

รายงานวิจัยฉบับสมบูรณ์

การสังเคราะห์วัสดุโครงสร้างนาโนเพื่อใช้เป็นตัวตรวจจับโฟตอน

Synthesis of nanostructured materials used for photonic sensors

โดย ศาสตราจารย์ ดร. สมชาย ทองเต็ม และคณะ

มิถุนายน 2558

สัญญาเลขที่ BRG5380020

รายงานวิจัยฉบับสมบูรณ์

การสังเคราะห์วัสดุโครงสร้างนาโนเพื่อใช้เป็นตัวตรวจจับโฟตอน

Synthesis of nanostructured materials used for photonic sensors

คณะผู้วิจัย

ศาสตราจารย์ ดร. สมชาย ทองเต็ม มหาวิทยาลัยเชียงใหม่

รองศาสตราจารย์ ธิติพันธุ์ ทองเต็ม มหาวิทยาลัยเชียงใหม่

ผู้ช่วยศาสตราจารย์ ดร. อนุกร ภู่เรืองรัตน์ มหาวิทยาลัยสงขลานครินทร์

อาจารย์ ดร. วัลย์ชัย พรมโนภาศ มหาวิทยาลัยเชียงใหม่

อาจารย์ ดร. สุลาวัลย์ ขาวผ่อง มหาวิทยาลัยเชียงใหม่

อาจารย์ ดร. เฉลิมชัย ปิละพงค์ มหาวิทยาลัยเชียงใหม่

อาจารย์ จุฑารัตน์ ก๋าวินจันทร์ มหาวิทยาลัยพะเยา

นางสาวหัสการ หอจงกล มหาวิทยาลัยเชียงใหม่

สนับสนุนโดยสำนักงานกองทุนสนับสนุนการวิจัย

และ

มหาวิทยาลัยเชียงใหม่

กิตติกรรมประกาศ

คณะผู้วิจัย ฯ ขอขอบคุณสำนักงานกองทุนสนับสนุนการวิจัย (ส.ก.ว.) กรุงเทพมหานคร และ มหาวิทยาลัยเชียงใหม่ ที่ได้ร่วมให้การสนับสนุนทุนวิจัยเป็นระยะเวลา 2 ปี

พร้อมกันนี้คณะผู้วิจัยขอขอบคุณ คณะวิทยาศาสตร์ มหาวิทยาลัยเชียงใหม่ ที่เอื้อเฟื้อสถานที่และครุภัณฑ์เพื่อการวิจัย รวมทั้งอำนวยความสะดวกต่าง ๆ ทำให้งานวิจัยนี้สำเร็จลุล่วงไปด้วยดี

(ศาสตราจารย์ ดร. สมชาย ทองเต็ม)
หัวหน้าโครงการวิจัย ฯ

บทคัดย่อ

ในงานวิจัยนี้ ได้สังเคราะห์ผลึก ZnO คล้ายดอกไม้, ZnO เข็มนาโนที่เจือด้วย Ce, $Nd(OH)_3$ และ Nd_2O_3 แท่งตันนาโน, $ZnMoO_4$ และ $La_2(MoO_4)_3$ ลักษณะรูปร่างต่าง ๆ, $CdMoO_4$, $PbMoO_4$ และ $PbWO_4$ อนุภาคนาโน, $MgWO_4$ และ $ZnWO_4$ อนุภาคนาโนที่เชื่อมต่อกันตามแนวแกนเส้นใย, วัสดุผสมนาโน Zn_2SnO_4-SnO_2, CdS โครงสร้างนาโนคล้ายต้นไม้ที่มีลำดับชั้น, ผลึกนาโนบริสุทธิ์ CdTe, Bi_2S_3 โครงสร้างนาโน และ Bi_2S_3 แท่งตันนาโนที่รวมกลุ่มกันคล้ายดอกไม้, อนุภาคนาโน $CuFeS_2$ และ $AgBiS_2$ และที่รวมกลุ่มกันคล้ายดอกไม้, โครงสร้างนาโน Cu_3BiS_3 ที่มีกิ่งก้าน, และ Cu_3SnS_4 อนุภาคนาโนและโครงสร้างนาโนคล้ายดอกไม้ โดยกระบวนการทางเคมีและฟิสิกส์ได้สำเร็จ ได้ศึกษาเฟสของผลึก ลักษณะรูปร่าง น้ำหนักที่ลดลง ทิศทางการเติบโตของผลึก การสั่นของอะตอม สถานะออกซิเดชัน สมบัติโฟตอนและการเร่งปฏิกิริยาเชิงแสงโดยใช้หลักการเปลี่ยนแปลงน้ำหนักตามความร้อน (TGA), เอ็กซ์เรย์ดิฟแฟรกชัน (XRD), การวิเคราะห์รามาน (Raman), ฟูเรียร์ทรานส์ฟอร์มอินฟราเรดสเปกโทรสโกปี (FTIR), จุลทรรศน์อิเล็กตรอนแบบส่องกราด (SEM) และการกระจายพลังงานรังสีเอกซ์ (EDX), จุลทรรศน์อิเล็กตรอนแบบส่องผ่าน (TEM), จุลทรรศน์อิเล็กตรอนแบบส่องผ่านที่มีการจำแนกสูง (HRTEM) และการเลือกพื้นที่การดิฟแฟรกชันของอิเล็กตรอน (SAED), จุลทรรศน์ที่สัมผัสด้วยแรงระดับอะตอม (AFM), การสร้างภาพด้วยโฟกัสไอออนบีม (FIB), เอ็กซ์เรย์โฟโตอิเล็กตรอนสเปกโทรสโกปี (XPS), สเปกโทรสโกปีของยูวีที่มองเห็นได้ และ สเปกโทรเมตรีการเปล่งแสง (PL) โดยพบว่ามีความสอดคล้องกับที่ได้จากการจำลอง นอกจากนี้ยังได้เสนอกลไกการเกิดวัสดุลักษณะรูปร่างต่าง ๆ ที่เป็นไปได้ตามผลทดลองที่เกิดขึ้นด้วย

คำหลัก: วัสดุนาโน; กระบวนการสังเคราะห์ทางเคมีและฟิสิกส์; เอ็กซ์เรย์ดิฟแฟรกชัน; จุลทรรศน์อิเล็กตรอน; สเปกโทรสโกปี; การเปล่งแสง; การเร่งปฏิกิริยาเชิงแสง

Abstract

In this research, flower-like ZnO crystals, Ce-doped ZnO nanoneedles, $Nd(OH)_3$ and Nd_2O_3 nanorods, $ZnMoO_4$ and $La_2(MoO_4)_3$ with different morphologies, $CdMoO_4$, $PbMoO_4$ and $PbWO_4$ nanoparticles, $MgWO_4$ and $ZnWO_4$ nanoparticles interconnecting along fibrous axes, Zn_2SnO_4-SnO_2 nanocomposites, hierarchical tree-like CdS nanostructure, purified CdTe nanocrystals, Bi_2S_3 nanostructures and Bi_2S_3 nanorods in flower-shaped bundles, $CuFeS_2$ and $AgBiS_2$ nanoparticles and flower-like clusters, nanostructure Cu_3BiS_3 dendrites, and Cu_3SnS_4 nanoparticles and nanostructured flowers were successfully synthesized by chemical and physical processes. Their crystalline phases, morphologies, weight losses, crystal growth directions, atomic vibration, oxidation states, photonic properties and photocatalysis were characterized by thermogravimetric analysis (TGA), X-ray diffraction (XRD), Raman spectroscopy, Fourier transform infrared (FTIR) spectroscopy, field emission scanning electron microscopy (FE-SEM) and energy dispersive X-ray (EDX) spectroscopy, transmission electron microscopy (TEM), high resolution transmission electron microscopy (HRTEM) and selected area electron diffraction (SAED), atomic force microscopy (AFM), focused ion beam (FIB) imaging, X-ray photoelectron spectroscopy (XPS), UV-visible spectroscopy and photoluminescence (PL) spectrometry, and were found to be in accordance with those of the simulation. Additionally, possible formation mechanisms were proposed according to the experimental results.

Keywords: Nanomaterials; Chemical and physical synthesis processes; X-ray diffraction; Electron microscopy; Spectroscopy; Photoluminescence; Photocatalysis

Executive Summary

ในงานวิจัยนี้ได้สังเคราะห์วัสดุโครงสร้างนาโนเพื่อใช้เป็นตัวตรวจจับโฟตอน และเร่งปฏิกิริยาเชิงแสงได้สำเร็จ จากนั้นศึกษาเฟสของผลึกโครงสร้างนาโน ระนาบผลึก ทิศทางการเติบโตและการกระจายขนาดผลึกนาโน แบบการสั่นของอะตอมในผลึก การเปล่งแสงและการดูดกลืนแสงยูวีมองเห็นได้ เพื่อหาช่องว่างพลังงานของผลผลิตที่สังเคราะห์ได้ รวมทั้งเสนอกลไกการเกิดผลผลิตที่มีลักษณะรูปร่างต่าง ๆ ในการวิจัยนี้ได้ตีพิมพ์เผยแพร่ผลงานวิจัยในฐานข้อมูล ISI, Sciencedirect และอื่น ๆ จำนวน 33 เรื่อง สร้างต้นแบบผลิตภัณฑ์จำนวน 2 ผลงาน อันประกอบด้วยอุปกรณ์สังเคราะห์วัสดุโดยให้อิเล็กตรอนไหลผ่านของแข็งโดยตรง และอุปกรณ์ชักใยด้วยไฟฟ้า (electrospinning equipment) ผลิตนักวิจัย/นักศึกษาระดับหลังปริญญาเอก ปริญญาเอก และ ปริญญาโท จำนวน 2, 4 และ 7 คน ตามลำดับ รวมทั้งได้รับรางวัลระดับต่าง ๆ มากกว่า 15 รางวัล

สารบัญ

กิตติกรรมประกาศ	**ii**
บทคัดย่อ	**iii**
Abstract	**iv**
Executive Summary	**v**
บทนำ	**1**
1. Characterization of ZnO flowers of hexagonal prisms with planar and hexagonal pyramid tips grown on Zn substrates by a hydrothermal process	2
2. Sonochemical synthesis, photocatalysis and photonic properties of 3 % Ce-doped ZnO nanoneedles	18
3. Template-free synthesis of neodymium hydroxide nanorods by microwave-assisted hydrothermal process, and of neodymium oxide nanorods by thermal decomposition	30
4. Effect of medium solvent ratios on morphologies and optical properties of α-$ZnMoO_4$, β-$ZnMoO_4$ and $ZnMoO_4 \cdot 0.8H_2O$ crystals synthesized by microwave-hydrothermal / solvothermal method	41
5. Microwave-assisted synthesis and optical property of $CdMoO_4$ nanoparticles	61
6. Effects of solution pH and processing cycle on nanostructured $La_2(MoO_4)_3$ produced by cyclic microwave radiation	75
7. Analysis of lead molybdate and lead tungstate synthesized by a sonochemical method	86
8. Photoemission and energy gap of $MgWO_4$ particles connecting as nanofibers synthesized by electrospinning-calcination combinations	95
9. Fabrication of $ZnWO_4$ nanofibers by a high direct voltage electrospinning process	108

10. Photocatalytic activity of Zn_2SnO_4-SnO_2 nanocomposites produced by sonochemistry in combination with high temperature calcination	129
11. Characterization and photonic absorption of hierarchical tree-like CdS nanostructure synthesized by solvothermal method	147
12. Characterization of nanostructured CdTe synthesized by solid state microwave-plasma process	154
13. Controlling morphologies of Bi_2S_3 nanostructures synthesized by glycolthermal method	164
14. Microwave-assisted hydrothermal synthesis of Bi_2S_3 nanorods in flower-shaped bundles	172
15. Cyclic microwave-assisted synthesis of $CuFeS_2$ nanoparticles using biomolecules as sources of sulfur and complexing agent	184
16. Transformation of cubic $AgBiS_2$ from nanoparticles to nanostructured flowers by a microwave-refluxing method	193
17. Cyclic microwave-assisted synthesis of Cu_3BiS_3 dendrites using L-cysteine as a sulfur source and complexing agent	204
18. Characterization of Cu_3SnS_4 nanoparticles and nanostructured flowers synthesized by a microwave-refluxing method	212
Output ที่ได้จากโครงการวิจัย	**228**
List of publications	**229**
ต้นแบบผลิตภัณฑ์ที่สร้างขึ้น	**234**
รายละเอียดผลงานวิจัยที่เผยแพร่ในวารสารวิชาการต่าง ๆ	**236**

บทนำ

ในปัจจุบัน การวิจัยวัสดุโครงสร้างนาโนกำลังเป็นที่สนใจกันมากทั้งในประเทศ และระดับนานาชาติ สำหรับประเทศไทยได้มีการนำเข้าวัสดุดังกล่าวจากต่างประเทศปีละเป็นจำนวนมากทั้งในลักษณะที่เป็นวัตถุดิบและสำเร็จรูป วัสดุต่าง ๆ เหล่านี้มีสมบัติกึ่งตัวนำที่มีความสำคัญทั้งในทางการค้าและอุตสาหกรรมเป็นอย่างมาก เช่น light emitting diodes (LEDs), solar cells, flat panel displays, photocatalysis และวัสดุกึ่งตัวนำอื่น ๆ ในงานวิจัยนี้สามารถสังเคราะห์วัสดุดังกล่าวให้มีลักษณะรูปร่างต่าง ๆ โดยกระบวนการทางเคมีและฟิสิกส์ได้สำเร็จ วัสดุเหล่านี้มีโครงสร้างระดับนาโน มีขนาดและลักษณะรูปร่างที่แตกต่างกัน ทำให้มีสมบัติทางเคมีและฟิสิกส์ที่แตกต่างกัน และย่อมแสดงสมบัติที่แตกต่างไปจากวัสดุที่เป็นก้อน การมีขนาดและลักษณะรูปร่างที่แตกต่างกันนี้ขึ้นอยู่กับ กระบวนการสังเคราะห์ สภาวะที่ใช้สังเคราะห์ และอื่น ๆ ในงานวิจัยนี้ได้สังเคราะห์วัสดุบริสุทธิ์ที่มีรูปร่างต่าง ๆ กัน มีสมบัติเปล่งแสง การเร่งปฏิกิริยาเชิงแสง และอื่น ๆ ได้สำเร็จ สามารถนำไปใช้ประโยชน์ต่าง ๆ ได้อย่างมีประสิทธิภาพ เพื่อเป็นการต่อยอดไปสู่ระดับการค้าและอุตสาหกรรมในประเทศ ลดการนำเข้าจากต่างประเทศ มีความสอดคล้องกับปรัชญาเศรษฐกิจพอเพียง ได้เผยแพร่ผลงานวิจัยในวารสารวิชาการระดับนานาชาติในฐานข้อมูลต่าง ๆ และสร้างต้นแบบผลิตภัณฑ์ เพื่อการศึกษาและวิจัยทางวิทยาศาสตร์ในอนาคต ได้ผลิตนักวิจัย/นักวิชาการระดับหลังปริญญาเอก ปริญญาเอก และปริญญาโท เพื่อให้มาตรฐานการศึกษาของมหาวิทยาลัยในประเทศไทยอยู่ในระดับที่สูงขึ้น ทั้งนี้ได้ดำเนินการวิจัยโดยมีรายละเอียดดังต่อไปนี้

1. Characterization of ZnO flowers of hexagonal prisms with planar and hexagonal pyramid tips grown on Zn substrates by a hydrothermal process

Abstract

Flower-like ZnO crystals on zinc substrates were synthesized by a simple hydrothermal method in different solutions containing 0.05, 0.10, 0.20, 0.30 and 0.40 g LiOH. X-ray diffraction (XRD), Fourier transform infrared (FTIR) spectroscopy, scanning electron microscopy (SEM), transmission electron microscopy (TEM) and selected area electron diffraction (SAED) showed that the products were wurtzite hexagonal ZnO flowers, composed of single crystalline hexagonal prisms grown along the [0001] direction with planar and hexagonal pyramid tips, including the Zn–O stretching vibration at 411.5 cm^{-1}. Photoluminescence (PL), excited by a 215 nm wavelength at room temperature, exhibited strong green emission at 543 nm.

Keywords: ZnO flower-like structure; Hexagonal prisms; Hydrothermal method

Introduction

Since the discovery of carbon nanotubes by Iijima in 1991, one dimensional (1D) nanomaterials, such as nanowires, nanotubes, nanorods and nanoribbons are very attractive for a number of worldwide researchers due to their unique physical, chemical and electron-transport properties, which are different from those of their corresponding bulks. They have widely potential applications in devices and interconnected integration in nanoelectronics and molecular electronics [1–4]. Zinc oxide with a 3.37 eV direct band gap and a 60 meV large exciton binding energy is an important semiconducting and piezoelectric material, which has novel photoelectric and electronic properties as well as its promising functionalities: catalytic, electric, optoelectronic and piezoelectric properties, solar cells, lasers and other nanodevices [2,5–8]. Thus considerable efforts have been directed towards the production of well-aligned 1D nanostructured ZnO on substrates

with specific optoelectronic and field-emission characteristics. These 1D nanorods were densely populated materials, and promoted rapid and effective diffusion of electrons through them for lasers and solar cells [9].

Physical and chemical methods such as vapor-phase approaches including pulsed laser deposition (PLD) [10], thermal evaporation [11–13] and chemical vapor deposition (CVD) [14,15] were used to synthesize the 1D metal oxide nanostructures deposited on substrates. These methods require high temperature and low pressure which are generally complex and expensive. Recently, hydrothermal route has been developed to synthesize ordered metal oxide nanostructures on substrates: ZnO [2,5,8], TiO_2 [16,17], Fe_3O_4 [18], CuO [19,20] and SnO_2 [21,22], by low temperature processing for controlling morphologies and phases and for scaling up production for commercial possibilities.

In this research, flower-like clusters of ZnO hexagonal prisms with planar and hexagonal pyramid tips were synthesized on zinc substrates by a hydrothermal method. The room temperature photoluminescence (PL) spectra of the flower-like ZnO nanostructures exhibited the sharp strong green emissions, which supports high potential optical applications.

Experimental procedure

All chemicals for this research were analytical grade and used without further purification. The ZnO hexagonal prisms with planar and hexagonal pyramid tips were fabricated on Zn substrates by a hydrothermal process at relatively low temperature. Test coupons of 15×15×0.25 mm Zn foils as Zn source and substrates were carefully cleaned in an ultrasound bath containing deionized water and alcohol. The test coupons in the 20 ml aqueous solutions containing 0.05, 0.10, 0.20, 0.30 and 0.40 g LiOH as OH^- source were hydrothermally processed in 30 ml Teflon-lined stainless steel autoclaves at 120 ^{o}C for 1–24 h in an electric oven and cooled them down to room temperature. In the end, the coupons were thoroughly rinsed by deionized water several times and ethanol,

dried in an electric oven at 70 ^{o}C under its atmospheric chamber for further characterization.

Crystalline phases and degree of the as-synthesized nanostructured samples were analyzed by X-ray diffractometer (XRD, Philips X'Pert MPD) operating at 20 kV 15 mA and using Cu-K_{α} line in 2θ of 20–60 deg. The morphology investigation was carried out by field emission scanning electron microscope (FE-SEM, JEOL JSM-6335F) operating at 35 kV, including transmission electron microscope (TEM, JEOL JEM-2010) and selected area electron diffractometer (SAED) operating at 200 kV. Fourier transform infrared (FTIR, Bruker Tensor 27) spectrometer was carried out in the range of 400–1,200 cm^{-1} at room temperature. The ZnO pellets with 1 cm in diameter for FTIR testing were prepared by 40 times dilution with KBr and pressed by 10 Torr pressure. Their optical properties were studied by a spectrophotometer (LS50B Perkin Elmer) using 215 nm excitation wavelength at room temperature.

Results and discussion

Crystal structure and phase of the as-synthesized ZnO grown on Zn substrates were characterized by XRD, as shown by the XRD patterns of Fig. 1. The XRD patterns corresponded with the (100), (002), (101), (102) and (110) planes at 2θ = 31.77, 34.45, 36.30, 47.53 and 56.06 deg for wurtzite hexagonal ZnO structure of the JCPDS no 36-1451, and the (100) (101) and (102) planes at 2θ = 39.03, 43.26 and 54.33 deg for hexagonal Zn structure of the JCPDS no 04-0831 [23]. No other characteristic peaks of impurities were detected in these samples. The spectra are very sharp, implying the high crystalline degree of the as-synthesized ZnO phase on Zn substrates. It should be noted that the relatively strong intensity peaks reflected and diffracted from the (101) and (002) crystallographic planes of wurtzite hexagonal ZnO phase. Possibly, these ZnO unit cells preferentially grew along the [101] and [002] directions, in accordance with the XRD pattern reported by Pei et al [24].

FTIR spectrum (Fig. 2) of the as-synthesized ZnO was recorded over the range of 400–1,200 cm^{-1}. The main absorbance appeared at 411.5 cm^{-1} corresponding to the Zn–O stretching vibration of tetrahedral units [25], each of which was composed of four oxygen atoms with one zinc atom inside.

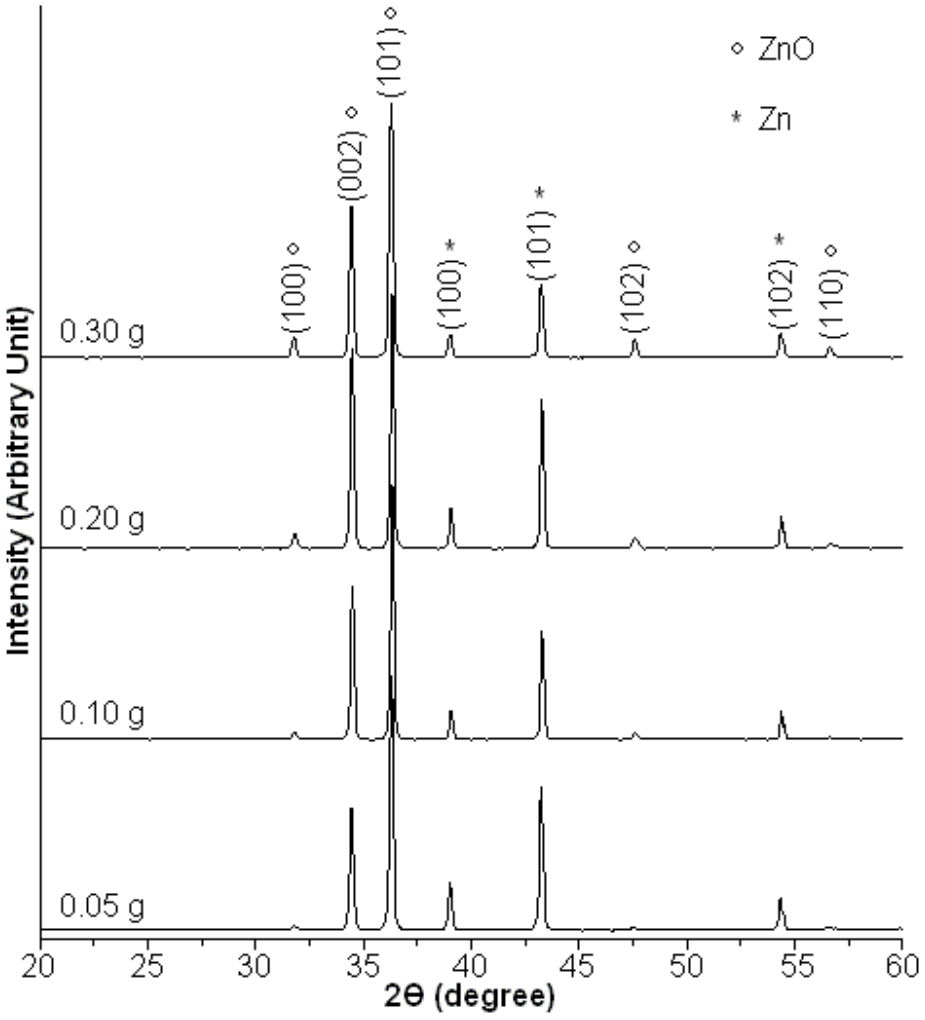


Fig. 1 XRD patterns of the as-synthesized ZnO phase on Zn substrates, hydrothermally synthesized in the solutions containing different contents of LiOH for 24 h.

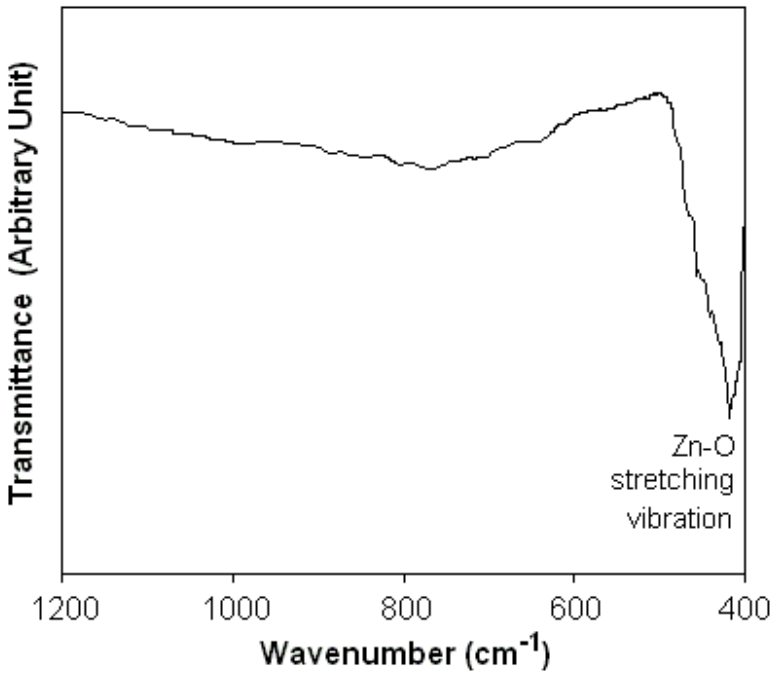


Fig. 2 FTIR spectrum of ZnO hydrothermally synthesized in the solution containing 0.30 g LiOH for 24 h.

SEM images (Fig. 3) show the ZnO solid grown on Zn substrates by hydrothermal synthesis of the solution containing 0.10 g LiOH at 120 ^{o}C for different lengths of time. For 1 h, ZnO nanorod arrays were synthesized and uniformly covered the entire surface of zinc substrate. When the time was lengthened to 6 h, the ZnO solid was densely oriented hexagonal nanorods in large-scale uniform arrays with 50 nm in diameter grown on the Zn surface. By prolonging the reaction time to 18 h and 24 h, flower-like clusters of hexagonal prisms grown out of ZnO flower cores were more obviously detected. The ZnO individual hexagonal prism has 100 nm in diameter and 1–2 μm in length. High magnification SEM image (inserted in Fig. 3d) presents ZnO crystal shaped like a hexagonal prism with angles between the two adjacent edges of 120 deg. Each of them has planar tip on top. Obviously, the elongation of these crystals was the result of anisotropic growth of different crystal faces. The hexagonally prismatic shaped ZnO crystals originated by an axial growth of the hexagon normal to the (0001)

crystallographic planes and directed along the c-axis of symmetry, including equatorial growth normal to the {10$\bar{1}$0} family planes and radially pointed out of the c-axis [26,27]. Alternately, the individual ZnO hexagonal prism is surrounded by six ±(10$\bar{1}$0), ±(1$\bar{1}$00) and ±(01$\bar{1}$0) prism planes with the acceleration of typical growth along the [0001] direction, leading to the formation of ZnO hexagonal prisms [26,28–30]. The solids appeared as high aspect ratio of hexagonal nanorods, identifying that the axial growth rate is faster than the equatorial growth rate [26].

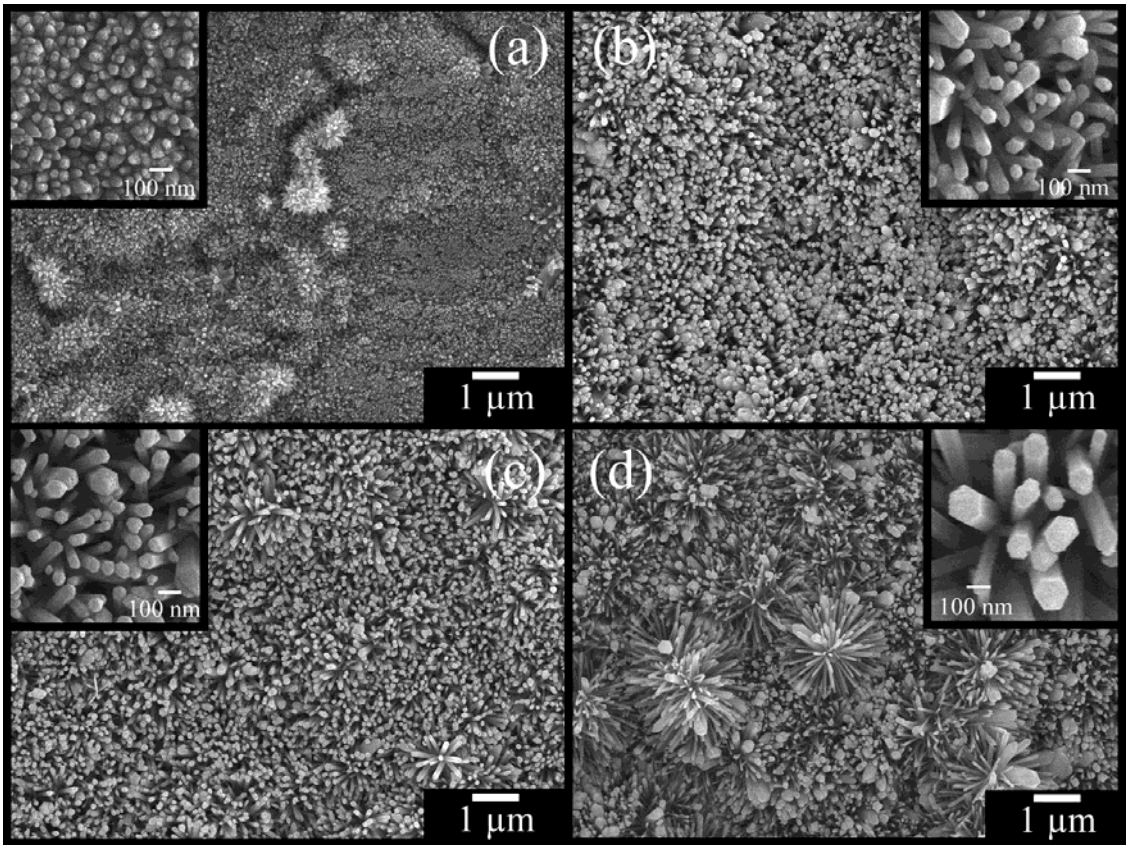


Fig. 3 SEM images of ZnO hydrothermally synthesized in the solution containing 0.10 g LiOH at 120 ^{o}C for (a-d) 1, 6, 18 and 24 h, respectively. High magnification images are shown as the insets.

Fig. 4 shows morphology development of the as-synthesized ZnO solids grown on Zn substrates by the 120 °C and 24 h hydrothermal reaction of the solutions containing different contents of LiOH. Clearly, the substrate was densely covered with ZnO hexagonal prisms of nanorods in the solution containing 0.05 g LiOH. The ZnO nanorod arrays were about 1 μm long and 200 nm in diameters on average. At the current stage, ZnO flower-like clusters of nanorods shaped of hexagonal prism grown out of the ZnO cores were also detected on some areas of the substrate.

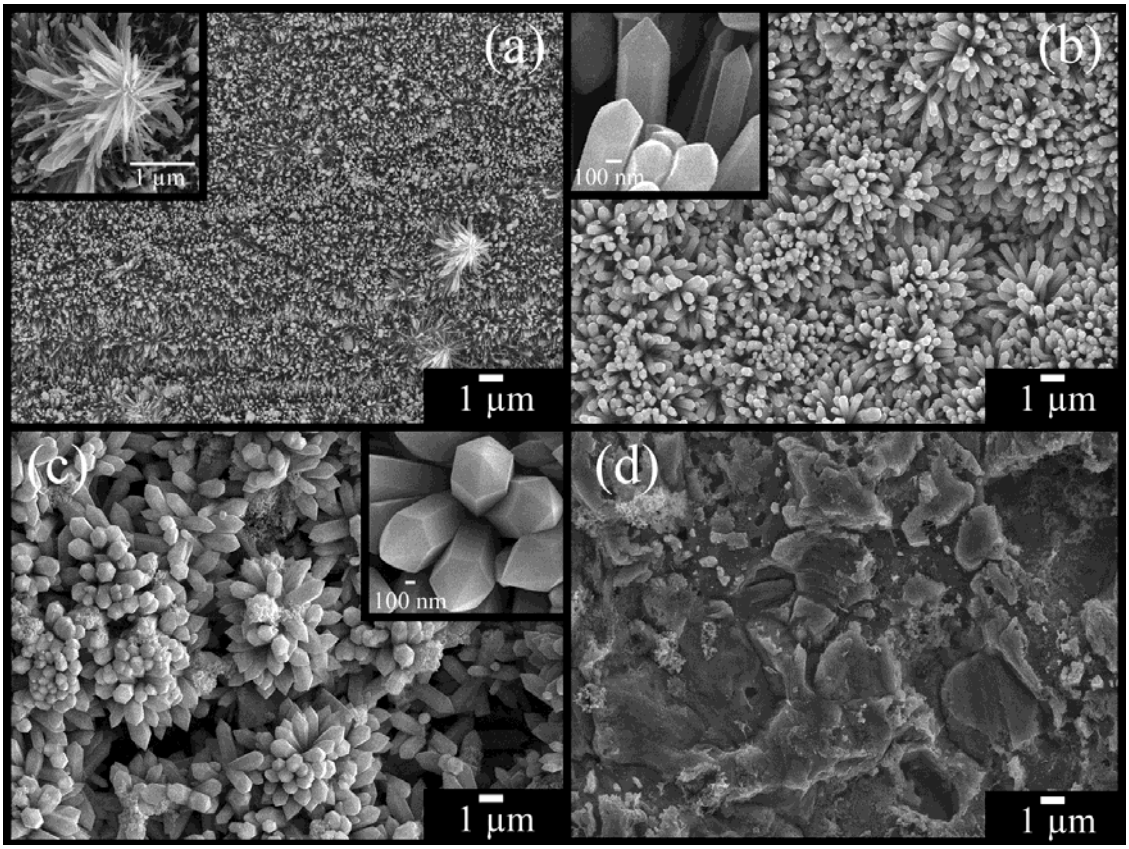


Fig. 4 SEM images of ZnO hydrothermally synthesized in the solutions containing (a-d) 0.05, 0.20, 0.30 and 0.40 g LiOH at 120 °C for 24 h, respectively. High magnification images are shown as the insets.

Upon increasing the contents of LiOH from 0.05 g to 0.20 g and 0.30 g, the Zn substrates were fully covered with flower-like clusters of ZnO prisms. The top-view of these images was enlarged. They (inserted in Fig. 4b and c) appeared as ZnO hexagonal prisms of nanorods. These images indicated that an individual ZnO nanorod exhibits an obvious hexagonal prism with hexagonal pyramid-like sharp tip of well-defined crystallographic faces, pointing in different directions like a petal of flowers. In 0.40 g LiOH solution, the flower-like clusters were no longer synthesized and the Zn substrate was covered with irregular shape of ZnO agglomerates.

Further structural characterization of the ZnO flower-like hexagonal prism arrays with hexagonal pyramid sharp tips grown on the zinc substrates was studied by TEM. Typical TEM images (Fig. 5a and b) of ZnO hexagonal prisms with hexagonal pyramid sharp tips broken from a ZnO flower of hexagonal prisms present the assembly of several well-aligned nanorods with sharp tips, with their approximate lengths of 600 nm. Their diameters were 80 nm uniform along the entire lengths with very smooth surfaces. SAED pattern (Fig. 5c) of a single ZnO petal appeared as systematic bright spots, suggesting that the nanorod was single crystal. The pattern was identified as the [$\bar{1}$10] electron beam projection on the ZnO petal [31]. The simulated pattern (Fig. 5d) [32] with a*, b* and c* lattice vectors in the [100], [010] and [001] directions are in systematic arrays, and in good accordance with the result obtained by current interpretation. Thus the product was really proved to be wurtzite ZnO, with the preferential growth of the ZnO nanorod along the [0001] direction [26,28,29]. To understand the characteristics of ZnO, it is necessary to study its growth mechanism. Wurtzite structured zinc oxide belongs to the P63mc space group with highly anisotropic structure along the c-axis. The (0001) plane terminated with Zn and the (000$\bar{1}$) plane with O. ZnO nanorods were easily synthesized by the nucleation and growth processes of the alternative arrangement of Zn and O atoms along the most favorable [0001] direction [26,33].

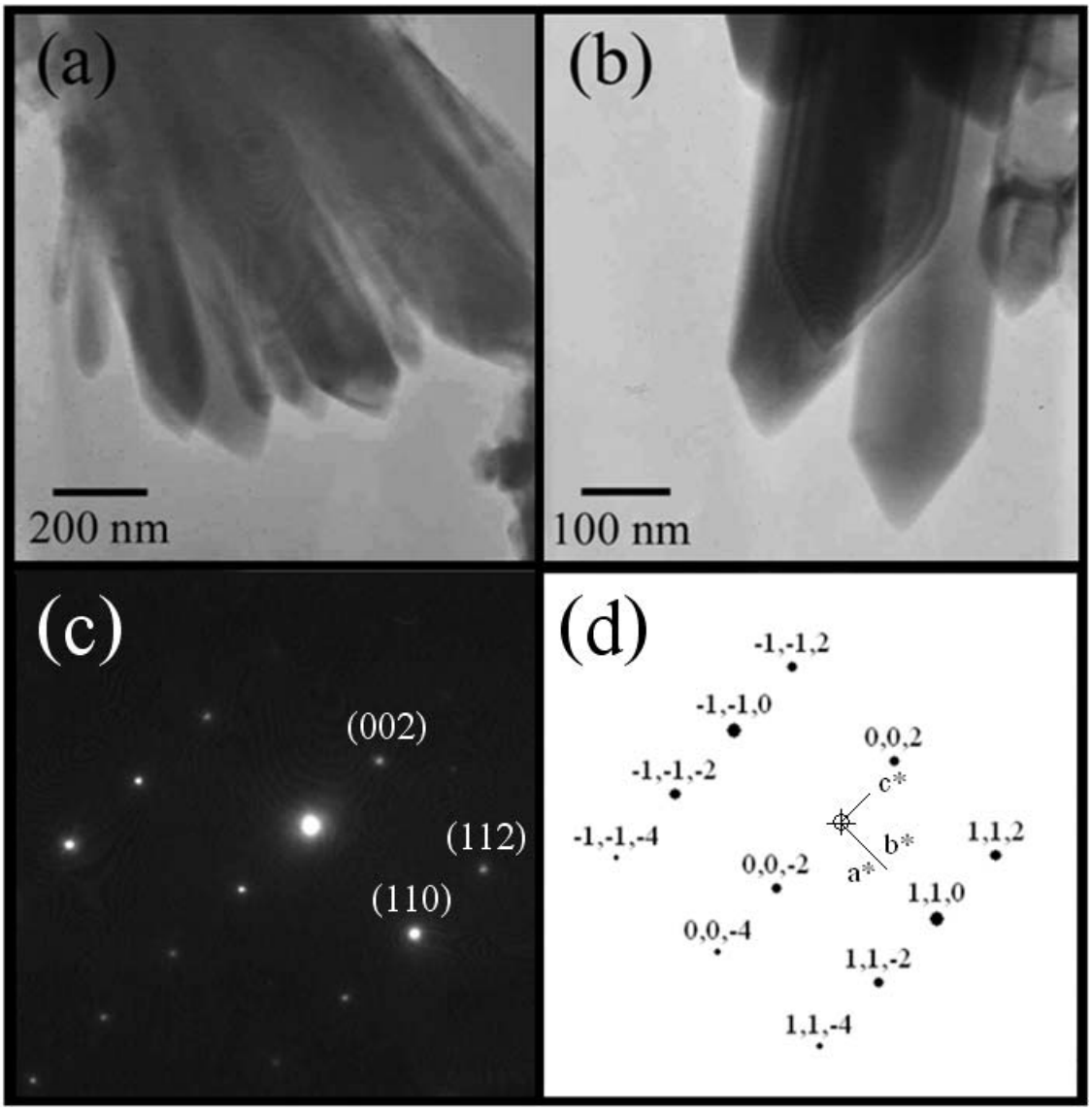


Fig. 5 (a, b) TEM images and (c) SAED pattern of hexagonal pyramid ZnO nanorods hydrothermally synthesized in the solution containing 0.30 g LiOH at 120 ^{o}C for 24 h, and (d) the simulation pattern of (c).

Fig. 6 shows a schematic diagram for a possible growth mechanism of ZnO hexagonal prisms with planar and hexagonal pyramid tips on Zn substrates. In a typical alkaline solution of synthetic approach, $[Zn(OH)_4]^{2-}$ served as basic growth units for the

formation of ZnO nuclei. In the present hydrothermal condition, Zn dissolved in the solution to form Zn^{2+} ions, which were further reacted with OH^- ions of LiOH to form $[Zn(OH)_4]^{2-}$. Subsequently, these $[Zn(OH)_4]^{2-}$ ions decomposed. ZnO molecular species were produced and nucleated as ZnO nuclei on Zn substrates. These ZnO nuclei grew to form hexagonal nanorod seeds. The hexagonal wurtzite ZnO with polar structure is hexagonal close packing of oxygen and zinc atoms in 3m point group and P63mc space group with zinc atoms in tetrahedral sites. Thus, the crystal characteristics of wurtzite ZnO exhibit well defined crystallographic faces: (0001) base and nonpolar low symmetry ($10\bar{1}0$) faces, with C_{6v} symmetry. In case of wurtzite ZnO polar crystal, each Zn^{2+} ion lies inside a tetrahedron of four oxygen ions. The Zn and O atoms are arranged alternatively along the c-axis such that the top face is the Zn-terminated (0001) plane and the bottom one the O-terminated ($000\bar{1}$) plane. The inherent asymmetry along the c-axis leads to the anisotropic growth of 1-D ZnO crystallites. The formation of hexagonal prisms in the present study was attributed to the difference in growth rates of different crystal faces. The hydrothermal growth rates of different planes are as follows: (0001) > ($10\bar{1}1$) > ($10\bar{1}0$). The more rapid of the plane grows, the faster of its disappearance becomes. Therefore, the relative growth rate of these crystalline faces was determined the aspect ratio and final shape of the ZnO nanorods. The (0001) plane disappeared due to its most rapid growth rate leading to the sharp tip at the end of the c axis. Growth rate of the ($10\bar{1}0$) plane was at the slowest, therefore, the solids remained to form hexagonal prisms with planar tips at lower pH (0.05 and 0.10 g LiOH), but the ($10\bar{1}1$) plane remain to form hexagonal pyramid-like tips. However, the polar (0001) face is metastable and subjected to be etched at higher pH (0.20 and 0.30 g LiOH). Possibly, Zn atoms of the (0001) metastable polar face reacted with the OH^- ions, forming hydroxide species. The side faces of hexagonal prisms on the six ±[$10\bar{1}0$], ± [$1\bar{1}00$] and ± [$01\bar{1}0$] symmetric directions were etched, remaining as hexagonal pyramid-like tips. Thus the one-dimensional growth continued to form hexagonal pyramid tips on top of ZnO nanorods [34,35].

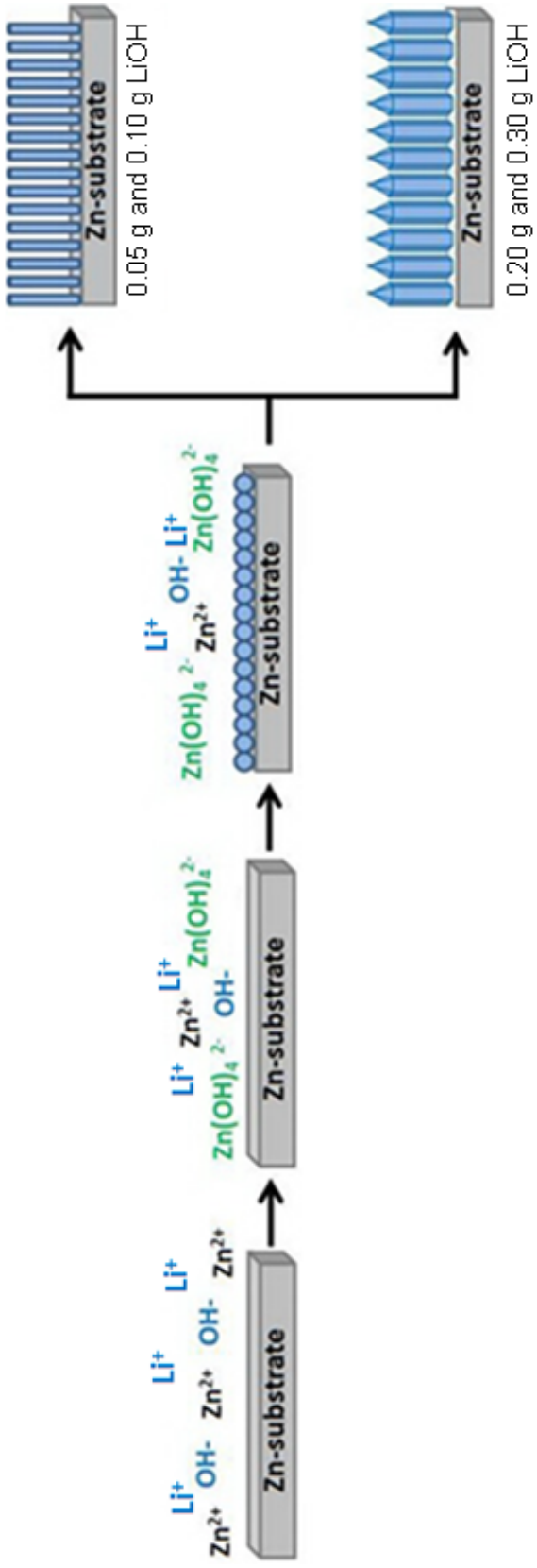


Fig. 6 Schematic diagram for a possible growth mechanism of ZnO hexagonal prisms with planar and hexagonal pyramid tips on Zn substrates.

The photoluminescence (PL) of ZnO was studied for its photonic applications. PL spectra (Fig. 7) of ZnO solids show the emission broad band at 505-625 nm in the visible range. They have the same strong green emission centered at 543 nm relating to different intrinsic defects originated during ZnO synthesis, but the exact mechanism is still ambiguous. There have been different proposed models to explain the emission from defects in ZnO crystal. The green emission at 542 nm originated from deep level associated with oxygen vacancies on outside walls of the ZnO nanorods [36,37]. Contrarily, the green emissions at 487 nm and 516 nm were believed to relate with oxygen vacancies, and the green-yellow emission at 574 nm to relate with oxygen vacancies [38]. In general, oxygen anions are so large that they are not able to reside in the interstitial sites of the ZnO solid synthesized by the 120 ^{o}C and 24 h hydrothermal method. The yellow-green emission at 573 nm is also known to be the presence of OH^{-} groups on the surface of ZnO nanorods, which were reduced by annealing the ZnO nanorods in oxygen atmosphere [39].

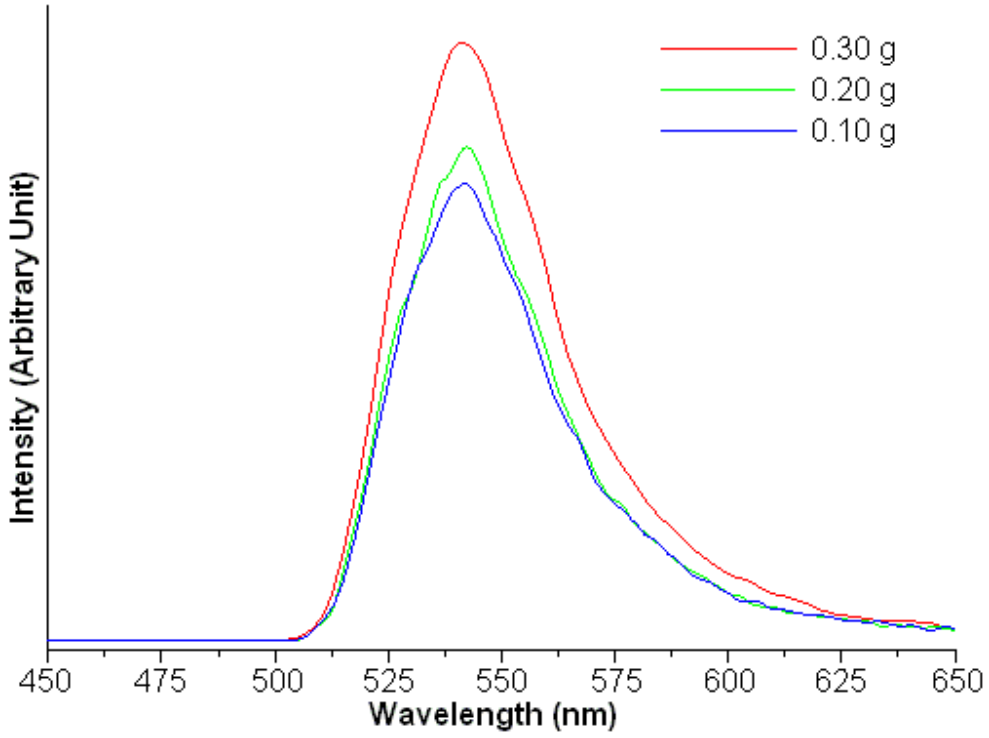


Fig. 7 PL spectra of ZnO hydrothermally synthesized in the solutions containing 0.10 g, 0.20 g and 0.30 g of LiOH for 24 h.

Conclusions

Wurtzite ZnO solids were successfully synthesized on zinc substrates by a simple hydrothermal method at 120 ^{o}C for 24 h using 0.05–0.40 g LiOH. The phase, morphology and photoluminescence were characterized by X-ray diffraction, electron microscopy and spectrophotometry. In this research, the products were hexagonal wurtzite ZnO structure with the as-grown flower-like clusters composed of hexagonal prisms with planar and hexagonal pyramid tips on Zn substrates grown along the [0001] direction. Photoluminescence spectra exhibited strong green emission at 543 nm due to the presence of oxygen vacancies in the solid.

References

[1] S. Iijima, Helical microtubules of graphitic carbon, Nature 354 (1991) 56–58.

[2] Z. Li, X. Huang, J. Liu, Y. Li and G. Li, Morphology control and transition of ZnO nanorod arrays by a simple hydrothermal method, Mater. Lett. 62 (2008) 1503–1506.

[3] A. Phuruangrat, T. Thongtem and S. Thongtem, Characterisation of one-dimensional CdS nanorods synthesised by solvothermal method, J. Experiment. Nanosci. 4 (2009) 47–54.

[4] T. Thongtem, C. Pilapong, J. Kavinchan, A. Phuruangrat and S. Thongtem, Microwave-assisted hydrothermal synthesis of Bi_2S_3 nanorods in flower-shaped bundles, J. Alloys Compd. 500 (2010) 195–199.

[5] C. Jia, X. Zhang, Y. Chen, Y. Su, Q. Zhou, M. Xin, Y. Lv and W. Kong, Liquid phase epitaxial growth and optical property of flower-like ZnO nanosheets on zinc foil, Appl. Surf. Sci. 254 (2008) 2331–2335.

[6] T. Thongtem, A. Phuruangrat and S. Thongtem, Characterization of nanostructured ZnO produced by microwave irradiation, Ceram. Int. 36 (2010) 257–262.

[7] A. Phuruangrat, T. Thongtem and S. Thongtem, Microwave-assisted synthesis of ZnO nanostructure flowers, Mater. Lett. 63 (2009) 1224–1226.

[8] Y. Tak and K. Yong, Controlled growth of well-aligned ZnO nanorod array using a novel solution method, J. Phys. Chem. B 109 (2005) 19263–19269.

[9] Z. Yang, C. Luan, W. Zhang, A. Liu and S. Tang, Fabrication and optical properties of ZnO nanostructured thin films via mechanical oscillation and hydrothermal method, Thin Solid Films 516 (2008) 5974–5980.

[10] K.A. Jeon, J.H. Kim and S.Y. Lee, Simple method for synthesis of silicon nanowire: pulsed laser deposition in furnace from p-Si wafer target, Prog. Solid State Chem. 33 (2005) 107–112.

[11] W. Lee, M.C. Jeong and J.M. Myoung, Catalyst-free growth of ZnO nanowires by metal-organic chemical vapour deposition (MOCVD) and thermal evaporation, Acta Mater. 52 (2004) 3949–3957.

[12] J.M. Wu, H.C. Shih, W.T. Wu, Y.K. Tseng, I.C. Chen, Thermal evaporation growth and the luminescence property of TiO_2 nanowires, J. Cryst. Growth 281 (2005) 384–390.

[13] S. Park, C. Hong, J. Kang, N. Cho and C. Lee, Growth of SnO_2 nanowires by thermal evaporation on Au-coated Si substrates, Curr. Appl. Phys. 9 (2009) S230–S233.

[14] F. Yu, D. Tang, K. Hai, Z. Luo, Y. Chen, X. He, Y. Peng, H. Yuan, D. Zhao and Y. Yang, Fabrication of SnO_2 one-dimensional nanosturctures with graded diameters by chemical vapor deposition method, J. Cryst. Growth 312 (2010) 220–225.

[15] R.R. Prabhakar, B. Varghese, W. Yuzhan, G. Xingyu and C.H. Sow, Carbon coated Nb_2O_5 nanowires as enhanced field emitters, Chem. Phys. Lett. 501 (2011) 431–436.

[16] F.D. Mai, W.L.W. Lee, J.L. Chang, S.C. Liu, C.W. Wu and C.C. Chen, Fabrication of porous TiO_2 film on Ti foil by hydrothermal process and its photocatalytic efficiency and mechanisms with ethyl violet dye, J. Hazard. Mater. 177 (2010) 864–875.

[17] Y. Su, S. Chen, N. Ma, X. Quan and H. Zhao, Photoelectrochemical characterization and application of direct-grown nanostructured anatase film via hydrothermal reactions, Separat. Purificat. Technol. 68 (2009) 255–260.

[18] J. Chen, K. Huang and S. Liu, Hydrothermal preparation of a protective Fe_3O_4 film on Fe foil, Corr. Sci. 50 (2008) 1982–1986.

[19] Z.A. Jiang, J.T. Chen, J. Wang, R.F. Zhuo, D. Yan, F. Zhang and P.X. Yan, CuO nanosheets synthesized by hydrothermal process, Chin. Phys. Lett. 26 (2009) 086202.

[20] Y. Liu, Y. Chu, M. Li, L. Li and L. Dong, In situ synthesis and assembly of copper oxide nanocrystals on copper foil via a mild hydrothermal process, J. Mater. Chem. 16 (2006) 192–198.

[21] Q. Zhao, Z. Li, C. Wu, X. Bai and Y. Xie, Facile synthesis and optical property of SnO_2 flower-like architectures, J. Nanopart. Res. 8 (2006) 1065–1069.

[22] H.T. Chen, X.L. Wu, Y.Y. Zhang, J. Zhu, Y.C. Cheng and P.K. Chu, A novel hydrothermal route to synthesize solid SnO_2 nanospheres and their photoluminescence property, Appl. Phys. A 97 (2009) 581–585.

[23] Powder Diffract. File, JCPDS-ICDD, 12 Campus Boulevard, Newtown Square, PA 19073-3273, U.S.A., 2001.

[24] L.Z. Pei, H.S. Zhao, W. Tan, H.Y. Yu, Y.W. Chen, C.G. Fan and Q.F. Zhang, Hydrothermal oxidization preparation of ZnO nanorods on zinc substrate, Physica E 42 (2010) 1333–1337.

[25] S.K. Nandi, S. Chakraborty, M.K. Bera and C.K. Maiti, Structural and optical properties of ZnO films grown on silicon and their applications in MOS devices in conjunction with ZrO_2 as a gate dielectric, Bull. Mater. Sci. 30 (2007) 247–254.

[26] S.P. Garcia and S. Semancik, Controlling the morphology of zinc oxide nanorods crystallized from aqueous solutions: the effect of crystal growth modifiers on aspect ratio, Chem. Mater. 19 (2007) 4016–4022.

[27] C.X. Xu, G.P. Zhu, J. Kasim, S.T. Tan, Y. Yang, X. Li, Z.X. Shen and X.W. Sun, Spatial distribution of defect in ZnO nanodisks, Curr. Appl. Phys. 9 (2009) 573–576.

[28] C.X. Xu, X.W. Sun, Z.L. Dong and M.B. Yu, Zinc oxide nanodisk, Appl. Phys. Lett. 85 (2004) 3878–3880.

[29] M. Wang, S.H. Hahn, J.S. Kim, J.S. Chung, E.J. Kim and K.K. Koo, Solvent-controlled crystallization of zinc oxide nano(micro)disks, J. Cryst. Growth 310 (2008) 1213–1219.

[30] D. Chu, Y. Zeng and D. Jiang, Controlled growth and properties of Pb^{2+} doped ZnO nanodisks, Mater. Res. Bull. 42 (2007) 814–819.

[31] S. Jattukul, S. Thongtem and T. Thongtem, Morphology development of ZnO produced by sonothermal process, Ceram. Int. 37 (2011) 2055–2059.

[32] C. Boudias and D. Monceau, CaRIne Crystallography 3.1, DIVERGENT S.A., Centre de Transfert, 60200 Compiègne, France, 1989–1998.

[33] W. Peng, S. Qu, G. Cong and Z. Wang, Synthesis and structures of morphology-controlled ZnO nano- and microcrystals, Cryst. Growth Des. 6 (2006) 1518–1522.

[34] J.H. Yang, J.H. Zheng, H.J. Zhai, L.L. Yang, L. Liu and M. Gao, Solvothermal growth of highly oriented wurtzite-structured ZnO nanotube arrays on zinc foil, Cryst. Res. Technol. 44 (2009) 619–623.

[35] D. Wang and C. Song, Controllable synthesis of ZnO nanorod and prism arrays in a large area, J. Phys. Chem. B 109 (2005) 12697–12700.

[36] H. Zhang, J. Feng, J. Wang and M. Zhang, Preparation of ZnO nanorods through wet chemical method, Mater. Lett. 61 (2007) 5202–5205.

[37] H. Gao, G. Fang, M. Wang, N. Liu, L. Yuan, C. Li, L. Ai, J. Zhang, C. Zhou, S. Wu and X. Zhao, The effect of growth conditions on the properties of ZnO nanorod dye-sensitized solar cells, Mater. Res. Bull. 43 (2008) 3345–3351.

[38] X. Wang, K. Huo, F. Zhang, Z. Hu, P.K. Chu, H. Tao, Q. Wu, Y. Hu and J. Zhu, Structural regulation and optical properties of one-dimensional ZnO nanomaterials in situ grown from and on brass substrates, J. Phys. Chem. C 113 (2009) 170–173.

[39] J. Lee, J. Chung and S. Lim, Improvement of optical properties of post-annealed ZnO nanorods, Physica E 42 (2010) 2143–2146.

2. Sonochemical synthesis, photocatalysis and photonic properties of 3 % Ce-doped ZnO nanoneedles

Abstract

ZnO nanostructured particles doped with 0-3 % Ce were successfully synthesized by an ultrasonic solution method. Phase and morphology characterized by XRD, FTIR, SEM, TEM, HRTEM, SAED and EDX revealed the presence of hexagonal wurtzite ZnO nanoneedles with E_{2H} vibration at 426 cm^{-1}, composing of the corresponding elements and growing in the [001] direction. The 3 % Ce-doped ZnO nanoneedles showed the 3.00 eV direct energy gap and 392.6 nm emission by UV-visible absorption and photoluminescence (PL) spectroscopy, including the most effective photocatalytic activity in the solution containing methylene blue.

Keywords: Electron microscopy; Spectroscopy; X-ray methods; Functional applications

Introduction

The II-VI semiconductors doped with rare-earth (RE) metals are very important for the present technology. They are promising for use as optoelectronic and luminescent devices: fluorescent lamps, cathode ray tube (CRT) phosphors and image intensifiers for X-ray screens [1]. RE atoms possessing special 4f shells are known as excellent candidates for luminescence centers of doped materials due to the transition of intra-4f or 4f–5d narrow emission line. The transitions play important roles in the absorption of RE atoms in the UV range. An energy transfer process from excited semiconductor host to doping lanthanide atoms promoted the doped nanocrystals to circumvent absorption of optically centers with remarkable improvement of luminescent properties [2,3].

Wurtzite ZnO (3.37 eV energy gap and 60 meV exciton binding energy at room temperature) is high electrochemical stability and nontoxicity n-type oxide [2,4-7]. It is one of the most dominant UV-activated photocatalysts for air and water treatment due to its high photosensitivity and oxidation potential, and low cost. Lanthanide-doped ZnO nanocrystals are one of new classes of luminescent materials for advanced display and lighting applications [1,2]. Thus ZnO is a promising candidate for treatment of environmental pollution, solving the problem of energy depletion and suitably doped with luminescence centers.

In this research, we succeeded in doping Ce into wurtzite ZnO by sonochemistry. Phase, morphologies, UV-visible absorption and photoluminescence were studied, including the investigation of photocatalytic property of Ce-doped ZnO under the UV light.

Experimental details

To prepare 0-3 % Ce-doped ZnO, 0.005 mole $Zn(NO_3)_2 \cdot 6H_2O$ and 0-3 mole % $Ce(NO_3)_3 \cdot 6H_2O$ were dissolved into 100 ml deionized water under vigorous stirring till complete dissolution. Subsequently, NH_4OH solution was slowly dropped into these solutions until the pH reaching at 9.5 and colorless solutions were achieved. Each of colorless solutions was sonicated in 35 kHz ultrasonic bath for 5 h. The precipitates were synthesized and collected for further characterization.

The photocatalytic activities of the as-synthesized samples were determined by measuring the degradation of methylene blue (MB) solution under UV light irradiation. The 500 mg photocatalyst was added to 100 ml 10^{-5} M MB aqueous solution. The solution was magnetically stirred for 60 min in the dark environment to establish adsorption/desorption equilibrium of MB on surfaces of the photocatalyst. Then the UV light was turned on to initiate the photocatalytic reaction.

Results and discussion

Fig. 1a shows XRD spectra of Ce-doped ZnO with different Ce^{3+} contents. For pure ZnO, the peaks were at 2θ of 32.11, 34.75, 36.59, 47.85 and 56.93 degree corresponding to the (100), (002), (101), (102) and (110) planes of hexagonal wurtzite ZnO of the JCPDS No. 36-1451 [8]. By doping Ce^{3+} in ZnO, only the ZnO peaks were still detected. No diffraction peaks of doping atoms or other phases were detected, indicating that the Ce^{3+} ions completely substituted for Zn^{2+} ions in ZnO lattice. Ce^{3+} concentration could be too low to be detected by XRD.

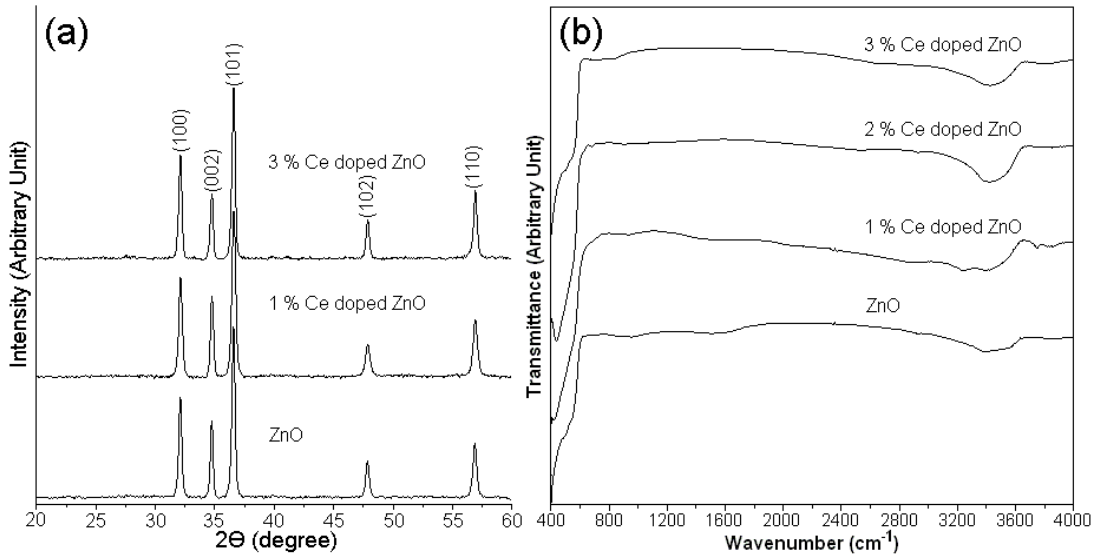


Fig. 1 (a) XRD and (b) FTIR spectra of ZnO with and without Ce doping.

FTIR spectra (Fig. 1b) of the 0, 1, 2 and 3 % Ce-doped ZnO, analyzed over the wavenumber of 400-4000 cm^{-1}, show strong bands at around 450-500 cm^{-1} with one broad band at 3300-3600 cm^{-1}. In this research, pure ZnO and 1-3 % Ce-doped ZnO show the same strong absorption bands at 426 cm^{-1} with the shoulders at 565 cm^{-1}, assigned as E_{2H} vibration and oxygen vacancies of wurtzite ZnO crystal, respectively [9]. For every two Ce^{3+} ions doped into ZnO crystal, one O^{2-} vacancy formed to maintain

electroneutrality of the crystal. Considering the ionic radii of Zn^{2+} and Ce^{3+} [6,10,11], it was likely that Ce^{3+} partially substituted for Zn^{2+} in the ZnO crystal. An absorption bands at 3300-3600 cm^{-1} is the O–H stretching of adsorbed water on the sample surface.

Pure ZnO (Fig. 2a) was nanoneedle-like particles with sharp tips on both ends. A base width at the middle and tapered tips were 100 nm and 25 nm with 1 μm long. By doping with Ce (Fig. 2b-d), the morphology of 1, 2 and 3 % Ce-doped ZnO remained as nanoneedles, but their lengths were increased to 2-3 μm. The elemental distribution of 3 % Ce-doped ZnO nanoneedles were characterized by EDX. Zn, O and Ce were shown on the elemental EDX-maps (result not shown), implying that Ce atoms were very distributive in the sample.

TEM and HRTEM images and SAED pattern (Fig. 3a, b) represent phase and morphology of pure ZnO nanoneedles with 800 nm long, uniform diameter and slightly rough surface. The HRTEM image was analyzed on edge part of a typical ZnO nanoneedle. The (002) fringe at right angle to the [001] growth direction with 2.61 Å apart were detected, in consistent with that of the bulk wurtzite ZnO crystal. Some defects were also detected. The SAED pattern shows a bright spot pattern of single crystal of hexagonal ZnO. Consider the 3 % Ce-doped ZnO images and SAED pattern (Fig. 3c, d), they revealed the straight nanoneedles of single crystal with smooth surface and 80 nm in diameter. The d-spacing values measured from the SAED pattern with zone axis of [1-10] are 1.62, 1.38 and 2.61 Å, well agree with the (110), (112) and (002) lattice planes of hexagonal ZnO phase, respectively. These indicated that 3 % Ce-doped ZnO nanoneedles grew along the [001] direction.

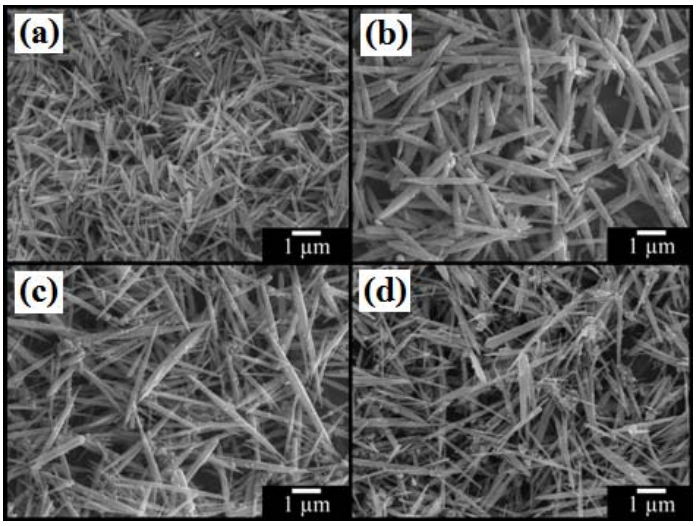


Fig. 2 SEM images of (a) undoped ZnO, and (b-d) 1, 2 and 3 % Ce-doped ZnO, respectively.

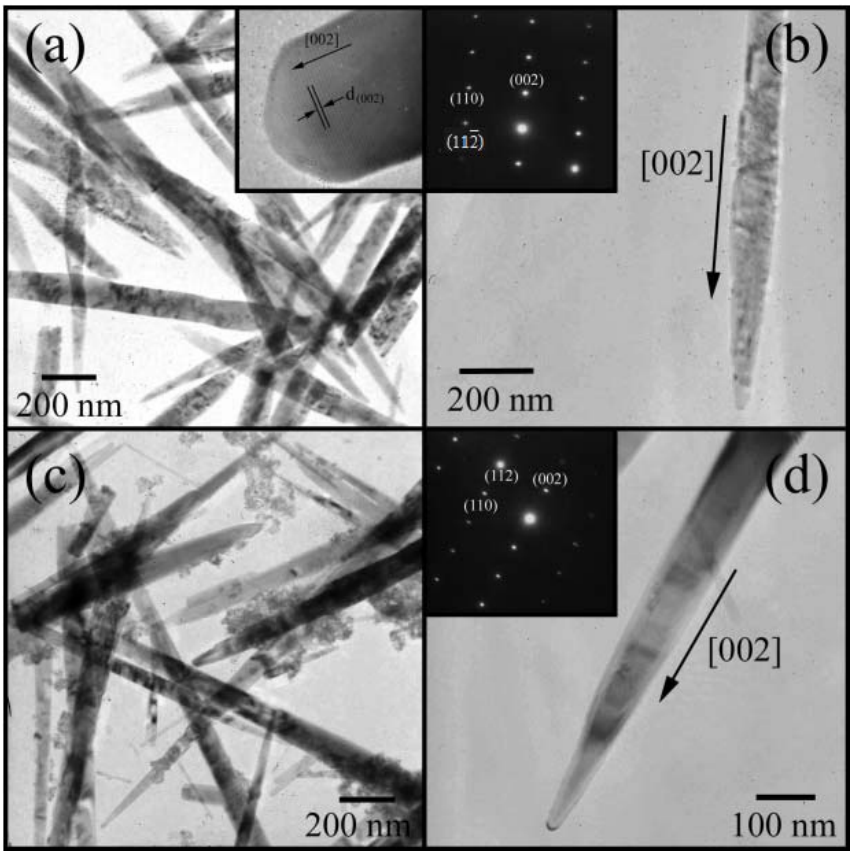


Fig. 3 TEM images, HRTEM images and SAED patterns of (a, b) pure ZnO and (c, d) 3 % Ce-doped ZnO.

Formation mechanism of ZnO nanoneedles proceeded in a sonochemical bath as follows. First, zinc nitrate, water and ammonium hydroxide absorbed ultrasound energy and followed by the dissociation process to form primary ions. Second, $[Zn(OH)_4]^{2-}$ complex ions formed and further decomposed to give ZnO molecules [12], which nucleated and grew as nanoneedles. Their preferential growth were along the [0001] direction due to the intrinsic anisotropy in growth rate (v) with v[0001] > v[01-10] > v[000-1]. The structure of ZnO single crystal can be described as a number of alternating planes of coordinated Zn^{2+} and O^{2-} ions, the positively charged Zn-(0001) and negatively charged O-(0001) polar surfaces. Due to the decreasing in the concentration of ZnO_2^{2-} monomers by the rapid nucleation of ZnO, the absorption of OH^- on the positively charged plane dominated the competition of ZnO_2^{2-} growth units. Thus, the OH^- ions stabilized the surface charge of Zn-(0001) to some degree, leading to the formation of nanoneedle-like ZnO along the [0001] direction [13,14]. When the doping material was also mixed, Ce^{3+} ions diffused and resided in the ZnO nanoneedles.

UV absorption (Fig. 4) of undoped ZnO and 3 % Ce-doped ZnO was investigated in 225-800 nm wavelength range. They presented well defined excitonic absorption peaks at 366 nm, corresponding to the band-to-band transition of ZnO [15], and at 370 nm of 3 % Ce-doped ZnO with red shifted absorption as compared to that for ZnO. The direct energy gaps of undoped ZnO and 3 % Ce-doped ZnO were determined to be 3.03 and 3.00 eV, respectively.

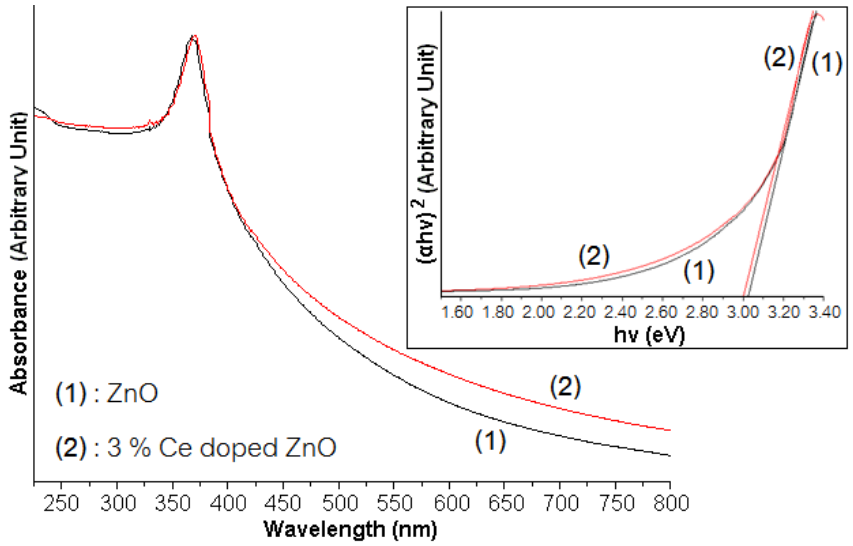


Fig. 4 UV-visible absorption and the $(\alpha h\nu)^2$ vs $h\nu$ plots of ZnO and 3 % Ce-doped ZnO.

PL spectra (Fig. 5) of ZnO with and without Ce doping were studied using 318 nm excitation wavelength. They showed broad emissions in the wavelength range of 325–600 nm. The 3 % Ce-doped ZnO showed higher emission intensity than any other products. Upon doing the Gaussian analysis for pure ZnO and 3 % Ce-doped ZnO with the highest intensity, the spectra were disintegrated into three emission peaks at 393.1, 442.9 and 495.6 nm for pure ZnO, and 392.6, 433.7 and 482.2 nm for 3 % Ce-doped ZnO – corresponding to the UV, blue and blue-green emissions, respectively [16,17]. The first was caused by the characteristic of near-band-edge emission of free exciton recombination process [18], but the second and third were possibly associated with oxygen vacancies [16] and other defects.

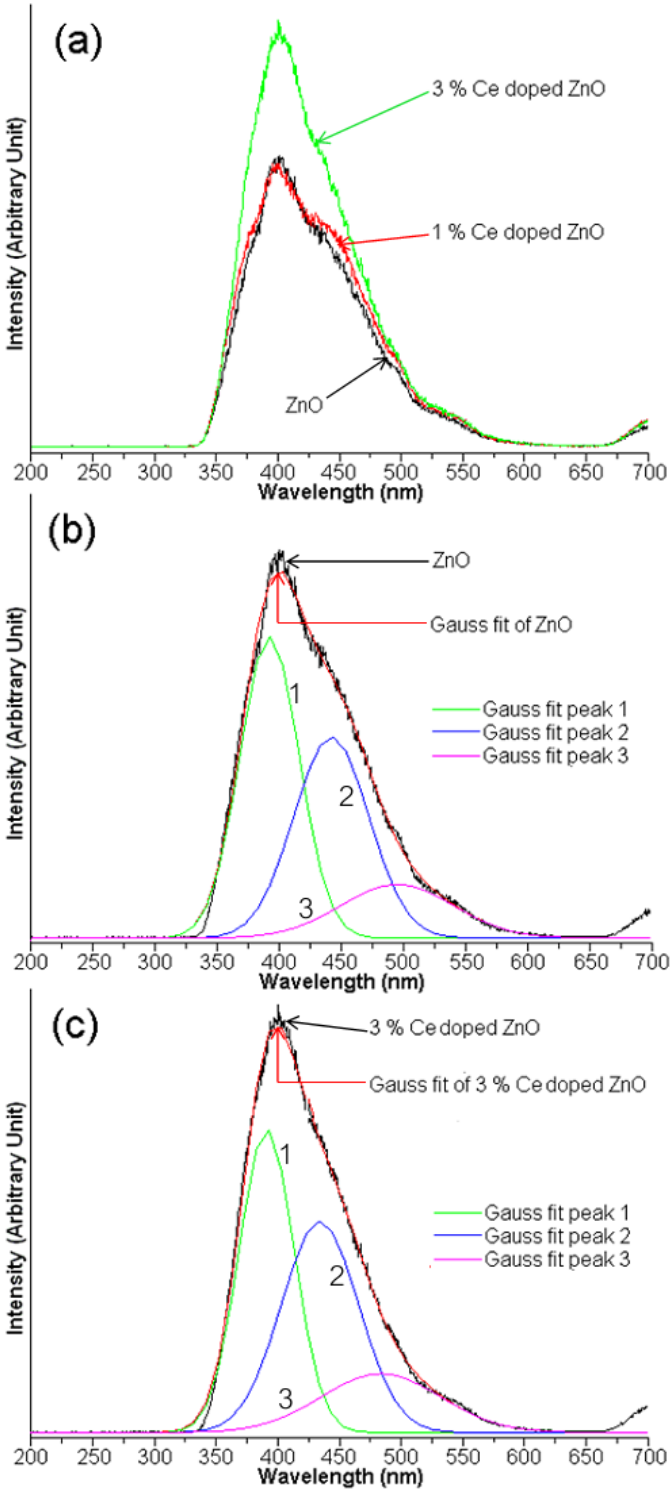


Fig. 5 (a) PL spectra of ZnO with and without Ce doping. Gaussian analysis of (b) ZnO and (c) 3 % Ce-doped ZnO.

MB is adopted as a representative organic pollutant to evaluate the photocatalytic performance of the as-synthesized Ce-doped ZnO. UV-visible absorbance (Fig. 6) of undoped ZnO and 3 % Ce-doped ZnO during photocatalysis for 0-300 min shows that the absorbance of MB for ZnO was gradually decreased, but that for 3 % Ce-doped ZnO was decreased at much faster rate. Fig. 7 shows the MB degradation rate for ZnO with and without Ce doping under UV light for different lengths of time. Obviously, 3 % Ce-doped ZnO shows the most effective in photocatalysis in these solutions. During the first 140 min, MB concentration was rapidly decreased to 32, 70 and 87 % for ZnO, 1 % Ce-doped ZnO and 3 % Ce-doped ZnO, respectively. For 240 min, the MB degradation efficiency for 3 % Ce-doped ZnO was higher than 98 %, 1.97 times the degradation efficiency of ZnO (49.81%). The higher the concentration of oxygen defects on the surfaces of Ce-doped ZnO nanocrystals is, the stronger the photocatalytic activity will be. Finally, the experimental results presented in this article will be very useful for the research on other metallic/semiconducting catalysts with high catalytic activities.

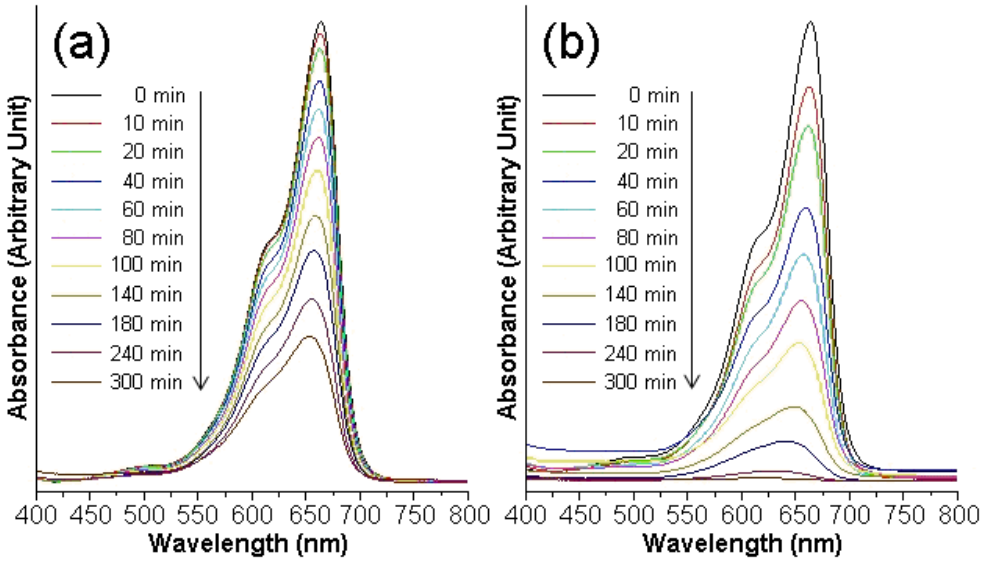


Fig. 6 UV-visible absorption of (a) pure ZnO and (b) 3 % Ce-doped ZnO.

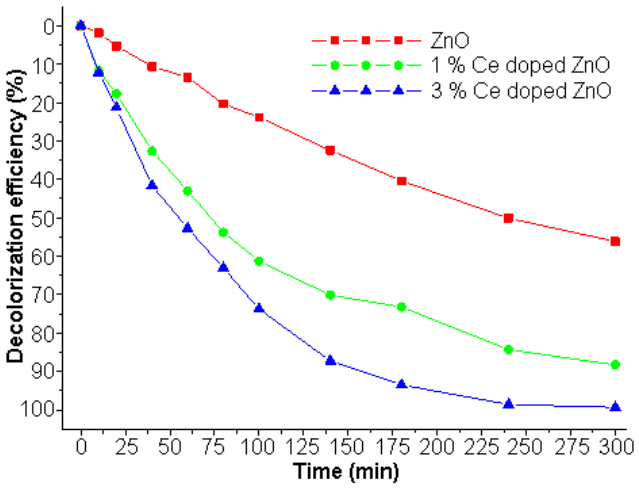


Fig. 7 Decolorization efficiencies of ZnO with and without Ce doping.

Conclusions

Undoped ZnO and 1-3 % Ce-doped ZnO nanoneedles were successfully synthesized in a controlled sonochemical process. The PL spectrum of 3 % Ce-doped ZnO showed a strong emission at 392.6 nm with other two weak visible emissions. The facile, reproducible and effective route presented a useful method for the RE^{3+}-doped ZnO system. High crystalline quality and good optical properties of the Ce-doped ZnO nanoneedles can lead the material to be a candidate for different applications in the future.

References

[1] J. Iqbal, X. Liu, H. Zhu, Z.B. Wu, Y. Zhang, D. Yu, R. Yu, Raman and highly ultraviolet red-shifted near band-edge properties of LaCe-co-doped ZnO nanoparticles, Acta Mater. 57 (2009) 4790–4796.

[2] Y.P. Du, Y.W. Zhang, L.D. Sun, C.H. Yan, Efficient energy transfer in monodisperse Eu-doped ZnO nanocrystals synthesized from metal acetylacetonates in high-boiling solvents, J. Phys. Chem. C 112 (2008) 12234–12241.

[3] J. Flor, S.A.M. de Lima, M.R. Davolos, Effect of reaction time on the particle size of ZnO and ZnO:Ce obtained by a sol–gel method, Progr. Colloid Polym. Sci. 128 (2004) 239–243.

[4] H.C. Gong, J.F. Zhong, S.M. Zhou, B. Zhang, Z.H. Li, Z.L. Du, Ce-induced single-crystalline hierarchical zinc oxide nanobrushes, Superlatt. Microstruct. 44 (2008) 183–190.

[5] Z. Sofiani, B. Derkowska, P. Dalasiński, M. Wojdyła, S. Dabos-Seignon, M. Alaoui Lamrani, L. Dghoughi, W. Bała, M. Addou, B. Sahraoui, Optical properties of ZnO and ZnO:Ce layers grown by spray pyrolysis, Optic Commun. 267 (2006) 433–439.

[6] D. Fangli, W. Ning, Z. Dongmei, S. Yingzhong, Preparation, characterization and infrared emissivity study of Ce-doped ZnO films, J. Rare Earths 28 (2010) 391–395.

[7] Y. Morinaga, K. Sakuragi, N. Fujimura, T. Ito, Effect of Ce doping on the growth of ZnO thin films, J. Cryst. Growth 174 (1997) 691–695.

[8] Powder Diffract. File, JCPDS-ICDD, 12 Campus Boulevard, Newtown Square, PA 19073-3273, U.S.A. (2001).

[9] G. Xiong, U. Pal, J.G. Serrano, K.B. Ucer, R.T. Williams, Photoluminescence and FTIR study of ZnO nanoparticles: the impurity and defect perspective, Phys. Stat. Sol. I 3 (2006) 3577–3581.

[10] C. Ge, C. Xie, S. Cai, Preparation and gas-sensing properties of Ce-doped ZnO thin-film sensors by dip-coating, Mater. Sci. Eng. B 137 (2007) 53–58.

[11] J.E. Huheey, E.A. Keiter, R.L. Keiter, Inorg. Chem.: Princ. Struct. React., 4th Ed., Harper Collins College Publ., NY 10022, U.S.A. (1993).

[12] P. Mishra, R.S. Yadav, A.C. Pandey, Growth mechanism and photoluminescence property of flower-like ZnO nanostructures synthesized by starch-assisted sonochemical method, Ultrason. Sonochem. 17 (2010) 560–565.

[13] B. Li, Y. Wang, Facile synthesis and enhanced photocatalytic performance of flower-like ZnO hierarchical microstructures, J. Phys. Chem. C 114 (2010) 890–896.

[14] D. Wang, C. Song, Controllable synthesis of ZnO nanorod and prism arrays in a large area, J. Phys. Chem. B 109 (2005) 12697–12700.

[15] H. Qin, W. Li, Y. Xia, T. He, Photocatalytic activity of heterostructures based on ZnO and N-doped ZnO, ACS Appl. Mater. Interface 3 (2011) 3152–3156.

[16] Z. Zhu, D. Yang, H. Liu, Microwave-assisted hydrothermal synthesis of ZnO rod-assembled microspheres and their photocatalytic performances, Adv. Powder Tech. 22 (2011) 493–497.

[17] C. Deng, H. Hu, G. Shao, C. Han, Facile template-free sonochemical fabrication of hollow ZnO spherical structures, Mater. Lett. 64 (2010) 852–855.

[18] J. Das, D. Khushalani, Nonhydrolytic route for synthesis of ZnO and its use as a recyclable photocatalyst, J. Phys. Chem. C 114 (2010) 2544–2550.

3. Template-free synthesis of neodymium hydroxide nanorods by microwave-assisted hydrothermal process, and of neodymium oxide nanorods by thermal decomposition

Abstract

Based on the 150 ^{o}C and 1 h microwave-assisted hydrothermal reaction of $Nd(NO_3)_3$ dissolved in deionized water with pH 10 adjusted by concentrated NH_4OH solution, the phase and morphology of the product, characterized by XRD, SEM and TEM analyses, were specified as hexagonal $Nd(OH)_3$ nanorods 50 nm in diameter and 700 nm long, growing along the [001] direction. TGA analysis showed the evaporation of adsorbed water and dehydration of $Nd(OH)_3$ to synthesize the final pure Nd_2O_3 product. With 500 ^{o}C and 2 h calcination of the $Nd(OH)_3$ self-template precursor, Nd_2O_3 nanorods were synthesized, retaining both the morphology and growth direction of the precursor.

Keywords: Microwave processing; Calcination; Electron microscopy; X-ray methods; Nanorods

Introduction

Since the discovery of carbon nanotubes (CNTs), a new structured carbon, in 1991 [1], one-dimensional (1D) nanostructures such as nanorods, nanowires, nanobelts and nanotubes have been promising materials for various electronic, optoelectronic, magnetic and photonic devices due to their unique physical and chemical properties – quite different from those of the corresponding bulk materials [2–4]. Rare earth oxides have been used in a number of scientific areas such as ceramic industries, and as catalysts for dehydrogenation, hydrogenation and esterification reactions, arising from their 4f electrons [2,5–9]. Among these, neodymium oxide (Nd_2O_3) has been widely used in luminescent materials for photonic applications, as a catalyst for the synthesis of ammonia and the oxidative coupling of methane, and as a protective coating [7,10].

Therefore, the preparation and characterization of Nd_2O_3 nanorods has attracted much interest in recent years. There are many reports on the synthesis of rare earth oxides with different morphologies, i.e. the synthesis of: uniform nanorods, nanowires and nanoplates of rare earth oxides (M_2O_3, M = Pr, Nd, Sm, Eu, Gd, Tb and Dy) by microwave irradiation [5]; Nd_2O_3 nanowires through a sol-gel process assisted by a porous anodic aluminum oxide (AAO) template [6]; rare earth oxide nanoparticles of Sm and Nd by hydrogen plasma-metal reaction [7]; $Ln(OH)_3$ (Ln = La, Pr, Nd, Sm, Eu, and Gd) by a simple wet chemical method [8]; Nd_2O_3 nanopowders by sol-gel auto-combustion [9]; Nd_2O_3 nanoparticles by a tartrate route [10]; and Nd_2O_3 nanoparticles [11] and rod-like Eu:Gd_2O_3 phosphor [12] via a hydrothermal route.

In the present research, we report the template-free synthesis of $Nd(OH)_3$ nanorods by the 150 ^{o}C and 1 h microwave-assisted hydrothermal (MH) reaction of $Nd(NO_3)_3$ solution with pH 10 adjusted by concentrated NH_4OH solution – a novel, facile, fast and environmentally benign low-temperature process. Subsequently, the $Nd(OH)_3$ nanorod self-template precursor was further calcined at 450 and 500 ^{o}C for 2 h to form Nd_2O_3 nanorods. This success may lead to large-scale synthesis applicable for a number of industries.

Experimental procedure

Neodymium (III) nitrate ($Nd(NO_3)_3$) and ammonium hydroxide (NH_4OH) were purchased from Sigma-Aldrich Co., and used without further purification. In a typical synthesis, 50 ml of aqueous 0.01 M $Nd(NO_3)_3$ was adjusted the pH to 10 by concentrated NH_4OH solution. It was transferred into a 100 ml Teflon-lined stainless-steel autoclave, which was filled with deionized water up to 80 % total capacity. The system was heated by 0-100 % 300 W microwave from room temperature to 150 ^{o}C for 20 min, held at this temperature for 1 h, and left cool down to room temperature. The resulting product was filtered, washed with distilled water and absolute ethanol, and dried at 80 ^{o}C for 12 h. Then the filtered product, the self-template precursor, was

further calcined at the rate of 5 ^{o}C.min^{-1} to 450, 500 and 550 ^{o}C and held at each of these temperatures for 2 h in ambient atmosphere to synthesize the final powders.

The weight loss (less), purified phase, structure and morphology of the as-synthesized products were characterized by a Shimadzu Scientific Instruments TGA-50 Thermogravimetric (TGA) analyzer under a stream of nitrogen at a heating rate of 10 ^{o}C.min^{-1}, a Bruker AXS D8 Advance Powder X-ray diffractometer (XRD) with K_{α} line from a copper target, a JEOL JSM-6335F field emission scanning electron microscope (FE-SEM) operating at 15 kV accelerating voltage with Au sputtering on the samples, and a JEOL JEM-2100F transmission electron microscope (TEM) and high resolution transmission electron microscope (HRTEM) including selective area electron diffractometer (SAED) operating at the accelerating voltage of 200 kV.

Results and discussion

Fig. 1 shows the thermogravimetric analysis (TGA) curve of the $Nd(OH)_3$ precursor. It shows continuous weight loss over a range of 50–650 ^{o}C, with a total weight loss of 15.44 %. Theoretically, $Nd(OH)_3$ decomposes to form Nd_2O_3 and H_2O:

$$2Nd(OH)_3 \longrightarrow Nd_2O_3 + 3H_2O \qquad (1)$$

Under the molar conservation of the (1) reaction, the calculated weight loss is 13.84 %, lower than that from TGA analysis. The precursor might absorb some moisture (water vapor) from the ambient atmosphere, which would evaporate during TGA analysis. The weight loss of the $Nd(OH)_3$ precursor was classified into three steps. First, weight loss in the temperature range of 50–270 ^{o}C was specified as the decomposition of adsorbed residual water on the surface of $Nd(OH)_3$. Second, weight loss at the temperature range 270–430 ^{o}C was due to the dehydration of $Nd(OH)_3$ to form NdOOH. Third, weight loss at 430–650 ^{o}C corresponded to the well-defined NdOOH dehydration into a hexagonal Nd_2O_3 structure [12–14]. In the present research, the TGA weight loss (Table 1) was very close to the theoretical value calculated from the molar conservation of products

and reactants of the (2) and (3) chemical reactions [12]. The dehydration of $Nd(OH)_3$ to form Nd_2O_3 can be written as follows:

$$2Nd(OH)_3 \longrightarrow 2NdOOH + 2H_2O \quad \text{at } 270\text{–}430\ ^{\circ}C \qquad (2)$$

$$2NdOOH \longrightarrow Nd_2O_3 + H_2O \quad \text{at } 430\text{–}650\ ^{\circ}C \qquad (3)$$

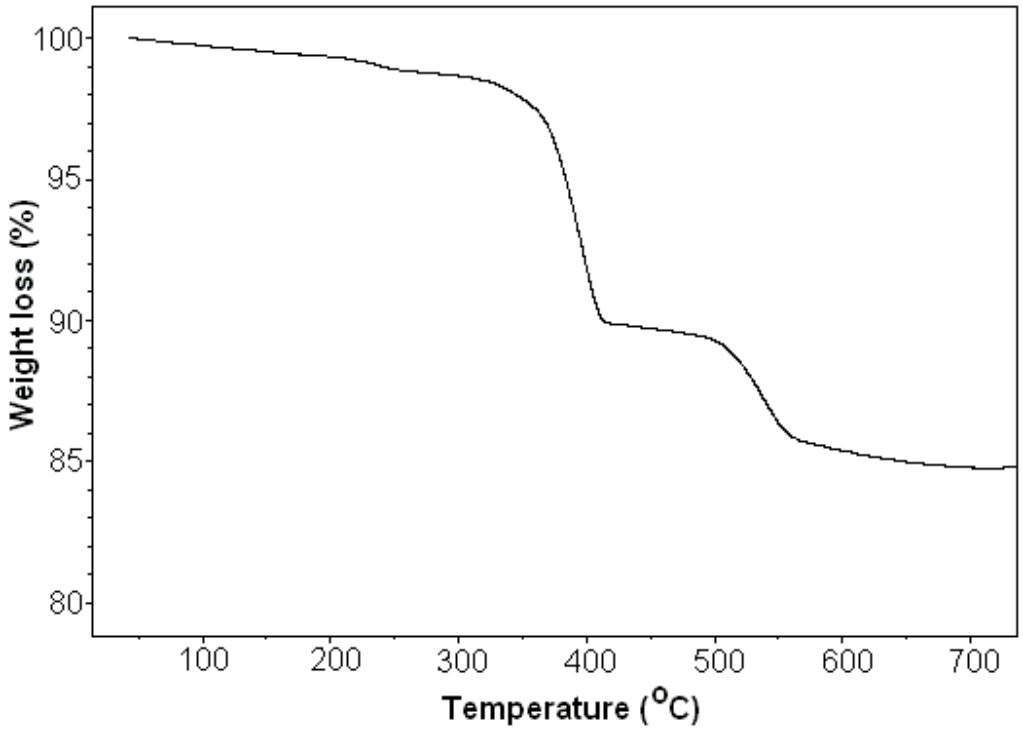


Fig. 1 TGA curve of $Nd(OH)_3$ precursor synthesized by the 150 °C and 1 h MH process.

Table 1 Weight loss of $Nd(OH)_3$ precursor characterized by TGA at 50-650 °C.

Temperature range (°C)	Reaction	TGA weight loss (%)	Theoretical weight loss (%)
50-270	Dehydration of water on $Nd(OH)_3$ surface	1.23	-
270-430	$2Nd(OH)_3 \longrightarrow 2NdOOH + 2H_2O$	8.91	9.23
430-650	$2NdOOH \longrightarrow Nd_2O_3 + H_2O$	5.30	4.61

The different phases of the products were analyzed by X-ray diffraction, as shown in Fig. 2. All diffraction peaks of the as-synthesized precursor were indexed as pure phase of hexagonal $Nd(OH)_3$, JCPDS No. 70-0214 [14]. Its diffraction peaks were at 2θ of 16.06, 27.90, 28.94, 32.34, 37.13, 40.59, 48.65, 49.26, 50.01, 57.11, 65.55, 71.73 and 79.42 deg, which were assigned as the (100), (110), (101), (200), (111), (201), (002), (300), (211), (112), (131), (302) and (231) planes, respectively. Upon calcination at 450, 500 and 550 $^{\circ}C$ for 2 h, the peaks were at 2θ of 26.88, 29.82, 30.80, 40.52, 47.44, 53.54, 57.00, 57.67, 61.89, 64.14, 68.76, 74.29 and 77.83 deg, specified as the (100), (002), (011), (012), (110), (103), (112), (201), (004), (202), (014), (023) and (121) planes of pure hexagonal Nd_2O_3 phase, in accordance with JCPDS No. 75-2255 [14]. Atomic diffusion became more violent with an increase in calcination temperature.

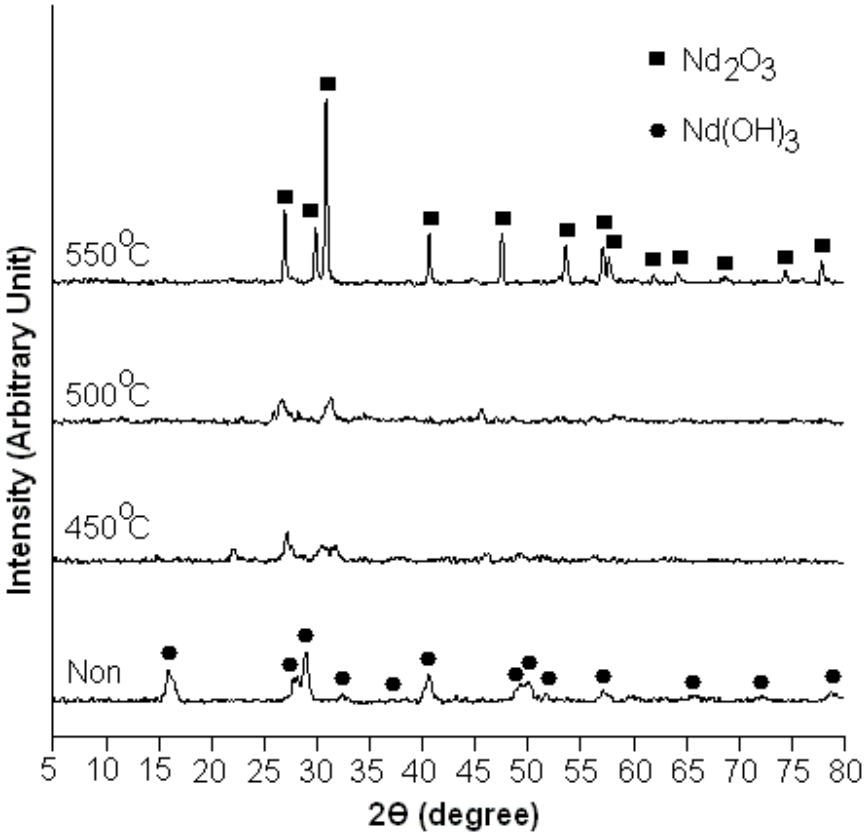


Fig. 2 XRD patterns of $Nd(OH)_3$ precursor, and Nd_2O_3 synthesized by the 450, 500 and 550 $^{\circ}C$ calcination of its precursor for 2 h.

In microwave-assisted hydrothermal (MH) synthesis, the final morphology of the product was controlled by surface chemistry, resulting in either oriented or random attachment of particles. During the MH process, Nd^{3+} ions reacted with hydroxyl ions of NH_4OH to form $Nd(OH)_3$ nanorods:

$$Nd^{3+} + 3OH^{-} \longrightarrow Nd(OH)_3 \quad (4)$$

In general, the morphology of the product was determined by the rates of nucleation and crystal growth, which were controlled by the inherent crystal structure and chemical potential of the precursor solution [15,16]. When the rate of nucleation was greater than that of crystal growth, the crystal size as well as its aspect ratio would be small. In contrast, fast crystal growth would lead to a large crystal with a high aspect ratio along the preferential direction [15]. At a high concentration of hydroxyl ions, the reaction of Nd^{3+} and OH^{-} to form $Nd(OH)_3$ was very fast, and the aggregation of particles led to the formation of nanorods. The concentrations of Nd^{3+} and OH^{-} were high enough to form $Nd(OH)_3$ in the shape of nanorods. Further calcination of $Nd(OH)_3$ nanorods in a furnace at 450–550 ^{o}C led to the dehydration process, with the formation of Nd_2O_3 by the following reaction:

$$2Nd(OH)_3 \longrightarrow Nd_2O_3 + 3H_2O \quad (5)$$

Under the optimum conversion condition (500 ^{o}C and 2 h), the final geometry of Nd_2O_3 nanorods was predetermined by the shape and size of the $Nd(OH)_3$ nanorods, functioning as self-template precursors.

Morphologies of the products were characterized by SEM, as shown in Fig. 3. Fig. 3a shows $Nd(OH)_3$ nanorods 700 nm long and 50 nm in diameter. The growth of $Nd(OH)_3$ nanorods was reliable in the reaction system without any catalyst, template or surfactant. The anisotropic growth of $Nd(OH)_3$ was mainly controlled by the inherent crystal structure and chemical potential of the solution [16]. For the crystal structure of $Nd(OH)_3$, all of the positive Nd^{3+} cations reside on the (001) face, with most of their dangling bonds coordinated with OH^{-} anions, alternately stacking along the [001] direction. Compared with the (110) and (100) planes, they have fewer ions with weaker

polarity than the (001) plane. This characteristic structure promotes the highest density of Nd^{3+} and OH^- ions along the [001] direction, which leads the (001) face to have the highest chemical potential and the most activity in relation to the surrounding growth conditions. Thus, the final crystal morphology is cooperative with the internal crystal structure and external reaction conditions [8]. It should be noted that calcination temperature was an important factor in determining the average particle size of the product. The particle size of Nd_2O_3 was increased with increasing calcination temperature. The degree of crystallinity was also increased. SEM analysis shows nanorod shapes with an estimated size of ~70 nm in diameter and ~500 nm in length from calcination at 450 and 500 ^{o}C for 2 h. Upon increasing the calcination temperature to 550 ^{o}C, but keeping the length of time at 2 h, they changed to nanoparticles with their sizes range of 80-200 nm.

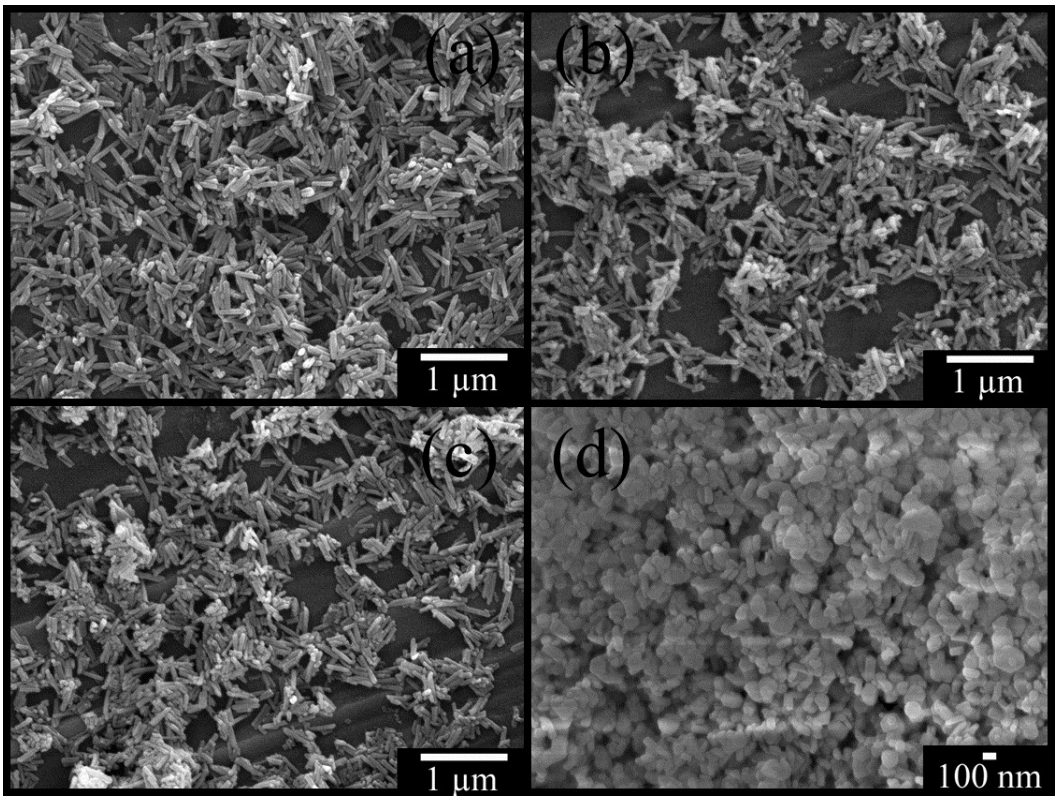


Fig. 3 SEM images of (a) $Nd(OH)_3$ nanorods synthesized by the 150 ^{o}C and 1 h MH process, and (b-d) Nd_2O_3 synthesized by the 450, 500 and 550 ^{o}C calcination of $Nd(OH)_3$ precursor for 2 h, respectively.

TEM images of $Nd(OH)_3$ and Nd_2O_3 are shown in Fig 4. The $Nd(OH)_3$ crystallites, synthesized by the microwave-assisted hydrothermal process, displayed uniform nanorods 20–40 nm in diameter and 200–400 nm in length (Fig. 4a). The morphology was almost the same when the $Nd(OH)_3$ precursor was calcined at either 450 ^{o}C or 500 ^{o}C for 2 h.

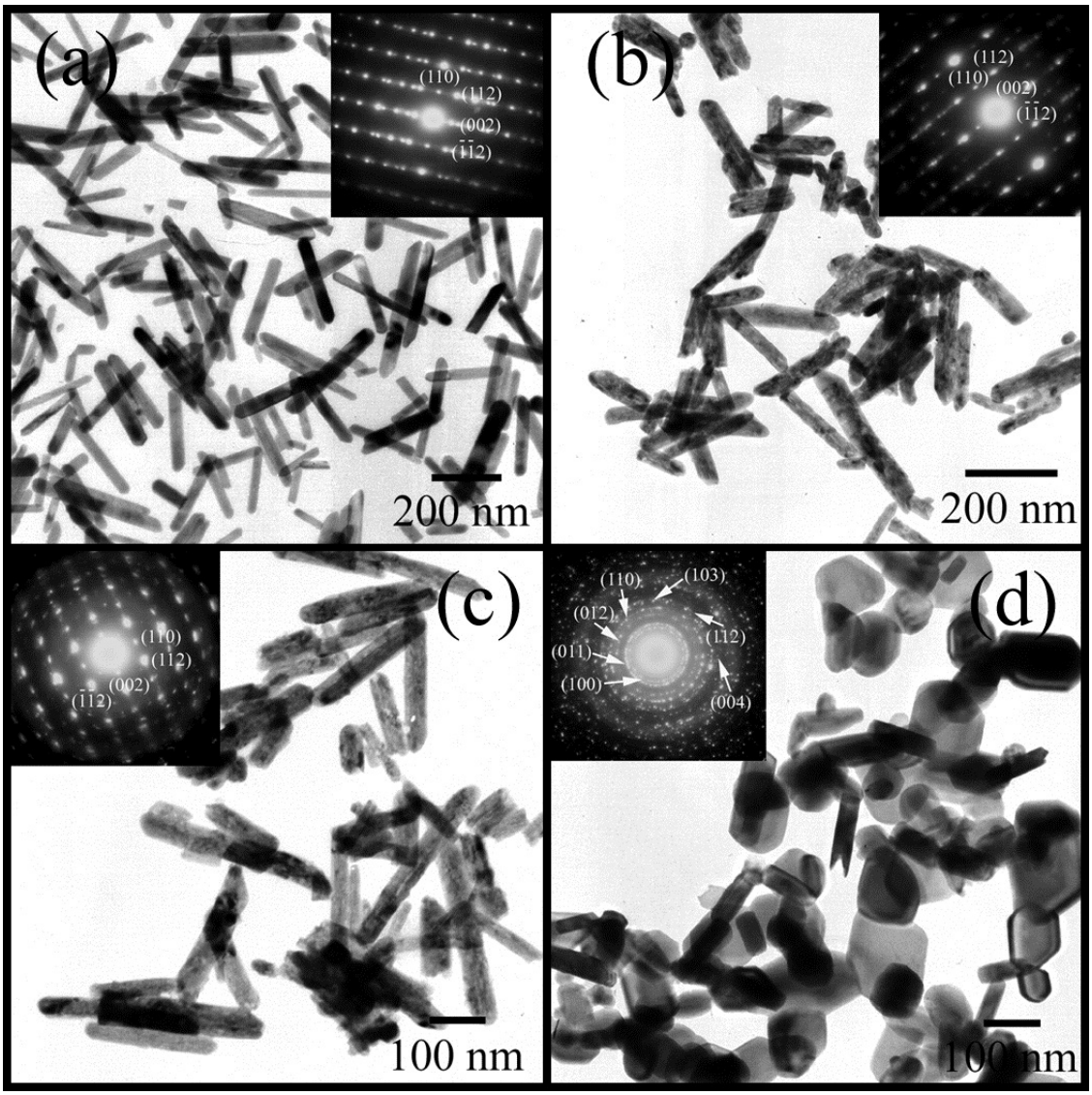


Fig. 4 TEM images and SAED patterns of (a) $Nd(OH)_3$ nanorods synthesized by the 150 ^{o}C and 1 h MH process, and (b-d) Nd_2O_3 synthesized by the 450, 500 and 550 ^{o}C calcination of $Nd(OH)_3$ precursor for 2 h, respectively.

But for 550 °C and 2 h calcination, the product became nanoparticles with an average size of 100 nm. At these stages, water evaporated and atomic diffusion proceeded. Selected area electron diffraction (SAED) patterns (insets of Fig. 4a-c) of the individual products corresponded to the (110), (112), (002) and (-1-12) planes with [2-20] as the zone axis, and were specified as $Nd(OH)_3$ and Nd_2O_3 single crystals [14] in accordance with the above XRD analysis. It should be noted that the planes of $Nd(OH)_3$ and Nd_2O_3 single crystals were the same, but their 2θ Bragg's angles were different. At 550 °C for 2 h, the SAED pattern (inset of Fig. 4d) was composed of concentric rings of bright spots, characterized as polycrystal. The interpreted pattern corresponded to the (100), (011), (012), (110), (103), (112) and (004) planes of Nd_2O_3 [14].

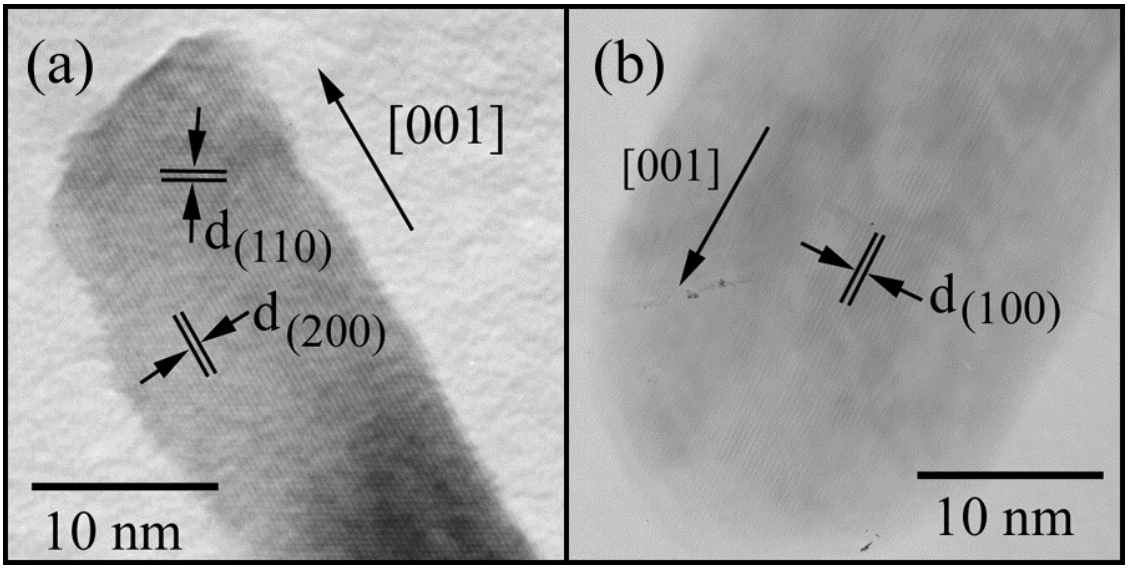


Fig. 5 HRTEM images of (a) $Nd(OH)_3$ nanorod synthesized by the 150 °C and 1 h MH process and (b) Nd_2O_3 nanorod synthesized by the 500 °C and 2 h calcination of $Nd(OH)_3$ nanorod precursor.

Fig. 5 shows typical HRTEM images of $Nd(OH)_3$ and Nd_2O_3 nanorods. Clearly, Fig. 5a reveals only d-spacing of the (110) and (200) planes, with a lattice spacing of about 0.321 and 0.278 nm for an individual $Nd(OH)_3$ nanorod. The HRTEM result suggested that the $Nd(OH)_3$ nanorod grew along the [001] direction, making angles of about 60° and 0° with the (110) and (200) lattice planes, respectively. Fig. 5b shows the

0.332 nm interplanar space, corresponding to d-spacing of the (100) plane of an individual Nd_2O_3 nanorod, parallel with its [001] growth direction.

Conclusions

Uniform Nd_2O_3 nanorods were successfully synthesized by the 500 ^{o}C and 2 h calcination of a $Nd(OH)_3$ nanorod precursor, which was synthesized by a one-step MH method at 150 ^{o}C for 1 h. Based on the experimental results, the final morphology of the one-dimensional (1D) Nd_2O_3 nanostructure was controlled by the morphology of the $Nd(OH)_3$ self-template nanorod and the calcination temperature. A possible growth mechanism of $Nd(OH)_3$ 1D nanorods was proposed, in which the growth was promoted by the highest number of Nd^{3+} and OH^{-} ions along the [001] direction.

References

[1] S. Iijima, Helical microtubules of graphitic carbon, Nature 354 (1991) 56–58.

[2] N. Zhang, R. Yi, L. Zhou, G. Gao, R. Shi, G. Qiu, X. Liu, Lanthanide hydroxide nanorods and their thermal decomposition to lanthanide oxide nanorods, Mater. Chem. Phys. 114 (2009) 160–167.

[3] X. Wang, Y. Li, Solution-based synthetic strategies for 1-D nanostructures, Inorg. Chem. 45 (2006) 7522–7534.

[4] H. Guan, Y. Zhang, Hydrothermal synthesis and characterization of hexagonal and monoclinic neodymium orthophosphate single-crystal nanowires, J. Solid State Chem. 177 (2004) 781–785.

[5] A.B. Panda, G. Glaspell, M.S. El-Shall, Microwave synthesis and optical properties of uniform nanorods and nanoplates of rare earth oxides, J. Phys. Chem. C 111 (2007) 1861–1864.

[6] X. Qu, J. Dai, J. Tian, X. Huang, Z. Liu, Z. Shen, P. Wang, Syntheses of Nd_2O_3 nanowires through sol–gel process assisted with porous anodic aluminum oxide (AAO) template, J. Alloys Compd. 469 (2009) 332–335.

[7] T. Liu, Y. Zhang, H. Shao, X. Li, Synthesis and characteristics of Sm_2O_3 and Nd_2O_3 nanoparticles, Langmuir 19 (2003) 7569–7572.

[8] L. Qian, Y. Gui, S. Guo, Q. Gong, X. Qian, Controlled synthesis of light rare-earth hydroxide nanorods via a simple solution route, J. Phys. Chem. Solids 70 (2009) 688–693.

[9] W. Yang, Y. Qi, Y. Ma, X. Li, X. Guo, J. Gao, M. Chen, Synthesis of Nd_2O_3 nanopowders by sol–gel auto-combustion and their catalytic esterification activity, Mater. Chem. Phys. 84 (2004) 52–57.

[10] B. Zhaorigetu, G. Ridi, L. Min, Preparation of Nd_2O_3 nanoparticles by tartrate route, J. Alloys Compd. 427 (2007) 235–237.

[11] L. Kępiński, M. Zawadzki, W. Miśta, Hydrothermal synthesis of precursors of neodymium oxide nanoparticles, Solid State Sci. 6 (2004) 1327–1336.

[12] C. Chang, F. Kimura, T. Kimura, H. Wada, Preparation and characterization of rod-like Eu:Gd_2O_3 phosphor through a hydrothermal routine, Mater. Lett. 59 (2005) 1037–1041.

[13] T. Thongtem, A. Phuruangrat, D.J. Ham, J.S. Lee, S. Thongtem, Controlled Gd_2O_3 nanorods and nanotubes by the annealing of $Gd(OH)_3$ nanorod and nanotube precursors and self-templates produced by a microwave-assisted hydrothermal process, CrystEngComm 12 (2010) 2962–2966.

[14] Powder Diffract. File, JCPDS-ICDD, 12 Campus Boulevard, Newtown Square, PA 19073-3273, U.S.A. 2001.

[15] W.B. Hu, D.T. Tian, Y.Z.Mi, G.H. Nie, Y.M. Zhao, Z.L. Liu, K.L. Yao, Synthesis and characterization of In_2O_3 nanocube via a solvothermal-calcination route, Mater. Chem. Phys. 118 (2009) 277–280.

[16] X. Wang, Y. Li, Synthesis and characterization of lanthanide hydroxide single-crystal nanowires, Angew. Chem. Int. Ed. 41 (2002) 4790–4793.

4. Effect of medium solvent ratios on morphologies and optical properties of α-$ZnMoO_4$, β-$ZnMoO_4$ and $ZnMoO_4 \cdot 0.8H_2O$ crystals synthesized by microwave-hydrothermal/solvothermal method

Abstract

$ZnMoO_4$ with different morphologies were successfully synthesized by microwave hydrothermal and microwave solvothermal methods, without the use of any additives. The different crystalline phases (α-$ZnMoO_4$, β-$ZnMoO_4$ and $ZnMoO_4 \cdot 0.8H_2O$), morphologies and optical properties of the samples were studied by X-ray diffraction, electron microscopy and spectroscopy, and were found to be influenced by the length of reaction time and the different volume ratios of ethylene glycol (EG) to water as medium solvents. In this research, the direct energy gap (E_g) and photonic emission wavelength were evaluated to be 3.13–3.51 eV and 366 nm, respectively.

Keywords: α-$ZnMoO_4$; β-$ZnMoO_4$; $ZnMoO_4 \cdot 0.8H_2O$; X-ray diffraction; Electron microscopy; Spectroscopy

Introduction

In recent years, semiconducting nanomaterials have received considerable attention due to their wide applications in the fabrication of optical and electronic devices. A group of metal molybdate such as $MmoO_4$ (M = Ca, Sr, Mg, Zn) are semiconductors, which are important in photoluminescence and photocatalysis. Among them, zinc molybdate has many attractive applications, especially in luminescence, scintillation and photocatalysis, and for using in battery electrodes and drug delivery system [1–5]. There are a variety of methods used to synthesize $ZnMoO_4$ such as hydrothermal method [3, 6, 7], conventional mixed oxide calcination [2], microwave irradiation [3] and Czochralski method [5].

However, a hybrid technique such as microwave-hydrothermal method exhibits much advantage and is frequently applied for synthesizing of (nano) materials and chemical compounds, mainly inorganic chemacals. In order to additionally enhance the reaction kinetics, a great amount of work has been done to hybridize the hydrothermal technique with microwave (MW). Particularly, microwave-hydrothermal and microwave-solvothermal methods are truly low-temperature processes for the synthesis of nanophase of different sizes and shapes. They consume less energy, environmentally friendly, and the reaction proceeding in a closed system. The kinetics of reaction is greatly increased with a small increase in temperature. New metastable products form and are generally single crystals [8–10]. In contrast to the conventional heating hydrothermal/solvothermal method, it requires a longer time (typically half to several days) and high electrical power of over a thousand watts. Microwave-assisted heating is a greener approach to synthesize materials with a shorter time (several minutes to hours) and with lower power consumption (hundreds of watts) as a consequence of directly and uniformly heating the contents.

In the current work, the synthesis of triclinic α-$ZnMoO_4$, monoclinic β-$ZnMoO_4$ and $ZnMoO_4 \cdot 0.8H_2O$ with different morphologies (rod-like, flower-like, rugby-like) by microwave hydrothermal and microwave solvothermal methods without the use of any additive and surfactant were investigated and reported.

Experiment

Materials and processing

5 mmol of each $Zn(NO_3)_2 \cdot 6H_2O$ and $(NH_4)_6Mo_7O_{24} \cdot 4H_2O$ was dissolved in 60 ml (constant volume) of deionized water and ethylene glycol with various ratios (Table 1) and vigorously stirred for 30 min. Then the solutions were transferred into glass vessels, which were tightly closed with covers equipped with safety valves on top. The systems were heated by a 270 W microwave (2.45 GHz) for different lengths of time. At the conclusion of the process, the system was naturally cooled to room temperature. Finally,

the products were washed with water and ethanol several times, and dried at 80 ^{o}C for 12 h for further characterization using different methods.

Table 1. Product code, reaction time and EG:H_2O volume ratio.

Product code	Time (min)	EG:H_2O volume ratio
E130	30	1 : 0
E160	60	
E190	90	
E4H1	30	4 : 1
E2H1	30	2 : 1
E1H1	30	1 : 1
E1H2	30	1 : 2
E1H4	30	1 : 4
H130	30	0 : 1
H160	60	
H190	90	
H1-2h	120	
H1-3h	180	

Characterizations

The as-synthesized products were characterized by X-ray diffractometer (XRD, SIEMENS D500) operating at 20 kV, 15 mA, and using Cu-Kα line, in combination with the database of the Joint Committee on Powder Diffraction Standards (JCPDS) [11]; scanning electron microscope (SEM, JEOL JSM-6335F) operating at 15 kV; transmission electron microscope (TEM, JEOL JEM-2010), high resolution transmission electron microscope (HRTEM) and selected area electron diffractometer (SAED) operating at 200 kV; Fourier transform infrared (FTIR, Bruker Tensor 27) spectrometer with KBr as a diluting agent and operated in the range of 4000–400cm^{-1}; Raman spectrometer (T64000 HORIBA Jobin Yvon) using a 50 mW and 514.5 nm wavelength Ar green laser; UV-visible spectrometer (Lambda 25 PerkinElmer) using a UV lamp with the resolution of 1 nm; and photoluminescence (PL) spectrometer (LS 50B PerkinElmer) using a 240 nm excitation wavelength at room temperature.

Results and discussion

XRD

As it is shown in Fig. 1, the influence of medium solvents and time on the formation of $ZnMoO_4$ phase was studied by XRD. For the samples synthesized in different EG:H_2O volume ratios for 30 min microwave irradiation, the volume ratio of the medium solvent had a crucial effect on the formation of $ZnMoO_4$ phase. The detected peaks of the samples synthesized in H_2O (H130) and in the mixture of EG and H_2O (1:4, 1:2 and 1:1 of EG:H_2O for E1H4, E1H2 and E1H1 samples) can be specified as pure $ZnMoO_4 \cdot 0.8H_2O$ phase of JCPDS no. 25-1025 [11]. When more EG was added to the medium solvents until at 4:1 and 1:0 of EG:H_2O, the mixture of α-$ZnMoO_4$ (JCPDS no. 35-0765) [11] and $ZnMoO_4 \cdot 0.8H_2O$ phases was detected in the E2H1 and E4H1 samples. When pure EG was used as a solvent, the XRD peaks of the E130 sample were identified to pure triclinic α-$ZnMoO_4$ phase (JCPDS no. 35-0765) [11]. This shows the loss of crystal water molecules this EG medium solvent. The crystalline phase became more perfect by increasing in the length of reaction time. The XRD peaks of the

E160 and E190 samples (Fig. 2a) became sharper and stronger, suggesting the enhancement of crystalline degree with prolonged time. When pure H_2O was used as a medium solvent instead, the influence of reaction time on the XRD patterns is also shown in Fig. 2b. For 30 and 60 min processing in H_2O medium solvent (H130 and H160 samples), pure $ZnMoO_4 \cdot 0.8H_2O$ phase of JCPDS no. 25-1025 [11] was detected. For 90 min long, some of the $ZnMoO_4 \cdot 0.8H_2O$ crystalline phase of the particles (H190) began transform into β-$ZnMoO_4$ phase (JCPDS no. 25-1024) [11]. Thus the mixture of $ZnMoO_4 \cdot 0.8H_2O$ and β-$ZnMoO_4$ phases were detected in the H190 sample. When the reaction time was lengthened to 2 h (H1-2h) and 3 h (H1-3h), the pure monoclinic β-$ZnMoO_4$ phase (according to the JCPDS no. 25-1024) [11] can be successfully synthesized. There were no other diffraction peaks of other phases were obviously detected. These results are in good evidence for the formation of $ZnMoO_4 \cdot 0.8H_2O$, α-$ZnMoO_4$ and β-$ZnMoO_4$ phases as shown by the following reaction scheme:

$$(NH_4)_6Mo_7O_{24} \cdot 4H_2O_{(s)} \longrightarrow 6NH_4^+{}_{(aq)} + Mo_7O_{24}^{6-}{}_{(aq)} + 4H_2O$$

$$Mo_7O_{24}^{6-}{}_{(aq)} + 8OH^-{}_{(aq)} \longrightarrow 7MoO_4^{2-}{}_{(aq)} + 4H_2O$$

$$Zn(NO_3)_2 \cdot 6H_2O_{(s)} \longrightarrow Zn^{2+}{}_{(aq)} + 2NO_3^{2-}{}_{(aq)} + 6H_2O$$

$$Zn^{2+}{}_{(aq)} + MoO_4^{2-}{}_{(aq)} + 0.8H_2O \longrightarrow ZnMoO_4 \cdot 0.8H_2O_{(s)}$$

$$ZnMoO_4 \cdot 0.8H_2O \longrightarrow \beta\text{-}ZnMoO_{4\,(s)} + 0.8H_2O$$

$$Zn^{2+}{}_{(aq)} + MoO_4^{2-}{}_{(aq)} \longrightarrow \alpha\text{-}ZnMoO_{4\,(s)}$$

Calculated lattice parameters are shown in Table 2. They are very close to those of the corresponding JCPDS database nos. 35-0765 for α-$ZnMoO_4$, 25-1024 for β-$ZnMoO_4$ and 25-1025 for $ZnMoO_4 \cdot 0.8H_2O$ crystalline phases [11].

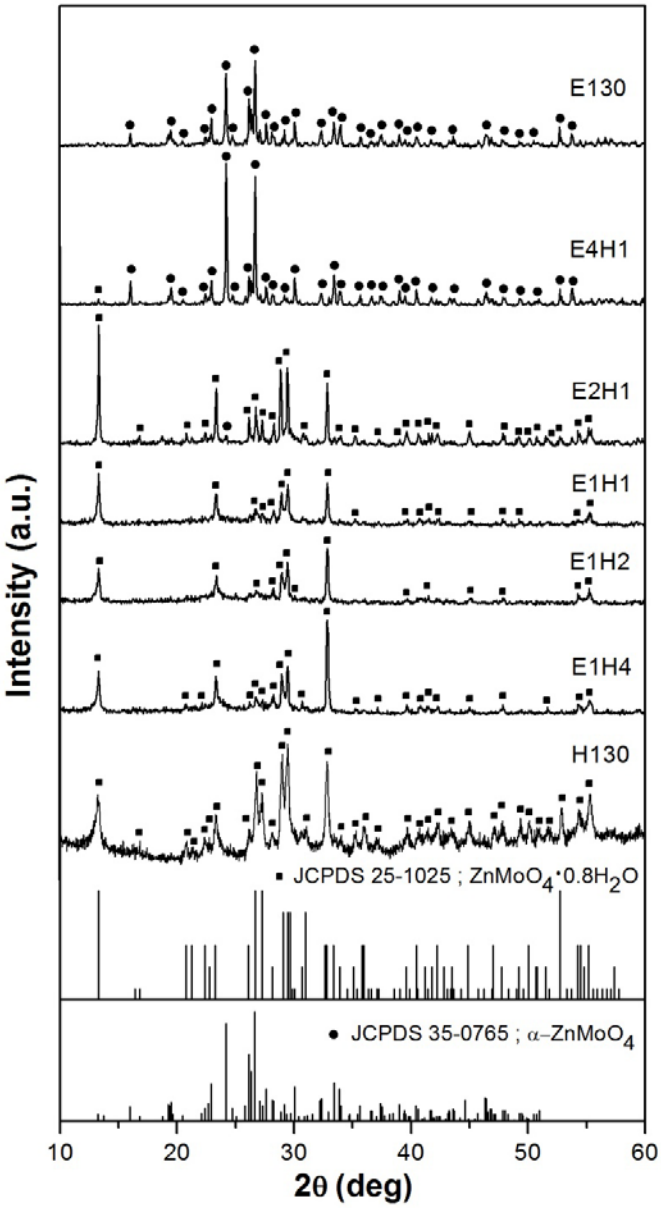

E130
E4H1
E2H1
E1H1
E1H2
E1H4
H130
▪ JCPDS 25-1025 ; ZnMoO4·0.8H2O
● JCPDS 35-0765 ; α–ZnMoO4
Intensity (a.u.)
10
20
30
40
50
60
2θ (deg)

Fig. 1 XRD patterns of the H130, E1H4, E1H2, E1H1, E2H1, E4H1 and E130 samples synthesized in 0:1, 1:4, 1:2, 1:1, 2:1, 4:1 and 1:0 volume ratios of EG:H_2O medium solvents for 30 min.

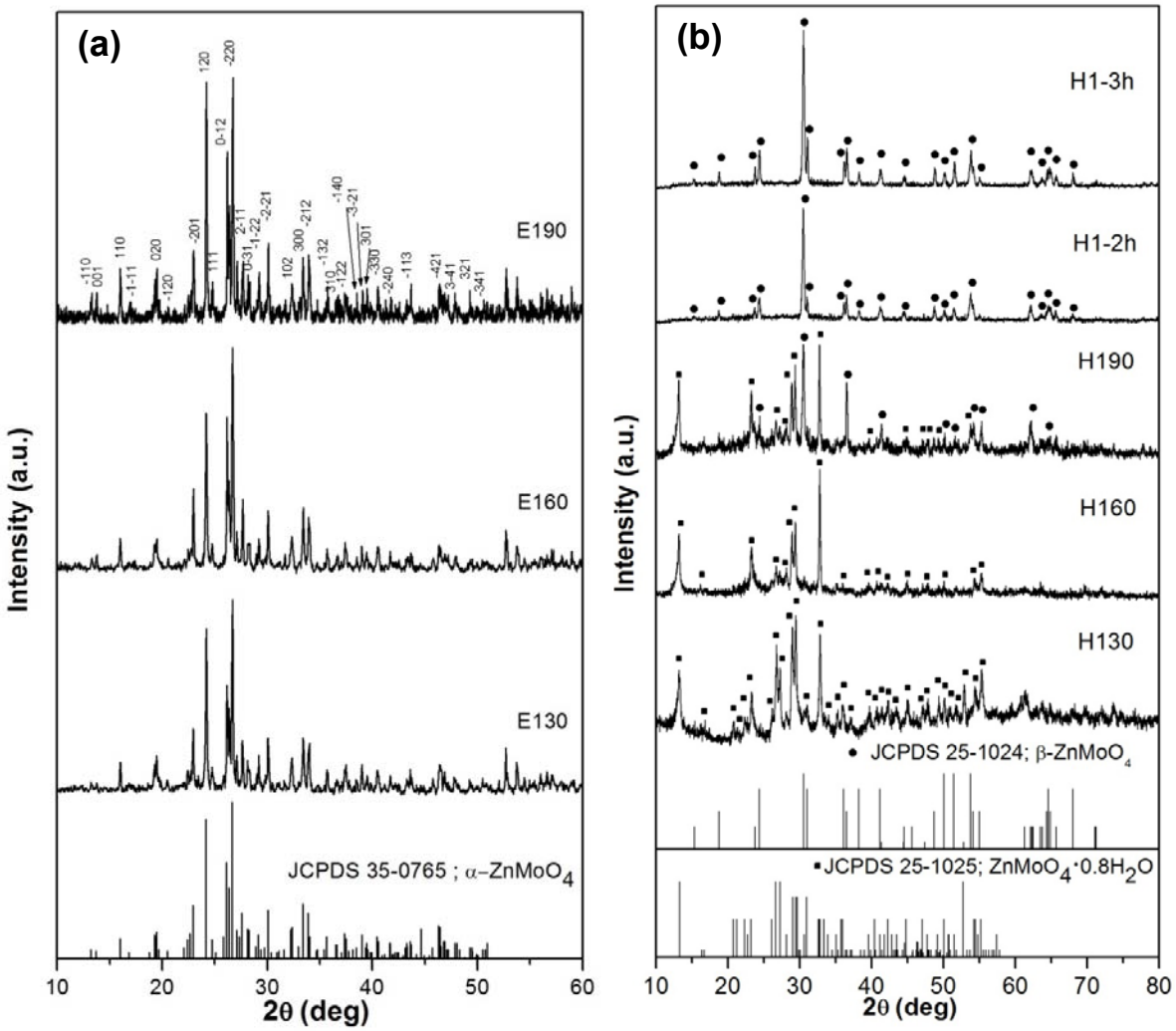


Fig. 2 XRD patterns of (a) the E130, E160 and E190 samples synthesized in pure EG for 30, 60 and 90 min; and (b) the H130, H160, H190, H1-2h and H1-3h samples synthesized in pure water for 30, 60, 90, 120 and 180 min, respectively.

Table 2. Comparing lattice parameters of $ZnMoO_4$ of different crystalline phases and those of the JCPDS database [11].

Sample	a	b	c	α	β	γ
$ZnMoO_4 \cdot 0.8H_2O$	10.2900	6.9100	6.9300	105.2300	117.7300	84.7500
H130	10.26174	6.89071	6.93312	105.18247	117.72608	84.71806
β-$ZnMoO_4$	4.7040	5.7540	4.9120	90.0000	90.1000	90.0000
H1-2h	4.81218	5.72650	4.92777		91.32811	
α-$ZnMoO_4$	8.3678	9.6916	6.9643	106.8720	101.7260	96.7340
E130	8.36447	9.68410	6.97094	106.80965	101.78322	96.72792

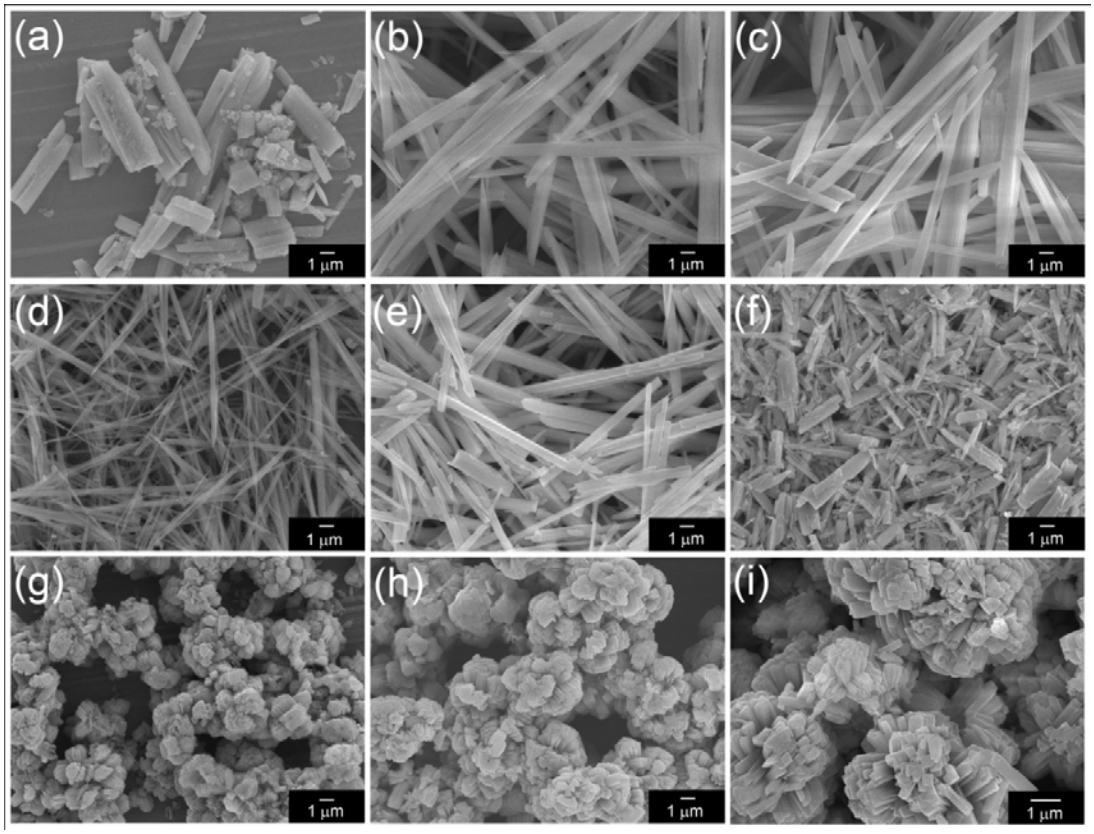


Fig. 3 SEM images of $ZnMoO_4$ synthesized in medium solvents of different EG:H_2O ratios: (a) H130, (b) E1H4, (c) E1H2, (d) E1H1, I E2H1, (f) E4H1 and (g) E130 for 30 min; (h) E160 for 60 min; and (i) E190 for 90 min.

SEM, TEM and SAED

Fig. 3. SEM images of $ZnMoO_4$ synthesized in the solvents of different EG:H_2O ratios for different lengths of reaction time. It can be seen that the sample H130 (Fig. 3a) which was synthesized in pure H_2O solvent for 30 min reaction time shows an irregularity in shape and size with the crystallite size of much larger than 1 μm. When the medium solvent was the mixture of EG and H_2O, rod-shaped particles began to show up. The samples of E4H1 (Fig. 3b) and E1H2 (Fig. 3c) had the same crystal size with the width of 0.6–2.4 μm range. For the EG:H_2O volume ratio of 1:1 (E1H1), the sample (Fig. 3d) formed as a rod-like structure with smaller in diameter of 0.1–0.6 μm, including the majority of the crystals had exceeded 6.0–11.5 μm in length. Due to the viscosity of EG (η = 21 mPa.s, 20 ^{o}C) is much higher than that of water (η =

1.0087x10^{-3} mPa.s, 20 ^{o}C) [12], the diffusion rate of ions in the EG:H_2O medium is significantly reduced. In this case, the quantity of EG can play the role in inhibiting the growth of anisotropic superstructures. The $ZnMoO_4$ side-walls were capped by hydroxyl groups of the solvent. The effect of hydrogen bonds between hydroxyl groups may exist as long chains and acted as a soft template, leading to the growth in the shape of rods. Upon further increasing in the EG volume (EG:H_2O = 2:1 by volume), $ZnMoO_4$ rods increased in diameter again (Fig. 3e) but decreased in length when the EG is much more than H_2O (EG:H_2O = 4:1 by volume, Fig. 3f). In the present case, the high concentration of EG in the medium solution has a tendency to limit the growth of particles. The adsorption and desorption processes on the surface of $ZnMoO_4$ particles were not well-controlled during microwaving, thus short rod-like particles originated. Fig. 3g–I shows the morphology of the E130, E160, E190 samples which were synthesized in pure EG solvent for 30, 60 and 90 min, respectively. All of them have the shape of flowers. The products were composed of a number of rod-like clusters and crystal size became much larger when the reaction time was lengthened. In this case, the high viscosity of EG is able to modify the mobility of the primary particles in suspension as well as their effective collision rates. Moreover, the predominance of EG in the solution has a higher viscosity as compared to that of water [13] and can limit the growth process, causing the reduction of the particle size and leading to the aggregation of particles in the shape of flowers.

The explanation shows that the medium solvents can play an important role in controlling the sample shapes. A polar solvent, which has permanent dipole moment, has relaxation process in microwave region. Thus it is a good candidate in the synthetic process. The dielectric constant of water at 25 ^{o}C is 78.4 and larger than ethylene glycol (dielectric constant at 25 ^{o}C = 40.3) [14]. These properties can be considered as the key factor to promote rapid heating to high temperature within a very short time. It can be seen that the sample obtained after 30 min reaction time in water solvent (H130) has irregular shape because of the more rapid rate of aggregation. When the reaction time

was increased to 60 min and the medium solvent was pure water (H160), the structure was in the shape of micro-size rods with a very high aspect ratio, 1.42 ± 0.45 μm in width and about 14.85–61.83 μm in length (Fig. 4a).

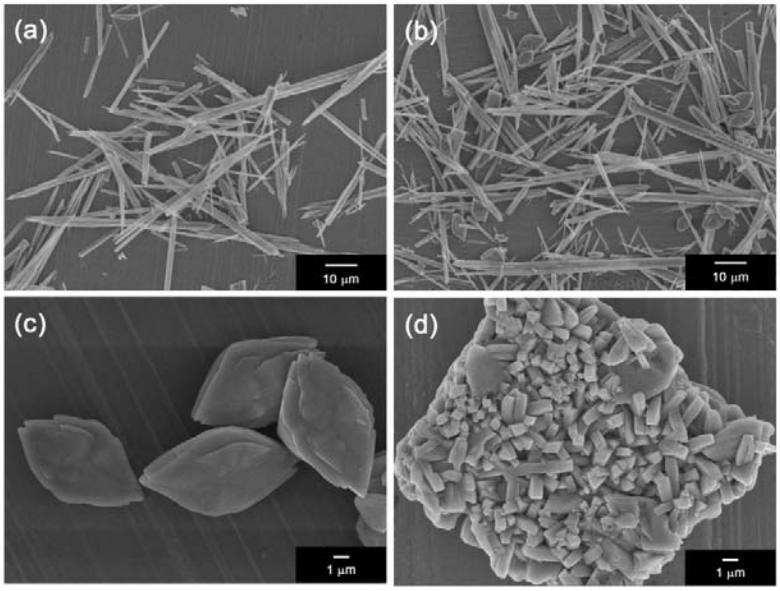


Fig. 4 SEM images of $ZnMoO_4$ synthesized in H_2O as a solvent for different lengths of reaction time: (a) H160 (60 min), (b) H190 (90 min), (c) H1-2h (2 h) and (d) H1-3h (3 h).

It can be seen that the H190 sample of Fig. 4b is composed of rod-shaped particles. The crystalline morphology of β-$ZnMoO_4$ obtained after 2 h reaction time is shown in Fig. 4c (H1-2h sample). Clearly, the rod-shape was no longer detected but the rugby-shaped $ZnMoO_4$ originated instead. By increasing the reaction time to 3 h (Fig. 4d), the agglomeration of rugby-shaped and rod-like particles clustered together as squares (H1-3h). Possibly, the crystallites can be nucleated and grew with the prolonged time.

Fig. 5 shows TEM and HRTEM images, and SAED and simulated patterns of the samples with different morphologies which were synthesized in different medium solvents. In medium solvent of EG:H_2O of 1:1 (E1H1), the sample was composed of nanorods (Fig. 5a). HRTEM images (Fig. 5b and c) show a nanorod which was single crystal and composed of a number of atoms in lattice arrays. Its growth was parallel to the (-220) plane of the single crystalline nanorod. Fig. 5d and g shows $ZnMoO_4$

morphologies in the shape of a flower and rugby, which were synthesized in EG (E130) and H_2O (H1-2h) as solvents, respectively. SAED patterns (Fig. 5e and h) of the samples appear as periodic arrays of bright spots, caused by electron diffraction through the crystallographic planes of single crystal. The calculated angles between any pairs of the directions belonging to these planes, and interplanar spaces determined from (h k l) are in accordance with those of the diffraction patterns on the films. The pattern of Fig. 5e corresponds to the (001), (201) and (200) planes of triclinic α-$ZnMoO_4$ with P-1 space group (JCPDS no. 35-0765) and of Fig. 5h corresponds to the (010), (110) and (100) planes of monoclinic β-$ZnMoO_4$ with P2-c space group (JCPDS no. 25-1024) [11]. Diffraction patterns with the [020] and [00-1] zone axis were simulated in Fig. 5f and I, respectively. The simulated spots with the specified crystallographic planes are in systematic and symmetric arrays, which are identified the existence of the patterns obtained by interpretation.

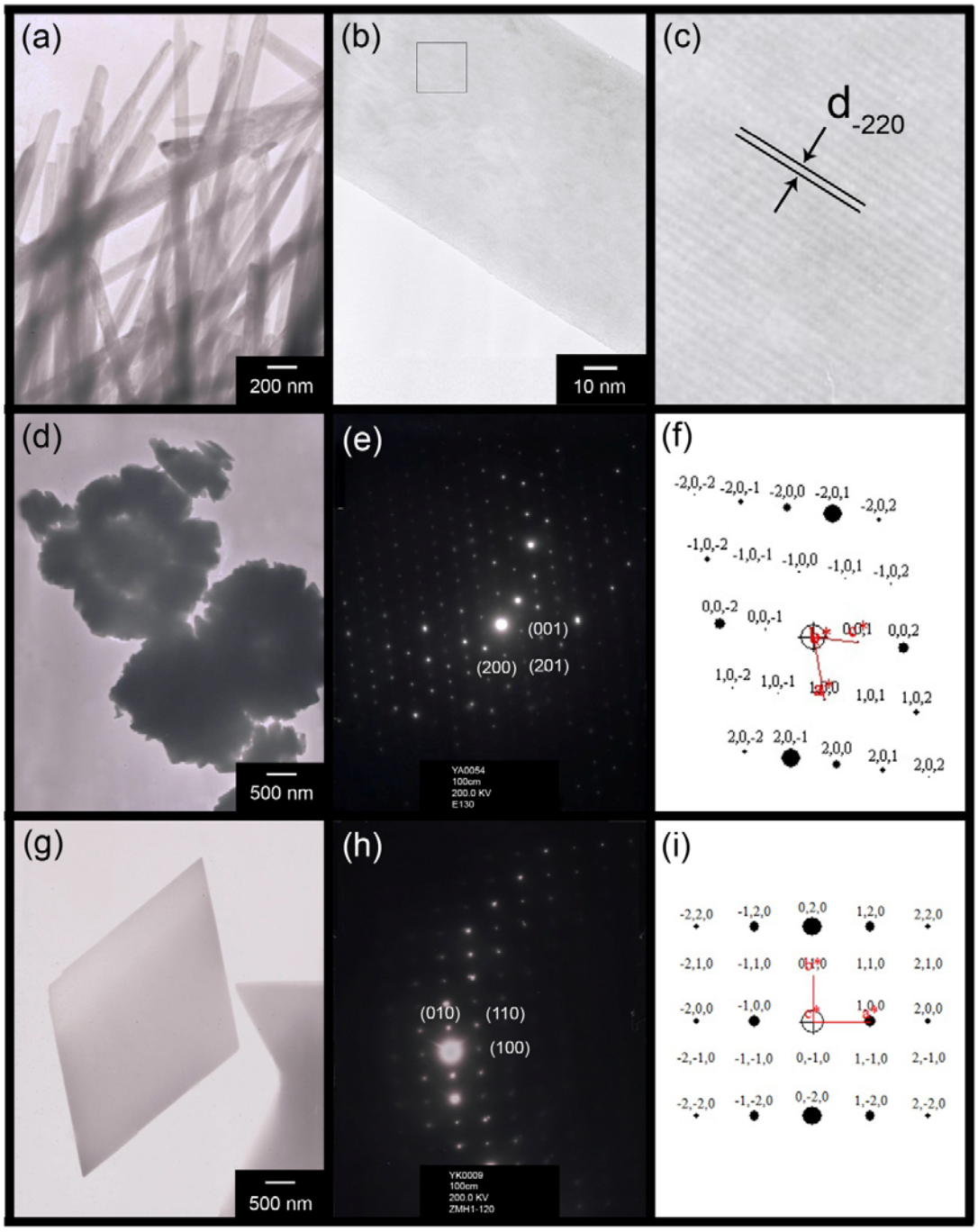


Fig. 5 TEM and HRTEM images, and SAED and simulated patterns of $ZnMoO_4$ particles synthesized in different medium solvents: (a)–(c) $ZnMoO_4 \cdot 0.8H_2O$ (E1H1), (d)–(f) α-$ZnMoO_4$ (E130), and (g)–(i) β-$ZnMoO_4$ (E1-2h).

Raman and FTIR analyses

Naturally, $ZnMoO_4$ was found in two different types of crystalline phase: α-triclinic and β-monoclinic. For the α-$ZnMoO_4$ triclinic structure, all zinc atoms are bonded to six oxygen atoms, forming the distorted octahedral [ZnO_6] units. The molybdenum atoms are coordinated to four oxygen atoms, resulting in the tetrahedral [MoO_4] units [15]. On the other hand, the β-$ZnMoO_4$ monoclinic structure has both Zn and Mo atoms bonded to six oxygen atoms, which promote the origin of distorted octahedral [ZnO_6]/[MoO_6] units, respectively [16].

Monoclinic β-$ZnMoO_4$ crystal has a wolframite-type structure belonging to the P2/c space group. Group theory calculation and symmetry of molybdate and tungstate crystals with a wolframite-type monoclinic structure present 3N = 36 degrees of freedom [17,18] show 36 distinct vibrational modes (Raman and infrared (IR)): $8A_g + 10B_g + 8A_u + 10B_u$ at the center (□) of Brillouin zone. Only A_g and B_g are Raman-active modes. Thus, only 18 active vibrational modes are expected in Raman spectra of β-$ZnMoO_4$ crystal ($8A_g + 10B_g$) [18]. Fig. 6 shows the Raman spectra of β-$ZnMoO_4$ microcrystals (H1-2h) synthesized by using water as a solvent for 2 h. The main Raman (A_g) mode with the strongest intensity peak at around 873 cm^{-1} is assigned to the symmetric stretching bonds of O–Mo–O. Two Raman (A_g and B_g) modes at approximately 773 cm^{-1} and 695 cm^{-1} are assigned to the asymmetric stretching bonds of O–Mo–O [18, 19].

The α-$ZnMoO_4$ crystal presents a triclinic structure with P_1 space group and C_1s point group symmetry [15, 18], and $ZnMoO_4 \cdot 0.8H_2O$ is the Anorthic crystalline phase. The strongest intensity peaks at 963 cm^{-1}, 946 cm^{-1} and 945 cm^{-1} were respectively detected in the samples of E130, E1H1 and H130, corresponding to the previous reports [20–22]. The α-$ZnMoO_4$ triclinic structure, metal molybdate has $[MoO_4]^{2-}$ molecular ionic groups with strong covalent Mo–O bonding. Their Raman vibrations are classified into two types, the internal and external modes. The first is caused by the oscillation inside the $[MoO_4]^{2-}$ molecular ionic groups with immobile mass center. The second is the lattice phonon vibration due to the motion of M^{2+} cations w.r.t the rigid molecular ionic units

[23]. There are no bridging Mo–O–Mo bonds between MoO_4 units, indicated as isolated $(MoO_4)^{2-}$ tetrahedral units. The crystals contained both ZnO_5 and ZnO_6 polyhedrons, deformed by the Jahn-Teller effect. Commonly, there was single-corner sharing of ZnO_5/ZnO_6 and MoO_4 with a number of Zn–O–Zn and Zn–O–Mo linkages inside, leading to the sharp peaks caused by Mo^{6+} bonding of isolated MoO_4 tetrahedrons [21].

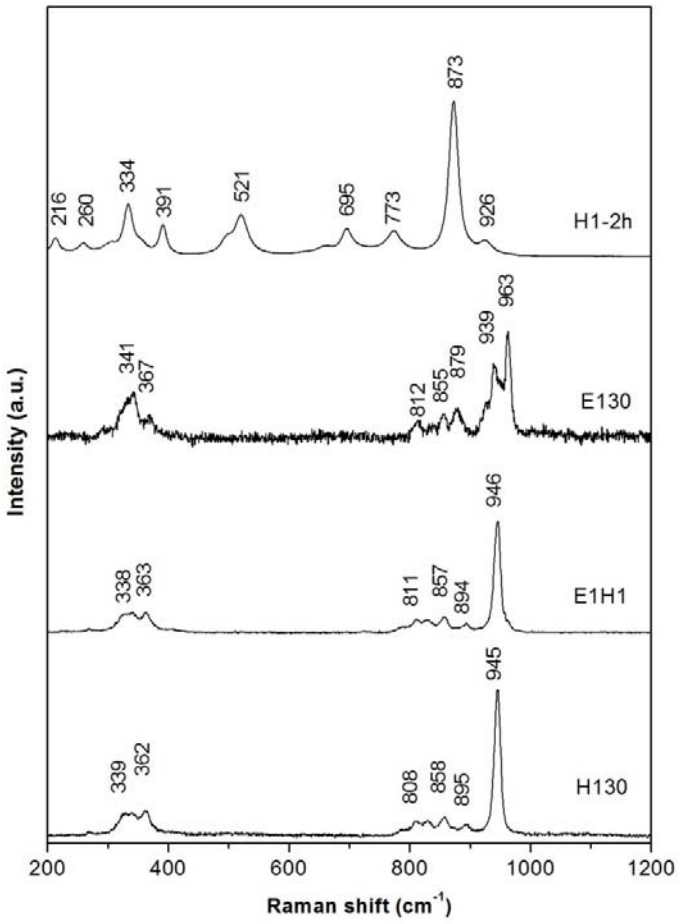


Fig. 6 Raman spectra of $ZnMoO_4$ (H130, E1H1, E130 and H1-2h) synthesized in different medium solvents.

FTIR spectra synthesized in different medium solvent and crystalline phase are showed in Fig. 7. The spectra of the samples prepared in H_2O (H130), EG:H_2O of 1:1 ratio (E1H1) with $ZnMoO_4 \cdot 0.8H_2O$ phase, and EG (E130) with α-$ZnMoO_4$ crystalline

phase contain the same wavenumbers at 964, 863, 745 and 409 cm^{-1}. Those were specified as the V_1 stretching of Mo–O in bridging Mo–O–Mo linkages, the V_1 stretching of $(MoO_4)^{2-}$ tetrahedrons, the V_3 stretching of Mo–O, and the V_4 Mo–O bending mode, respectively [20, 25]. When H_2O was used as a medium solvent for 2 h reaction time with the formation of β-$ZnMoO_4$ monoclinic structure (H1-2h), the bands shifted to 829, 654, 516 and 409 cm^{-1}, corresponding to the A_u mode assigned to the O–Mo–O symmetric stretching of the distorted octahedral [MoO_6] units, an A_u mode with distorted octahedral [MoO_6] units assigned as an anti-symmetric stretching, A_u mode related to the anti-asymmetric stretching of the distorted octahedral [MoO_6]-[MoO_6] units in a chain, and the A_u mode ascribed to an O–Zn–O anti-symmetric stretching of distorted octahedral [ZnO_6] units, respectively [18].

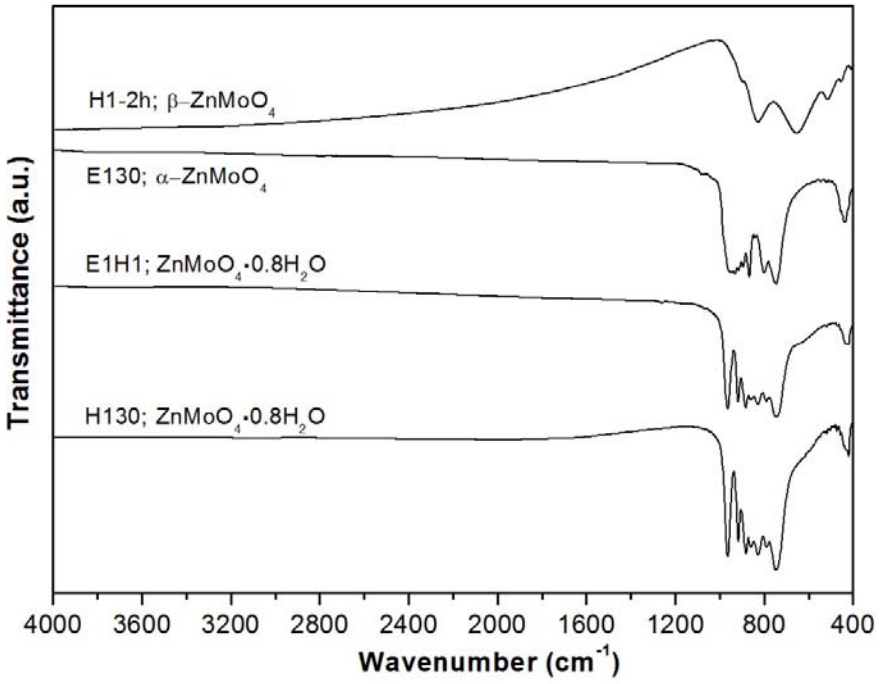


Fig. 7 FTIR spectra of $ZnMoO_4$ (H130, E1H1, E130 and H1-2h) synthesized in different EG:H_2O medium solvent ratios.

UV-visible and PL analyses

UV-visible absorption of the H130, E1H1, E130 and H1-2h samples are shown in Fig. 8, which indicated an exponential decreasing of the photonic absorbance attenuated through the materials. For crystalline semiconductors, the UV absorption near band edge follows the equation.

$$\alpha h\nu = (h\nu - E_g)^n$$

, where α, h, ν, and E_g are the absorbance, Planck constant, photon frequency and photonic energy band gap, respectively. The parameter n is a pure number associated with the different types of electronic transitions: n = ½, 2, 3/2 or 3 for direct-allowed, indirect allowed, direct-forbidden and indirect-forbidden transitions, respectively [18, 24].

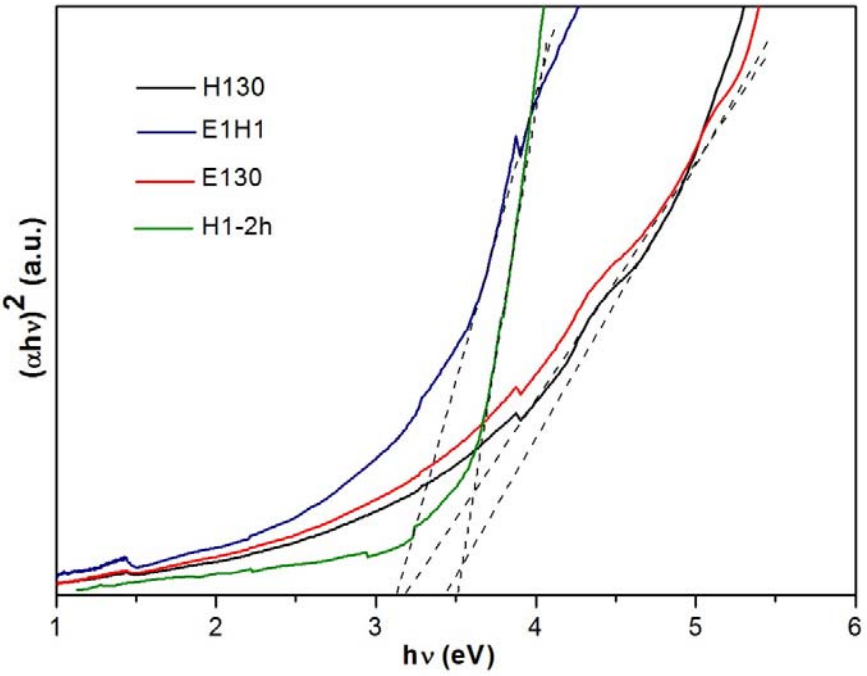


Fig. 8 UV-visible absorption of $ZnMoO_4$ (H130, E1H1, E130 and H1-2h) synthesized in different medium solvents.

The direct E_g was determined by extrapolating the linear portion of the curve to zero absorption to be 3.13–3.51 eV — very close to that for $xMoO_3$-(1-x)ZnO [25] and $ZnMoO_4$ nanofibers of the previous report [20], but less than that estimated for perfect $ZnMoO_4$ [26].

By using a 280 nm excitation wavelength, the PL emission peaks of the H130, E1H1, E130 and H1-2h samples (Fig. 9) presented broad bands over the 320-600 nm range with a strong blue emission peaks centered at the same wavelengths of 366 nm due to the transitions between Mo_{4d} and O_{2p} states — in accordance with other reports [2, 20]. In the present research, the PL emission was in the same range as the direct E_g, relating to the direct transition in the crystals.

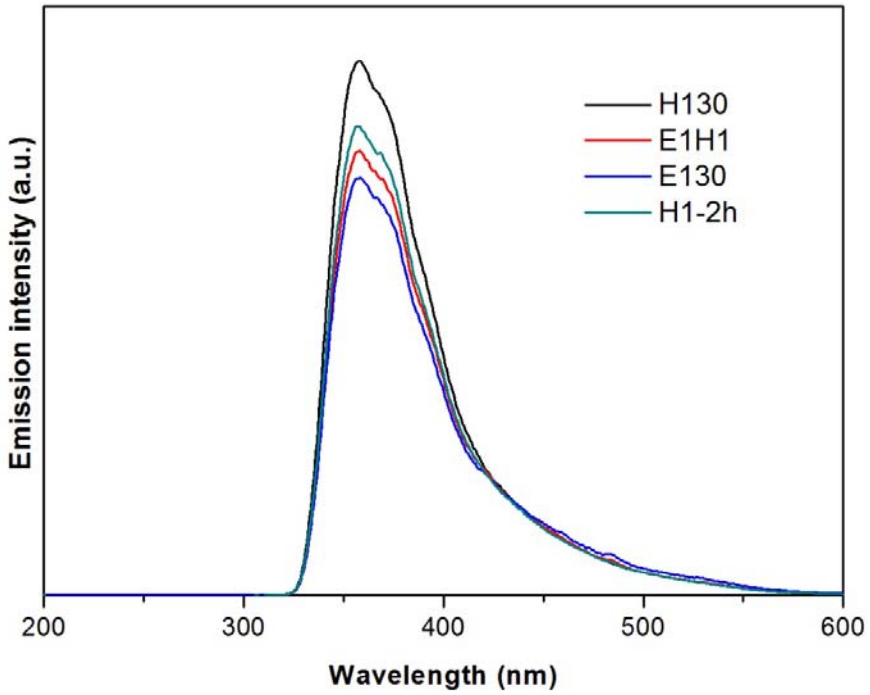


Fig. 9 PL spectra of $ZnMoO_4$ (H130, E1H1, E130 and H1-2h) synthesized in different EG:H_2O medium solvent ratios.

Conclusions

α-$ZnMoO_4$, β-$ZnMoO_4$ and $ZnMoO_4 \cdot 0.8H_2O$ crystals were successfully synthesized by hydrothermal/solvothermal method with different EG:H_2O solvent ratios. SEM and TEM show the as-synthesized $ZnMoO_4$ with different morphologies (rod, rugby and flower). Vibration wavenumbers provided the evidence of different crystalline phases of $ZnMoO_4$. The optical band gap values of the samples are approximately 3.13–3.51 eV and PL emission shows the peaks at 366 nm.

References

[1] G.K. Choi, J.R. Kim, S.H. Yoon, K.S. Hong. Microwave dielectric properties of scheelite (A = Ca, Sr, Ba) and wolframite (A = Mg, Zn, Mn) $AmoO_4$ compounds. J Eur. Ceram. Soc. 27 (2007) 3063–3067.

[2] J.H. Ryu, S.M. Koo, J.W. Yoon, C.S. Lim, K.B. Shim. Synthesis of nanocrystalline $MmoO_4$ (M=Ni, Zn) phosphors via a citrate complex route assisted by microwave irradiation and their photoluminescence. Mater Lett. 60 (2006) 1702–1705.

[3] G. Zhang, S. Yu, Y. Yang, W. Jiang, S. Zhang, B. Huang. Synthesis, morphology and phase transition of the zinc molybdates $ZnMoO_4 \cdot 0.8H_2O$/α-$ZnMoO_4$/$ZnMoO_4$ by hydrothermal method. J Cryst Growth. 312 (2010) 1866–1874.

[4] Y. Li, G. Weisheng, B. Bo, G. Kaijie. Yeast-directed hydrothermal synthesis of $ZnMoO_4$ hollow microspheres and its photocatalytic degradation of auramine O. 2009 Internat Conf Energy Environm Tech. IEEE; 2009, doi:10.1109/ICEET.2009.631

.[5] A.M. Dubovik, Y.Y. Vostretsov, B.V. Grinyov, F.A. Danevich, H. Kraus, L.L. Nagornaya, et al. Research and development of $ZnBO_4$ (B = W, Mo) crystal scintillators for dark matter and double beta decay searching. Acta Phys Pol A. 117 (2010) 15–19.

[6] Y.R. Jiang, W.W. Lee, K.T. Chen, M.C. Wang, K.H. Chang, C.C. Chen. Hydrothermal synthesis of β-$ZnMoO_4$ crystals and their photocatalytic degradation of Victoria Blue R and phenol. J. TaiwanInst.Chem.Eng. (2013), http://dx.doi.org/10.1016/j.jtice.2013.05.007.

[7] L.S. Cavalcante, J.C. Sczancoski, M. Siu Li, E. Longo, J.A. Varela. B-$ZnMoO_4$ microcrystals synthesized by the surfactant-assisted hydrothermal. Colloids and Surfaces A. 396 (2012) 346–351.

[8] M. L. Moreira, G. P. Mambrini, D. P. Volanti, E. R. Leite, M.O. Orlandi, P.S. Pizani, V. R. Mastelaro, C. O. Paiva-Santos, E. Longo, and J. A. Varela. Hydrothermal Microwave: A New Route to Obtain Photoluminescent Crystalline $BaTiO_3$ Nanoparticles. Chem. Mater. 20 (2008) 5381–5387.

[9] S. Komarneni, R. Pidugu, Q. H. Li and R. Roy. Microwave-hydrothermal processing of metal powders. J. Mater. Res. 10 (1995) 1687–1692.

[10] S. Komarneni. Nanophase materials by hydrothermal, microwave-hydrothermal and microwave-solvothermal methods. Current Sci. 85 (2003) 1730–1734.

[11] Powder Diffract. File, JCPDS-ICDD, 12 Campus Boulevard, Newtown Square, PA 19073-3273, U.S.A. 2001.

[12] F. Teng, S. Santhanagopalan, R. Lemmens, X. Geng, P. Patel, D. D. Meng. In situ growth of $LiFePO_4$ nanorod arrays under hydrothermal condition. Solid State Sciences (2010) doi:10.1016/j.solidstatesciences.2010.02.017.

[13] V. S. Marques, L. S. Cavalcante, J. C. Sczancoski, A. F. P. Alcantara, M. O. Orlandi, E. Moraes, E. Longo, J. A. Varela, M. Siu Li, and M. R. M. C. Santos. Effect of Different Solvent Ratios (Water/Ethylene Glycol) on the Growth Process of $CaMoO_4$ Crystals and Their Optical. J Cryst Growth. 10 (2010) 4752–4762.

[14] T. Thongtem, A Phuruangrat, S Thongtem. Preparation and characterization of nanocrystalline $SrWO_4$ using cyclic microwave radiation. Curr. Appl. Phys. 8 (2008) 189–197.

[15] W. Reichelt, T. Weber, T. Sohnel and S. Dabritz. Mischkristallbildung im System $CuMoO_4/ZnMoO_4$. Z. Anorg. Allg. Chem. 626 (2000) 2020–2027.

[16] K.Pavani, A. Ramanan. Influence of 2-Aminopyridine on the Formation of Molybdates under Hydrothermal Conditions. Eur. J. Inorg. Chem. (2005) 3080–3087.

[17] L. H. Hoang, N. T. M. Hien, W. S. Choi, Y. S. Lee, K. Taniguchi, T. Arima, S. Yoon, X. B. Chena and I. S. Yang. Temperature-dependent Raman scattering study of multiferroic $MnWO_4$. J. Raman Spectrosc. 41 (2010) 1005–1010.

[18] L.S. Cavalcante, E. Moraes, M.A.P. Almeida, C.J. Dalmaschio, N.C. Batista, J.A. Varela, E. Longo, M. Siu Li, J. Andres, A. Beltran. A combined theoretical and experimental study of electronic structure and optical properties of □-$ZnMoO_4$. Polyhedron. 54 (2013) 13–25.

[19] M. Markova-Velichkova, R. Iordanova, Y. Dimitriev. Glass formation in the V_2O_5-MoO_3-ZnO system. Phys. Status Solidi C. 8 (2011) 3159.

[20] Y. Keereeta, T. Thongtem, S. Thongtem. Characterization of $ZnMoO_4$ nanofibers synthesized by electrospinning-calcination combinations. Mater Lett. 68 (2012) 265–268.

[21] L. Aleksandrov, T. Komatsu, R. Iordanova, Y. Dimitriev. Structure study of MoO_3-ZnO-B_2O_3 glasses by Raman spectroscopy and formation of α-$ZnMoO_4$ nanocrystals. Optical Materials. 33 (2011) 839–845.

[22] J. Šubcik, L. Koudelka, P. Mošner, L. Montagne, B. Revel, I. Gregora. Structure and properties of MoO_3-containing zinc borophosphate glasses. J. Non-Cryst. Solids. 355 (2009) 970–975.

[23] A. Phuruangrat, T. Thongtem, S. Thongtem. Preparation, characterization and photoluminescence of nanocrystalline calcium molybdate. J. Alloys Compd. 481 (2009) 568–572.

[24] Y. Keereeta, T. Thongtem, S. Thongtem. Fabrication of $ZnWO_4$ nanofibers by a high direct voltage electrospinning process. J. Alloys Compd. 509 (2011) 6689–6695.

[25] Bhattacharya S, Kar T, Bar AK, Roy D, Graca MPF, Valente MA. Structural behaviors and optical properties of semiconducting zinc-molybdate glass nanocomposites. Sci Adv Mater. 3 (2011) 284–288.

[26] Spassky DA, Vasilev AN, Kamenskikh IA, Mikhailin VV, Savon AE, Hizhnyi YA, et al. Electronic structure and luminescence mechanisms in ZnMoO4 crystals. J Phys. 23 (2011) 365501–10.

5. Microwave-assisted synthesis and optical property of $CdMoO_4$ nanoparticles

Abstract

Microwave-assisted synthesis is a novel method used to synthesize $CdMoO_4$ nanoparticles in propylene glycol. The effects of reaction time, and microwave power on phase, morphologies, and optical properties of $CdMoO_4$ nanoparticles were studied, using X-ray diffraction (XRD), Raman spectroscopy, Fourier transform infrared spectroscopy (FTIR), transmission electron microscopy (TEM), and UV-visible spectroscopy. The present analyses proved that these crystalline powders were scheelite-type tetragonal structured $CdMoO_4$, with the crystallite size of 14-20 nm, and 4.51-4.73 eV band gaps, controlled by the synthetic conditions.

Keywords: Cadmium molybdate, Nanoparticles, Scheelite-type structure, UV-visible absorption

Introduction

Metal molybdates and tungstates have two type structures, depending on the size of bivalent cations, - the scheelite (ionic radius > 0.99 Å: Ca, Sr, Ba, Pb) and wolframite (ionic radius < 0.77 Å: Mg, Mn, Fe, Co, Ni, Zn) [1-3]. They have attracted considerable interest for a number of researchers, due to their promising technological importance in a wide range of applications, including photoluminescence, scintillating materials, humidity sensors, photoelectric devices, photonic crystals, light weight filler materials, photocatalysts, and chemical reactors [1-6].

Cadmium molybdate ($CdMoO_4$) is one of metallic molybdate compounds with scheelite structure, and has a body-center orthorhombic primitive cell with C_{4h}^6 space group. Each site of Cd and Mo is surrounded by eight oxygen (octahedron) and four equivalent oxygen (tetrahedron) sites, respectively. The calculation of the electronic structure shows that the Cd_{4d} state localize at the bottom region of the O_{2p} valence band,

and the Cd_{5s} state has a significant contribution to the bottom of the conduction band, composed of the Mo_{4d} state [7]. $CdMoO_4$ is an interesting material owning to its excellent optical and chemical properties, electronic excitation at VUV synchrotron radiation, pressure-induced phase transformations, and ^{111}Cd and ^{113}Cd spin-lattice relaxation. As a wide band gap semiconductor of 3.25 eV, $CdMoO_4$ is expected to be a photocatalyst under UV radiation [5-8].

Recently, there are some reports on the synthesis of $CaMoO_4$. For example, Ma et al. [1] reported the synthesis of $CdMoO_4$ nanoparticles with good crystallization at 90 ^oC for 20 h by a hydrothermal method. It showed the emission peak at 390 nm, using 330 nm excitation wavelength. Liu and Tan [7] synthesized $CdMoO_4$ nanorods by hydrothermal at relatively low temperature, and tested on the electrochemical properties for using as cathode material of lithium rechargeable batteries. Ma et al. [9] showed that the photoluminescence properties of $CdMoO_4$ nanoparticles were controlled by its shape and size, determined by the pH of the solutions. There are some reported on the synthesis of $CdMoO_4$ hollow microspheres composed of nanoparticles by a facile aqueous reaction process without using templates and other additives by Zhen et al. [4], Wang et al. [6], and Zhen et al. [8]. Comparing to the large amount synthesis using microwave radiation, this method has been considered to be a good process for preparation of other metal molybdates and tungstates [2,10-12], due to the convenience of morphology and size controlling, simple and one step synthesis, uniform composition and phase, and large scale synthesis for industrial application.

In the present research, the microwave-assisted synthesis of highly crystalline $CdMoO_4$ nanocrystals with particle size smaller than 50 nm was firstly reported. The effects of reaction time and microwave power on phase, morphologies and optical properties of $CdMoO_4$ nanoparticles were studied, and compared with those of the co-precipitation method.

Experiment

The analytical grade chemicals, such as cadmium (II) nitrate tetrahydrate ($Cd(NO_3)_2 \cdot 4H_2O$, 99.99 %), sodium molybdate 64ehydrate ($Na_2MoO_4 \cdot 2H_2O$, ≥ 99.5 %) and propylene glycol ($C_3H_8O_2$, 99.99 %) were bought from Sigma-Aldrich, and used without further purification.

To synthesize $CdMoO_4$ nanoparticles, each 0.005 mole of $Cd(NO_3)_2 \cdot 4H_2O$ and $Na_2MoO_4 \cdot 2H_2O$ was separately dissolved in 15.00 ml propylene glycol, mixed and stirred for 30 min. Then the solution was transferred into a microwave oven and heated at 20 % (each cycle: the microwave was on for 24 s and off for 96 s) of 180-600 W for 20-60 min. At the completion of the reaction, white powders were produced, collected and washed with distilled water and absolute ethanol, and dried in air at 80 ^{o}C for 24 h.

The products were characterized and recorded on a Philips X'Pert MPD X-ray diffractometer (XRD) equipped by a graphitic monochromator with Cu Kα radiation (λ = 0.154056 nm), using a scanning rate of 0.02 deg/s over the 2θ range of 15° – 60°. FTIR spectra were recorded on Perkin Elmer Spectrum RX FTIR Spectrometer with KBr as a diluting agent and operated in the range of 400-4,000 cm^{-1} with the resolution of 4 cm^{-1}. Raman vibrations of the products were detected by a HORIBA JOBIN YVON T64000 Raman spectrometer with 50 mW and 514.5 nm wavelength Ar laser. Transmission electron microscopic (TEM) images, and selected area electron diffraction (SAED) patterns were taken on a JEOL JEM-2010, employing at an accelerating voltage of 200 kV. UV-visible spectra were carried out by a Lambda 25 spectrometer using UV lamp with the resolution of 1 nm.

Results and discussion

$CdMoO_4$ has scheelite structure with lattice constants of a = 5.1550 Å and c = 11.1940 Å and has $I4_1/a$ or C_{4h}^6 space group. This structure has eight symmetry elements, and a body-centered orthorhombic ($a \neq b \neq c$, $\alpha = \beta = \gamma = 90^{o}$) primitive cell that includes two formula units of $CdMoO_4$. Each Mo site is surrounded by four

equivalent O sites at a bond length of 1.75 Å to form $[MoO_4]^{2-}$ anions in approximately tetrahedral symmetry. Each Cd site is surrounded by eight O sites at bond lengths of 2.40 Å and 2.44 Å in approximately octahedral symmetry. $CdMoO_4$ has strong covalent bonds of Mo–O in $[MoO_4]^{2-}$ molecular ionic units and weak coupling between $[MoO_4]^{2-}$ anions and Cd^{2+} cations [7,11-15].

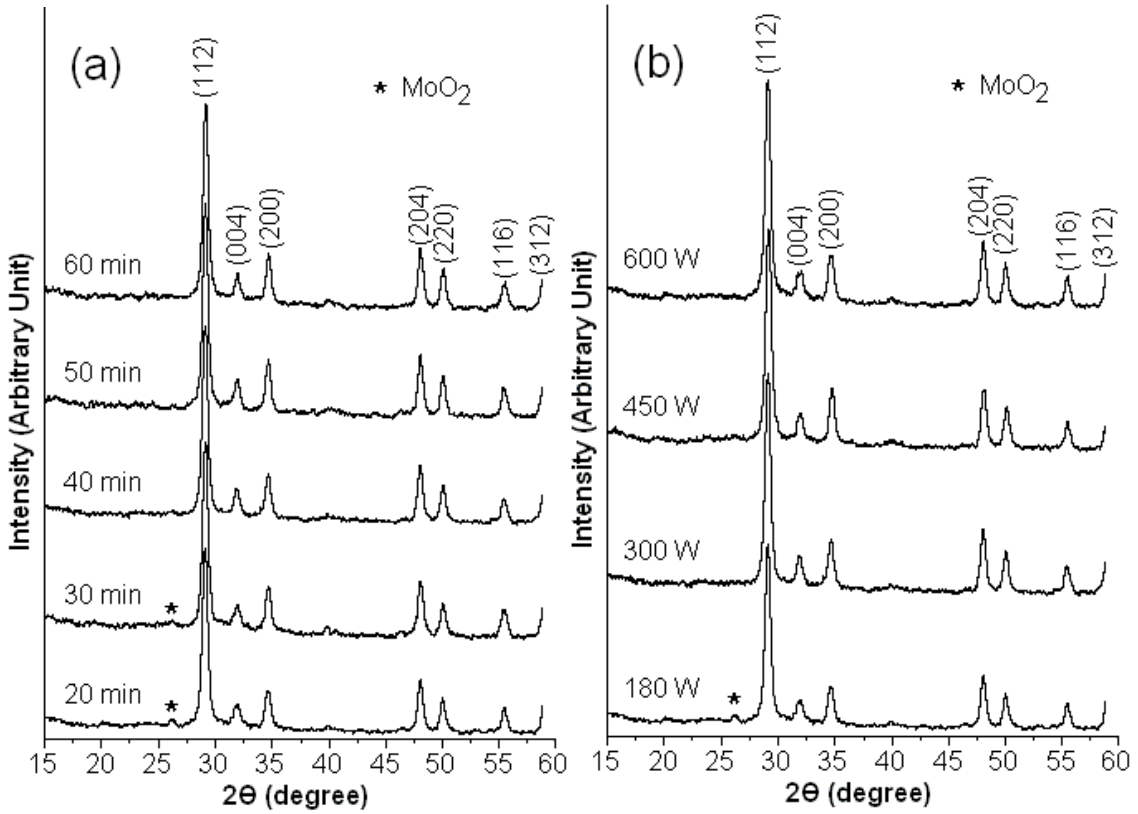


Fig. 1 XRD patterns of $CdMoO_4$ synthesized using a microwave radiation at (a) 180 W for 20-60 min, and (b) 180-600 W for 20 min.

Fig. 1 shows the XRD patterns of the products synthesized at difference microwave radiation powers and lengths of reaction time. For the microwave radiation at 180 W for 20 and 30 min, the products were composed of tetragonal $CdMoO_4$ and MoO_2, comparing to the JCPDS nos. 07-0209 for $CdMoO_4$ (a = b = 5.1550 Å, and c = 11.1940 Å, $\alpha = \beta = \gamma = 90^{\circ}$), and 01-0615 [16] for MoO_2 as the main phase and impurity, respectively. Upon using 180 W microwave radiation and the reaction times of 40, 50,

and 60 min or increasing the microwave radiation power from 180 W to 300, 450 and 600 W with the reaction time remaining at 20 min, the products became the only pure tetragonal $CdMoO_4$ phase with no detection of any impurity. The XRD peaks became stronger and shaper with the increase in the microwave radiation power and length of reaction time, indicating that the crystalline degree of the tetragonal $CdMoO_4$ phase became higher. At 600 W and 20 min, lattice parameters were calculated using the plane spacing equation of tetragonal structure [17] and Bragg's law for diffraction. They were a = b = 5.1619 Å, and c = 11.1952 Å, in accordance with those of the JCPDS database no. 07-0209 [16].

Approximate crystallite sizes (L) of $CdMoO_4$ nanocrystals synthesized under different conditions were calculated from Scherrer formula [17]

$$L = \frac{\lambda k}{B\cos\theta} \qquad (1)$$

where λ, θ, k, and B are the wavelength of Cu-K_α radiation (1.54056 Å), Bragg angles of the (112) planes, a constant (0.89), and full widths at half maximum of the (112) peaks, respectively. Calculated crystallite sizes of $CdMoO_4$ nanocrystals synthesized under microwave radiation power of 180 W for 20, 30, 40, 50 and 60 min are 15.00, 15.24, 15.52, 15.55 and 15.60 nm, and under microwave radiation powers of 300, 450 and 600 W for 20 min are 15.55, 16.18 and 20.20 nm, respectively. The crystallite size increases are 4 % by increasing the length of time from 20 min to 60 min with the microwave power remaining at 180 W, and 35 % by increasing the microwave power from 180 W to 600 W with the length of time remaining at 20 min. These analyses implied that microwave radiation power and length of reaction time played the role in the phase, crystalline degree and crystallite sizes of $CdMoO_4$ nanoparticles. The microwave power had stronger influence on them than the length of reaction time.

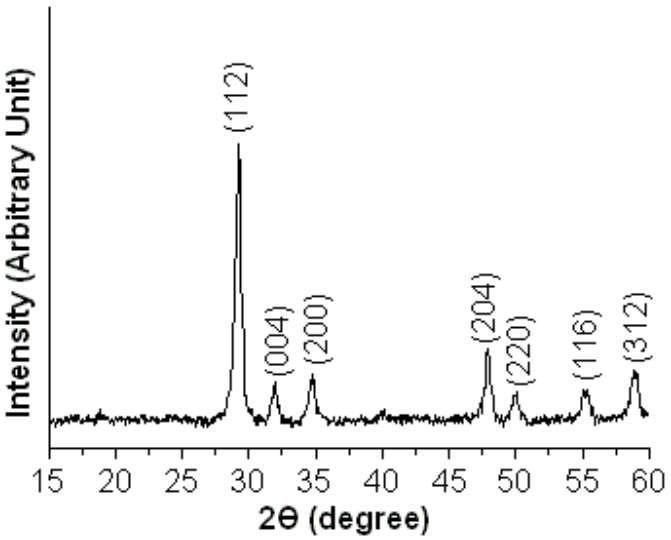


Fig. 2 XRD pattern of $CdMoO_4$ synthesized by co-precipitation method at room temperature for 48 h.

Comparing to the non-microwave radiation method, $Cd(NO_3)_2{\cdot}4H_2O$ and $Na_2MoO_4{\cdot}2H_2O$ as cadmium and molybdate sources were mixed in 30.00 ml propylene glycol. Upon stirring for 24 h, the colorless solution changed into white colloidal solution. The experiment was continued stirring until 48 h completion, and white precipitates were synthesized. After washing and drying, they were characterized by XRD (Fig. 2). The product was identified to be pure tetragonal $CdMoO_4$ phase, comparing to the JCPDS No. 07-0209 [16], but the intensity peaks became lessened. These results proved that the microwave radiation played the role in accelerating the crystalline degree of $CdMoO_4$ powders.

In lattice space, scheelite compounds ($CaMoO_4$, $CaWO_4$, $SrMoO_4$, $SrMoO_4$, etc.) correspond to S_4 symmetry. A group theoretical analysis of the scheelite structure yields 26 lattice modes at the Γ point of Brillouin zone: $3A_g + 5A_u + 5B_g + 3B_u + 5E_g + 5E_u$. The 13 g modes are Raman-active, and the 13 u modes are infrared active ($4A_u$ and $4E_u$), acoustic ($1A_u$ and $1E_u$), and silent ($3B_u$). The Raman active phonon modes can be classified into two types of vibrations, the internal and external modes (rotation and translation) with respect to (w.r.t.) the $[MoO_4]^{2-}$ tetrahedrons. Among them, seven modes

are internal stretching vibrations of $V_1(A_g)$, $V_3(B_g)$ and $V_3(E_g)$, and bending of $V_2(A_g)$, $V_2(B_g)$, $V_4(B_g)$ and $V_4(E_g)$. The six remains are external modes – three rotations, two translations, and an unidentified mode. The internal modes correspond to normal vibrations of the $[MoO_4]^{2-}$ tetrahedrons, while the external modes involve motions of the metallic atoms (e.g. Ca, Sr, Ba and Cd etc.) w.r.t. $[MoO_4]^{2-}$ tetrahedrons [10-12,15,18-20]. It is expected that the frequencies and wavenumbers of the internal stretching modes are higher than those of the external ones, because the internal covalent bonding within the $[MoO_4]^{2-}$ tetrahedrons is stronger than the external lattice binding. Fig. 3a shows Raman spectra of $CdMoO_4$ produced by microwave radiation method under different conditions. They show strong Raman peaks that indicate a strong interaction between the ions, which mainly arise from the stretching and bending vibrations of the shorter metal–oxygen bonds within the anionic groups. All Raman spectra were identified as $V_1(A_g)$, $V_3(B_g)$, $V_3(E_g)$, $V_4(E_g, B_g)$, and $V_2(A_g, B_g)$ at 862, 820, 755, 396 and 309 cm^{-1}, respectively. Three rotation and two translation modes of $[MoO_4]^{2-}$ units were detected at 280, 192, 153, 135 and 102 cm^{-1}, respectively. These results are in accordance with those reported in the literatures [15,20] (Table 1), although their wavenumber vibration modes were not exactly the same values, due to the difference of geometries, particle sizes, and nature of the products.

For T_d-symmetry, the scheelite structure has four vibrations, specified as $V_1(A_1)$, V_2I, $V_3(F_2)$ and $V_4(F_2)$. In lattice space, its IR spectrum is in accordance with the S_4 symmetry. The correlations of the $T_d \leftrightarrow S_4$ symmetries are $A_1 \leftrightarrow A$, $E \leftrightarrow A + B$, and $F_2 \leftrightarrow B + E$. There was no detection of the V_1 mode. Only the V_2, V_3 and V_4 modes were detected. Fig. 3b shows FTIR spectra of $CdMoO_4$ produced by microwave radiation method under different conditions. For the present analysis, a strong transmittance mode specified as Mo-O anti-symmetric stretching vibration (V_3) of $[MoO_4]^{2-}$ tetrahedrons was detected at 743-895 cm^{-1}, and additional weak peak of Mo-O bending mode (V_4) at 423 cm^{-1}. These results are in accordance with those previously reported [10-12].

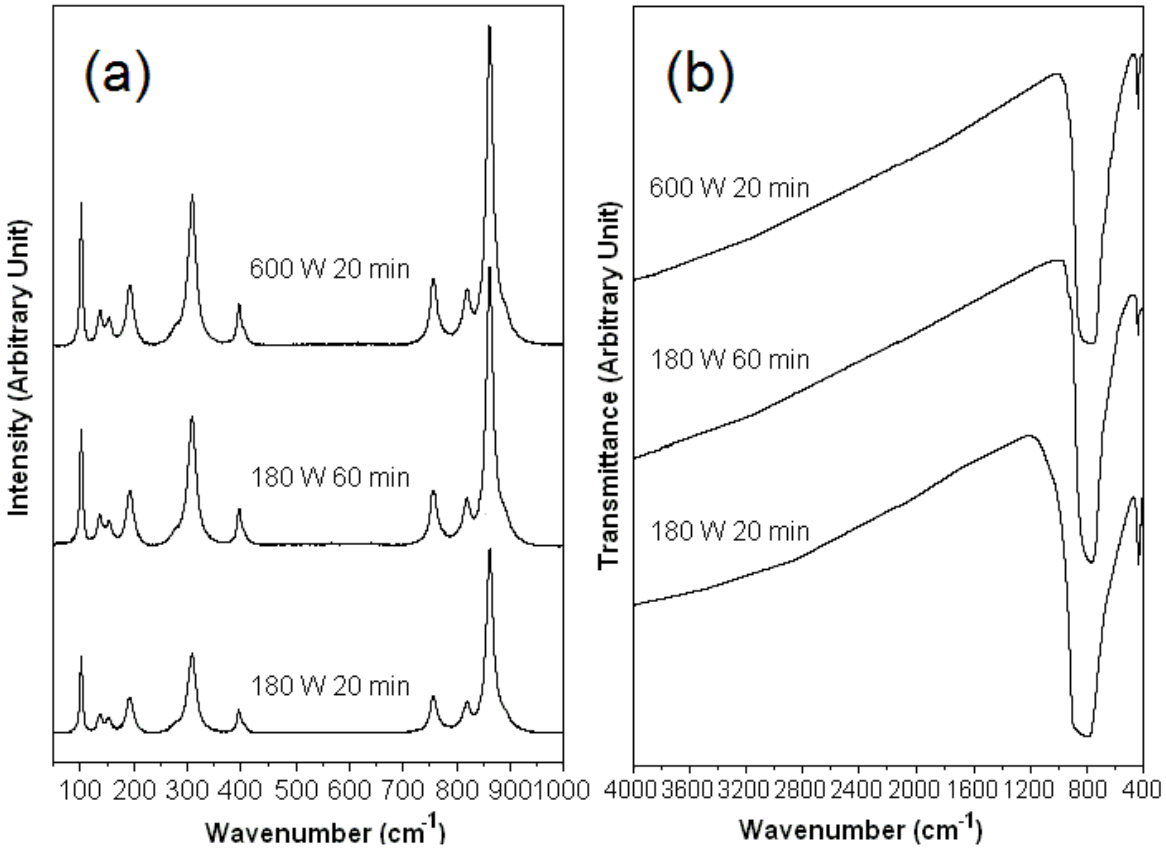


Fig. 3 (a) Raman and (b) FTIR spectra of $CdMoO_4$ synthesized using a microwave radiation at 180 W 20 min, 180 W 60 min, and 600 W 20 min.

Table 1. Raman vibration modes of $CdMoO_4$ obtained from this work and those reported in the literatures. (S = Strong, M = Medium, W = Weak, V = Very, R = Rotation, and T = Translation)

Vibration mode	Raman Intensity	Wavenumber (cm^{-1})		
		This work	Daturi et al. [15]	Jayaraman et al. [20]
$V_1(A_g)$	VS	862	863	867
$V_3(B_g)$	W	820	822	825
$V_3(E_g)$	W	755	759	761
$V_4(E_g, B_g)$	M	396	402	399
	M		396	401
$V_2(A_g, B_g)$	M	309	308	309
R	VW	280	277	282
R	M	192	189	193
R	VW	153	173	154
T	M	135	150	137
	M		135	107
T	S	102	101	103

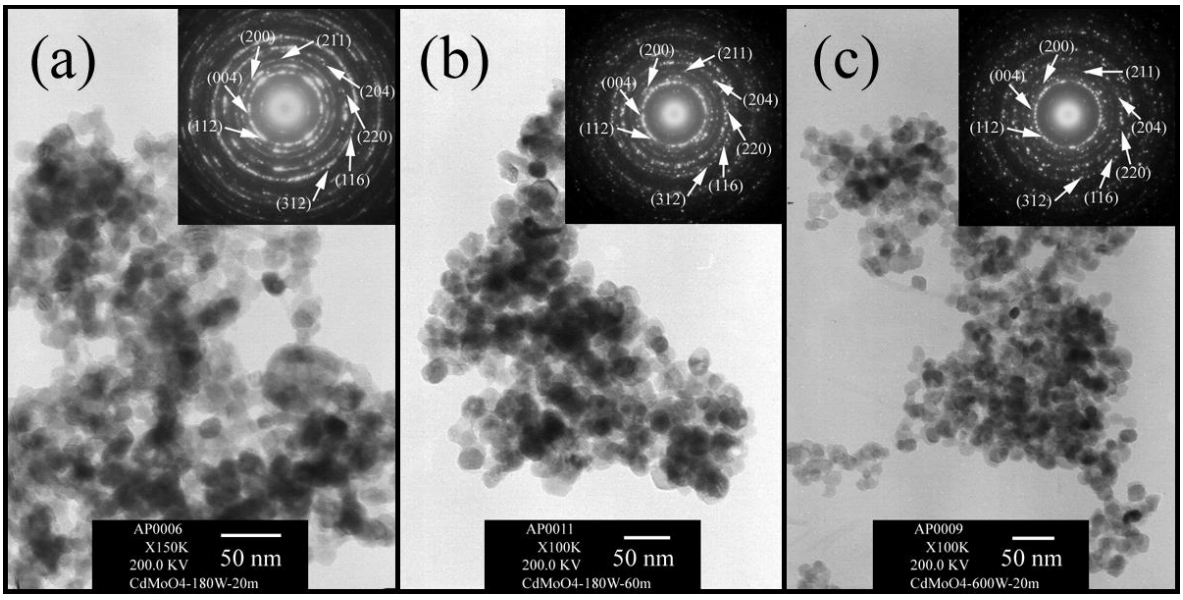


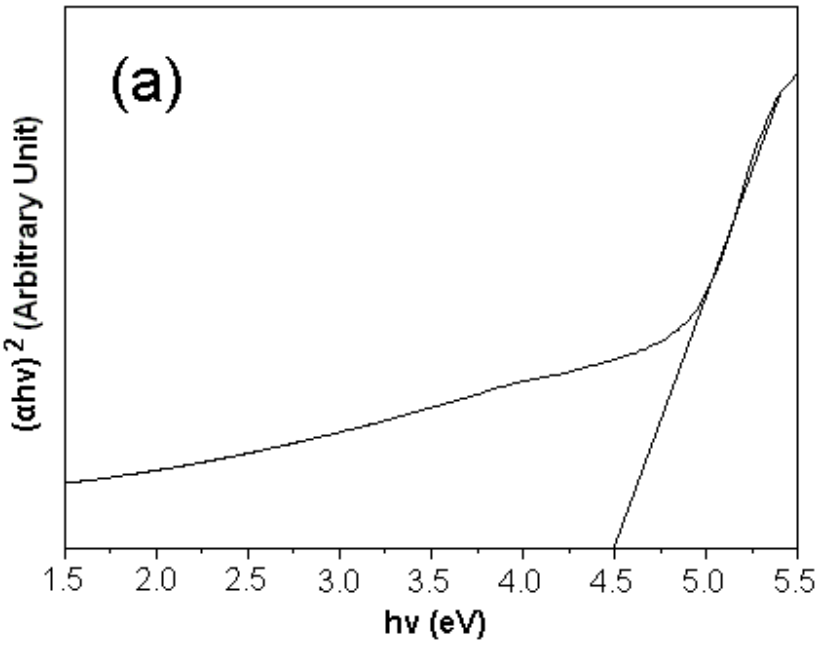
Fig. 4 TEM images and SAED patterns of $CdMoO_4$ synthesized using a microwave radiation at (a) 180 W 20 min, (b) 180 W 60 min, and (c) 600 W 20 min.

TEM images of the $CdMoO_4$ nanocrystallines obtained from different conditions under microwave radiation method are shown in Fig. 4 and their SAED patterns were inserted inside. At 180 W 20 min, the product was composed of clusters of spherical nanoparticles with average particle size and standard deviation of 14.16 ± 2.18 nm. By increasing the reaction time from 20 min to 60 min or microwave power from 180 W to 600 W, the products are perfectly and homogeneously spherical nanoparticles with average particle size of 15.19 ± 1.95 nm at 180 W for 60 min, and 19.99 ± 2.72 nm at 600 W for 20 min. Obviously, the increase of the particle size of $CdMoO_4$ nanoparticles was by increasing in the microwave power and reaction time of the microwave radiation synthetic process. Their SAED patterns show bright fully concentric rings of poly-nanocrystalline $CdMoO_4$ – corresponding to the (112), (004), (200), (211), (204), (220), (116) and (312) planes. It should be noted that the particle sizes of tetragonal $CdMoO_4$ crystallites can be controlled under the microwave radiation process by varying the microwave power and reaction time.

The direct band gap energy (E_g) of $CdMoO_4$ nanoparticles was calculated by Wood and Tauc method [19]. The optical band gap is associated with the absorbance and photon energy by the following equation

$$\alpha h\nu \propto (h\nu - E_g)^2 \qquad (2)$$

where α, h, ν, and E_g are the absorbance, Planck constant, frequency, and optical band gap. The plots of $(\alpha h\nu)^2$ and hv of $CdMoO_4$ nanoparticles at 180 W 20 min, 180 W 60 min, and 600 W 20 min are shown in Fig. 5. The E_g of $CdMoO_4$ nanoparticles was evaluated by extrapolating the linear portions of the curves to the zero absorbance. The energy band gaps are 4.51, 4.65, and 4.73 eV for 180 W 20 min, 180 W 60 min, and 600 W 20 min, respectively. In fact, energy band gap is influenced by several factors, such as bond distortion, degree of structural order–disorder, and defects of the crystal [18].



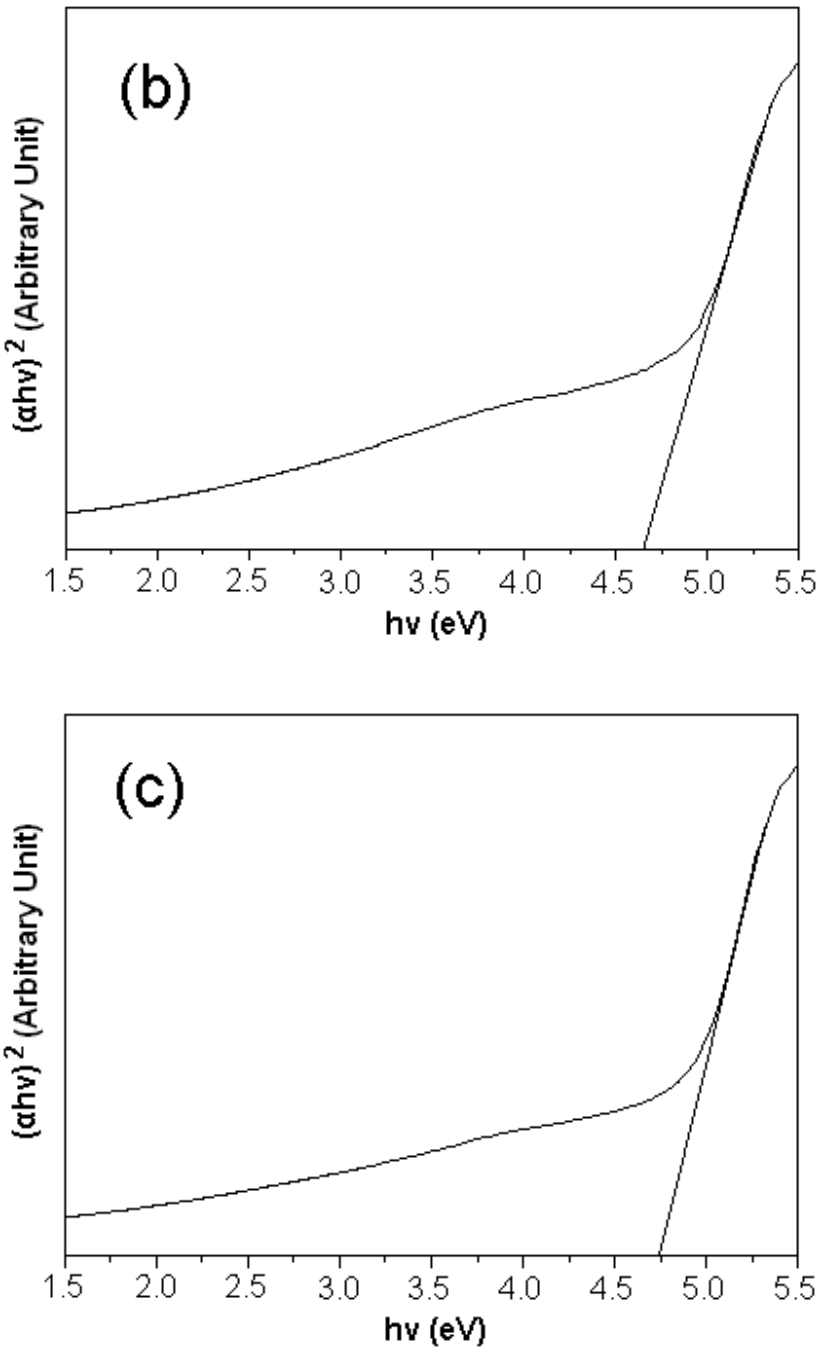


Fig. 5 The $(\alpha h\nu)^2$ and hv plots of $CdMoO_4$ nanoparticles synthesized at (a) 180 W 20 min, (b) 180 W 60 min, and (c) 600 W 20 min.

Conclusions

$CdMoO_4$ nanoparticles were synthesized by the microwave radiation method under different conditions. XRD patterns, TEM images, and UV-visible absorbance revealed that these crystalline powders were scheelite-type tetragonal structure with $I4_1/a$ space group, the particle size range of 14-20 nm, and 4.51-4.73 eV band gaps. Raman spectra showed the vibration as $V_1(A_g)$, $V_3(B_g)$, $V_3(E_g)$, $V_4(E_g, B_g)$, and $V_2(A_g, B_g)$ at 862, 820, 755, 396 and 309 cm^{-1}, with three rotation and two translation modes at 280, 192, 153, 135 and 102 cm^{-1}, respectively. The FTIR analysis shows a strong transmittance mode specified as Mo-O anti-symmetric stretching vibration (V_3) and Mo-O bending mode (V_4) of $[MoO_4]^{2-}$ tetrahedrons at 743-895 cm^{-1} and 423 cm^{-1}, respectively.

References

[1] X. Jiang, J. Ma, B. Lin, Y. Ren, J. Liu, X. Zhu and J. Tao, J. Am. Ceram. Soc. 90 (2007) 977–979.

[2] A. Phuruangrat, T. Thongtem and S. Thongtem, J. Phys. Chem. Solids 70 (2009) 955–959.

[3] X. Wu, J. Du, H. Li, M. Zhang, B. Xi, H. Fan, Y. Zhu and Y. Qian, J. Solid State Chem. 180 (2007) 3288–3295.

[4] L. Zhen, W.S. Wang, C.Y. Xu, W.Z. Shao, M.M. Ye and Z.L. Chen, Scripta Mater. 58 (2008) 461–464.

[5] W.S. Wang, L. Zhen, C.Y. Xu and W.Z. Shao, Cryst. Growth Des. 9 (2009) 1558-1568.

[6] L. Zhou, W. Wang, H. Xu and S. Sun, Cryst. Growth Des. 8 (2008) 3595-3601.

[7] H. Liu and L. Tan, Ionics 16 (2010) 57–60.

[8] W.S. Wang, L. Zhen, C.Y. Xu, B.Y. Zhang and W.Z. Shao, J. Phys. Chem. B 110 (2006) 23154-23158.

[9] Y. Ren, J. Ma, Y. Wang, X. Zhu, B. Lin, J. Liu, X. Jiang and J. Tao, J. Am. Ceram. Soc. 90 (2007) 1251–1254.

[10] T. Thongtem, A. Phuruangrat and S. Thongtem, Mater. Lett. 62 (2008) 454–457.

[11] A. Phuruangrat, T. Thongtem and S. Thongtem, J. Alloy. Comd. 481 (2009) 568–572.

[12] A. Phuruangrat, T. Thongtem and S. Thongtem, J. Cryst. Growth 311 (2009) 4076–4081.

[13] M. Fujita, M. Itoh, T. Katagiri, D. Iri, M. Kitaura and V.B. Mikhailik, Phys. Rev. B 77 (2008) 155118-1 – 155118-7.

[14] Y. Abraham, N. A. W. Holzwarth, and R. T. Williams, Phys. Rev. B 62 (2000) 1733-1741.

[15] M. Daturi, G. Busca, M.M. Borel, A. Leclaire and P. Piaggio, J. Phys. Chem. B 101 (1997) 4358-4369.

[16] Powder Diffract. File, JCPDS-ICDD, 12 Campus Boulevard, Newtown Square, PA 19073-3273, U.S.A. (2001).

[17] C. Suryanarayana and M.G. Norton, X-ray Diffraction, A Practical Approach, NY, Plenum Press, (1998).

[18] J.C. Sczancoski, L.S. Cavalcante, M.R. Joya, J.W.M. Espinosa, P.S. Pizani, J.A. Varela and E. Longo, J. Colloid Interf. Sci. 330 (2009) 227-236.

[19] J.C. Sczancoski, L.S. Cavalcante, M.R. Joya, J.A. Varela, P.S. Pizani and E. Longo, Chem. Eng. J. 140 (2008) 632-637.

[20] A. Jayaraman, S.Y. Wang and S.K. Sharma, Phys. Rev. B 52 (1995) 9886-9889.

6. Effects of solution pH and processing cycle on nanostructured $La_2(MoO_4)_3$ produced by cyclic microwave radiation

Abstract

$La_2(MoO_4)_3$ with different morphologies were successfully produced by a facile cyclic microwave radiation (CMR) processing of a 2:3 molar ratio lanthanum to molybdenum of $La(NO_3)_3{\cdot}6H_2O$ and $(NH_4)_6Mo_7O_{24}{\cdot}4H_2O$ in the solutions with different pH values adjusted by 2M NaOH for different processing cycles. XRD, SEM, TEM, HRTEM and SAED showed that $La_2(MoO_4)_3$ microflowers of nanoflake-like petals could be produced by a 180 W CMR for 15 cycles in the solutions with the pH 7 and 8. The 904 and 887 cm^{-1} Raman symmetric stretching modes as well as the 320 cm^{-1} asymmetric bending modes were detected, and direct energy gaps of the UV–visible spectroscopy were 3.47 and 3.85 eV, respectively. The formation mechanism was also proposed in relation to the experimental results.

Keywords: Semiconductors; Scanning electron microscopy; Transmission electron microscopy; X-ray diffraction

Introduction

Presently, chemists and materials scientists are paying much attention to study micro and nanostructured $La_2(MoO_4)_3$ materials, due to their novel morphologies, chemical and physical properties, including their potential applications for high-performance phosphors, catalysts, positive thermal expansion materials, and ionic conductors [1,2]. There have been several routes used to develop the materials: $La_2(MoO_4)_3$ phosphors with various Eu^{3+} concentrations by a facile co-precipitation process [1], positive thermal expansion lanthanum molybdate by rapid solidification with a CO_2 laser [2], monodisperse $La_2(MoO_4)_3$:Yb, Tm microarchitectures with uniform waxberry-like morphology by a facile surfactant-assisted hydrothermal route with SLS

used as a structure directing agent [3], 3D flower-like $La_2(MoO_4)_3$:Eu microarchitectures by a facile hydrothermal process in the presence of AOT [4], uniform 3D $La_2(MoO_4)_3$ nanostructures with a pompon shape by a simple surfactant-free hydrothermal approach [5], and pomponlike $La_2(MoO_4)_3$ microstructures assembled with single-crystalline nanoflakes via a surfactant-assisted ultrasound route [6]. In the present research, $La_2(MoO_4)_3$ with different morphologies were produced by a facile cyclic microwave radiation (CMR) reaction, the environmentally benign rapid process, without using any surfactants or additives.

Experiment

To produce $La_2(MoO_4)_3$ with different morphologies, lanthanum nitrate hexahydrate ($La(NO_3)_3{\cdot}6H_2O$) and ammonium molybdate tetrahydrate ($(NH_4)_6Mo_7O_{24}{\cdot}4H_2O$) with 2:3 molar ratio La:Mo were separately dissolved in 15 ml de-ionized water, mixed, and followed by pH adjusting using 2M NaOH. At the present stage, the mixtures turned into white colloid. Subsequently, they were processed by a 180 W cyclic microwave radiation (CMR) for 6, 9, 12, and 15 cycles. Each cycle was 20 s on for every 40 s interval. Frequency of the microwave radiation for the present research was 2,450 MHz. Finally, the products with and without processing by the CMR were washed with water and ethanol, and dried at 80 ^{o}C for 12 h. Phases, morphologies, structures, vibration modes and energy gaps of the products were characterized by X-ray diffraction (XRD, SIEMENS D500) operating at 20 kV and 15 mA, using K_α line from a copper target; scanning electron microscopy (SEM, JEOL JSM-6335F) operating at 15 kV; transmission electron microscopy (TEM, JEOL JEM-2010), high resolution transmission electron microscopy (HRTEM) and selected area electron diffraction (SAED) operating at 200 kV; Raman spectroscopy (T64000 HORIBA Jobin Yvon) using a 50 mW and 514.5 nm wavelength Ar green laser; and UV-visible spectrometry (Lambda 25 PerkinElmer) using a UV lamp with the resolution of 1 nm.

Results and discussion

XRD

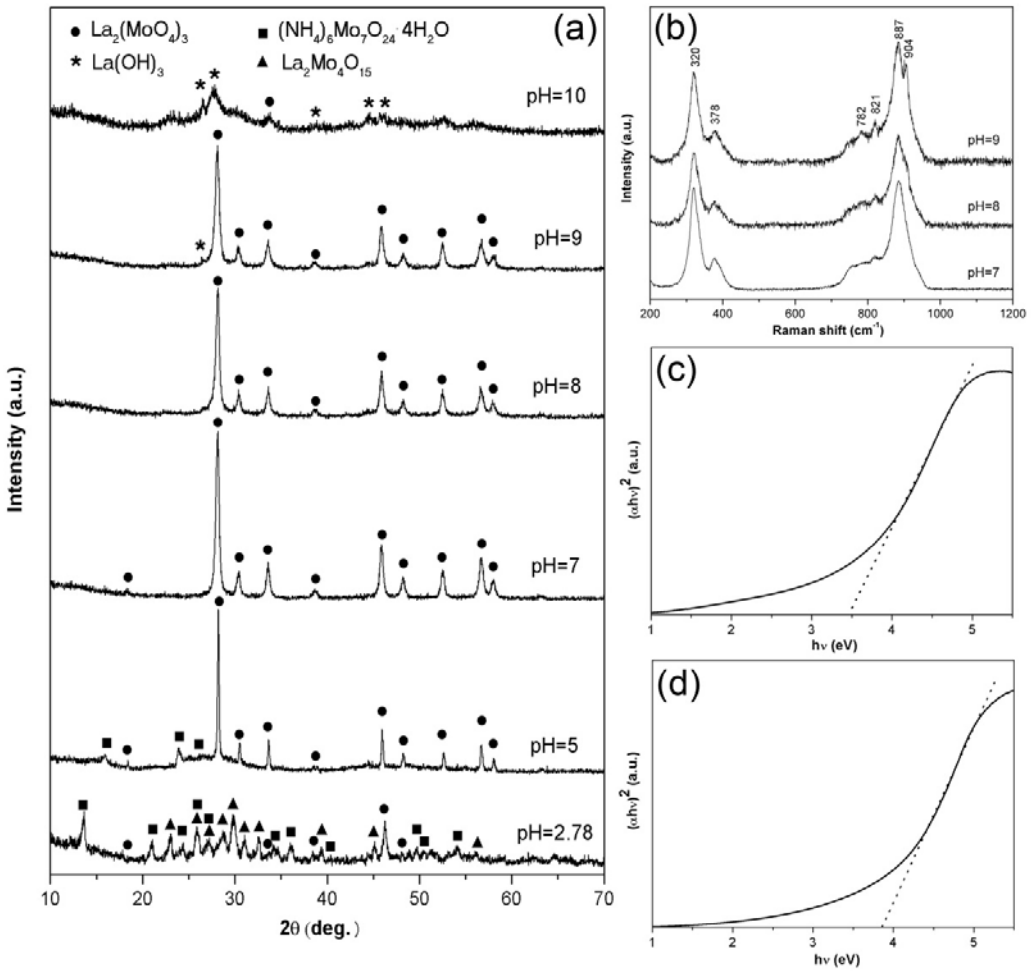


Fig. 1 (a, b) XRD and Raman spectra of the products produced in the solutions with different pH values, and (c, d) UV-visible absorption of $La_2(MoO_4)_3$ produced in the solutions of pH 7 and 8 by 180 W CMR for 15 cycles, respectively.

Crystallographic planes of XRD spectra produced in the solutions with different pH values by a 180 W CMR for 15 cycles (Fig. 1a) were indexed and compared with those of the JCPDS database nos: 01-0135, 45-0407, 23-1146, and 36-1481 for $(NH_4)_6Mo_7O_{24}{\cdot}4H_2O$, $La_2(MoO_4)_3$, $La_2Mo_4O_{15}$ and $La(OH)_3$), respectively [7]. In the solution with the pH 2.78 (free of NaOH), the product was the mixture of $La_2(MoO_4)_3$,

$La_2Mo_4O_{15}$, and $(NH_4)_6Mo_7O_{24}{\cdot}4H_2O$. When 2M NaOH was added to the solution until its pH was 5, the product contained $La_2(MoO_4)_3$ with some $(NH_4)_6Mo_7O_{24}{\cdot}4H_2O$ residue. At the pH 7 and 8, the products were pure tetragonal $La_2(MoO_4)_3$ phase with no impurity detection. At the pH 9 and 10, additional $La(OH)_3$ was detected. Upon increasing the pH from 9 to 10, the intensity of $La(OH)_3$ peaks became higher but that of $La_2(MoO_4)_3$ was lower. For the present 180 W CMR and 15 cycles analysis, pure $La_2(MoO_4)_3$ was successfully produced in the solutions with the pH 7 and 8.

Raman analysis

To further ascertain the presence of $La_2(MoO_4)_3$, the products produced by the 180 W CMR and 15 cycles in the solutions with the pH of 7, 8 and 9 were characterized by Raman spectroscopy. Their Raman shifts (Fig. 1b) at 904 and 887 cm^{-1} corresponded to the symmetric stretching modes, and those at 821 and 782 cm^{-1} to the asymmetric stretching modes. The vibrations at 378 and 320 cm^{-1} were the symmetric and asymmetric bending modes of MoO_4^{2-} tetrahedrons, respectively. Below these wavenumber values, they were specified as the translation and lattice vibrations [2]. It should be noted that the Raman spectra contain prominent peaks at the same wavenumbers although the three products were produced at different pH values, which reflected their purity. Those produced in the pH 7 and 8 solutions were pure phase of $La_2(MoO_4)_3$, but that in the pH 9 solution was the mixed phases of $La_2(MoO_4)_3$ and $La(OH)_3$.

SEM, TEM, HRTEM and SAED

SEM, TEM and HRTEM images (Figs. 2-4) show the product morphologies, produced by the 180 W CMR in the solutions with different pH values and processing cycles. At the pH 2.78 (free of NaOH) and 15 cycle processing (Fig. 2a), the product was nanoparticles clustered together as irregular microparticles with different orientations.

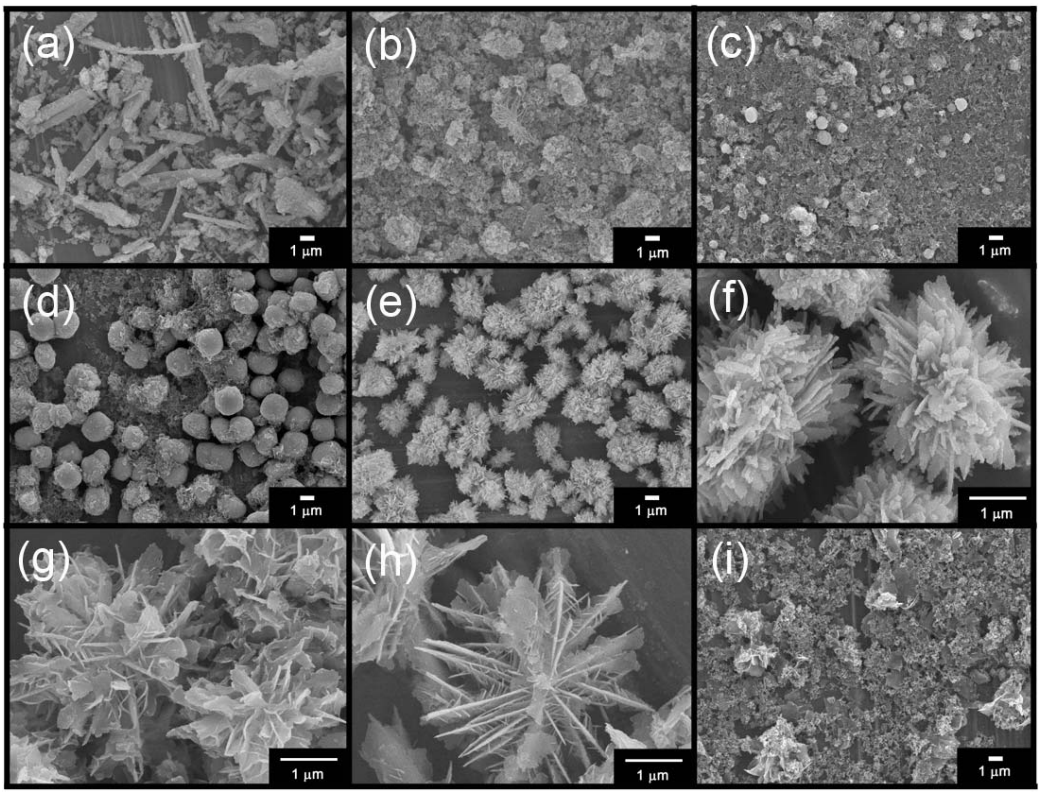


Fig. 2 SEM images of the products produced in the solutions with the pH of (a) 2.78, (b) 4, (c) 5, (d) 6, (e, f) 7, (g) 8, (h) 9, and (i) 10, by 180 W CMR for 15 cycles.

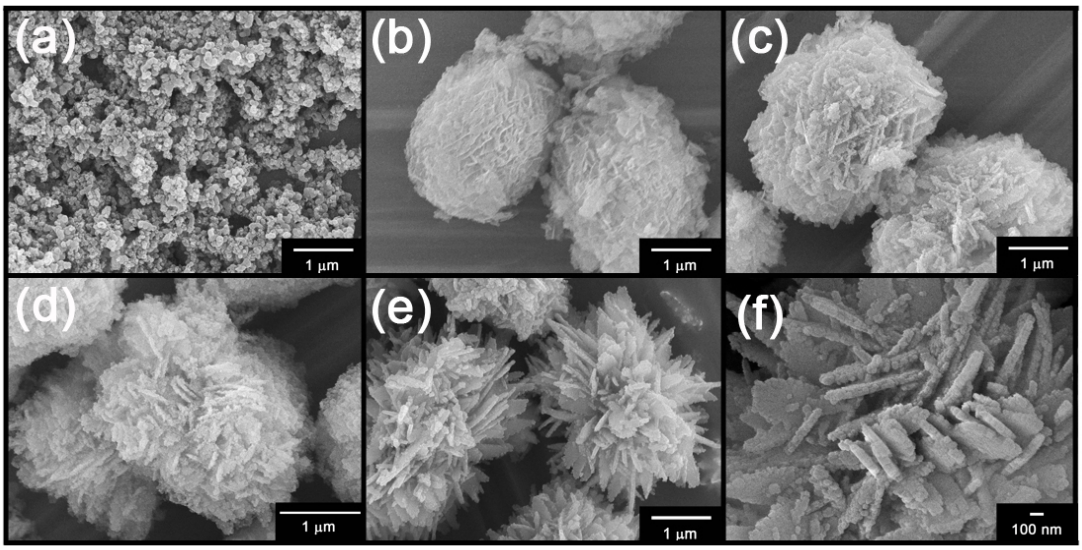


Fig. 3 SEM images of the products produced in the solutions with the pH 7: (a) before, (b-e) after processing by the 180 W CMR for 6, 9, 12 and 15 cycles, and (f) the enlarged image of (e), respectively.

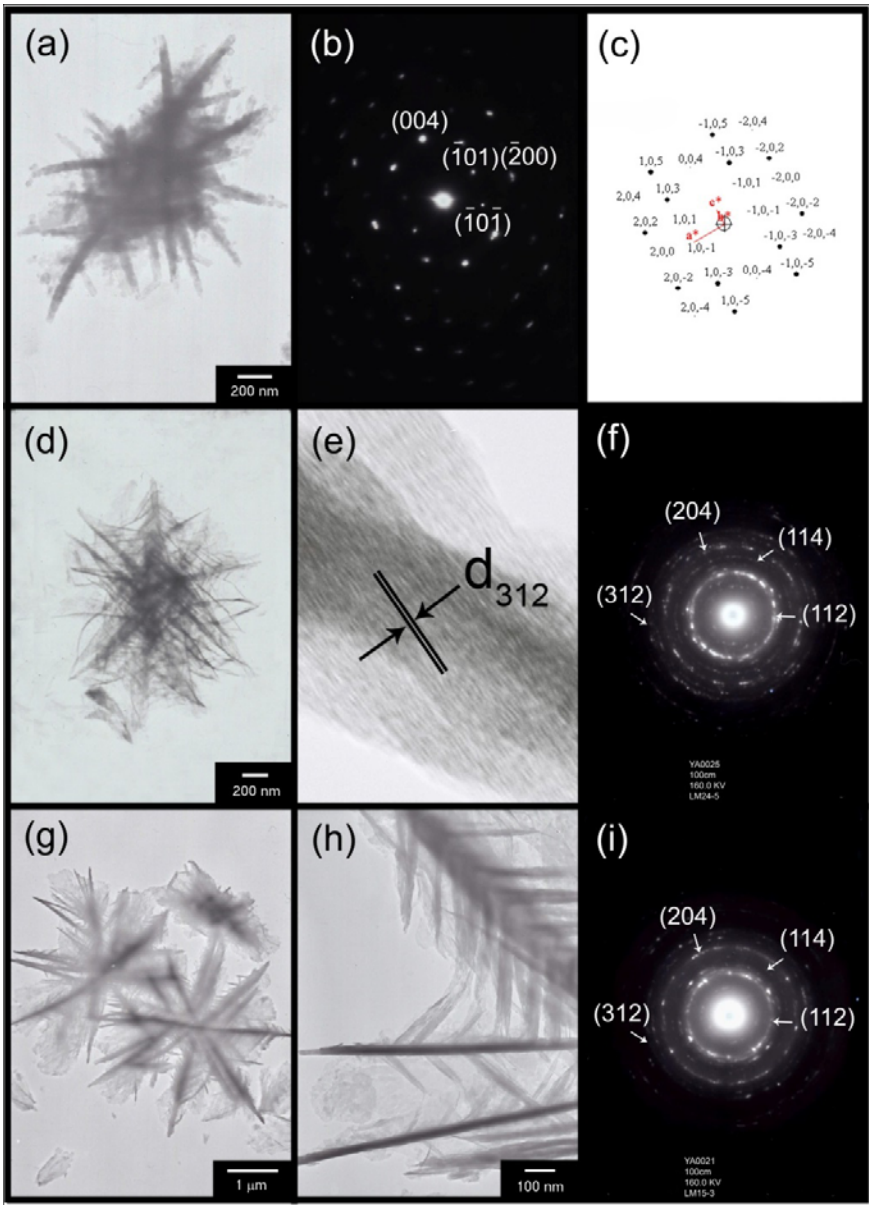


Fig. 4 TEM and HRTEM images, and SAED patterns of the products produced in the solutions with the pH of (a, b) 7, (d-f) 8, (g-i) 9 by 180 W CMR for 15 cycles, and (c) the simulated pattern of (b).

Upon increasing pH of the solution to 4, 5 and 6 (by adding 2M NaOH) but keeping the processing cycle to be the same at 15 cycles (Fig. 2b-d), the products were developed in sequence: nanoparticles and microparticles, nanoparticles and round microparticles, and nanoparticles and larger round microparticles. At these states (pH 2.78, 4, 5 and 6),

the products contained some impurities. At the pH 7 and 8, and 15 cycle processing (Figs. 2e-g, 3e & f, and 4a & d), the products (pure $La_2(MoO_4)_3$ phase) were microflowers of nanoflake-like petals. By increasing only the pH from 8 to 9 and 10 (Figs. 2h & i, and 4g & h), the products (mixed phases of $La_2(MoO_4)_3$ and $La(OH)_3$) were microflowers of nanoflake-like petals, and sponges, respectively. For comparison, the product produced in the solution of pH 7 without processing by the CMR (Fig. 3a) was composed of a number of nanoparticles with different orientations. In the present research, the effect of processing cycles was also studied. Upon processing by 180 W CMR of the solution with the pH 7 for 12 cycles (Fig. 3d), 9 cycles (Fig. 3c) and 6 cycles (Fig. 3b), the products were microparticles of nanoflakes, smaller microparticles of nanoflakes, and microparticles, respectively. The development of product morphologies by the solution pH and processing cycle was also summarized in Table 1. In order to present the crystalline product produced in the solution with the pH 8 by 180 W CMR for 15 cycles (Fig. 4d), the product was characterized by high resolution TEM, as shown in Fig. 4e. Its (312) lattice plane belonging to $La_2(MoO_4)_3$ phase was detected. This implied that the petal of the microflower was single crystal. A petal of the microflower produced in the solution with the pH 7 by 180 W CMR for 15 cycles (Fig. 4a), was characterized by SAED, as shown in Fig. 4b. The SAED pattern was indexed [8] and specified that the petal was $La_2(MoO_4)_3$ single crystal [7,8]. It was in accordance with its simulated pattern [9] (Fig. 4c), showing that the electron diffraction pattern could exist in reality. Other two microflowers produced in the solutions with the pH 8 and 9 by 180 W CMR for 15 cycles (Fig. 4d and g) were also characterized by SAED, as shown in Fig. 4f and i. These two SAED patterns were indexed [8] to correspond with the (112), (114), (204) and (312) crystallographic planes of $La_2(MoO_4)_3$ polycrystalline [7,8] microflowers. Also, these two patterns were composed of diffuse and hollow concentric rings, which were the indication of nanostructured microflowers.

Table 1. Morphology development of the products produced by the 180 W CMR of the solutions with different pH values and processing cycles, as compared to the product without processing by the CMR.

pH	Cycles	Morphologies
2.78 (Free of NaOH)	15	Nanoparticles clustered together to be irregular microparticles with different orientations
4	15	Nanoparticles and microparticles
5	15	Nanoparticles and round microparticles
6	15	Nanoparticles and larger round microparticles
7	Without processing by CMR	Nanoparticles
7	15	Microflowers of nanoflake-like petals
8	15	Microflowers of nanoflake-like petals
9	15	Microflowers of nanoflake-like petals
10	15	Sponges
7	12	Microparticles of nanoflakes
7	9	Smaller microparticles of nanoflakes
7	6	Microparticles

Formation mechanism

When $La(NO_3)_3 \cdot 6H_2O$ and $(NH_4)_6Mo_7O_{24} \cdot 4H_2O$ solutions were mixed with and without NaOH adding, a number of nuclei were produced. Concurrently, they clustered together to form nanoparticles (white colloid). Upon processing the mixtures by a 180 W cyclic microwave radiation for 15 cycles, larger nanoparticles were produced. At the pH 2.78 (free of NaOH), some nanoparticles clustered together to be irregular microparticles of mixed phases. When 2M NaOH was added to the solutions until their pH values were 4, 5 and 6 in sequence, the products were the mixtures of nanoparticles and microparticles with the increasing in the content of microparticles and the degree of

purity. The basicity of the solutions was further increased until at the pH values of 7, 8 and 9, these products became microflowers of nanoflake-like petals. The microflowers were pure phase of $La_2(MoO_4)_3$ only those produced in the solutions with the pH 7 and 8. In the solution with the pH 9, some $La(OH)_3$ impurity was also produced, due to the excess of hydroxyl ions. In the pH 10 solution, the product was sponges of mixed phases of $La_2(MoO_4)_3$ and $La(OH)_3$. Upon increasing the basicity from the pH 9 to 10, the content of the first constituent became lowered and that of the second one was raised up. It should be noted that OH^- ions not only controlled the purity of the products but also functioned as a template in directing the product morphologies. By decreasing the processing times of the pH 7 mixtures from 15 cycles to 12, 9, and 6 cycles, the products gradually turned into microparticles of nanoflakes, smaller microparticles of nanoflakes, and microparticles, respectively. During the CMR process, $La_2(MoO_4)_3$ was produced by the reaction.

$$14La^{3+} + 3Mo_7O_{24}^{6-} + 12H_2O \longrightarrow 7La_2(MoO_4)_3 + 24H^+$$

UV-visible spectroscopy

UV-visible absorption of pure $La_2(MoO_4)_3$ microflowers with nanoflake-like petals produced in the solutions with the pH 7 and 8 by 180 W CMR for 15 cycles was characterized by a UV-visible spectrophotometer, as shown in Fig. 1c and d. For the photon energy ($h\nu$) of more than energy gap (E_g), the relationship between the square absorbance and the photon energy for direct interband transitions was linearly increased with the increasing of photon energy. The inclination of the linear portion of the curve was caused by the UV absorption for charged transition from the topmost occupied state of valence band to the bottommost unoccupied state of the conduction band. For the photon energy with less than energy gap, the absorption curve became different from linearity, caused by the UV absorption for charged transition relating to defects [10,11]. The direct energy gaps of the $La_2(MoO_4)_3$ microflowers produced in the solutions with

the pH 7 and 8 were determined to be 3.47 and 3.85 eV, respectively, a promising material for high-performance phosphor.

Conclusions

$La_2(MoO_4)_3$ with different morphologies were successfully produced by facile CMR processing of the solutions containing $La(NO_3)_3 \cdot 6H_2O$ and $(NH_4)_6Mo_7O_{24} \cdot 4H_2O$ with different pH values and processing cycles. In the present research, $La_2(MoO_4)_3$ microflowers produced in the solutions with the pH 7 and 8 presented their direct energy gaps of 3.47 and 3.85 eV, respectively.

References

[1] Y. Tian, B. Chen, R. Hua, J. Sun, L. Cheng, H. Zhong, X. Li, J. Zhang, Y. Zheng, T. Yu, L. Huang, H. Yu, Optical transition, electron-phonon coupling and fluorescent quenching of $La_2(MoO_4)_3$:Eu^{3+} phosphor, J. Appl. Phys. 109 (2011) 053511-1–053511-6.

[2] E.J. Liang, H.L. Huo, Z. Wang, M.J. Chao, J.P. Wang, Rapid synthesis of $A_2(MoO_4)_3$ (A = Y^{3+} and La^{3+}) with a CO_2 laser, Solid State Sci. 11 (2009) 139–143.

[3] Zh. Chen, W. Bu, N. Zhang, J. Shi, Controlled construction of monodisperse $La_2(MoO_4)_3$:Yb,Tm, microarchitectures with upconversion luminescent property, J. Phys. Chem. C 112 (2008) 4378–4383.

[4] N. Zhang, W. Bu, Y. Xu, D. Jiang, J. Shi, Self-assembled flowerlike europium-doped lanthanide molybdate microarchitectures and their photoluminescence properties, J. Phys. Chem. C 111 (2007) 5014–5019.

[5] W. Bu, Y. Xu, N. Zhang, H. Chen, Z. Hua, J. Shi, Controlled construction of uniform pompon-shaped microarchitectures self-assembled from single-crystalline lanthanum molybdate nanoflakes, Langmuir 23 (2007) 9002–9007.

[6] Y. Ding, Ch. Li, R. Guo, Facile fabrication of pomponlike microarchitectures of lanthanum molybdate via an ultrasound route, Ultras. Sonochem. 17 (2010) 46–54.

[7] Powder Diffract. File, JCPDS-ICDD, 12 Campus Boulevard, Newtown Square, PA 19073-3273, U.S.A. 2001.

[8] K.W. Andrews, D.J. Dyson, S.R. Keown, Interpret. Electr. Diffract. Patterns, Plenum Press, New York, 1971.

[9] C. Boudias, D. Monceau, CaRIne Crystallography 3.1, DIVERGENT S.A., Centre de Transfert, 60200 Compiègne, France, 1989–1998.

[10] J. Kavinchan, T. Thongtem, S. Thongtem, Cyclic microwave assisted synthesis of Sb_2S_3 dumb-bells using polyvinylpyrrolidone as a template and splitting agent, Mater. Lett. 64 (2010) 2388–2391.

[11] Y. Keereeta, T. Thongtem, S. Thongtem, Fabrication of $ZnWO_4$ nanofibers by a high direct voltage electrospinning process, J. Alloys Compd., 509 (2011) 6689–6695.

7. Analysis of lead molybdate and lead tungstate synthesized by a sonochemical method

Abstract

Lead molybdate and lead tungstate nanopaticles were successfully synthesized by a sonochemical method for 1 h. XRD patterns showed the body-centered tetragonal structures of $PbMoO_4$ and $PbWO_4$, and were in accordance with those of the simulation and JCPDS software. Calculated lattice parameters are a = b = 5.4233 Å and c = 12.1253 Å for $PbMoO_4$, and 5.4570 Å and 12.0995 Å for $PbWO_4$. They are in accordance with those of the corresponding JCPDS software. TEM images show that the particles were 29.09 ± 5.22 nm and 21.05 ± 2.68 nm for $PbMoO_4$ and $PbWO_4$, respectively. Raman and FTIR vibrations were investigated to identify a definite existence of the structures.

Keywords: Nanostructures; Chemical synthesis; X-ray diffraction; Raman spectroscopy; Electron microscopy

Introduction

Metal molybdates and tungstates are the materials, which have highly potential and widely applications: photoluminescence, solid-state lasers, optical fibers, scintillating materials, humidity sensors, magnetic materials and catalysts [1-3]. Recently, $PbMoO_4$ has gained attractive interest for using as acousto-optic deflectors and modulators due to its high figure of merit, low optical loss in the range 420-3900 nm and good mechanical impedance for acoustic matching, ion conductors and effective low-temperature scintillators of nuclear instruments [4,5]. $PbWO_4$ is a good candidacy in radiation detection of high energy physics and nuclear physics due to its high density (8.3 g/cm^3), short radiation length (less than 10 ns for a large part of light output), high irradiation damage resistance (10^7 rad for undoped and 10^8 rad for La-doped $PbWO_4$),

small Moliere radius, fast decay time and non-hygroscopic materials, and low production cost [6-8].

There are various methods used to synthesize the molybdates and tungstates, such as wet chemical processes [1-3,8], hydrothermal reactions [7] and microwave radiation [9]. It is very interesting to develop other facile methods for the synthesis of these materials with short reaction time under a mild condition. Sonochemical is very attractive process used for synthesizing these nanosized materials. Ultrasonic radiation (20 kHz-10 MHz) is supplied to molecules, which undergo chemical reaction by the acoustic cavitation – formation (nucleation) of bubbles, growth by the diffusion of solute vapor into the bubbles, and collapse of bubbles (mechanical action) in a liquid solution when their maximum sizes are excessive. During the collapsing process (with less than 1 ns), the temperature and cooling rate are extremely high (5,000-25,000 K, exceeding 10^{11} K/s), causing chemical bonds to be broken. For volatile precursors, gas phase reactions are predominant and amorphous nanoparticles are synthesized. For non-volatile precursors and the reactions are in liquid solutions, the products are nanoamorphous particles and nanocrystalline - depending on the temperature surrounding the collapsing bubbles. In general, the products synthesized by this process are nanomaterials (amorphous or crystalline) with different shapes, sizes and structures [10]. When ultrasonic radiation is supplied to chemical solutions, their molecules vibrate - the problems of concentration and temperature gradients were solved. The radiation has the influence on the reaction to proceed with efficiency and very short time. Subsequently, pure products were synthesized [11]. At present, a simple and fast sonochemical assisted process for synthesizing nanocrystallines of $PbMoO_4$ and $PbWO_4$ is reported.

Experiment

$PbMO_4$ (M = Mo and W) nanocrystals were synthesized using 0.005 mol each of $Pb(NO_3)_2.2H_2O$ and $Na_2MO_4.2H_2O$ dissolved in 50 ml ethylene glycol. The solution was

transferred in an ultrasonic bath (BANDELIN SONOREX - RK 102 H, 120/480 W, 35 kHz), and sonicated for 1 h. The final products were washed with de-ionized water and absolute ethanol, dried at 70 ^{o}C for 12 h, and intensively characterized: XRD (SIEMENS D500) using Cu K_{α} line (1.5406 Å [3]), Raman spectrometer (HORIBA JOBIN YVON T64000) with 50 mW and 514.5 nm wavelength Ar laser, FTIR (BRUKER TENSOR27) with KBr as a diluting agent and operated in the range 400-4,000 cm^{-1}, and TEM (JEOL JEM-2010) operated at 200 kV. Specimen preparation for TEM analysis was to sonicate the products in a beaker containing absolute ethanol for 15 min each, drop the solutions on copper grids, and dry them in ambient atmosphere for 24 h.

Results and discussion

XRD patterns of $PbMO_4$ synthesized by sonochemical method are shown in Fig. 1a. Their XRD patterns were interpreted to be the tetragonal structures of $PbMoO_4$ and $PbWO_4$ with $I4_1/a$ space group, comparing to the JCPDS nos. 08-0475 for $PbMoO_4$ and 08-0476 for $PbWO_4$ [12]. Lattice parameters were calculated using an equation of plane spacing for the tetragonal structure and Bragg's law for diffraction [13]: a = b = 5.4233 Å and c = 12.1253 Å for $PbMoO_4$, and 5.4570 Å and 12.0995 Å for $PbWO_4$, respectively. They are in accordance with the corresponding values of the JCPDS software [12].

To specify that the diffraction patterns of the products could exist in reality, XRD patterns of $PbMO_4$ with $I4_1/a$ space group were simulated using CaRIne Version 3.1 program [14]. The simulated XRD patterns are shown in Fig. 1b. The 2θ Bragg's angles and intensities of different crystallographic planes from the experiment, simulation and JCPDS nos. 08-0475 and 08-0476 [12] were summarized in Tables 1 and 2. These values for both products are in good accordance. Low intensity peaks of the (211) and (222) planes of JCPDS no. 08-0476 [12] were not detected by the experiment and simulation.

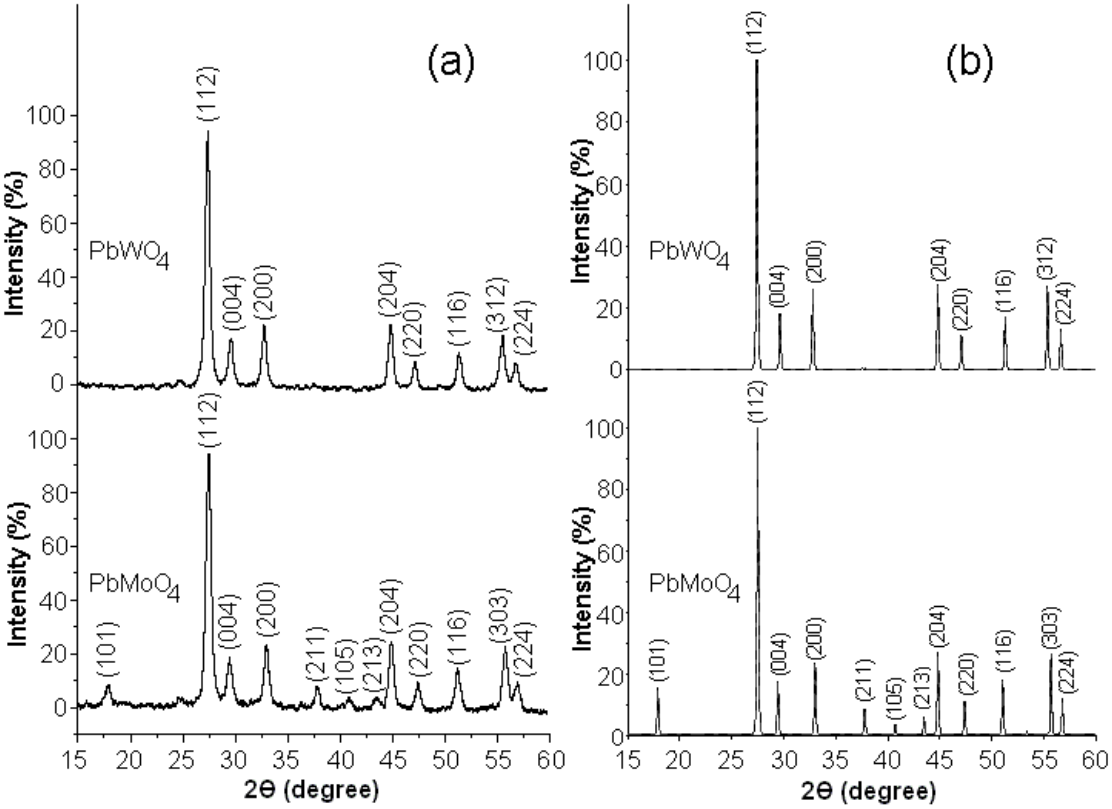


Fig. 1 (a) XRD patterns of $PbMO_4$ and (b) their simulations.

For body-centered tetragonal $PbMO_4$ structure, $(MO_4)^{2-}$ tetrahedrons have S_4 symmetry in crystallographic lattice [15]. Raman spectra of the products (Fig. 2) show wavenumbers at 872.57 cm^{-1} for $PbMoO_4$ and 906.43 cm^{-1} for $PbWO_4$, associated with $\nu_1(A_g)$ vibrations in the tetrahedral $(MO_4)^{2-}$ units. Those at 769.92 and 744.87 cm^{-1} for $PbMoO_4$, and 769.57 and 752.93 cm^{-1} for $PbWO_4$ were split from the ν_3 mode to become $\nu_3(B_g)$ and $\nu_3(E_g)$, respectively. Two modes at 300-400 cm^{-1} were interpreted as the stronger $\nu_2(A_g)$ and weaker $\nu_4(B_g)$ of the regular $(MO_4)^{2-}$ tetrahedrons. Vibration modes at 169.12 cm^{-1} for $(MoO_4)^{2-}$ and 178.35 cm^{-1} for $(WO_4)^{2-}$ rotating about the z axis are much less energies than those of other modes [8,15-17]. Vibrational energies of $(MO_4)^{2-}$ ions were rather small. Thus, bonding of the $(MO_4)^{2-}$ anionic tetrahadrons is quite strong, comparing to the bonding between the anionic and cationic units.

Table 1. The 2θ Bragg's angles (deg.) and diffraction intensities (%) of $PbMoO_4$ obtained from the experiment, simulation and JCPDS no. 08-0475 [12].

Plane	JCPDS 08-0475		Experiment		Simulation	
	2θ	Intensity	2θ	Intensity	2θ	Intensity
(101)	17.87	12.00	17.83	7.52	17.90	15.00
(112)	27.47	100.00	27.44	100.00	27.50	100.00
(004)	29.48	20.00	29.44	16.03	29.44	17.40
(200)	32.93	25.00	32.97	32.97	33.01	23.10
(211)	37.72	8.00	37.74	8.11	37.80	8.50
(105)	40.76	6.00	40.84	4.41	40.72	3.70
(213)	43.43	8.00	43.41	4.07	43.48	5.70
(204)	44.81	30.00	44.87	26.25	44.81	26.60
(220)	47.31	14.00	47.42	10.06	47.37	10.80
(116)	51.07	18.00	51.21	16.23	51.04	17.90
(303)	55.55	25.00	55.74	23.94	55.65	27.60
(224)	56.71	12.00	56.95	10.23	56.76	11.60

Table 2. The 2θ Bragg's angles (deg.) and diffraction intensities (%) of $PbWO_4$ obtained from the experiment, simulation and JCPDS no. 08-0476 [12].

Plane	JCPDS 08-0476		Experiment		Simulation	
	2θ	Intensity	2θ	Intensity	2θ	Intensity
(112)	27.42	100.00	27.40	100.00	27.39	100.00
(004)	29.66	20.00	29.50	18.17	29.51	18.50
(200)	32.75	30.00	32.76	20.06	32.80	25.90
(211)	37.54	2.00	-	-	-	-
(204)	44.74	35.00	44.84	24.15	44.69	27.70
(220)	47.02	16.00	47.12	9.44	47.06	11.40
(222)	49.56	1.00	-	-	-	-
(116)	51.23	20.00	51.31	14.71	51.06	17.40
(312)	55.29	35.00	55.50	16.95	55.31	27.00
(224)	56.57	16.00	56.72	8.16	56.63	12.50

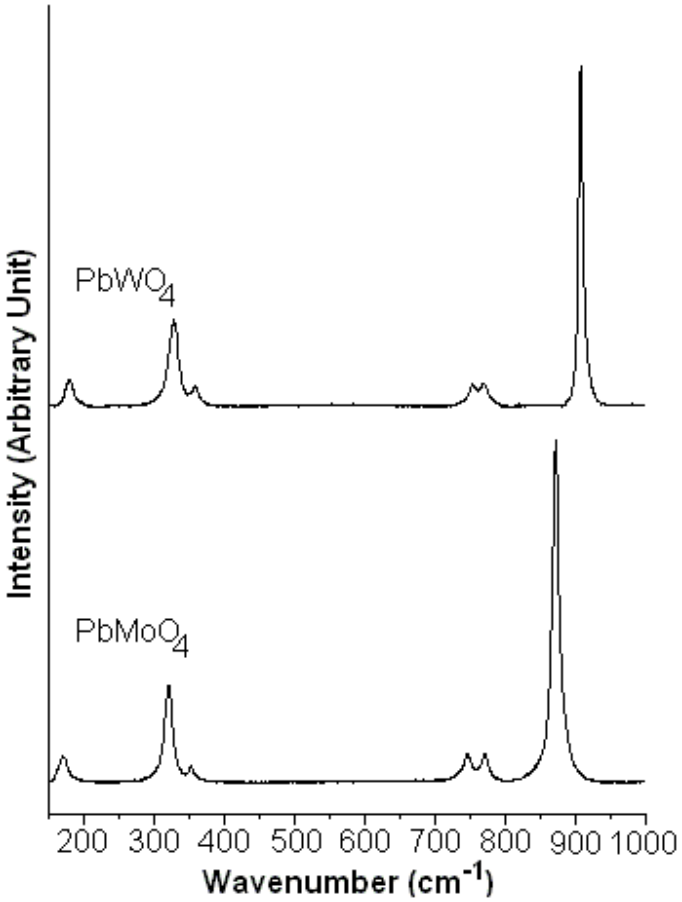


Fig. 2 Raman spectra of $PbMO_4$.

FTIR transmittance modes (Fig. 3) of the products were detected at 730-879 cm^{-1} for $PbMoO_4$, and 738-879 cm^{-1} for $PbWO_4$, specified as the antisymmetric stretching vibrations of $(MO_4)^{2-}$ tetrahedrons [18,19].

TEM analysis shows that each product (Fig. 4) was composed of a number of dispersed nanosized particles with round shape. By respective measuring of 160 and 150 particles for $PbMoO_4$ and $PbWO_4$ on the TEM images, their particle size distribution curves (Fig. 5) are very close to bell shapes with normal distribution. The averages and standard deviations are 29.09 ± 5.22 nm for $PbMoO_4$, and 21.05 ± 2.68 nm for $PbWO_4$. The narrow particle size distributions and homogenous particles favor luminescent properties [11].

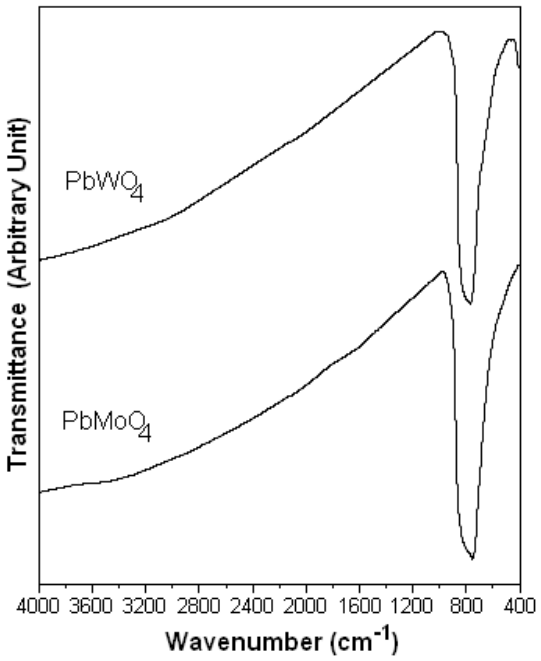


Fig. 3 FTIR spectra of $PbMO_4$.

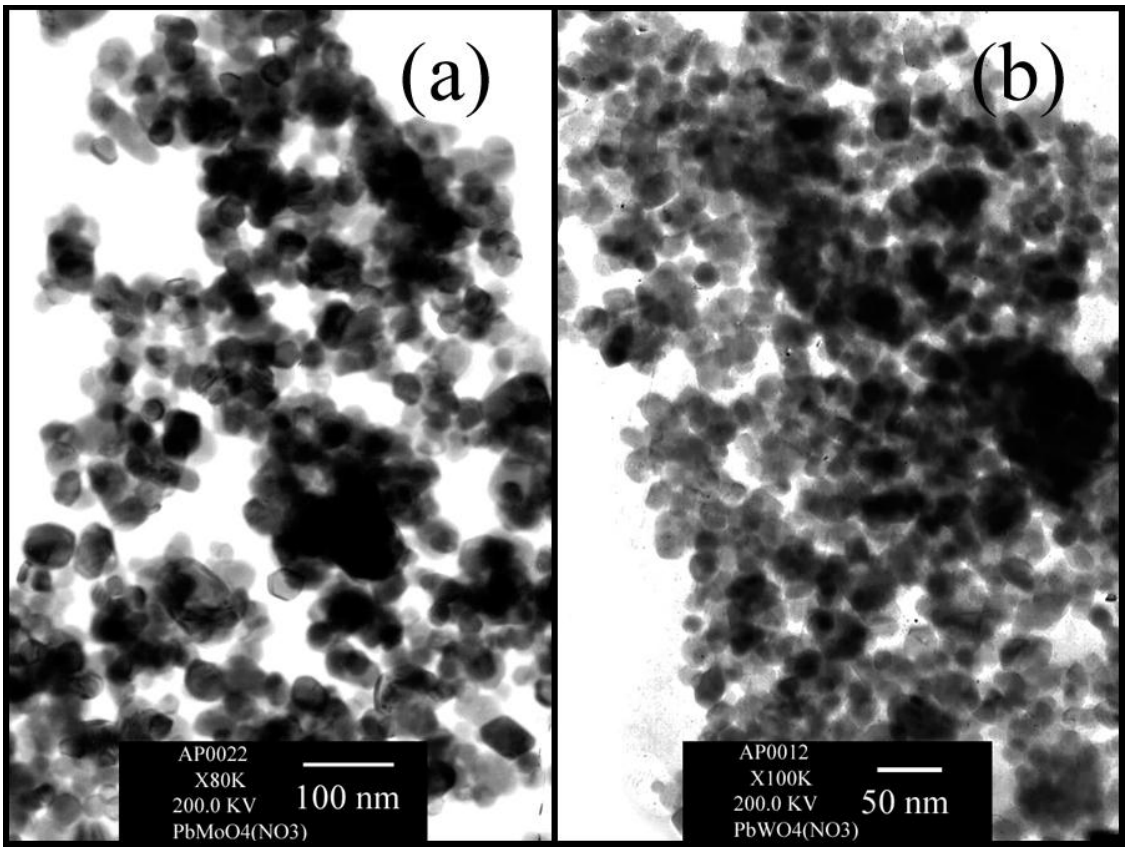


Fig. 4 TEM images of (a) $PbMoO_4$ and (b) $PbWO_4$ nanoparticles.

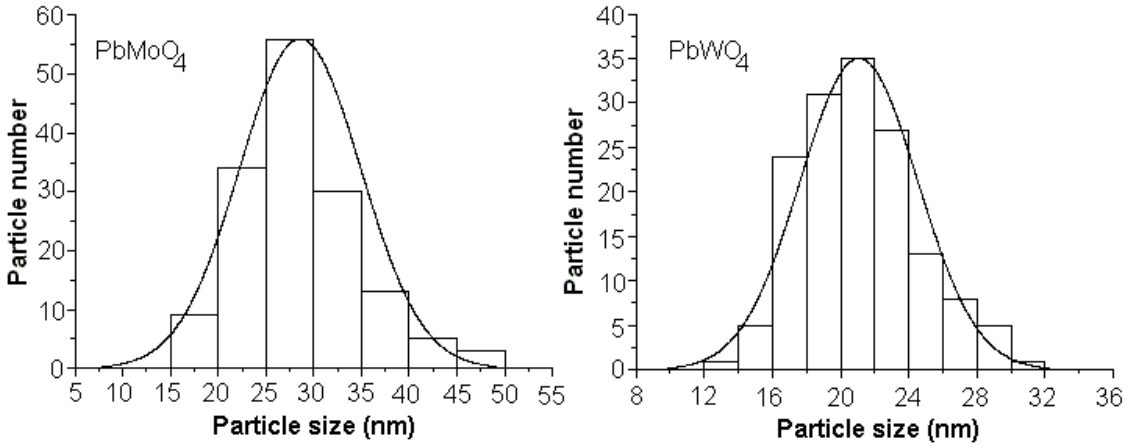


Fig. 5 Particle size distribution curves of $PbMO_4$.

Conclusions

$PbMoO_4$ and $PbWO_4$ nanoparticles were successfully synthesized from $Pb(NO_3)_2.2H_2O$ and $Na_2MO_4.2H_2O$ in ethylene glycol by a sonochemical method. XRD patterns obtained by the experiment are in good accordance with those obtained by the simulation and JCPDS software [12]. A definite existence of the tetragonal $PbMO_4$ structures was confirmed by the Raman and FTIR vibrations of these products. TEM images showed that they were composed of dispersed nanoparticles with normal size distributions, having the influence on the photoluminescent properties.

References

[1] F.M. Pontes, M.A.M.A. Maurera, A.G. Souza, E. Longo, E.R. Leite,R. Magnani, M.A.C. Machado, P.S. Pizani, J.A. Varela, J. Eur. Ceram. Soc. 23 (2003) 3001-3007.

[2] J. Liu, J. Ma, B. Lin, Y. Ren, X. Jiang, J. Tao, X. Zhu, Ceram. Inter. 34 (2008) 1557-1560.

[3] J.C. Sczancoski, L.S. Cavalcante, M.R. Joya, J.A. Varela, P.S. Pizani, E. Longo, Chem. Eng. J. 140 (2008) 632-637.

[4] N. Senguttuvan, S.M. Babu, R. Dhanasekaran, Mater. Chem. Phys. 49 (1997) 120-123.

[5] D. Piwowarska, S.M. Kaczmarek, M. Berkowski, J. Non-Cryst. Solids 354 (2008) 4437-4442.

[6] G. Wang, C. Hao, Mater. Res. Bull. 44 (2009) 418-421.

[7] W. Zhao, X. Song, G. Chen, G. Tian, S. Sun, Mater. Lett. 63 (2009) 285-288.

[8] L.S. Cavalcante, J.C. Sczancoski, V.C. Albarici, J.M.E. Matos, J.A. Varela, E. Longo, Mater. Sci. Eng. B 150 (2008) 18-25.

[9] T. Thongtem, A. Phuruangrat, S. Thongtem, Curr. Appl. Phys. 8 (2008) 189-197.

[10] A. Gedanken, Ultrason. Sonochem. 11 (2004) 47-55.

[11] T. Thongtem, A. Phuruangrat, S. Thongtem, Appl. Surf. Sci. 254 (2008) 7581-7585.

[12] Powder Diffract. File, JCPDS-ICDD, 12 Campus Boulevard, Newtown Square, PA 19073-3273, U.S.A. (2001).

[13] C. Suryanarayana, M.G. Norton, X-ray Diffraction, A Practical Approach, Plenum Press, New York (1998).

[14] C. Boudias, D. Monceau, CaRIne Crystallography 3.1, DIVERGENT S.A., Centre de Transfert, 60200 Compiègne, France (1989-1998).

[15] A.A. Kaminskii, C.L. McCray, H.R. Lee, S.W. Lee, D.A. Temple, T.H. Chyba, W.D. Marsh, J.C. Barnes, A.N. Annanenkov, V.D. Legun, H.J. Eichler, G.M.A. Gad, K. Ueda, Opt. Commun. 183 (2000) 277-287.

[16] H. S. Lee, S. D. Lee, J. H. Lee, M. S. Jang, Ferroelectrics 107 (1990) 151-154.

[17] J. Xu, S. Wang, M. H. Manghnani, L. C. Ming, J. Bologh, High Press. Res. 3 (1990) 254-256.

[18] A.P. de Azevedo Marques, D.M.A. de Melo, C.A. Paskocimas, P. S. Pizani, M.R. Joya, E.R. Leite, E. Longo, J. Solid State Chem. 179 (2006) 671-678.

[19] G.M. Clark, W.P. Doyle, Spectrochim. Acta 22 (1966) 1441-1447.

8. Photoemission and energy gap of $MgWO_4$ particles connecting as nanofibers synthesized by electrospinning-calcination combinations

Abstract

Mixtures of magnesium acetate tetrahydrate ($(CH_3COO)_2Mg{\cdot}4H_2O$), ammonium tungstate tetrahydrate ($(NH_4)_6W_7O_{24}{\cdot}4H_2O$), and poly (vinyl alcohol) with the molecular weight of 72,000 were electrospun through a + 15 kV direct voltage to form fibers on ground flat aluminum foils. The electrospun fibers of 1.5, 3.0, and 4.5 mmol of each starting material containing 1.3 g poly (vinyl alcohol) were further calcined at 500–700 ^{o}C for 3 h constant length of time. At 500 and 600 ^{o}C calcination, both monoclinic and anorthic phases of $MgWO_4$ particles with different sizes connecting as fibrous assemblies were detected. Upon increasing the calcination temperature to 700 ^{o}C, only monoclinic phase of facet nanoparticles interconnecting along the fibrous axes with 4.19 eV indirect band gap and 461 nm photoemission was synthesized. In the present research, formation of $MgWO_4$ molecules as well as nucleation and growth of nanoparticles was also proposed.

Keywords: $MgWO_4$ nanofibers, Electrospinning, Indirect band gap

Introduction

Two majorities of AWO_4 (A^{2+} = divalent cations) naturally crystallized on Earth are tetragonal scheelite ($I4_1/a$ space group) with large cationic radii (> 0.099 nm: Ba, Ca, Sr, Pb, Eu), and monoclinic wolframite (P2/c space group) with small cationic radii (< 0.077 nm: Co, Cd, Fe, Mn, Mg, Ni, Zn). For the first, each W^{6+} ion is surrounded by four O^{2-} ions forming $(WO_4)^{2-}$ tetrahedral unit. But for the second, each W^{6+} ion is surrounded by six O^{2-} ions forming $(WO_6)^{6-}$ octahedral complex [1-6]. $MgWO_4$ is a semiconducting material, containing both light (Mg and O) and heavy (W) elements. It is very interesting for different technological applications: luminescence, scintillation [7,8], tunable

microwave applications [9] and tunable solid state lasers [10]. Thus the study of photonic absorption and emission of $MgWO_4$ particles interconnecting as fiber-like assemblies became increasingly attractive for a number of applications.

Basically, electrospinning equipment is composed of three components: a direct current (d.c.) power supply, a long hollow needle and an electrical conducting screen. During electrospinning, a drop of polymeric solution at the tip of the hollow needle is charged by a positive d.c. high voltage. The mutual positive charge repulsion on the polymeric droplet is created. When the applied d.c. voltage is increased, the liquid droplet is stretched to be a conical shape, known as Taylor cone. Upon further increasing the d.c. voltage until it is sufficiently high, the repulsive force overcomes the surface tension of the polymeric liquid, and the jet of liquid is ejected out of the Taylor cone. Meanwhile, the liquid jet evaporates and solidifies, leaving behind the polymeric fibers deposited on the ground conducting screen [11,12].

There are several parameters playing the role in electrospun fibers: (a) variable parameters of electrospinning equipment (applied voltage at the needle tips as well as electric field inside fibers, pressure used to push the liquid out of the hollow needles, and a distance between the needle tip and ground conducting screen), (b) solution properties (viscosity, surface tension, elasticity and conductivity) and (c) ambient parameters (temperature, humidity and wind blow). These can play the role in the surface morphologies of electrospun fibers, fibrous diameter, number of beads including their shape and size, and defects (pores) on fibers [11,12]. Inclination (vertical or horizontal) of the hollow needle also has the influence on electrospun fibers.

To the best of our knowledge, no $MgWO_4$ nanofibers have ever been synthesized by electrospinning and high temperature calcination. It is therefore for us to use the mixture of inorganic and organic salts dissolving in poly (vinyl alcohol) (PVA) to synthesize inorganic-polymeric fibers, which would transform into nanofibers by subsequent calcination at high temperature. This success may lead to new industrial process by direct high voltage electrospinning.

Experiment

Different contents of magnesium acetate tetrahydrate ($(CH_3COO)_2Mg{\cdot}4H_2O$), ammonium (meta) tungstate tetrahydrate ($(NH_4)_6W_7O_{24}{\cdot}4H_2O$), and poly (vinyl alcohol) (PVA, 72,000 MW) were thoroughly mixed by dissolving in 30 ml deionized water each with 30 min stirring. Each of these mixtures was electrospun through a horizontal plastic syringe, biased with a + 15 kV direct voltage to form fibers on a ground flat aluminum foil placed 15 cm apart. The fibers were also calcined at 500, 600, and 700 ºC for 3 h constant length of time, and left them cool down to room temperature. The products synthesized from different contents of the starting materials with and without subsequent calcination at high temperatures were summarized and encoded (Table 1).

Table 1. Product codes of the present research.

Product code	$(CH_3COO)_2Mg{\cdot}4H_2O$ (mmol)	$(NH_4)_6W_7O_{24}{\cdot}4H_2O$ (mmol)	PVA (g)	Calcination temperature (^{o}C) / time (h)
P1	1.5	1.5	0.9	Non
P2	1.5	1.5	1.1	Non
P3	1.5	1.5	1.3	Non
P3C1	1.5	1.5	1.3	500 / 3
P4	3.0	3.0	1.3	Non
P4C1	3.0	3.0	1.3	500 / 3
P5	4.5	4.5	1.3	Non
P5C1	4.5	4.5	1.3	500 / 3
P5C2	4.5	4.5	1.3	600 / 3
P5C3	4.5	4.5	1.3	700 / 3

These products were further characterized by X-ray diffractometer (XRD, SIEMENS D500) operating at 20 kV 15 mA, and using Cu-K_α line, in combination with the database of the Joint Committee on Powder Diffraction Standards (JCPDS) [13];

scanning electron microscope (SEM, JEOL JSM-6335F) operating at 15 kV; transmission electron microscope (TEM, JEOL JEM-2010), high resolution transmission electron microscope (HRTEM) and selected area electron diffractometer (SAED) operating at 200 kV; atomic force microscope (AFM, NanoScope IIIa, MMAFML N, Veeco) with silicon tip driven at a frequency of 200-300 kHz tapping mode; UV-visible spectrometer (Lambda 25 PerkinElmer) using a UV lamp with the resolution of 1 nm; and photoluminescence (PL) spectrometer (LS 50B PerkinElmer) using a 290 nm excitation wavelength at room temperature.

Results and discussion

XRD

XRD spectra (Fig 1a) of the P5C1, P5C2 and P5C3 products show that chemical reactions of the starting materials were completed. $MgWO_4$ with anorthic (JCPDS No 45-0412) and monoclinic (JCPDS No 72-2191) [13] were successfully synthesized. During electrospinning by a + 15 kV direct voltage, $(CH_3COO)_2Mg{\cdot}4H_2O$ reacted with $(NH_4)_6W_7O_{24}{\cdot}4H_2O$ to synthesize $MgWO_4$ molecules, blended in the PVA template.

$$7Mg^{2+} + (W_7O_{24})^{6-} + 4H_2O \longrightarrow 7MgWO_4 + 8H^{+} \qquad (1)$$

$(CH_3COO)_2Mg{\cdot}4H_2O$ and $(NH_4)_6W_7O_{24}{\cdot}4H_2O$ could remain in the template but their concentrations were too low to be detected by XRD. By calcination at 500 ^{o}C for 3 h, PVA evaporated and decomposed. The PVA was no longer detected at 494 ^{o}C and above [14]. At the same time, the $(CH_3COO)_2Mg{\cdot}4H_2O$ and $(NH_4)_6W_7O_{24}{\cdot}4H_2O$ residues combined to form $MgWO_4$ molecules, which nucleated and grew to be particles (mixed phases) with different orientations. Upon increasing of the calcination temperature to 600 ^{o}C, the anorthic phase became lessened, with the greater extent of the monoclinic one. At 700 ^{o}C and 3 h calcination, only the monoclinic crystal structure was detected, and the product was the best crystal – the atoms resided in perfect crystal lattice. Its calculated lattice parameters [15] (Table 2) were very close to those of the standard values [13], which supported the presence of $MgWO_4$ with monoclinic crystal system. By

using the Scherrer formula [15], crystallite sizes of the P5C1, P5C2 and P5C3 products were calculated and summarized in Table 2. Crystallite sizes of both anorthic and monoclinic phases were increased with the increasing in the calcination temperatures, but the rate of increasing for the first was slower than that for the second. It should be noted that the anorthic crystallites were smaller than the monoclinic ones.

Table 2. Lattice parameters and crystallite sizes of the P5C1, P5C2 and P5C3 products.

Product	Lattice parameter (nm)			Crystallite size (nm)	
	a	b	c	Anorthic	Monoclinic
P5C1	-	-	-	15.0	23.0
P5C2	-	-	-	29.6	68.8
P5C3	0.465	0.564	0.490	-	69.8

XRD pattern of monoclinic $MgWO_4$ was simulated [16] as shown in Fig 1b. In the present research, the 2θ Bragg's angles and peak intensities of the experiment, simulation and JCPDS database were in good accordance. Simulated crystal structure of monoclinic $MgWO_4$ (inset of Fig 1b) was explained as network of interconnecting zigzag chains of alternate MgO_6 and WO_6 distorted octahedrons running along the [001] direction, with Mg ions in the O ion polyhedrons [10].

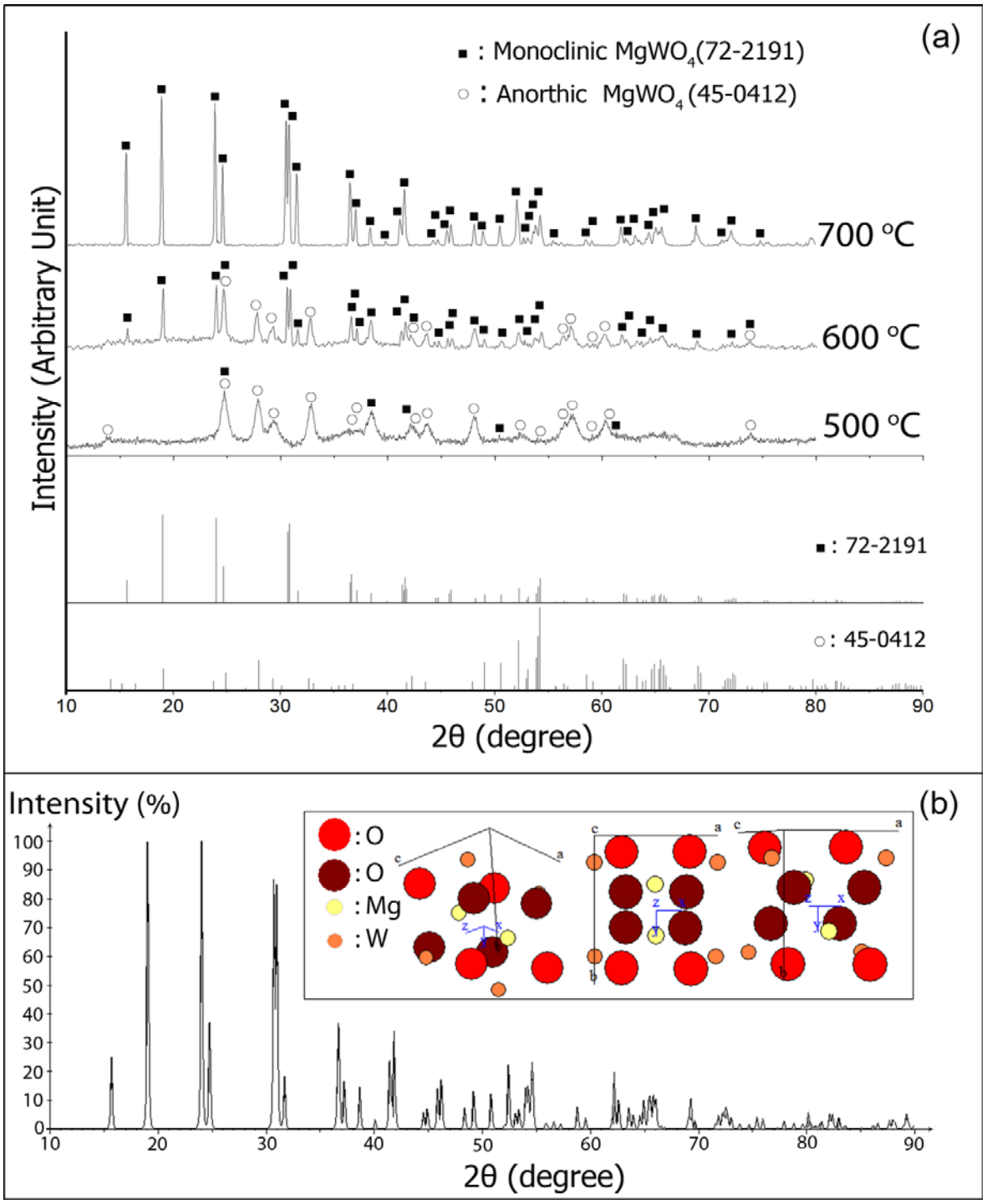


Fig. 1 (a) XRD spectra of the P5C1, P5C2 and P5C3 products, compared with the anorthic and monoclinic $MgWO_4$ phases. (b) Simulated XRD pattern and crystal structure of monoclinic $MgWO_4$.

SEM, TEM, HRTEM, SAED and AFM

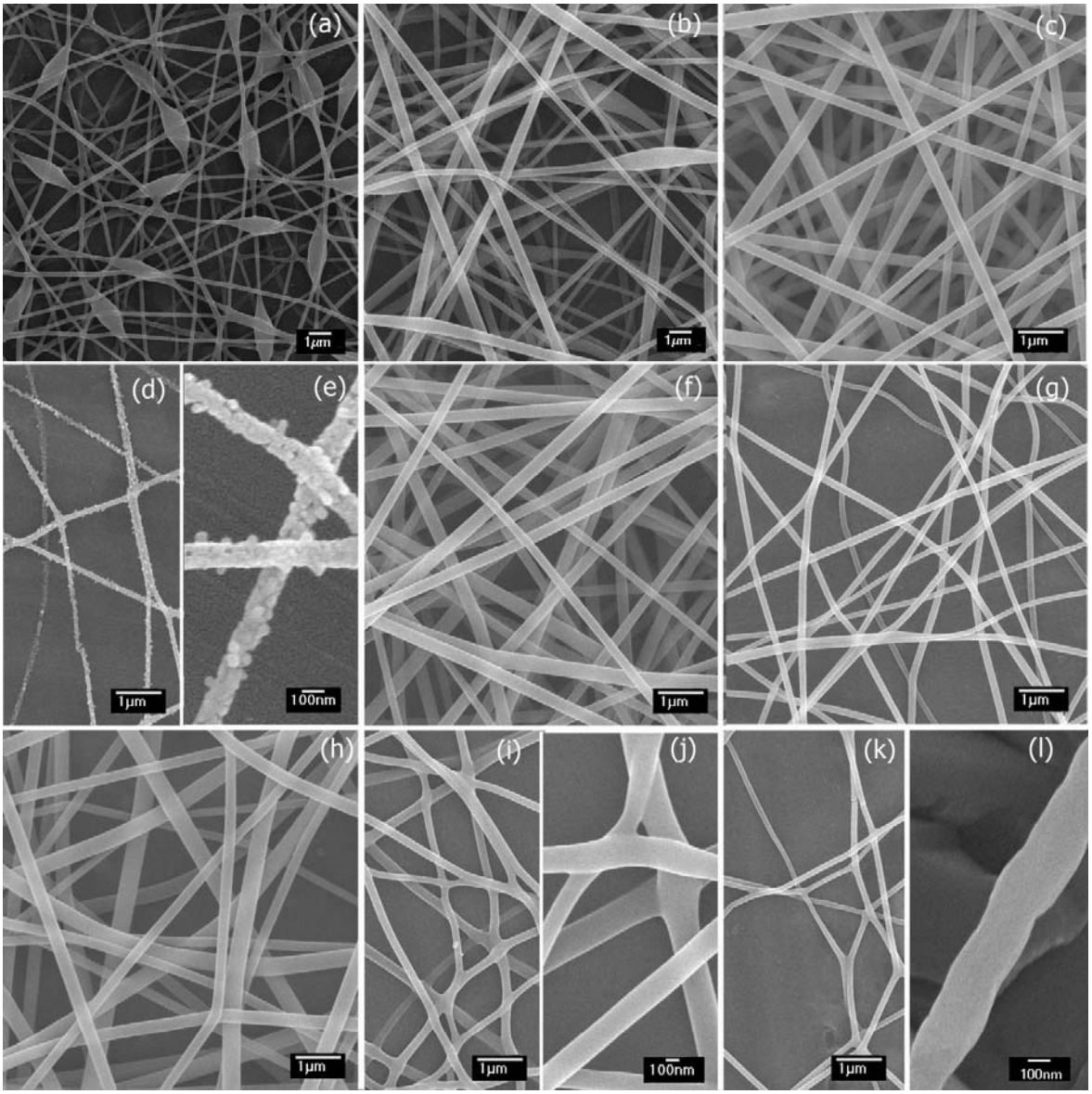


Fig. 2 SEM images of the (a) P1, (b) P2, (c) P3, (d, e) P3C1, (f) P4, (g) P4C1, (h) P5, (i, j) P5C1, (k) P5C2 and (l) P5C3 products.

SEM, TEM and HRTEM images (Figs 2 and 3a-d) show external surfaces of the products electrospun from different contents of the starting materials, before and after calcination at 500, 600, and 700 ºC for 3 h constant length of time. Before calcination,

some beads were detected on the P1 and P2 products (Fig 2a, b) but no longer detected on the P3 product (Fig 2c). Upon increasing the amount of PVA, the beads became lessened. Finally, they were no longer detected. These showed that the increase of viscosity of the mixtures played the role in the absence of beads on the electrospun fibers. The mixture of 1.5 mmol $(CH_3COO)_2Mg{\cdot}4H_2O$), 1.5 mmol $(NH_4)_6W_7O_{24}{\cdot}4H_2O$ and 1.3 g PVA has the viscosity and density high enough to form the bead-free electrospun fibers.

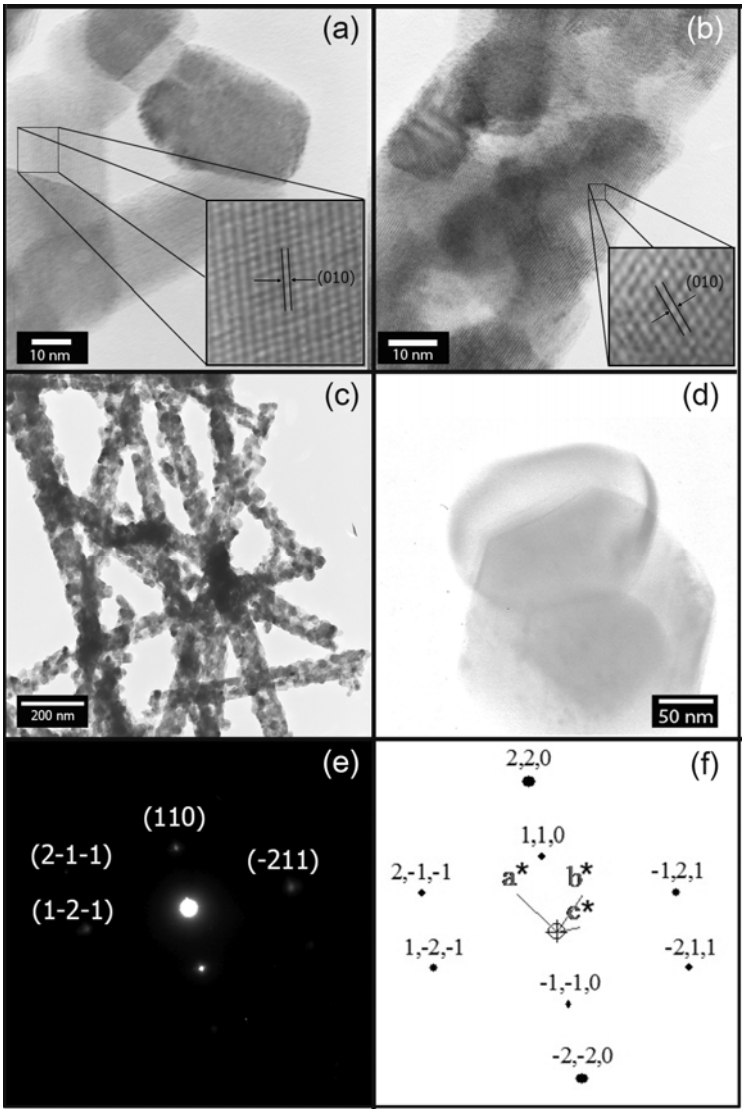


Fig. 3 TEM and HRTEM images, and SAED and simulated patterns of the (a) P3C1, (b, c) P5C1 and (d-f) P5C3 products.

By increasing the amount of the starting materials but keeping the amount of PVA constant at 1.3 g, the products were still to be bead-free electrospun fibers (Fig 2f, h). $MgWO_4$ molecules and nanoparticles in the fibers became denser, proved by the P3C1, P4C1 and P5C1 products (Figs 2d, e, g, i, j, and 3a-c). Surfaces of the fibers were roughened. The products were composed of interconnecting of facet nanoparticles along the fibrous axes. Upon increasing the calcination temperature of the P5C1 product from 500 ^{o}C to 600 ^{o}C (P5C2) and 700 ^{o}C (P5C3) (Figs 2k, l, and 3d), both the nanoparticles and fibers were enlarged. A number of the (010) crystallographic planes of typical nanoparticles of the P3C1 and P5C1 products (insets of Fig 3a and b) were detected by HRTEM - revealing the presence of crystalline $MgWO_4$ in the fibers. A SAED pattern of the P5C3 product (Fig 3e) corresponded to the database of the monoclinic $MgWO_4$ [13], and the pattern obtained by simulation (Fig 3f) [16].

AFM images and surface roughness of the P4C1 and P5C1 products are shown in Fig 4. After 500 °C and 3 h calcination, the fibers were very rough and uneven, which reflected on their surface energy. Root mean square (RMS) values and maximum heights were 19.671 nm and 60.275 nm for the first, and 4.761 nm and 27.421 nm for the second, respectively. Each of these products contained particles with different sizes connecting as fiber-like assembly - in accordance with the above SEM and TEM analyses.

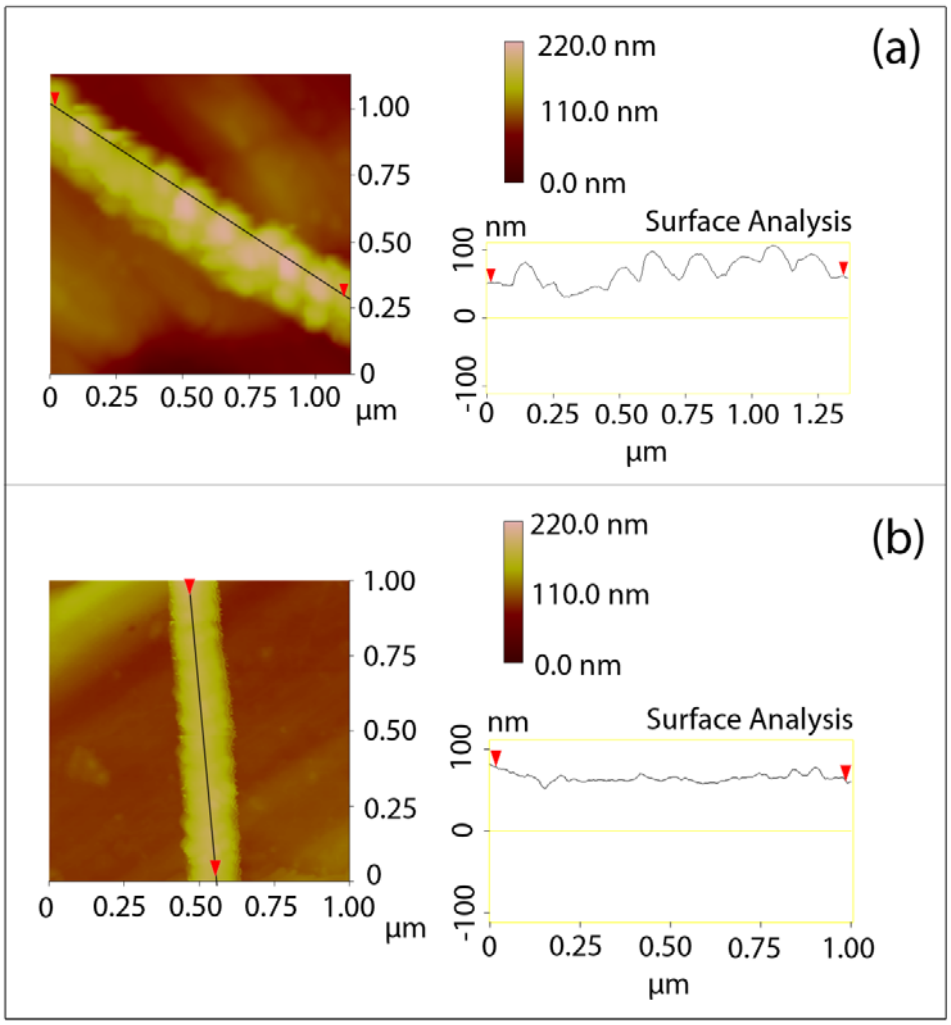


Fig. 4 AFM images and surface roughness of the (a) P4C1 and (b) P5C1 products.

PL emission and UV-visible absorption

By using 290 nm excitation wavelength, PL emissions (Fig 5a) of the P5C1, P5C2 and P5C3 products were detected at 461 nm - in accordance with the report of Danevich et al. [8]. The different emission was caused by the distorted $(WO_6)^{6-}$ octahedrons, Jahn-Teller effect, and the perturbation of $(WO_4)^{2-}$ tetrahedrons induced by defects [17].

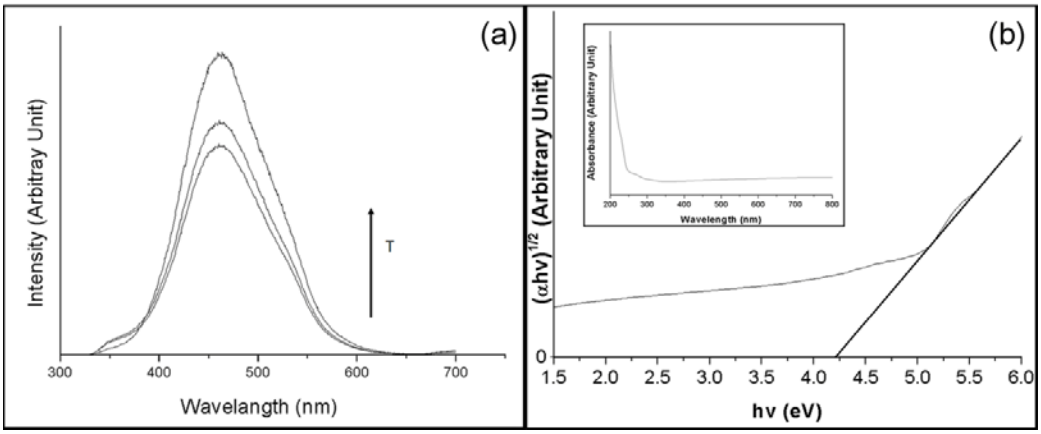


Fig. 5 (a) PL emission of the P5C1, P5C2 and P5C3 products, and (b) UV-visible absorption of the P5C3 product.

UV-visible absorption (Fig 5b) of P5C3 indicated an exponential decreasing of photonic absorption attenuated through the product. Its indirect E_g was determined, by extrapolating linear portion of the curve to zero absorption, to be 4.19 eV - very close to that reported by Lacomba-Perales et al. [1], and Kim et al. [18]. Particle-sizes and morphologies could play the role in the absorbance characteristics [19,20], having the influence on the energy gap.

Conclusions

The mixture of 4.5 mmol $(CH_3COO)_2Mg{\cdot}4H_2O$, 4.5 mmol $(NH_4)_6W_7O_{24}{\cdot}4H_2O$ and 1.3 g PVA was electrospun through a +15 kV direct voltage to form $MgWO_4$-PVA fibers, which were followed by 700 ^{o}C calcination for 3 h to form interconnecting facet nanoparticles of $MgWO_4$ along the fibrous axes with 4.19 eV indirect band gap and 461 nm PL emission – the promising nanofibers for a variety of applications.

References

[1] R. Lacomba-Perales, J. Ruiz-Fuertes, D. Errandonea, D. Martínez-García, A. Segura, Optical absorption of divalent metal tungstates: Correlation between the band-gap energy and the cation ionic radius, EPL 83 (2008) 37002 (5pp).

[2] Z. Lou, M. Cocivera, Cathodoluminescence of $CaWO_4$ and $SrWO_4$ thin films prepared by spray pyrolysis, Mater. Res. Bull. 37 (2002) 1573–1582.

[3] S.H. Yu, B. Liu, M.S. Mo, J.H. Huang, X.M. Liu, Y.T. Qian, General synthesis of single-crystal tungstate nanorods/nanowires: a facile, low-temperature solution approach, Adv. Funct. Mater. 13 (2003) 639–647.

[4] A. GolubovićĆ, R. GajićĆ, Z. DohčevićĆ-MitrovićĆ, S. NikolićĆ, Nd induced changes in IR spectra of $CaWO_4$ single crystals, J. Alloys Comp. 415 (2006) 16–22.

[5] X. Wang, H. Xu, H. Wang, H. Yan, Morphology-controlled $BaWO_4$ powders via a template-free precipitation technique, J. Crys. Growth 284 (2005) 254–261.

[6] J.T. Kloprogge, M.L. Weier, L.V. Duong, R.L. Frost, Microwave-assisted synthesis and characterisation of divalent metal tungstate nanocrystalline minerals: ferberite, hübnerite, sanmartinite, scheelite and stolzite, Mater. Chem. Phys. 88 (2004) 438–443.

[7] V.B. Mikhailik, H. Kraus, V. Kapustyanyk, M. Panasyuk, Y. Prots, V. Tsybulskyi, L. Vasylechko, Structure, luminescence and scintillation properties of the $MgWO_4$-$MgMoO_4$ system, J. Phys.: Condens. Matter. 20 (2008) 365219 (8pp).

[8] F.A. Danevich, D.M. Chernyak, A.M. Dubovik, B.V. Grinyov, S. Henry, H. Kraus, V.M. Kudovbenko, V.B. Mikhailik, L.L. Nagornaya, R.B. Podviyanuk, O.G. Polischuk, I.A. Tupitsyna, Y.Y. Vostretsov, $MgWO_4$ – A new crystal scintillator, Nucle. Instrum. Metho. Phys. Res. A 608 (2009) 107–115.

[9] M. Zhang, J. Zhai, J. Zhang, H. Jiang, X. Yao, Effect of $MgWO_4$ content on properties of $Ba_{0.5}Sr_{0.5}TiO_3$ composite ceramics for tunable microwave applications, Mater. Res. Bulle. 46 (2011) 1102–1106.

[10] E. Cavalli, A. Belletti, M.G. Brik, Optical spectra and energy levels of the Cr^{3+} ions in MWO_4 (M = Mg, Zn, Cd) and $MgMoO_4$ crystals, J. Phys. Chem. Solids 69 (2008) 29–34.

[11] J.M. Deitzel, J. Kleinmeyer, D. Harris, N.C.B. Tan, The effect of processing variables on the morphology of electrospun nanofibers and textiles, Polymer 42 (2001) 261–272.

[12] Z.M. Huang, Y.Z. Zhang, M. Kotaki, S. Ramakrishna, A review on polymer nanofibers by electrospinning and their applications in nanocomposites, Compos. Sci. Tech. 63 (2003) 2223–2253.

[13] Powder Diffract. File, JCPDS-ICDD, 12 Campus Boulevard, Newtown Square, PA 19073-3273, U.S.A., (2001).

[14] S. Wannapop, T. Thongtem, S. Thongtem, Characterization of $SrWO_4$-PVA and $SrWO_4$ spiders' webs synthesized by electrospinning, Ceram. Int., 37 (2011) 3499–3507.

[15] C. Suryanarayana, M.G. Norton, X-ray Diffract., A Pract. Appro., Plenum Press, New York, 1998.

[16] C. Boudias, D. Monceau, CaRIne Crystallography 3.1, DIVERGENT S.A., Centre de Transfert, 60200 Compiègne, France, 1989–1998.

[17] V.B. Mikhailik, H. Kraus, D. Wahl, H. Ehrenberg, M.S. Mykhaylyk, Optical and luminescence studies of $ZnMoO_4$ using vacuum ultraviolet synchrotron radiation, Nucle. Instrum. Metho. Phys. Res. A 562 (2006) 513–516.

[18] D.W. Kim, I.S. Cho, S.S. Shin, S. Lee, T.H. Noh, D.H. Kim, H.S. Jung, K.S. Hong, Electronic band structures and photovoltaic properties of MWO_4 (M = Zn, Mg, Ca, Sr) compounds, J. Solid State Chem. 184 (2011) 2103–2107.

[19] M. Hojamberdiev, G. Zhu, Y. Xu, Template-free synthesis of $ZnWO_4$ powders via hydrothermal process in a wide pH range, Mater. Res. Bull. 45 (2010) 1934–1940.

[20] Y. Keereeta, T. Thongtem, S. Thongtem, Fabrication of $ZnWO_4$ nanofibers by a high direct voltage electrospinning process, J. Alloy Comp. 509 (2011) 6689–6695.

9. Fabrication of $ZnWO_4$ nanofibers by a high direct voltage electrospinning process

Abstract

Mixtures of zinc acetate dihydrate, ammonium metatungstate hydrate, and 5 wt%, 6 wt%, and 7 wt% of poly (vinyl alcohol) (PVA) were electrospun by a +15 kV direct voltage to produce fibers. In the present research, the electrospun fibers of 6 wt% PVA were further calcined at 400-600 °C for 3 h. The sanmartinite monoclinic structured $ZnWO_4$ was detected by X-ray diffractometer (XRD) and selected area electron diffraction (SAED), weight loss by thermogravimetric analyser (TGA), morphology and particle size by scanning and transmission electron microscopes (SEM, TEM) and atomic force microscope (AFM), including their vibration modes by Fourier transform infrared spectrometer (FTIR) and Raman spectrometer. The 4.42 eV direct energy gap (E_g) and 460 nm emission wavelength, caused by the electronic transition of $(WO_6)^{2-}$ octahedrons, were determined by UV-visible absorption and photoluminescence (PL) spectrometers. A possible formation mechanism of $ZnWO_4$ nanofibers was also proposed according to the experimental results.

Keywords: Semiconductors; Nanofabrications; Luminescence; Scanning electron microscopy; X-ray diffraction

Introduction

Recently, nanostructured materials such as nanowires, nanorods, nanotubes and nanofibers have received considerable attention for a variety of applications [1]; especially, nanofibers or non-woven textiles [2]. They have attractive properties and novel potential applications for using as solar cells, electromagnetic shielding materials, non-wetting textiles, medical prosthesis, and liquid crystal devices [3,4]. A possible process used to produce nanofibrous inorganic materials is by electrospinning, which is now becoming increasingly popular [5] even for the industrial scale production. It is able

to produce continuous polymer fibers with diameters of micro- and nano-scale through the action of an external electric field imposed in a polymer solution or melt [2]. By using the inorganic material and polymer mixtures as the starting precursors, the inorganic material-polymer electrospun fibers are able to be produced easily. When diameters of the electrospun fibers are lessened from micrometers to sub-micrometers or nanometers, there appear some amazing characteristics such as very large surface area to volume ratio, flexibility in surface functionality, and superior mechanical performance [4]. Subsequently, inorganic nanofibers are able to be produced by the calcination of inorganic material-polymer electrospun fibers obtained by electrospinning of the sol–gel solution [6].

Among different semiconducting materials, $ZnWO_4$ has excellent properties and strong potential application in various fields such as photoluminescence [7-9], Raman laser converters [7], photocatalyst [7], and scintillator material [7,10]. $ZnWO_4$ belongs to the monoclinic sanmartinite-type structure with P2/c space group [11]. In the past decade, nanosized $ZnWO_4$ has been produced by several processes such as co-precipitation [7], Czochralski technique [12], hydrothermal method [8,13-15], microwave-assisted synthesis [16], and polymerized complex method [17].

To produce non-woven fibers by the electrospinning process, a positive high direct voltage is applied to a liquid droplet, ejected out of the tip of a hollow needle. The droplet is charged and stretched – known as Taylor cone. If the molecular cohesion of the liquid - such as polymeric solution or melt, and the direct voltage are sufficiently high, a very long thin charged liquid jet will be formed. During flying, the jet dries and solidifies - caused by the external electric field inside. Finally, the fiber is produced, and deposited on a grounded collector [4].

In the present research, $ZnWO_4$-PVA electrospun fibers were firstly produced by the lab-made electrospinning equipment. They are very novel and promising material for a variety of applications. These electrospun fibers were subsequently calcined at high temperature to form $ZnWO_4$ nanofibers. To the best of our knowledge, there are no

$ZnWO_4$ nanofibers have ever been produced by the present process. It is therefore for us to use the mixture of inorganic materials and polymer to produce the inorganic material-polymer electrospun fibers, which would transformed into nanofibrous inorganic material by subsequent calcination at high temperature. Moreover, the success in producing the solid nanofibrous material may lead to new industrial process under the action of an external electric field.

Experimental procedure

Basing on the conventional sol-gel process - 1:1 molar ratio of Zn:W of zinc acetate dihydrate ($Zn(CH_3COO)_2 \cdot 2H_2O$, 99.0%) and ammonium metatungstate hydrate ($H_{26}N_6O_{40}W_{12} \cdot H_2O$, 99.0%) was dissolved in 10 ml deionized water, and stirred for 10 min. Then 20 ml aqueous solutions of 5 wt%, 6 wt%, and 7 wt% poly (vinyl alcohol) (PVA, 125,000 MW) were added to the precursor solutions, with 30 min vigorous stirring in a 80 °C water bath. Each of the solution mixtures was loaded into a plastic syringe on a horizontal platform. A piece of flat aluminum foil was vertically placed 15 cm away for collecting the fibers. Electrospinning was done by ejecting a jet of inorganic material-polymeric solution out of the long hollow needle, and a +15 kV of a d.c. power supply was simultaneously applied at the needle tip. Finally a dense web of electrospun fibers was collected on the grounded aluminum foil. The fibers produced from 6 wt% PVA solution was calcined by increasing from room temperature (T_R) at a rate of 5 ºC/min until reaching 400 ºC, 500 ºC, and 600 ºC, held at each of these temperatures for 3 h, and left the system to cool down to room temperature. The products were characterized using thermogravimetric analyser (TGA, Shimadzu TGA-50 analyzer, Japan) using a heating rate of 5 °C/min; X-ray diffractometer (XRD, SIEMENS D500, Germany) operating at 20 kV, 15 mA, and using Cu-K_α line, in combination with the database of the Joint Committee on Powder Diffraction Standards (JCPDS) [11]; scanning electron microscope (SEM, JEOL JSM-6335F, Japan) operating at 15 kV; transmission electron microscope (TEM, JEOL JEM-2010, Japan), high resolution transmission electron

microscope (HRTEM) and selected area electron diffractometer (SAED) operating at 200 kV; atomic force microscope (AFM, NanoScope IIIa, MMAFML N, Veeco, U.S.A.) with silicon tip driven at a frequency of 200-300 kHz tapping mode; Fourier transform infrared spectrometer (FTIR, Bruker Tensor 27, Germany) with KBr as a diluting agent and operated in the range of 4000-400 cm^{-1}; Raman spectrometer (T64000 HORIBA Jobin Yvon, U.S.A.) using a 50 mW and 514.5 nm wavelength Ar green laser; UV-visible spectrometer (Lambda 25 PerkinElmer, U.S.A.) using a UV lamp with the resolution of 1 nm; and photoluminescence (PL) spectrometer (LS 50B PerkinElmer, U.S.A.) using a 280 nm excitation wavelength at room temperature.

Results and discussion

XRD

XRD patterns of the electrospun fibers after calcination at 400 °C, 500 °C and 600 °C are presented in Fig. 1. Comparing to the JCPDS database no. 15-0774 [11], they corresponded to sanmartinite structured $ZnWO_4$ with monoclinic crystal system and P2/c space group. In the present study, temperature was found to have influence on the crystallinity and purity of $ZnWO_4$ fibers; especially, the relatively high temperature calcination. At 400 ^{o}C, XRD revealed that the product was not perfectly pure $ZnWO_4$. It contained some residual PVA at 2θ of approximately 22.5 ^{o} [18]. Upon increasing the calcination temperatures to be 500 °C and 600 °C, the spectra became sharper and the XRD intensities were stronger. The crystalline degree of the products was much improved. No PVA was detected by the XRD. At 600 °C calcination, the product was the best pure crystal. Its degree of crystallinity was the highest, and the atoms resided in the perfect crystal lattice. By using the Scherrer formula [19], the crystallite sizes obtained by 400 ^{o}C, 500 ^{o}C, and 600 ^{o}C calcination for 3 h were 16 nm, 30 nm, and 105 nm, respectively.

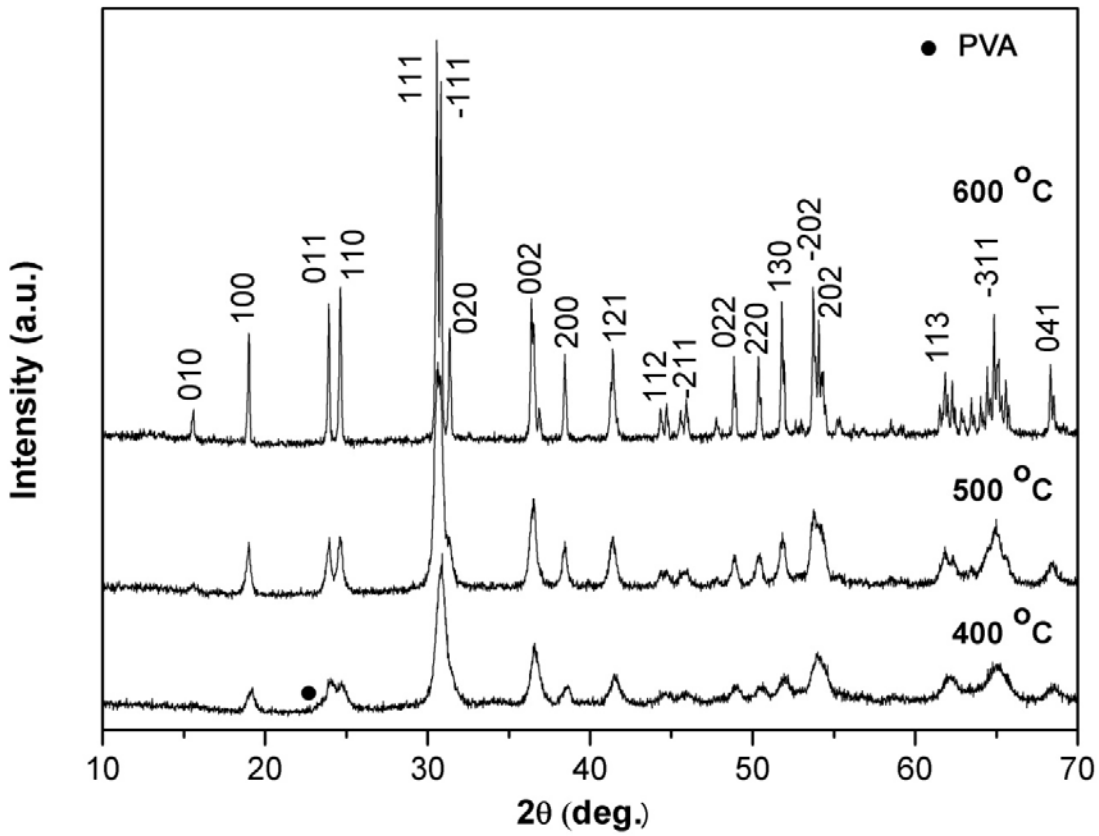


Fig. 1 XRD patterns of the electrospun fibers after calcination at 400 °C, 500 °C, and 600 °C for 3 h.

TGA

Fig. 2 shows the thermal behavior of PVA and $ZnWO_4$-PVA electrospun fibers characterized by TGA analyzer with a heating rate of 5 °C/min. The weight loss of pure PVA exhibited the degradation process as follows. The first weight loss was 10.5 %, due to the evaporation of loosely bound water at 32-200 °C. The second was the large amount of weight loss for 79.3 %, predominantly caused by the decomposition of PVA structure at 200-420 °C. The third was 8.3 %, by the breaking of PVA backbone at 420-490 °C. The weight loss tended to terminate upon further heating to above 490 °C [20]. When the $ZnWO_4$-PVA electrospun fibers were characterized, their weight losses were divided into three different steps.

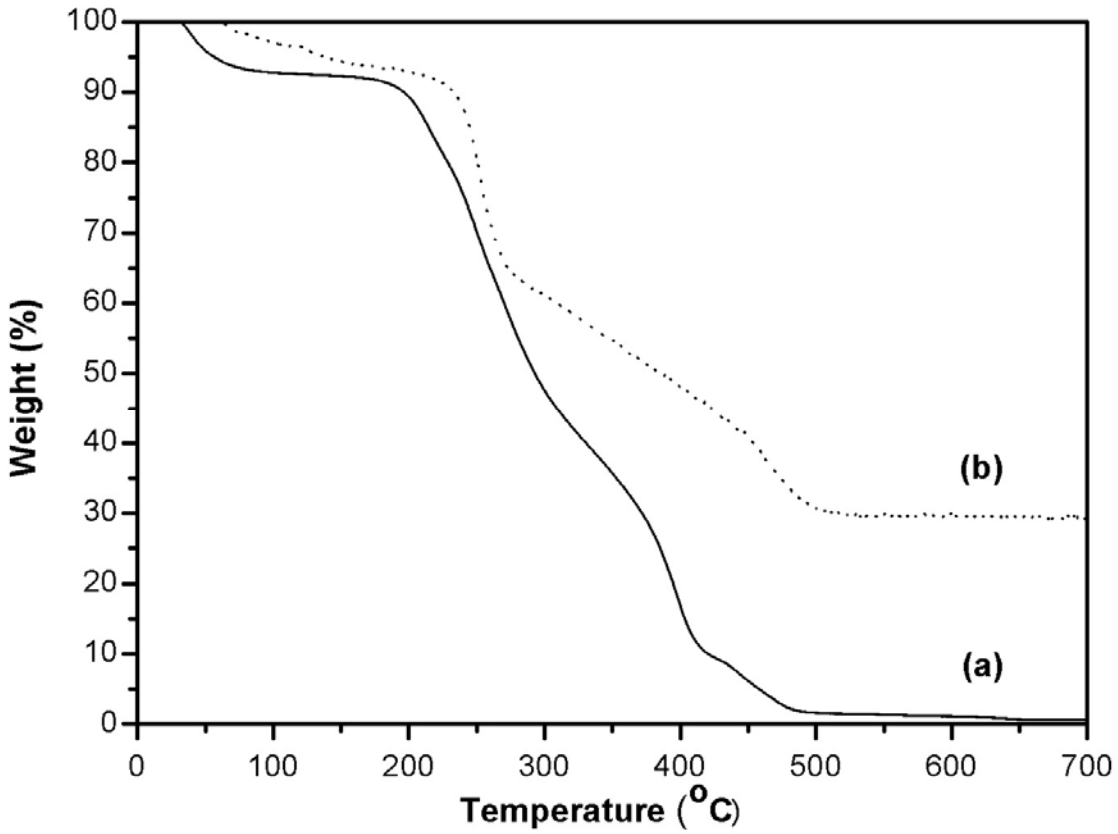


Fig. 2 TGA curves of (a) PVA, and (b) $ZnWO_4$-PVA electrospun fibers produced from 6 wt% PVA solution.

The first weight loss in the temperature range of 32 - 226 °C was 11.2 %, and associated with water evaporation. The second weight loss of 45.7 % at 226 °C - 420 °C was caused by the decomposition of PVA. The final weight loss of 15.5 % in the temperature range of 420-519 °C was likely to be the oxidation and decomposition of the PVA main chain. These last two steps were attributed to the loss of PVA and organic compound blended in the fibers. At a temperature above 519 °C, there was no significant change in their weight. Thus, pure crystalline $ZnWO_4$ fibers were assumed to be produced at a temperature of 519 °C and above – very close to the reports of Zhao et al. (486 ^{o}C) [10], and Ryu et al. (550 ^{o}C) [17]. Comparing between PVA and $ZnWO_4$-

PVA electrospun fibers, their weight and weight loss percents of each steps were different, mainly caused by the evaporation and decomposition of water and PVA.

SEM, TEM, AFM, and SAED

Fig. 3a-c shows SEM images of the electrospun fibers produced from the solutions of 5 wt%, 6 wt% and 7 wt% PVA. These products were composed of fibers shaped like a web of spiders, with their smooth surfaces. The as-electrospun nuclei blended in the fibers were not able to be detected by SEM. For 5 wt% PVA, some beads were also detected. When the content of PVA was increased from 5 wt% to 7 wt%, diameters of the fibers were also increased and the beads were no longer detected. This implies that the electrospun beaded fibers were influenced by the stability of the jet of inorganic material-polymeric solutions, and PVA contents. It should be noted that at low PVA content, the web was composed of fibers and beads. At sufficiently high PVA content, it was exactly right to eject the inorganic material-polymeric solution through the syringe out of the long hollow needle [21], and the product was composed of the bead-free fibers. The diameters of the fibers of Fig. 3b were in the range of 100-250 nm. When they were calcined at 400 °C, 500 °C and 600 °C for 3 h - shown in Fig. 3d-f, the fibers became thinner with their surfaces roughened. These were caused by the evaporation of PVA and volatile components. The nuclei grew up, due to the high temperature calcination – indicating that these products were composed of a number of solid nanoparticles joined together in lines shaped like fibers. Upon increasing the calcination temperature, the evaporation rate of PVA and the crystalline degree of inorganic material became higher. At 600 °C, PVA was completely decomposed, and the polycrystalline fibers were produced. At this stage, the diameters of the fibers were in the range of 50-100 nm. The nanoparticles grew up to be larger particles with the average diameter of 100 nm.

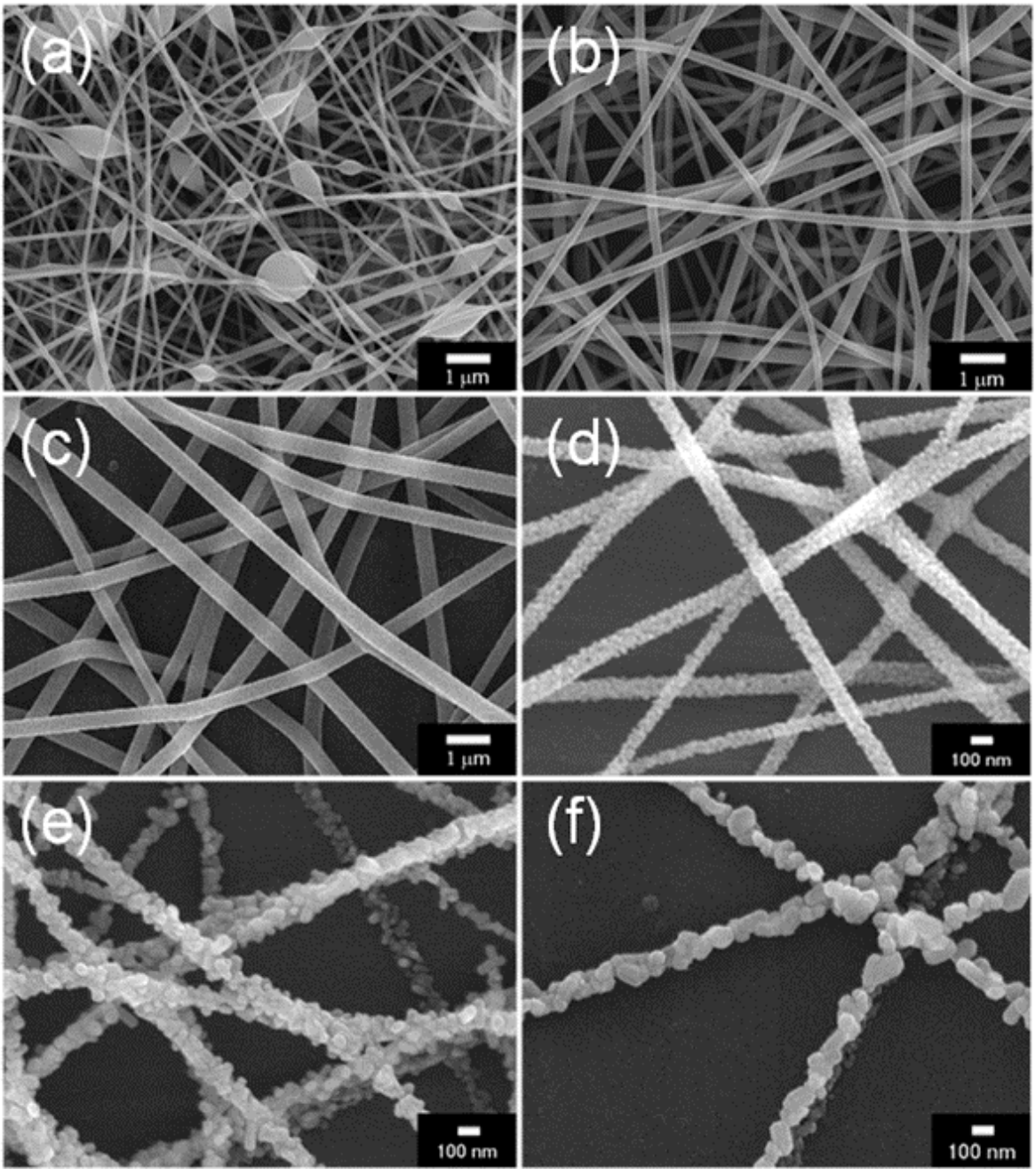


Fig. 3 SEM images of the electrospun fibers using different PVA contents of (a-c) 5 wt%, 6 wt%, and 7 wt%, and (d-f) the electrospun fibers of (b) after calcination at 400 °C, 500 °C, and 600 °C for 3 h, respectively.

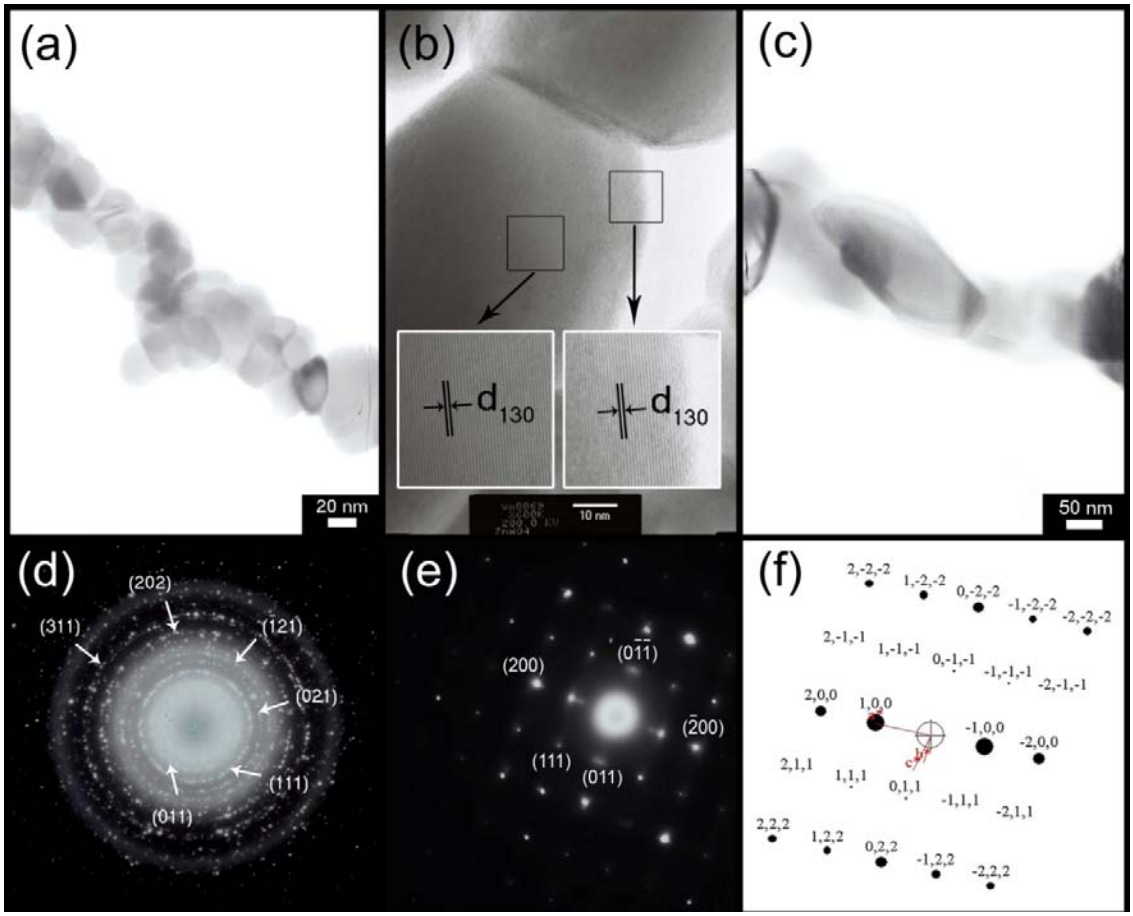


Fig. 4 TEM and HRTEM images, and SAED and simulated patterns of the electrospun fibers after calcination at (a, b and d) 500 °C and (c, e and f) 600 °C for 3 h.

Typical TEM and HRTEM images of electrospun fibers after calcination at 500 °C and 600 °C for 3 h are shown in Fig. 4a-c. The results confirmed that the fibers with 500 °C calcination were composed of a number of nanoparticles with average diameter of 50 nm. The corresponding SAED pattern (Fig. 4d) was indexed [22] and specified as $ZnWO_4$ (JCPDS database no. 15-0774) [11]. The (130) lattice planes (Fig. 4b) were also detected as clear and coherent parallel stripes, composing the crystalline structured $ZnWO_4$. The analysis implies that each of the nanoparticles is single crystal. Upon increasing the calcination temperature from 500 °C to 600 °C, the average size of

crystalline particles was increased by 1.5 times of the precursor or about 75 nm in diameter – joined together to form fiber-like assembly. Fig. 4e and f shows SAED and simulated patterns of its single crystal. This SAED pattern was indexed [22] and specified as $ZnWO_4$ (JCPDS database no. 15-0774) [11]. It was also in accordance with that obtained by the simulation [23]. This product was really proved to be monoclinic sanmartinite-type structured $ZnWO_4$.

External morphologies of the electrospun fibers with their corresponding height profiles before (A), and after (B,C) calcination at 500 °C are shown in Fig. 5. In the present research, the as-spun fiber appeared as smooth and even surface, with 250 nm diameter. After calcination at 500 °C, the fiber became thinner. Its surface was roughened and uneven. This product contained different sized particles, connected as fiber-like assembly - in accordance with the above SEM and TEM analyses.

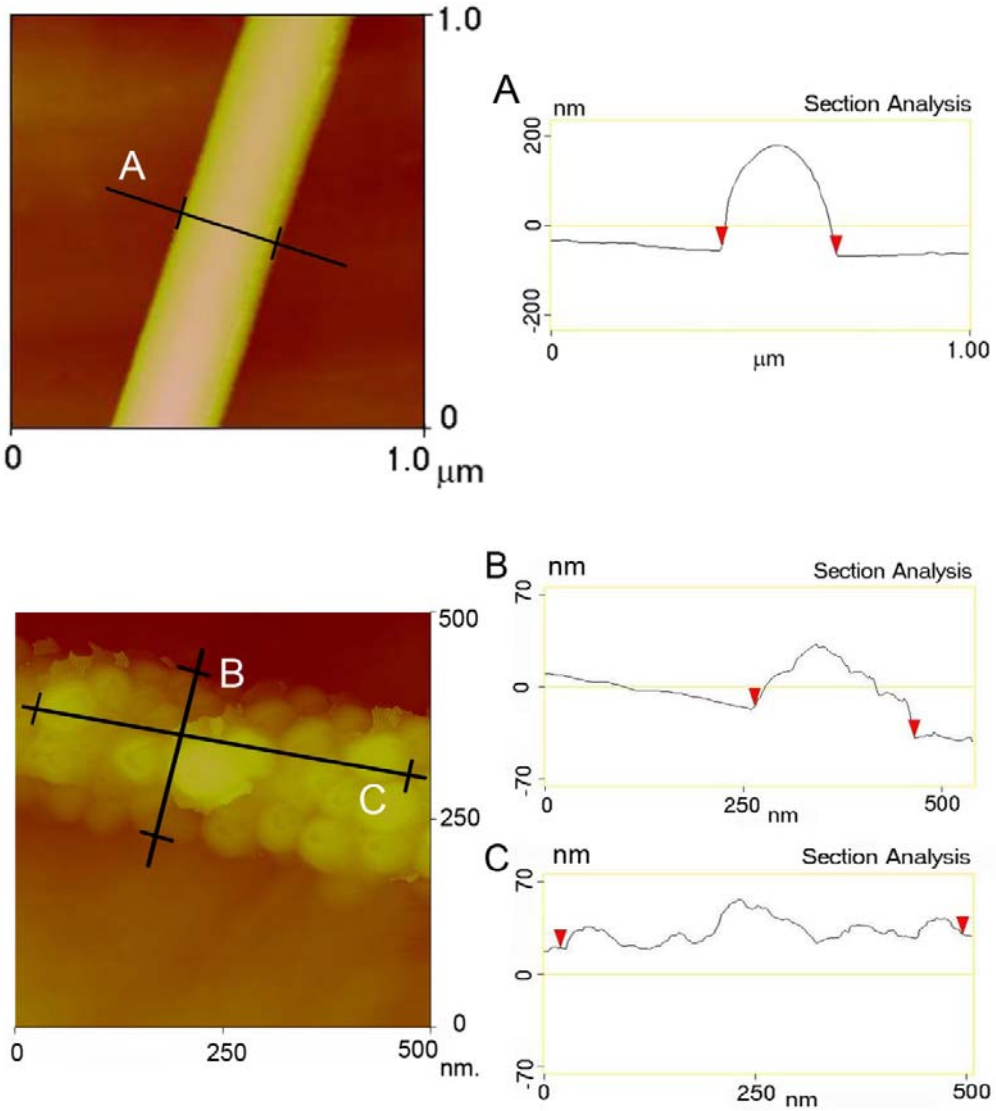


Fig. 5 AFM images and height profiles of the electrospun fibers before (A), and after (B,C) calcination at 500 °C for 3 h.

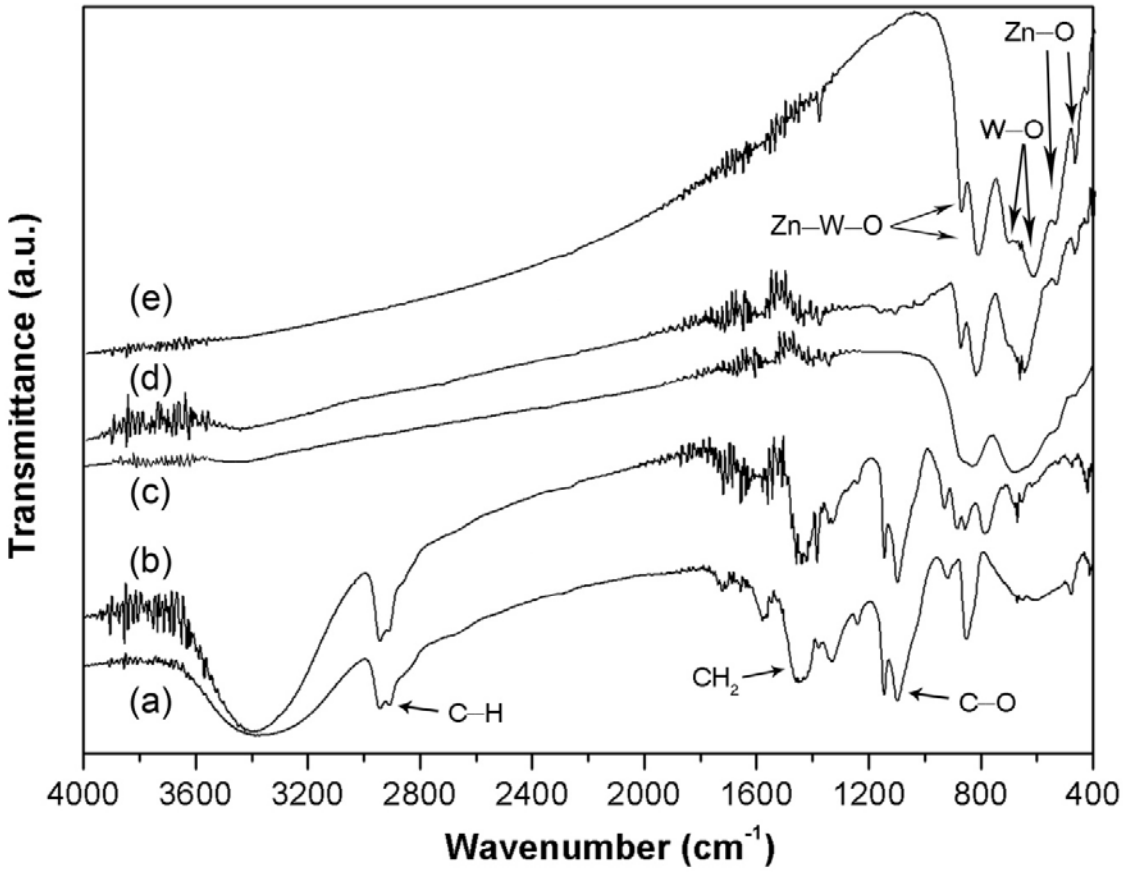


Fig. 6 FTIR spectra of (a) PVA, and (b-e) $ZnWO_4$-PVA electrospun fibers before and after calcination at 400 °C, 500 °C, and 600 °C for 3 h, respectively.

FTIR

To explain the structure of the products in more detail, they were characterized by FTIR in the range between 4000 and 400 cm^{-1}. The FTIR spectra (Fig. 6) were provided further insight into the structure of PVA (MW = 125,000), and $ZnWO_4$-PVA electrospun fibers with and without calcination at 400 °C, 500 °C and 600 °C. Obviously, the major vibrational modes associated with poly (vinyl alcohol) were the following. The O–H stretching of alcohol and residual water was detected at 3600-3200 cm^{-1}. The vibrational mode at 2943 cm^{-1} corresponds to the C–H stretching of alkyl groups. The C=O stretching mode was detected at 1721 cm^{-1}, CH_2 bending mode at 1448 cm^{-1}, and

C–O stretching mode of carboxyl at 1098 cm^{-1} [24,25]. When the $ZnWO_4$-PVA as-spun fibers were characterized by FTIR, additional six modes were detected at 1000-450 cm^{-1}. They were the stretching and bending modes of Zn–O–W (880, 826 cm^{-1}), W–O in $(WO_6)^{2-}$ octahedrons (709, 660 cm^{-1}), and Zn–O (540, 475 cm^{-1}), respectively [10,17]. Once, the $ZnWO_4$-PVA electrospun fibers were calcined at high temperature, the PVA began to evaporate and decompose. At higher temperatures, the evaporation rates were faster and the PVA spectra became lessened. Until at 600 °C calcination, the vibrational modes of PVA were no longer detected, and those of $ZnWO_4$ were the strongest.

Raman analysis

The Raman spectra of $ZnWO_4$-PVA electrospun fibers with 400 °C, 500 °C, and 600 °C calcination are shown in Fig. 7. It should be noted that the Raman peaks of the electrospun fibers with 400 °C calcination were broadened, caused by the dispersion of the crystallite sizes and relaxation of the $ZnWO_4$ particles [7]. When the calcination temperatures were increased to be 500 °C and 600 °C, the $ZnWO_4$ crystals were improved and its crystalline degree was increased. These promoted the atoms to concurrently vibrate at the same mode and the intensity increased in the strength. The spectra show the peaks at 195 cm^{-1} which was interpreted as $V(A_g)$ involving the Zn^{2+} cations. The peaks at 277 cm^{-1} were specified as $V_{def}(A_g)$ of the cationic sublattices. Those at 344 and 409 cm^{-1} were assigned as $r(B_g)$ and $\delta(A_g)$ deformation modes, and at 783 cm^{-1} and 901 cm^{-1} as antisymmetric B_g and symmetric A_g modes of the terminal WO_2 groups, including at 515 and 547 cm^{-1} as $V_{sym}(B_g)$ and $V_{sym}(A_g)$, and at 678 and 710 cm^{-1} as $V_{as}(A_g)$ and $V_{as}(B_g)$ modes of the $(W_2O_4)_n$ chains, reported by Kloprogge et al. [16], respectively. These last two vibrations were reported as B_g and A_g internal stretching modes, reported by Errandonea et al. [26] and Siriwong et al. [27]. The Raman spectra were also used to prove the crystalline $ZnWO_4$.

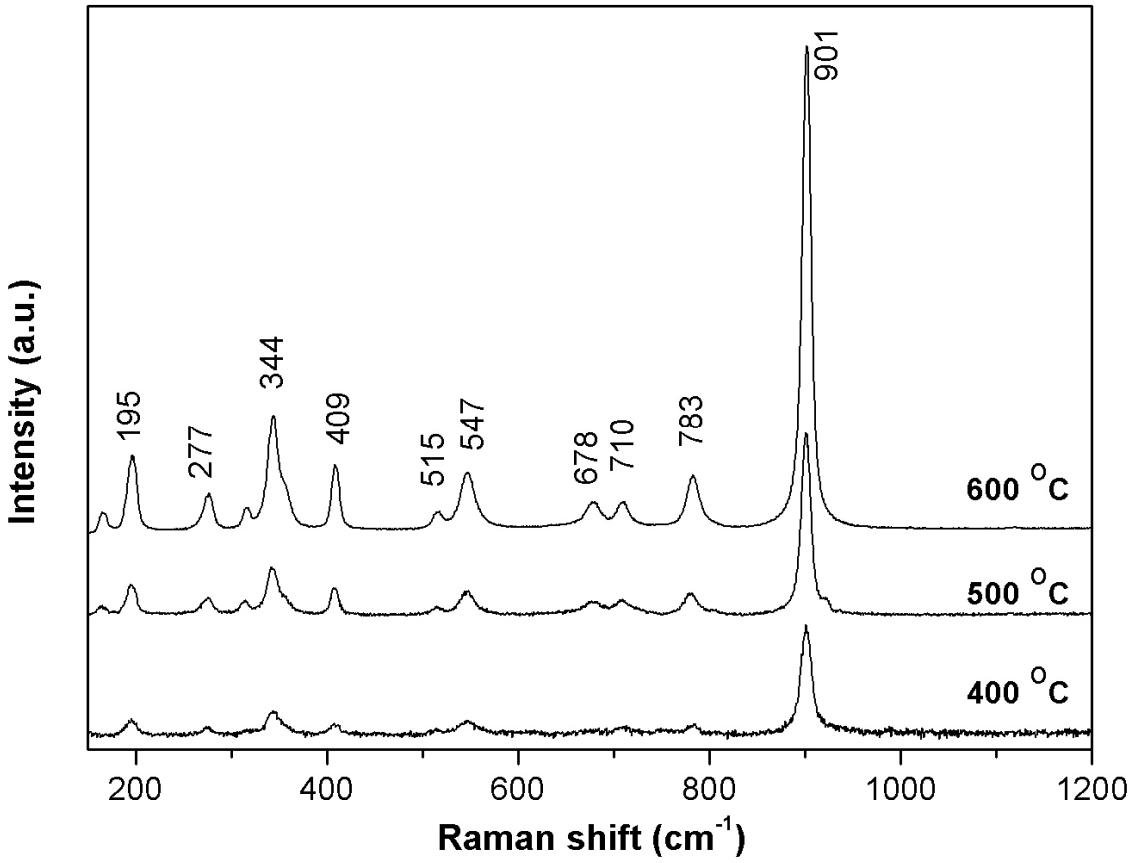


Fig. 7 Raman spectra of $ZnWO_4$-PVA electrospun fibers after calcination at 400 °C, 500 °C, and 600 °C for 3 h.

Formation mechanism

A possible formation mechanism of $ZnWO_4$-PVA electrospun fibers produced by electrospinning was proposed according to the above results as follows. The mixture solution of zinc acetate dihydrate, ammonium metatungstate hydrate and PVA was ejected out of a hollow needle as a non-woven fiber. Concurrently, a high direct voltage was supplied to the needle tip. The external electric field $(\vec{E})$ developed inside the fiber, axially pointed towards the grounded collector. Thus the fiber was heated up. Zinc acetate dihydrate reacted with ammonium metatungstate hydrate to produce $ZnWO_4$ molecules, which nucleated and blended in PVA template.

$$12Zn(CH_3COO)_2{\cdot}2H_2O + H_{26}N_6O_{40}W_{12}{\cdot}H_2O + 31H_2O \longrightarrow 12ZnWO_4 + 48CO_2 + 105H_2 + 3N_2 \quad (1)$$

At this stage, $ZnWO_4$-PVA electrospun product shaped like fibers formed and deposited as a web of fibers on a grounded aluminum foil (Figs. 3a-c, and 5 (left top)). Upon calcination at 400-600 °C, PVA and residual water evaporated and decomposed. $ZnWO_4$ nuclei grew to form nanoparticles (Figs. 3d-f, 4a-c, and 5 (left bottom)). The rates of evaporation and decomposition increased with the increasing in the calcination temperature. At 600 °C, PVA and water were no longer detected (Figs. 1, 4e, and 6e). A number of the nanoparticles joined together in line shaped like a web of nanofibers.

UV-visible absorption

UV-visible absorption of $ZnWO_4$-PVA electrospun fibers after calcination at 600 °C is shown in Fig. 8, which indicated an exponential decreasing of the photonic absorbance attenuated through the material. For crystalline semiconductors, the UV absorption near band edge follows the equation.

$$\alpha h\nu = (h\nu - E_g)^n \quad (2)$$

where α, h, ν, and E_g are the absorbance, Planck constant, photon frequency, and photonic energy band gap, respectively. The parameter n is a pure number associated with the different types of electronic transitions: n = 1/2, 2, 3/2 or 3 for direct-allowed, indirect-allowed, direct-forbidden and indirect-forbidden transitions, respectively [10,15,28,29]. It should be noted that the absorption was controlled by two photon energy ($h\nu$) ranges – the high and low energies. When the photon energy is greater than the energy band gap (E_g), absorption is linearly increased with the increasing of photon energy. The steep inclination of the linear portion of the curve was caused by the UV absorption for charged transition from the topmost occupied state of valence band to the bottommost unoccupied state of the conduction band. For the photon energy with less than E_g, the absorption curve became different from linearity, which was caused by the UV absorption for charged transition relating to defect levels. Its direct energy gap

was determined by extrapolating the linear portion curve of the $(\alpha h\nu)^2$ vs $h\nu$ plot to $\alpha = 0$ (zero absorption). For the present work, direct energy gap was 4.42 eV – very close to those of 3.9-4.4 eV reported by Lacomba-Perales et al. [30], and 4.01 eV reported by Zhao et al. [10].

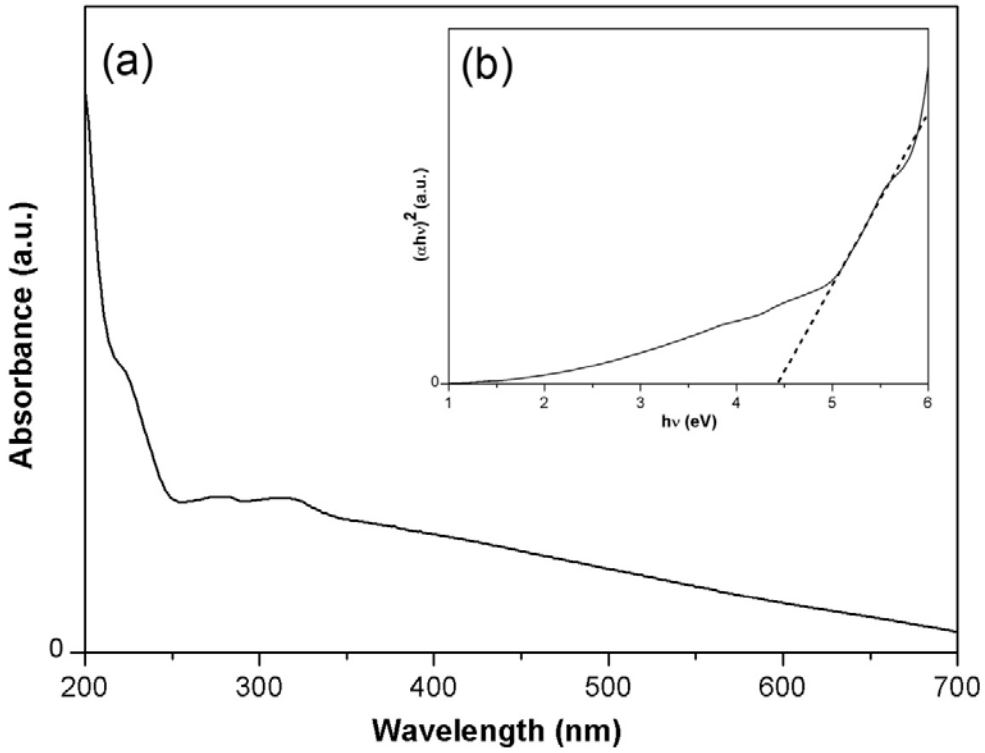


Fig. 8 UV-visible absorption of $ZnWO_4$-PVA electrospun fibers after calcination at 600 °C for 3 h.

For tungstates, the top occupied states of valence band correspond to O_{2p}, and the lowest unoccupied states of conduction band to W_{5d} [27]. For bivalent metal tungstates, the hybridization of the valence states of the metal with O_{2p} and W_{5d} states played an important role in determining the energy band gap. A wide band gap was achieved for those of the tungstates with the s states of the bivalent cations hybridized with the O_{2p} and W_{5d} states, while a narrow band gap was caused by the p, d, and f states hybridization. As for a wide band gap of $ZnWO_4$, the s states hybridization seemed to be taken into account in the electronic transition. The transition of excitons (electron-hole

pairs) between the O_{2p} and W_{5d} orbitals of pure WO_3 was induced by photonic absorption – the O_{2p} orbitals constituted the valence band, and the W_{5d} orbitals the conduction band. For transition metal tungstates - $ZnWO_4$ excluded, the valence orbitals of the transition metal cations ($Co^{II}(3d^7)$, $Ni^{II}(3d^8)$, $Cu^{II}(3d^9)$) hybridized with the W_{5d} orbitals to make the constitution of the conduction band different. For $Zn^{II}(3d^{10})$, the only possibility is to form the conduction band composed of Zn_{3s} and W_{5d} states, in order to enlarge the energy band gap (E_g) [28]. However, particle-sizes and morphologies were found to play the role in the absorbance characteristics [15], which have the influence on the energy gap as well.

PL emission

The optical property of $ZnWO_4$ nanofibers with calcination at high temperatures was studied using 280 nm excitation wavelength, and the results are shown in Fig. 9.

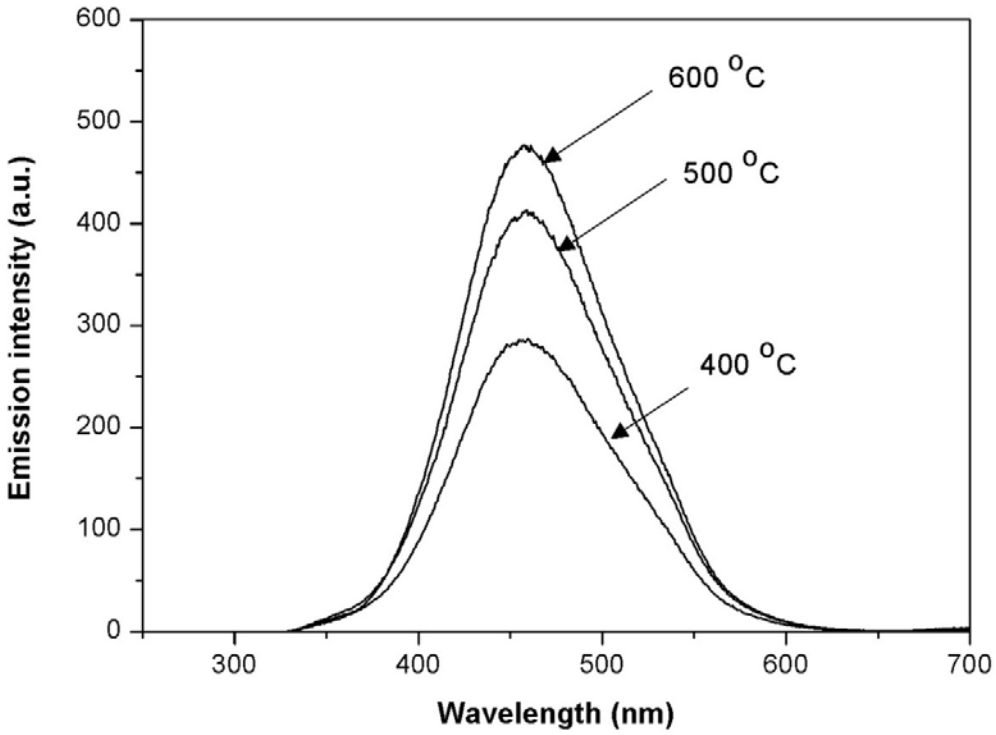


Fig. 9 PL emission of $ZnWO_4$-PVA electrospun fibers after calcination at 400 °C, 500 °C, and 600 °C for 3 h.

In this research, the emission peaks presented broad bands over the 350−600 nm range with a strong blue emission peaks centered at the same wavelengths of 460 nm – in accordance with the report of Chen et al. [31]. The transitions were caused by the hybridization of the W_{5d} and O_{2p} states with very strong tendency for self-trapping of the $(WO_6)^{2-}$ octahedral structure of $ZnWO_4$, in response to this PL emission [15]. The luminescence intensity was increased with the increasing of the calcination temperature, in accordance with the improvement of crystalline degree characterized by the above XRD analysis.

Conclusions

A solution of zinc acetate dihydrate and ammonium metatungstate hydrate with 1:1 molar ratio of Zn:W was prepared and further mixed with 5 wt%, 6 wt%, and 7 wt% PVA, to form three mixtures. By using the +15 kV direct voltage, these mixtures were electrospun to form the webs of $ZnWO_4$-PVA fibers on the ground aluminum foils. In the present research, the electrospun fibers of 6 wt% PVA were further calcined at 400-600 °C for 3 h to form $ZnWO_4$ nanofibers. At 600 °C, the product was $ZnWO_4$ nanoparticles joined together in line shaped like a web of spiders with their direct energy gap of 4.42 eV caused by the hybridization of Zn_{3s} and W_{5d} states, and luminescence at 460 nm (blue) by the transition of the $(WO_6)^{2-}$ octahedrons – one of the promising materials for a variety of applications.

References

[1] Z.W. Fu, J. Ma, Q.Z. Qin, Nanostructured $LiCoO_2$ and $LiMn_2O_4$ fibers fabricated by a high frequency electrospinning, Solid State Ionics 176 (2005) 1635–1640.

[2] J.M. Deitzel, J. Kleinmeyer, D. Harris, N.C.B. Tan, The effect of processing variables on the morphology of electrospun nanofibers and textiles, Polymer 42 (2001) 261–272.

[3] J. Lyons, C. Li, F. Ko, Melt-electrospinning part I: Processing parameters and geometric properties, Polymer 45 (2004) 7597–7603.

[4] Z.M. Huang, Y.Z. Zhang, M. Kotaki, S. Ramakrishna, A review on polymer nanofibers by electrospinning and their applications in nanocomposites, Compos. Sci. Tech. 63 (2003) 2223–2253.

[5] P. K. Panda, S. Ramakrishna, Electrospinning of alumina nanofibers using different precursors, J. Mater. Sci. 42 (2007) 2189–2193.

[6] J.Y. Li, H. Dai, Q. Li, X.H. Zhong, X.F. Ma, J. Meng, X.Q. Cao, Lanthanum zirconate nanofibers with high sintering-resistance, Mater. Sci. Eng. B 133 (2006) 209–212.

[7] A. Kalinko, A. Kuzmin, Raman and photoluminescence spectroscopy of zinc tungstate powders, J. Lumin. 129 (2009) 1144–1147.

[8] G. Huang, C. Zhang, Y. Zhu, $ZnWO_4$ photocatalyst with high activity for degradation of organic contaminants, J. Alloys Compd. 432 (2007) 269–276.

[9] R.P. Jia, G.X. Zhang, Q.S. Wu, Y.P. Ding, $ZnWO_4$-TiO_2 composite nanofilms: Preparation, morphology, structure and photoluminescent enhancement, Mater. Lett. 61 (2007) 1793–1797.

[10] X. Zhao, W. Yao, Y. Wu, S. Zhang, H. Yang, Y. Zhu, Fabrication and photoelectrochemical properties of porous $ZnWO_4$ film, J. Solid State Chem. 179 (2006) 2562–2570.

[11] Powder Diffract. File, JCPDS-ICDD, 12 Campus Boulevard, Newtown Square, PA 19073-3273, U.S.A., 2001.

[12] A. Kornylo, A. Jankowska-Frydel, B. Kuklinski, M. Grinberg, N. Krutiak, Z. Moroz, M. Pashkowsky, Spectroscopic properties of $ZnWO_4$ single crystal doped with Fe and Li impurities, Radiat. Meas. 38 (2004) 707–710.

[13] H. Fu, J. Lin, L. Zhang, Y. Zhu, Photocatalytic activities of a novel $ZnWO_4$ catalyst prepared by a hydrothermal process, Appl. Catal. A 306 (2006) 58–67.

[14] F.S. Wen, X. Zhao, H. Huo, J.S. Chen, E. Shu-Lin, J.H. Zhang, Hydrothermal synthesis and photoluminescent properties of $ZnWO_4$ and Eu^{3+} - doped $ZnWO_4$, Mater. Lett. 55 (2002) 152–157.

[15] M. Hojamberdiev, G. Zhu, Y. Xu, Template-free synthesis of $ZnWO_4$ powders via hydrothermal process in a wide pH range, Mater. Res. Bull. 45 (2010) 1934–1940.

[16] J.T. Kloprogge, M.L. Weier, L. V. Duong, R. L. Frost, Microwave-assisted synthesis and characterisation of divalent metal tungstate nanocrystalline minerals: ferberite, hübnerite, sanmartinite, scheelite and stolzite, Mater. Chem. Phys. 88 (2004) 438–443.

[17] J.H. Ryu, C.S. Lim, K.H. Auh, Synthesis of $ZnWO_4$ nanocrystalline powders, by the polymerized complex method, Mater. Lett. 57 (2003) 1550–1554.

[18] K. Pal, A.K. Banthia, D.K. Majumdar, Preparation and characterization of polyvinyl alcohol–gelatin hydrogel membranes for biomedical applications, AAPS PharmSciTech. 8 (2007) Art. No. 21, DOI: 10.1208/pt080121.

[19] C. Suryanarayana, M.G. Norton, X-ray Diffract., A Pract. Appro., Plenum Press, New York, 1998.

[20] E.A. El-hefian, M.M. Nasef, A.H. Yahaya, The preparation and characterization of chitosan / poly (vinyl alcohol) blended films, E-J. Chem. 7 (2010) 1212–1219.

[21] B. Ding, H.Y. Kim, S.C. Lee, D.R. Lee, K.J. Choi, Preparation and characterization of nanoscaled poly (vinyl alcohol) fibers via electrospinning, Fibers and Polymers 3 (2002) 73–79.

[22] K.W. Andrews, D.J. Dyson, S.R. Keown, Interpret. Electr. Diffract. Patterns, Plenum Press, New York, 1971.

[23] C. Boudias, D. Monceau, CaRIne Crystallography 3.1, DIVERGENT S.A., Centre de Transfert, 60200 Compiègne, France, 1989–1998.

[24] H.S. Mansur, R.L. Oréfice, A.A.P. Mansur, Characterization of poly (vinyl alcohol) / poly (ethylene glycol) hydrogels and PVA-derived hybrids by small-angle X-ray scattering and FTIR spectroscopy, Polymer 45 (2004) 7193–7202.

[25] H.S. Mansur, C.M. Sadahira, A.N. Souza, A.A.P. Mansur, FTIR spectroscopy characterization of poly (vinyl alcohol) hydrogel with different hydrolysis degree and chemically crosslinked with glutaraldehyde, Mater. Sci. Eng. C 28 (2008) 539–548.

[26] D. Errandonea, F. J. Manjón, N. Garro, P. Rodríguez-Hernández, S. Radescu, A. Mujica, A. Muñoz, C. Y. Tu, Combined Raman scattering and ab initio investigation of pressure-induced structural phase transitions in the scintillator $ZnWO_4$, Phys. Rev. B, 78 (2008) 054116-1–054116-12.

[27] P. Siriwong, T. Thongtem, A. Phuruangrat, S. Thongtem, Hydrothermal synthesis, characterization, and optical properties of wolframite $ZnWO_4$ nanorods, CrystEngComm, 13 (2011) 1564–1569.

[28] T. Montini, V. Gombac, A. Hameed, L. Felisari, G. Adami, P. Fornasiero, Synthesis, characterization and photocatalytic performance of transition metal tungstates, Chem. Phys. Lett. 498 (2010) 113–119.

[29] O. Yayapao, T. Thongtem, A. Phuruangrat, S. Thongtem, CTAB-assisted hydrothermal synthesis of tungsten oxide microflowers, J. Alloys Compd. 509 (2011) 2294–2299.

[30] R. Lacomba-Perales, J. Ruiz-Fuertes, D. Errandonea, D. Martínez-García, A. Segura, Optical absorption of divalent metal tungstates: Correlation between the band-gap energy and the cation ionic radius, Europhys. Lett. 83 (2008) Art. No. 37002, DOI: 10.1209/0295-5075/83/37002.

[31] S.J. Chen, J.H. Zhou , X.T. Chen, J. Li, L.H. Li, J.M. Hong, Z. Xue, X.Z. You, Fabrication of nanocrystalline $ZnWO_4$ with different morphologies and sizes via hydrothermal route, Chem. Phys. Lett. 375 (2003) 185–190.

10. Photocatalytic activity of Zn_2SnO_4-SnO_2 nanocomposites produced by sonochemistry in combination with high temperature calcination

Abstract

Zn_2SnO_4 nanocubes-SnO_2 (ZTO(NC)-SnO_2) and Zn_2SnO_4 nanoparticles-SnO_2 (ZTO(NP)-SnO_2) were successfully produced by a combination of sonochemical route in mixture solvents of different contents of ethylene glycol – de-ionized water and high temperature calcination. The phase and morphology were characterized by X-ray powder diffraction (XRD), field emission scanning electron microscopy (FE-SEM), transmission electron microscopy (TEM) and energy-dispersive X-ray spectroscopy (EDS). ZTO(NP)-SnO_2 nanocomposites exibit higher photocatalytic activity than ZTO(NC)-SnO_2 through the degradation of methylene blue (MB) dye under UV light.

Keywords: Sonochemistry-calcination combination; ZTO(NC)-SnO_2; ZTO(NP)-SnO_2; Photocatalysis

Introduction

Photocatalysis using metal oxide as catalysts has been widely studied for promoting degradation of organic pollutants. The present process, photon with energies corresponding to or exceeding the energy band gap of the semiconducting catalyst can excite electrons from the valence band (VB) to the conduction band (CB), producing high-energy electron-hole pairs. They can react with water and dissolving oxygen to produce •OH free radicals with high chemical activity and with the dye molecules adsorbed on the surface of metal oxide photocatalyst. Thus the dye molecules will be photodegradated by the oxidation–reduction reaction [1–5]. However, high recombination rate between photo-generated electrons and holes is a major factor to reduce the photocatalytic efficiency. Coupling of different semiconducting oxides such as CuO-ZnO [6], TiO_2-SnO_2 [7], Fe_2O_3-SnO_2 [8], $NaBiO_3$-Bi_2O_3 [9] and TiO_2-Fe_2O_3 [10] has been

widely studied and proved to be good photocatalysts by promoting the high quantum yield of electron–hole pair separation. Moreover parameters such as small particle size, high surface area, controlled porosity and tailor-designed pore size distribution are important factors for enhancement of the photocatalytic efficiency [3, 11, 12].

Zn_2SnO_4 (ZTO) is one type of mixed oxide which has possibility in the photocatalytic application due to its high electron diffusivity, high electrical conductivity and favorable stability in acidic and basic solutions [2, 13–17]. For SnO_2, it is widely studied for photocatalysis and its band gap is in accordance with ZTO. The CB edge potential of ZTO is more negative than that of SnO_2 thus electrons easily transfers to the CB of the SnO_2, leading to the effective electron–hole pair separation [17, 18]. Therefore, ZTO and SnO_2 are the interesting coupling semiconductors for photocatalysis of this work.

In this report, the ZTO(NC)-SnO_2 and ZTO(NP)-SnO_2 composites can be produced by the simple and commercially feasible method of the sonochemical route and calcination combination. Their photocatalytic activity evaluated through the degradation efficiency of MB was found to be improved.

Experimental procedure

To synthesize the ZTO-SnO_2 nanocomposites, each 0.010 mole of tin(II) chloride dihydrate ($SnCl_2 \cdot 2H_2O$) and zinc nitrate hexahydrate ($Zn(NO_3)_2 \cdot 6H_2O$) was dissolved in different solvents of ethylene glycol (EG) – de-ionized water mixture: 0 % w/w EG (100 % w/w de-ionized water), 40 % w/w EG, 75 % w/w EG and 100 % w/w EG, and continuously stirred for 20 min at room temperature. The pH of the solutions was adjusted to 4, 7 and 10 using 3 M NaOH. Then the solutions were irradiated by 35 kHz ultrasonic radiation for 15 min. White precipitates were produced, separated by filtration, washed for several times by de-ionized water and absolute ethanol, and dried in air at 70 ^{o}C for 24 h. Each precursor powder produced in 100 % w/w de-ionized water and 100 % w/w ethylene glycol solvents was divided into four parts. One was used as a

reference, and each of the three remains were further calcined at 400 ^{o}C, 600 ^{o}C and 900 ^{o}C in an ambient atmosphere for 1 h to form white powder.

The products were characterized by an X-ray diffractometer (XRD, Philips X' Pert MPD) operating at 20 kV, 15 mA with Cu K_{α} radiation (1.5405 Å) at a scanning rate of 0.02 deg/s in the 2θ range of 10–80 deg; a scanning electron microscope (SEM, JEOL JSM-6335F) operating at 15 kV; a transmission electron microscope (TEM, JEOL JEM-2010) operating at 200 kV; and a UV-visible spectrometer (Lambda 25 PerkinElmer) using a UV lamp with the resolution of 2.0 nm.

The photocatalytic activity of the ZTO(NC)-SnO_2 and ZTO(NP)-SnO_2 products were investigated through the degradation of methylene blue (MB) dye aqueous solutions. Each 100 mg product was suspended in 100 ml $6.0x10^{-6}$ M MB solution, which was stirred for 1 h in the dark condition to establish an adsorption–desorption equilibrium of MB dye on the ZTO-SnO_2 surfaces. Photocatalysis was initiated by two 15 W UV lamps for different lengths of time. Absorbance peaks at 663 nm wavelength, determined by UV-visible spectrometer, were assumed to be linearly dependent on the concentration of MB before and after photocatalysis. Decolorization efficiency (%) was calculated by $\frac{I_o - I}{I_o} x100$, where I_o and I were the absorbance intensities of the solutions before and after photocatalysis, respectively.

Results and discussion

Phase and morphology

Fig. 1a shows diffraction patterns of the products which were produced in 100 % w/w water as a solvent with the pH of 4, 7 and 10. In this research, the pH is an important parameter for the formation of $ZnSn(OH)_6$ phase and its crystalline degree. Amorphous SnO_2 with tetragonal crystal structure (JCPDS No. 01-0657) [19] was produced in the solution with the pH 4. In the solution with the higher pH of 7, $ZnSn(OH)_6$ mixed with SnO_2 phase began to be detected. Eventually, the product was

pure $ZnSn(OH)_6$ with high crystalline degree under the highest alkaline condition at the pH 10. The diffraction peaks of the product are in good accordance with those of the standard $ZnSn(OH)_6$ phase (JCPDS No. 73-2384) [19]. Therefore, the higher alkaline condition can form pure $ZnSn(OH)_6$ powder with effectively.

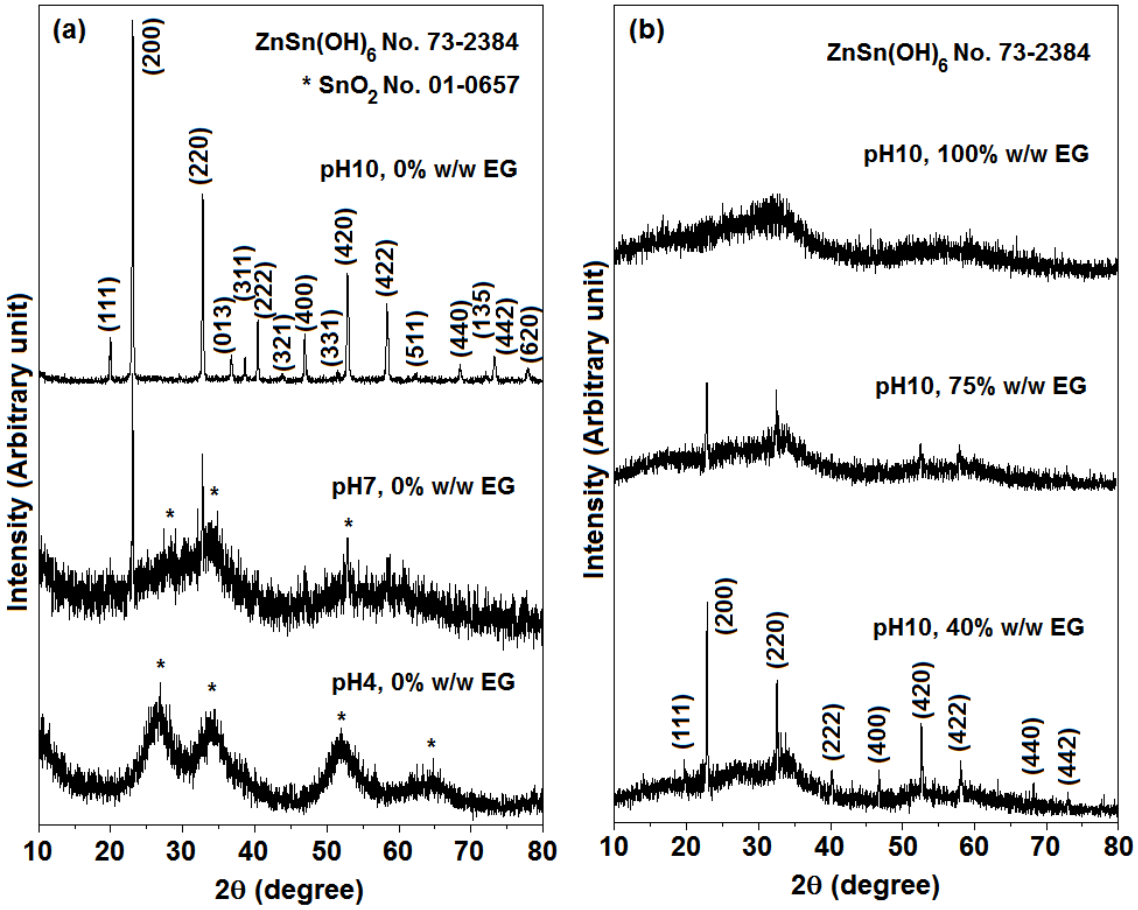


Fig. 1 XRD patterns of the products produced in (a) 100 % w/w water at the pH of 4, 7 and 10, (b) EG-water mixture solvent containing 40, 75 and 100 % w/w EG at the pH of 10.

Fig. 1b shows diffraction patterns of the products which were produced at different w/w contents of ethylene glycol in water. The peak intensity of $ZnSn(OH)_6$ was gradually decreased with the increasing in ethylene glycol and completely formed

amorphous $ZnSn(OH)_6$ at 100 % w/w ethylene glycol. There were no diffraction lines assigned to any crystalline phase, indicating that amorphous $ZnSn(OH)_6$ was produced. The growth of $ZnSn(OH)_6$ concerned the thermal stability of the starting materials, controlled by the interaction with the solvent. The starting materials in the solvent having high-dielectric constant can undergo decomposition and form the precursor nuclei at lower temperature than those in the solvent having low-dielectric constant [20]. In this case, ethylene glycol has low-dielectric constant than water. Thus the starting reagents in ethylene glycol can slowly undergo decomposition and form $ZnSn(OH)_6$ nuclei less complete than the reagents in water solvent, producing the $ZnSn(OH)_6$ amorphous phase in 100 % w/w EG.

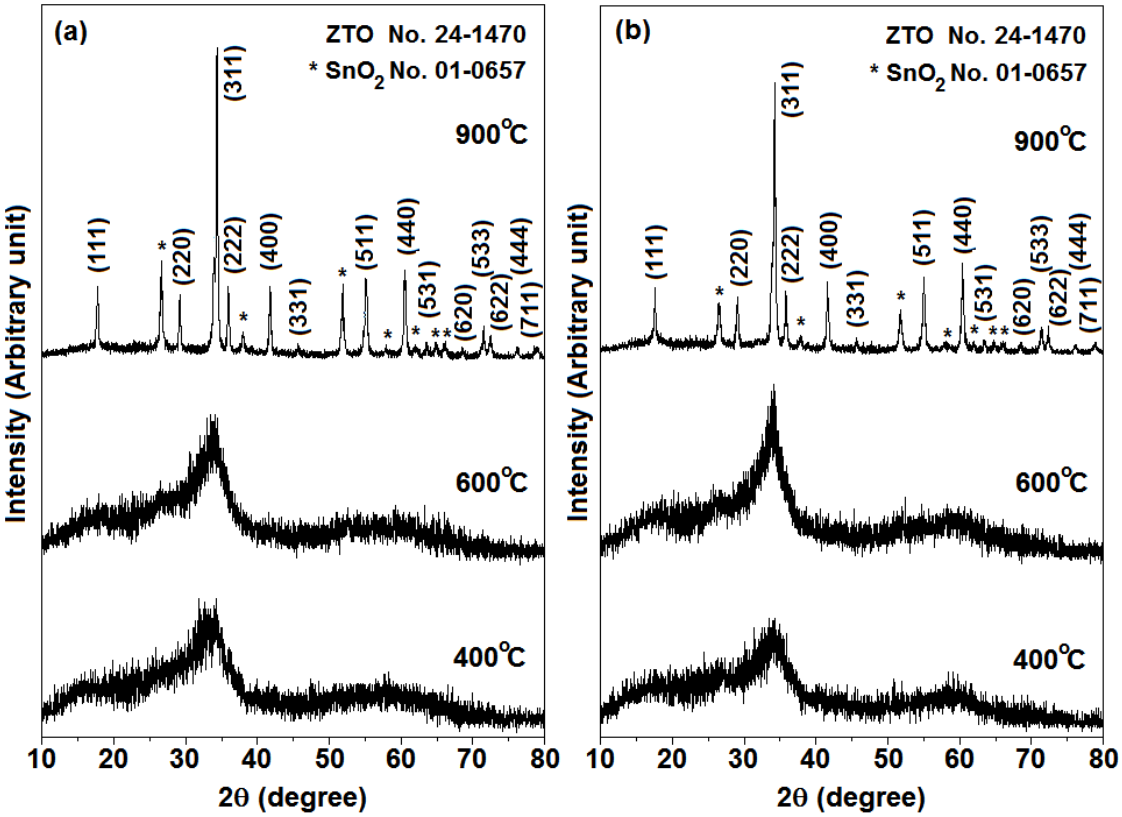


Fig. 2 XRD patterns of the products produced in (a) 100 % w/w water and (b) 100 % w/w ethylene glycol with the pH of 10 and followed by calcination at 400, 600 and 900 ^{o}C for 1 h.

The crystalline phases of the calcination products in water and ethylene glycol as solvents are illustrated in Fig. 2. In water solvent, the product before calcination was $SrSn(OH)_6$ phase with high crystalline degree (Fig. 1a) transformed into high amorphous degree of Zn_2SnO_4-SnO_2 composites after calcination at 400 ^{o}C and 600 ^{o}C, and became completely ZTO-SnO_2 crystal at 900 ^{o}C, according to Zn_2SnO_4 (JCPDS No. 24-1470) and SnO_2 (JCPDS No. 01-0657) [19]. By using ethylene glycol as a solvent, the product before calcination was amorphous $ZnSn(OH)_6$ (Fig. 1b). Its crystalline degree was increased with the increasing in the calcination temperature and became completely crystalline ZTO-SnO_2 composites at 900 ^{o}C calcination.

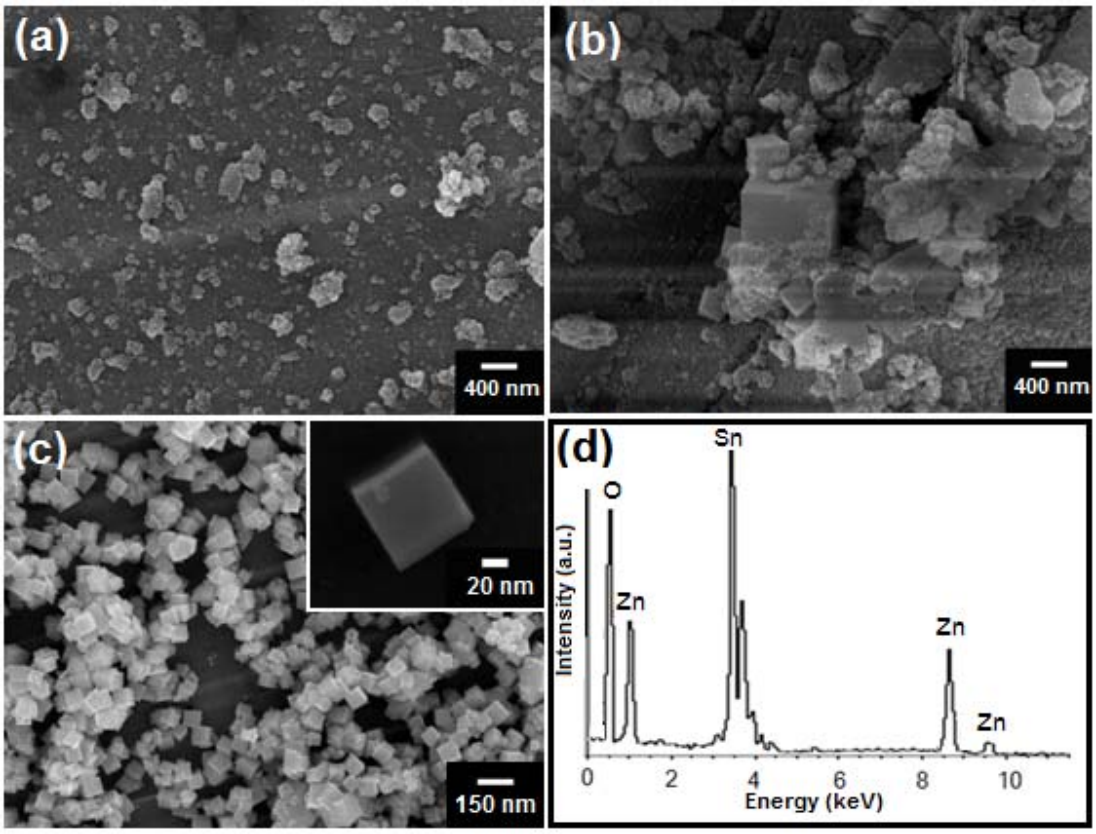


Fig. 3 (a–c) SEM images of the products produced in 100 % w/w water as a solvent at the pH of 4, 7 and 10, respectively. (d) EDS spectrum of the product produced in 100 % w/w water as a solvent at the pH of 10.

Fig. 3 shows SEM images and EDS spectrum of the precursors produced under different pH conditions. At the pH of 4 and 7, a number of particles were produced. Upon increasing the pH to 10, homogeneous cubes (average length of 80 nm) of $ZnSn(OH)_6$ were completely produced. The atomic composition of $ZnSn(OH)_6$ was analyzed by EDS, corresponding to the prominent peaks of Zn, Sn and O elements of the Zn-L_α, Zn-K_α, Zn-K_β, Sn-L_α and O-K_α lines without any impurity detection. Fig. 4 shows SEM images of the post-calcined products produced in different mixture solvents at the pH 10. SEM images of the ZTO-SnO_2 composites present the increasing in the number of ZTO nanoparticles instead of the ZTO nanocubes when the amount of ethylene glycol in water was increased. The really fine ZTO(NP)-SnO_2 was produced in the 100 % w/w ethylene glycol as a solvent. Ethylene glycol molecules with negative charge of two hydroxyl groups at both ends adsorbed on the positively charged surface of the particles. They could retard the preferential growth and finally lead to the formation of ZTO(NP)-SnO_2 instead of ZTO(NC)-SnO_2 [20].

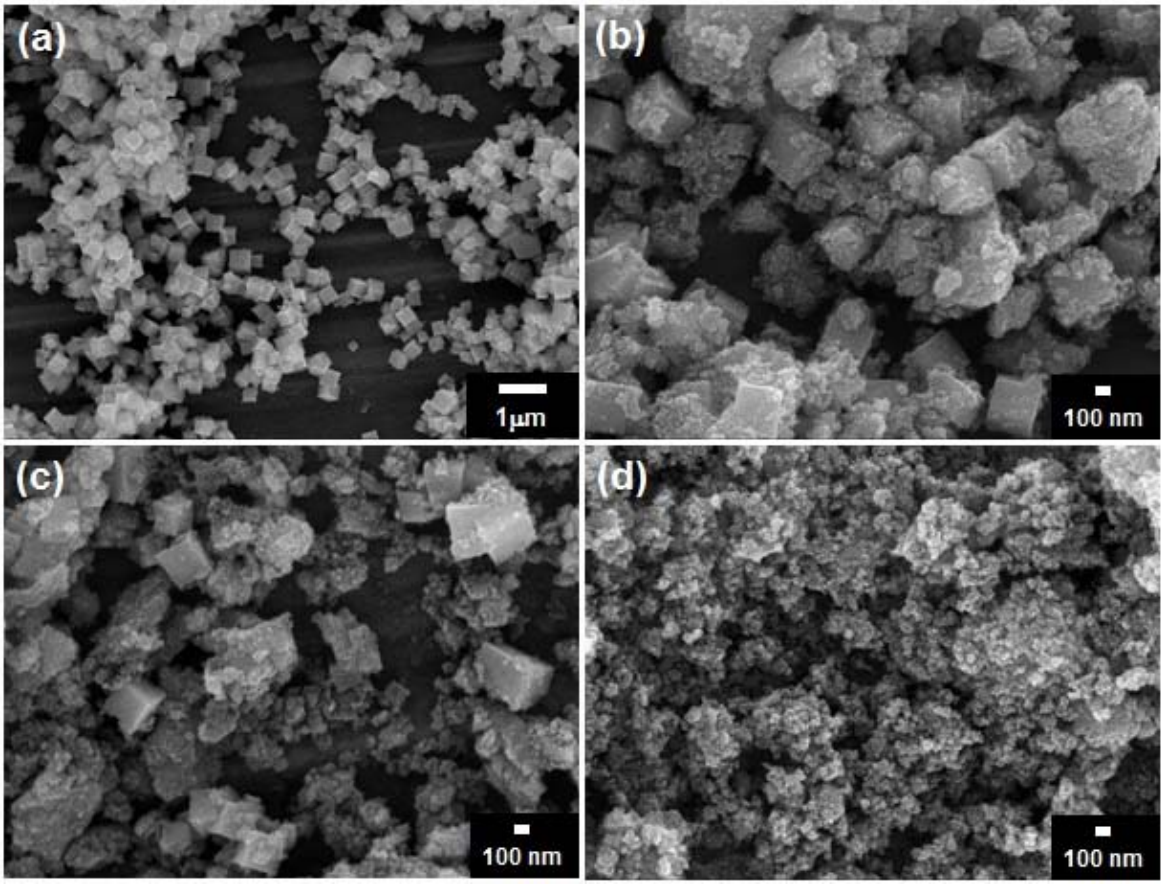


Fig. 4 (a–d) SEM images of ZTO-SnO_2 composites produced in EG-water mixture solvent containing 0, 40, 75 and 100 % w/w EG at the pH of 10 and followed by calcination at 900 ^{o}C for 1h.

The $ZnSn(OH)_6$ precursors were produced from metal salts ($SnCl_2{\cdot}2H_2O$ and $Zn(NO_3)_2{\cdot}6H_2O$) and alkali (NaOH) as starting reagents. Sn^{2+} ions were oxidized by dissolving O_2 to form Sn^{4+} ions. Subsequently, Sn^{4+} and Zn^{2+} reacted with OH^- in alkaline solution to form $ZnSn(OH)_6$. The $ZnSn(OH)_6$ precursors are thermodynamically unstable. The post-calcination of the metastable $ZnSn(OH)_6$ led to the recrystallization process by transforming $ZnSn(OH)_6$ into ZTO-SnO_2 composites with stable structure. Meanwhile, $ZnSn(OH)_6$ precursors still retained their original morphology in the ZTO-SnO_2 composites. The formation of ZTO-SnO_2 composites from $SnCl_2{\cdot}2H_2O$ and $Zn(NO_3)_2{\cdot}6H_2O$ as starting materials can be explained by the following.

$$Zn^{2+} + Sn^{2+} + 4OH^{-} + H_2O + 0.5O_2(g) \longrightarrow ZnSn(OH)_6(s) \quad (1)$$

$$2ZnSn(OH)_6(s) \longrightarrow Zn_2SnO_4(s)\text{-}SnO_2 \text{ composites} + 6H_2O(g) \quad (2)$$

A possible growth mechanism of different morphologies of $ZnSn(OH)_6$ crystal in the solutions containing water and ethylene glycol is schematically illustrated in Fig. 5. First, Sn^{2+} ions were oxidized by dissolving O_2 to form Sn^{4+} ions. Then, Zn^{2+} and Sn^{4+} ions in the aqueous solution easily form $ZnSn(OH)_6$ precipitates by forming bonds with OH^{-} in alkaline aqueous solution. These $ZnSn(OH)_6$ precipitates grew to form larger particles. Self-aggregated particles were able to cluster together to form aggregates as well. With the prolonging reaction time, $ZnSn(OH)_6$ precursors exhibit a well-defined cubic structure with the crystallite size of 85 nm under ultrasonic radiation and finally transformed into the ZTO(NC)-SnO_2 composites by the 900 ^{o}C calcination.

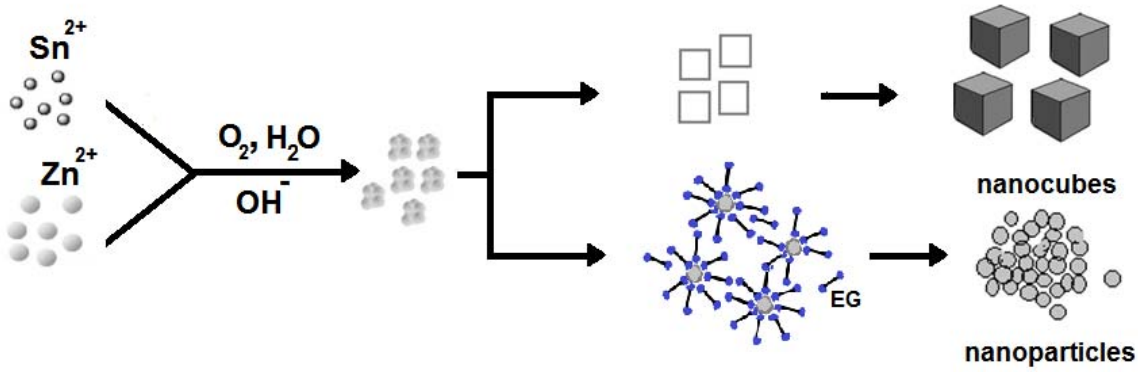


Fig. 5 Schematic illustration for the formation of $ZnSn(OH)_6$ precursors.

The TEM image of ZTO-SnO_2 nanocomposites produced in water solvent (Fig. 6a) reveals the SnO_2 nanoparticles distributed on surface of the ZTO perfect nanocubes. In ethylene glycol as a solvent, the product (Fig. 6c) is the nanoparticles of ZTO-SnO_2. The selected area electron diffraction (SAED) patterns of ZTO-SnO_2 powder (Fig. 6b and d) confirm the polycrystalline structure. The diffraction rings can be indexed to cubic ZTO and tetragonal SnO_2 in accordance with the XRD analysis.

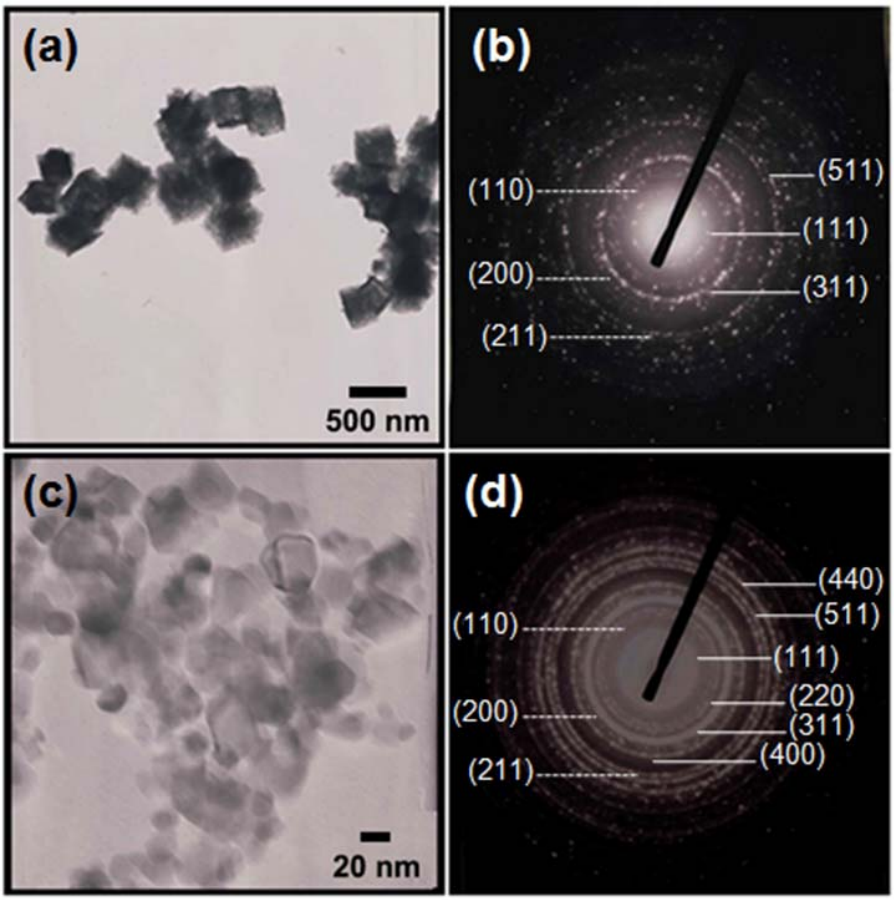


Fig. 6 TEM images and SAED patterns of ZTO-SnO_2 composites produced in (a, b) 100 % w/w water and (c, d) 100 % w/w ethylene glycol at the pH of 10 and followed by calcination at 900 ^{o}C for 1h. Solid and dotted lines are for Zn_2SnO_4 (ZTO) and SnO_2 phases, respectively.

Photocatalysis

The ZTO(NP)-SnO_2 composites produced in 100 % w/w ethylene glycol (EG) solvent was used for photocatalytic testing (Fig. 7). At the beginning, the color of MB dye solution was blue. When the photocatalyst was applied in the dark condition for 60 min, the concentration of MB dye decreased remarkably due to the adsorption of dye molecules on surface of the photocatalyst. Then the photocatalysis was initiated by UV light, and the blue solution was decolorized for different lengths of time. Each

absorbance was determined from the UV-visible intensity at 663 nm wavelength of the individual peak.

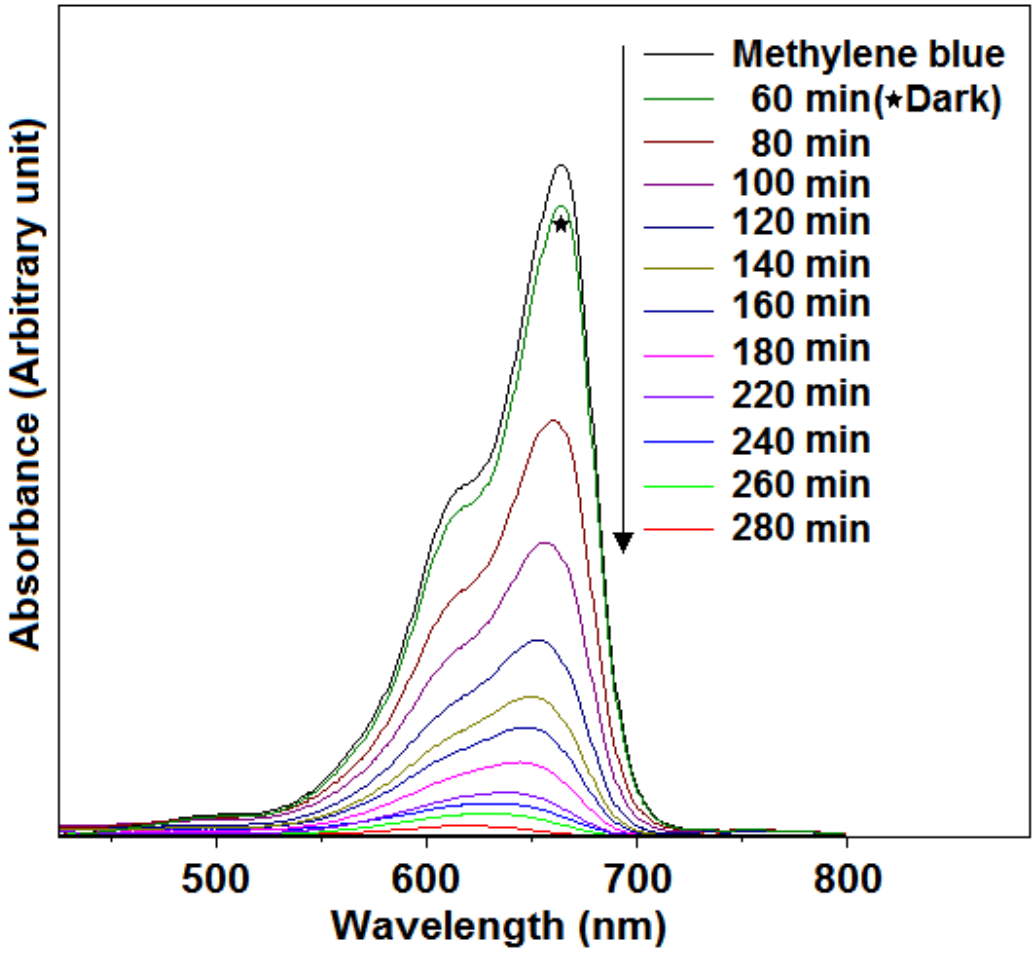


Fig. 7 UV–visible absorption of MB dye in the solution containing ZTO(NP)-SnO_2 composites in the dark and under UV light for different lengths of time.

The decolorization efficiency (Fig. 8) of the MB dye solutions containing ZTO(NC)-SnO_2 and ZTO(NP)-SnO_2 used as photocatalytic materials was compared with that of the MB dye solution without the catalyst. The decolorization efficiency of ZTO(NP)-SnO_2 was 98.6 % within 220 min, and the solution color changed from blue to milky white. The color was more milky white than the MB dye solution containing the ZTO(NC)-SnO_2 (decolorization efficiency = 85.1 % within 220 min) due to the smaller size and larger surface area [3, 11]. A number of photocatalytic materials with high performance have

been reported. Among them, the photocatalytic activities of SnO_2, ZnO doped SnO_2 and Zn_2SnO_4 were 51, 65 and 81 % under UV radiation by 295, 295 and 245 min, respectively [2]. By the use of Zn_2SnO_4 as a photocatalyst, the first-order reaction fitted to a straight line with the reaction rate constant of 5.8×10^{-3} min^{-1} [16]. For the 3 % Ho-doped ZnO as a photocatalyst, the degradation of MB was 98.26 % by 300 min under UV radiation [21]. Methyl orange (MO) solution containing ZnO/SnO_2 (33.3 mol% Sn) photocatalyst with 500 ^{o}C and 10 h calcination was completely decolorized within 60 min under UV radiation [22]. ZnO/SnO_2 photocatalyst calcined at 350 ^{o}C for 2 h can promote the rate of decolorization of MO which was completely decolorized by 35 min [23]. Thus ZTO(NP)-SnO_2 is one of the candidate for using as a photocatalyst for environmental treatment.

The degradation kinetics of MB dye solution of ZTO(NC)-SnO_2 and ZTO(NP)-SnO_2 could be evaluated. The pseudo first-order kinetics model was used and fitted to the equation

$$-\ln\left(\frac{C_t}{C_0}\right) = kt \qquad (3)$$

, where k is the apparent pseudo-first-order rate constant of the degradation, and C_t and C_0 are the concentration of MB dye at any reaction time t and initial concentration, respectively [21, 24, 25]. The k values of Fig. 9 were derived from the plots of $-\ln(C_t/C_0)$ versus irradiation time (t). The rate constant k was calculated and found that the degradation of MB shows apparent pseudo-first-order kinetics of 1.763×10^{-2} and 8.893×10^{-3} min^{-1} for the ZTO(NP)-SnO_2 and ZTO(NC)-SnO_2 nanocomposites, respectively. To test the photocatalytic stability, the photocatalysts were recycled and reused, as shown in Fig. 10. The performance was still unchanged although the catalyst was reused for five times.

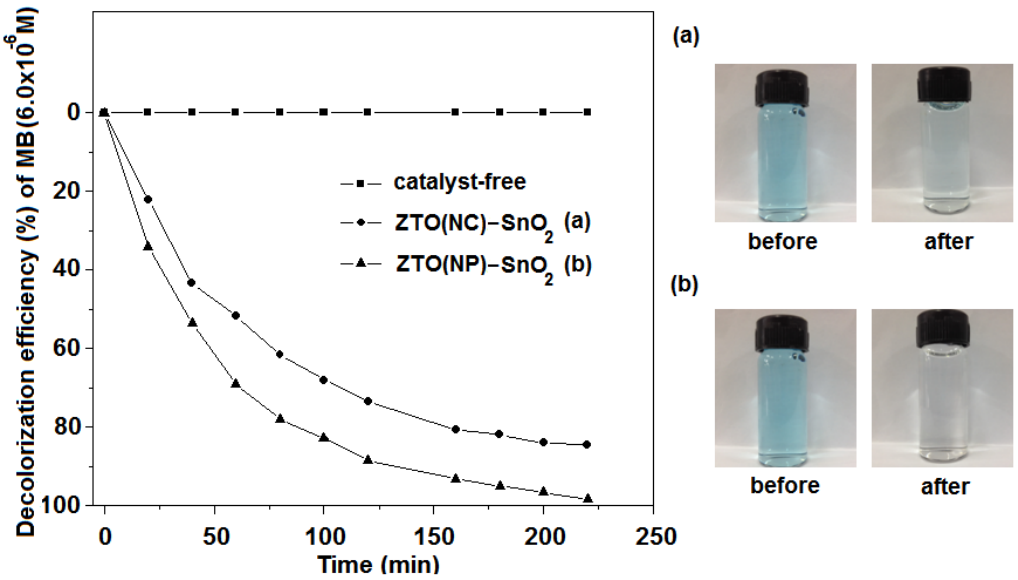


Fig. 8 Decolorization efficiency of MB dye in the solutions containing ZTO(NC)-SnO_2 and ZTO(NP)-SnO_2 composites as compared with that in the catalyst-free solution, and the MB aqueous solution of both before and after testing.

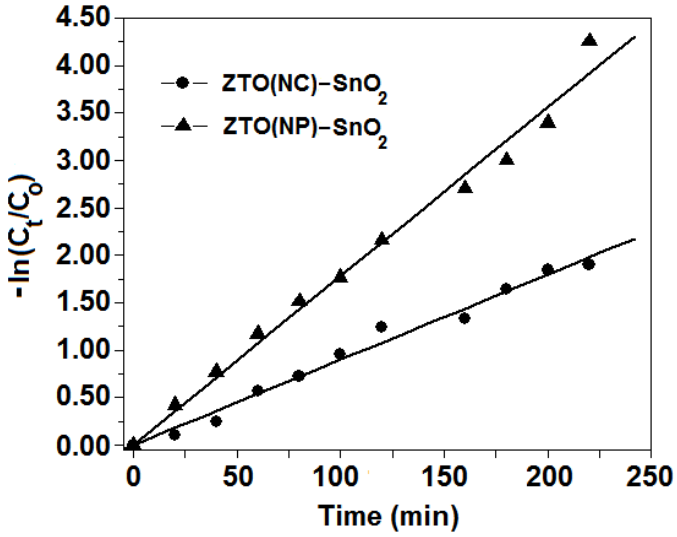


Fig. 9 The pseudo first-order kinetics plot of the MB aqueous solution containing ZTO(NC)-SnO_2 and ZTO(NP)-SnO_2.

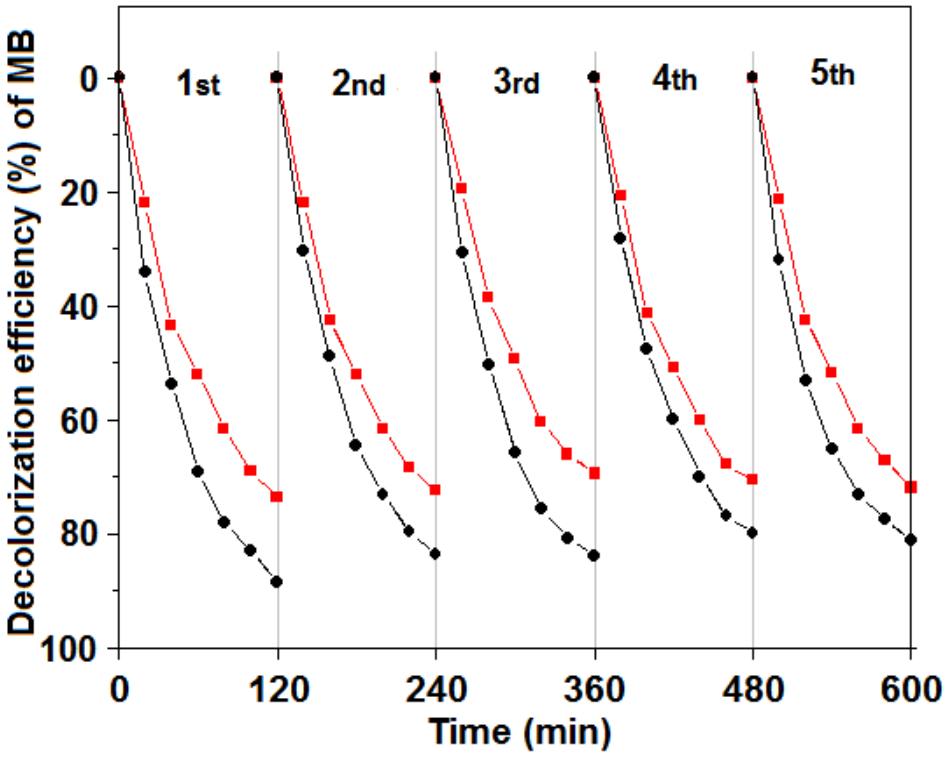


Fig. 10 The cycle performance of the ZTO(NC)-SnO_2 (red) and ZTO(NP)-SnO_2 (black) photocatalysts.

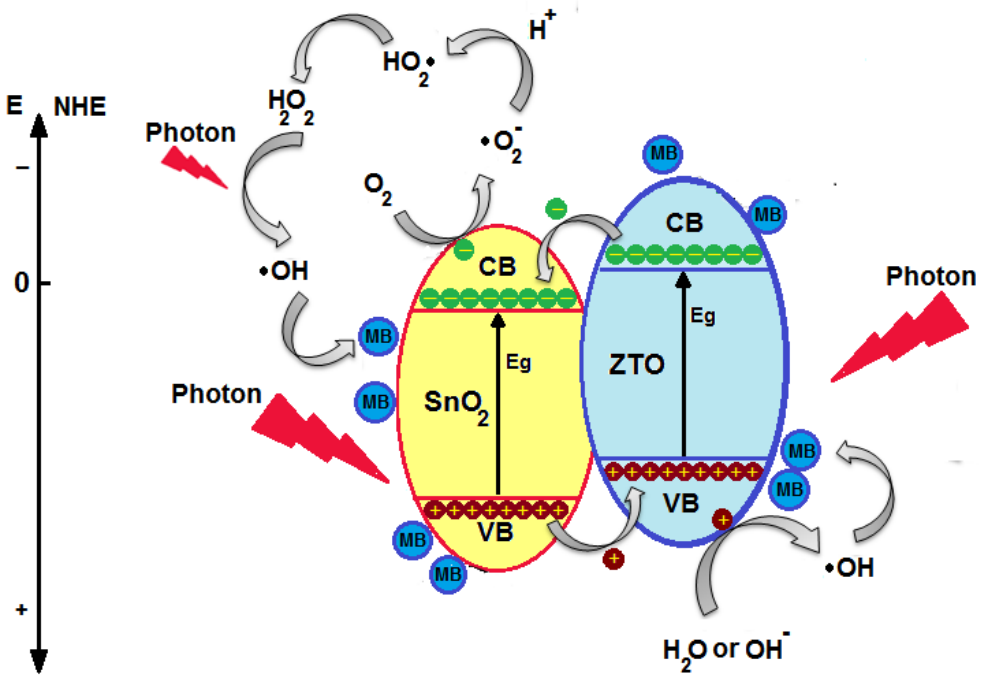


Fig. 11 Schematic illustration of the ZTO-SnO_2 nanocomposited photocatalyst.

The energy gap (E_g) values of SnO_2, Zn_2SnO_4 (ZTO) and ZTO-SnO_2 have been reported: $E_g(SnO_2)$ = 3.61 eV, E_g(ZTO) = 3.69 eV and E_g(ZTO-SnO_2) = 3.63 eV [17], and their energy levels have been determined [13, 17]. The phenomena for the high photocatalytic activity of ZTO-SnO_2 composites can be explained by the proposed mechanism (Fig. 11). The ZTO-SnO_2 photocatalyst could be excited by the photon which has sufficient energy to generate the photo-induced electron-hole pairs. The CB edge potential of ZTO is more negative than that of SnO_2, and the VB of SnO_2 is more positive than that of ZTO [18]. The local electric field at the ZTO-SnO_2 interface pushes the photogenerated electrons toward the CB of SnO_2, while the holes on the VB of SnO_2 diffuse to VB of ZTO. The photogenerated electrons can be effectively collected by SnO_2 and holes by ZTO, leading to the effective separation of photogenerated electrons and holes. Thus the electron–hole recombination process was prohibited and the ZTO-SnO_2 composites exhibit enhanced performance as compared to SnO_2 and ZTO alone. During processing, holes react with water (H_2O) molecules or hydroxyl (OH^-) ions in the

reaction system to form hydroxyl radicals (•OH), and electrons react with adsorbing oxygen (O_2) to generate superoxide radical ($\bullet O_2^-$). The process is strong oxidizing performance for degradation of the organic substances [4, 9, 26]. The oxidizing power of the •OH radicals is strong enough to completely oxidize organic pollutants. These reactive species may also contribute to the oxidative pathways: the degradation of methylene blue dye (Fig. 12) [27, 28].

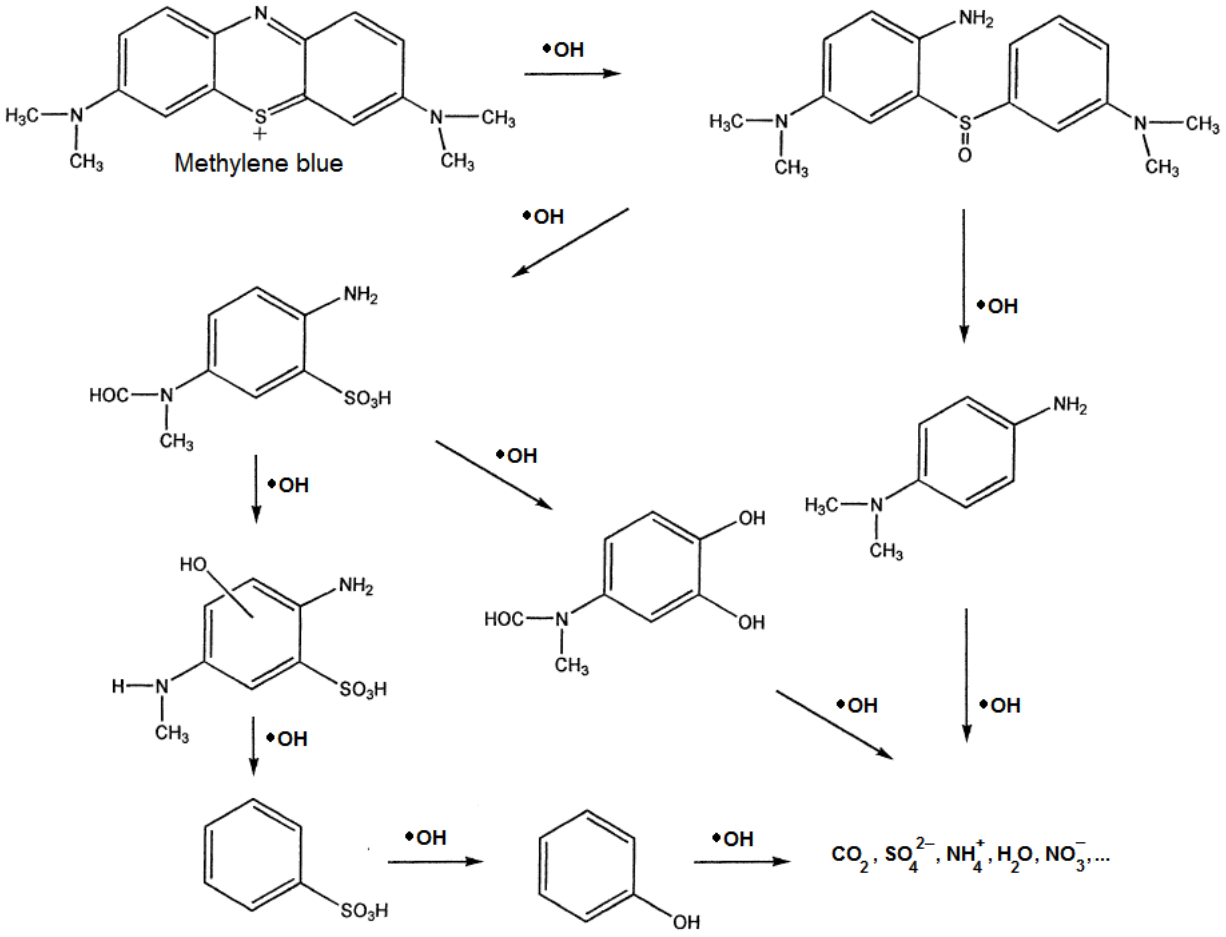


Fig. 12 Photocatalytic degradation pathway of MB.

Conclusions

The really fine $ZnSn(OH)_6$ precursors with nanocubes and nanoparticles could be successfully produced at room temperature by short reaction time of sonochemistry in de-ionized water and ethylene glycol, respectively. Due to the thermodynamically

unstable of the $ZnSn(OH)_6$ precursors, they were transformed into the ZTO-SnO_2 by high temperature calcination. The ZTO-SnO_2 nanocomposites exhibit enhanced photocatalytic performance. In this research, ZTO(NP)-SnO_2 presents higher activity than ZTO(NC)-SnO_2, enhanced by the relative smaller size and larger surface area.

References

[1] P. Junploy, S. Thongtem, T. Thongtem, Superlatt. Microstruct. 57 (2013) 1–10.

[2] A.A. Firooz, A.R. Mahjoub, A.A. Khodadadi, M. Movahedi, Chem. Eng. J. 165 (2010) 735–739.

[3] D. Chen, Recent Pat. Nanotechnol. 2 (2008) 183–189.

[4] L. Ge, C. Han, J. Liu, Appl. Catal. B 108–109 (2011) 100–107.

[5] L. Zhang, W. Wang, S. Sun, Y. Sun, E. Gao, Z. Zhang, Appl. Catal. B 148–149 (2014) 164–169.

[6] T. Chang, Z. Li, G. Yun, Y. Jia, H. Yang, Nano-Micro Lett. 5 (2013) 163–168.

[7] R. Zhang, H. Wu, D. Lin, W. Pan, J. Am. Ceram. Soc. 92 (2009) 2463–2466.

[8] L.P. Zhu, N.C. Bing, D.D. Yang, Y. Yang, G.H. Liao, L.J. Wang, CrystEngComm 13 (2011) 4486–4490.

[9] L. Cheng, Y. Kang, Mater. Lett. 117 (2014) 94–97.

[10] O. Akhavan, Appl. Surf. Sci. 257 (2010) 1724–1728.

[11] J. Zhu, J. Yang, Z.F. Bian, J. Ren, Y.M. Liu, Y. Cao, H.X. Li, H.Y. He, K.N. Fan, Appl. Catal. B 76 (2007) 82–91.

[12] Z. Zhang, W. Wang, D. Jiang, J. Xu, Appl. Surf. Sci. 292 (2014) 948–953.

[13] M.A. Alpuche-Aviles, Y. Wu, J. Am. Chem. Soc. 131 (2009) 3216–3224.

[14] M.J. Kim, S.H. Park, Y.D. Huh, Bull. Korean Chem. Soc. 32 (2011) 1757–1760.

[15] Z. Ai, S. Lee, Y. Huang, W. Ho, L. Zhang, J. Hazard. Mater. 179 (2010) 141–150.

[16] C.G. Anchieta, D. Sallet, E.L. Foletto, S.S. da Silva, O. Chiavone-Filho, C.A.O. do Nascimento, Ceram. Internat. 40 (2014) 4173–4178.

[17] B. Li, L. Luo, T. Xiao, X. Hu, L. Lu, J. Wang, Y. Tang, J. Alloys Compd. 509 (2011) 2186–2191.

[18] T.J. Coutts, D.L. Young, X. Li, W.P. Mulligan, X. Wu, J. Vac. Sci. Technol. A 18 (2000) 2646–2660.

[19] Powder Diffract. File, JCPDS-ICDD, 12 Campus Boulevard, Newtown Square, PA 19073-3273, U.S.A., 2001.

[20] M. Vaseem, A. Umar, Y.B. Hahn, Metal Oxide Nanostructures and Their Applications Edited by A. Umar and Y.B. Hahn, 5 (2010) 1–36.

[21] A. Phuruangrat, O. Yayapao, T. Thongtem, S. Thongtem, Superlatt. Microstruct. 67 (2014) 118–126.

[22] C. Wang, X. Wang, B.Q. Xu, J. Zhao, B. Mai, P. Peng, G. Sheng, J. Fu, J. Photochem. Photobio. A 168 (2004) 47–52.

[23] M. Zhang, T. An, X. Hu, C. Wang, G. Sheng, J. Fu, Appl. Catal. A 260 (2004) 215–222.

[24] K. Zhang, W.C. Oh, Bull. Korean Chem. Soc. 31 (2010) 1589–1595.

[25] Z. Shami, N. Sharifi-Sanjani, CrystEngComm 16 (2014) 910–921.

[26] W. Li, D. Wu, Y. Yu, P. Zhang, J. Yuan, Y. Cao, Y Cao, J. Xu, Physica E 58 (2014)118–123.

[27] A. Houas, H. Lachheb, M. Ksibi, E. Elaloui, C. Guillard, J.M. Herrmann, Appl. Catal. B 31 (2001) 145–157.

[28] H.L. Wang, D.Y. Zhao, W.F. Jiang, Desalinat. Water Treat. 51 (2013) 2826–2835.

11. Characterization and photonic absorption of hierarchical tree-like CdS nanostructure synthesized by solvothermal method

Abstract

Hierarchical tree-like wurtzite CdS nanostructure was successfully synthesized by the 200 ^{o}C and 24 h solvothermal reaction of cadmium nitrate and thiourea as starting materials in 1:1 volume ratio of diethylenetriamine and ethylenediamine as a mixed solvent. Phase and morphology of the as-synthesized CdS product were characterized by X-ray diffraction (XRD), Raman spectroscopy and transmission electron microscopy (TEM), including its photonic absorption by UV-visible spectroscopy. XRD spectrum and TEM image showed hexagonal wurtzite CdS structure with a 1-2 μm prototypical cluster, composed of a number of limbed nanorods. Its Raman spectrum was specified as the first-order (1LO) and second-order (2LO) longitudinal optical phonon modes at 298 and 599 cm^{-1}. UV-visible spectrum shows an absorption peak centered at around 489 nm, assigned as the excitonic transition, blue shifted comparing to its bulk.

Keywords: Electron microscopy; Spectroscopy; X-ray techniques

Introduction

Among the II–VI semiconducting materials, cadmium sulfide (CdS) with 2.42 eV direct band gap at room temperature has received much attention for a number of researchers, due to its excellent properties for luminescence and photochemistry. It has a wide variety of applications, such as light-emitting diodes, solar cells and optoelectronic devices [1,2]. Over the past decade, different morphologies were produced, including nanorods [1], microflowers [2], nanostructured mutipods [3], nanowires [4,5], nanotubes [6] and nanoribbons [7,8]. They were successfully synthesized by both physical and chemical processes: solvothermal/hydrothermal [1-4],

dc electrochemical deposition [5], chemical vapor deposition (CVD) [6,7] and microwave radiation [8]. Among them, the solvothermal route, reaction of precursors in a closed system in the presence of an organic solvent at a temperature higher than the boiling temperature of the solvent, is one of the most effective synthetic methods for synthesizing nanostructured CdS [1] controlled by a variety of parameters. In this work, a hierarchical tree-like CdS nanostructure was synthesized by a facile solvothermal method and its optical property was also studied.

Experiment

To synthesize hierarchical tree-like wurtzite CdS nanostructure, each 0.005 mol of cadmium nitrate ($Cd(NO_3)_2$) and thiourea (NH_2CSNH_2) was dissolved in 50 ml of 1:1 volume ratio of diethylenetriamine and ethylenediamine mixture under 30 min stirring at room temperature. Subsequently, the solution was solvothermally processed at 200 ^{o}C for 24 h, and left cool down to room temperature. At the conclusion, orange precipitate was synthesized, separated by filtration, washed with de-ionized water and absolute ethanol, and dried at 70 ^{o}C for 12 h, for further characterization by X-ray diffraction (XRD), Raman spectrometry, transmission electron microscopy (TEM) with equipped energy dispersive X-ray (EDX) spectroscopy and UV-visible spectroscopy.

Results and discussion

XRD spectrum (Fig. 1) of the as-synthesized CdS product was indexed using Bragg's law for diffraction, and specified as wurtzite hexagonal CdS structure with P63mc space group, comparing to the JCPDS database no. 41-1049 [9]. No other characteristic peaks of impurities were detected, showing that the product was pure phase. The spectrum shows sharp and narrow diffraction peaks with different intensities, indicating that the as-synthesized CdS product was good crystalline. The (002) diffraction peak was higher than the others, implying that the product has a preferred ordering orientation growth along the c-axis. Calculated lattice parameters for wurtzite

hexagonal CdS structure using Bragg's law for diffraction and plane-spacing equation [10] were a = b = 0.413 nm and c = 0.669 nm, in accordance with those of the JCPDS database.

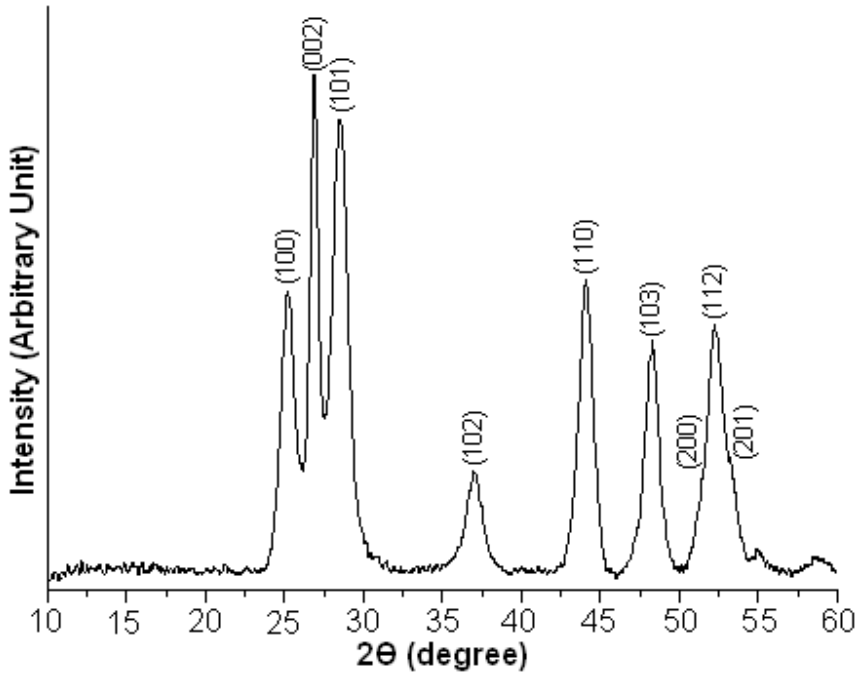


Fig. 1 XRD spectrum of the as-synthesized CdS product.

The c-orientation degree of the as-synthesized CdS product was explained by a relative texture coefficient (TC) [3] of the (002) peak calculated using the formula,

$$TC002 = \frac{\left(I002 / I^{o}002\right)}{\left[I002 / I^{o}002 + I100 / I^{o}100\right]} \qquad (1)$$

, where TC_{002} is the relative texture coefficient of the (002) over (100) diffraction peaks. I_{002} and I_{100} are the diffraction intensities of the (002) and (100) experimental peaks, including I^{o}_{002} and I^{o}_{100} the corresponding intensities of the randomly oriented CdS powder of the JCPDS database, respectively. Texture coefficient of random crystallographic orientation wurtzite CdS structure is 0.5. In the present research, the calculated TC_{002} is 0.55, which supports the preferential orientation of the as-synthesized CdS product grew along the [001] direction.

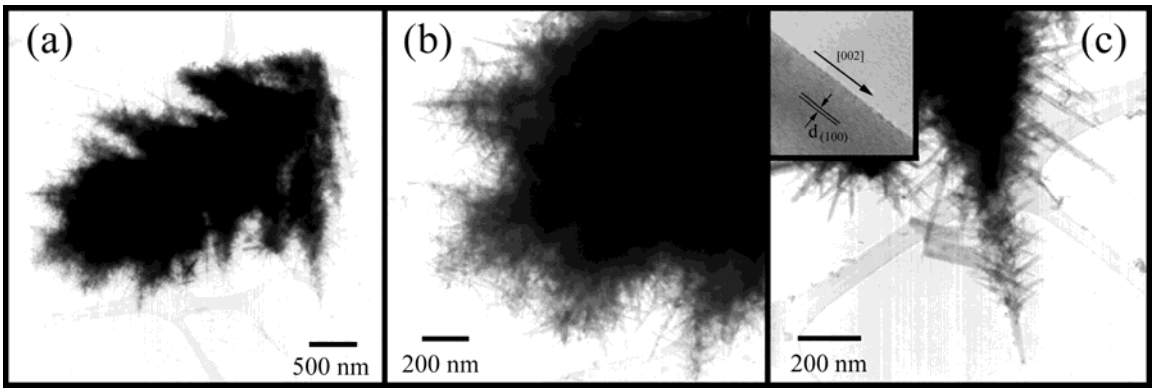


Fig. 2 TEM images at different magnifications of hierarchical tree-like wurtzite CdS nanostructure.

Fig. 2 shows TEM images of the as-synthesized CdS product of a hierarchical tree-like CdS nanostructure with 1-2 μm prototypical cluster, composing of a number of limbed nanorods. At high magnification, the branches were composed of small nanorods with 20-30 nm in diameter and 100-200 nm in length, growing out of hierarchical tree-like CdS nanostructured trunks. HRTEM image (inset of Fig. 2c) revealed that the hierarchical tree-like CdS nanostructured nanorods grew out along the [001] direction. Qualitative and quatitative analyses of the as-synthesized CdS product were characterized by EDX. It presents three L_{α}, L_{β_1} and L_{β_2} lines of Cd at 3.13, 3.32 and 3.53 keV, and a $K_{\alpha_{1,2}}$ line of S at 2.31 keV. The molar ratio of Cd:S was 0.98:1 in good accordance with the stoichiometric CdS phase. The $K_{\alpha_{1,2}}$ and K_{β} lines of Cu at 8.04 and 8.91 keV as well as C-$K_{\alpha_{1,2}}$ line at 0.28 keV of Cu grid with C film coated on top were also detected [11].

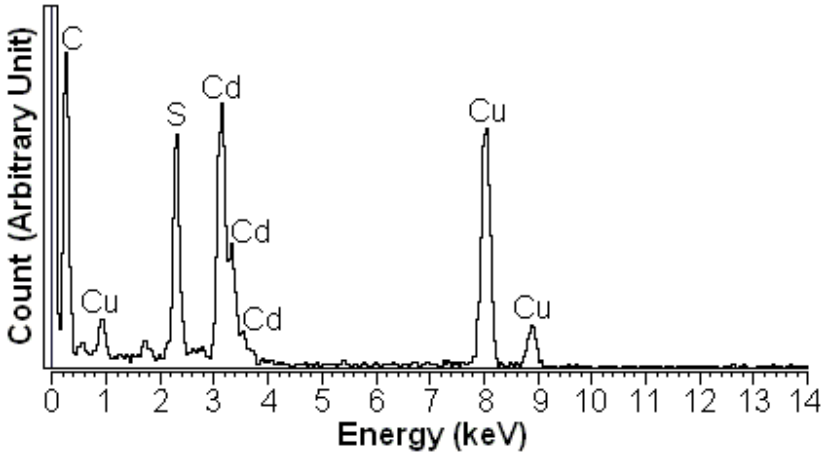


Fig. 3 EDX spectrum of a hierarchical tree-like CdS nanostructure.

Hexagonal wurtzite structured CdS belongs to a C^4_{6V} space group. According to factor group analysis, its Raman active modes are $1A_1 + 1E_1 + 2E_2$ (E_2^H and E_2^L). Only the $2B_2$ modes are silent. Phonon polarization of the A_1 branch is in the z direction, and those of the doubly degenerate E_1 and E_2 are in the xy plane. The wurtzite structure is noncentrosymmetric, thus both A_1 and E_1 modes split into longitudinal optical (LO) and transverse optical (TO) components [12]. Raman spectroscopy of hierarchical tree-like CdS nanostructure was at 298 and 599 cm^{-1} wavenumbers, assigned as the first (1LO) and second (2LO) longitudinal optical phonon modes [4,12], comparing to the characteristic Raman spectrum of bulk CdS at 297.5 and 599 cm^{-1} corresponding to the 1LO and 2LO reported by Singh et al [13]. The 1LO Raman wavenumber of the hierarchical tree-like CdS nanostructure was blue shifted due to the phonon confinement in the transverse direction and the transition of elementary excitons in the longitudinal direction and strain effect [13].

Energy level and band gap of CdS were calculated and reported by Ge et al [2]. For this material, S3p character is the highest occupied molecular orbital level, and Cd3d + S3p hybrid is the lowest unoccupied molecular orbital level. Upon photoexcitation, charged particles transferred from the S3p orbital to the empty Cd3d + S3p hybrid, including the formation of photogenerated electron-hole pairs. The optical absorbance spectrum of hierarchical tree-like CdS nanostructure (Fig. 4) showed

strong absorption edge at 489 nm. Obviously, blue-shift to a shorter wavelength was detected, comparing to its CdS bulk (515 nm) - caused by the quantum confinement effect [14,15]. Fig. 4 shows UV-visible absorption of hierarchical tree-like wurtzite CdS nanostructure. Its band gap was determined at zero absorbance to be 3.93 eV. In the present research, band gap and maximum absorption of hierarchical tree-like CdS nanostructure are blue-shifted comparing to bulk CdS (2.42 eV) [8].

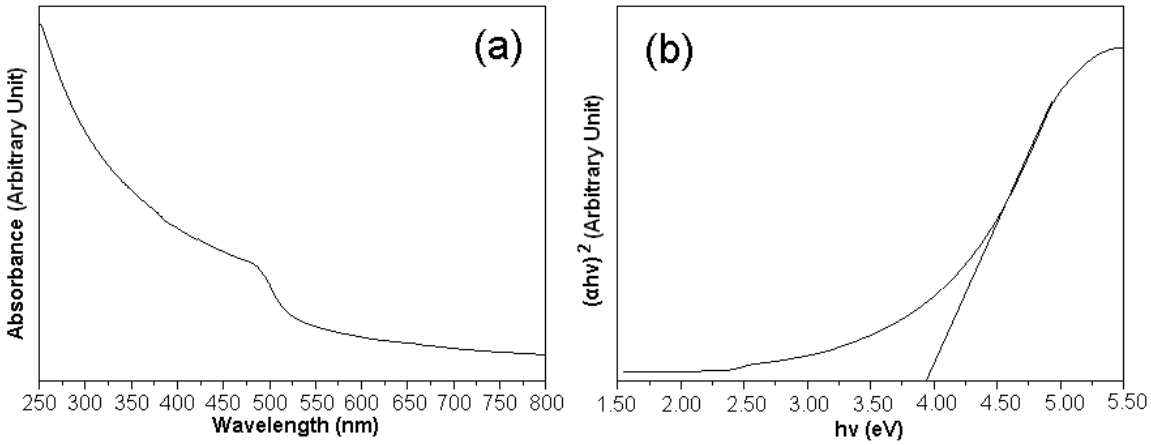


Fig. 4 (a) UV-visible spectrum and (b) $(\alpha hv)^2$ vs hv curve of the hierarchical tree-like wurtzite CdS nanostructure.

Conclusions

Hexagonal wurtzite CdS nanostructure was successfully synthesized by the 200 ^{o}C and 24 h solvothermal method. XRD and TEM analyses revealed that the product was hierarchical tree-like CdS nanostructure with a 1-2 μm prototypical cluster, composed of a number of limbed nanorods. UV-visible absorption spectrum was blue shift at 489 nm, assigned as the exitonic absorption comparing to its bulk.

References

[1] Dalvand P, Mohammadi MR, Fray DJ. Mater Lett 2011;65:1291–4.

[2] Ge M, Cui Y, Liu L, Zhou Zh. Appl Surf Sci 2011;257:6595–600.

[3] Phuruangrat A, Thongtem T, Thongtem S. Chalcogen Lett 2010;7:605–8.

[4] Phuruangrat A, Thongtem T, Thongtem S. Curr Appl Phys 2009;9:S201–4.

[5] Mondal SP, Dhar A, Ray SK. Mater Sci Semicond Proc 2007;10:185–93.

[6] Shen XP, Yuan AH, Wang F, Hong JM, Xu Zh. Solid State Commun 2005;133:19–22.

[7] Wang Y, Wang GZ, Yau MY, To CY, Ng DHL. Chem Phys Lett 2005;407:510–5.

[8] Zhu JJ, Wang H, Zhu JM, Wang J. Mater Sci Eng B 2002;94:136–40.

[9] Powder Diffract. File, JCPDS-ICDD, 12 Campus Boulevard, Newtown Square, PA 19073-3273, USA 2001.

[10] Suryanarayana C, Norton MG. X-ray Diffract., A Pract. Appro., Plenum Press, New York, 1998.

[11] Oxford Instruments Analytical, Halifax Rd, High Wycombe Bucks HP12 3SE, UK.

[12] Phuruangrat A, Thongtem T, Thongtem S. Mater Lett 2009;63:1538–41.

[13] Singh V, Chauhan Pr. Chalcogen Lett 2009;6:421–6.

[14] Yang XH, Wu QSh, Li L, Ding YP, Zhang GX. Colloid Surf A 2005;264:172–8.

[15] Maleki M, Mirdamadi Sh, Ghasemzadeh R, Ghamsari MS. Mater Lett 2008;62:1993–5.

12. Characterization of nanostructured CdTe synthesized by solid state microwave-plasma process

Abstract

Purified cubic CdTe nanocrystals were synthesized from 1:1 molar ratio of Cd:Te using 900 W microwave plasma. The phase was detected using X-ray diffraction (XRD), which are in accordance with those of the simulation, and selected area electron diffraction (SAED). Raman spectroscopic, scanning electron microscopic (SEM) and focused ion beam (FIB) techniques showed that the products were nanocrystals with fundamental transverse optical (1TO) and longitudinal optical (1LO) vibrations at 140 cm^{-1} and 169 cm^{-1}, respectively. Its direct energy gap (E_g) was determined to be 1.6 eV.

Keywords: Nanostructured CdTe; X-ray diffraction; Raman spectroscopy; Focused ion beam technique; UV-visible absorption

Introduction

CdTe is one of the II–VI semiconducting materials, which has a direct band gap of 1.5 eV at room temperature [1]. It is widely used as photovoltaic detectors, photo-electrochemical cells [1], space charge limited diodes, infrared (IR) detectors [2], and high efficiency solar cells [3]. There are a number of processes used to synthesize this material – tetrapod nanocrystals by a facile one-pot synthetic method [4], nanocrystals in tri-octylphosphine-dodecylamine mixture [5], nanocrystals in aqueous solution [6], nanoparticles in aqueous solution by colloidal method [7], thin film by thermal evaporation and close spaced sublimation [1,2,8,9], thin film by spray deposition in the presence of electric field [10], thin film by sintering [3], thin film by pulsed laser deposition [11], thin film by chemical solution method [12], thin film by electrochemical method [13], and epilayer by vapor phase epitaxy [14].

Microwave radiation (2,450 MHz) is coherent and polarized [15]. When this radiation is supplied to chemicals, one or more of the components is capable of coupling with it. This can lead to higher heating rate than that achieved by conventional method. The entire volume of materials is internally heated up. Microwave radiation can solve the problems of temperature and concentration gradients. By focusing large amount of microwave radiation into the system, the vibrating electric field applied a force on charged particles which vibrated accordingly. Vibrations of the reactants have the influence on the reaction to proceed with efficiency. Subsequently, pure products were synthesized [15,16].

In the present research, nanostructured CdTe was synthesized by solid state microwave-plasma process. This process is rapid, done in closed system, and safe for lives. The synthesized product is also pure, although it was synthesized by solid state reaction process. The product was then characterized using different techniques.

Experiment

To synthesize CdTe nanocrystals, Cd and Te powders (purum, analytical grade, Fluka) were used without further purification. Solid mixture of 1:1 molar ratio Cd:Te was thoroughly mixed, loaded into silica tubes (11 mm I.D. x 100 mm long), and placed in a horizontal (H) quartz tube. The tube was tightly closed and evacuated to 3.9±0.2 kPa absolute pressure for removal of air. Subsequently, argon was gradually fed into this H tube. The procedure was repeated three times. Finally, argon in the H tube was evacuated to a constant value of 3.9±0.2 kPa absolute pressure. The solid mixture was heated in a manner of batch run by a 2,450 MHz microwave with 900 W output power to produce plasma. Each batch, the solids were heated for 10 min, left to cool down in vacuum to room temperature, and thoroughly mixed. The process was repeated under the same condition until at the completion of 10, 20 and 30 min. The products were then analyzed using X-ray powder diffractometer (XRD) with a 1.5418 Å wavelength of Cu-K_α line, scanning electron microscope (SEM) operated at 15 kV, focused ion beam (FIB)

technique operated at 30 kV, and selected area electron diffractometer (SAED) operated at 200 kV, Raman spectrometer using 30 mW He-Ne laser with 632.8 nm (red) wavelength, and UV-visible spectrometer operated at the 300-850 nm wavelength range with the 0.5 $nm.sec^{-1}$ scanning rate.

Results and discussion

XRD spectra of the products synthesized for different lengths of time are shown in Fig. 1. The XRD spectra were interpreted as CdTe cubic structure with F-43m space group, comparing to the JCPDS database no 15-0770 [17]. Their diffraction peaks corresponding to the (111), (220), (311), (400), and (331) planes are at 2θ = 23.84, 39.36, 46.48, 56.84, and 62.48 deg, respectively. By increasing the length of time to 30 min, the product's crystalline degree was the highest. The reactants have more chance to form new product (CdTe), and the atoms have more chance to arrange themselves in their crystal lattices. Its lattice parameter (a) was calculated using Bragg's law for diffraction and the plane-spacing equation for cubic structure [18], and is summarized in Table 1. This parameter is 0.6496±0.0020 nm, which is very close to that of the JCPDS database no 15-0770 (a = 0.6481 nm) - confirming the detection of cubic lattice structured CdTe.

An XRD diffraction pattern of CdTe was also simulated using the CaRIne program [19] in combination with the calculated lattice parameter, and is shown in Fig. 1. The 2θ Bragg's angles and diffraction intensities of different peaks of the experiment, simulation and JCPDS database no 15-0770 [17] are shown in Table 1. Both 2θ Bragg's angles and diffraction intensities of different peaks obtained from the experiment, simulation and JCPDS database are in good accordance.

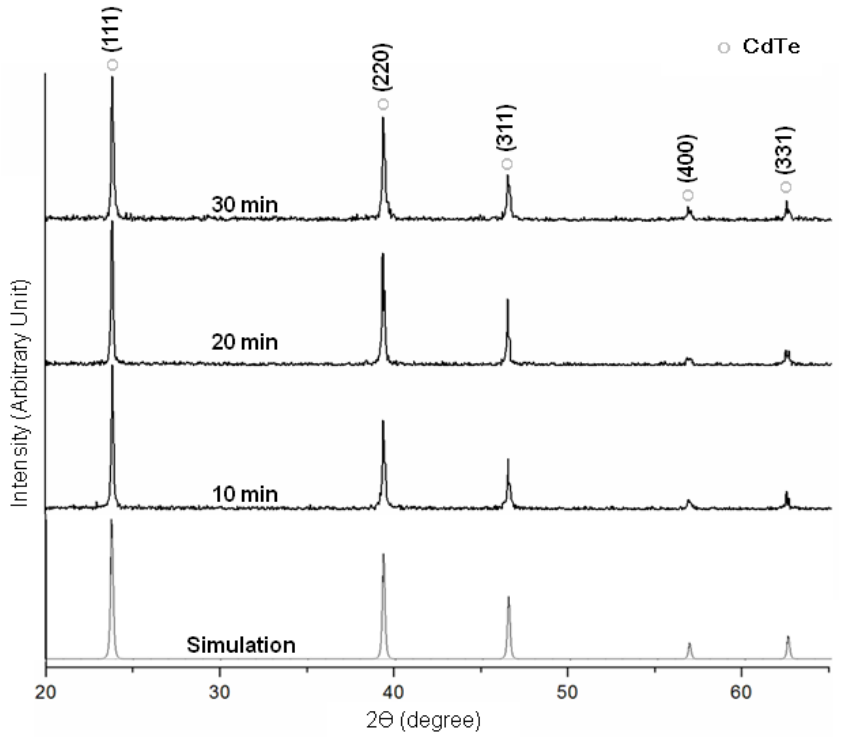


Fig. 1 XRD spectra of cubic structured CdTe synthesized by the solid state microwave-plasma process for 10 min, 20 min, and 30 min, including its simulation.

Table 1. The 2θ Bragg's angles (deg) and diffraction intensities (%) of nanostructured CdTe obtained from the 30 min experiment, simulation and JCPDS database no 15-0770, including its calculated lattice parameter (a, nm) for different crystallographic planes.

Plane	Experiment		Simulation		JCPDS database		a
	2θ	Intensity	2θ	Intensity	2θ	Intensity	
(111)	23.84	100	23.78	100	23.76	100	0.6522
(220)	39.36	71.65	39.32	75.3	39.31	60	0.6500
(311)	46.48	32.08	46.48	44.7	46.43	30	0.6478
(400)	56.84	10.16	56.83	11.4	56.82	6	0.6507
(331)	62.48	14.43	62.47	16.4	62.35	10	0.6473
							0.6496±0.0020

Fig. 2 shows SAED patterns of nanostructured CdTe synthesized by the 900 W microwave plasma for 10 and 30 min. The patterns appear as white concentric rings, characterized as polycrystals. These rings are diffuse and hollow showing that the product was composed of a number of nanosized crystals. At the present stage, the electron beam reflected and diffracted from polycrystals to form the concentric rings. Interplanar spaces (d) were calculated using their diffraction ring diameters [20], and compared with those of the JCPDS database no 15-0770 [17]. They both correspond to the (111), (220), (311), (400), and (331) crystallographic planes of the products and were specified as cubic CdTe.

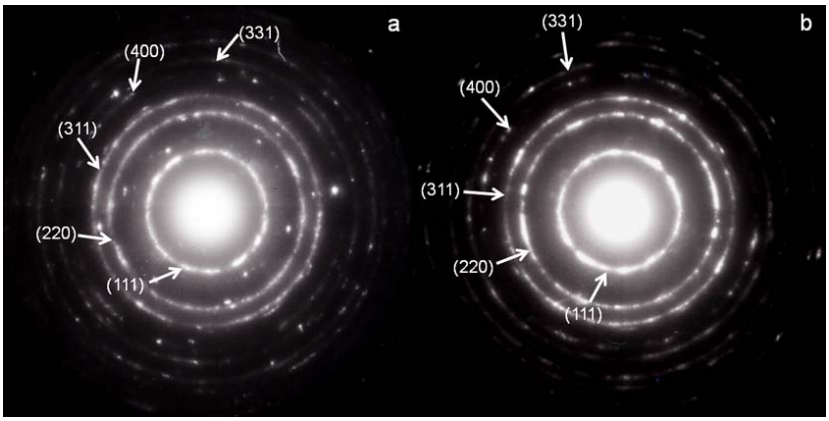


Fig. 2 SAED patterns of nanostructured CdTe, synthesized by 900 W microwave plasma for (a) 10 min, and (b) 30 min.

Morphology of the product (Fig. 3), synthesized by 900 W microwave plasma for 10 and 30 min, was investigated by SEM and FIB. Both of them show that the product was composed of a number of nanoparticles gathering together in the shape of spheres, aligning in different orientations. These spheres were larger with increasing the length of time. It should be noted that the detections of nanostructured CdTe by SEM and FIB are in good accordance with the interpretation of the SAED, explained above.

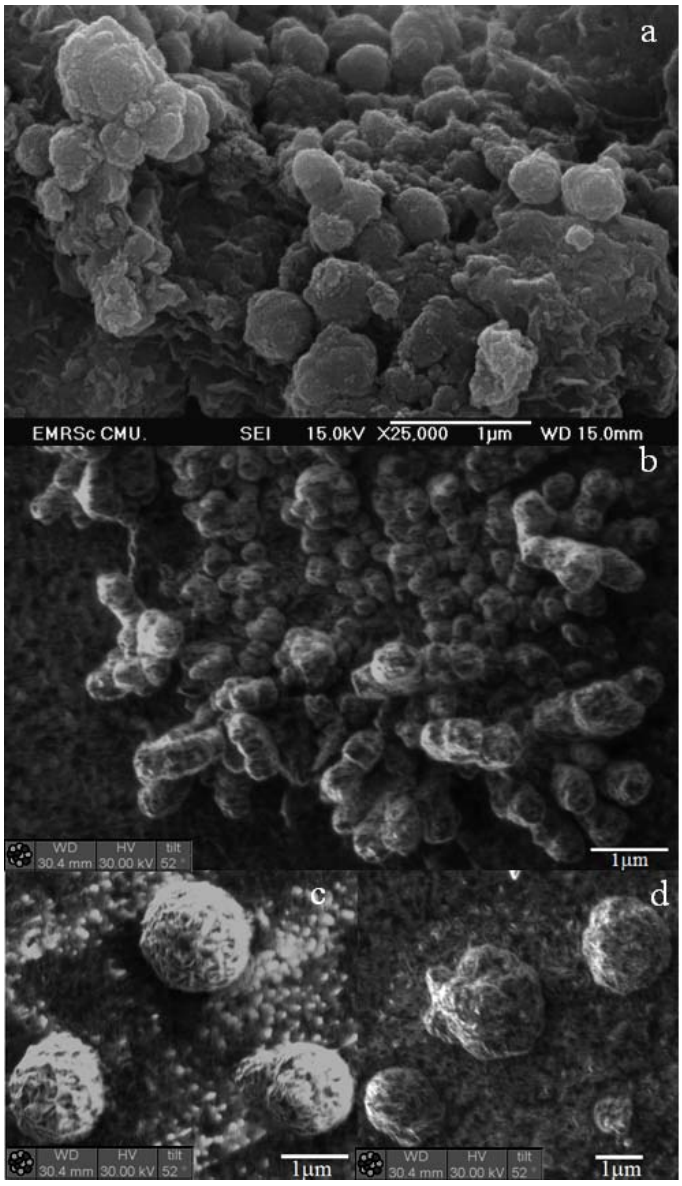


Fig. 3 SEM and FIB images of nanostructured CdTe synthesized by 900 W microwave plasma for (a, b) 10 min, and (c, d) 30 min.

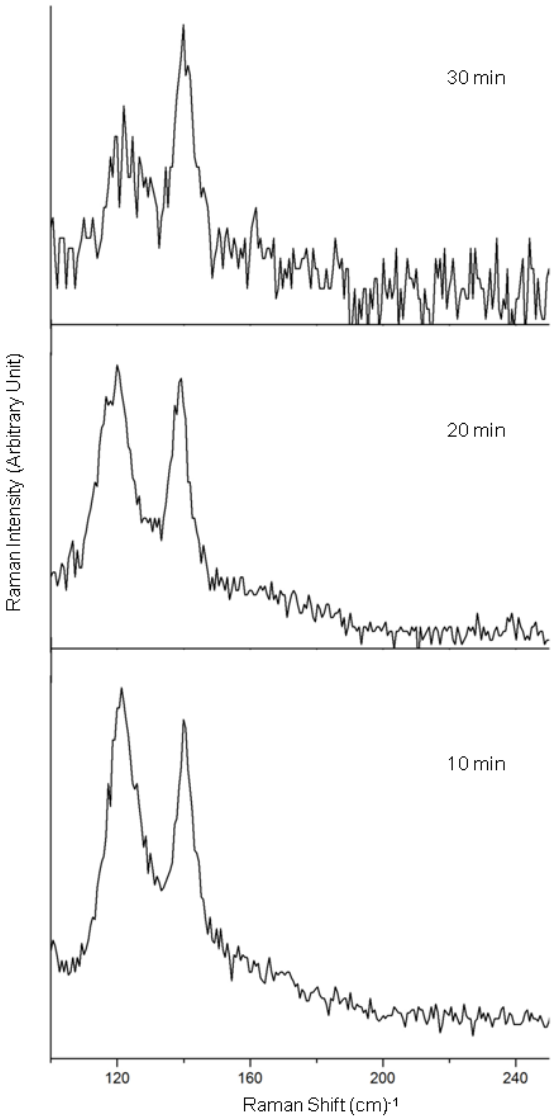


Fig. 4 Raman shifts of nanostructured CdTe, synthesized by 900 W microwave plasma for 10 min, 20 min, and 30 min.

The presence of cubic CdTe can be analyzed using a Raman spectrometer. For this case, test specimens are non-destructive and can be re-used for other purposes. The Raman shifts (Fig. 4) show the vibration modes of CdTe, corresponding to the fundamental transverse optical (1TO) and longitudinal optical (1LO) vibrations at 140 cm^{-1} and 169 cm^{-1}, respectively. They are in good accordance with those obtained by Dutta et al. who specified the 1TO, and 1LO Raman shifts of CdTe at 141, and 166 cm^{-1} [21],

and by Campos et al. at 141, and 167 cm^{-1} [22], respectively. Other peaks at 120 cm^{-1} were caused by the residual Te [22], although the Te peaks were not detected by XRD measurement – its concentration could be too low to be detected by the XRD analysis. By increasing the length of time, this 120 cm^{-1} peak became lower – implying that the Te content became lessened. It should be noted that the 140 cm^{-1} peak was influenced not only by the vibration of cubic CdTe, but also the residual Te [22]. Comparing to the XRD results, the 140 cm^{-1} peak was dominantly influenced by the vibration of nanostructured CdTe.

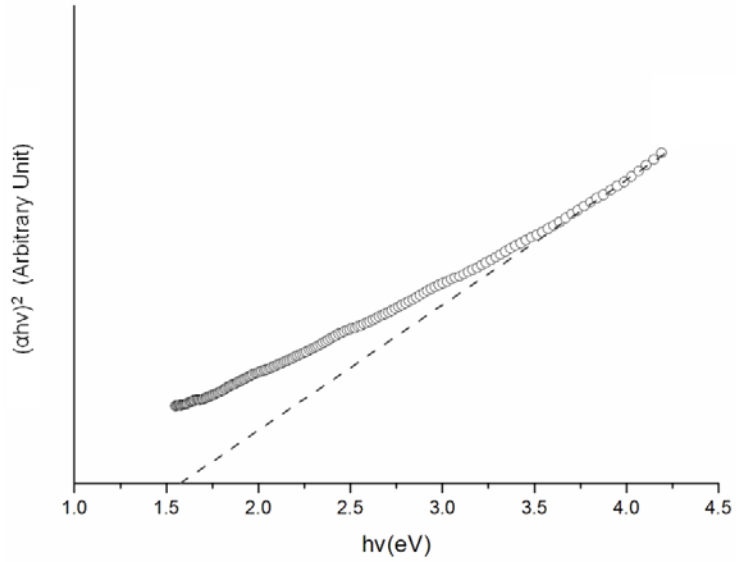


Fig. 5 The $(\alpha h\nu)^2$ and $h\nu$ plot of nanostructured CdTe, synthesized by 900 W microwave plasma for 30 min.

The UV-visible spectrum of nanostructured CdTe, synthesized by 900 W microwave plasma for 30 min, was investigated using UV-visible spectrometer at room temperature. Its direct energy band gap (E_g) was calculated from the $(\alpha h\nu)^2$ vs $h\nu$ plot (Fig. 5), where α, h and ν are the absorbance, Planck constant and frequency [23], respectively. The absorbance increases with increasing photon energy ($h\nu$). The direct band gap of the semiconducting nanostructured CdTe was determined by extrapolating the broken line to the photon energy axis at $\alpha = 0$, which gives the energy band gap of CdTe to be 1.6 eV. This value is in accordance with 1.64 eV of the as-deposited CdTe

film determined by Kokate et al. [23], and 1.6 eV of the cubic CdTe film by Pandey et al. [11]. These energy band gaps are also influenced by film thickness, particle-size, and degree of crystallinity [2].

Conclusions

Purified cubic CdTe nanocrystals were successfully synthesized by the solid state microwave plasma process. Its 1TO and 1LO modes were respectively detected at 140 cm^{-1} and 169 cm^{-1}, including the determined direct band gap (E_g) of 1.6 eV.

References

[1] S. Lalitha, S.Zh. Karazhanov, P. Ravindran, S. Senthilarasu, R. Sathyamoorthy, J. Janabergenov, Physica B 387, 227 (2007).

[2] R. Sathyamoorthy, Sa.K. Narayandass, D. Mangalaraj, Solar Energy Mater. Solar Cells 76, 339 (2003).

[3] S. Kumar, S.K. Sharma, T.P. Sharma, M. Husain, J. Phys. Chem. Solids 61, 1809 (2000).

[4] H. Lee, S.W. Yoon, J.P. Ahn, Y.D. Suh, J.S. Lee, H. Lim, D. Kim, Solar Energy Mater. Solar Cells 93, 779 (2009).

[5] S.F. Wuister, F. van Driel, A. Meijerink, J. Lumines. 102-103, 327 (2003).

[6] A.S. Susha, A.M. Javier, W.J. Parak, A.L. Rogach, Coll. Surf. A 281, 40 (2006).

[7] J.H. Kim, H. Kim, K. Cho, S. Kim, Solid State Comm. 136, 220 (2005).

[8] S. Chandramohan, R. Sathyamoorthy, P. Sudhagar, D. Kanjilal, D. Kabiraj, K. Asokan, Thin Solid Films 516, 5508 (2008).

[9] M.E. Hernández-Torres, R. Silva-González, G. Casarrubias-Segura, J.M. Gracia-Jiménez, Solar Energy Mater. Solar Cells 90, 2241 (2006).

[10] V.V. Ison, A.R. Rao, V. Dutta, Solar Energy Mater. Solar Cells 93, 1507 (2009).

[11] S.K. Pandey, U. Tiwari, R. Raman, Ch. Prakash, V. Krishna, V. Dutta, K. Zimik, Thin Solid Films 473, 54 (2005).

[12] M. Sotelo-Lerma, R.A. Zingaro, S.J. Castillo, J. Organomet. Chem. 623, 81 (2001).

[13] X. Mathew, J.P. Enriquez, Solar Energy Mater. Solar Cells 63, 347 (2000).

[14] N.V. Sochinskii, M. Abellán, J. Rodríguez-Fernández, E. Diéguez, J. Franc, P. Hlidek, P. Praus, V. Babentsov, Superlatt. Microstruct. 45, 228 (2009).

[15] S. Bhunia, D.N. Bose, J. Cryst. Growth 186, 535 (1998).

[16] C. Gabriel, S. Gabriel, E.H. Grant, B.S.J. Halstead, D.M.P. Mingos, Chem. Soc. Rev. 27, 213 (1998).

[17] Powder Diffract. File, JCPDS Internat. Centre Diffract. Data, PA 19073-3273, U.S.A. (2001).

[18] C. Suryanarayana, M.G. Norton, X-ray Diffract, A Practical Approach, Plenum Press, New York (1998).

[19] C. Boudias, D. Monceau, CaRIne Crystallography 3.1, DIVERGENT S.A., Centre de Transfert, 60200 Compiègne, France, (1989-1998).

[20] K.W. Andrews, D.J. Dyson, S.R. Keown, Interpret. Electr. Diffract. Patter., 2nd ed, Plenum Press, NY, (1971).

[21] V.V. Ison, A.R. Rao, V. Dutta, Solid State Sci. 11, 2003 (2009).

[22] C.E.M. Campos, K. Ersching, J.C. de Lima, T.A. Grandi, H. Höhn, P.S. Pizani, J. Alloys Compd. 466, 80 (2008).

[23] A.V. Kokate, M.R. Asabe, P.P. Hankare, B.K. Chougule, J. Phys. Chem. Solids 68, 53 (2007).

13. Controlling morphologies of Bi_2S_3 nanostructures synthesized by glycolthermal method

Abstract

Single crystalline orthorhombic Bi_2S_3 nanostructures with different morphologies were synthesized by the 180 ^{o}C and 12 h glycolthermal reactions, using ethylene glycol, propylene glycol and polyethylene glycol with different molecular weights as solvents. The as-synthesized products were characterized by X-ray diffraction (XRD), transmission electron microscopy (TEM), high resolution transmission electron microscopy (HRTEM), and selected area electron diffraction (SAED). In the present research, different solvents played the role in the product morphologies. A formation mechanism of Bi_2S_3 nanostructures was also proposed.

Keywords: Semiconductors; X-ray techniques; Electron microscopy

Introduction

Generally, nanostructured materials exhibit novel properties, comparing to their bulks due to their quantum confinement effect and number of free electrons. Much effort has been dedicated to achieve in controlling over the morphologies [1-3]. Among them, ceria nanospindles as a catalyst for oxidation of CO were synthesized via a simple template-free solvothermal treatment [4], large-scale synthesis of single-crystalline and uniform CeO_2 nanorods by a precipitation method [5], and CeO_2 nanoplates, nanotubes, and nanorods by CTAB assisted hydrothermal synthesis, including the study of their morphologies on the oxidation of CO [6].

Over the past decades, chalcogenide semiconductors (A_2X_3, A = Sb, Bi, As, and X = S, Se, Te) have received considerable attention due to their wide applications in television cameras with photoconducting targets, thermoelectric devices, optoelectronic devices, and IR spectroscopy photovoltaic converters, including their unique thermal,

mechanical, electron transport, phonon transport, optical and non-linear optical properties [2,3,7]. Particularly, Bi_2S_3 is a low direct band gap (1.3-1.7 eV) layered semiconductor that crystallizes in orthorhombic system with a promising candidate for a number of applications. It has large absorption coefficient, and is an ideal candidate for solar cells and photodetectors in the visible region, including thermoelectric applications [2,7-10].

Glycols such as ethylene glycol, 1,2-propadiol and polyethylene glycol with different molecular weights (MWs) are novel solvents for synthesizing nanostructured materials with different morphologies [11-15]. In this research, the synthesis of Bi_2S_3 with different morphologies by glycolthermal method using ethylene glycol (EG), propylene glycol (PG), polyethylene glycol (PEG) with different MWs as solvents was reported.

Experiment

All chemicals with analytical grade were used without further purification. In this experiment, 0.01 mol $Bi(NO_3)_3 \cdot 5H_2O$ and 0.015 mol L-cysteine were dissolved in 75 ml of different glycol solvents including EG, PG and PEG with different MWs of 200, 300, 400 and 600 under 1 h vigorous stirring. PEG with MW of 200 was encoded as PEG-200, and similarly for others. Each solution was loaded into a 80 ml Teflon-lined stainless-steel autoclave. The autoclaves were tightly closed and put in an oven at 180 ^{o}C for 12 h. At the conclusion, deep gray precipitates were synthesized, repeatedly washed with distilled water and absolute ethanol, and dried in vacuum at 60 ^{o}C for 4 h for further characterization.

Results and discussion

XRD patterns (Fig. 1) of the as-synthesized products in different glycols were indexed as pure orthorhombic Bi_2S_3 with Pbnm space group (JCPDS database no. 17-0320) [16] with its calculated lattice parameters [17] of 11.1300, 11.260 and 3.960 Å.

Strong sharp reflection peaks indicated that well-crystallized products were synthesized through the glycolthermal process.

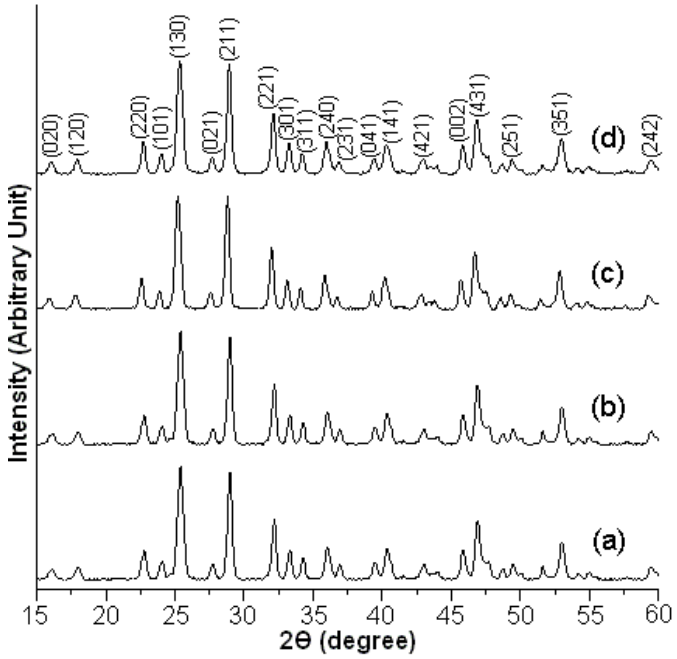


Fig. 1 XRD patterns of Bi_2S_3 nanostructures synthesized in (a-d) EG, PG, PEG-300, and PEG-600, respectively.

TEM images (Fig. 2a-f) of Bi_2S_3 nanostructures synthesized in different solvents revealed different product morphologies. A large number of Bi_2S_3 nanorods and nanowires were synthesized in EG and PG, respectively. They were well segregated with 50 nm diameter and 200-1200 nm long for nanorods, and 50 nm diameter and as long as 4 μm for nanowires. It should be noted that no individual nanorods and nanowires were synthesized in other glycols, showing that EG and PG have the advantage in forming the segregated nanorods and nanowires. TEM image of the as-synthesized Bi_2S_3 in PEG-200 indicates that the product was a cluster of typical straw-sheaves, composed of high agglomeration of numerous nanorods with radial radiation out of their center. Each straw-sheaf was approximately 4 μm long. In this research, nanostructured microflowers composed of petals with different shapes and sizes were synthesized in PEG-300, PEG-400 and PEG-600. Spherical Bi_3S_2 microflowers

synthesized in PEG-300 were clearly detected. A number of nanoneedles radially radiated from a common point to build up microflowers. Bi_2S_3 architecture synthesized in PEG-400 was composed of well-aligned nanorods pointed out of a common center to form 4 μm microflower. Upon increasing the MW of PEG to 600, a typical TEM image presents Bi_2S_3 microflowers of nanororods, growing out of centers. Each microflower consisted of nanorods with 20−50 nm diameter and several hundred nanometers long. In conclusion, different solvents played the key role in the formation of Bi_2S_3 nanostructures with different morphologies.

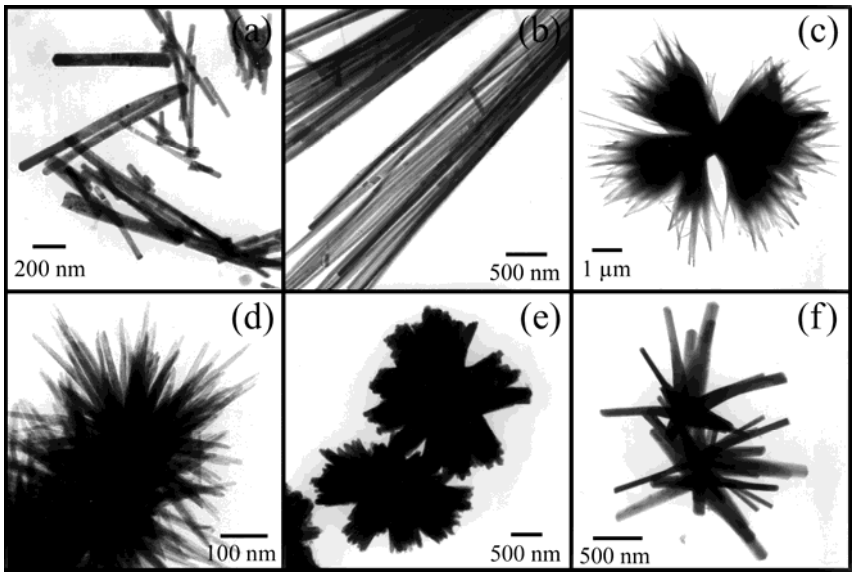


Fig. 2 TEM images of Bi_2S_3 nanostructures synthesized in (a-f) EG, PG, PEG-200, PEG-300, PEG-400 and PEG-600, respectively.

Bi_2S_3 nanowires were further characterized by TEM, SAED and HRTEM (Fig. 3). Bi_2S_3 long uniform nanowires with 35 nm diameter growing along the c axis were detected. The HRTEM image, recorded on two different nanowires, revealed the presence of single crystalline nanowires with 3.96 Å lattice spacing of the (220) planes of orthorhombic Bi_2S_3 [16]. Due to lowest excess energy of the (001) planes than others [18], the nanowires preferentially grew along the [001] direction – in accordance with the previous report [19].

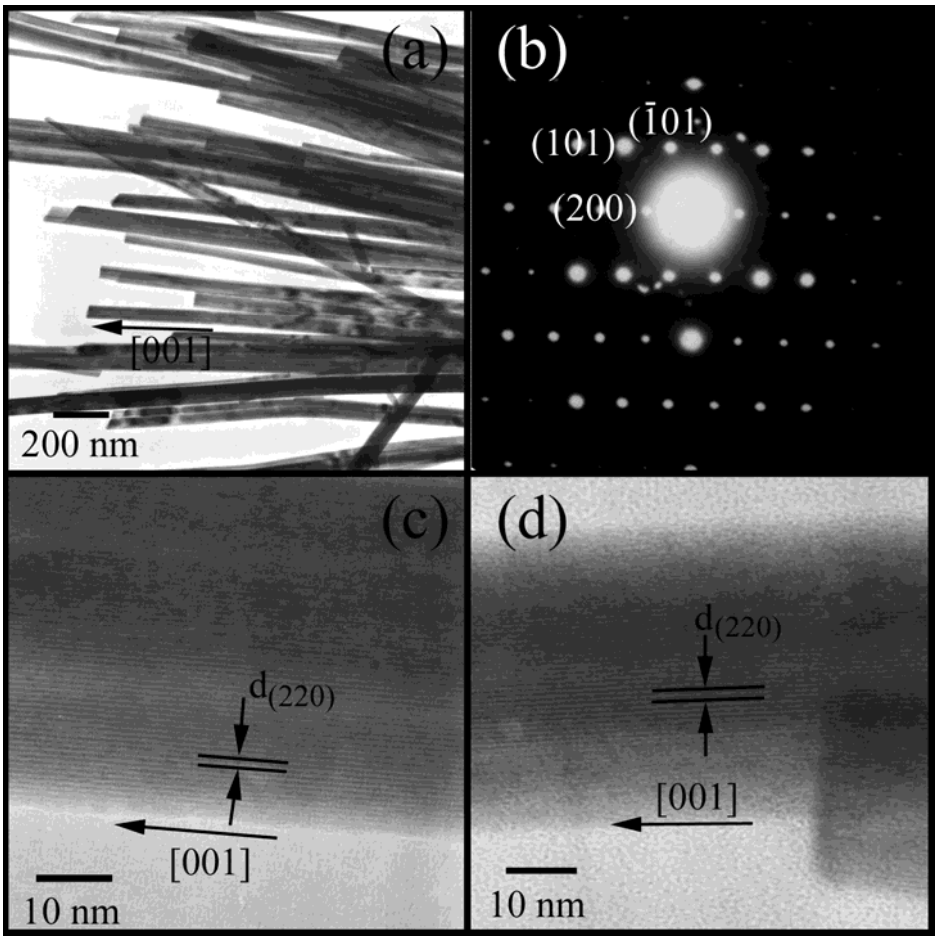


Fig. 3 TEM and HRTEM images, and SAED pattern of Bi_2S_3 nanowires synthesized in PG.

Bi_2S_3 microflower (Fig. 4a and b) shows an individual Bi_2S_3 flower-like structure with perfect geometry, assembled by tens of uniform nanorods with 0.75-1 μm long and 40-80 nm diameter. SAED pattern (Fig. 4c) was indexed through the [010] electron beam direction and specified as orthorhombic Bi_2S_3 [16]. HRTEM image (Fig. 4d) of the individual Bi_2S_3 nanorod clearly presents 3.96 Å lattice spacing of orthorhombic Bi_2S_3 [16]. The Bi_2S_3 nanorod building up the flower-like structure was single crystal composed of the (220) parallel planes, and has the preferred growth along the [001] direction.

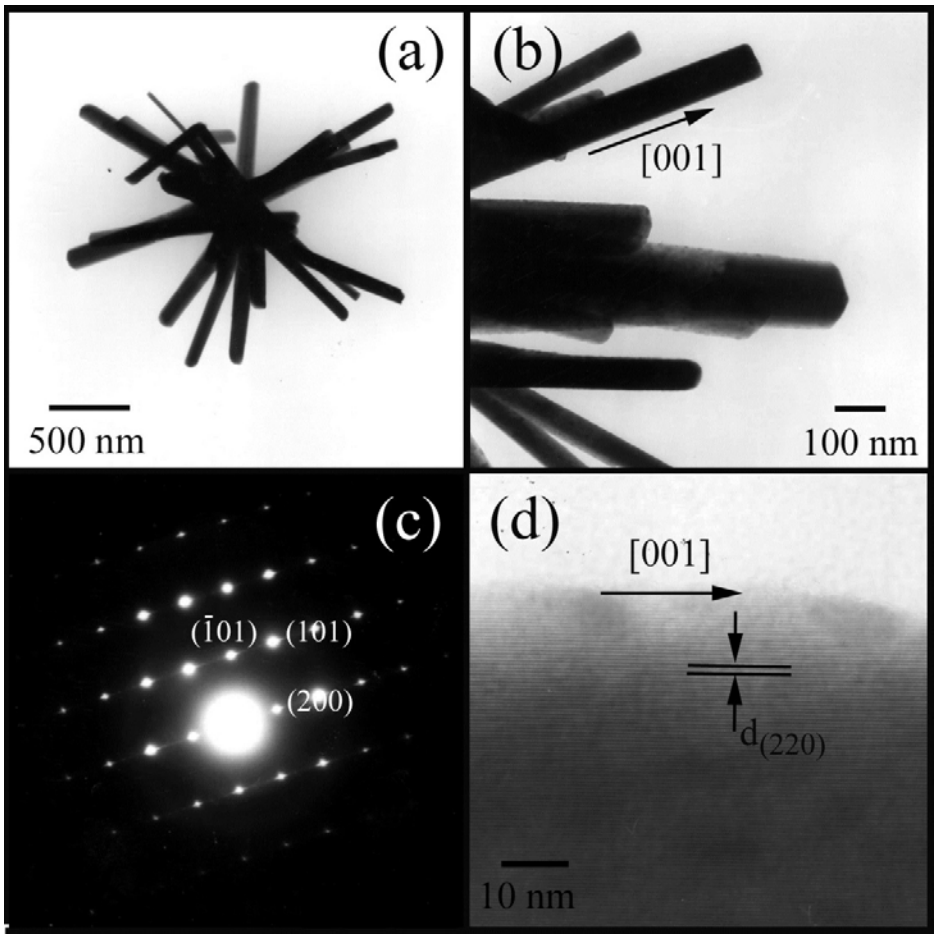


Fig. 4 TEM and HRTEM images, and SAED pattern of Bi_2S_3 nanowires synthesized in PEG-600.

Basing on the above, a formation mechanism of Bi_2S_3 with different morphologies was proposed. Although the exact mechanism is still unclear, the interaction between Bi^{3+} and S^{2-} ions assumingly played a significant role in the formation of Bi_2S_3 nanostructures. Two paths were possible. (1) Initially, Bi^{3+} ions were solvated by glycol molecules. Afterwards S^{2-} ions synthesized from L-cysteine through the hydrolysis reaction might attack the Bi^{3+} ions, inducing the formation of bond between Bi^{3+} and S^{2-}. (2) Alternately, Bi^{3+} ions might react with L-cysteine to form complexes. Subsequently, the complexes glycolthermally decomposed to form Bi_2S_3 molecules. During processing, Bi_2S_3 molecules of these two paths gradually nucleated, and provided as seeds for

crystalline growing. Concurrently different templates (EG, PG, PEG-200, PEG-300, PEG-400 and PEG-600) modeled the growing Bi_2S_3 nuclei to be perfect nanorods, nanowires, straw-sheaves of nanorods, and microflowers of nanorods [1-3,20].

Conclusions

Nanorods, nanowires, straw-sheaves and microflowers of nanostructured orthorhombic Bi_2S_3 were synthesized by the 180 ^{o}C and 12 h glycolthermal reactions, and were found to be controlled by different solvents: EG, PG and PEG with different MWs.

References

[1] Tang C, Wang C, Su F, Zang C, Yang Y, Zong Z, Zhang Y. Solid State Sci 2010;12:1352–6.

[2] Thongtem T, Pilapong C, Kavinchan J, Phuruangrat A, Thongtem S. J Alloy Compd 2010;500:195–9.

[3] Zhu G, Liu P. Cryst Res Technol 2009;44:713–20.

[4] Zhang D, Niu F, Yan T, Shi L, Du X, Fang J. Appl Surf Sci 2011;257:10161–7.

[5] Pan C, Zhang D, Shi L, Fang J. Eur J Inorg Chem 2008;2008:2429–36.

[6] Pan C, Zhang D, Shi L. J Solid State Chem 2008;181:1298–306.

[7] Lu J, Han Q, Yang X, Lu L, Wang X. Mater Lett 2007;61:3425–8.

[8] Begum A, Hussain A, Rahman A. Mater Sci Appl 2011;2:163–8.

[9] Yu Y, Sun WT. Mater Lett 2009;63:1917–20.

[10] Tang CJ, Zhang YX, Dou XC, Li GH. J Cryst Growth 2010;312:692–7.

[11] Zhang D, Yan T, Shi L, Pan C, Zhang J. Appl Surf Sci 2009;255:5789–94.

[12] Phuruangrat A, Ekthammathat N, Thongtem T, Thongtem S. J Alloy Compd 2011;509:10150–4.

[13] Zhang D, Fu H, Shi L, Pan C, Li Q, Chu Y, Yu W. Inorg. Chem. 2007;46:2446–51.

[14] Phuruangrat A, Thongtem T, Thongtem S. Appl Surf Sci 2008;254:7553–8.

[15] Thongtem T, Phuruangrat A, Thongtem S. J Ceram Proc Res 2008;9:189–91.

[16] Powder Diffract. File, JCPDS-ICDD, 12 Campus Boulevard, Newtown Square, PA 19073-3273, U.S.A. 2001.

[17] Suryanarayana C, Norton MG. X-ray Diffract. Plenum Press, NY. 1998.

[18] Phuruangrat A, Thongtem T, Thongtem S. Mater Lett 2009;63:1538–41.

[19] Wang Y, Chen J, Wang P, Chen L, Chen YB, Wu LM. J Phys Chem C 2009;113:16009–14.

[20] Wu J, Qin F, Cheng G, Li H, Zhang J, Xie Y, Yang HJ, Lu Z, Yu X, Chen R. J Alloy Comd 2011;509:2116–26.

14. Microwave-assisted hydrothermal synthesis of Bi_2S_3 nanorods in flower-shaped bundles

Abstract

Bi_2S_3 nanorods in flower-shaped bundles were successfully synthesized from the decomposition of Bi-thiourea complexes under the microwave-assisted hydrothermal process. X-ray powder diffraction (XRD) patterns and field emission scanning electron microscopy (FE-SEM) show that Bi_2S_3 has the orthorhombic phase and appears as nanorods in flower shaped bundles. A transmission electron microscopic (TEM) study reveals the independent single Bi_2S_3 nanorods with their growth along the [001] direction. A possible formation mechanism of Bi_2S_3 nanorods in flower shaped bundles is also proposed and discussed. Their UV-vis spectrum shows the absorbance at 596 nm, with its direct energy band gap of 1.82 eV.

Keywords: Semiconductors; Chemical synthesis; Luminescence; Scanning electron microscopy; Transmission electron microscopy; X-ray diffraction

Introduction

In recent years, the fabrication of nanomaterials and nanodevices has been widely and deeply researched due to the novel properties comparing to their normal counterparts, and strong dependence on their characteristics such as shape, size and crystallinity [1,2]. Among them, one-dimensional (1D) nanostructures possess unique physical, chemical, and electron-transport properties, different from those of bulky and isotropic materials [2-4].

Binary metal chalcogenides of $A_2^{V}X_3^{VI}$ (A = As, Sb, Bi; X = S, Se, Te) semiconductors have a number of applications including photoconducting targets of television cameras, electronic and optoelectronic devices, thermoelectric devices, and infrared (IR) spectroscopy [2,4-6]. Bismuth sulfide (Bi_2S_3) has a 1.3 eV direct band gap,

and is suitable for application in photovoltaic materials, photodiode arrays, sensors and IR spectroscopy photovoltaic converters, thermoelectric cooling technologies based on the Peltier effect [2,3,5,7-10]. The convention hydrothermal (CH) method has been widely used to synthesize the Bi_2S_3 nanomaterials [1-7]. It was able to control the morphologies: nanorods, nanowires, agglomerated particles and urchinlike [1-8].

Herein, an economical method to synthesize Bi_2S_3 nanorods in flower-shaped bundles by microwave-assisted hydrothermal (MH) method is reported. This method is simple, fast and inexpensive, as compared to the convention hydrothermal (CH) one.

Experimental procedure

The analytical grade chemicals: bismuth nitrate pentahydrate ($Bi(NO_3)_3 \cdot 5H_2O$), thiourea (NH_2CSNH_2) and polyvinylpyrrolidone (PVP) were used without further purification. To synthesize Bi_2S_3 flower-like structure, 0.005 mole $Bi(NO_3)_3 \cdot 5H_2O$ and 0.001 mole NH_2CSNH_2 were dissolved in 60 ml distilled water, and followed by 0.5 ml 37 % HNO_3 and 0.5 g PVP adding, respectively. The mixture was stirred for 30 min at room temperature and put into a 100 ml Teflon-lined autoclave, which was tightly closed, heated up to 200 ^{o}C by a 300 W microwave radiation, held at this temperature for 1 h, and then naturally cooled to room temperature. After the microwave-assisted hydrothermal process, the product was filtered, washed with distilled water and absolute ethanol for several times, and dried at 80 ^{o}C for 24 h. This process was also repeated by using the convention hydrothermal method, heated by an electric oven, at 200 ^{o}C for 24 h.

The products were analyzed using an X-ray diffractometer (D8 Advance, Bruker Ltd., Germany) with Cu Kα radiation in the 2θ range from 10 to 80 deg. The Raman spectra was recorded on HORIBA JOBIN YVON T64000 Raman spectrometer using 50 mW Ar Laser with λ = 514.5 nm. The morphology of the product was characterized by a JSM-6335F scanning electron microscope (SEM, JEOL Ltd., Japan) and JEM-2010 transmission electron microscope (TEM, JEOL Ltd., Japan). The room temperature UV-

visible spectrum was collected on a UV/VIS spectrometer Perkin Elmer LAMBDA 40 at wavelength range of 200-1300 nm with the scanning rate of 0.5 $nm.s^{-1}$.

Results and discussion

Fig. 1a shows the XRD patterns of the products synthesized by the MH and CH methods. All diffraction peaks match very well with the Bi_2S_3 JCPDS no. 17-0320 [11] with no detection of any impurities. The XRD intensity synthesized by the MH is higher than that synthesized by the CH. It implies that Bi_2S_3 synthesized by the first is better crystalline than Bi_2S_3 synthesized by the second. All the diffraction peaks of the Bi_2S_3 nanorods in flower-shaped bundles were shifted towards the lower angles, as compared to the JCPDS database, caused by an increase in their interplanar spaces. This may be attributed to the existence of the stress in the lattice of Bi_2S_3 nanorods in flower-shaped bundles. EDX spectrum of Bi_2S_3 produced by the MH method (un-shown result) detected only Bi and S peaks, in accordance with its constituents. Quantitative EDX analysis showed that the atomic ratio of Bi:S is 38:62, very close to the composition of Bi_2S_3. A definite existence of Bi_2S_3 was analyzed using a Raman spectrometer as shown in Fig. 1b. The spectra show four vibration modes, at 139.6, 253.7, 310.0 and 968.9 cm^{-1}. The first is in accordance with the 139.4 cm^{-1} mode of Bi_2S_3 nanorods, specified as the surface phonon vibration [12]. The second corresponds with the vibration mode of Bi_2S_3 nanorods at 252.0 cm^{-1} and 259 cm^{-1}, [12,13] and Bi_2S_3 nanoribbons and hierarchical nanostructures at 250 cm^{-1}, specified as the vibration mode of Bi-S bonds [14,15]. The detections of the third and fourth were in accordance with those of Bi_2S_3 nanorods at 312 and 975 cm^{-1} [13]. In the FTIR spectrum of PVP, it shows the wave numbers at 3450, 2930, 1675, 1420 and 1290 cm^{-1} - assigned to be the OH stretching vibration, CH_2 unsymmetrical stretching vibration, CO stretching vibration, CH_2 bending vibration and CN stretching vibration, respectively [16,17]. There was no detection of these impurity peaks in the FTIR spectrum of Bi_2S_3 (un-shown result), which implied that the product was pure phase.

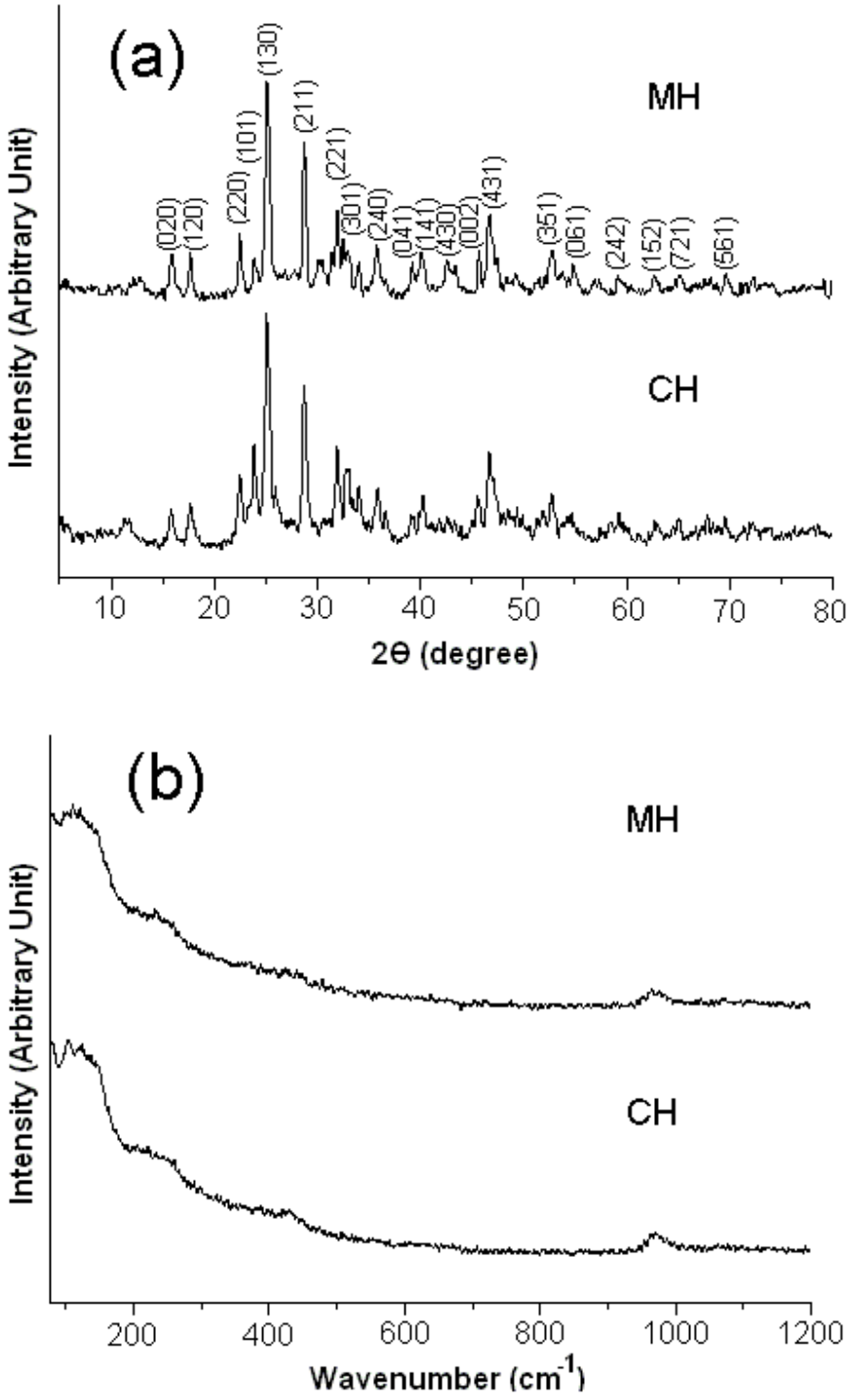


Fig. 1 (a) XRD patterns and (b) Raman spectra of Bi_2S_3 synthesized by the conventional hydrothermal and microwave-assisted hydrothermal methods.

SEM images of Bi_2S_3, prepared by the MH and CH methods, are given in Fig. 2. Only Bi_2S_3 irregular crystalline (Fig. 2a) with the average size of 1.5 μm was synthesized by the CH process. These nanorods agglomerate together to form clusters, and are not separate as independent nanorod bundles. Comparing to the synthesis of large-scale single-crystalline Bi_2S_3 nanowires by a simple one-step hydrothermal reaction of $Bi(NO_3)_3 \cdot 5H_2O$ and $Na_2S_2O_3$ at 180 ^{o}C for 2 days, the product contained a large quantity of nanowires with their lengths of hundreds of nanometers to a few microns range [18]. When microwave radiation was used as the heating source, the clearly independent Bi_2S_3 nanorods in flower-shaped bundles were detected. The use of microwave radiation as heating source shows the formation of uniform and perfect Bi_2S_3 flower-like bundles with the approximate diameter of 3-4 μm including the approximate length of the nanorods of 1-2 μm. The anisotropic growth of the Bi_2S_3 crystallites was further confirmed by the TEM analysis.

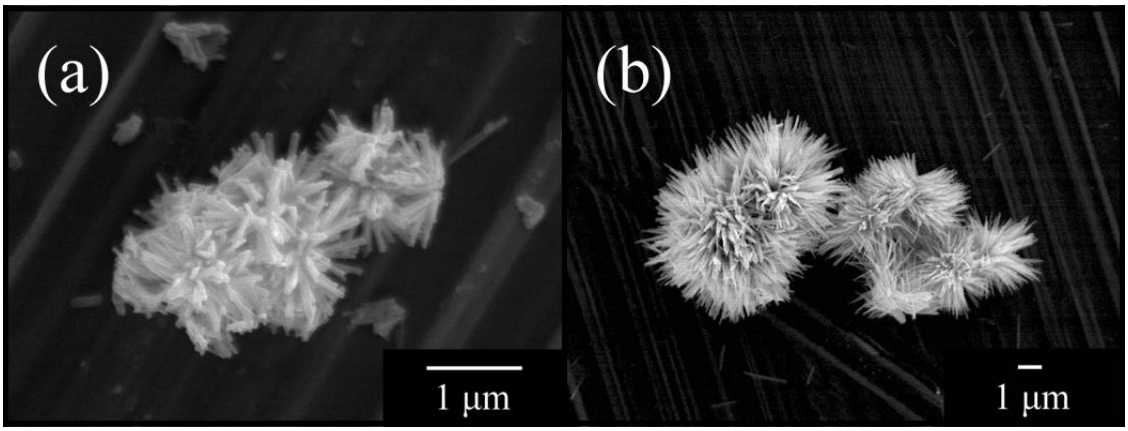


Fig. 2 SEM images of Bi_2S_3 nanorods in bundles synthesized by the (a) conventional hydrothermal and (b) microwave-assisted hydrothermal methods.

Fig. 3 shows TEM images of Bi_2S_3 nanorods in flower-shaped bundles synthesized by the MH method. The Bi_2S_3 flowers of Fig. 3a and b are composed of more than a hundred of individual Bi_2S_3 nanorods grow from the Bi_2S_3 cores. It is clearly that the morphology of Bi_2S_3 nanorods in flower-shaped bundles with 3 - 5.5 μm in size is in accordance with the SEM image (Fig. 2b) shown above. Fig. 3c shows the broken

Bi_2S_3 nanorods form the Bi_2S_3 flower-like cores. The length of the individual nanorod of Bi_2S_3 is approximately 500-1500 nm. The growth direction of Bi_2S_3 nanorods in flower shaped bundles was studied using high resolution transmission electron microscopy (HRTEM) and selected area electron diffraction (SAED). They were characterized on areas 1 and 2 of TEM image (Fig. 3c). HRTEM images of Fig. 4a and c show lattice fringes of crystallographic planes with 3.96 Å space in parallel with the nanorods, corresponding to the (220) planes of orthorhombic Bi_2S_3 phase. The HRTEM images demonstrate that the Bi_2S_3 nanorods synthesized by the MH and CH methods grow along the [001] direction – in accordance with the growth direction of Bi_2S_3 nanorods and nanowires characterized by other researchers [1,3,19]. Both SAED patterns in areas 1 and 2 appear as bright spots composing electron diffraction patterns (Fig. 4b and d), revealing that individual Bi_2S_3 nanorods broken from flower-like cores are single crystal Bi_2S_3 with high degree of crystallinity. The SAED patterns can be indexed as the orthorhombic phase of Bi_2S_3 (JCPDS no. 17-0320) with the same [-110] zone axes, which further confirm that the structure of the nanorods is orthorhombic phase, in accordance with the XRD analysis.

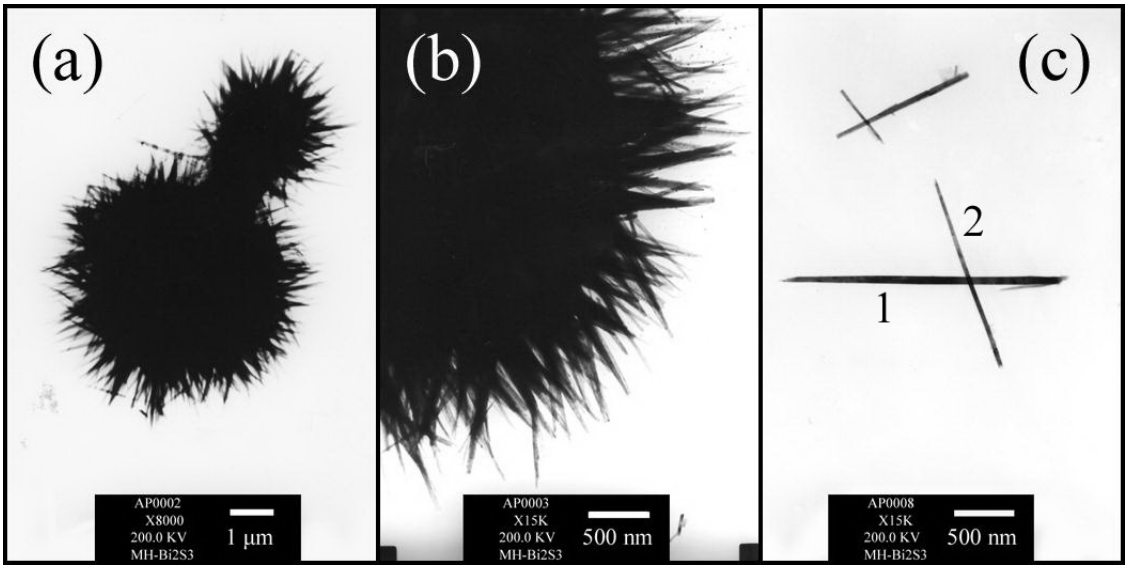


Fig. 3 TEM images of Bi_2S_3 nanorods in flower shaped bundles synthesized by the MH method at (a) low and (b) high magnifications. (c) The broken nanorods from the flower-like cores.

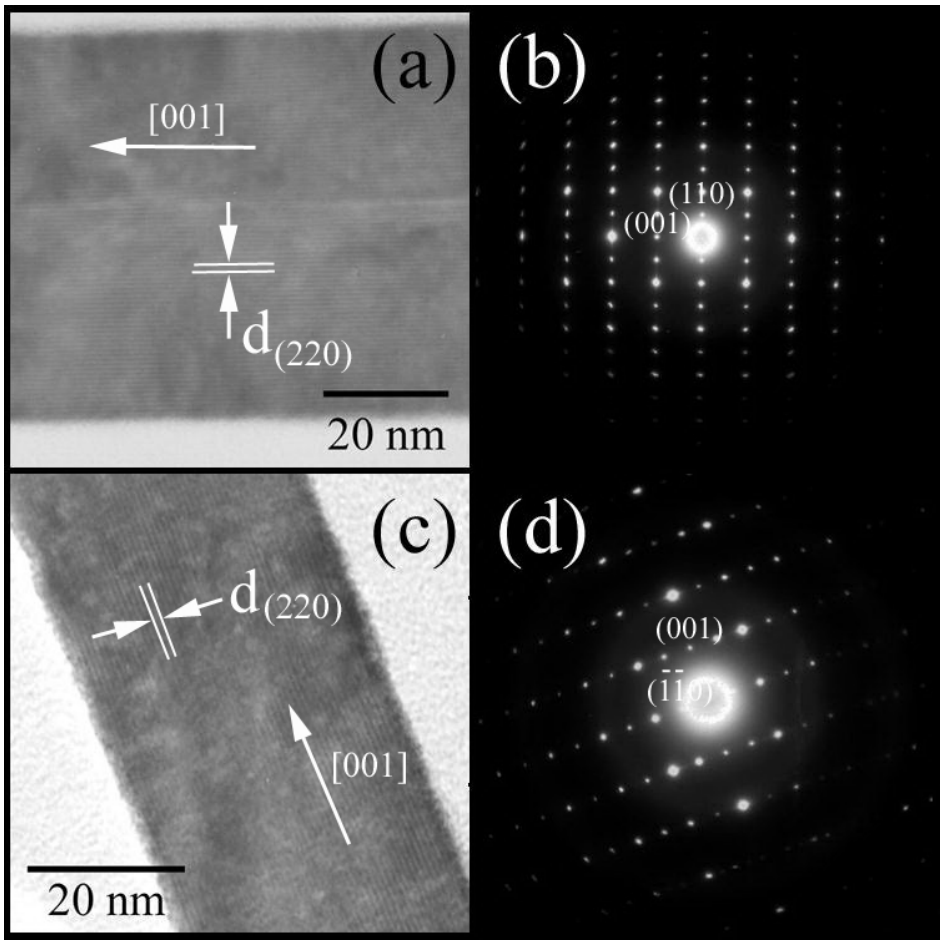


Fig. 4 HRTEM images and SAED patterns of Bi_2S_3 nanorods in bundles synthesized by the (a, b) conventional hydrothermal, and (c, d) microwave-assisted hydrothermal methods.

The formation mechanism of Bi_2S_3 nanorods in flower-shaped bundles is schematically shown in Fig. 5. First, the strong complex action between Bi^{3+} and thiourea (TU) leads to the formation of Bi–TU complexes [9]. For NH_2CSNH_2 compound, it has pair electrons on nitrogen and sulfur atoms, which have the great coordinating ability with inorganic metal cations, such as Cd^{2+}, Cu^{2+} and Pb^{2+} to form the metal-thiourea complexes [20]. Under microwave-assisted hydrothermal process, the Bi–TU complexes decomposed and formed the Bi_2S_3 nuclei. Then the Bi_2S_3 nanorods grew on

the surface of Bi_2S_3 nuclei to form Bi_2S_3 nanorods in flower shaped bundles. The formation reactions may be described as follows.

$$Bi^{3+} + TU \longrightarrow Bi–TU\ complexes \quad (1)$$

$$Bi–TU\ complexes \longrightarrow Bi_2S_3 \quad (2)$$

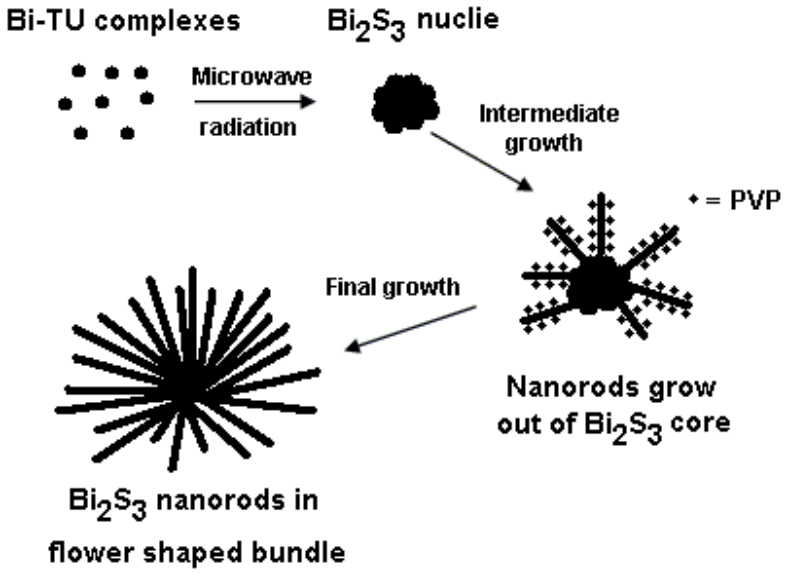


Fig. 5 Schematic illustration for the formation mechanism of Bi_2S_3 nanorods in flower shaped bundles.

The growth process of Bi_2S_3 nanorods in flower shaped bundles contains mainly two stages – the nucleation and crystal growth. For the present research, $Bi(NO_3)_3$ reacts with TU to form Bi–TU complexes at the initial stage. At the intermediate stage, the Bi–TU complexes decomposed to produce Bi_2S_3 nuclei by the microwave-assisted hydrothermal process. At this stage, PVP adsorbed on Bi_2S_3 nuclei - leading to the Bi_2S_3 nucleation as seeds which act as initial nuclei for particle growth. When the particles reach the critical dimension, PVP absorbed on the small particles by the side linked Bi_2S_3 units forming infinite chains parallel to the c-axis acting as a template for the formation of Bi_2S_3 nanorods in flower shaped bundles. The final stage is the Bi_2S_3 nanorods in flower shaped bundles, obtained by a novel microwave hydrothermal method, are homogeneous in size and form much similar to a flower with thorns found in

nature [9,10,21]. In general, the growth of 1D Bi_2S_3 nanomaterials is a preferential growth direction along the c-axis due to the difference bonding in Bi_2S_3 structure. Bi_2S_3 is a lamellar structure with linked Bi_2S_3 units forming infinite chains parallel to the c-axis. The stronger covalent bond between the planes perpendicular to the c-axis supports higher growth rate along the c-axis. The much weaker van der Waals bonding between the planes perpendicular to the a-axis limits the growth of the fibers in the horizontal direction and supports their cleavage to form one dimensional nanostructure [22].

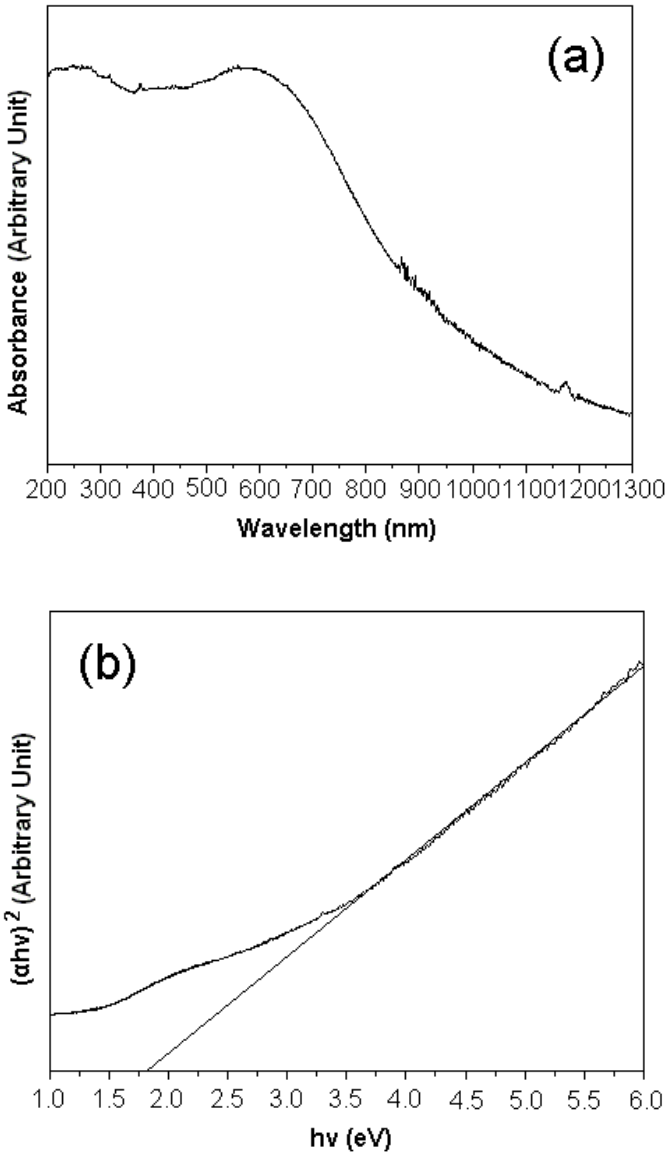


Fig. 6 (a) UV-vis absorbance, and (b) $(\alpha h\nu)^2$ vs $h\nu$ curve of Bi_2S_3 nanorods in flower shaped bundles synthesized by the microwave-assisted hydrothermal method.

The optical property of the product was investigated by UV-visible spectroscopy. Fig. 6 presents the UV-vis absorbance spectrum, and $(\alpha h\nu)^2$ vs $h\nu$ curve of Bi_2S_3 nanorods in flower shaped bundles synthesized by the MH method. The UV-vis spectrum showed the blue shifted absorption at 596 nm as compared to the 953 nm absorption for bulk Bi_2S_3 [23]. It can be attributed to the excitonic absorbance due to the quantum confinement at low dimension compared to its bulk counterparts [23]. The direct band gap of the product was calculated from its optical absorption spectrum by plotting $(\alpha h\nu)^2$ vs $h\nu$ curve where α is the absorbance, h the Planck constant and ν the frequency [24] is shown in Fig. 6b. The direct band gap (E_g) of the Bi_2S_3 semiconducting nanorods in flower shaped bundles was determined to be at 1.82 eV. This value is in good agreement with the 1.85 eV band gap of Bi_2S_3 nanowires [22], and 1.8 eV band gap of Bi_2S_3 thin films [24].

Conclusions

Microwave-assisted hydrothermal reaction has emerged as an alternative route of fine powder synthesis. It was demonstrated that this simple method can be used to synthesize Bi_2S_3 nanostructure. XRD, SEM and TEM analyses proved that the product is orthorhombic Bi_2S_3 nanorods in flower shaped bundles with the size of 3 - 5.5 μm. The microwave-assisted hydrothermal process for the synthesis of nanomaterials is shown to be very effective, inexpensive, short reaction time and environmentally benign. The direct energy band gap of the product was determined to be 1.82 eV – in agreement with those of other researchers.

References

[1] Z.J. Zhang and X.Y. Chen, J. Phys. Chem. Solids, 70 (2009) 1121-1131.

[2] L. Tian, H.Y. Tan, and J.J. Vittal, Cryst. Growth Des., 8 (2008) 734-738.

[3] C.J. Tang, G.Z. Wang, H.Q. Wang, Y.X. Zhang and G.H. Li, Mater. Lett., 62 (2008) 3663-3665.

[4] Q. Han, J. Chen, X. Yang, L. Lu and X. Wang, J. Phys. Chem. C, 111 (2007) 14072-14077.

[5] J. Lu, Q. Han, X. Yang, L. Lu and X. Wang, Mater. Lett., 61 (2007) 3425-3428.

[6] G. Xie, Z.P. Qiao, M.H. Zeng, X.M. Chen and S.L. Gao, Cryst. Growth Des., 4 (2004) 513-516.

[7] X. Zhu, J. Ma, Y. Wang, J. Tao, B. Lin, Y. Ren, X. Jiang and J. Liu, Ceram. Int., 34 (2008) 249-251.

[8] Y. Jiang, Y.J. Zhu and Z.L. Xu, Mater. Lett., 60 (2006) 2294-2298.

[9] A. Phuruangrat, T. Thongtem and S. Thongtem, Mater. Lett., 63 (2009) 1496-1498.

[10] T. Thongtem, A. Phuruangrat, S. Wannapop and S. Thongtem, Mater. Lett., 64 (2010) 122-124.

[11] Powder Diffract. File, JCPDS-ICDD, 12 Campus Boulevard, Newtown Square, PA 19073-3273, U.S.A., (2001).

[12] X. Yang, X. Wang and Z. Zhang, Mater. Chem. Phys., 95 (2006) 154-157.

[13] J. Ota and S.K. Srivastava, J. Phys. Chem. C, 111 (2007) 12260-12264.

[14] Y. Sun, Q. Han, J. Lu, X. Yang, L. Lu and X. Wang, Mater. Lett., 62 (2008) 3730-3732.

[15] Q. Han, Y. Sun, X. Wang, L. Chen, X. Yang and L. Lu, J. Alloys Compd., 481 (2009) 520-525.

[16] X. Sui, Y. Liu, C. Shao, Y. Liu and C. Xu, Chem. Phys. Lett., 424 (2006) 340-344.

[17] T.T. Tseng and W.J. Tseng, Ceram. Int., 35 (2009) 2837-2844.

[18] Y. Yu and W.T. Sun, Mater. Lett., 63 (2009) 1917-1920.

[19] Y. Yu, C.H. Jin, R.H. Wang, Q. Chen and L.M. Peng, J. Phys. Chem. B, 109 (2005) 18772-18776.

[20] S.H. Yu, J. Yang, Z.H. Han, Y. Zhou, R.Y. Yang, Y.T. Qian and Y.H. Zhang, J. Mater. Chem., 9 (1999) 1283-1287.

[21] D.P. Volanti, D. Keyson, L.S. Cavalcante, A.Z. Simões, M.R. Joya, E. Longo, J.A. Varela, P.S. Pizani, A.G. Souza, J. Alloy. Compd., 459 (2008) 537-542.

[22] W. Li, Mater. Lett., 62 (2008) 243-245.

[23] M. Salavati-Niasari, D. Ghanbari and F. Davar, J. Alloy. Compd., 488 (2009) 442-447.

[24] V.V. Killedar, S.N. Katore and C.H. Bhosale, Mater. Chem. Phys., 64 (2000) 166-169.

15. Cyclic microwave-assisted synthesis of $CuFeS_2$ nanoparticles using biomolecules as sources of sulfur and complexing agent

Abstract

Copper iron sulfide ($CuFeS_2$) nanoparticles were successfully synthesized by a 300 W cyclic microwave radiation, exposing onto ethylene glycol containing $Cu(CH_3COO)_2$, $FeCl_3{\cdot}6H_2O$ or $FeCl_2{\cdot}4H_2O$ and L-cysteine biomolecules. X-ray diffraction (XRD), field emission scanning electron microscopy (FE-SEM), transmission electron microscopy (TEM), Raman spectrometry and X-ray photoelectron spectroscopy (XPS) revealed the presence of pure tetragonal chalcopyrite $CuFeS_2$ nanoparticles with valence states of Cu^{+}, Fe^{3+} and S^{2-} and four Raman shifts at 215.0–218.6, 280.2–281.4, 394.4–394.9 and 472.2–473.4 cm^{-1}. A formation mechanism of the products was also proposed according to the experimental results.

Keywords: Electron microscopy; Nanocrystalline materials; Spectroscopy; X-ray techniques

Introduction

Chalcopyrite copper iron sulfide ($CuFeS_2$) is a I-III-VI_2 ternary compound known as an antiferromagnetic semiconductor, which has narrow band gap (0.5–0.6 eV), very high Néel temperature (550 ^{o}C) and innovative electrical, optical and magnetic properties [1–5]. It has potential applications for cathodes of lithium-ion batteries [6], solar cells [1] and thermoelectric devices [5]. Different methods have been investigated for the synthesis of $CuFeS_2$: nanorods and nanoparticles by hydrothermal synthesis [1,7], single crystalline nanowires and hexagonal plate-like chalcopyrite by solvothermal process [2,6], spherical and pyramidal nanocrystals by thermal decomposition and reaction of metal-dithiocarbamate or acetylacetonate precursors with sulfur in an organic solvent mixture [3], and a combination of mechanical alloying and spark plasma sintering [5].

In this research, cyclic microwave radiation was used for the synthesis of $CuFeS_2$ nanoparticles using L-cysteine biomolecules as sources of sulfur and complexing agent. The process is more rapid and efficient than that achieved by a conventional one. Additionally, it can solve the problems of temperature and concentration gradients and provides uniform growth media.

Experiment

To synthesize $CuFeS_2$, 1 mmol $Cu(CH_3COO)_2$, 3 mmol $FeCl_3{\cdot}6H_2O$ or $FeCl_2{\cdot}4H_2O$ and 2 mmol $C_3H_7NO_2S$ (L-cysteine) were mixed in 40 ml ethylene glycol (EG) to form solutions which were processed by a 300 W cyclic microwave radiation (CMR) for 5–40 cycles. Each cycle, microwave radiation was on for 40 s every 40 s interval. In the end, the precipitates were separated, rinsed and dried at 70 ^{o}C for 24 h to form CA-1 and CA-2 products, where CA, 1 and 2 were for those synthesized using $Cu(CH_3COO)_2$, $FeCl_3{\cdot}6H_2O$ and $FeCl_2{\cdot}4H_2O$, respectively.

Results and discussion

XRD

The crystalline structure and chemical composition of the as-synthesized products were characterized by XRD of which the patterns (Fig. 1) were compared with the JCPDS database No. 01-0842 [8]. All diffraction peaks of CA-1 and CA-2 were readily indexed to be tetragonal chalcopyrite $CuFeS_2$. Their XRD peaks were similar in height and very sharp, implying that the products were composed of a number of particles with the same size and high crystalline degree.

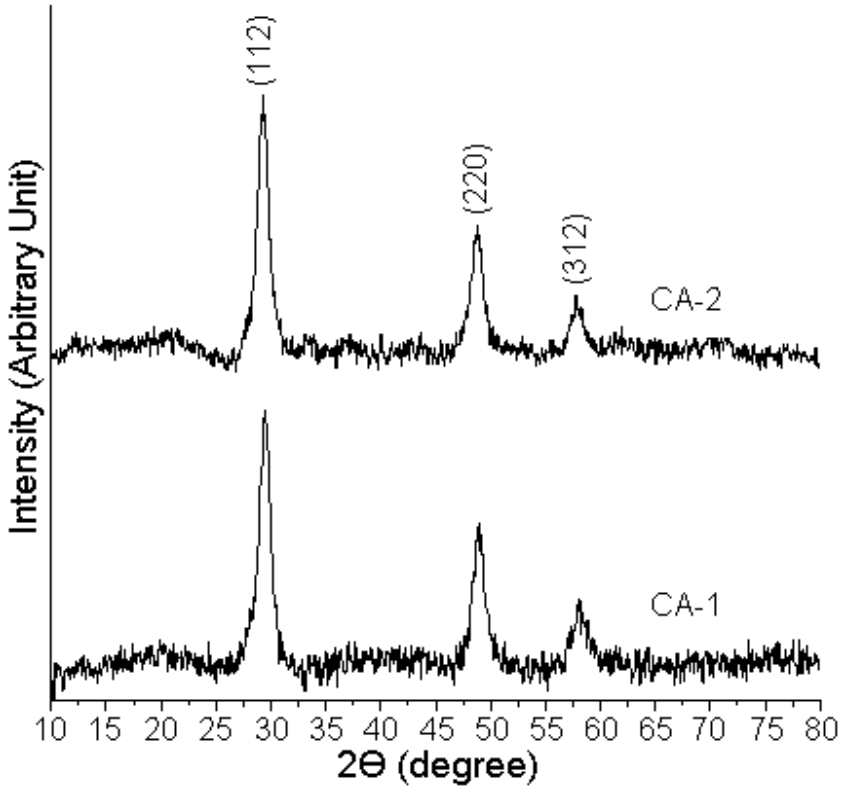


Fig. 1 XRD patterns of CA-1 and CA-2 synthesized for 40 cycles.

SEM, TEM, EDX and SAED

An effect of different iron sources on morphologies was investigated by SEM and EDX (Fig. 2). The CA-1 product contained 10–20 nm nanoparticles in clusters. Each cluster appeared as rough surface which was the proof of loosely packed nanoparticles grouping together [9]. For the CA-2 product, it was composed of nanoparticles in irregular clusters, in accordance with the above XRD analysis. EDX spectra of both products revealed the presence of Cu, Fe and S as fundamental elements, sputtered Au for conductivity improving, including C and O of polymer tape.

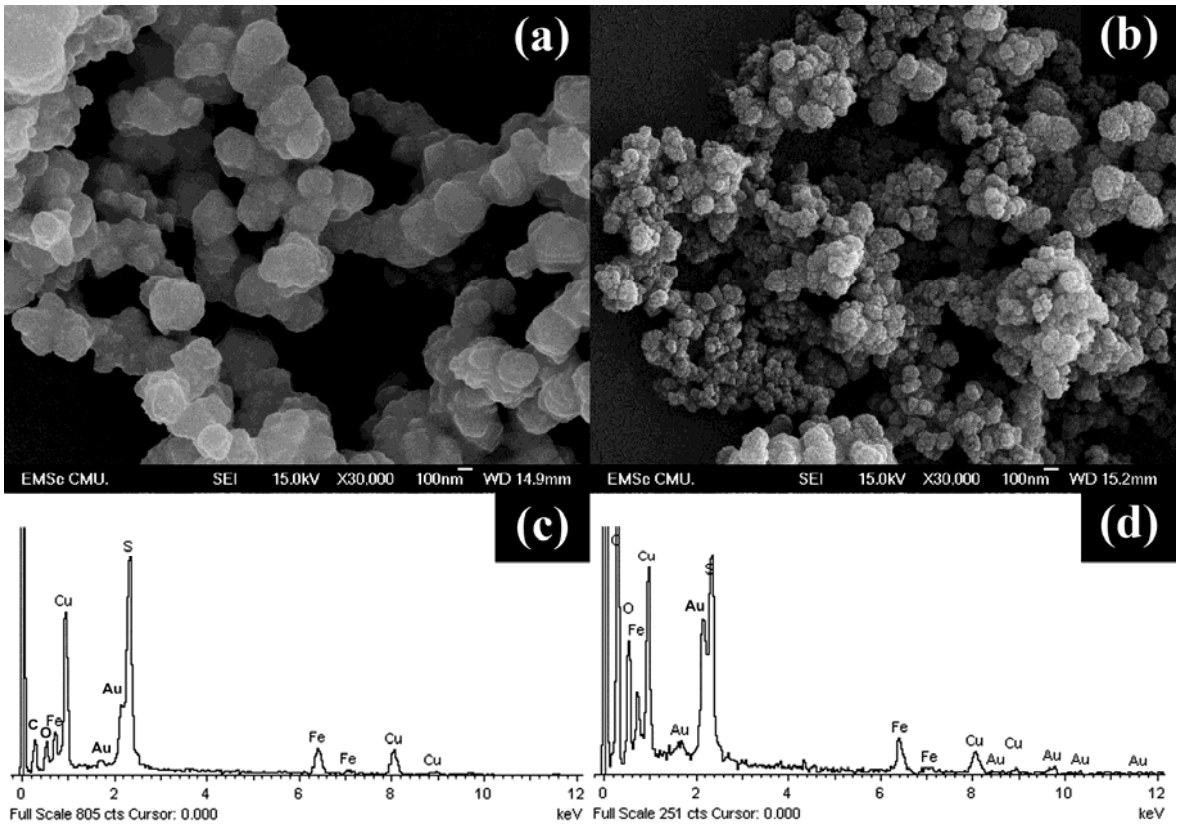


Fig. 2 SEM images and EDX spectra of (a, c) CA-1 and (b, d) CA-2 synthesized for 40 cycles.

The nanoparticles were further investigated by TEM and SAED (Fig. 3). For 40 cycles, intensive contrast at dark edges surrounding small bright areas indicates that CA-1 was composed of a number of nanoparticles cluster together, which was not able to be detected by SEM. The product presents the really fine nanoparticles. Upon decreasing the processing time from 40 cycles to 20 and 5 cycles, the products remained as clusters of nanoparticles with reducing their sizes in sequence. By changing the iron source from $FeCl_3 \cdot 6H_2O$ to $FeCl_2 \cdot 4H_2O$, clusters of nanoparticles were still detected. SAED patterns of these products were composed of diffuse and hollow concentric rings, specified as polynanocrystalline $CuFeS_2$ [8].

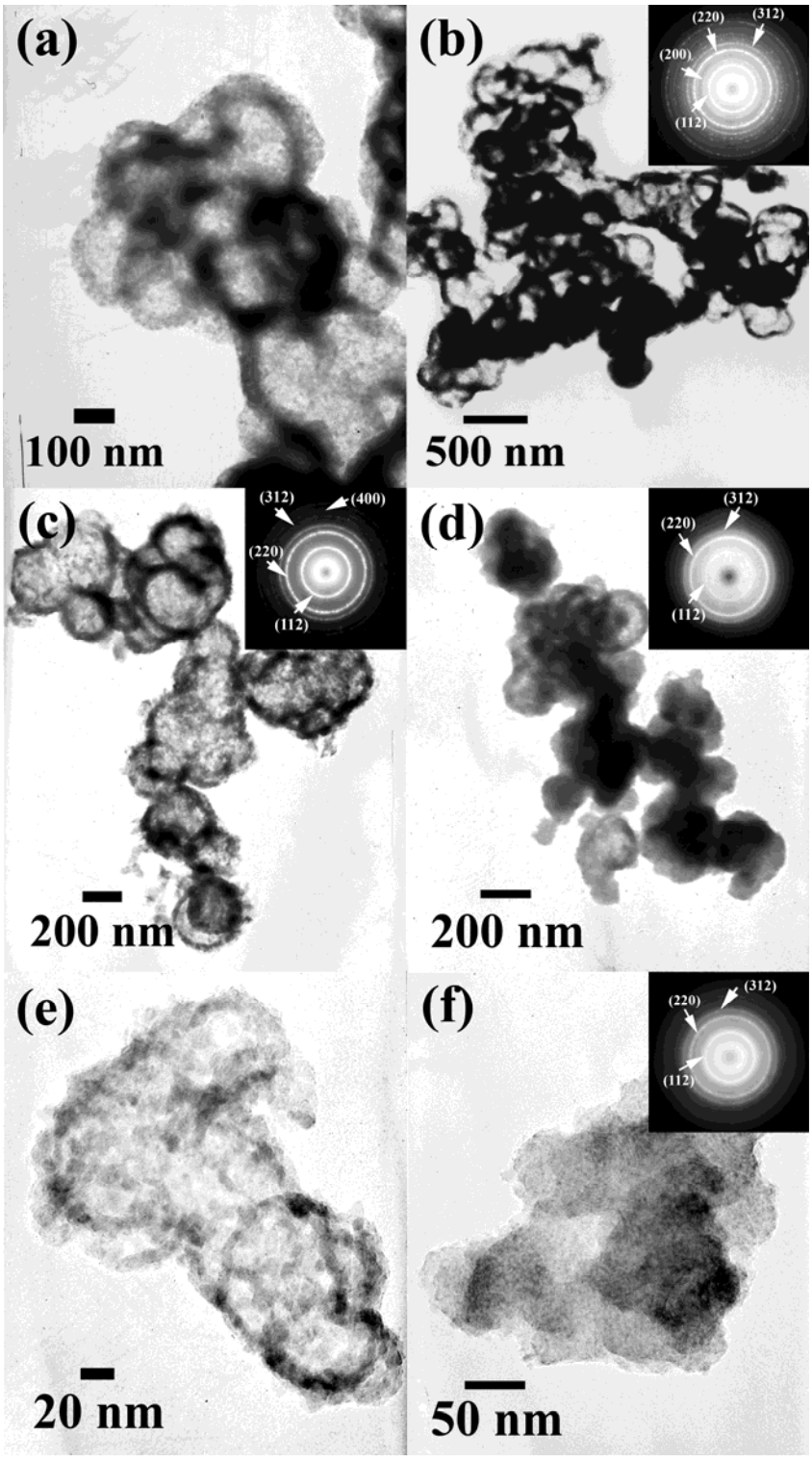


Fig. 3 TEM images and SAED patterns of (a-d) CA-1 synthesized for 40, 40, 20 and 5 cycles, including those of (e, f) CA-2 synthesized for 40 cycles, respectively.

Raman and XPS spectra

Raman spectra of $CuFeS_2$ (Fig. 4) shows four Raman shifts at 215.0–218.6, 280.2–281.4 (A_1 modes), 394.4–394.9 (B_2 modes) and 472.2–473.4 (E modes) cm^{-1}, in accordance with the previous report [10]. A slight difference of Raman peaks was observed, caused by systematic downshift of Raman peaks of the CA-1 comparing with those of the CA-2. Band positions and relative intensities of the Raman peaks could slightly vary from one spectrum to another due to the orientation of crystal lattice and optical properties, including the presence of local impurities or defects inside [10,11].

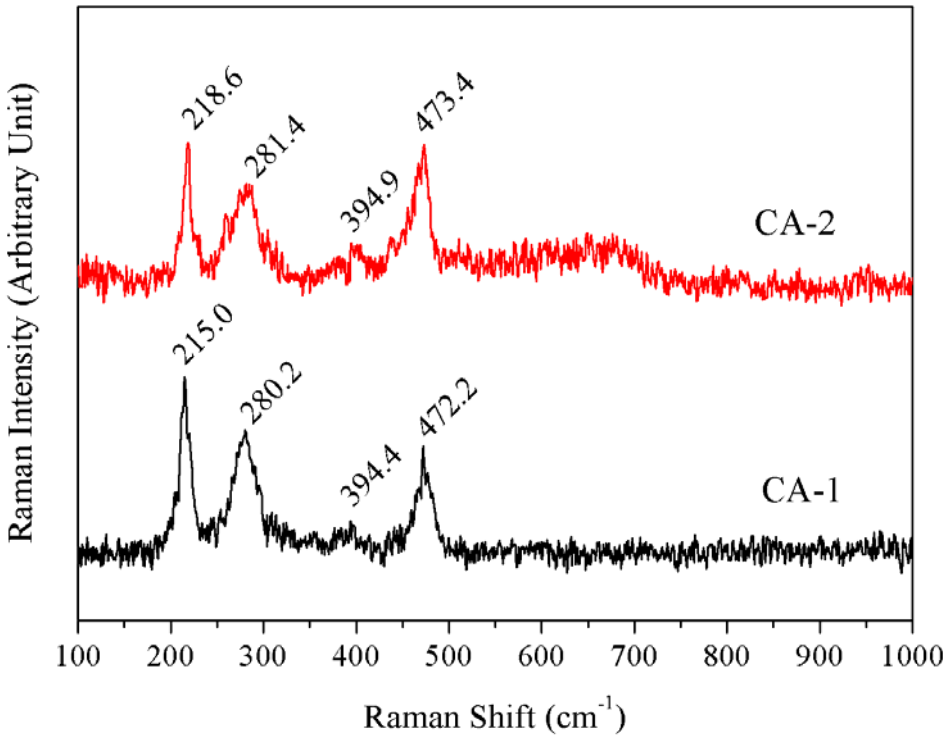


Fig. 4 Raman spectra of CA-1 and CA-2 synthesized for 40 cycles.

XPS spectra of copper, iron and sulfur containing in CA-1 and CA-2 are shown in Fig. 5. The Cu2p core-level spectra show the analyzed binding energy (BE) of $Cu2p_{3/2}$ (932.3−932.5 eV) and $Cu2p_{1/2}$ (952.2−952.5 eV) peaks, corresponding to Cu^{+}. No $Cu2p_{3/2}$ satellite peak at 942 eV of Cu^{2+} was detected. For the Fe2p core-level spectra,

BE of $Fe2p_{3/2}$ (711.3−711.5 eV) and $Fe2p_{1/2}$ (725.8−726.2 eV) were in good accordance with Fe^{3+}.

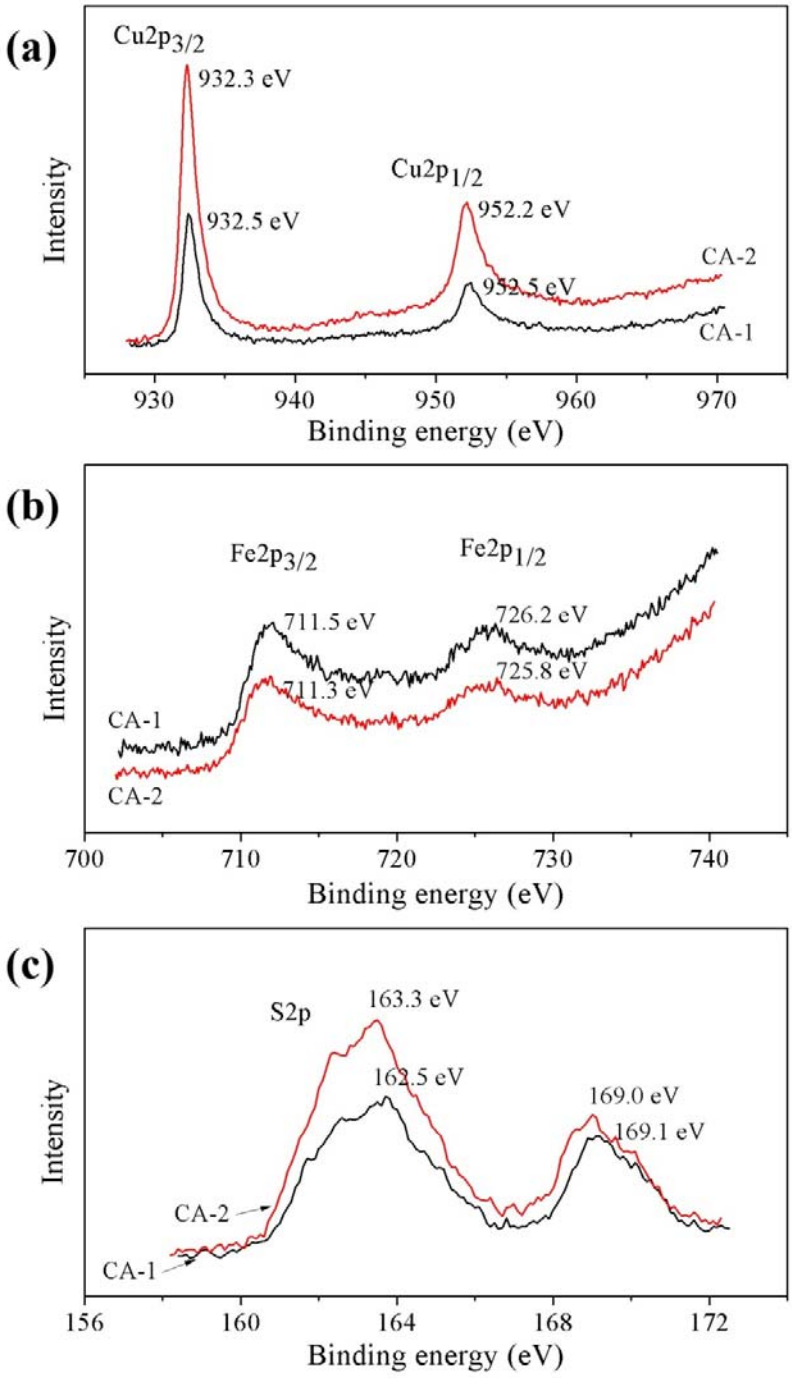


Fig. 5 XPS spectra of (a−c) Cu, Fe and S containing in CA-1 and CA-2 synthesized for 40 cycles, respectively.

The S2p core-level spectra reveal BE of $S2p_{3/2}$ (162.5−163.3 eV), corresponding to S^{2-} [2,3,12]. Furthermore, additional peaks were detected at 169.0−169.1 eV and were likely to be from the oxidized parts of the products during the synthesis. Other minor peaks of C1s (284.5−285.3 eV) and O1s (531.3−531.5 eV) were also detected [2]. They belonged to the coated carbon for conductivity improvement for XPS analysis and absorbed gaseous molecules.

Formation mechanism

Mixtures of $Cu(CH_3COO)_2$, $FeCl_3{\cdot}6H_2O$ and L-cysteine biomolecules in EG were processed by CMR to form $CuFeS_2$ with valence states of Cu^{+}, Fe^{3+} and S^{2-}. Possibly, $Cu(CH_3COO)_2$ was reduced by EG, a well-known reducing agent, by transforming Cu^{2+} into Cu^{+} intermediate ions [13−16], which further combined with L-cysteine to form [Cu(L−cysteine) complexes]. Concurrently, Fe^{3+} formed [Fe(L−cysteine) complexes] with L-cysteine. During CMR, these complexes were combined and decomposed with the formation of $CuFeS_2$ nuclei. Alternately, [Cu–Fe(L-cysteine) complexes] could form with the subsequent formation of $CuFeS_2$ nuclei.

When $FeCl_2{\cdot}4H_2O$ was used instead of $FeCl_3{\cdot}6H_2O$, $CuFeS_2$ with valence states of Cu^{+}, Fe^{3+} and S^{2-} was also synthesized. Oxidation-reduction of Fe^{2+} and Cu^{2+} proceeded, including the formation of complexes and $CuFeS_2$ nuclei in sequence as above.

The nuclei grew by forming $CuFeS_2$ nanoparticles and clustering in groups with reducing their surface energies.

Conclusions

Pure tetragonal $CuFeS_2$ nanoparticles were successfully synthesized by a 300 W CMR, exposing onto EG containing $Cu(CH_3COO)_2$, $FeCl_3{\cdot}6H_2O$ or $FeCl_2{\cdot}4H_2O$ and L-

cysteine precursors for 5–40 cycles. Four Raman shifts were detected at 215.0–218.6, 280.2–281.4, 394.4–394.9 and 472.2–473.4 cm^{-1}, and BE of Cu^{+} at 932.3−932.5 eV ($Cu2p_{3/2}$) and 952.2−952.5 eV ($Cu2p_{1/2}$), Fe^{3+} at 711.3−711.5 eV ($Fe2p_{3/2}$) and 725.8−726.2 eV ($Fe2p_{1/2}$), and S^{2-} at 162.5−163.3 eV ($S2p_{3/2}$). In this research, Fe-sources played the same role in crystalline degree and size distribution of the products.

References

[1] Chen KT, Chiang CJ, Ray D. Mater Lett 2013;95:172–4.

[2] Wang MX, Wang LS, Yue GH, Wang X, Yan PX, Peng DL. Mater Chem Phys 2009;115:147–50.

[3] Wang YHA, Bao N, Gupta A. Solid State Sci 2010;12:387–90.

[4] Disale SD, Garje SS. Appl Organometal Chem 2009;23:492–7.

[5] Li J, Tan Q, Li JF. J Alloy Compd 2013;551:143–9.

[6] Ding W, Wang X, Peng H, Hu L. Mater Chem Phys 2013;137:872–6.

[7] Hu J, Lu Q, Deng B, Tang K, Qian Y, Li Y, et al. Inorg Chem Commun 1999;2:569–71.

[8] Powder Diffract File, JCPDS-ICDD, 12 Campus Boulevard, Newtown Square, PA 19073-3273, USA (2001).

[9] Zhang DE, Xie Q, Wang MY, Zhang XB, Li SZ, Han GQ, et al. Solid State Sci 2010;12:1529–33.

[10] Wang C, Xue S, Hu J, Tang K. Jpn J Appl Phys 2009;48:023003(3pp).

[11] White SN. Chem Geol 2009;259:240–52.

[12] Kuzuya T, Itoh K, Ichidate M, Wakamatsu T, Fukunaka Y, Sumiyama K. Electrochim Acta 2007;53:213–7.

[13] Anzlovar A, Orel ZC, Zigon M. J Nanosci Nanotechnol 2008;8:3516–25.

[14] Ningthoujam RS, Gajbhiye NS, Sharma S. Pramana-J Phys 2009;72:577–86.

[15] Carotenuto G, Pepe GP, Nicolais L. Eur Phys J B 2000;16:11–7.

[16] Orel ZC, MatijeviĆ E, Goia DV. J Mater Res 2003;18:1017–22.

16. Transformation of cubic $AgBiS_2$ from nanoparticles to nanostructured flowers by a microwave-refluxing method

Abstract

Cubic $AgBiS_2$ nanoparticles and flower-like clusters were successfully synthesized by microwave refluxing of CH_3COOAg, $Bi(NO_3)_3{\cdot}5H_2O$ and thiosemicarbazide ($NH_2NHCSNH_2$) in ethylene glycol. The phase was detected by X-ray diffraction (XRD) and selected area electron diffraction (SAED). The SAED pattern was also in accordance with that of the simulation. Scanning and transmission electron microscopy (SEM and TEM) revealed the gradual transformation of nanoparticles into flower-like clusters by microwave power increasing. Their UV-visible absorption and photoluminescence (PL) emission were detected by spectrometry. Possible formation mechanism of nanoparticles and nanostructured flowers was also proposed according to the experimental results.

Keywords: Electron microscopy; Spectroscopy; X-ray methods; Functional applications

Introduction

At present, I-V-VI ternary chalcogenides are very attractive materials, especially silver bismuth sulfide ($AgBiS_2$). It is a promising candidate for using as novel semiconductors [1] and has high potential for use as optoelectric and thermoelectric devices including optical recording media [2].

Microwave refluxing is a distillation process by microwave radiation involving the condensation of vapors and the return of the condensate (liquid produced by condensation of steam) to the original system. This process is very simple, fast, effective and environmentally benign. It can solve the problems of temperature and concentration gradients, and provides uniform growth media. It has been developed and widely used in industrial and laboratory distillations [3].

The motivation of doing this research is to synthesize $AgBiS_2$ crystals the shape and size of nanoparticles and flower-like clusters by a microwave-assisted refluxing method. The success in this synthesis may lead to different applications in the near future.

Experiment

In this research, 1 mmol CH_3COOAg, 1 mmol $Bi(NO_3)_3 \cdot 5H_2O$ and 2 mmol thiosemicarbazide ($NH_2NHCSNH_2$) with 1:1:2 molar ratio Ag:Bi:S were dissolved in 50 ml of different solvents - ethylene glycol (EG), propylene glycol (PG), ethylene diamine (ED) and water. Each 50 ml solution was refluxed by 100, 300, 600 and 800 W microwave radiation for 20, 40 and 60 min. Finally, black precipitates were synthesized, separated by filtration, washed with de-ionized water and ethanol, and dried at 70 °C for 12 h.

The products were then characterized by different methods: X-ray diffractometer (XRD, SIEMENS D500, Germany) operating at 20 kV, 15 mA, and using Cu-K_α line in combination with the database of the Joint Committee on Powder Diffraction Standards (JCPDS) [4]; scanning electron microscope (SEM, JEOL JSM-6335F, Japan) operating at 15 kV; transmission electron microscope (TEM, JEOL JEM-2010, Japan) and selected area electron diffractometer (SAED) operating at 200 kV; UV-visible spectrometer (Lambda 25 PerkinElmer, U.S.A.) using a UV lamp with the resolution of 1 nm; and photoluminescence (PL) spectrometer (LS 50B PerkinElmer, U.S.A.) using a 300 nm excitation wavelength at room temperature.

Results and discussion

XRD

XRD patterns (Fig. 1a) of the products synthesized by 800 W microwave refluxing of the starting agents dissolved in different solvents for 60 min. They were indexed and specified as cubic $AgBiS_2$ (JCPDS no. 04-0699) [4] without impurity detection only in the EG. Upon reducing the lengths of microwave refluxing time from 60 min to 40 and 20 min (Fig. 1b), the chemical reaction became incomplete and some Bi_2S_3 (JCPDS no. 06-0333) [4] residue was also detected.

To save the consumption energy, the refluxing power of microwave was gradually reduced step by step from 800 W to 600, 300 and 100 W (Fig. 1c). The product was the still pure $AgBiS_2$ phase but the crystalline degree was lessened.

Electron microscopy

The as-synthesized products with different morphologies were characterized by SEM and TEM. At 100 W (Figs. 2a and 3a), the product was composed of a number of nanoparticles oriented in different directions. They are crystals with facets and angles. Their size distribution (Fig. 3c) is in the 30-100 nm range, with the average of 58.14 $\pm$ 11.87 nm. By increasing the refluxing power of the microwave, the products (Figs. 2b-d and 4a, b) gradually transformed into flower-like clusters at 800 W. SAED patterns of nanoparticles (Fig. 3b) and a petal of the flower-like cluster (Fig. 4c) were both indexed to correspond with polycrystalline and single crystalline $AgBiS_2$ [5], respectively. The interpreted pattern was also in accordance with that obtained by simulation (Fig. 4d).

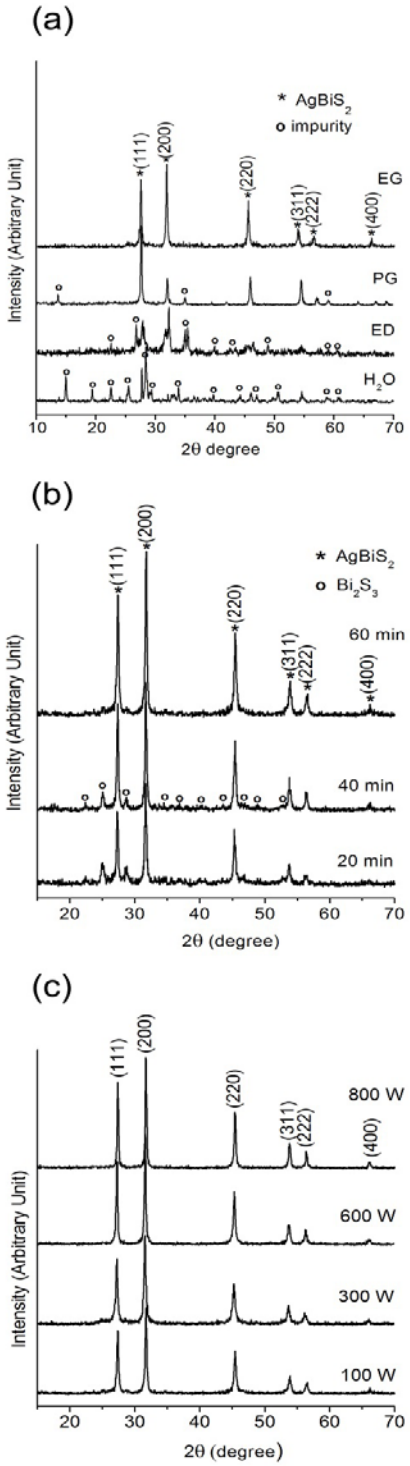


Fig. 1 XRD patterns of $AgBiS_2$ synthesized by a microwave-assisted refluxing method in (a) different solvents at 800 W microwave for 60 min, (b) EG at 800 W microwave for different lengths of time and (c) EG at different heating powers for 60 min.

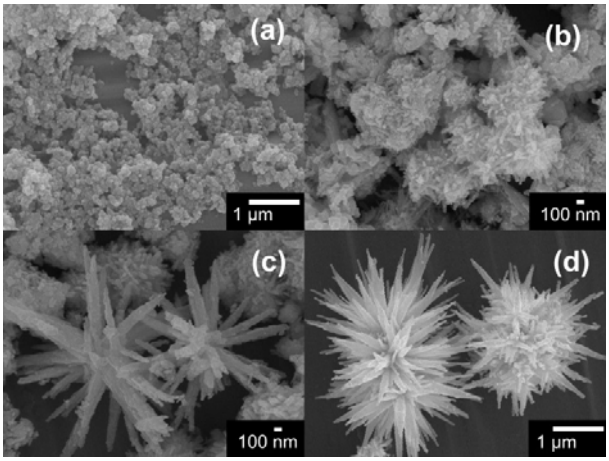


Fig. 2 SEM images of $AgBiS_2$ synthesized by (a-d) 100, 300, 600 and 800 W microwave refluxing method in EG for 60 min, respectively.

Proposed mechanism

To synthesize $AgBiS_2$ by a microwave-assisted refluxing method, CH_3COOAg, $Bi(NO_3)_3 \cdot 5H_2O$ and thiosemicarbazide (TS) were dissolved in ethylene glycol (EG). Ag^+ and Bi^{3+} ions formed complexes with thiosemicarbazide during stirring. At this stage, free ions of Ag^+, Bi^{3+} and S^{2-} were very low. Thus, Ag_2S and Bi_2S_3 formations were prohibited.

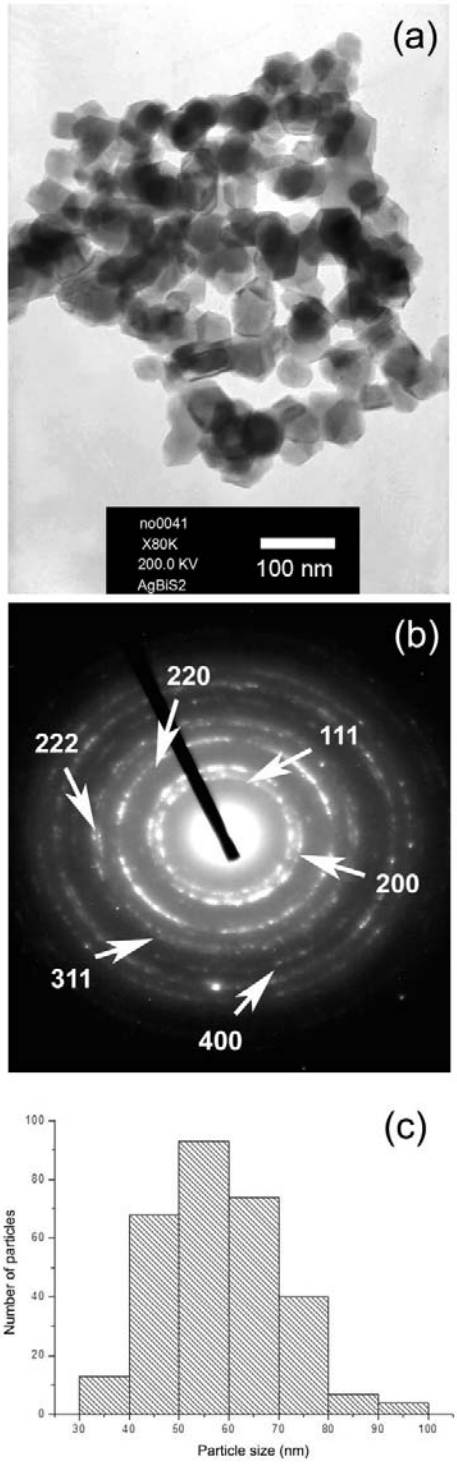


Fig. 3 (a) TEM image, (b) SAED pattern and (c) size distribution of $AgBiS_2$ nanoparticles synthesized by 100 W microwave refluxing method in EG for 60 min.

During the microwave refluxing, the complexes were decomposed to synthesize $(AgBiS_2)_n$ nuclei. The decomposition proceeded with rather slow rates. Their concentration was lower than that obtained by the direct ion-exchange reaction. Finally, $AgBiS_2$ nuclei were synthesized in EG by the microwave-assisted refluxing method.

$$Ag^{+} + Bi^{3+} + TS \longrightarrow \text{Ag-Bi-TS complexes} \quad (1)$$

$$\text{Ag-Bi-TS complexes} \longrightarrow (AgBiS_2)_n \quad (2)$$

$$(AgBiS_2)_n \longrightarrow n(AgBiS_2) \quad (3)$$

Alternately, Ag-TS and Bi-TS complexes could form and were decomposed to synthesize $AgBiS_2$ nuclei.

$$Ag^{+} + TS \longrightarrow \text{Ag-TS complexes} \quad (4)$$

$$Bi^{3+} + TS \longrightarrow \text{Bi-TS complexes} \quad (5)$$

$$\text{Ag-TS complexes} + \text{Bi-TS complexes} \longrightarrow n(AgBiS_2) \quad (6)$$

Due to the 100 W microwave refluxing, $AgBiS_2$ nanoparticles were synthesized by the orientation growth process. At higher refluxing power, the atoms were vibrated violently by a very strong force. Thus the nanoparticles gradually transformed into flower-like clusters at 800 W. In this research, the microwave refluxing played a key role in the decomposition of the complexes, formation of $(AgBiS_2)_n$ nuclei (nucleation), and the oriented growth of $AgBiS_2$ crystals [1,2].

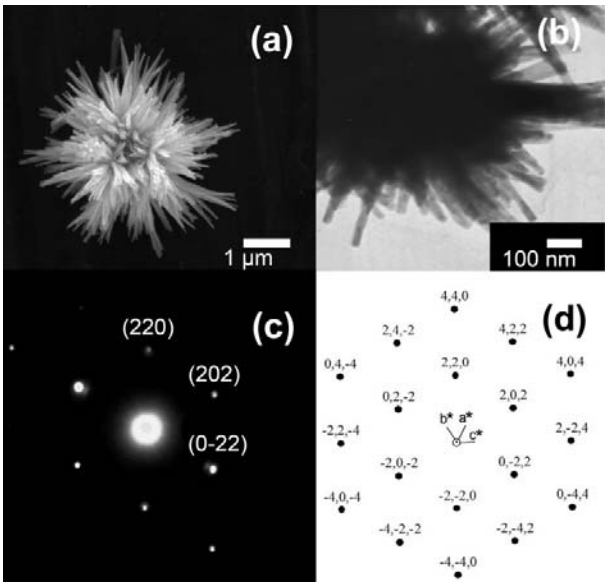


Fig. 4 (a, b) TEM images and (c) SAED pattern of a petal of $AgBiS_2$ flower synthesized by 800 W microwave refluxing method in EG for 60 min, and (d) its simulated pattern.

Absorption and emission

UV-visible absorption (Fig. 5) of the as-synthesized nanoparticles and flower-like clusters indicated an exponential decreasing of optical absorption attenuated through the $AgBiS_2$ solids. Their allowed direct energy gaps were determined, by extrapolating linear portions of the curves to zero absorption, to be 2.91 eV for nanoparticles and 2.82 eV for flower-like clusters – in accordance with 2.88 eV of thin film reported by Ibrahim and Soliman [6].

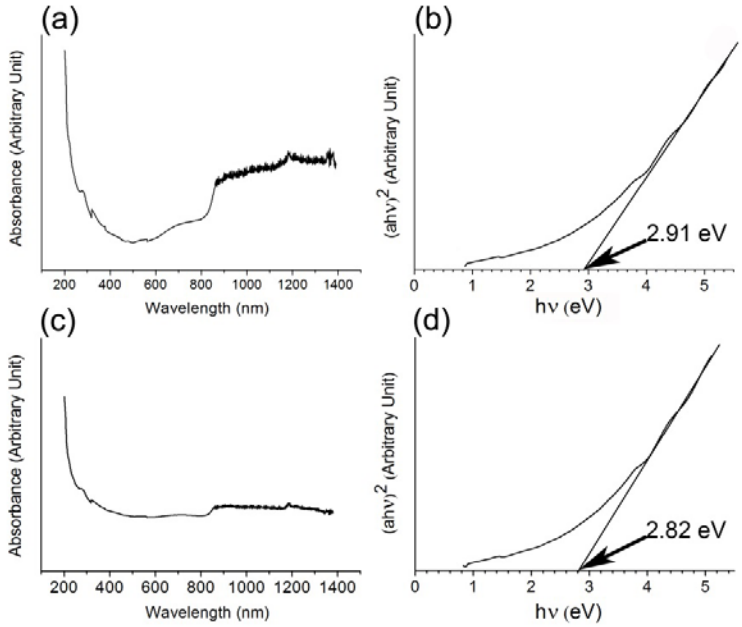


Fig. 5 UV-visible absorption and the $(\alpha h\nu)^2$ and $h\nu$ plots of $AgBiS_2$ (a, b) nanoparticles, and (c, d) flower-like clusters.

PL emissions of different products (Fig. 6) were characterized using 300 nm excitation wavelength at room temperature. Their emission peaks were detected at the same wavelengths of 422.5 nm (2.93 eV) with two shoulders at 444.5 nm and 486.0 nm. The main emission peaks were specified as the recombination of electrons and holes in trapped surface states residing in the forbidden region [7,8]. But for the shoulders, they were caused by the shallow levels of donors and acceptors between the valence and conduction bands [9]. The present result corresponded to the 435 nm (2.85 eV) of $AgBiS_2$ nanostructured flowers and hexapod [10].

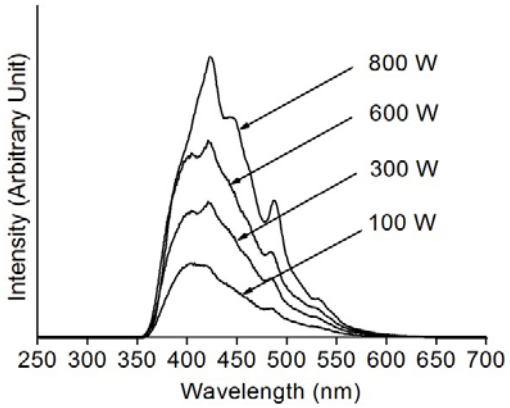


Fig. 6 PL emissions of $AgBiS_2$ synthesized by 100, 300, 600 and 800 W microwave refluxing in EG for 60 min.

Conclusions

Pure cubic $AgBiS_2$ crystals the shape and size of nanoparticles and flower-like clusters were successfully synthesized by 100 W and 800 W microwave refluxing in ethylene glycol for 60 min. The phase was detected by XRD and SAED. SEM and TEM revealed the transformation of the as-synthesized nanoparticles at 100 W into flower-like clusters at 800 W. Their allowed direct energy gaps were determined to be 2.91 eV for nanoparticles and 2.82 eV for flower-like clusters, including their PL emission wavelengths were 422.5 nm.

References

[1] D. Chen, G. Shen, K. Tang, X. Jiang, L. Huang, Y. Jin and Y. Qian, Microwave synthesis of $AgBiS_2$ dendrites in aqueous solution, Inorg. Chem. Commun. 6 (2003) 710–712.

[2] G. Shen, D. Chen, K. Tang and Y. Qian, Novel polyol route to $AgBiS_2$ nanorods, J. Cryst. Growth 252 (2003) 199–201.

[3] http://en.wikipedia.org (14/5/2012).

[4] Powder Diffract File, JCPDS-ICDD, 12 Campus Boulevard, Newtown Square, PA 19073-3273, U.S.A. 2001.

[5] K.W. Andrews, D.J. Dyson and S.R. Keown, Interpret. Electr. Diffract. Patterns, Plenum Press, New York, 1971.

[6] A.M. Ibrahim and L.I. Soliman, Optical properties of $AgBiS_2$ thin films, Fizika A 5 (1996) 177–183.

[7] M.X. Wang, G.H. Yue, X.Y. Fan, P.X. Yan, Properties and characterization of Cu_3SbS_3 nanowires synthesized by solvothermal route, J. Cryst. Growth 310 (2008) 3062–3066.

[8] G.H. Yue, X. Wang, L.S. Wang, W. Wang, D.L. Peng, Synthesis of single crystal $CuAlS_2$ nanowires via a low temperature direct polyol route, Phys. Lett. A 372 (2008) 5995–5998.

[9] G. Harichandran, N.P. Lalla, Facile synthesis of $CuAlS_2$ nanorods, Mater. Lett. 62 (2008) 1267–1269.

[10] T. Thongtem, J. Jaroenchaichana and S. Thongtem, Cyclic microwave-assisted synthesis of flower-like and hexapod silver bismuth sulfide, Mater. Lett. 63 (2009) 2163–2166.

17. Cyclic microwave-assisted synthesis of Cu_3BiS_3 dendrites using L-cysteine as a sulfur source and complexing agent

Abstract

Nanostructured Cu_3BiS_3 dendrites were successfully synthesized from CuCl, $BiCl_3$ and L-cysteine in ethylene glycol (EG), using cyclic microwave radiation (CMR). The phase was detected by X-ray diffraction (XRD) and selected area electron diffraction (SAED), and was in accordance with that obtained by the simulation. Scanning and transmission electron microscopic (SEM and TEM) techniques revealed the gradual transformation of nanoparticles to nanostructured dendrites, due to the increase of microwave power. Photoluminescence of Cu_3BiS_3 dendrites was a blue emission centered at 367 nm.

Keywords: Characterization methods; Luminescence; Nanomaterials; Solar energy materials; X-ray techniques

Introduction

Due to the linear and non-linear properties of I-V-VI ternary compounds, a number of studies have been devoted to the technological applications of these semiconducting materials. They have high potential for use as optoelectronic and thermoelectric devices, including optical recording media [1]. Copper bismuth sulfide (Cu_3BiS_3), with the mineral name wittichenite [2], is one of the promising materials for use as p-type semiconductors [3,4], and as solar absorbers in photovoltaic devices [5]. It can be synthesized by different methods: powders in polyacrylic acid matrix [3]; nanorods via a simple ethanol-thermal route [4]; thin films by reactive sputter deposition on hot substrates [5]; nanocrystallines by a hydrothermal decomposition process [6]; and others.

Microwaving is a process used for the synthesis of nanostructured materials. It can solve the problems of temperature and concentration gradients, and provides uniform growth media. By focusing microwave radiation into solutions, the vibrating electric field applies a force on dissolving species to induce vibrations with different modes. The processing is more rapid and efficient than that achieved by a conventional one, even at a low microwave power [7,8]. To avoid over-boiling, CMR was used instead of continuous.

Our motivation was to synthesize novel Cu_3BiS_3 dendritic crystals using a genetically coded amino acid (L-cysteine) by CMR. No one has ever succeeded in synthesizing Cu_3BiS_3 dendrites by this process.

Experiment

To synthesize nanostructured Cu_3BiS_3 dendrites, 3 mmol CuCl and 1 mmol $BiCl_3$ were dissolved in 30 ml EG to form a solution. Then 3 mmol L-cysteine ($C_3H_7NO_2S$) was added with 30 min continuous stirring. Samples of the solution were irradiated using 300–700 W CMR (30 s on for every 30 s interval) for 40 cycles. Finally, precipitates were synthesized, separated by filtration, washed with de-ionized water and absolute ethanol, and dried at 70 °C for 24 h, for further characterization.

Results and discussion

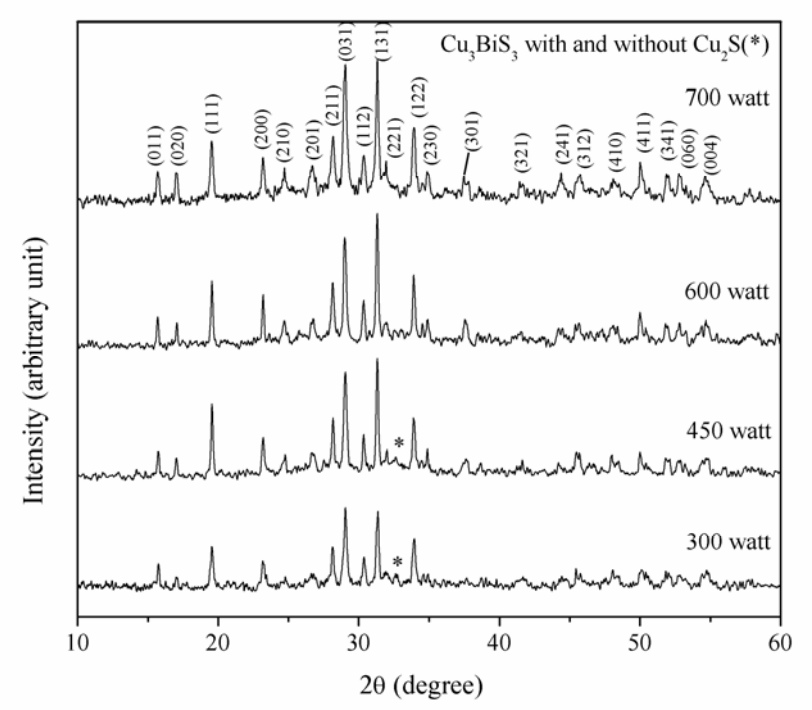


Fig. 1 XRD patterns of Cu_3BiS_3 synthesized at different microwave powers.

Fig. 1 shows XRD patterns of the products synthesized by 300–700 W CMR. At 300 W, the XRD pattern was composed of rather broad peaks, specifying that the product's degree of crystallinity was quite low. Comparing the XRD pattern to the JCPDS database (nos. 43-1479 and 02-1272) [2], this product was proved to be orthorhombic Cu_3BiS_3 mixed with Cu_2S impurity. The strongest intensity peak at 31.3 ^{o} was found to correspond with the (131) crystallographic plane of the Cu_3BiS_3 phase, which was specified as the main product. When the microwave power was increased, the XRD pattern became sharper. At 700 W, the pattern was composed of the sharpest peaks. At this stage, the degree of crystallinity was the highest – implying that the atoms had arranged themselves in the best order. By increasing microwave power, the impurities were lessened as well. Until microwaving at powers of 600 and 700 W, the products were pure single-phase orthorhombic Cu_3BiS_3.

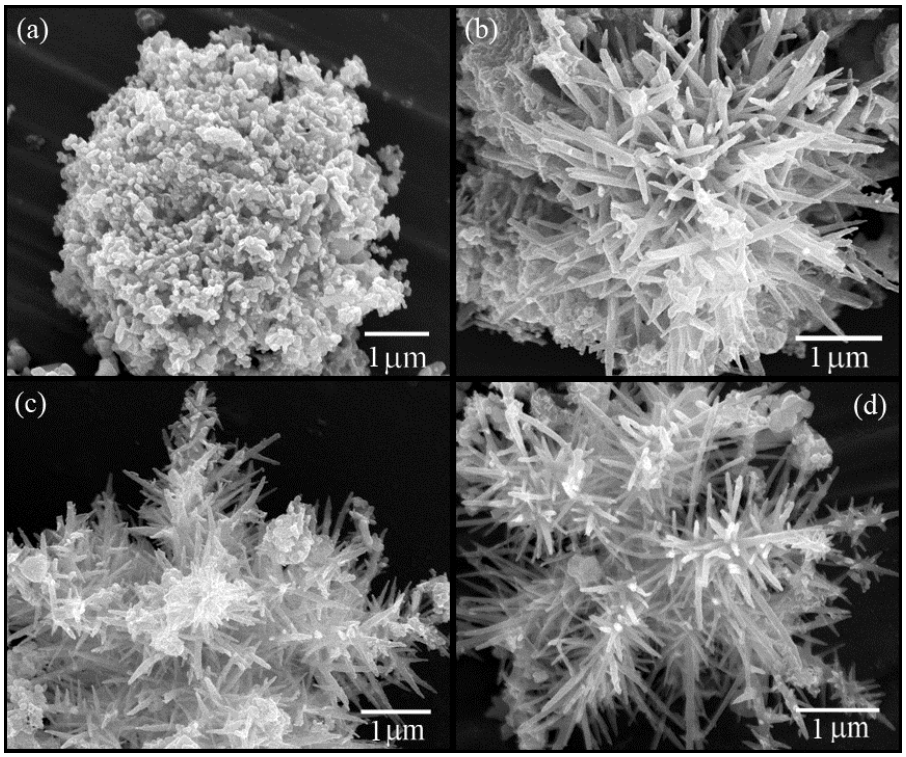


Fig. 2 SEM images of Cu_3BiS_3 synthesized at (a-d) 300, 450, 600, and 700 W, respectively.

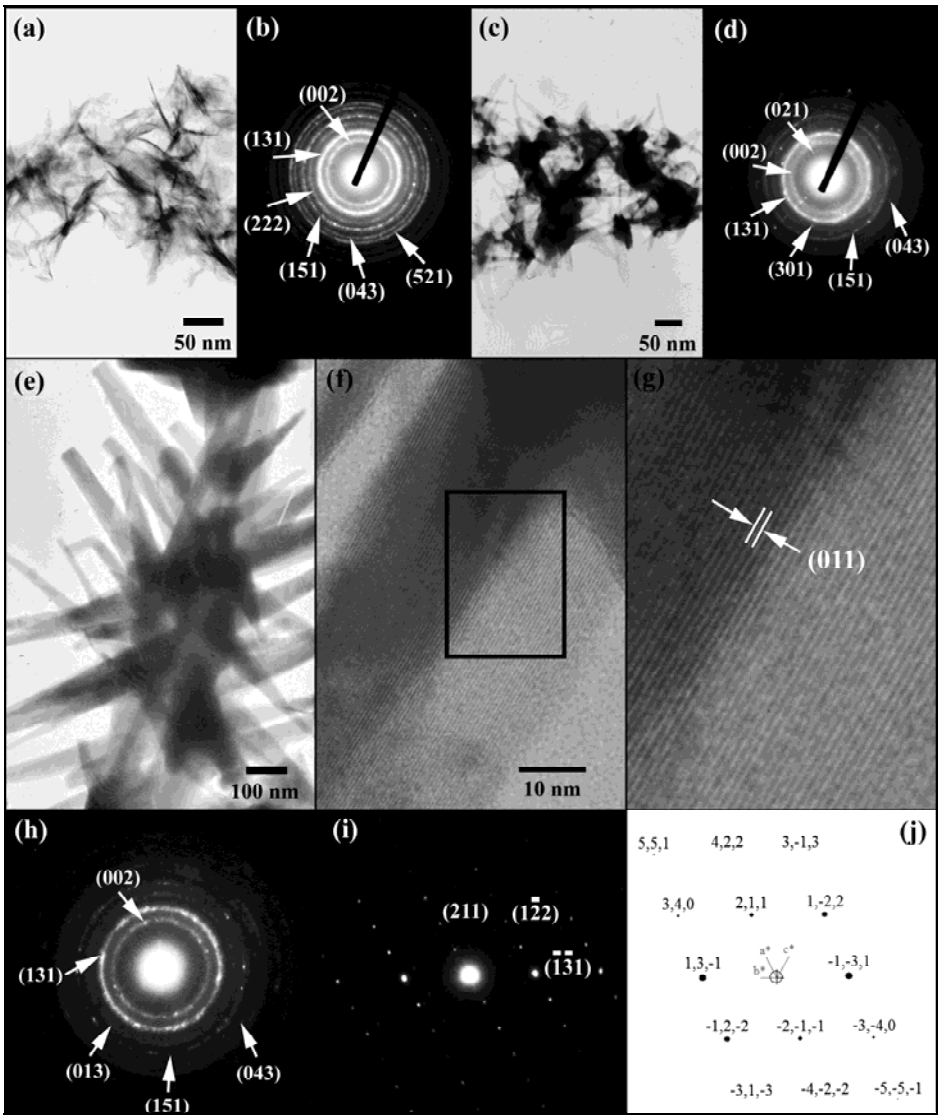


Fig. 3 TEM and HRTEM images, and SAED patterns of Cu_3BiS_3 synthesized at (a, b) 450 W, (c, d) 600 W, and (e-i) 700 W. (j) Simulated pattern of (i).

SEM and TEM images show nanostructured Cu_3BiS_3 synthesized using different microwave powers. At 300 W, the product (Fig. 2a) was composed of a number of nanoparticles with different orientations. By increasing the powers from 300 W to 450 and 600 W (Figs. 2b, 2c, 3a, and 3c), some of the products were gradually transformed into dendrites. At these stages, the products were mixtures of nanoparticles and dendrites. It should be noted that their morphologies appear on SEM images are in

three dimensions, but those on TEM images are in two dimensions. At 700 W (Figs. 2d and 3e), the whole product consisted of dendrites with different orientations. This phenomenon proved that microwave radiation at higher powers has a strong influence on vibrating atoms to form a crystal lattice, and that orthorhombic Cu_3BiS_3 unit cells were able to arrange themselves to fit with both nanoparticles and dendrites. When a dendrite, produced at 700 W, was characterized using HRTEM (Fig. 3f and 3g), a number of the (011) planes 5.6 Å apart were detected – implying that the dendrite was single crystal. SAED patterns of the whole products, synthesized using 450, 600, and 700 W (Fig. 3b, 3d and 3h), appear as concentric rings of bright spots of polycrystals; but that of a dendrite synthesized at 700 W (Fig. 3i) was composed of systematic spots of diffraction electrons from a single crystal. The patterns for both polycrystals and single crystal were interpreted [9], and specified as orthorhombic Cu_3BiS_3 [2], with the electron beam for the interpretation of Fig. 3i in the [4-3-5] direction. No Cu_2S impurity was detected in the SAED pattern of the product synthesized at 450 W, due to the very low Cu_2S concentration in this host. An electron diffraction pattern (Fig. 3j) was also simulated [10], using the [4-3-5] direction as a zone axis. It appears as a systematic array of spots, corresponding to that obtained by the interpretation of Fig. 3i – showing that this electron diffraction pattern of the product could exist in reality.

In this research, CuCl and $BiCl_3$ were dissolved in EG to form a solution. L-cysteine, a genetically coded amino acid, was used as a sulfur source and complexing agent. By adding L-cysteine to the solution, Cu^+ and Bi^{3+} ions coordinated with it to form complexes.

$$Cu^+ + \text{L-cysteine} \xrightarrow{coordination} [\text{Cu(L-cysteine) complexes}]$$

$$Bi^{3+} + \text{L-cysteine} \xrightarrow{coordination} [\text{Bi(L-cysteine) complexes}]$$

Under 700 W CMR, these complexes decomposed, and Cu_3BiS_3 nuclei were synthesized very rapidly. At this stage, the number of free ions was very low. Thus, Cu_2S and Bi_2S_3 formations were inhibited [1,11,12].

$$[\text{Cu(L-cysteine) complexes}] + [\text{Bi(L-cysteine) complexes}] \xrightarrow{decomposition} Cu_3BiS_3(\text{nuclei})$$

Concurrently, [Cu-Bi(L-cysteine) complexes] could possibly form by the reaction

$$Cu^{+} + Bi^{3+} + \text{L-cysteine} \xrightarrow{coordination} \text{[Cu-Bi(L-cysteine) complexes]}$$

These complexes were then decomposed by CMR.

$$\text{[Cu-Bi(L-cysteine) complexes]} \xrightarrow{decomposition} Cu_3BiS_3\text{(nuclei)}$$

These nuclei grew to synthesize Cu_3BiS_3 dendrites. Dendritic growth was promoted by the strong atomic vibrations. Thus these atoms had more chances to arrange themselves in perfect order to form dendritic crystals. In the present research, CMR played a key role in the growth of Cu_3BiS_3 crystals: both in the decomposition of the complexes, and in the nucleation and growth of Cu_3BiS_3. By using CMR, the process is rapid and homogenous, providing a uniform growth environment; thus crystalline dendrites were rapidly synthesized. At 300 W CMR, the nucleation rate of Cu_3BiS_3 was slower; Cu_2S at very low concentration thus had a better chance to nucleate as a second phase contained in this nanoparticle product.

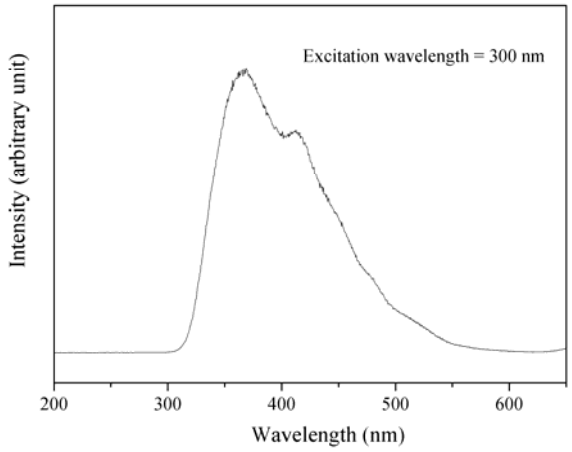


Fig. 4 PL emission of Cu_3BiS_3 dendrites synthesized at 700 W.

Photoluminescence (PL) of Cu_3BiS_3 dendrites was studied at room temperature, using 300 nm excitation wavelength from a xenon laser. The spectrum (Fig. 4) was blue emission centered at 367 nm, with the shoulder at 412 nm (caused by some defects that originated during the synthesis process). These Cu_3BiS_3 dendrites were I-V-VI ternary – promising materials for use in solar energy converters and optical nanodevices.

Conclusions

Nanostructured Cu_3BiS_3 dendrites were successfully synthesized by CMR. The phase was detected using XRD and SAED. SEM and TEM images showed that, with increasing microwave power, nanoparticles were gradually transformed into dendritic single crystals composed of a number of (011) parallel crystallographic planes. PL emission of the Cu_3BiS_3 dendrites was blue emission centered at 367 nm.

References

[1] Jiasong Z, Weidong X, Huaidong J, Wen C, Lijun L, Xinyu Y, Xiaojuan L, Haitao L. Mater Lett 2010;64:1499-502.

[2] Powder Diffract File, JCPDS-ICDD, 12 Campus Boulevard, Newtown Square, PA 19073-3273, U.S.A. 2001.

[3] Hu H, Gomez-Daza O, Nair PK. J Mater Res 1998;13:2453-6.

[4] Chen D, Shen G, Tang K, Liu X, Qian Y, Zhou G. J Cryst Growth 2003;253:512-6.

[5] Gerein NJ, Haber JA. Chem Mater 2006;18:6297-302.

[6] Hu J, Deng B, Wang C, Tang K, Qian Y. Mater Chem Phys 2003;78:650-4.

[7] Wang G, Hao C. Mater Res Bull 2009;44:418-21.

[8] Sczancoski JC, Cavalcante LS, Joya MR, Espinosa JWM, Pizani PS, Varela JA, Longo E. J Colloid Interf Sci 2009;330:227-36.

[9] Andrews KW, Dyson DJ, Keown SR. Interpret Electr Diffract Pattern, 2nd ed, New York, Plenum Press 1971.

[10] Boudias C, Monceau D, CaRIne Crystallography 3.1, DIVERGENT S.A., Centre de Transfert, 60200 Compiègne, France 1989-1998.

[11] Thongtem T, Jaroenchaichana J, Thongtem S. Mater Lett 2009;63:2163-6.

[12] Chen D, Shen G, Tang K, Jiang X, Huang L, Jin Y, Qian Y. Inorg Chem Commun 2003;6:710-12.

18. Characterization of Cu_3SnS_4 nanoparticles and nanostructured flowers synthesized by a microwave-refluxing method

Abstract

Cu_3SnS_4 nanoparticles and nanostructured flowers were synthesized by 100, 300, 600 and 800 W microwave refluxing of the mixture containing 3 mmol $CuCl_2{\cdot}2H_2O$, 1 mmol $SnCl_2{\cdot}2H_2O$ and 4 mmol thiosemicarbazide ($NH_2NHCSNH_2$) in 50 ml ethylene glycol ($HOCH_2CH_2OH$). X-ray diffraction (XRD), selected area electron diffraction (SAED), X-ray photoelectron spectroscopy (XPS), scanning and transmission electron microscopy (SEM and TEM), Raman analysis, and photoluminescence (PL) spectrophotometry revealed the morphology transformation of pure tetragonal Cu_3SnS_4 with nanoparticles at 100 W into 3D-hierarchical flower-like structure at 800 W, including the presence of $2Cu^{+}$, Cu^{2+}, Sn^{4+} and $4S^{2-}$ containing in the sulfide, the PL emission of the 3D-hierarchical flower-like Cu_3SnS_4 at 366 nm, and the prominent Raman peak of Cu-Sn vibration at 319 cm^{-1}. In this research, a formation mechanism was also proposed according to the experimental results.

Keywords: Microwave-refluxing method; X-ray diffraction; Electron microscopy; X-ray photoelectron spectroscopy

Introduction

At present, I-IV-VI ternary semiconducting compounds, such as Cu–Sn–E (E = S; Se), have been very attractive, due to their mid-band-gap semiconductors and non-linear optical properties [1]. For Cu, Sn and S, they can form several sulfides, such as $CuSn_{3.75}S_8$, Cu_2SnS_3, $Cu_2Sn_3S_7$, Cu_3SnS_4, Cu_4SnS_4 and $Cu_4Sn_7S_{16}$ [2–4]. Among them, Cu_3SnS_4 (CTS) is one of a semiconducting material which has the potential to be used in solar cells and as a photocatalyst. Generally, optical band gap of CTS material is influenced by different morphologies and structures, crystalline degree, and different

types and concentration of defects. Lin et al. have estimated optical band gap of the Cu_3SnS_4 (CTS) nanocrystals to be 1.43 eV, the optimal value for solar energy converters [5]. Furthermore, the optical band gap of 3D-hierarchical flower-like Cu_3SnS_4 (CTS) microspheres was evaluated to be 1.38 eV by Chen et al. [6], who stated the potential application in solar energy conversion and photocatalysis. Optical properties of Cu_3SnS_4 sprayed thin film with 500 ^oC annealing were measured and the direct energy gap of the film was determined by Bouaziz et al. to be 1.22 eV [7]. The energy band gap of tetragonal Cu_3SnS_4 with 500 ^oC sulfurization temperature was reported by Guan et al. to be 1.22 eV [8]. Thin film of Cu_3SnS_4 was grown by sulfidation of Sn-Cu metallic precursors in a S_2 atmosphere at 520 ^oC to form orthorhombic CTS thin film with 1.60 eV band gap, reported by Fernandes et al. [9]. CTS thin film was prepared by a spray pyrolysis technique and followed by annealing at 550 ^oC in an atmosphere containing sulfur to form polycrystalline orthorhombic Cu_3SnS_4 thin film which was determined its direct energy gap of 1.8 eV by Chalapathi et al. [10]. The Cu-Sn-S precursor was sulfurized in sulfur containing atmosphere at 500 ^oC to form Cu_3SnS_4 thin film by Su et al., and its optical energy gap was determined to be 1.47 eV [11]. The energy gap of orthorhombic (Pmn21) Cu_3SnS_4 with petrukite structure thin film, deposited by dc magnetron sputtering and followed by sulfurization in N_2 + S_2 vapor atmosphere at 520 ^oC, was determined to be 1.60 eV by Fernandes et al. [12]. Thus Cu_3SnS_4 is a very important semiconductor which attracts great attention of its promising optical, thermal and mechanical properties [1].

Microwave radiations (2.45 GHz) are coherent and polarized [13]. They are able to couple with charged particles, and cause them to be heated up very rapidly. In general, materials are classified into three groups: reflectors (bulk metals and alloys), transmitters (fused-silica and fluoropolymers) and absorbers (inorganic materials, powdered metals, metal oxides and metal halides) [14]. Thus containers should appropriately be chosen. Microwave-assisted synthesis is a very interesting process for synthesizing of different materials. When microwave is applied to substances, at least

one of their components is able to couple with the radiation. Comparing to a conventional method, it can accelerate the reaction rate, and consume lesser reaction time. It is able to solve the problems of temperature and concentration gradients, including to provide uniform growth media. Due to a large amount of microwave energy passing through the solution, the vibrating electric field induces charged particles to vibrate accordingly. This process is very simple, fast, effective and environmentally benign [15, 16]. Microwave refluxing is a distillation process which a microwave radiation involves in the evaporation of liquid, condensation of vapor and the return of condensate to the original system. It has been developed and widely used in industrial and laboratory distillation processes [17].

In this research, Cu_3SnS_4 with nanoparticles and flower-like clusters were synthesized by a microwave-assisted refluxing method. This success may lead to different applications in the near future.

Experiment

To synthesize Cu_3SnS_4, 3 mmol $CuCl_2{\cdot}2H_2O$, 1 mmol $SnCl_2{\cdot}2H_2O$ and 4 mmol thiosemicarbazide (TBZ) were dissolved in 50 ml of ethylene glycol (EG). Each 50 ml solution was refluxed by 100, 300, 600 and 800 W microwave for 15, 30 and 60 min. Finally, black precipitates were synthesized, separated by filtration, washed with deionized water and ethanol, and dried at 70 ^{o}C for 12 h. The products were characterized by an X-ray diffractometer (XRD, SIEMENS D500) operating at 20 kV 15 mA and using Cu-K_α line in combination with the database of the Joint Committee on Powder Diffraction Standards (JCPDS) [18]; a scanning electron microscope (SEM, JEOL JSM-6335F) operating at 15 kV; a transmission electron microscope (TEM, JEOL JEM-2010) and selected area electron diffraction (SAED) technique operating at 200 kV; X-ray photoelectron spectrometer (XPS, Axis Ultra^{DLD}, Kratos analytical) operating at 15 kV 10 mA in a chamber with $5x10^{-9}$ torr; and a photoluminescence (PL) spectrometer (LS 50B PerkinElmer) using 300 nm excitation wavelength at room temperature.

Results and discussion

XRD

XRD patterns (Fig. 1a) of the products synthesized by 800 W microwave refluxing of the starting agents dissolved in ethylene glycol. They were indexed and specified as tetragonal Cu_3SnS_4 (JCPDS no. 33-0501) [18] without impurity detection. Its mineral name is known as kuramite [5, 18]. Upon reducing the lengths of microwave refluxing time from 60 min to 30 and 15 min, the XRD peaks for the production in EG were broadened, and the crystalline degree of these pure products was lowered. To save the energy consumption, the refluxing power of microwave was gradually reduced step by step from 800 W to 600, 300 and 100 W at a constant length of refluxing time for 60 min (Fig. 1b). The products were still pure Cu_3SnS_4 phase, but the crystalline degree was lessened.

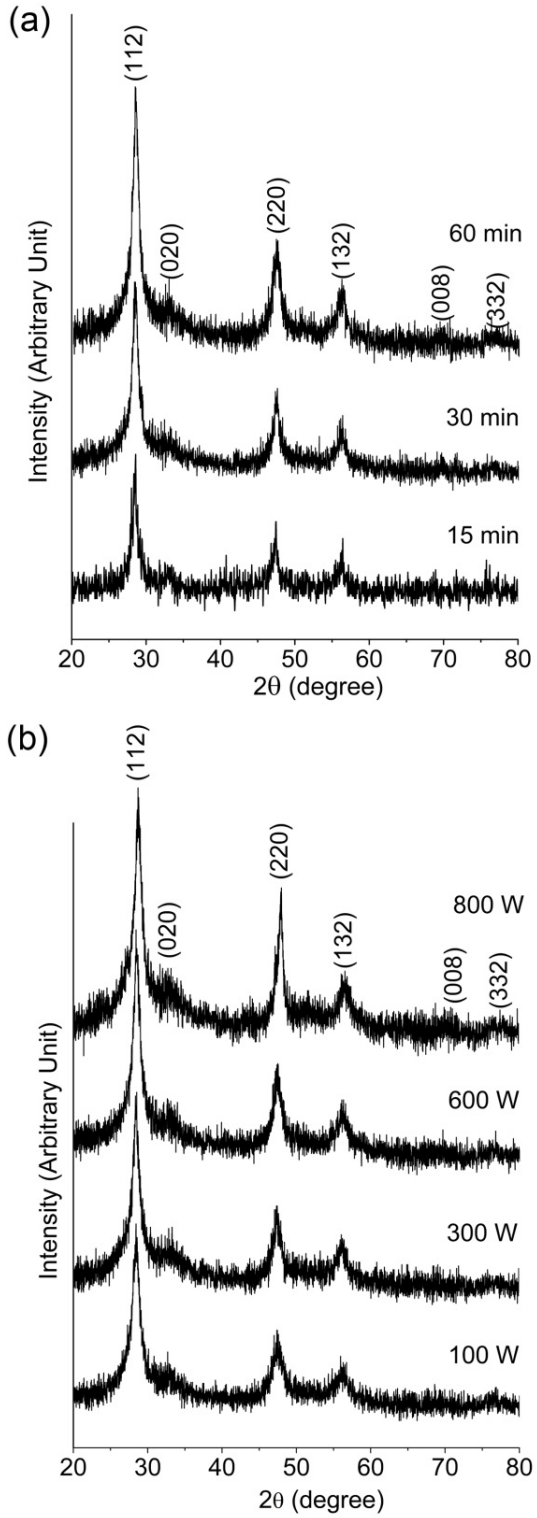


Fig. 1 XRD patterns of Cu_3SnS_4 synthesized by a microwave-assisted refluxing method in ethylene glycol at (a) 800 W microwave for 15, 30 and 60 min, and (b) 100, 300, 600 and 800 W for 60 min.

Electron microscopy

The SEM and TEM images of Cu_3SnS_4 synthesized by a 800 W microwave refluxing method for 15, 30 and 60 min are shown in Fig. 2a–e. For 15 min and 800 W microwave refluxing, the product was incomplete nanostructured flowers. They became complete flowers until the length of time was as long as 60 min. By fixing the length of time to be 60 min at different microwave powers (Fig. 3), the as-synthesized products with different morphologies were synthesized. At 100 W, the product was composed of a number of nanoparticles clustered together in group. By increasing the refluxing power of the microwave from 100 W to 300, 600 and 800 W, the nanoparticles gradually transformed into incomplete flowers at 300 and 600 W, and into complete flower-like structure at 800 W. In this research, both powers of microwave and lengths of time have the influence to determine the product morphologies, including their crystalline degrees. A SAED pattern (Fig. 2f) of nanostructured flowers was diffuse and hollow, and was identified to correspond with polynanocrystals of tetagonal Cu_3SnS_4 (JCPDS no. 33-0501) [18].

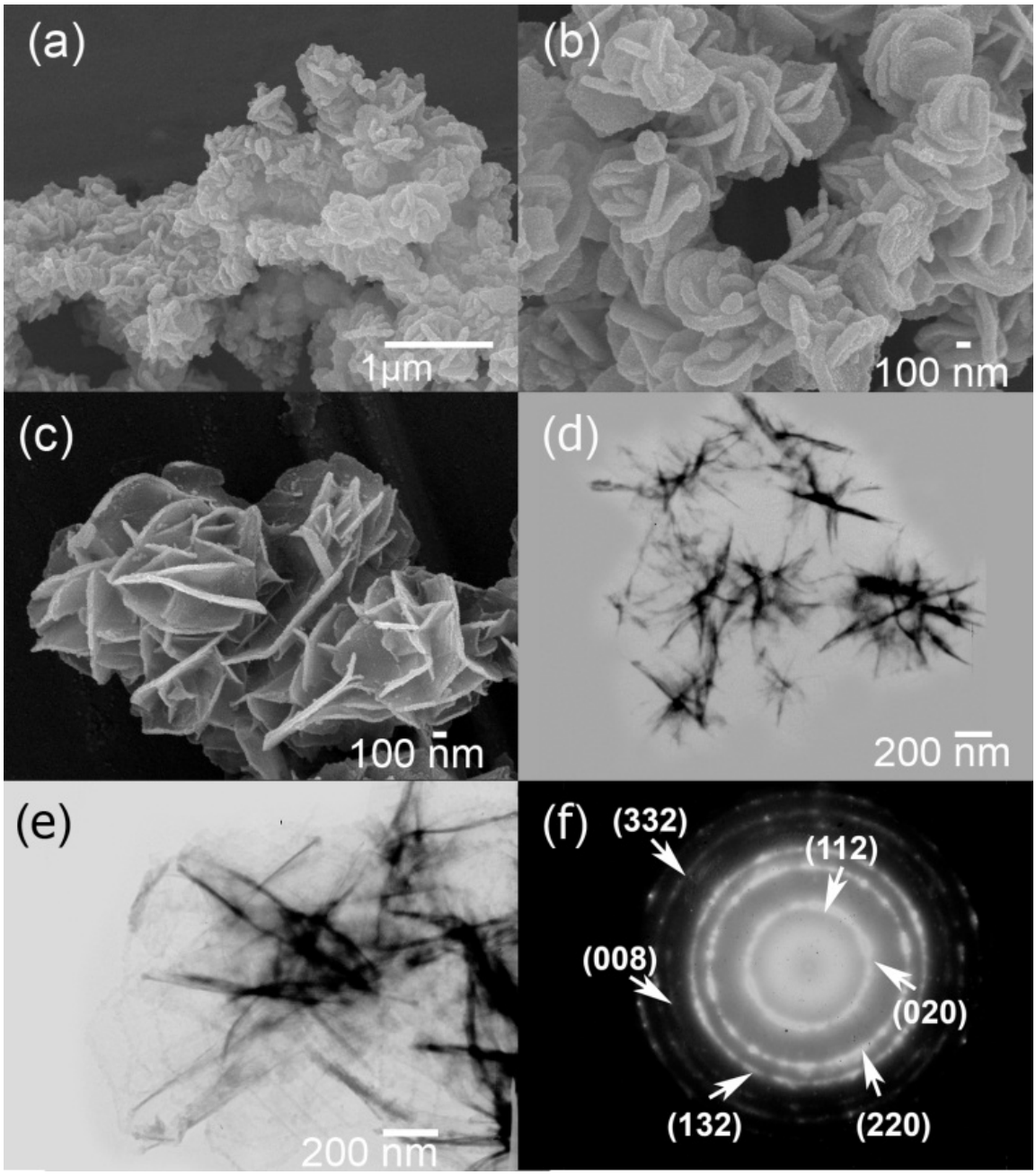


Fig. 2 (a–c) SEM images of Cu_3SnS_4 synthesized at 800 W microwave refluxing method in ethylene glycol for 15, 30 and 60 min, respectively. (d, e) TEM images and (f) SAED pattern of Cu_3SnS_4 flowers synthesized by a 800 W microwave refluxing method for 60 min.

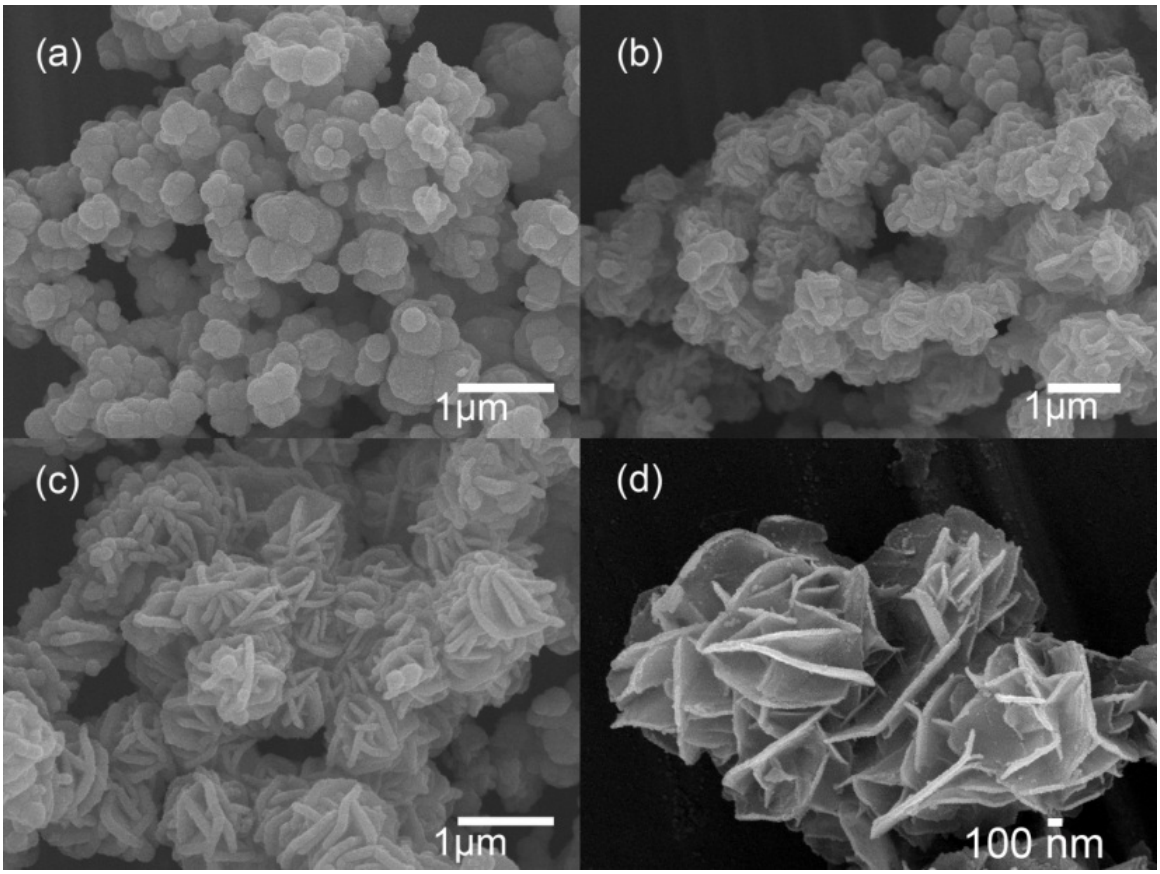


Fig. 3 SEM images of Cu_3SnS_4 synthesized by (a–d) 100, 300, 600 and 800 W microwave refluxing method in ethylene glycol for 60 min, respectively.

XPS

The XPS spectra of Cu_3SnS_4 nanostructured flowers (Fig. 4) revealed the presence of copper, tin and sulfur peaks. The Cu (2p) core level spectrum indicates the observed binding energy (BE) for Cu ($2p_{3/2}$) (932.4 eV) and ($2p_{1/2}$) (952.4 eV), corresponding to the reported value for Cu^{+}. The Cu ($2p_{3/2}$) satellite peak at 942.8 eV identified as Cu^{2+} was also detected. Obviously, there were both Cu^{2+} and Cu^{+} ions in the as-synthesized Cu_3SnS_4 product. The photoelectron spectrum of Sn (3d) core levels at 486.6 eV of Sn ($3d_{5/2}$) and 495.1 eV of Sn ($3d_{3/2}$) belongs to Sn^{4+}. No evidence of Sn^{2+} (binding energy at 485.2 eV) was detected in the spectrum. The S (2p) core-level

spectrum indicates the binding energy at 161.7 eV [1, 5, 19–25]. Furthermore, additional peak was detected at 169.0 eV and was likely to be from the oxidized parts of the product during the synthesis. The present analysis reveals that the Cu_3SnS_4 flowers were composed of $2Cu^{+}$, Cu^{2+}, Sn^{4+} and $4S^{2-}$. The presence of both Cu(I) and Cu(II) in the complex charge balance Cu_3SnS_4 was also detected by Benedetto et al. [26, 27]. The kuramite CTS phase is a p-type semiconductor [5], which exhibits a marked paramagnetism originated by the presence of Cu(II) [27]. Its stoichiometric formula is written as $Cu(I)_2Cu(II)SnS_4$ with a random distribution of Cu(I), Cu(II) and Sn(IV) ions in the available tetrahedral sites [27]. In the present research, other minor peaks of C1s (284.9 eV) and O1s (531.4 eV) were also detected [1, 20–22]. They belonged to the coated carbon to improve electrical conductivity for XPS analysis and the absorbed gaseous molecules in the characterized product. Based on the Cu (2p), Sn (3d) and S (2p) core level peaks of Cu_3SnS_4, the atomic ratio of Cu:Sn:S was determined to be 3.04:1.00:3.82 – very close to the stoichiometric ratio of the sulfide, and in accordance with the report of Yi et al. [28].

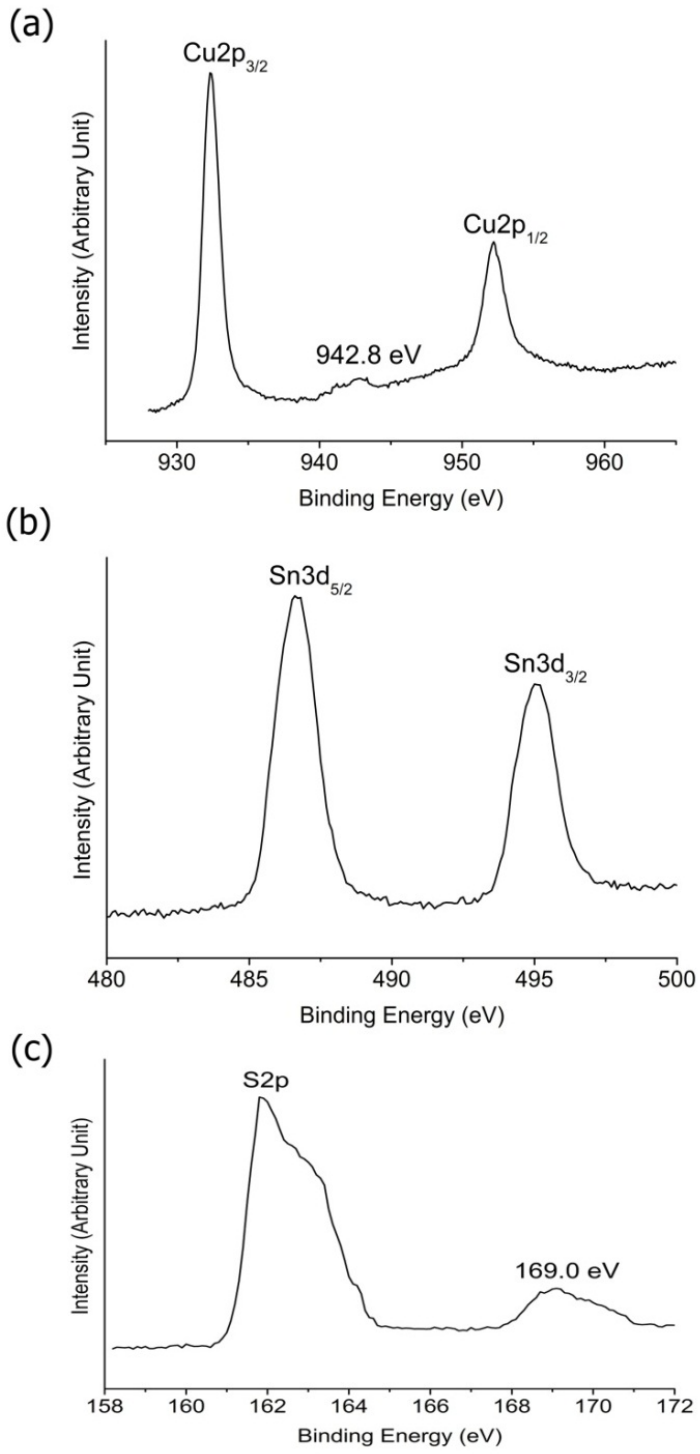


Fig. 4 (a–c) Cu2p, Sn3d and S2p core levels of nanostructured flower-like Cu_3SnS_4 synthesized by 800 W microwave refluxing for 60 min.

Raman analysis

Fig. 5 shows the Raman peaks of flower-like Cu_3SnS_4 synthesized by 800 W microwave refluxing for 60 min at 296, 319 and 449 cm^{-1}. The 319 cm^{-1} prominent Raman peak can be specified as Cu-Sn vibration analogy to other sulfide complexes [4, 8, 9].

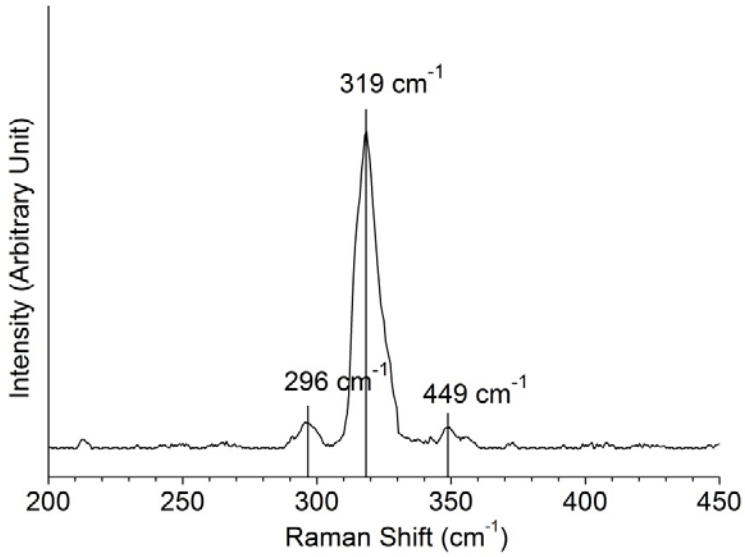


Fig. 5 Raman spectrum of Cu_3SnS_4 synthesized by 800 W microwave refluxing for 60 min.

Proposed mechanism

To synthesize Cu_3SnS_4 by a microwave-assisted refluxing method, $CuCl_2{\cdot}2H_2O$, $SnCl_2{\cdot}2H_2O$ and thiosemicarbazide with 3:1:4 molar ratio Cu:Sn:S were dissolved in ethylene glycol ($HOCH_2CH_2OH$). It is well known that thiosemicarbazide ($NH_2NHCSNH_2$) is usually considered as a bidentate ligand of which sulfur and nitrogen atoms are in favorable positions to form five-membered rings and able to form complexes with transition metals [29]. In the present research, copper (II) coordinated thiosemicarbazide (TBZ). Cu^{2+} ions were reduced to Cu^{+} ions by thiosemicarbazide and the Cu^{+} ions further coordinated thiosemicarbazide to form stable Cu^{I}–TBZ complexes [1]. Cu^{2+} ions

were reduced to Cu^{+} ions by ethylene glycol as well [30–33]. According to the difference in the standard Gibbs free energy (ΔG^{o}): ΔG^{o} (Cu^{2+}/Cu^{+}) = -14.76 kJ; ΔG^{o} (Sn^{4+}/Sn^{2+}) = -28.95 kJ, Sn^{2+} ions could be slowly oxidized to Sn^{4+} by Cu^{2+} ions under a certain condition [34]. During stirring, Cu^{+}, Cu^{2+} and Sn^{4+} ions formed complexes with thiosemicarbazide. At this stage, free ions of Cu^{+}, Cu^{2+}, Sn^{4+} and S^{2-} were very low, and the formation of CuS, Cu_2S, SnS and SnS_2 was prohibited.

$$Cu^{2+}(aq) + e^{-} \longrightarrow Cu^{+}(aq), \quad \Delta G^{o}(Cu^{2+}/Cu^{+}) = -14.76\ kJ \qquad (1)$$

$$Sn^{4+}(aq) + 2e^{-} \longrightarrow Sn^{2+}(aq), \quad \Delta G^{o}(Sn^{4+}/Sn^{2+}) = -28.95\ kJ \qquad (2)$$

$$2Cu^{2+}(aq) + Sn^{2+}(aq) \longrightarrow 2Cu^{+}(aq) + Sn^{4+}(aq), \quad \Delta G^{o}(\text{reaction}) = -570\ J \qquad (3)$$

$$Cu^{I}(aq) + TBZ \longrightarrow Cu^{I}\text{-TBZ complex} \qquad (4)$$

$$Cu^{II}(aq) + TBZ \longrightarrow Cu^{II}\text{-TBZ complex} \qquad (5)$$

$$Sn^{IV}(aq) + TBZ \longrightarrow Sn^{IV}\text{-TBZ complex} \qquad (6)$$

During microwave refluxing, the complexes were decomposed several steps to form Cu_3SnS_4. The decomposition proceeded with rather slow rate. The concentrations of the decomposed species were lower than that obtained by the direct ion-exchange reaction. Finally, Cu_3SnS_4 nuclei were synthesized in EG by the microwave-assisted refluxing method.

$$Cu^{I}\text{-TBZ complex} + Cu^{II}\text{-TBZ complex} + Sn^{IV}\text{-TBZ complex} \longrightarrow (Cu_3SnS_4)_n \text{ ----------} \longrightarrow n Cu_3SnS_4 \qquad (7)$$

The nuclei grew to form nanoparticles which clustered together in groups at 100 W microwave power. Further, each of nanoparticles transformed into complete flowers at 800 W microwave power within 60 min.

PL emission

PL emission (Fig. 6) of Cu_3SnS_4 synthesized by 800 W microwave refluxing method in EG for 60 min was determined using 300 nm excitation wavelength at room temperature. The emission peak of the 3D-hierarchical flower-like Cu_3SnS_4 was detected at 366 nm wavelength (3.39 eV), due to the interband electron-hole recombination process. It should be noted that the transition between bands could involve electronic levels in the vicinity to the bottom of the lowest empty band and at the top of the highest occupied band [23]. The emission was very close to the reports of Hu et al. who excited the Cu_3SnS_4 nanoshell tubes using 234 nm Xe light source and determined the PL emission of the Cu_3SnS_4 nanoshell tubes to be 345 nm [1], and of Xiong et al. who excited Cu_3SnS_4 nanorods using 264 nm and determined the PL emission of the Cu_3SnS_4 nanorods to be 319 nm of blue light [23]. These results show that PL emissions of Cu_3SnS_4 were influenced by different morphologies of the products and excitation wavelengths.

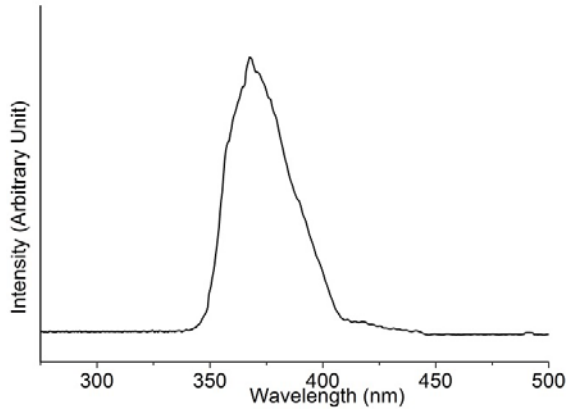


Fig. 6 PL emission of Cu_3SnS_4 synthesized by 800 W microwave refluxing for 60 min.

Conclusions

Pure tetragonal Cu_3SnS_4 with nanoparticles and 3D-hierarchical flower-like structure were successfully synthesized by microwave refluxing of $CuCl_2{\cdot}2H_2O$, $SnCl_2{\cdot}2H_2O$ and thiosemicarbazide in ethylene glycol. In this research, the Cu_3SnS_4

products were composed of $2Cu^{+}$ (BE = 932.4 and 952.4 eV), Cu^{2+} (BE = 942.8 eV), Sn^{4+} (BE = 486.6 and 495.1 eV) and $4S^{2-}$ (BE = 161.7 eV), including the PL emission at 366 nm for the 3D-hierarchical flower-like Cu_3SnS_4, and the prominent Raman peak of Cu-Sn vibration at 319 cm^{-1}.

References

[1] H. Hu, Z. Liu, B. Yang, X. Chen, Y. Qian, J. Cryst. Growth 284 (2005) 226–234.

[2] M. Bouaziz , J. Ouerfelli, S.K. Srivastava, J.C. Bernède, M. Amlouk, Vacuum 85 (2011) 783–786.

[3] M. Bouaziz, M. Amlouk, S. Belgacem, Thin Solid Films 517 (2009) 2527–2530.

[4] A.-J. Cheng, M. Manno, A. Khare, C. Leighton, S.A. Campbell, E.S. Aydil, J. Vac. Sci. Technol. A 29 (2011) 051203 (11 pp.).

[5] X. Lin, A. Steigert, M.Ch. Lux-Steiner, A. Ennaoui, RSC Adv. 2 (2012) 9798–9800.

[6] F. Chen, J. Zai, M. Xu, X. Qian, J. Mater. Chem. A 1 (2013) 4316–4323.

[7] M. Bouaziz, J. Ouerfelli, M. Amlouk, S. Belgacem, Phys. Stat. Sol. (a) 204 (2007) 3354–3360.

[8] H. Guan, H. Shen, C. Gao, X. He, J. Mater. Sci.: Mater. Electron. 24 (2013) 1490–1494.

[9] P.A. Fernandes, P.M.P. Salomé, A.F. da Cunha, J. Phys. D: Appl. Phys. 43 (2010) 215403 (11 pp.).

[10] U. Chalapathi, Y.B. Kishore Kumar, S. Uthanna, V. Sundara Raja, Solid State Phys.: AIP Conf. Proc. 1447 (2012) 649–650.

[11] Z. Su, K. Sun, Z. Han, F. Liu, Y. Lai, J. Li, Y. Liu, J. Mater. Chem. 22 (2012) 16346–16352.

[12] P.A. Fernandes, P.M.P. Salomé, A.F. da Cunha, Phys. Stat. Sol. C 7 (2010) 901–904.

[13] S. Bhunia, D.N. Bose, J. Cryst. Growth 186 (1998) 535–542.

[14] J.W. Lekse, A. M. Pischera, J.A. Aitken, Mater. Res. Bull. 42 (2007) 395–403.

[15] C. Gabriel, S. Gabriel, E.H. Grant, B.S.J. Halstead, D.M.P. Mingos, Chem. Soc. Rev. 27 (1998) 213–223.

[16] K.J. Rao, B. Vaidhyanathan, M. Ganguli, P.A. Ramakrishnan, Chem. Mater. 11 (1999) 882–895.

[17] N. Tipcompor, S. Thongtem, T. Thongtem, Ceram. Interl. 39 (2013) S383–S387.

[18] Powder Diffract. File, JCPDS-ICDD, 12 Campus Boulevard, Newtown Square, PA 19073-3273, U.S.A. 2001.

[19] J.Q. Hu, B. Deng, K.B. Tang, C.R. Wang, Y.T. Qian, J. Mater. Res. 16 (2001) 3411–3415.

[20] M.X. Wang, L.S. Wang, G.H. Yue, X. Wang, P.X. Yan, D.L. Peng, Mater. Chem. Phys. 115 (2009) 147–150.

[21] Y.H.A. Wang, N. Bao, A. Gupta, Solid State Sci. 12 (2010) 387–390.

[22] T. Kuzuya, K. Itoh, M. Ichidate, T. Wakamatsu, Y. Fukunaka, K. Sumiyama, Electrochim. Acta 53 (2007) 213–217.

[23] Y. Xiong, Y. Xie, G. Du, H. Su, Inorg. Chem. 41 (2002) 2953–2959.

[24] M. Bouaziz, K. Boubaker, M. Amlouk, S. Belgacem, J. Phase Equil. Diffus. 31 (2010) 498–503.

[25] X. Chen, X. Wang, C. An, J. Liu, Y. Qian, J. Cryst. Growth 256 (2003) 368–376.

[26] F. Di Benedetto, F. d'Acapito, I Bencistà, A. De Luca, G. Fornaciai, S. Frizzera, M. Innocenti, G. Montegrossi, L.A. Pardi, M. Romanelli, Phys. Stat. Sol. C 1-3 (2013) Doi 10.1002/pssc.201200753.

[27] F. Di Benedetto, D. Borrini, A. Caneschi, G. Fornaciai, M. Innocenti, A. Lavacchi, C.A. Massa, G. Montegrossi, W. Oberhauser, L.A. Pardi, M. Romanelli, Phys. Chem. Miner. 38 (2011)483–490.

[28] L. Yi, D. Wang, M. Gao, CrystEngComm 14 (2012) 401–404.

[29] T.V. Koksharova, S.V. Kurando, I.V. Stoyanova, Russ. J. Gen. Chem. 82 (2012) 1481–1484.

[30] A. Anzlovar, Z.C. Orel, M. Zigon, J. Nanosci. Nanotechnol. 8 (2008) 3516–3525.

[31] R.S. Ningthoujam, N.S. Gajbhiye, S. Sharma, Pramana-J. Phys. 72 (2009) 577–586.

[32] G. Carotenuto, G.P. Pepe, L. Nicolais, Eur. Phys. J. B 16 (2000) 11–17.

[33] Z.C. Orel, E. MatijeviĆ, D.V. Goia, J. Mater. Res. 18 (2003) 1017–1022.

[34] D.R. Gaskell, Introduction to Metallurgical Thermodynamics, McGraw-Hill Book Company, New York, 1981.

Output ที่ได้จากโครงการวิจัย

ตัวชี้วัด	ผลลัพธ์ที่ได้จริง
(1) จำนวนบทความวิจัยในฐาน ISI, Sciencedirect และ อื่น ๆ	33
(2) จำนวนนักศึกษาระดับปริญญาโท (คน)	7
(3) จำนวนนักศึกษาระดับปริญญาเอก (คน)	4
(4) จำนวนนักวิจัยระดับหลังปริญญาเอก (คน)	2
(5) ต้นแบบผลิตภัณฑ์	2
(6) รางวัลจากงานวิจัย	>15
(7) การแลกเปลี่ยนนักศึกษา-อาจารย์	6
(8) การเชิญผู้เชี่ยวชาญต่างประเทศ	1

List of publications

(1) Patcharanan Junploy, Somchai Thongtem, Titipun Thongtem, Anukorn Phuruangrat, Photocatalytic activity of Zn_2SnO_4-SnO_2 nanocomposites produced by sonochemistry in combination with high temperature calcination, Superlattices and Microstructures 74 (2014) 173–183.

(2) Yanee Keereeta, Titipun Thongtem, Somchai Thongtem, Effect of medium solvent ratios on morphologies and optical properties of α-$ZnMoO_4$, β-$ZnMoO_4$ and $ZnMoO_4 \cdot 0.8H_2O$ crystals synthesized by microwave-hydrothermal / solvothermal method, Superlattices and Microstructures 69 (2014) 253–264.

(3) Patcharanan Junploy, Titipun Thongtem, Somchai Thongtem, Anukorn Phuruangrat, Decolorization of Methylene Blue by Ag/$SrSnO_3$ Composites under Ultraviolet Radiation, Journal of Nanomaterials 2014 (2014) Article ID: 261395 (9 pp).

(4) Jarupat Sungpanich, Titipun Thongtem, Somchai Thongtem, Photocatalysis of WO_3 Nanoplates Synthesized by Conventional–Hydrothermal and Microwave–Hydrothermal Methods and of Commercial WO_3 Nanorods, Journal of Nanomaterials 2014 (2014) Article ID: 739251 (8 pp).

(5) Narongrit Tipcompor, Somchai Thongtem, Titipun Thongtem, Characterization of Cu_3SnS_4 nanoparticles and nanostructured flowers synthesized by a microwave-refluxing method, Japanese Journal of Applied Physics 52 (2013) 111201 (4 pp).

(6) Narongrit Tipcompor, Somchai Thongtem, Titipun Thongtem, Characterization of cubic $AgSbS_2$ nanostructured flowers synthesized by microwave-assisted refluxing method, Journal of Nanomaterials 2013 (2013) Article ID: 970489 (6 pp).

(7) Kamonwan Aup-Ngoen, Titipun Thongtem, Somchai Thongtem, Anukorn Phuruangrat, Cyclic microwave-assisted synthesis of $CuFeS_2$ nanoparticles using biomolecules as sources of sulfur and complexing agent, Materials Letters 101 (2013) 9–12.

(8) Nuengruethai Ekthammathat, Titipun Thongtem, Anukorn Phuruangrat, Somchai Thongtem, Photoluminescence of hexagonal ZnO nanorods hydrothermally grown on

Zn foils in KOH solutions with different values of basicity, Journal of Nanomaterials 2013 (2013) Art. ID 208230 (4 pp).

(9) Oranuch Yayapao, Somchai Thongtem, Anukorn Phuruangrat, Titipun Thongtem, Sonochemical synthesis, photocatalysis and photonic properties of 3 % Ce-doped ZnO nanoneedles, Ceramics International 39 (2013) S563–S568.

(10) Narongrit Tipcompor, Somchai Thongtem, Titipun Thongtem, Transformation of cubic $AgBiS_2$ from nanoparticles to nanostructured flowers by a microwave-refluxing method, Ceramics International 39 (2013) S383–S387.

(11) Patcharanan Junploy, Somchai Thongtem, Titipun Thongtem, Photoabsorption and photocatalysis of $SrSnO_3$ produced by a cyclic microwave radiation, Superlattices and Microstructures 57 (2013) 1–10.

(12) Nuengruethai Ekthammathat, Titipun Thongtem, Anukorn Phuruangrat, Somchai Thongtem, Characterization of ZnO flowers of hexagonal prisms with planar and hexagonal pyramid tips grown on Zn substrates by a hydrothermal process, Superlattices and Microstructures 53 (2013) 195–203.

(13) Yanee Keereeta, Titipun Thongtem, Somchai Thongtem, Effects of solution pH and processing cycle on nanostructured $La_2(MoO_4)_3$ produced by cyclic microwave radiation, Current Applied Physics 12 (2012) S139–S143.

(14) Narongrit Tipcompor, Titipun Thongtem, Anukorn Phuruangrat, Somchai Thongtem, Characterization of $SrCO_3$ and $BaCO_3$ nanoparticles synthesized by cyclic microwave radiation, Materials Letters 87 (2012) 153–156.

(15) Anukorn Phuruangrat, Titipun Thongtem, Somchai Thongtem, Characterization and photonic absorption of hierarchical tree-like CdS nanostructure synthesized by solvothermal method, Materials Letters 80 (2012) 114–116.

(16) Anukorn Phuruangrat, Somchai Thongtem, Titipun Thongtem, Template-free synthesis of neodymium hydroxide nanorods by microwave-assisted hydrothermal process, and of neodymium oxide nanorods by thermal decomposition, Ceramics International 38 (2012) 4075–4079.

(17) Arrak Klinbumrung, Titipun Thongtem, Somchai Thongtem, Characterization of orthorhombic α-MoO_3 microplates produced by a microwave plasma process, Journal of Nanomaterials 2012 (2012) Article ID 930763 (5 pp).

(18) Anukorn Phuruangrat, Titipun Thongtem, Somchai Thongtem, Solvothermal synthesis of CdS nanorods using poly(vinyl butyral-co-vinyl alcohol-co-vinyl acetate) as a capping agent in ethylenediamine solvent, Powder Technology 221 (2012) 383–386.

(19) Anukorn Phuruangrat, Jun Song Chen, Xiong Wen Lou, Oranuch Yayapao, Somchai Thongtem, Titipun Thongtem, Hydrothermal synthesis and electrochemical properties of α-MoO_3 nanobelts used as cathode materials for Li-ion batteries, Applied Physics A 107 (2012) 249–254.

(20) Surangkana Wannapop, Titipun Thongtem, Somchai Thongtem, Photoemission and energy gap of $MgWO_4$ particles connecting as nanofibers synthesized by electrospinning-calcination combinations, Applied Surface Science 258 (2012) 4971–4976.

(21) Hathai Sinaim, Dong Jin Ham, Jae Sung Lee, Anukorn Phuruangrat, Somchai Thongtem, Titipun Thongtem, Free-polymer controlling morphology of α-MoO_3 nanobelts by a facile hydrothermal synthesis, their electrochemistry for hydrogen evolution reactions and optical properties, Journal of Alloys and Compounds 516 (2012) 172–178.

(22) Anukorn Phuruangrat, Somchai Thongtem, Titipun Thongtem, Controlling morphologies of Bi_2S_3 nanostructures synthesized by glycolthermal method, Materials Letters 72 (2012) 104–106.

(23) Nuengruethai Ekthammathat, Titipun Thongtem, Anukorn Phuruangrat, Somchai Thongtem, Microwave-assisted synthesis and characterization of uniform $LaPO_4$ nanorods, Journal of Experimental Nanoscience 7 (2012) 616–623.

(24) Yanee Keereeta, Titipun Thongtem, Somchai Thongtem, Characterization of $ZnMoO_4$ nanofibers synthesized by electrospinning-calcination combinations, Materials Letters 68 (2012) 265–268.

(25) Yanee Keereeta, Titipun Thongtem, Somchai Thongtem, Fabrication of $ZnWO_4$ nanofibers by a high direct voltage electrospinning process, Journal of Alloys and Compounds 509 (2011) 6689–6695.

(26) Wonchai Promnopas, Titipun Thongtem, Somchai Thongtem, Characterization of nanostructured CdTe synthesized by solid state microwave-plasma process, Chalcogenide Letters 8 (2011) 1–7.

(27) Kamonwan Aup-Ngoen, Somchai Thongtem, Titipun Thongtem, Cyclic microwave-assisted synthesis of Cu_3BiS_3 dendrites using L-cysteine as a sulfur source and complexing agent, Materials Letters 65 (2011) 442–445.

(28) Oranuch Yayapao, Titipun Thongtem, Anukorn Phuruangrat, Somchai Thongtem, CTAB-assisted hydrothermal synthesis of tungsten oxide microflowers, Journal of Alloys and Compounds 509 (2011) 2294–2299.

(29) Anukorn Phuruangrat, Nuengruethai Ekthammathat, Titipun Thongtem, Somchai Thongtem, Microwave-assisted synthesis and optical property of $CdMoO_4$ nanoparticles, Journal of Physics and Chemistry of Solids 72 (2011) 176–180.

(30) Anukorn Phuruangrat, Titipun Thongtem, Somchai Thongtem, Preparation and characterization of nano-crystalline $LiNi_{0.5}Co_{0.5}VO_4$ by tartate precursor combustion method, International Journal of Nano Dimension 1 (2010) 111–118.

(31) Anukorn Phuruangrat, Titipun Thongtem, Somchai Thongtem, Synthesis of nanocrystalline metal molybdates using cyclic microwave radiation, Materials Science - Poland 28 (2010) 557–563.

(32) Titipun Thongtem, Chalermchai Pilapong, Jutarat Kavinchan, Anukorn Phuruangrat, Somchai Thongtem, Microwave-assisted hydrothermal synthesis of Bi_2S_3 nanorods in flower-shaped bundles, Journal of Alloys and Compounds 500 (2010) 195–199.

(33) Anukorn Phuruangrat, Titipun Thongtem, Somchai Thongtem, Analysis of lead molybdate and lead tungstate synthesized by a sonochemical method, Current Applied Physics 10 (2010) 342–345.

ต้นแบบผลิตภัณฑ์ที่สร้างขึ้น



อุปกรณ์สังเคราะห์วัสดุโดยให้อิเล็กตรอนไหลผ่านของแข็งโดยตรง

โดย

สมชาย ทองเต็ม, ธิติพันธุ์ ทองเต็ม และ ชเนษฎ์ วิชาศิลป์



อุปกรณ์ชักใยด้วยไฟฟ้า

โดย

สมชาย ทองเต็ม, ธิติพันธุ์ ทองเต็ม, สุรางคนา วรรณภพ, จารุภัทร ซึงพานิช และ ญาณี คีรีต๊ะ

รายละเอียดผลงานวิจัยที่เผยแพร่ในวารสารวิชาการต่าง ๆ

Superlattices and Microstructures 74 (2014) 173–183

Contents lists available at ScienceDirect

Superlattices and Microstructures

journal homepage: www.elsevier.com/locate/superlattices

Photocatalytic activity of Zn_2SnO_4–SnO_2 nanocomposites produced by sonochemistry in combination with high temperature calcination

Patcharanan Junploy [a], Somchai Thongtem [b,c,*], Titipun Thongtem [a,c,*], Anukorn Phuruangrat [d]

[a] Department of Chemistry, Faculty of Science, Chiang Mai University, Chiang Mai 50200, Thailand
[b] Department of Physics and Materials Science, Faculty of Science, Chiang Mai University, Chiang Mai 50200, Thailand
[c] Materials Science Research Center, Faculty of Science, Chiang Mai University, Chiang Mai 50200, Thailand
[d] Department of Materials Science and Technology, Faculty of Science, Prince of Songkla University, Hat Yai, Songkhla 90112, Thailand

ARTICLE INFO

Article history:
Received 9 March 2014
Received in revised form 11 June 2014
Accepted 20 June 2014
Available online 2 July 2014

Keywords:
Sonochemistry–calcination combination
ZTO(NC)–SnO_2
ZTO(NP)–SnO_2
Photocatalysis

ABSTRACT

Zn_2SnO_4 nanocubes–SnO_2 (ZTO(NC)–SnO_2) and Zn_2SnO_4 nanoparticles–SnO_2 (ZTO(NP)–SnO_2) were successfully produced by a combination of sonochemical route in mixture solvents of different contents of ethylene glycol – de-ionized water and high temperature calcination. The phase and morphology were characterized by X-ray powder diffraction (XRD), field emission scanning electron microscopy (FE-SEM), transmission electron microscopy (TEM) and energy-dispersive X-ray spectroscopy (EDS). ZTO(NP)–SnO_2 nanocomposites exhibit higher photocatalytic activity than ZTO(NC)–SnO_2 through the degradation of methylene blue (MB) dye under UV light.

© 2014 Elsevier Ltd. All rights reserved.

1. Introduction

Photocatalysis using metal oxide as catalysts has been widely studied for promoting degradation of organic pollutants. The present process, photon with energies corresponding to or exceeding the

* Corresponding authors at: Department of Physics and Materials Science, Faculty of Science, Chiang Mai University, Chiang Mai 50200, Thailand. Tel.: +66 (0)53 941924; fax: +66 (0)53 943445 (S. Thongtem). Department of Chemistry, Faculty of Science, Chiang Mai University, Chiang Mai 50200, Thailand. Tel.: +66 (0)53 943344; fax: +66 (0)53 892277 (T. Thongtem).
E-mail addresses: schthongtem@yahoo.com (S. Thongtem), ttpthongtem@yahoo.com (T. Thongtem).

http://dx.doi.org/10.1016/j.spmi.2014.06.015
0749-6036/© 2014 Elsevier Ltd. All rights reserved.

energy band gap of the semiconducting catalyst can excite electrons from the valence band (VB) to the conduction band (CB), producing high-energy electron–hole pairs. They can react with water and dissolving oxygen to produce ·OH free radicals with high chemical activity and with the dye molecules adsorbed on the surface of metal oxide photocatalyst. Thus the dye molecules will be photodegradated by the oxidation–reduction reaction [1–5]. However, high recombination rate between photo-generated electrons and holes is a major factor to reduce the photocatalytic efficiency. Coupling of different semiconducting oxides such as CuO–ZnO [6], TiO_2–SnO_2 [7], Fe_2O_3–SnO_2 [8], $NaBiO_3$–Bi_2O_3 [9] and TiO_2–Fe_2O_3 [10] has been widely studied and proved to be good photocatalysts by promoting the high quantum yield of electron–hole pair separation. Moreover parameters such as small particle size, high surface area, controlled porosity and tailor-designed pore size distribution are important factors for enhancement of the photocatalytic efficiency [3,11,12].

Zn_2SnO_4 (ZTO) is one type of mixed oxide which has possibility in the photocatalytic application due to its high electron diffusivity, high electrical conductivity and favorable stability in acidic and basic solutions [2,13–17]. For SnO_2, it is widely studied for photocatalysis and its band gap is in accordance with ZTO. The CB edge potential of ZTO is more negative than that of SnO_2 thus electrons easily transfers to the CB of the SnO_2, leading to the effective electron–hole pair separation [17,18]. Therefore, ZTO and SnO_2 are the interesting coupling semiconductors for photocatalysis of this work.

In this report, the ZTO(NC)–SnO_2 and ZTO(NP)–SnO_2 composites can be produced by the simple and commercially feasible method of the sonochemical route and calcination combination. Their photocatalytic activity evaluated through the degradation efficiency of MB was found to be improved.

2. Experimental procedure

To synthesize the ZTO–SnO_2 nanocomposites, each 0.010 mol of tin(II) chloride dihydrate ($SnCl_2 \cdot 2H_2O$) and zinc nitrate hexahydrate ($Zn(NO_3)_2 \cdot 6H_2O$) was dissolved in different solvents of ethylene glycol (EG) – de-ionized water mixture: 0% w/w EG (100% w/w de-ionized water), 40% w/w EG, 75% w/w EG and 100% w/w EG, and continuously stirred for 20 min at room temperature. The pH of the solutions was adjusted to 4, 7 and 10 using 3 M NaOH. Then the solutions were irradiated by 35 kHz ultrasonic radiation for 15 min. White precipitates were produced, separated by filtration, washed for several times by de-ionized water and absolute ethanol, and dried in air at 70 °C for 24 h. Each precursor powder produced in 100% w/w de-ionized water and 100% w/w ethylene glycol solvents was divided into four parts. One was used as a reference, and each of the three remains were further calcined at 400 °C, 600 °C and 900 °C in an ambient atmosphere for 1 h to form white powder.

The products were characterized by an X-ray diffractometer (XRD, Philips X' Pert MPD) operating at 20 kV, 15 mA with Cu Kα radiation (1.5405 Å) at a scanning rate of 0.02°/s in the 2θ range of 10–80°; a scanning electron microscope (SEM, JEOL JSM-6335F) operating at 15 kV; a transmission electron microscope (TEM, JEOL JEM-2010) operating at 200 kV; and a UV–visible spectrometer (Lambda 25 PerkinElmer) using a UV lamp with the resolution of 2.0 nm.

The photocatalytic activity of the ZTO(NC)–SnO_2 and ZTO(NP)–SnO_2 products were investigated through the degradation of methylene blue (MB) dye aqueous solutions. Each 100 mg product was suspended in 100 ml 6.0×10^{-6} M MB solution, which was stirred for 1 h in the dark condition to establish an adsorption–desorption equilibrium of MB dye on the ZTO–SnO_2 surfaces. Photocatalysis was initiated by two 15 W UV lamps for different lengths of time. Absorbance peaks at 663 nm wavelength, determined by UV–visible spectrometer, were assumed to be linearly dependent on the concentration of MB before and after photocatalysis. Decolorization efficiency (%) was calculated by $\frac{I_o - I}{I_o} \times 100$, where I_o and I were the absorbance intensities of the solutions before and after photocatalysis, respectively.

3. Results and discussion

3.1. Phase and morphology

Fig. 1a shows diffraction patterns of the products which were produced in 100% w/w water as a solvent with the pH of 4, 7 and 10. In this research, the pH is an important parameter for the formation

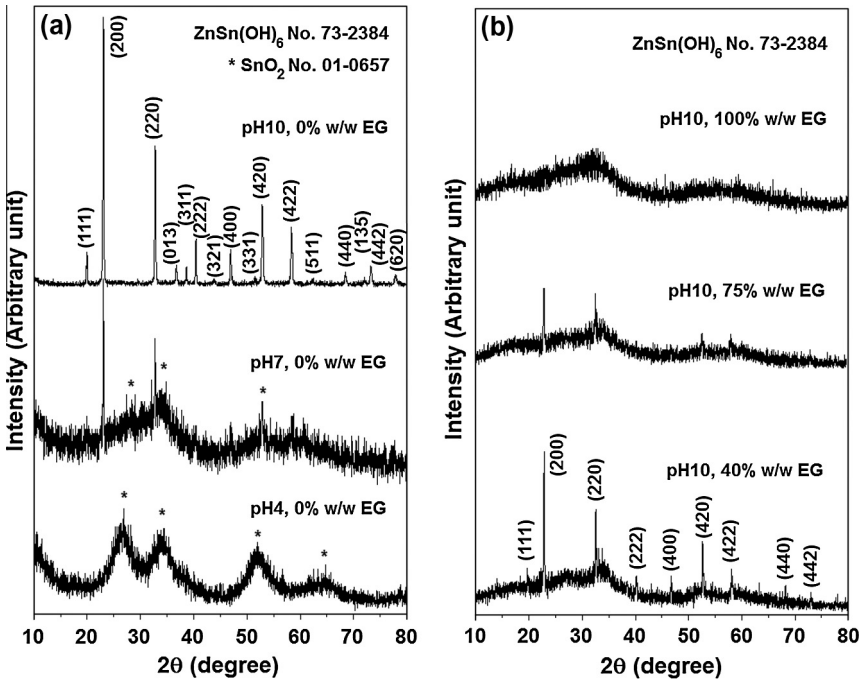


Fig. 1. XRD patterns of the products produced in (a) 100% w/w water at the pH of 4, 7 and 10, (b) EG–water mixture solvent containing 40%, 75% and 100% w/w EG at the pH of 10.

of $ZnSn(OH)_6$ phase and its crystalline degree. Amorphous SnO_2 with tetragonal crystal structure (JCPDS No. 01-0657) [19] was produced in the solution with the pH 4. In the solution with the higher pH of 7, $ZnSn(OH)_6$ mixed with SnO_2 phase began to be detected. Eventually, the product was pure $ZnSn(OH)_6$ with high crystalline degree under the highest alkaline condition at the pH 10. The diffraction peaks of the product are in good accordance with those of the standard $ZnSn(OH)_6$ phase (JCPDS No. 73-2384) [19]. Therefore, the higher alkaline condition can form pure $ZnSn(OH)_6$ powder with effectively.

Fig. 1b shows diffraction patterns of the products which were produced at different w/w contents of ethylene glycol in water. The peak intensity of $ZnSn(OH)_6$ was gradually decreased with the increasing in ethylene glycol and completely formed amorphous $ZnSn(OH)_6$ at 100% w/w ethylene glycol. There were no diffraction lines assigned to any crystalline phase, indicating that amorphous $ZnSn(OH)_6$ was produced. The growth of $ZnSn(OH)_6$ concerned the thermal stability of the starting materials, controlled by the interaction with the solvent. The starting materials in the solvent having high-dielectric constant can undergo decomposition and form the precursor nuclei at lower temperature than those in the solvent having low-dielectric constant [20]. In this case, ethylene glycol has low-dielectric constant than water. Thus the starting reagents in ethylene glycol can slowly undergo decomposition and form $ZnSn(OH)_6$ nuclei less complete than the reagents in water solvent, producing the $ZnSn(OH)_6$ amorphous phase in 100% w/w EG.

The crystalline phases of the calcination products in water and ethylene glycol as solvents are illustrated in Fig. 2. In water solvent, the product before calcination was $SrSn(OH)_6$ phase with high crystalline degree (Fig. 1a) transformed into high amorphous degree of Zn_2SnO_4–SnO_2 composites after calcination at 400 °C and 600 °C, and became completely ZTO–SnO_2 crystal at 900 °C, according to Zn_2SnO_4 (JCPDS No. 24-1470) and SnO_2 (JCPDS No. 01-0657) [19]. By using ethylene glycol as a solvent, the product before calcination was amorphous $ZnSn(OH)_6$ (Fig. 1b). Its crystalline degree was increased with the increasing in the calcination temperature and became completely crystalline ZTO–SnO_2 composites at 900 °C calcination.

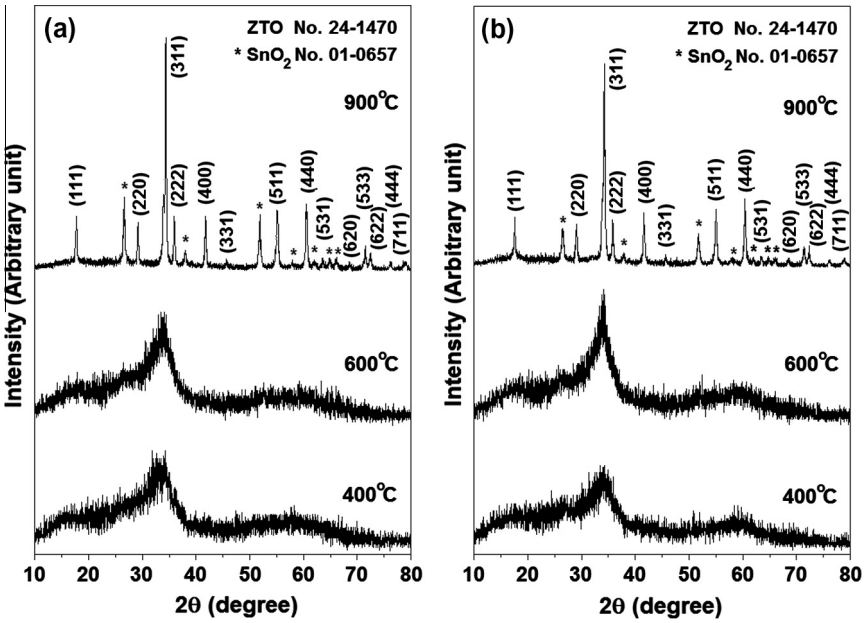


Fig. 2. XRD patterns of the products produced in (a) 100% w/w water and (b) 100% w/w ethylene glycol with the pH of 10 and followed by calcination at 400, 600 and 900 °C for 1 h.

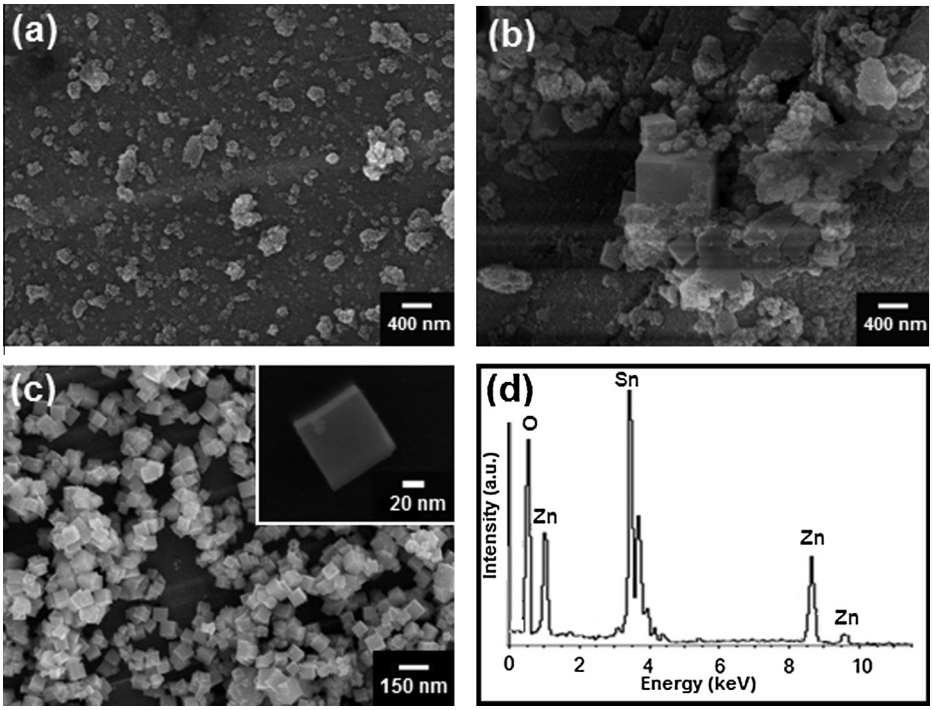


Fig. 3. (a–c) SEM images of the products produced in 100% w/w water as a solvent at the pH of 4, 7 and 10, respectively. (d) EDS spectrum of the product produced in 100% w/w water as a solvent at the pH of 10.

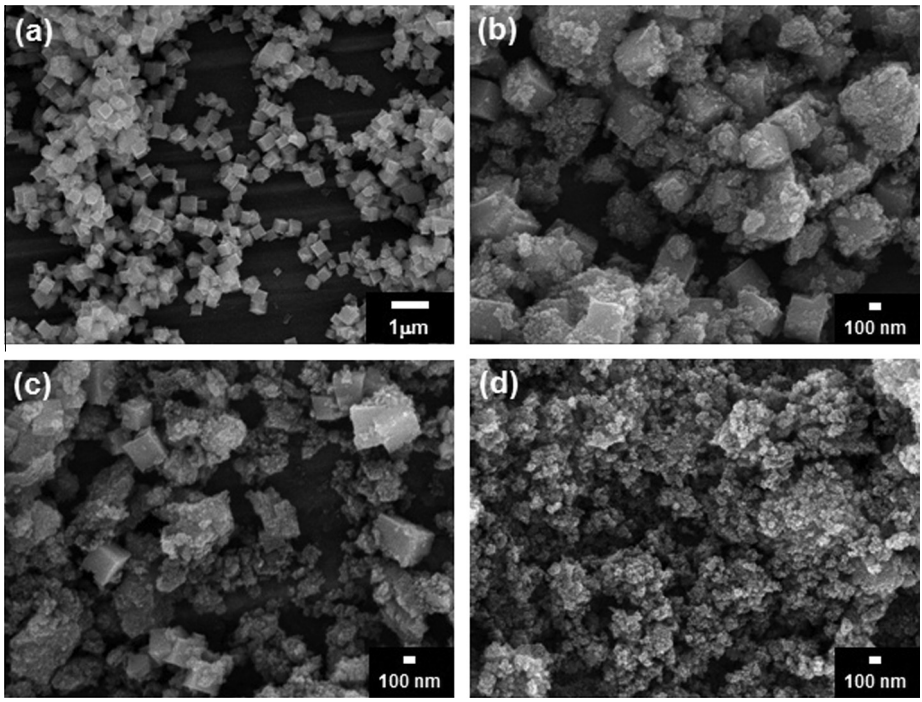


Fig. 4. (a–d) SEM images of ZTO–SnO_2 composites produced in EG–water mixture solvent containing 0%, 40%, 75% and 100% w/w EG at the pH of 10 and followed by calcination at 900 °C for 1 h.

Fig. 3 shows SEM images and EDS spectrum of the precursors produced under different pH conditions. At the pH of 4 and 7, a number of particles were produced. Upon increasing the pH to 10, homogeneous cubes (average length of 80 nm) of $ZnSn(OH)_6$ were completely produced. The atomic composition of $ZnSn(OH)_6$ was analyzed by EDS, corresponding to the prominent peaks of Zn, Sn and O elements of the Zn-L_α, Zn-K_α, Zn-K_β, Sn-L_α and O-K_α lines without any impurity detection. Fig. 4 shows SEM images of the post-calcined products produced in different mixture solvents at the pH 10. SEM images of the ZTO–SnO_2 composites present the increasing in the number of ZTO nanoparticles instead of the ZTO nanocubes when the amount of ethylene glycol in water was increased. The really fine ZTO(NP)–SnO_2 was produced in the 100% w/w ethylene glycol as a solvent. Ethylene glycol molecules with negative charge of two hydroxyl groups at both ends adsorbed on the positively charged surface of the particles. They could retard the preferential growth and finally lead to the formation of ZTO(NP)–SnO_2 instead of ZTO(NC)–SnO_2 [20].

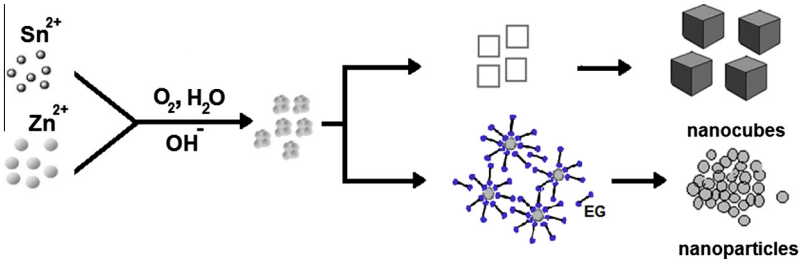


Fig. 5. Schematic illustration for the formation of $ZnSn(OH)_6$ precursors.

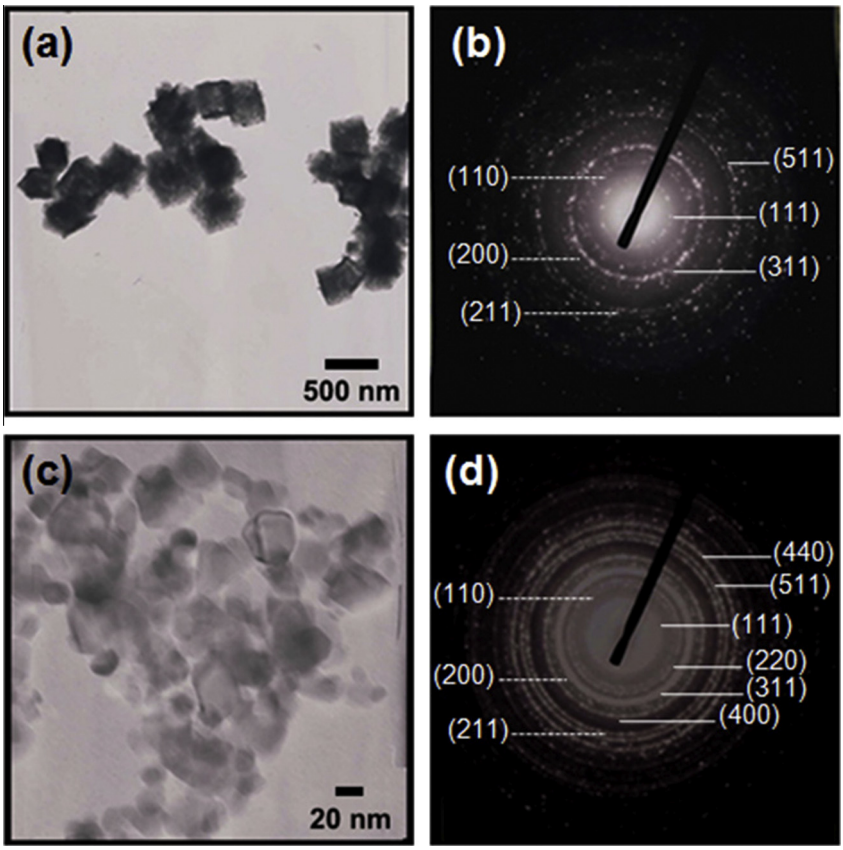


Fig. 6. TEM images and SAED patterns of ZTO–SnO_2 composites produced in (a and b) 100% w/w water and (c and d) 100% w/w ethylene glycol at the pH of 10 and followed by calcination at 900 °C for 1 h. Solid and dotted lines are for Zn_2SnO_4 (ZTO) and SnO_2 phases, respectively.

The $ZnSn(OH)_6$ precursors were produced from metal salts ($SnCl_2{\cdot}2H_2O$ and $Zn(NO_3)_2 \cdot 6H_2O$) and alkali (NaOH) as starting reagents. Sn^{2+} ions were oxidized by dissolving O_2 to form Sn^{4+} ions. Subsequently, Sn^{4+} and Zn^{2+} reacted with OH^- in alkaline solution to form $ZnSn(OH)_6$. The $ZnSn(OH)_6$ precursors are thermodynamically unstable. The post-calcination of the metastable $ZnSn(OH)_6$ led to the recrystallization process by transforming $ZnSn(OH)_6$ into ZTO–SnO_2 composites with stable structure. Meanwhile, $ZnSn(OH)_6$ precursors still retained their original morphology in the ZTO–SnO_2 composites. The formation of ZTO–SnO_2 composites from $SnCl_2 \cdot 2H_2O$ and $Zn(NO_3)_2 \cdot 6H_2O$ as starting materials can be explained by the following.

$$Zn^{2+} + Sn^{2+} + 4OH^- + H_2O + 0.5O_2(g) \rightarrow ZnSn(OH)_6(s) \quad (1)$$

$$2ZnSn(OH)_6(s) \rightarrow Zn_2SnO_4(s) - SnO_2\,\text{composites} + 6H_2O(g) \quad (2)$$

A possible growth mechanism of different morphologies of $ZnSn(OH)_6$ crystal in the solutions containing water and ethylene glycol is schematically illustrated in Fig. 5. First, Sn^{2+} ions were oxidized by dissolving O_2 to form Sn^{4+} ions. Then, Zn^{2+} and Sn^{4+} ions in the aqueous solution easily form $ZnSn(OH)_6$ precipitates by forming bonds with OH^- in alkaline aqueous solution. These $ZnSn(OH)_6$ precipitates grew to form larger particles. Self-aggregated particles were able to cluster together to

form aggregates as well. With the prolonging reaction time, $ZnSn(OH)_6$ precursors exhibit a well-defined cubic structure with the crystallite size of 85 nm under ultrasonic radiation and finally transformed into the ZTO(NC)–SnO_2 composites by the 900 °C calcination.

The TEM image of ZTO–SnO_2 nanocomposites produced in water solvent (Fig. 6a) reveals the SnO_2 nanoparticles distributed on surface of the ZTO perfect nanocubes. In ethylene glycol as a solvent, the product (Fig. 6c) is the nanoparticles of ZTO–SnO_2. The selected area electron diffraction (SAED) patterns of ZTO–SnO_2 powder (Fig. 6b and d) confirm the polycrystalline structure. The diffraction rings can be indexed to cubic ZTO and tetragonal SnO_2 in accordance with the XRD analysis.

3.2. Photocatalysis

The ZTO(NP)–SnO_2 composites produced in 100% w/w ethylene glycol (EG) solvent was used for photocatalytic testing (Fig. 7). At the beginning, the color of MB dye solution was blue. When the photocatalyst was applied in the dark condition for 60 min, the concentration of MB dye decreased remarkably due to the adsorption of dye molecules on surface of the photocatalyst. Then the photocatalysis was initiated by UV light, and the blue solution was decolorized for different lengths of time. Each absorbance was determined from the UV–visible intensity at 663 nm wavelength of the individual peak. The decolorization efficiency (Fig. 8) of the MB dye solutions containing ZTO(NC)–SnO_2 and ZTO(NP)–SnO_2 used as photocatalytic materials was compared with that of the MB dye solution without the catalyst. The decolorization efficiency of ZTO(NP)–SnO_2 was 98.6% within 220 min, and the solution color changed from blue to milky white. The color was more milky white than the MB dye solution containing the ZTO(NC)–SnO_2 (decolorization efficiency = 85.1% within 220 min) due to the smaller size and larger surface area [3,11]. A number of photocatalytic materials with high performance have been reported. Among them, the photocatalytic activities of SnO_2, ZnO doped SnO_2 and Zn_2SnO_4 were 51%, 65% and 81% under UV radiation by 295, 295 and 245 min, respectively [2]. By the use of Zn_2SnO_4 as a photocatalyst, the first-order reaction fitted to a straight line with the reaction rate constant of 5.8×10^{-3} min^{-1} [16]. For the 3% Ho-doped ZnO as a photocatalyst, the degradation of MB was 98.26% by 300 min under UV radiation [21]. Methyl orange (MO) solution containing ZnO/SnO_2 (33.3 mol% Sn) photocatalyst with 500 °C and 10 h calcination was completely decolorized within 60 min under UV radiation [22]. ZnO/SnO_2 photocatalyst calcined at 350 °C for 2 h can promote the rate of decolorization of MO which was completely decolorized by 35 min [23]. Thus ZTO(NP)–SnO_2 is one of the candidate for using as a photocatalyst for environmental treatment.

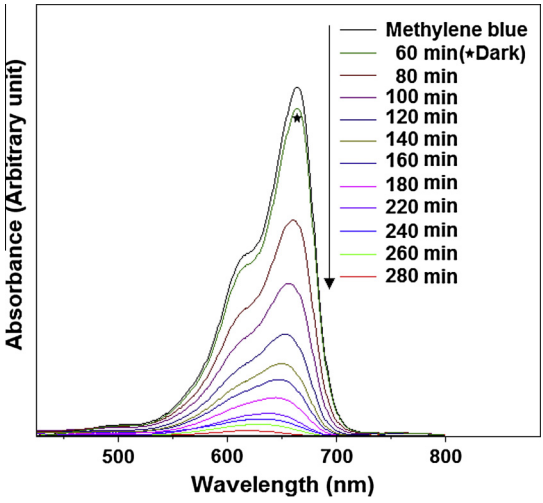


Fig. 7. UV–visible absorption of MB dye in the solution containing ZTO(NP)–SnO_2 composites in the dark and under UV light for different lengths of time.

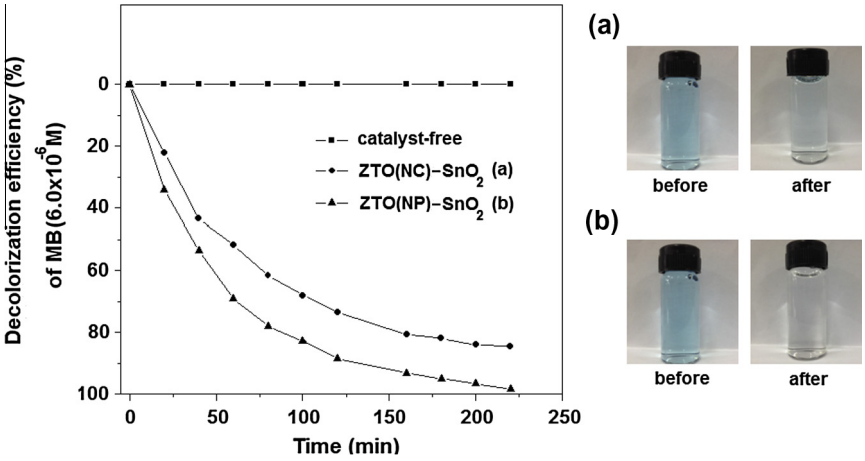


Fig. 8. Decolorization efficiency of MB dye in the solutions containing ZTO(NC)–SnO_2 and ZTO(NP)–SnO_2 composites as compared with that in the catalyst-free solution, and the MB aqueous solution of both before and after testing.

The degradation kinetics of MB dye solution of ZTO(NC)–SnO_2 and ZTO(NP)–SnO_2 could be evaluated. The pseudo first-order kinetics model was used and fitted to the equation

$$-\ln\left(\frac{C_t}{C_0}\right) = kt, \tag{3}$$

where k is the apparent pseudo-first-order rate constant of the degradation, and C_t and C_0 are the concentration of MB dye at any reaction time t and initial concentration, respectively [21,24,25]. The k values of Fig. 9 were derived from the plots of $-\ln(C_t/C_0)$ versus irradiation time (t). The rate constant k was calculated and found that the degradation of MB shows apparent pseudo-first-order kinetics of 1.763×10^{-2} and 8.893×10^{-3} min^{-1} for the ZTO(NP)–SnO_2 and ZTO(NC)–SnO_2 nanocomposites, respectively. To test the photocatalytic stability, the photocatalysts were recycled and reused, as shown in Fig. 10. The performance was still unchanged although the catalyst was reused for five times.

The energy gap (E_g) values of SnO_2, Zn_2SnO_4 (ZTO) and ZTO–SnO_2 have been reported: $E_g(SnO_2) = 3.61$ eV, $E_g(ZTO) = 3.69$ eV and $E_g(ZTO–SnO_2) = 3.63$ eV [17], and their energy levels have

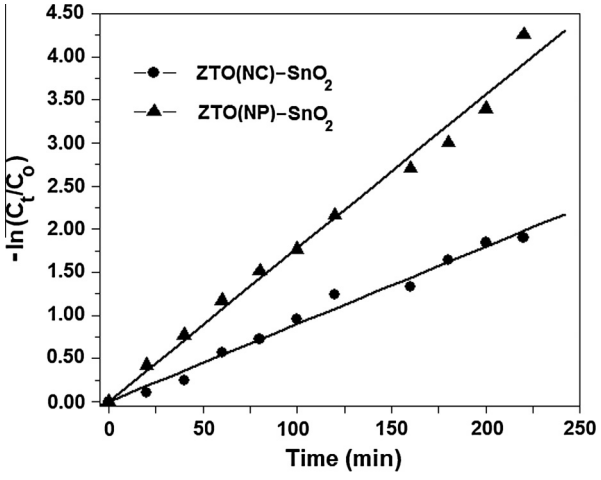


Fig. 9. The pseudo first-order kinetics plot of the MB aqueous solution containing ZTO(NC)–SnO_2 and ZTO(NP)–SnO_2.

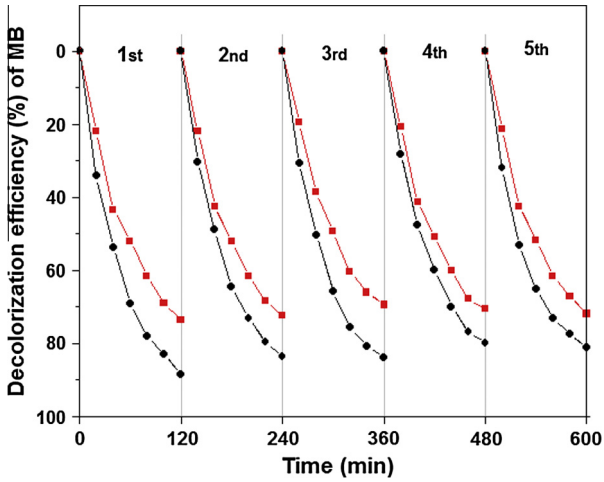


Fig. 10. The cycle performance of the ZTO(NC)–SnO_2 (red) and ZTO(NP)–SnO_2 (black) photocatalysts. (For interpretation of the references to color in this figure legend, the reader is referred to the web version of this article.)

been determined [13,17]. The phenomena for the high photocatalytic activity of ZTO–SnO_2 composites can be explained by the proposed mechanism (Fig. 11). The ZTO–SnO_2 photocatalyst could be excited by the photon which has sufficient energy to generate the photo-induced electron–hole pairs. The CB edge potential of ZTO is more negative than that of SnO_2, and the VB of SnO_2 is more positive than that of ZTO [18]. The local electric field at the ZTO–SnO_2 interface pushes the photogenerated electrons toward the CB of SnO_2, while the holes on the VB of SnO_2 diffuse to VB of ZTO. The photogenerated electrons can be effectively collected by SnO_2 and holes by ZTO, leading to the effective separation of photogenerated electrons and holes. Thus the electron–hole recombination process was prohibited

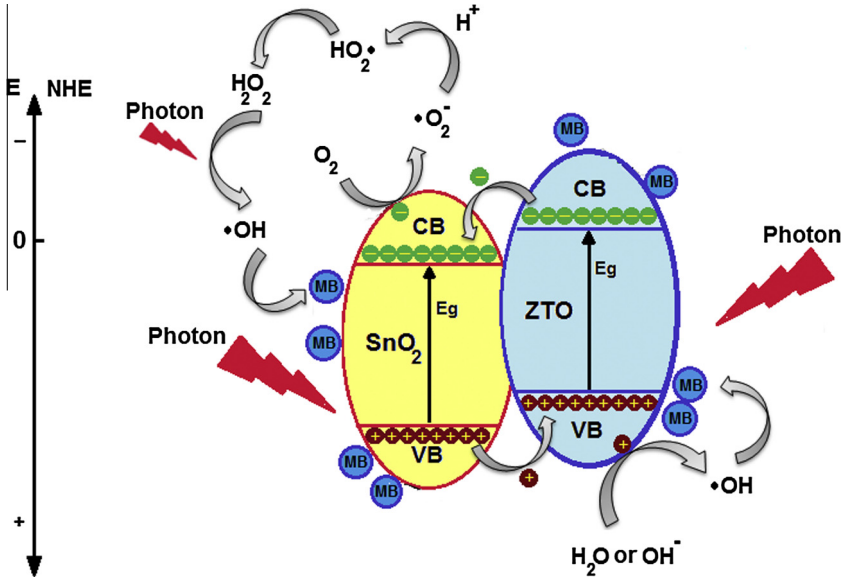


Fig. 11. Schematic illustration of the ZTO–SnO_2 nanocomposited photocatalyst.

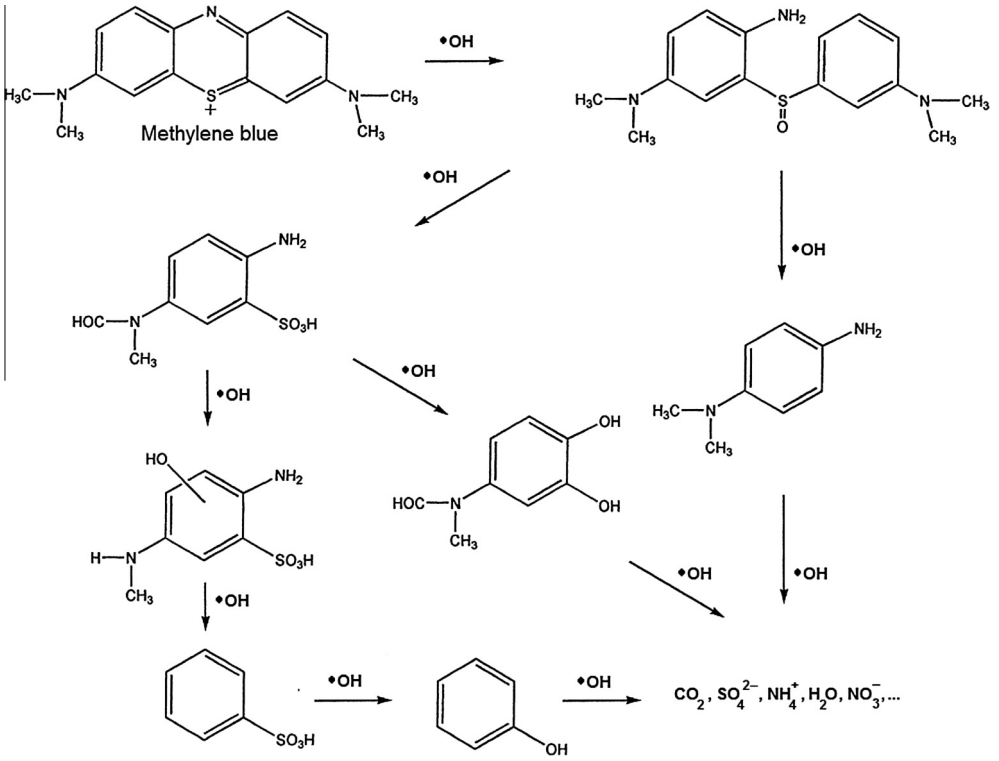


Fig. 12. Photocatalytic degradation pathway of MB.

and the ZTO–SnO_2 composites exhibit enhanced performance as compared to SnO_2 and ZTO alone. During processing, holes react with water (H_2O) molecules or hydroxyl (OH^-) ions in the reaction system to form hydroxyl radicals (·OH), and electrons react with adsorbing oxygen (O_2) to generate superoxide radical ($\cdot O_2^-$). The process is strong oxidizing performance for degradation of the organic substances [4,9,26]. The oxidizing power of the ·OH radicals is strong enough to completely oxidize organic pollutants. These reactive species may also contribute to the oxidative pathways: the degradation of methylene blue dye (Fig. 12) [27,28].

4. Conclusions

The really fine $ZnSn(OH)_6$ precursors with nanocubes and nanoparticles could be successfully produced at room temperature by short reaction time of sonochemistry in de-ionized water and ethylene glycol, respectively. Due to the thermodynamically unstable of the $ZnSn(OH)_6$ precursors, they were transformed into the ZTO–SnO_2 by high temperature calcination. The ZTO–SnO_2 nanocomposites exhibit enhanced photocatalytic performance. In this research, ZTO(NP)–SnO_2 presents higher activity than ZTO(NC)–SnO_2, enhanced by the relative smaller size and larger surface area.

Acknowledgements

We wish to thank the Thailand Research Fund (TRF) for providing financial support through the Royal Golden Jubilee Ph.D. Program and the TRF Research Grant BRG5380020, and the Thailand's Office of the Higher Education Commission through the National Research University (NRU) Project for Chiang Mai University (CMU), including the Graduate School of CMU through a general support.

References

[1] P. Junploy, S. Thongtem, T. Thongtem, Superlattices Microstruct. 57 (2013) 1–10.
[2] A.A. Firooz, A.R. Mahjoub, A.A. Khodadadi, M. Movahedi, Chem. Eng. J. 165 (2010) 735–739.
[3] D. Chen, Recent Pat. Nanotechnol. 2 (2008) 183–189.
[4] L. Ge, C. Han, J. Liu, Appl. Catal. B 108–109 (2011) 100–107.
[5] L. Zhang, W. Wang, S. Sun, Y. Sun, E. Gao, Z. Zhang, Appl. Catal. B 148–149 (2014) 164–169.
[6] T. Chang, Z. Li, G. Yun, Y. Jia, H. Yang, Nano-Micro Lett. 5 (2013) 163–168.
[7] R. Zhang, H. Wu, D. Lin, W. Pan, J. Am. Ceram. Soc. 92 (2009) 2463–2466.
[8] L.P. Zhu, N.C. Bing, D.D. Yang, Y. Yang, G.H. Liao, L.J. Wang, CrystEngComm 13 (2011) 4486–4490.
[9] L. Cheng, Y. Kang, Mater. Lett. 117 (2014) 94–97.
[10] O. Akhavan, Appl. Surf. Sci. 257 (2010) 1724–1728.
[11] J. Zhu, J. Yang, Z.F. Bian, J. Ren, Y.M. Liu, Y. Cao, H.X. Li, H.Y. He, K.N. Fan, Appl. Catal. B 76 (2007) 82–91.
[12] Z. Zhang, W. Wang, D. Jiang, J. Xu, Appl. Surf. Sci. 292 (2014) 948–953.
[13] M.A. Alpuche-Aviles, Y. Wu, J. Am. Chem. Soc. 131 (2009) 3216–3224.
[14] M.J. Kim, S.H. Park, Y.D. Huh, Bull. Korean Chem. Soc. 32 (2011) 1757–1760.
[15] Z. Ai, S. Lee, Y. Huang, W. Ho, L. Zhang, J. Hazard. Mater. 179 (2010) 141–150.
[16] C.G. Anchieta, D. Sallet, E.L. Foletto, S.S. da Silva, O. Chiavone-Filho, C.A.O. do Nascimento, Ceram. Int. 40 (2014) 4173–4178.
[17] B. Li, L. Luo, T. Xiao, X. Hu, L. Lu, J. Wang, Y. Tang, J. Alloys Compd. 509 (2011) 2186–2191.
[18] T.J. Coutts, D.L. Young, X. Li, W.P. Mulligan, X. Wu, J. Vac. Sci. Technol. A 18 (2000) 2646–2660.
[19] Powder Diffract, File, JCPDS-ICDD, 12 Campus Boulevard, Newtown Square, PA 19073-3273, U.S.A., 2001.
[20] M. Vaseem, A. Umar, Y.B. Hahn, Metal Oxide Nanostructures and Their Applications, in: A. Umar, Y.B. Hahn (Eds.) 5 (2010) 1–36.
[21] A. Phuruangrat, O. Yayapao, T. Thongtem, S. Thongtem, Superlattices Microstruct. 67 (2014) 118–126.
[22] C. Wang, X. Wang, B.Q. Xu, J. Zhao, B. Mai, P. Peng, G. Sheng, J. Fu, J. Photochem. Photobiol. A 168 (2004) 47–52.
[23] M. Zhang, T. An, X. Hu, C. Wang, G. Sheng, J. Fu, Appl. Catal. A 260 (2004) 215–222.
[24] K. Zhang, W.C. Oh, Bull. Korean Chem. Soc. 31 (2010) 1589–1595.
[25] Z. Shami, N. Sharifi-Sanjani, CrystEngComm 16 (2014) 910–921.
[26] W. Li, D. Wu, Y. Yu, P. Zhang, J. Yuan, Y. Cao, Y. Cao, J. Xu, Physica E 58 (2014) 118–123.
[27] A. Houas, H. Lachheb, M. Ksibi, E. Elaloui, C. Guillard, J.M. Herrmann, Appl. Catal. B 31 (2001) 145–157.
[28] H.L. Wang, D.Y. Zhao, W.F. Jiang, Desalination Water Treat. 51 (2013) 2826–2835.

Superlattices and Microstructures 69 (2014) 253–264

Contents lists available at ScienceDirect

Superlattices and Microstructures

journal homepage: www.elsevier.com/locate/superlattices

Effect of medium solvent ratios on morphologies and optical properties of α-$ZnMoO_4$, β-$ZnMoO_4$ and $ZnMoO_4 \cdot 0.8H_2O$ crystals synthesized by microwave-hydrothermal/solvothermal method

Yanee Keereeta [a], Titipun Thongtem [b,c,*], Somchai Thongtem [a,c,*]

[a] Department of Physics and Materials Science, Faculty of Science, Chiang Mai University, Chiang Mai 50200, Thailand
[b] Department of Chemistry, Faculty of Science, Chiang Mai University, Chiang Mai 50200, Thailand
[c] Materials Science Research Center, Faculty of Science, Chiang Mai University, Chiang Mai 50200, Thailand

ARTICLE INFO

Article history:
Received 6 February 2014
Accepted 19 February 2014
Available online 10 March 2014

Keywords:
α-$ZnMoO_4$
β-$ZnMoO_4$
$ZnMoO_4 \cdot 0.8H_2O$
X-ray diffraction
Electron microscopy
Spectroscopy

ABSTRACT

$ZnMoO_4$ with different morphologies were successfully synthesized by microwave hydrothermal and microwave solvothermal methods, without the use of any additives. The different crystalline phases (α-$ZnMoO_4$, β-$ZnMoO_4$ and $ZnMoO_4 \cdot 0.8H_2O$), morphologies and optical properties of the samples were studied by X-ray diffraction, electron microscopy and spectroscopy, and were found to be influenced by the length of reaction time and the different volume ratios of ethylene glycol (EG) to water as medium solvents. In this research, the direct energy gap (E_g) and photonic emission wavelength were evaluated to be 3.13–3.51 eV and 366 nm, respectively.
© 2014 Published by Elsevier Ltd.

1. Introduction

In recent years, semiconducting nanomaterials have received considerable attention due to their wide applications in the fabrication of optical and electronic devices. A group of metal molybdate

* Corresponding authors. Address: Department of Chemistry, Faculty of Science, Chiang Mai University, Chiang Mai 50200, Thailand. Tel.: +66 (0)53 943344; fax: +66 (0)53 892277 (T. Thongtem). Address: Department of Physics and Materials Science, Faculty of Science, Chiang Mai University, Chiang Mai 50200, Thailand. Tel.: +66 (0)53 941924; fax: +66 (0)53 943445 (S. Thongtem).
E-mail addresses: ttpthongtem@yahoo.com (T. Thongtem), schthongtem@yahoo.com (S. Thongtem).

http://dx.doi.org/10.1016/j.spmi.2014.02.011
0749-6036/© 2014 Published by Elsevier Ltd.

such as $MMoO_4$ (M = Ca, Sr, Mg, Zn) are semiconductors, which are important in photoluminescence and photocatalysis. Among them, zinc molybdate has many attractive applications, especially in luminescence, scintillation and photocatalysis, and for using in battery electrodes and drug delivery system [1–5]. There are a variety of methods used to synthesize $ZnMoO_4$ such as hydrothermal method [3,6,7], conventional mixed oxide calcination [2], microwave irradiation [3] and Czochralski method [5].

However, a hybrid technique such as microwave-hydrothermal method exhibits much advantage and is frequently applied for synthesizing of (nano) materials and chemical compounds, mainly inorganic chemicals. In order to additionally enhance the reaction kinetics, a great amount of work has been done to hybridize the hydrothermal technique with microwave (MW). Particularly, microwave-hydrothermal and microwave-solvothermal methods are truly low-temperature processes for the synthesis of nanophase of different sizes and shapes. They consume less energy, environmentally friendly, and the reaction proceeding in a closed system. The kinetics of reaction is greatly increased with a small increase in temperature. New metastable products form and are generally single crystals [8–10]. In contrast to the conventional heating hydrothermal/solvothermal method, it requires a longer time (typically half to several days) and high electrical power of over a thousand watts. Microwave-assisted heating is a greener approach to synthesize materials with a shorter time (several minutes to hours) and with lower power consumption (hundreds of watts) as a consequence of directly and uniformly heating the contents.

In the current work, the synthesis of triclinic α-$ZnMoO_4$, monoclinic β-$ZnMoO_4$ and $ZnMoO_4{\cdot}0.8H_2O$ with different morphologies (rod-like, flower-like, rugby-like) by microwave hydrothermal and microwave solvothermal methods without the use of any additive and surfactant were investigated and reported.

2. Experiment

2.1. Materials and processing

5 mmol of each $Zn(NO_3)_2{\cdot}6H_2O$ and $(NH_4)_6Mo_7O_{24}{\cdot}4H_2O$ was dissolved in 60 ml (constant volume) of deionized water and ethylene glycol with various ratios (Table 1) and vigorously stirred for 30 min. Then the solutions were transferred into glass vessels, which were tightly closed with covers equipped with safety valves on top. The systems were heated by a 270 W microwave (2.45 GHz) for different lengths of time. At the conclusion of the process, the system was naturally cooled to room temperature. Finally, the products were washed with water and ethanol several times, and dried at 80 °C for 12 h for further characterization using different methods.

Table 1
Product code, reaction time and EG:H_2O volume ratio.

Product code	Time (min)	EG:H_2O volume ratio
E130	30	1: 0
E160	60	
E190	90	
E4H1	30	4:1
E2H1	30	2:1
E1H1	30	1:1
E1H2	30	1:2
E1H4	30	1:4
H130	30	0:1
H160	60	
H190	90	
H1-2h	120	
H1-3h	180	

2.2. Characterizations

The as-synthesized products were characterized by X-ray diffractometer (XRD, SIEMENS D500) operating at 20 kV, 15 mA, and using Cu Kα line, in combination with the database of the Joint Committee on Powder Diffraction Standards (JCPDS) [11]; scanning electron microscope (SEM, JEOL JSM-6335F) operating at 15 kV; transmission electron microscope (TEM, JEOL JEM-2010), high resolution transmission electron microscope (HRTEM) and selected area electron diffractometer (SAED) operating at 200 kV; Fourier transform infrared (FTIR, Bruker Tensor 27) spectrometer with KBr as a diluting agent and operated in the range of 4000–400 cm^{-1}; Raman spectrometer (T64000 HORIBA Jobin Yvon) using a 50 mW and 514.5 nm wavelength Ar green laser; UV–visible spectrometer (Lambda 25 PerkinElmer) using a UV lamp with the resolution of 1 nm; and photoluminescence (PL) spectrometer (LS 50B PerkinElmer) using a 240 nm excitation wavelength at room temperature.

3. Results and discussion

3.1. XRD

As it is shown in Fig. 1, the influence of medium solvents and time on the formation of $ZnMoO_4$ phase was studied by XRD. For the samples synthesized in different EG:H_2O volume ratios for 30 min microwave irradiation, the volume ratio of the medium solvent had a crucial effect on the formation of $ZnMoO_4$ phase. The detected peaks of the samples synthesized in H_2O (H130) and in the mixture of EG and H_2O (1:4, 1:2 and 1:1 of EG:H_2O for E1H4, E1H2 and E1H1 samples) can be specified as pure $ZnMoO_4{\cdot}0.8H_2O$ phase of JCPDS No. 25-1025 [11]. When more EG was added to the medium solvents until at 2:1 and 4:1 of EG:H_2O, the mixture of α-$ZnMoO_4$ (JCPDS No. 35-0765) [11] and $ZnMoO_4{\cdot}0.8H_2O$ phases was detected in the E2H1 and E4H1 samples.

When pure EG was used as a solvent, the XRD peaks of the E130 sample were identified to pure triclinic α-$ZnMoO_4$ phase (JCPDS No. 35-0765) [11]. This shows the loss of crystal water molecules this EG medium solvent. The crystalline phase became more perfect by increasing in the length of reaction time. The XRD peaks of the E160 and E190 samples (Fig. 2a) became sharper and stronger, suggesting the enhancement of crystalline degree with prolonged time. When pure H_2O was used as a medium solvent instead, the influence of reaction time on the XRD patterns is also shown in Fig. 2b. For 30 and 60 min processing in H_2O medium solvent (H130 and H160 samples), pure $ZnMoO_4{\cdot}0.8H_2O$ phase of JCPDS No. 25-1025 [11] was detected. For 90 min long, some of the $ZnMoO_4{\cdot}0.8H_2O$ crystalline phase of the particles (H190) began transform into β-$ZnMoO_4$ phase (JCPDS No. 25-1024) [11]. Thus the mixture of $ZnMoO_4{\cdot}0.8H_2O$ and β-$ZnMoO_4$ phases were detected in the H190 sample. When the reaction time was lengthened to 2 h (H1-2h) and 3 h (H1-3h), the pure monoclinic β-$ZnMoO_4$ phase (according to the JCPDS No. 25-1024) [11] can be successfully synthesized. There were no other diffraction peaks of other phases were obviously detected. These results are in good evidence for the formation of $ZnMoO_4{\cdot}0.8H_2O$, α-$ZnMoO_4$ and β-$ZnMoO_4$ phases as shown by the following reaction scheme:

$$(NH_4)_6Mo_7O_{24}\cdot 4H_2O_{(s)} \longrightarrow 6NH^{+}_{4(aq)} + Mo_7O^{6-}_{24(aq)} + 4H_2O$$

$$Mo_7O^{6-}_{24(aq)} + 8OH^{-}_{(aq)} \longrightarrow 7MoO^{2-}_{4(aq)} + 4H_2O$$

$$Zn(NO_3)_2\cdot 6H_2O_{(s)} \longrightarrow Zn^{2+}_{(aq)} + 2NO^{2-}_{3(aq)} + 6H_2O$$

$$Zn^{2+}_{(aq)} + MoO^{2-}_{4(aq)} + 0.8H_2O \longrightarrow ZnMoO_4\cdot 0.8H_2O_{(s)}$$

$$ZnMoO_4\cdot 0.8H_2O \longrightarrow \beta\text{-}ZnMoO_{4(s)} + 0.8H_2O$$

$$Zn^{2+}_{(aq)} + MoO^{2-}_{4(aq)} \longrightarrow \alpha\text{-}ZnMoO_{4(s)}$$

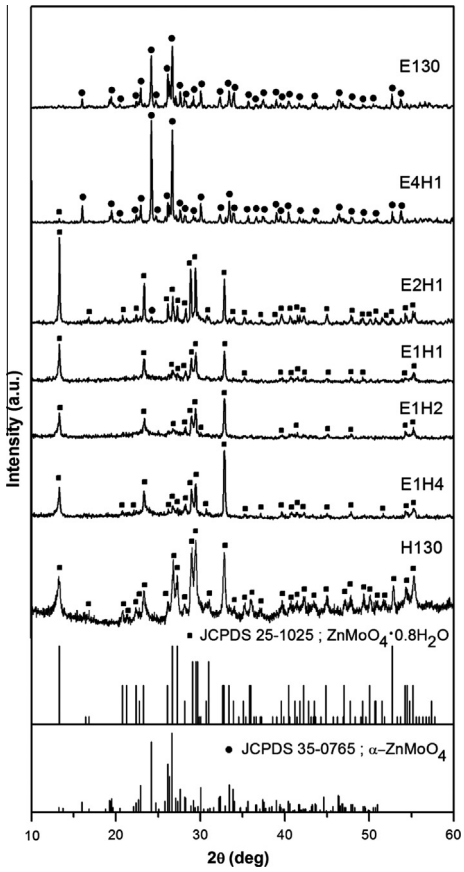


Fig. 1. XRD patterns of the H130, E1H4, E1H2, E1H1, E2H1, E4H1 and E130 samples synthesized in 0:1, 1:4, 1:2, 1:1, 2:1, 4:1 and 1:0 volume ratios of EG:H_2O medium solvents for 30 min.

Calculated lattice parameters are shown in Table 2. They are very close to those of the corresponding JCPDS database Nos. 35-0765 for α-$ZnMoO_4$, 25-1024 for β-$ZnMoO_4$ and 25-1025 for $ZnMoO_4{\cdot}0.8H_2O$ crystalline phases [11].

3.2. SEM, TEM and SAED

Fig. 3. SEM images of $ZnMoO_4$ synthesized in the solvents of different EG:H_2O ratios for different lengths of reaction time. It can be seen that the sample H130 (Fig. 3a) which was synthesized in pure H_2O solvent for 30 min reaction time shows an irregularity in shape and size with the crystallite size of much larger than 1 μm. When the medium solvent was the mixture of EG and H_2O, rod-shaped particles began to show up. The samples of E1H4 (Fig. 3b) and E1H2 (Fig. 3c) had the same crystal size with the width of 0.6–2.4 μm range. For the EG:H_2O volume ratio of 1:1 (E1H1), the sample (Fig. 3d) formed as a rod-like structure with smaller in diameter of 0.1–0.6 μm, including the majority of the crystals had exceeded 6.0–11.5 μm in length. Due to the viscosity of EG (η = 21 mPa s, 20 °C) is much higher than that of water ($\eta = 1.0087 \times 10^{-3}$ mPa s, 20 °C) [12], the diffusion rate of ions in the EG:H_2O medium is significantly reduced. In this case, the quantity of EG can play the role in inhibiting the growth of anisotropic superstructures. The $ZnMoO_4$ side-walls were capped by hydroxyl groups of the solvent. The effect of hydrogen bonds between hydroxyl groups may exist as long chains and acted

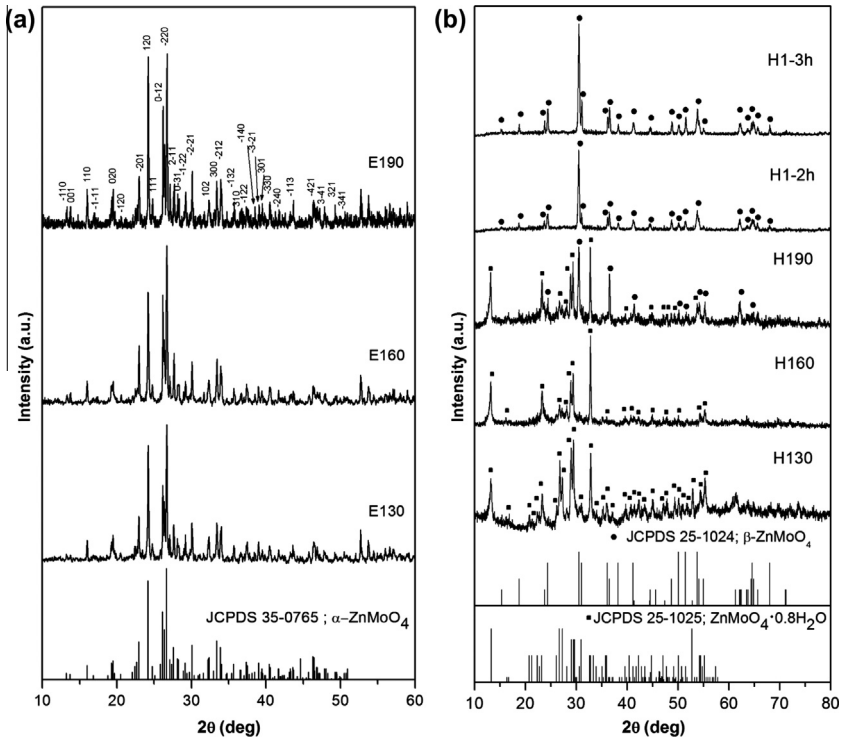


Fig. 2. XRD patterns of (a) the E130, E160 and E190 samples synthesized in pure EG for 30, 60 and 90 min; and (b) the H130, H160, H190, H1-2h and H1-3h samples synthesized in pure water for 30, 60, 90, 120 and 180 min, respectively.

Table 2
Comparing lattice parameters of $ZnMoO_4$ of different crystalline phases and those of the JCPDS database [11].

Sample	*a*	*b*	*c*	*α*	*β*	*γ*
$ZnMoO_4{\cdot}0.8H_2O$	10.2900	6.9100	6.9300	105.2300	117.7300	84.7500
H130	10.26174	6.89071	6.93312	105.18247	117.72608	84.71806
β-$ZnMoO_4$	4.7040	5.7540	4.9120	90.0000	90.1000	90.0000
H1-2h	4.81218	5.72650	4.92777		91.32811	
α-$ZnMoO_4$	8.3678	9.6916	6.9643	106.8720	101.7260	96.7340
E130	8.36447	9.68410	6.97094	106.80965	101.78322	96.72792

as a soft template, leading to the growth in the shape of rods. Upon further increasing in the EG volume (EG:H_2O = 2:1 by volume), $ZnMoO_4$ rods increased in diameter again (Fig. 3e) but decreased in length when the EG is much more than H_2O (EG:H_2O = 4:1 by volume, Fig. 3f). In the present case, the high concentration of EG in the medium solution has a tendency to limit the growth of particles. The adsorption and desorption processes on the surface of $ZnMoO_4$ particles were not well-controlled during microwaving, thus short rod-like particles originated. Fig. 3g–i shows the morphology of the E130, E160, E190 samples which were synthesized in pure EG solvent for 30, 60 and 90 min, respectively. All of them have the shape of flowers. The products were composed of a number of rod-like clusters and crystal size became much larger when the reaction time was lengthened. In this case, the high viscosity of EG is able to modify the mobility of the primary particles in suspension as well as their effective collision rates. Moreover, the predominance of EG in the solution has a higher

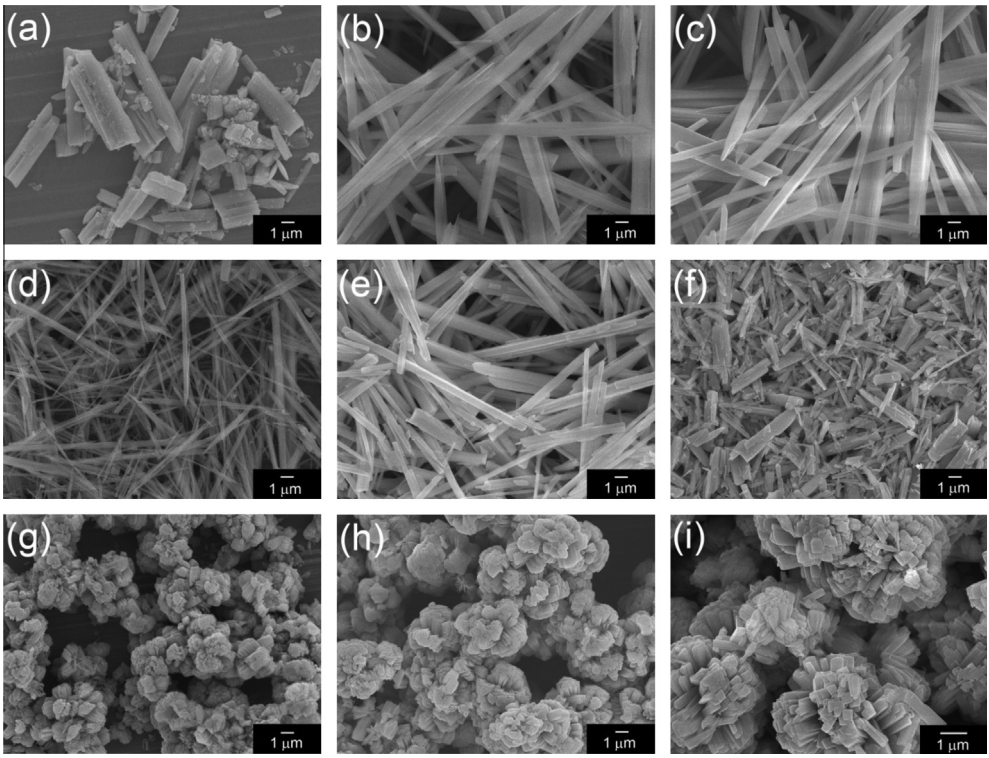


Fig. 3. SEM images of $ZnMoO_4$ synthesized in medium solvents of different EG:H_2O ratios: (a) H130, (b) E1H4, (c) E1H2, (d) E1H1, (e) E2H1, (f) E4H1 and (g) E130 for 30 min; (h) E160 for 60 min; and (i) E190 for 90 min.

viscosity as compared to that of water [13] and can limit the growth process, causing the reduction of the particle size and leading to the aggregation of particles in the shape of flowers.

The explanation shows that the medium solvents can play an important role in controlling the sample shapes. A polar solvent, which has permanent dipole moment, has relaxation process in microwave region. Thus it is a good candidate in the synthetic process. The dielectric constant of water at 25 °C is 78.4 and larger than ethylene glycol (dielectric constant at 25 °C = 40.3) [14]. These properties can be considered as the key factor to promote rapid heating to high temperature within a very short time. It can be seen that the sample obtained after 30 min reaction time in water solvent (H130) has irregular shape because of the more rapid rate of aggregation. When the reaction time was increased to 60 min and the medium solvent was pure water (H160), the structure was in the shape of microsize rods with a very high aspect ratio, 1.42 ± 0.45 μm in width and about 14.85–61.83 μm in length (Fig. 4a). It can be seen that the H190 sample of Fig. 4b is composed of rod-shaped particles. The crystalline morphology of β-$ZnMoO_4$ obtained after 2 h reaction time is shown in Fig. 4c (H1-2h sample). Clearly, the rod-shape was no longer detected but the rugby-shaped $ZnMoO_4$ originated instead. By increasing the reaction time to 3 h (Fig. 4d), the agglomeration of rugby-shaped and rod-like particles clustered together as squares (H1-3h). Possibly, the crystallites can be nucleated and grew with the prolonged time.

Fig. 5 shows TEM and HRTEM images, and SAED and simulated patterns of the samples with different morphologies which were synthesized in different medium solvents. In medium solvent of EG:H_2O of 1:1 (E1H1), the sample was composed of nanorods (Fig. 5a). HRTEM images (Fig. 5b and c) shows a nanorod which was single crystal and composed of a number of atoms in lattice arrays. Its growth was parallel to the (-220) plane of the single crystalline nanorod. Fig. 5d and g shows $ZnMoO_4$

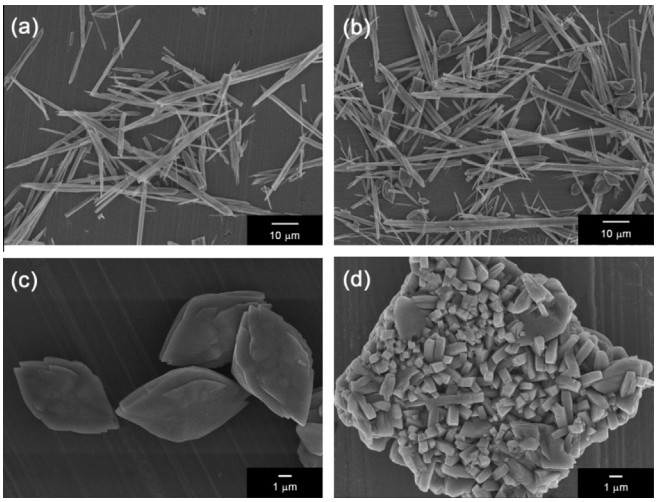


Fig. 4. SEM images of $ZnMoO_4$ synthesized in H_2O as a solvent for different lengths of reaction time: (a) H160 (60 min), (b) H190 (90 min), (c) H1-2h (2 h) and (d) H1-3h (3 h).

morphologies in the shape of a flower and rugby, which were synthesized in EG (E130) and H_2O (H1-2h) as solvents, respectively. SAED patterns (Fig. 5e and h) of the samples appear as periodic arrays of bright spots, caused by electron diffraction through the crystallographic planes of single crystal. The calculated angles between any pairs of the directions belonging to these planes, and interplanar spaces determined from (hkl) are in accordance with those of the diffraction patterns on the films. The pattern of Fig. 5e corresponds to the (001), (201) and (200) planes of triclinic α-$ZnMoO_4$ with *P*-1 space group (JCPDS No. 35-0765) and of Fig. 5h corresponds to the (010), (110) and (100) planes of monoclinic β-$ZnMoO_4$ with P2-c space group (JCPDS No. 25-1024) [11]. Diffraction patterns with the [020] and [00–1] zone axis were simulated in Fig. 5f and i, respectively. The simulated spots with the specified crystallographic planes are in systematic and symmetric arrays, which are identified the existence of the patterns obtained by interpretation.

3.3. Raman and FTIR analyses

Naturally, $ZnMoO_4$ was found in two different types of crystalline phase: α-triclinic and β-monoclinic. For the α-$ZnMoO_4$ triclinic structure, all zinc atoms are bonded to six oxygen atoms, forming the distorted octahedral [ZnO_6] units. The molybdenum atoms are coordinated to four oxygen atoms, resulting in the tetrahedral [MoO_4] units [15]. On the other hand, the β-$ZnMoO_4$ monoclinic structure has both Zn and Mo atoms bonded to six oxygen atoms, which promote the origin of distorted octahedral [ZnO_6]/[MoO_6] units, respectively [16].

Monoclinic β-$ZnMoO_4$ crystal has a wolframite-type structure belonging to the P2/c space group. Group theory calculation and symmetry of molybdate and tungstate crystals with a wolframite-type monoclinic structure present 3N = 36 degrees of freedom [17,18] show 36 distinct vibrational modes (Raman and infrared (IR)): $8A_g + 10B_g + 8A_u + 10B_u$ at the center (τ) of Brillouin zone. Only A_g and B_g are Raman-active modes. Thus, only 18 active vibrational modes are expected in Raman spectra of β-$ZnMoO_4$ crystal ($8A_g + 10B_g$) [18]. Fig. 6 shows the Raman spectra of β-$ZnMoO_4$ microcrystals (H1-2h) synthesized by using water as a solvent for 2 h. The main Raman (A_g) mode with the strongest intensity peak at around 873 cm^{-1} is assigned to the symmetric stretching bonds of O–Mo–O. Two Raman (A_g and B_g) modes at approximately 773 cm^{-1} and 695 cm^{-1} are assigned to the asymmetric stretching bonds of O–Mo–O [18,19].

The α-$ZnMoO_4$ crystal presents a triclinic structure with P_1 space group and C_1s point group symmetry [15,18], and $ZnMoO_4{\cdot}0.8H_2O$ is the Anorthic crystalline phase. The strongest intensity peaks at

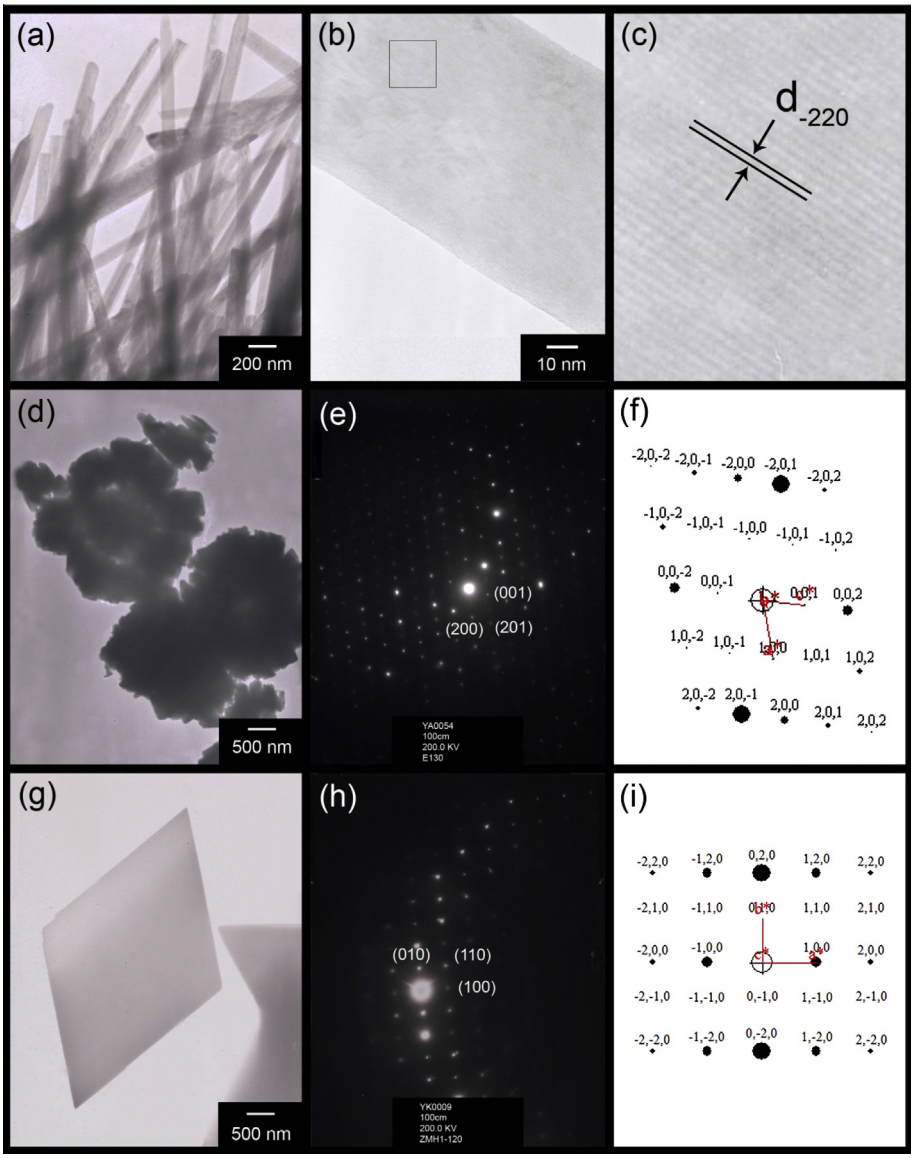


Fig. 5. TEM and HRTEM images, and SAED and simulated patterns of $ZnMoO_4$ particles synthesized in different medium solvents: (a)–(c) $ZnMoO_4{\cdot}0.8H_2O$ (E1H1), (d)–(f) α-$ZnMoO_4$ (E130), and (g)–(i) β-$ZnMoO_4$ (H1-2h).

963 cm^{-1}, 946 cm^{-1} and 945 cm^{-1} were respectively detected in the samples of E130, E1H1 and H130, corresponding to the previous reports [20–22]. The α-$ZnMoO_4$ triclinic structure, metal molybdate has $[MoO_4]^{2-}$ molecular ionic groups with strong covalent Mo–O bonding. Their Raman vibrations are classified into two types, the internal and external modes. The first is caused by the oscillation inside the $[MoO_4]^{2-}$ molecular ionic groups with immobile mass center. The second is the lattice phonon vibration due to the motion of M^{2+} cations w.r.t the rigid molecular ionic units [23]. There are no bridging Mo–O–Mo bonds between MoO_4 units, indicated as isolated $(MoO_4)^{2-}$ tetrahedral units. The crystals contained both ZnO_5 and ZnO_6 polyhedrons, deformed by the Jahn–Teller effect. Commonly, there was

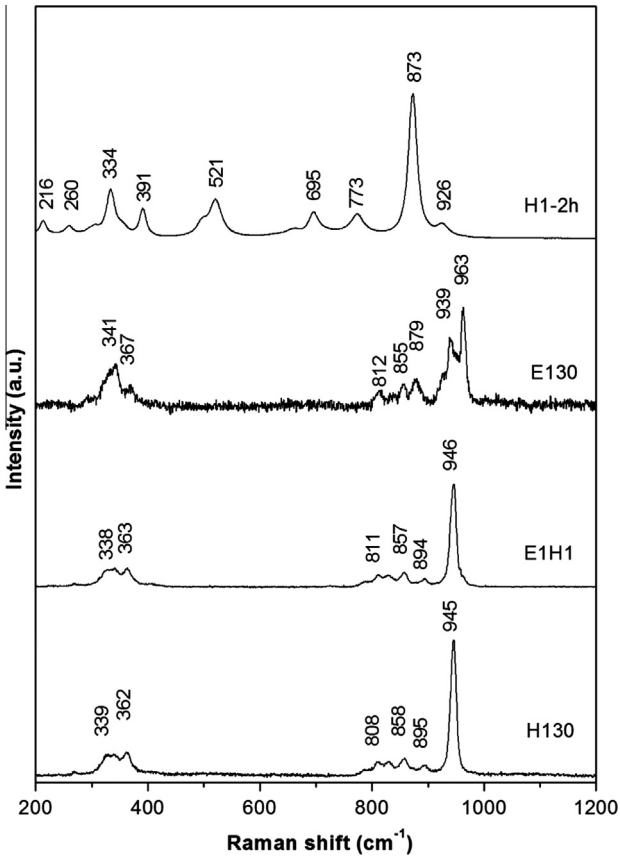


Fig. 6. Raman spectra of $ZnMoO_4$ (H130, E1H1, E130 and H1-2h) synthesized in different medium solvents.

single-corner sharing of ZnO_5/ZnO_6 and MoO_4 with a number of Zn–O–Zn and Zn–O–Mo linkages inside, leading to the sharp peaks caused by Mo^{6+} bonding of isolated MoO_4 tetrahedrons [21].

FTIR spectra synthesized in different medium solvent and crystalline phase are showed in Fig. 7. The spectra of the samples prepared in H_2O (H130), EG:H_2O of 1:1 ratio (E1H1) with $ZnMoO_4{\cdot}0.8H_2O$ phase, and EG (E130) with α-$ZnMoO_4$ crystalline phase contain the same wavenumbers at 964, 863, 745 and 409 cm^{-1}. Those were specified as the ν_1 stretching of Mo–O in bridging Mo–O–Mo linkages, the ν_1 stretching of $(MoO_4)^{2-}$ tetrahedrons, the ν_3 stretching of Mo–O, and the ν_4 Mo–O bending mode, respectively [20,25]. When H_2O was used as a medium solvent for 2 h reaction time with the formation of β-$ZnMoO_4$ monoclinic structure (H1-2h), the bands shifted to 829, 654, 516 and 409 cm^{-1}, corresponding to the A_u mode assigned to the O–Mo–O symmetric stretching of the distorted octahedral $[MoO_6]$ units, an A_u mode with distorted octahedral $[MoO_6]$ units assigned as an anti-symmetric stretching, A_u mode related to the anti-asymmetric stretching of the distorted octahedral $[MoO_6]$–$[MoO_6]$ units in a chain, and the A_u mode ascribed to an O–Zn–O anti-symmetric stretching of distorted octahedral $[ZnO_6]$ units, respectively [18].

3.4. UV–visible and PL analyses

UV–visible absorption of the H130, E1H1, E130 and H1–2 h samples are shown in Fig. 8, which indicated an exponential decreasing of the photonic absorbance attenuated through the materials. For crystalline semiconductors, the UV absorption near band edge follows the equation.

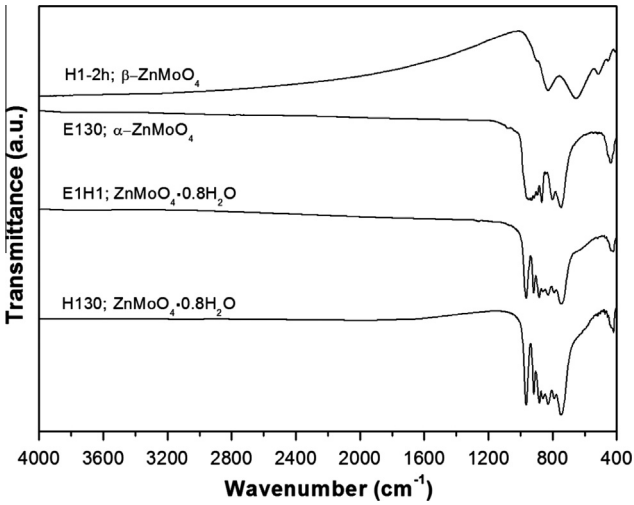


Fig. 7. FTIR spectra of $ZnMoO_4$ (H130, E1H1, E130 and H1-2h) synthesized in different EG:H_2O medium solvent ratios.

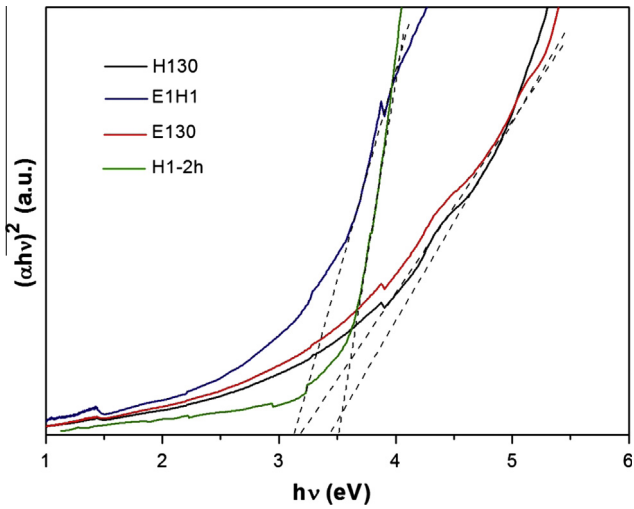


Fig. 8. UV–visible absorption of $ZnMoO_4$ (H130, E1H1, E130 and H1-2h) synthesized in different medium solvents.

$$\alpha h\nu = (h\nu - E_g)^n$$

where α, h, ν, and E_g are the absorbance, Planck constant, photon frequency and photonic energy band gap, respectively. The parameter n is a pure number associated with the different types of electronic transitions: $n = 1/2$, 2, 3/2 or 3 for direct-allowed, indirect allowed, direct-forbidden and indirect-forbidden transitions, respectively [18,24].

The direct E_g was determined by extrapolating the linear portion of the curve to zero absorption to be 3.13–3.51 eV — very close to that for $xMoO_3$–$(1-x)ZnO$ [25] and $ZnMoO_4$ nanofibers of the previous report [20], but less than that estimated for perfect $ZnMoO_4$ [26].

By using a 240 nm excitation wavelength, the PL emission peaks of the H130, E1H1, E130 and H1–2h samples (Fig. 9) presented broad bands over the 320–600 nm range with a strong blue emission

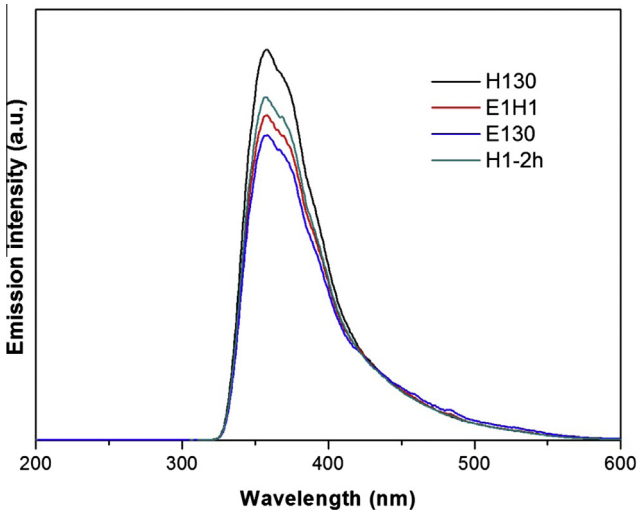


Fig. 9. PL spectra of $ZnMoO_4$ (H130, E1H1, E130 and H1-2h) synthesized in different EG:H_2O medium solvent ratios.

peaks centered at the same wavelengths of 366 nm due to the transitions between Mo_{4d} and O_{2p} states — in accordance with other reports [2,20]. In the present research, the PL emission was in the same range as the direct E_g, relating to the direct transition in the crystals.

4. Conclusions

α-$ZnMoO_4$, β-$ZnMoO_4$ and $ZnMoO_4{\cdot}0.8H_2O$ crystals were successfully synthesized by hydrothermal/solvothermal method with different EG:H_2O solvent ratios. SEM and TEM show the as-synthesized $ZnMoO_4$ with different morphologies (rod, rugby and flower). Vibration wavenumbers provided the evidence of different crystalline phases of $ZnMoO_4$. The optical band gap values of the samples are approximately 3.13–3.51 eV and PL emission shows the peaks at 366 nm.

Acknowledgements

We wish to thank the Thailand Research Fund (TRF) for providing financial support through the Royal Golden Jubilee Ph.D. Program and the TRF Research Grant BRG5380020, and the Thailand's Office of the Higher Education Commission through the National Research University (NRU) Project for Chiang Mai University (CMU), including the Graduate School of CMU through a general support.

References

[1] G.K. Choi, J.R. Kim, S.H. Yoon, K.S. Hong, Microwave dielectric properties of scheelite (A = Ca, Sr, Ba) and wolframite (A = Mg, Zn, Mn) $AMoO_4$ compounds, J Eur. Ceram. Soc. 27 (2007) 3063–3067.
[2] J.H. Ryu, S.M. Koo, J.W. Yoon, C.S. Lim, K.B. Shim, Synthesis of nanocrystalline $MMoO_4$ (M = Ni, Zn) phosphors via a citrate complex route assisted by microwave irradiation and their photoluminescence, Mater. Lett. 60 (2006) 1702–1705.
[3] G. Zhang, S. Yu, Y. Yang, W. Jiang, S. Zhang, B. Huang, Synthesis, morphology and phase transition of the zinc molybdates $ZnMoO_4{\cdot}0.8H_2O$/α-$ZnMoO_4$/$ZnMoO_4$ by hydrothermal method, J. Cryst. Growth 312 (2010) 1866–1874.
[4] Y. Li, G. Weisheng, B. Bo, G. Kaijie, Yeast-directed hydrothermal synthesis of ZnMoO4 hollow microspheres and its photocatalytic degradation of auramine O., Int. Conf. Energy Environ. Technol. IEEE 2009 (2009), http://dx.doi.org/10.1109/ICEET.2009.631.
[5] A.M. Dubovik, Y.Y. Vostretsov, B.V. Grinyov, F.A. Danevich, H. Kraus, L.L. Nagornaya, et al, Research and development of $ZnBO_4$ (B = W, Mo) crystal scintillators for dark matter and double beta decay searching, Acta Phys. Pol. A 117 (2010) 15–19.

[6] Y.R. Jiang, W.W. Lee, K.T. Chen, M.C. Wang, K.H. Chang, C.C. Chen, Hydrothermal synthesis of β-$ZnMoO_4$ crystals and their photocatalytic degradation of Victoria Blue R and phenol, J. Taiwan Inst. Chem. Eng. (2013), http://dx.doi.org/10.1016/j.jtice.2013.05.007.
[7] L.S. Cavalcante, J.C. Sczancoski, M. Siu Li, E. Longo, J.A. Varela, β-ZnMoO4 microcrystals synthesized by the surfactant-assisted hydrothermal, Colloids Surf. A 396 (2012) 346–351.
[8] M.L. Moreira, G.P. Mambrini, D.P. Volanti, E.R. Leite, M.O. Orlandi, P.S. Pizani, V.R. Mastelaro, C.O. Paiva-Santos, E. Longo, J.A. Varela, Hydrothermal microwave: a new route to obtain photoluminescent crystalline $BaTiO_3$ nanoparticles, Chem. Mater. 20 (2008) 5381–5387.
[9] S. Komarneni, R. Pidugu, Q.H. Li, R. Roy, Microwave-hydrothermal processing of metal powders, J. Mater. Res. 10 (1995) 1687–1692.
[10] S. Komarneni, Nanophase materials by hydrothermal, microwave-hydrothermal and microwave-solvothermal methods, Curr. Sci. 85 (2003) 1730–1734.
[11] Powder Diffract, File, JCPDS-ICDD, 12 Campus Boulevard, Newtown Square, PA 19073–3273, USA, 2001.
[12] F. Teng, S. Santhanagopalan, R. Lemmens, X. Geng, P. Patel, D.D. Meng, In situ growth of $LiFePO_4$ nanorod arrays under hydrothermal condition, Solid State Sci. (2010) 1–4.
[13] V.S. Marques, L.S. Cavalcante, J.C. Sczancoski, A.F.P. Alcantara, M.O. Orlandi, E. Moraes, E. Longo, J.A. Varela, M. Siu Li, M.R.M.C. Santos, Effect of different solvent ratios (water/ethylene glycol) on the growth process of $CaMoO_4$ crystals and their optical, J. Cryst. Growth 10 (2010) 4752–4762.
[14] T. Thongtem, A. Phuruangrat, S. Thongtem, Preparation and characterization of nanocrystalline $SrWO_4$ using cyclic microwave radiation, Curr. Appl. Phys. 8 (2008) 189–197.
[15] W. Reichelt, T. Weber, T. Sohnel, S. Dabritz, Mischkristallbildung im system $CuMoO_4/ZnMoO_4$, Z. Anorg. Allg. Chem. 626 (2000) 2020–2027.
[16] K. Pavani, A. Ramanan, Influence of 2-aminopyridine on the formation of molybdates under hydrothermal conditions, Eur. J. Inorg. Chem. (2005) 3080–3087.
[17] L.H. Hoang, N.T.M. Hien, W.S. Choi, Y.S. Lee, K. Taniguchi, T. Arima, S. Yoon, X.B. Chena, I.S. Yang, Temperature-dependent Raman scattering study of multiferroic $MnWO_4$, J. Raman Spectrosc. 41 (2010) 1005–1010.
[18] L.S. Cavalcante, E. Moraes, M.A.P. Almeida, C.J. Dalmaschio, N.C. Batista, J.A. Varela, E. Longo, M. Siu Li, J. Andres, A. Beltran, A combined theoretical and experimental study of electronic structure and optical properties of α-$ZnMoO_4$, Polyhedron 54 (2013) 13–25.
[19] M. Markova-Velichkova, R. Iordanova, Y. Dimitriev, Glass formation in the V_2O_5–MoO_3–ZnO system, Phys. Status Solidi C 8 (2011) 3159.
[20] Y. Keereeta, T. Thongtem, S. Thongtem, Characterization of $ZnMoO_4$ nanofibers synthesized by electrospinning–calcination combinations, Mater. Lett. 68 (2012) 265–268.
[21] L. Aleksandrov, T. Komatsu, R. Iordanova, Y. Dimitriev, Structure study of MoO_3–ZnO–B_2O_3 glasses by Raman spectroscopy and formation of α-$ZnMoO_4$ nanocrystals, Opt. Mater. 33 (2011) 839–845.
[22] J. Šubcik, L. Koudelka, P. Mošner, L. Montagne, B. Revel, I. Gregora, Structure and properties of MoO_3-containing zinc borophosphate glasses, J. Non-Cryst. Solids 355 (2009) 970–975.
[23] A. Phuruangrat, T. Thongtem, S. Thongtem, Preparation, characterization and photoluminescence of nanocrystalline calcium molybdate, J. Alloys Compd. 481 (2009) 568–572.
[24] Y. Keereeta, T. Thongtem, S. Thongtem, Fabrication of $ZnWO_4$ nanofibers by a high direct voltage electrospinning process, J. Alloys Compd. 509 (2011) 6689–6695.
[25] S. Bhattacharya, T. Kar, A.K. Bar, D. Roy, M.P.F. Graca, M.A. Valente, Structural behaviors and optical properties of semiconducting zinc-molybdate glass nanocomposites, Sci. Adv. Mater. 3 (2011) 284–288.
[26] D.A. Spassky, A.N. Vasilev, I.A. Kamenskikh, V.V. Mikhailin, A.E. Savon, Y.A. Hizhnyi, et al, Electronic structure and luminescence mechanisms in $ZnMoO_4$ crystals, J. Phys. 23 (2011) 365501–365510.

Hindawi Publishing Corporation
Journal of Nanomaterials
Volume 2014, Article ID 261395, 9 pages
http://dx.doi.org/10.1155/2014/261395

Research Article

Decolorization of Methylene Blue by $Ag/SrSnO_3$ Composites under Ultraviolet Radiation

Patcharanan Junploy,[1] Titipun Thongtem,[1] Somchai Thongtem,[2,3] and Anukorn Phuruangrat[4]

[1] *Department of Chemistry, Faculty of Science, Chiang Mai University, Chiang Mai 50200, Thailand*
[2] *Department of Physics and Materials Science, Faculty of Science, Chiang Mai University, Chiang Mai 50200, Thailand*
[3] *Materials Science Research Center, Faculty of Science, Chiang Mai University, Chiang Mai 50200, Thailand*
[4] *Department of Materials Science and Technology, Faculty of Science, Prince of Songkla University, Hat Yai, Songkhla 90112, Thailand*

Correspondence should be addressed to Titipun Thongtem; ttpthongtem@yahoo.com and Somchai Thongtem; schthongtem@yahoo.com

Received 22 January 2014; Revised 23 May 2014; Accepted 25 May 2014

Academic Editor: Tianxi Liu

Copyright © 2014 Patcharanan Junploy et al. This is an open access article distributed under the Creative Commons Attribution License, which permits unrestricted use, distribution, and reproduction in any medium, provided the original work is properly cited.

$SrSn(OH)_6$ precursors synthesized by a cyclic microwave radiation (CMR) process were calcined at 900°C for 3 h to form rod-like $SrSnO_3$. Further, the rod-like $SrSnO_3$ and $AgNO_3$ in ethylene glycol (EG) were ultrasonically vibrated to form rod-like $Ag/SrSnO_3$ composites, characterized by X-ray diffraction (XRD), X-ray photoelectron spectroscopy (XPS), electron microscopy (EM), Fourier transform infrared (FTIR) spectroscopy, and UV-visible analysis. The photocatalyses of rod-like $SrSnO_3$, 1 wt%, 5 wt%, and 10 wt% $Ag/SrSnO_3$ composites were studied for degradation of methylene blue (MB, $C_{16}H_{18}N_3SCl$) dye under ultraviolet (UV) radiation. In this research, the 5 wt% $Ag/SrSnO_3$ composites showed the highest activity, enhanced by the electron-hole separation process. The photoactivity became lower by the excessive Ag nanoparticles due to the negative effect caused by reduction in the absorption of UV radiation.

1. Introduction

Strontium stannate ($SrSnO_3$) is a type of ABO_3 perovskite, at which A is commonly an alkaline earth such as Ca, Sr, and Ba, and B is a p-block posttransition metal in the periodic table. ABO_3 perovskite has been used for energy conversion, lithium ion batteries, stable capacitors, oxygen-permeable ceramic membranes, and gas sensors [1–4]. In recent years, $SrSnO_3$ has been widely used in photocatalytic applications [4–6]. Development of semiconductors to enhance photocatalytic activity by being deposited with noble transition metals like Ag, Au, Pt, and Ir has been intensively investigated. The noble metal/semiconducting oxide composites are able to slow down the rate of electron-hole recombination, due to the better charged separation of electrons and holes. The electrons accumulated on the metal and holes remained on the photocatalytic surfaces [7]. Silver nanoparticles exhibit unexpectedly high photocatalytic activities toward different types of reactions compared to the bulk and promote the performance of photocatalysis [8].

$SrSnO_3$ has been synthesized by different methods such as solid state reaction at a temperature above 1,000°C [2], hydrothermal method [3, 4], microemulsion [9], and polymeric precursor method [10]. Recently, microwave radiation has been used for the synthesis of materials, including inorganic complexes, oxides, and sulfides. Microwave radiation has shown very rapid growth in its application to materials science and engineering due to its unique reaction effect, such as rapid volumetric heating and the consequent dramatic increase in reaction rate [11, 12]. Silver nanoparticles can be deposited on substrates by polyol organic agent as a reducing agent in assisting the nucleation and growth of nanoparticles on a variety of substrates including silicon/carbon composite microspheres, polymer nanofibers, and TiO_2 nanoparticles [13–15].

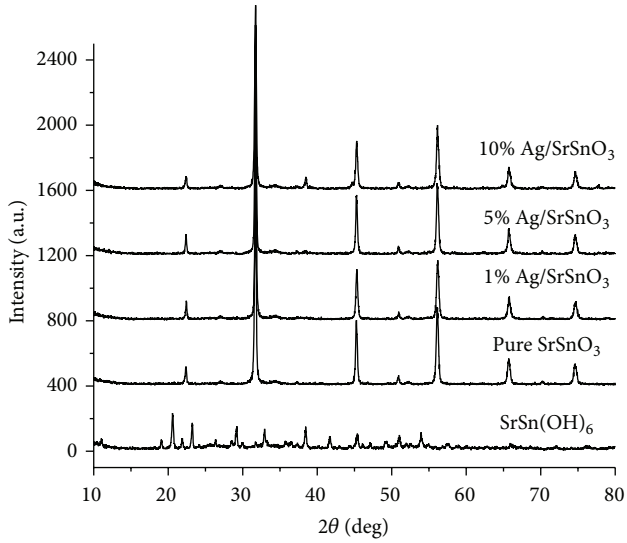


Figure 1: XRD patterns of $SrSn(OH)_6$ precursors, pure $SrSnO_3$, 1 wt%, 5 wt%, and 10 wt% $Ag/SrSnO_3$ composites.

In the present research, a cyclic microwave radiation (CMR) used for the synthesis of rod-like $SrSn(OH)_6$ precursors in surfactant-free solution with fast reaction time is reported. Metallic silver nanoparticles were doped with $SrSnO_3$ products to form $Ag/SrSnO_3$ composites, which are new candidates for photocatalysis for waste water treatment.

2. Experimental Procedures

To synthesize $SrSn(OH)_6$ precursors, 0.005 mol strontium acetate ($(CH_3CO_2)_2Sr$) and 0.005 mol tin(II) chloride dihydrate ($SnCl_2{\cdot}2H_2O$) were dissolved in 80 mL deionized water with 30 min continuous stirring at room temperature. The pH was adjusted to 12 using 3 M NaOH with continuous stirring for 1 h until white suspension was obtained. The mixture was irradiated by a 180 W cyclic microwave radiation (1 min on for every 1 min interval) for 30 cycles. The white precipitates were synthesized, separated using a filtered paper, rinsed with deionized water for several times and absolute ethanol, and dried in air at 70°C for 24 h. In the end, the $SrSn(OH)_6$ precursors were calcined in ambient atmosphere at 900°C for 3 h to form the $SrSnO_3$ product.

To synthesize $Ag/SrSnO_3$ composites, 1 wt%, 5 wt%, and 10 wt% $AgNO_3$ and 1 g $SrSnO_3$ were dispersed in 50 mL of ethylene glycol (EG, $C_2H_6O_2$) under magnetic stirring. The solutions were ultrasonically vibrated for 15 min to form products which were separated by filtering, washed with absolute ethanol, and dried in air at 70°C for 24 h to form $Ag/SrSnO_3$ composites. The final composites were labeled with 1 wt% $Ag/SrSnO_3$, 5 wt% $Ag/SrSnO_3$, and 10 wt% $Ag/SrSnO_3$.

The final products were characterized by an X-ray diffractometer (XRD, Philips X'Pert MPD) operating at 20 kV, 15 mA with Cu-K_α line (λ = 0.1542 nm) at a scanning rate of 0.02 deg/s over the 2θ range of 10–80 deg; X-ray photoelectron spectroscopy (XPS, Kratos Axis Ultra DLD) with a monochromatic Al Kα (1486.6 eV) radiation as the excitation source at 15 kV with spectrum calibration using a C1s electron peak at 285.1 eV; a Fourier transform infrared spectrometer (FTIR, Bruker Tensor 27) with KBr as a diluting agent operating in the range of 1000–400 cm^{-1}; a scanning electron microscope (SEM, JEOL JSM-6335F) operating at 15 kV equipped with an Oxford Instruments INCA energy-dispersive X-ray (EDX) analyzer using Si(Li) as a detector; a transmission electron microscope (TEM, JEOL JEM-2010) with a selected area electron diffractometer (SAED) operating at 200 kV; and a UV-visible spectrometer (Lambda 25 Perkin Elmer) using a UV lamp with the resolution of 2.0 nm. Photocatalytic activities of the products were investigated by studying the degradation of methylene blue (MB, $C_{16}H_{18}N_3SCl$) dye in 100 mL 5.0×10^{-6} M MB aqueous solutions by 100 mg photocatalyst each. The solutions were stirred in the dark condition for 1 h to establish an adsorption-desorption equilibrium of MB dye on the catalyst. Then, the solutions were irradiated by two 15 W UV lamps for different lengths of time for further analysis using the UV-visible spectrometer. The decolorization efficiency was calculated by

$$\text{Decolorization efficiency}\,(\%) = \frac{C_o - C}{C_o} \times 100, \quad (1)$$

where C_o and C were the initial and final concentrations of MB, respectively.

3. Results and Discussion

XRD patterns of different products are shown in Figure 1. The precursors were specified as hexagonal $SrSn(OH)_6$ phase of the JCPDS database number 09-0086 [16]. Upon calcination of the precursors at 900°C for 3 h, the products with high diffraction intensity and better crystalline degree were readily indexed to be orthorhombic perovskite structured $SrSnO_3$ of the JCPDS database number 77-1798 [16]. Then, $SrSnO_3$ products were doped with Ag nanoparticles to form $Ag/SrSnO_3$ composites. Comparing the patterns of the 1 wt% $Ag/SrSnO_3$, 5 wt% $Ag/SrSnO_3$, and 10 wt% $Ag/SrSnO_3$ composites to those of the JCPDS database number 09-0086 [16], they were still being identified as pure orthorhombic $SrSnO_3$ phase. No other peaks were detected in the XRD patterns of 1 wt% and 5 wt% $Ag/SrSnO_3$ composites. Possibly, concentration of Ag was too low to be detected. In case of 10 wt% $Ag/SrSnO_3$ composites, additional two peaks at 2θ of 38.50 and 77.84 deg were detected and specified as the (111) and (311) peaks of cubic Ag of the JCPDS database number 02-1098 [16], due to the reduction process $Ag^+ \rightarrow Ag^0$ by EG during ultrasonic vibration process. This detection indicated that Ag nanoparticles were only deposited on the $SrSnO_3$ surface. The average Ag particle size was estimated by Debye-Scherrer formula

$$D = \frac{0.9\lambda}{\beta \cos\theta}, \quad (2)$$

where λ is wave length of X-ray (0.15418 nm for Cu K_α), β is full width at half maximum (FWHM) in radian, θ is the

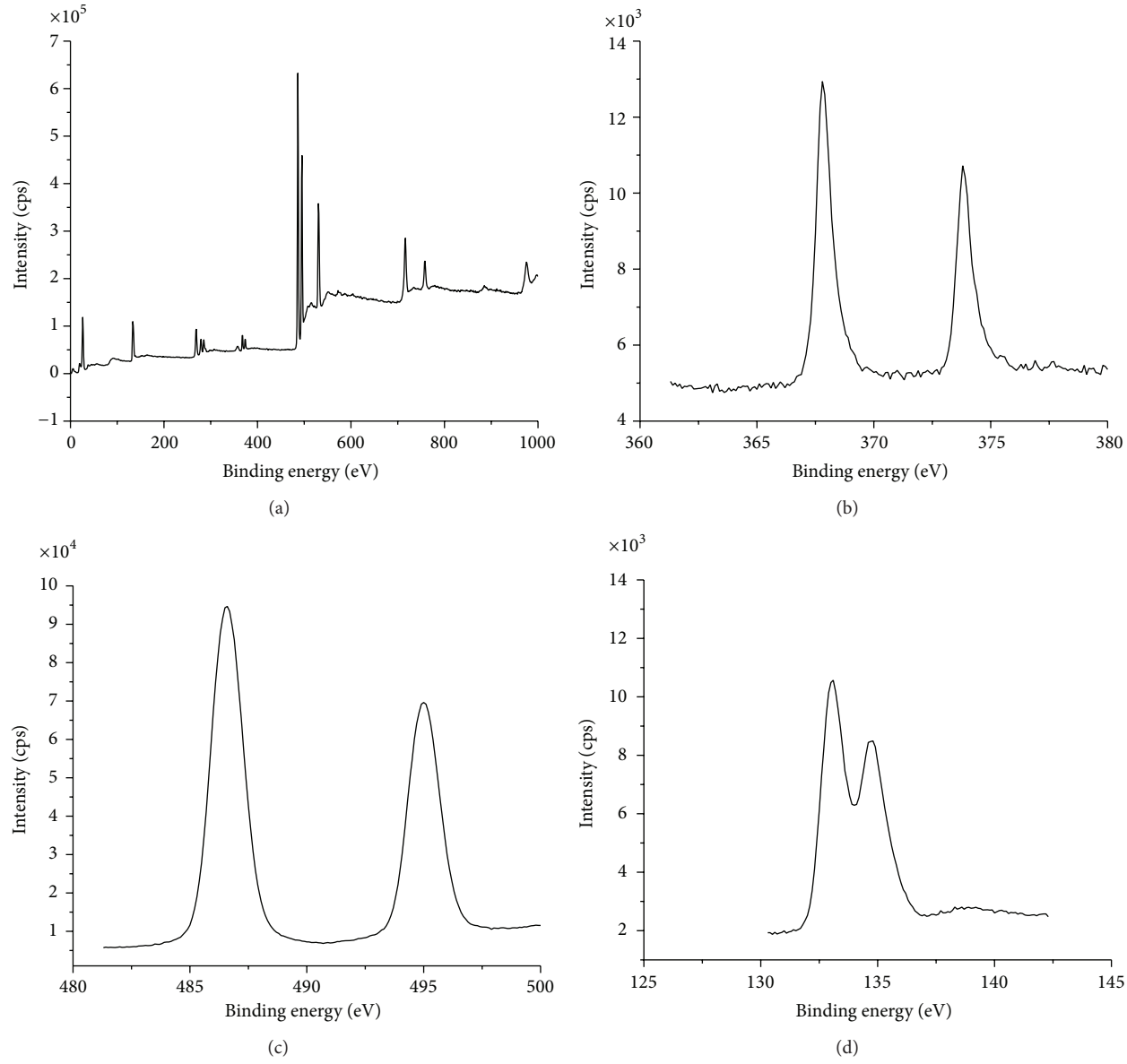


Figure 2: XPS spectra of (a) 10 wt% $Ag/SrSnO_3$, (b) Ag3d, (c) Sn3d, and (d) Sr3d.

diffraction angle, and D is particle diameter size [17]. The average particle size is 28.5 nm.

The 10 wt% $Ag/SrSnO_3$ composites were analyzed by XPS to identify the metallic state of silver (Ag^0) on the surface of the composites, as shown in Figure 2. The XPS analysis reveals the existing peaks of strontium, carbon (tape), silver, tin, and oxygen, consistent with the chemical components of the $Ag/SrSnO_3$ composites. The binding energy of C1s line (285.1 eV) was used to calibrate all the binding energies. The analysis reveals the silver 3d spectral lines of spin-orbit doublet peaks with a splitting of 6.07 eV at the binding energy of 367.77 and 373.84 eV for $Ag3d_{5/2}$ and $Ag3d_{3/2}$, respectively. These binding energies correspond with those of the metallic silver of the previous reports [18–21], indicating the presence of Ag^0 in $SrSnO_3$ matrix. The Sn3d peaks of 10 wt% $Ag/SrSnO_3$ composites appear at 486.60 eV of $Sn3d_{5/2}$ and 494.98 eV of $Sn3d_{3/2}$, corresponding to Sn^{4+} [22]. The Sr3d spectrum with spin-orbit doublet peaks corresponds to $Sr3d_{5/2}$ and $Sr3d_{3/2}$ peaks at 133.04 and 134.74 eV, respectively. They are in accordance with Sr^{2+} [23].

The as-synthesized pure $SrSnO_3$ and 1 wt%, 5 wt%, and 10 wt% $Ag/SrSnO_3$ composites were analyzed by FTIR at room temperature over the range from 400 to 1000 cm^{-1} (Figure 3). The vibration of the SnO_3^{2-} stannate groups of pure $SrSnO_3$ was detected as high intensity band at 677 cm^{-1} [24]. Moreover, the bands became shallower with increase in the amount of Ag contained in the $Ag/SrSnO_3$ composites, which indicates the interaction between silver and oxygen atoms in the stannate group of $SrSnO_3$. The result proved

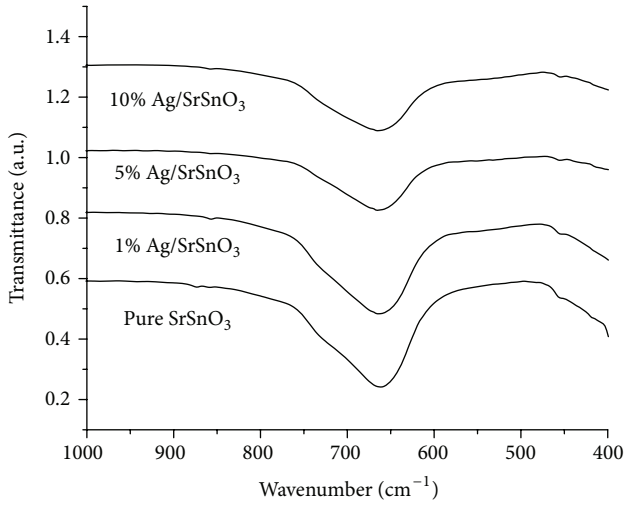


Figure 3: FTIR spectra of pure $SrSnO_3$, 1 wt%, 5 wt%, and 10 wt% $Ag/SrSnO_3$ composites.

that Ag nanoparticles were attached to the surface of $SrSnO_3$ samples.

The products were analyzed by electron microscopy (EM), energy dispersive X-ray (EDX) spectroscopy, and selected area electron diffraction (SAED), as shown in Figures 4, 5, 6, and 7. The $SrSn(OH)_6$ precursors demonstrate the formation of rod-like product with the size distribution of about 300–745 nm in diameter and one to several microns in length. For pure $SrSnO_3$, it still retains the morphology as the $SrSn(OH)_6$ precursors, but the rods became thinner with smooth surface due to the loss of hydroxyl group of the rod-like $SrSn(OH)_6$ precursors by transforming into rod-like $SrSnO_3$. The 10 wt% $Ag/SrSnO_3$ composites remained at the same size and shape as pure $SrSnO_3$ with the aggregated Ag nanoparticles (about 30 nm) formed on the surfaces of $SrSnO_3$ rods. The EDX qualitative analyses of 10 wt% $Ag/SrSnO_3$ composites were recorded as the mapping images of Ag, Sr, Sn, and O, which show the distributive Ag nanoparticles over the $SrSnO_3$ matrix. The EDX spectrum also corresponds to the four prominent peaks belonging to the Sr-L_α, Sn-L_α, O-$K_{\alpha 1,2}$, and Ag-L_α lines without any impurity detection. A SAED pattern shows diffraction rings of the polycrystalline rod-like $SrSn(OH)_6$ precursors corresponding to the (301), (222), (512), and (441) crystallographic planes of the JCPDS database number 09-0086 [16]. SAED patterns of two single crystalline rods of pure $SrSnO_3$ and 10 wt% $Ag/SrSnO_3$ composites were indexed and specified as $SrSnO_3$ orthorhombic phase of the JCPDS database number 77-1798 [16] in accordance with the patterns obtained by simulation. It should be noted that Ag nanoparticles were not detected in the 10 wt% $Ag/SrSnO_3$ composites because the SAED interpretation was selected for characterization only on a very small area.

Figure 8 presents the UV-visible absorption spectra of pure $SrSnO_3$ and 1 wt%, 5 wt%, and 10 wt% $Ag/SrSnO_3$ composites. In this research, the absorption intensity increased significantly around 300 nm in short wavelength for pure $SrSnO_3$ rods, but it did not show the absorption in the visible region, corresponding to the previous reports [4, 24]. By doping with Ag, its absorption intensity on the short-wavelength side was steeply increased compared to that of pure $SrSnO_3$ rods. A small absorption band in the visible region at 437 nm started appearing in the absorption spectrum of the 1 wt% $Ag/SrSnO_3$ composites and gradually shifted to the lower wavelength of 435 nm in the 10 wt% $Ag/SrSnO_3$ composites. Detection of the absorption spectra in the visible light region for $Ag/SrSnO_3$ composites indicates an increase in the absorption intensity with an increase in the Ag content. It is well known that surface plasmon bands appearing in the visible region are characteristic of the noble metal nanoparticles with sizes ranging from 2 nm to 100 nm [25] and surface plasmons are collective oscillations of free electrons at metallic surface [26]. This absorption band is attributed to the characteristic surface plasmon resonance (SPR) phenomenon of free electron in the conduction bands of Ag nanoparticles. When Ag nanoparticles were irradiated by visible light, a large oscillating electric field originated around the metallic particles [26–30]. Clearly, this result indicates the presence of Ag nanoparticles contained in $SrSnO_3$ matrix synthesized by the ultrasonic vibration.

The degradation of MB dye in aqueous solution containing 5 wt% $Ag/SrSnO_3$ composites (Figure 9) under ultraviolet radiation was studied. The intensity decrease in the characteristic absorption peak of MB dye at 663 nm for different lengths of time clearly shows the efficiency of catalytic activity of the photocatalyst. For the decolorization efficiency of MB (Figure 10), almost no degradation of MB dye was detected in the catalyst-free solution although the exposure time was as long as 320 min. This result indicates that the contribution of self-degradation was negligible. But for the solutions containing pure $SrSnO_3$, 1 wt% $Ag/SrSnO_3$, 5 wt% $Ag/SrSnO_3$, and 10 wt% $Ag/SrSnO_3$ composites, the decolorization efficiencies within 320 min were 84.8, 86.3, 99.5, and 92.6%, respectively. These implied that 5 wt% $Ag/SrSnO_3$ composites were the best photocatalyst for waste water treatment. The excess of Ag nanoparticles can cause deficiency in the photocatalytic activity of 10 wt% $Ag/SrSnO_3$ composites by lowering the absorption of UV light, leading to the decrease in UV light utilization with negative effect to the photocatalytic process [31]. Moreover, the 5 wt% $Ag/SrSnO_3$ composites were recycled and reused five times to test the photocatalytic stability shown in Figure 11. The photocatalyst is still performing the decolorization efficiency at almost the same rate.

The photocatalysis for organic compounds decomposed by $SrSnO_3$ with and without Ag nanoparticles doping under ultraviolet radiation is proposed (Figure 12). For $SrSnO_3$, electrons in valence band (VB) were excited and transferred to conduction band (CB) under UV light radiation. Then, the photogenerated holes in VB combined with hydroxyl anions to form $^{\bullet}OH$ oxidative species which would further decompose the organic compounds. The rapid recombination rate of electron-hole pairs can lead to low photocatalytic activity. When Ag nanoparticles were added to the $SrSnO_3$ product, the Ag nanoparticles acted as electron traps, inhibiting the electron-hole recombination process. Subsequently, the

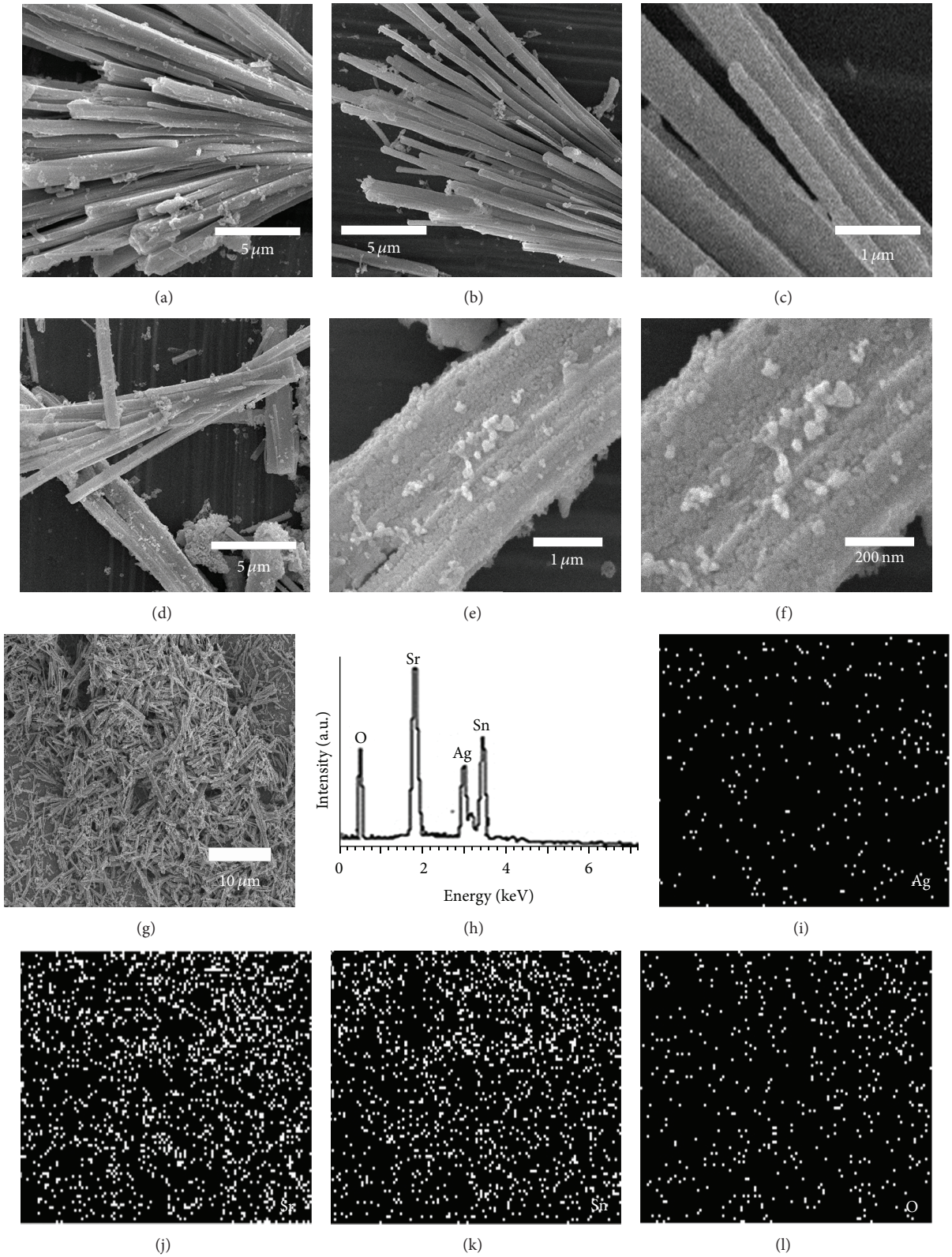


Figure 4: SEM images of (a) $SrSn(OH)_6$ precursors, (b, c) pure $SrSnO_3$, and (d–g) 10 wt% $Ag/SrSnO_3$ composites. (h) EDX spectrum of 10 wt% $Ag/SrSnO_3$ composites and (i–l) EDX mapping for Ag, Sr, Sn, and O of 10 wt% $Ag/SrSnO_3$ composites, respectively.

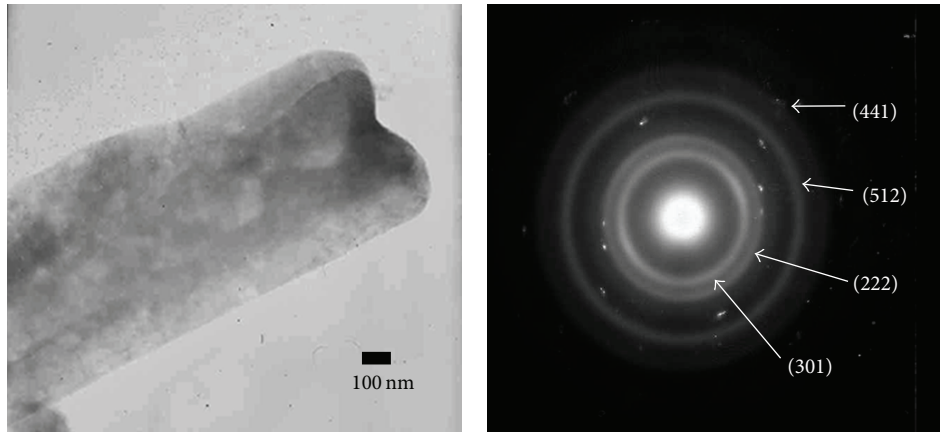


Figure 5: TEM image and SAED pattern of SrSn $(OH)_6$precursors.

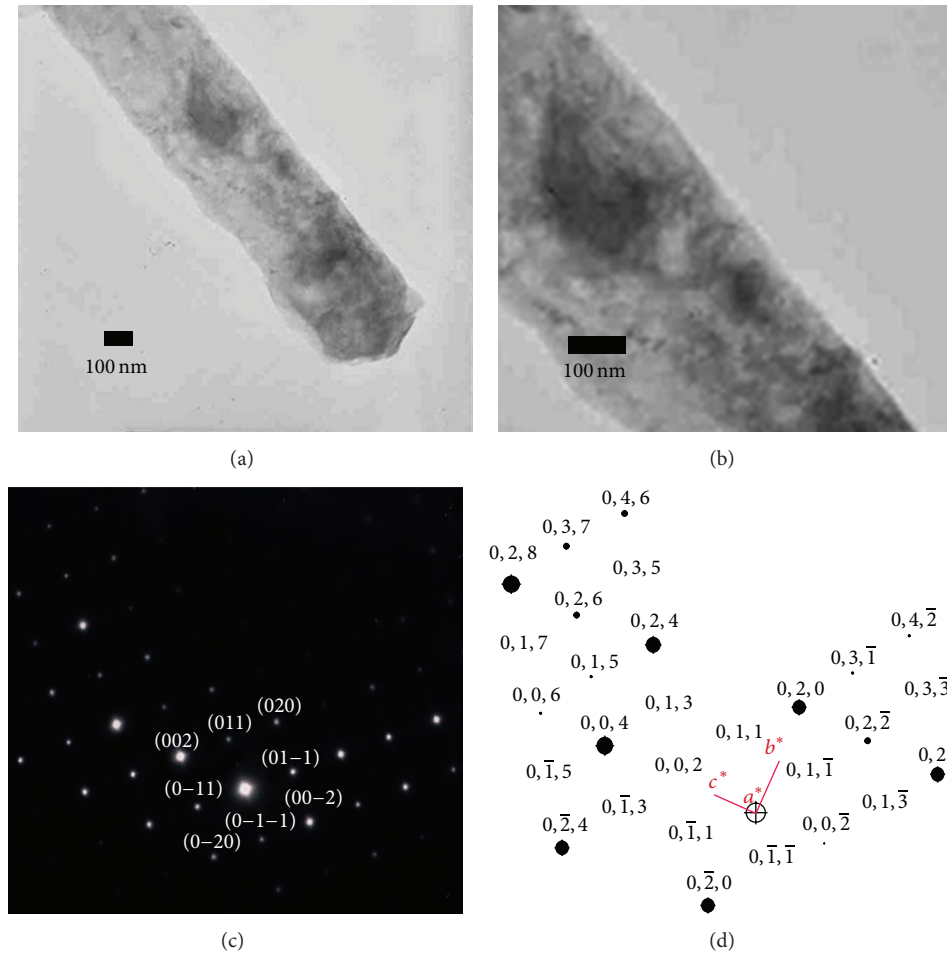


Figure 6: (a, b) TEM images and (c, d) SAED and simulated patterns of pure $SrSnO_3$, respectively.

trapped electrons were transferred to the adsorbed O_2, which acted as electron acceptors. Thus $^{\bullet}O_2^-$ oxidative species were generated and could effectively oxidize the MB dye. Holes still remained in the VB of $SrSnO_3$ and combined with H_2O to form H^+ ions and $^{\bullet}OH$ radicals. These oxidative species could effectively break down toxic organic substances back into original chemical forms of CO_2 and H_2O creating a cleaner

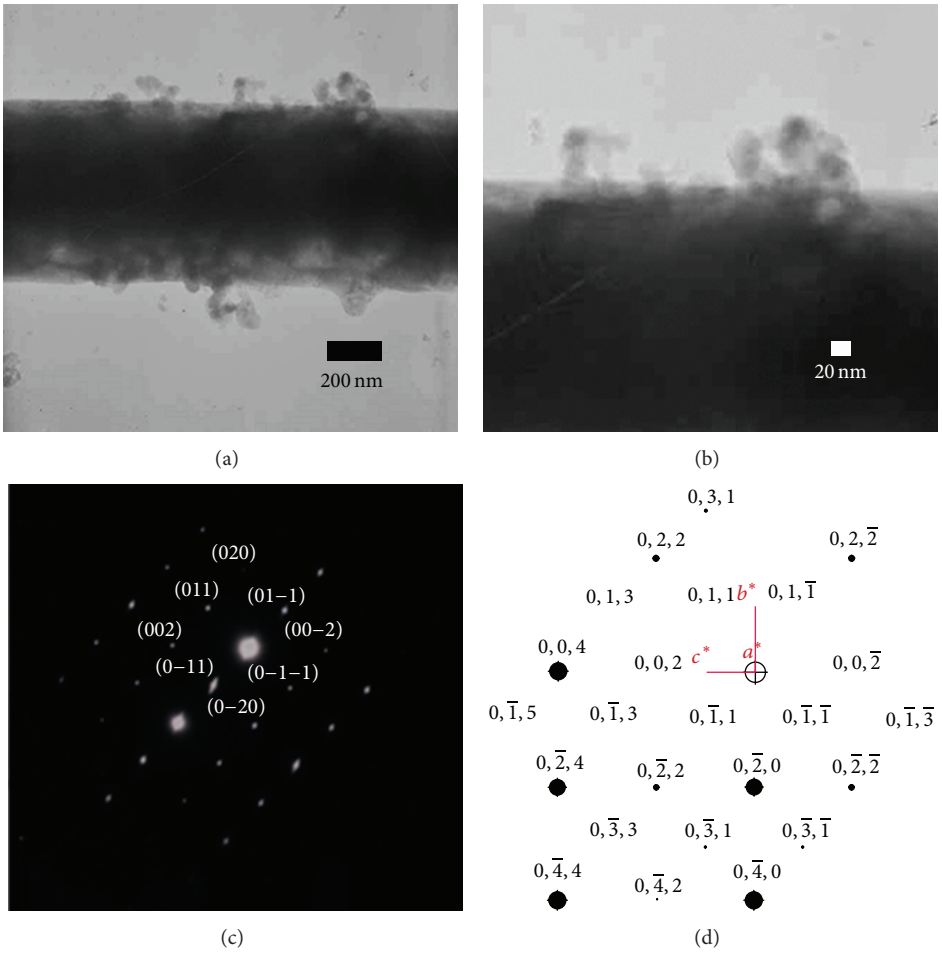


Figure 7: (a, b) TEM images and (c, d) SAED and simulated patterns of 10 wt% Ag/$SrSnO_3$ composites, respectively.

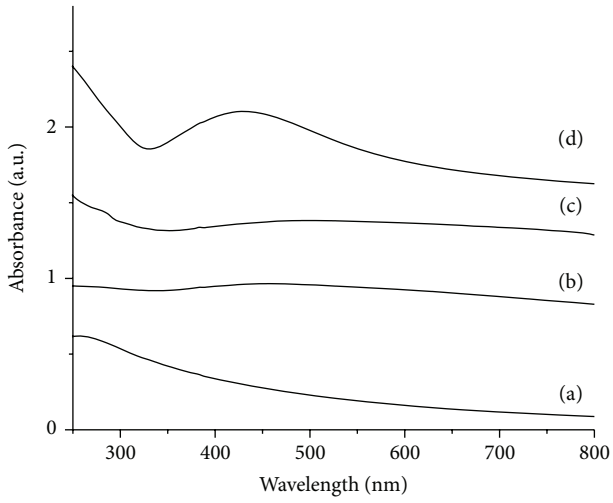


Figure 8: UV-visible absorption of (a) pure $SrSnO_3$ and (b–d) 1 wt%, 5 wt%, and 10 wt% Ag/$SrSnO_3$ composites, respectively.

and safer environment [32]. The recombination of electron-hole pairs was inhibited, and the photochemical reaction for waste water treatment was enhanced [33, 34].

4. Conclusions

A solution containing strontium acetate and tin(II) chloride dihydrate with the pH of 12 was processed by a cyclic microwave radiation (CMR) to form $SrSn(OH)_6$ precursors, which were calcined at 900°C for 3 h to form $SrSnO_3$. Further, the $SrSnO_3$ precursors and $AgNO_3$ in ethylene glycol were ultrasonically vibrated to form Ag/$SrSnO_3$ composites, which were tested for photocatalysis under ultraviolet radiation for the degradation of MB dye as an organic model. In this research, the 5 wt% Ag/$SrSnO_3$ composites showed the best photocatalyst due to the enhancement of electron-hole separation process.

Conflict of Interests

The authors declare that there is no conflict of interests regarding the publication of this paper.

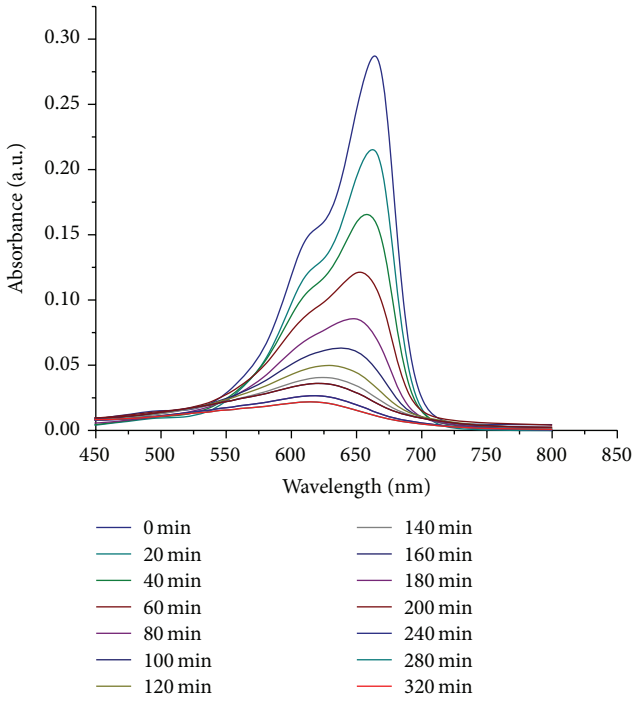


FIGURE 9: UV-visible absorption of MB photocatalyzed by the 5 wt% $Ag/SrSnO_3$ composites under UV light for different lengths of time.

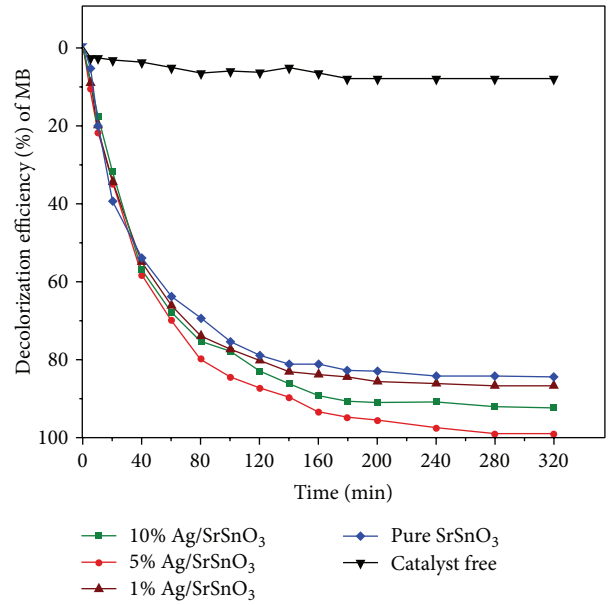


FIGURE 10: Decolorization efficiencies of MB dye dissolving in different solutions of photocatalyst-free, pure $SrSnO_3$, and 1 wt%, 5 wt%, and 10 wt% $Ag/SrSnO_3$ composites under UV light for different lengths of time.

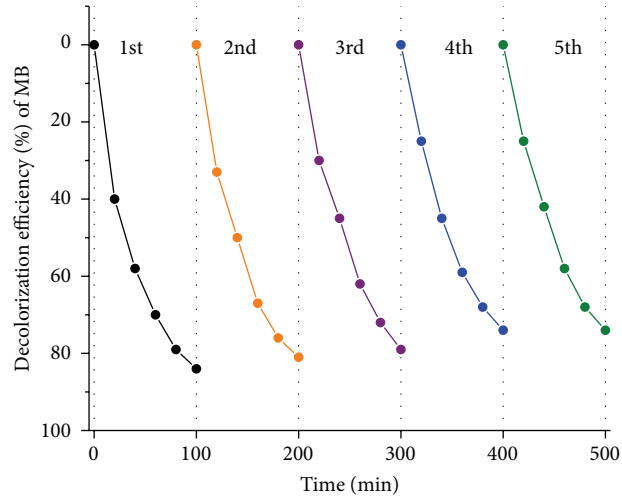


FIGURE 11: Cycling runs of photodecolorization efficiencies of MB photocatalyzed by 5 wt% $Ag/SrSnO_3$ composites.

Acknowledgments

The authors wish to thank the Thailand Research Fund (TRF) for providing financial support through the Royal Golden Jubilee Ph.D. Program and the TRF Research Grant BRG5380020 and the Thailand's Office of the Higher Education Commission through the National Research University (NRU) Project for Chiang Mai University (CMU), including the Graduate School of CMU through a general support.

References

[1] N. Zidi, S. Omeiri, B. Hadjarab, A. Bouguelia, A. Akroun, and M. Trari, "Transport properties and photo electrochemical characterization of oxygen-deficient $ASnO_{3-\delta}$ (A=Ca, Sr and Ba)," *Physica B*, vol. 405, no. 16, pp. 3355–3359, 2010.

[2] M. C. F. Alves, S. Boursicot, S. Ollivier et al., "Synthesis of $SrSnO_3$ thin films by pulsed laser deposition: Influence of substrate and deposition temperature," *Thin Solid Films*, vol. 519, no. 2, pp. 614–618, 2010.

[3] C. Li, Y. Zhu, S. Fang et al., "Preparation and characterization of $SrSnO_3$ nanorods," *Journal of Physics and Chemistry of Solids*, vol. 72, no. 7, pp. 869–874, 2011.

[4] D. Chen and J. Ye, "$SrSnO_3$ nanostructures: synthesis, characterization, and photocatalytic properties," *Chemistry of Materials*, vol. 19, no. 18, pp. 4585–4591, 2007.

[5] C. W. Lee, D. W. Kim, I. S. Cho et al., "Simple synthesis and characterization of $SrSnO_3$ nanoparticles with enhanced photocatalytic activity," *International Journal of Hydrogen Energy*, vol. 37, no. 14, pp. 10557–10563, 2012.

[6] W. F. Zhang, J. Tang, and J. Ye, "Photoluminescence and photocatalytic properties of $SrSnO_3$ perovskite," *Chemical Physics Letters*, vol. 418, no. 1–3, pp. 174–178, 2006.

[7] H. Sinaim, A. Phuruangrat, S. Thongtem, and T. Thongtem, "Synthesis and characterization of heteronanostructured Ag nanoparticles/MoO_3 nanobelts composites," *Materials Chemistry and Physics*, vol. 132, no. 2-3, pp. 358–363, 2012.

[8] G. Li, K. Chao, C. Ye, and H. Peng, "One-step synthesis of Ag nanoparticles supported on $AgVO_3$ nanobelts," *Materials Letters*, vol. 62, no. 4-5, pp. 735–738, 2008.

[9] J. Ahmed, C. K. Blakely, S. R. Bruno, and V. V. Poltavets, "Synthesis of $MSnO_3$ (M = Ba, Sr) nanoparticles by reverse micelle method and particle size distribution analysis by whole powder pattern modeling," *Materials Research Bulletin*, vol. 47,

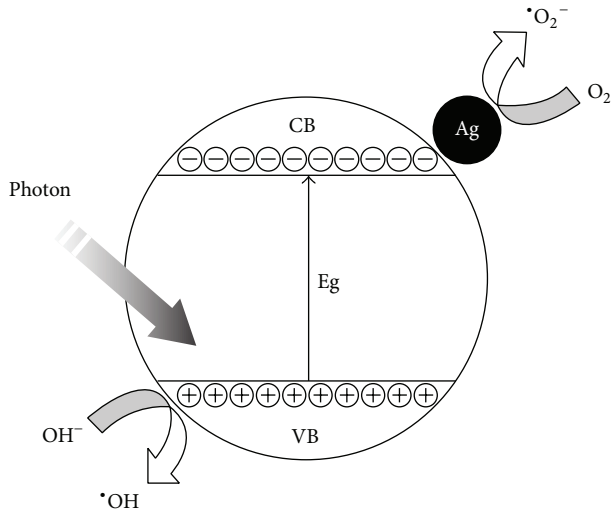


Figure 12: Schematic diagram for the photocatalysis of $Ag/SrSnO_3$ composites.

no. 9, pp. 2282–2287, 2012.

[10] M. C. F. Alves, M. R. Nascimento, S. J. G. Lima et al., "Influence of synthesis conditions on carbonate entrapment in perovskite $SrSnO_3$," *Materials Letters*, vol. 63, no. 1, pp. 118–120, 2009.

[11] T. Ding and J. Zhu, "Microwave heating synthesis of HgS and PbS nanocrystals in ethanol solvent," *Materials Science and Engineering B: Solid-State Materials for Advanced Technology*, vol. 100, no. 3, pp. 307–313, 2003.

[12] T. Thongtem, A. Phuruangrat, and S. Thongtem, "Characterization of nano- and micro-crystalline CdS synthesized using cyclic microwave radiation," *Journal of Physics and Chemistry of Solids*, vol. 69, no. 5-6, pp. 1346–1349, 2008.

[13] E. Kwon, H. S. Lim, Y. K. Sun, and K. D. Suh, "Improved rate capability of lithium-ion batteries with Ag nanoparticles deposited onto silicon/carbon composite microspheres as an anode material," *Solid State Ionics*, vol. 237, pp. 28–33, 2013.

[14] Q. Liu, S. Sun, H. Li et al., "Preparation, characterization and photocatalytic activities of $ZrWMoO_8$/Ag composites with core-shell structure," *Applied Surface Science*, vol. 261, pp. 593–597, 2012.

[15] G. Li, H. Liu, H. Zhao et al., "Chemical assembly of TiO_2 and TiO_2@Ag nanoparticles on silk fiber to produce multifunctional fabrics," *Journal of Colloid and Interface Science*, vol. 358, no. 1, pp. 307–315, 2011.

[16] Powder Diffract File, JCPDS-ICDD, Delaware County, Pa, USA, 2001.

[17] T. Theivasanthi and M. Alagar, "Electrolytic synthesis and characterization of silver nanopowder," *Nano Biomedicine and Engineering*, vol. 4, no. 2, pp. 58–65, 2012.

[18] B. Yu, K. M. Leung, Q. Guo, W. M. Lau, and J. Yang, "Synthesis of Ag-TiO2 composite nano thin film for antimicrobial application," *Nanotechnology*, vol. 22, no. 11, Article ID 115603, 2011.

[19] S. Hu, F. Li, and Z. Fan, "A convenient method to prepare AG deposited N-TiO_2 composite nanoparticles via NH_3 plasma treatment," *Bulletin of the Korean Chemical Society*, vol. 33, no. 7, pp. 2309–2314, 2012.

[20] W. Song, Y. Wang, H. Hu, and B. Zhao, "Fabrication of surface-enhanced Raman scattering-active ZnO/Ag composite microspheres," *Journal of Raman Spectroscopy*, vol. 38, no. 10, pp. 1320–1325, 2007.

[21] X. Zhu, Z. Zhang, K. Wang et al., "A facile route to mechanically durable responsive surfaces with reversible wettability switching," *New Journal of Chemistry*, vol. 36, no. 5, pp. 1280–1284, 2012.

[22] M. Kwoka, L. Ottaviano, M. Passacantando, S. Santucci, G. Czempik, and J. Szuber, "XPS study of the surface chemistry of L-CVD SnO_2 thin films after oxidation," *Thin Solid Films*, vol. 490, no. 1, pp. 36–42, 2005.

[23] V. Kozhukharov, M. Machkova, P. Ivanov, H. J. M. Bouwmeester, and R. van Doorn, "Surface analysis of doped lanthanide cobalt perovskites by X-ray photoelectron spectroscopy," *Journal of Materials Science Letters*, vol. 15, no. 19, pp. 1727–1729, 1996.

[24] P. Junploy, S. Thongtem, and T. Thongtem, "Photoabsorption and photocatalysis of $SrSnO_3$ produced by a cyclic microwave radiation," *Superlattices and Microstructures*, vol. 57, pp. 1–10, 2013.

[25] K. Mollazadeh-Moghaddam, B. V. Moradi, R. Dolatabadi-Bazaz, M. Shakibae, and A. R. Shahverdi, "An enhancing effect of gold nanoparticles on the lethal action of 2450 MHz electromagnetic radiation in microwave oven," *Avicenna Journal of Medical Biotechnology*, vol. 3, no. 4, pp. 195–200, 2011.

[26] S. S. Gasaymeh, S. Radiman, L. Y. Heng, E. Saion, and G. H. M. Saeed, "Synthesis and characterization of silver/polyvinilpirrolidone (Ag/PVP) nanoparticles using gamma irradiation techniques," *African Physical Review*, vol. 4, pp. 31–41, 2010.

[27] L. S. Daniel, H. Nagai, and M. Sato, "Absorption spectra and photocurrent densities of Ag nanoparticle/TiO_2 composite thin films with various amounts of Ag," *Journal of Materials Science*, vol. 48, no. 20, pp. 7162–7170, 2013.

[28] X. Yin, W. Que, D. Fei, F. Shen, and Q. Guo, "Ag nanoparticle/ZnO nanorods nanocomposites derived by a seed-mediated method and their photocatalytic properties," *Journal of Alloys and Compounds*, vol. 524, pp. 13–21, 2012.

[29] R. Chahal, S. Mahendia, A. K. Tomar, and S. Kumar, "Effect of ultraviolet irradiation on the optical and structural characteristics of in-situ prepared PVP-Ag nanocomposites," *Digest Journal of Nanomaterials and Biostructures*, vol. 6, no. 1, pp. 301–308, 2011.

[30] Q. Wang, S. Wang, W. Hang, and Q. Gong, "Optical resonant absorption and third-order nonlinearity of (Au,Ag)-TiO_2 granular composite films," *Journal of Physics D: Applied Physics*, vol. 38, no. 3, pp. 389–391, 2005.

[31] S. Hu, F. Li, and Z. Fan, "Preparation of SiO_2-coated TiO_2 composite materials with enhanced photocatalytic activity under UV light," *Bulletin of the Korean Chemical Society*, vol. 33, no. 6, pp. 1895–1899, 2012.

[32] C. Wu and J. Chern, "Kinetics of photocatalytic decomposition of methylene blue," *Industrial and Engineering Chemistry Research*, vol. 45, no. 19, pp. 6450–6457, 2006.

[33] C. Yu and J. C. Yu, "Sonochemical fabrication, characterization and photocatalytic properties of Ag/$ZnWO_4$ nanorod catalyst," *Materials Science and Engineering B: Solid-State Materials for Advanced Technology*, vol. 164, no. 1, pp. 16–22, 2009.

[34] C. Gu, C. Cheng, H. Huang, T. Wong, N. Wang, and T. Zhang, "Growth and photocatalytic activity of dendrite-like ZnO@Ag heterostructure nanocrystals," *Crystal Growth & Design*, vol. 9, no. 7, pp. 3278–3285, 2009.

Hindawi Publishing Corporation
Journal of Nanomaterials
Volume 2014, Article ID 739251, 8 pages
http://dx.doi.org/10.1155/2014/739251

Research Article

Photocatalysis of WO_3 Nanoplates Synthesized by Conventional-Hydrothermal and Microwave-Hydrothermal Methods and of Commercial WO_3 Nanorods

Jarupat Sungpanich,[1] Titipun Thongtem,[2,3] and Somchai Thongtem[1,3]

[1] *Department of Physics and Materials Science, Faculty of Science, Chiang Mai University, Chiang Mai 50200, Thailand*
[2] *Department of Chemistry, Faculty of Science, Chiang Mai University, Chiang Mai 50200, Thailand*
[3] *Materials Science Research Center, Faculty of Science, Chiang Mai University, Chiang Mai 50200, Thailand*

Correspondence should be addressed to Titipun Thongtem; ttpthongtem@yahoo.com
and Somchai Thongtem; schthongtem@yahoo.com

Received 6 May 2014; Accepted 5 July 2014; Published 7 August 2014

Academic Editor: Sheng-Rui Jian

Copyright © 2014 Jarupat Sungpanich et al. This is an open access article distributed under the Creative Commons Attribution License, which permits unrestricted use, distribution, and reproduction in any medium, provided the original work is properly cited.

The degradation of methylene blue (MB) dye by tungsten oxide (WO_3) photocatalyst synthesized by the 200°C conventional-hydrothermal (C-H) and 270 W microwave-hydrothermal (M-H) methods and commercial WO_3 was studied under UV light irradiation for 360 min. The photocatalysts were characterized by X-ray diffraction (XRD), scanning electron microscopy (SEM), transmission electron microscopy (TEM), Fourier transform infrared (FTIR) spectroscopy, Raman spectrophotometry, and UV visible spectroscopy to determine phase, morphology, vibration mode, and optical property. The BET analysis revealed the specific surface area of 29.74, 37.25, and 33.56 m^2/g for the C-H WO_3 nanoplates, M-H WO_3 nanoplates, and commercial WO_3 nanorods, respectively. In this research, the M-H WO_3 nanoplates have the highest photocatalytic efficiency of 90.07% within 360 min, comparing to the C-H WO_3 nanoplates and even commercial WO_3 nanorods.

1. Introduction

In the past decade, nanostructured materials with zero-dimensional quantum dots, one-dimensional nanofibers, nanotubes, and nanorods, and two-dimensional nanoplates and nanodisks have been widely synthesized and studied of their novel properties which are different from their counterparts [1]. Particularly, transition metal oxide based nanostructured semiconductors have become a rapid expansion in modern materials science, physics, and chemistry [2, 3]. Tungsten oxide is an *n*-type semiconductor having attractive properties, especially as photochromic and electrochromic materials, and novel potential applications for using as gas sensors [3–5], humidity sensors [6], electrochromic devices [7], and photocatalysts [1, 5, 8, 9]. During the last several decades, nanostructured WO_3 has been synthesized by different processes: hydrothermal method [5, 9, 10], microwave radiation [11], microwave plasma [12], microwave-assisted hydrothermal synthesis [8, 13], and sol-gel [6, 7]. Most previous approaches to the synthesis of WO_3 nanomaterials such as conventional-hydrothermal and microwave-hydrothermal methods have several advantages. Komarneni [14] reported that these methods consumed less energy and were cost-effective and environmental friendly, and that the products are high purified single crystal. Although the hydrothermal process is slow kinetics at any given temperature, a combination of microwave and hydrothermal systems has been used to increase the kinetics of crystallization [14]. Due to the environmental remedy and energy-saving, photocatalytic semiconductors have been carried out. Sun et al. [15] described two main limitations for the wide use of the semiconductors: the low solar energy conversion efficiency due to their wide band gap and the high recombination rate of photo-induced electron-hole pairs. WO_3 as one of the photocatalytic materials has been extensively investigated, mainly due to its high activities for hydrogen evolution from water and degradation

of pollutants for water treatment [9, 16, 17]. The physical and chemical properties of the solid semiconductor surfaces are controlled by the synthesis method [18]. In the previous research [13], WO_3 nanoplates were successfully synthesized by a 270 W microwave-hydrothermal reaction for 180 min and the formation mechanism was also proposed according to the experimental results. At present, photocatalysis of WO_3 nanoplates synthesized by the conventional-hydrothermal (C-H) method at 200°C for 12 h, WO_3 nanoplates synthesized by the 270 W microwave-hydrothermal (M-H) method for 180 min [13], and commercial (com) WO_3 nanorods was investigated by determining the photodegradation of methylene blue (MB) dye under UV light irradiation.

2. Experimental Procedure

2.1. Synthesis. To synthesize WO_3 nanoplates, 1 mmol sodium tungstate ($Na_2WO_4{\cdot}2H_2O$, 99.0%) and 0.2 g citric acid ($C_6H_8O_7{\cdot}H_2O$) were dissolved in 40 mL deionized water with 10 min vigorous magnetic stirring till complete dissolution. Subsequently, 37% HCl was dropped to the solution until pH reaching 1. Then the solution was vigorously stirred by a magnetic stirrer for 30 min until the turbid yellow solution was obtained. Each of the turbid yellow solutions was transferred into Teflon lined stainless steel autoclaves, which were heated at 120, 160, and 200°C for 12 h. In the end, the autoclaves were naturally cooled to room temperature. The as-synthesized yellow precipitates were washed with ethanol and distilled water three times and dried at 80°C for 24 h for further studies. The system was also processed by the 270 W microwave-hydrothermal reaction for 180 min.

2.2. Characterization. The final products were characterized by Rigaku MiniFlex X-ray diffractometer with Cu-K_α radiation (λ = 1.54178 Å) ranging from 10° to 80°, in combination with database of the Joint Committee on Powder Diffraction Standards (JCPDS) [19]. The scanning electron microscopic (SEM) images were carried out by field emission scanning electron microscopy (JEOL JSM-6335F). Transmission electron microscopic (TEM) and high-resolution transmission electron microscopic (HRTEM) images and selected area electron diffraction (SAED) pattern were taken on a transmission electron microscope (JEOL JEM-2010) accelerating at a voltage of 200 kV. Fourier transform infrared (FTIR) spectra were recorded on a Bruker Tensor 27 spectrometer with KBr as a diluting agent and operated in the range of 400–4000 cm^{-1}. Raman spectra were recorded on a T64000 HORIBA Jobin Yvon spectrometer using a 50 mW and 514.5 nm wavelength Ar green laser. UV-visible absorption spectra were recorded on a Lambda 25 Perkin Elmer spectrometer using a UV lamp with 1 nm resolution ranging from 300 to 1000 nm. The Brunauer-Emmett-Teller (BET) surface area was determined by a Quantachrome Autosorb 1-MP.

2.3. Photocatalysis. Photocatalytic activities of the WO_3 nanoplates synthesized by the M-H and C-H methods and the commercial WO_3 (Merck) nanorods were tested in a methylene blue ($C_{16}H_{18}N_3SCI$, MB) aqueous media under UV radiation. The initial concentration of 100 mL aqueous MB solution was set as 1×10^{-5} mol/L and loaded with 0.1 g WO_3. The suspension was irradiated by a 18 W UV lamp with the average light intensity of 50.7 W/m^2. The concentration of MB was traced by UV-visible spectroscopy (Lambda 25 Perkin Elmer) in the range of 450–900 nm and the absorbance at the characteristic band of 664 nm was used to determine MB concentration.

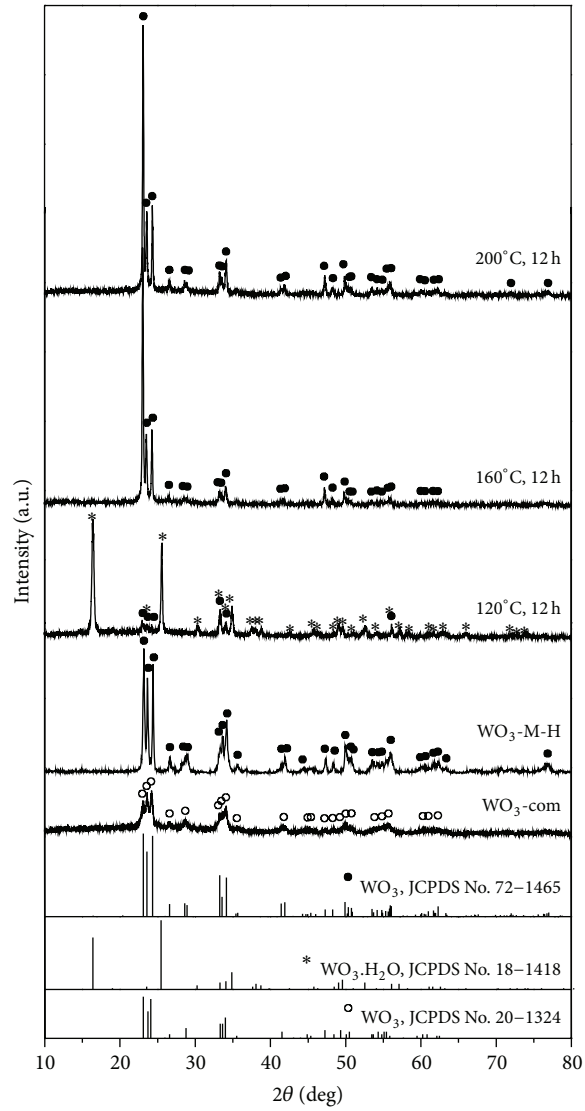


Figure 1: XRD patterns of the products synthesized by the C-H at 120, 160, and 200°C for 12 h and M-H at 270 W for 180 min and commercial (com) WO_3.

3. Results and Discussion

3.1. XRD. Comparing XRD spectra (Figure 1) of the products synthesized by the C-H method at 120, 160, and 200°C for 12 h with the JCPDS database (WO_3, No. 72-1465) [19], they corresponded with pure monoclinic crystal system and P21/n

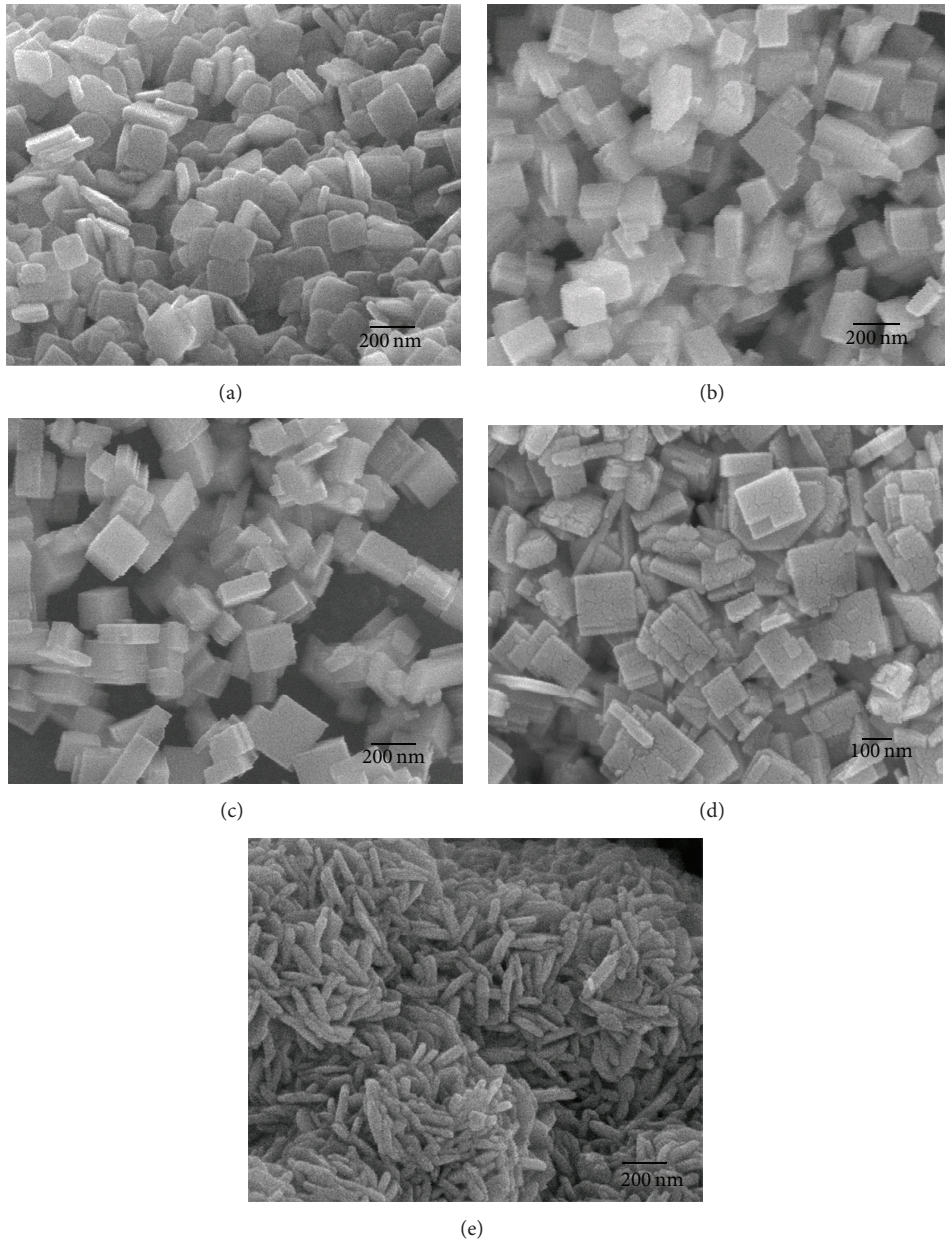


Figure 2: SEM images of the products, respectively, synthesized by the (a)–(c) C-H at 120, 160, and 200°C for 12 h and (d) M-H at 270 W for 180 min and (e) commercial WO_3.

space group at the synthesis temperatures of 160 and 200°C for 12 h. At 120°C, the product was composed of mixed phases of monoclinic WO_3 and orthorhombic $WO_3 \cdot H_2O$ (JCPDS No. 18-1418) [19]. Upon increasing the operation temperature to 160 and 200°C, pure monoclinic phase of WO_3 was detected. Their XRD intensity peaks were strengthened in sequence with the increase in the test temperature from 160°C to 200°C. In addition, the diffraction peaks of WO_3 synthesized by 270 W microwave-hydrothermal processed for 180 min [13] are also identical to the monoclinic phase of the JCPDS No. 72-1465 [19]. For commercial WO_3, the XRD pattern confirmed that the powder was composed of orthorhombic phase of WO_3 (JCPDS No. 20-1324) [19].

3.2. SEM. Morphologies of the products synthesized at 120, 160, and 200°C for 12 h were characterized by SEM as shown in Figures 2(a)–2(c). It can be clearly seen that irregular nanoplates of the products gradually transformed into completely rectangular shape by increasing the synthesis temperature. The particles were randomly oriented in different directions as those of the previous report [13]. The C-H synthesis surface of WO_3 was smoother than the M-H synthesis one (Figure 2(d)). Some traces of cracks were also detected on the M-H rectangular nanoplates. These cracks can play the role in promoting the product porosity. In this research, the C-H nanoplates are 50–100 nm thick, thicker than WO_3 nanoplates of the M-H. These imply that stability

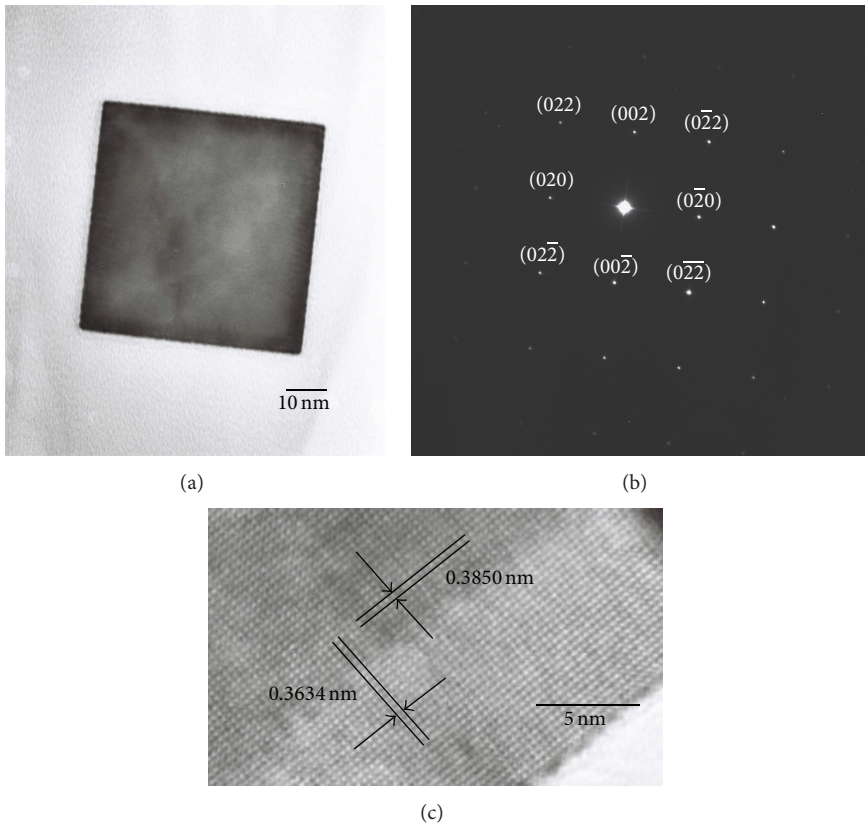


Figure 3: (a) TEM image, (b) SAED pattern, and (c) HRTEM image of WO_3 synthesized by the C-H at 200°C for 12 h.

of the pressure, temperature, and prolonged time can play a role in the crystal growth. The growth mechanism can be explained as follows: tiny nuclei formed by the reaction of $Na_2WO_4{\cdot}2H_2O$ and $C_6H_8O_7{\cdot}H_2O$ in the solution with the pH of 1 and grew as orthorhombic $WO_3{\cdot}H_2O$ irregular nanoplates at 120°C. By increasing the temperature to 160 and 200°C, monoclinic WO_3 rectangular nanoplates with anisotropic growth rate were detected, especially, at 200°C. It should be noted that the growth of WO_3 nanoparticles could be changed during phase transformation and was controlled by citric acid [13]. The SEM image of commercial WO_3 was also shown in Figure 2(e). It was composed of nanoparticles clustered together in the shape of nanorods with <100 nm diameter and ~200 nm length.

3.3. TEM. The morphology and phase of the product synthesized by the C-H at 200°C for 12 h were characterized by TEM, HRTEM, and SAED and are shown in Figure 3. In this research, the WO_3 product was shaped like rectangular nanoplates with the width and length of several 10 nm. SAED pattern of the product was indexed [19] to correspond with the (0 2 2), (0 0 2), (0 −2 2), (0 −2 0), (0 −2 −2), (0 0 −2), (0 2 −2), and (0 2 0) planes, specified as single crystalline WO_3 [19]. The electron beam was in the [1 0 0] direction. The HRTEM image of the product revealed the presence of lattice plane separation of 0.3850 nm and 0.3634 nm corresponding to the interlayer stacking of the (0 0 2) and (2 0 0) crystallographic planes of WO_3 (JCPDS No. 72-1465) [19], respectively.

3.4. FTIR. The FTIR spectra (Figure 4(a)) provided further insight into the structure of the products synthesized by the C-H at different temperatures for 12 h and commercial WO_3. At 120°C synthesis, the major vibration modes associated with O–H stretching of residual water was detected at 3655–3122 cm^{-1}, C=O stretching modes at 1626 cm^{-1}, C–O stretching modes of carboxyl at 948 cm^{-1}, O–W–O stretching modes at 814 and 746 cm^{-1}, and W–O–W stretching modes at 669 cm^{-1} [20–23]. Upon increasing the temperature from 120°C to 160°C and 200°C, the O–H and C=O stretching modes were no longer detected. For commercial WO_3, the observed peak was assigned to W–O bonding.

3.5. Raman Analysis. A definite existence of the products synthesized by the C-H at different temperatures for 12 h and commercial WO_3 was revealed by Raman analysis (Figure 4(b)). For WO_3 synthesized at 160 and 200°C and commercial WO_3, two main peaks are typical O–W–O stretching modes of crystalline WO_3 at 802 cm^{-1} (symmetric) for the shorter bonds, and 712 cm^{-1} (asymmetric) for the longer ones. Weak peaks at 610 cm^{-1} are assigned as the O–W–O stretching modes of WO_3. Those at 325, 273, and 241 cm^{-1} are specified as W–O–W bending modes of the

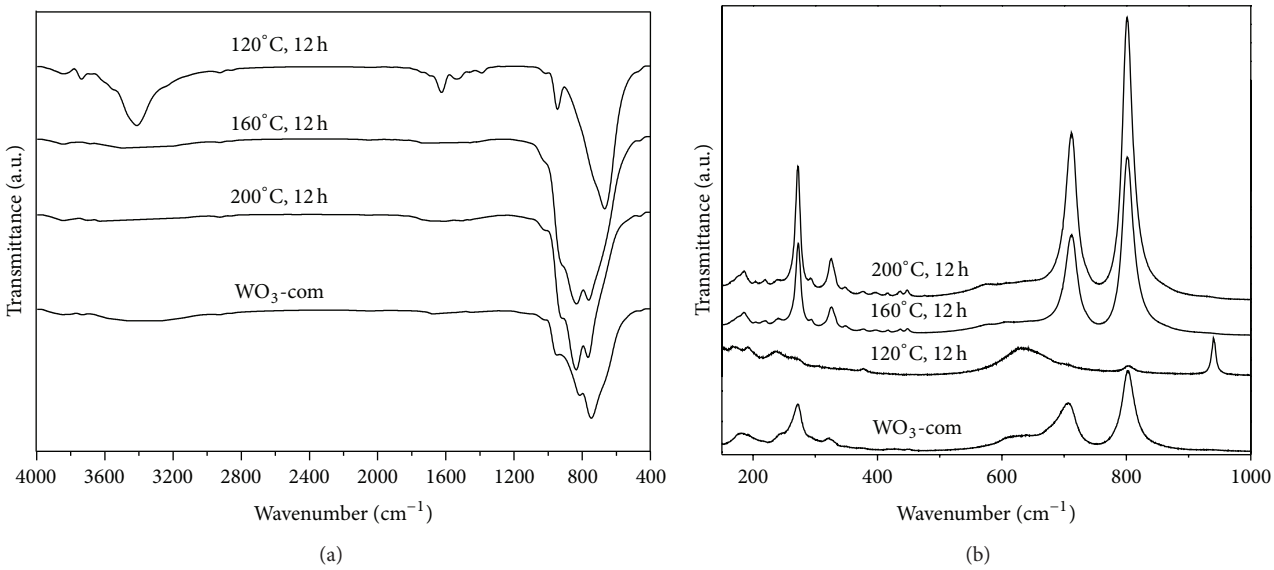


Figure 4: (a) FTIR and (b) Raman spectra of the products synthesized by the C-H at 120, 160, and 200°C for 12 h and commercial WO_3.

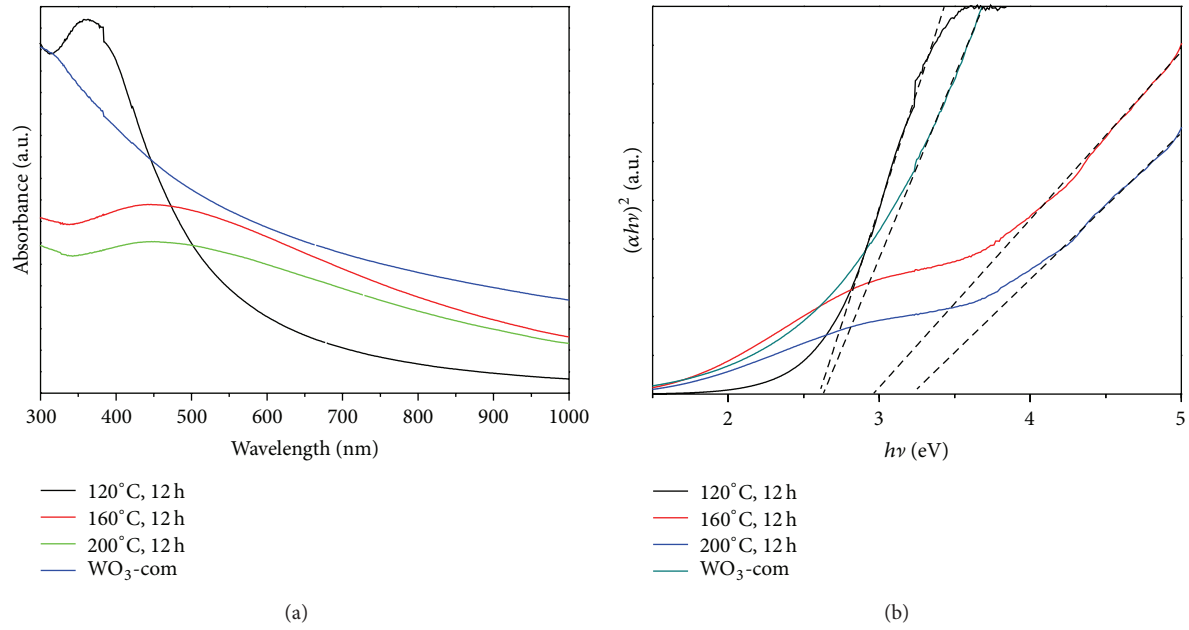


Figure 5: (a) UV-visible absorption and (b) the plot of $(\alpha h\nu)^2$ versus $h\nu$ of the products synthesized by the C-H at 120, 160, and 200°C for 12 h and commercial WO_3.

bridging oxygen. The peaks at 186 cm^{-1} are attributed to the lattice vibration. Additional mode belonging to W=O stretching of the product processed at 120°C for 12 h was also detected at 940 cm^{-1} [20, 23–27].

3.6. UV-Visible Absorption. UV-visible absorption of the products synthesized by the C-H at different temperatures for 12 h and commercial WO_3 is shown in Figure 5. For crystalline semiconductors, the UV absorption near band edge follows the following Wood and Tauc equation [28]:

$$\alpha h\nu = \left(h\nu - E_g\right)^n, \quad (1)$$

where α is the absorbance, h is the Planck constant, ν is the photon frequency, E_g is the energy gap, and n is a pure number associated with the different types of charged

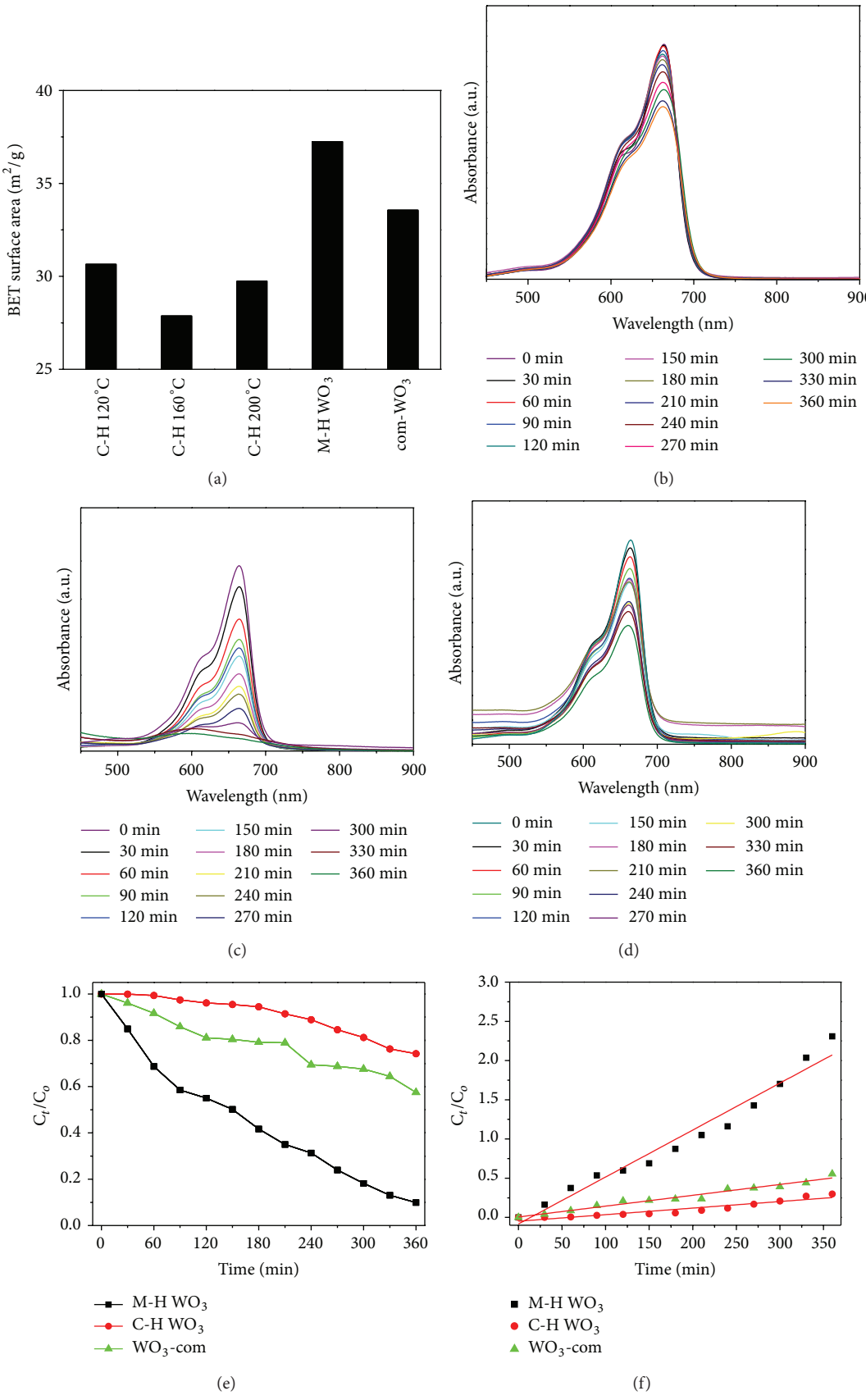


Figure 6: (a) BET surface areas of the products synthesized by the C-H at 120, 160, and 200°C for 12 h and M-H at 270 W for 180 min and commercial (com) WO_3. (b)–(d) UV-visible absorption spectra and (e), (f) photocatalytic degradation kinetics of MB dye by the WO_3 photocatalysts of the 200°C C-H and 270 W M-H and the commercial WO_3 irradiated with UV light for different lengths of time.

transition. The transitions are directly allowed, indirectly allowed, directly forbidden, and indirectly forbidden for n equals 1/2, 2, 3/2, and 3, respectively. The absorption was controlled by two photon energy ranges relative to energy gap. For $h\nu > E_g$, absorption is linearly increased with the increasing of photon energy caused by the transition of electrons from the topmost occupied state of valence band to the bottommost unoccupied state of conduction band. For $h\nu < E_g$, the absorption curves are different from linearity, caused by charged transition relating to defects. In the present research, direct energy gaps of the products synthesized by the C-H at 120, 160, and 200°C for 12 h were determined to be 2.60, 2.96, and 3.22 eV, respectively [2, 29, 30]. In addition, the direct band gap of commercial WO_3 was determined to be 2.63 eV [8].

3.7. BET Analysis. The BET analysis was used to determine surface area of the products (Figure 6(a)). It was found that pure WO_3 of the M-H (37.25 m^2/g) has larger surface area than the product of the C-H and commercial WO_3 (33.56 m^2/g). Surface area of the product synthesized by the C-H at 120°C for 12 h ($WO_3 \cdot H_2O$) was determined to be 30.65 m^2/g. Pure WO_3 products at 160 and 200°C for 12 h were determined to be 27.87 and 29.74 m^2/g, respectively. The M-H processed WO_3 nanostructure has different size distributions due to thermal stress during rapid heating, and the M-H product is also shown as rough surface. The traces of cracks on the M-H nanoplates and small debris separation have the influence to increase surface area.

3.8. Photocatalysis. The photocatalytic activities of WO_3 synthesized by the 200°C C-H and 270 W M-H and of the commercial WO_3 photocatalyst were evaluated by identifying the degradation of methylene blue ($C_{16}H_{18}N_3SCI$, MB) under UV radiation. Before UV irradiation, 100 mL of 1×10^{-5} mol/L MB aqueous solution containing 0.1 g of photocatalyst was magnetically stirred in the dark for 30 min. For comparison, WO_3 synthesized by the 200°C of the C-H for 12 h, WO_3 of the 270 W M-H for 180 min, and commercial WO_3 were used as photocatalytic materials for degrading MB under UV radiation. Figures 6(b)–6(d) show the UV-visible absorption spectra of MB in aqueous solution containing WO_3 synthesized by the C-H and M-H methods and commercial WO_3 for different lengths of irradiation time. The characteristic absorption peaks of MB at 664 nm gradually decrease with the prolonging irradiation time. For WO_3 photocatalyst of the M-H, the characteristic absorption peak decreases almost disappear within 360 min. The MB degradation under a series of the experimental conditions is shown in Figure 6(e), where C_o and C_t are the initial concentration after the equilibrium absorption and residual concentration of MB within the length of time (t), respectively. The MB concentration of WO_3 photocatalyst of the C-H decreases slower than WO_3 of the M-H and commercial one under UV radiation. The degradation efficiencies for the M-H, commercial, and C-H photocatalysts were 90.07%, 42.53%, and 25.80% within 360 min irradiation, respectively. These results corresponded with the BET analysis. Not only surface area plays the role in the photocatalytic activity but the crystalline composition of the photocatalyst also shows an important effect [31]. The crystalline structure and morphology of the M-H and C-H WO_3 (monoclinic, nanoplates) are difference from those of commercial WO_3 (orthorhombic, nanorods). They also have the influence to control the photocatalytic rate. The Langmuir-Hinshelwood (L-H) kinetics model was used to investigate the degradation of MB solution and the pseudo-first-order rate equation was given by [18]

$$\ln\left(\frac{C_o}{C_t}\right) = k_{\text{app}}t, \tag{2}$$

where C_o is the equilibrium concentration after absorption, C_t is the concentration of MB at time t, and k_{app} represents the apparent pseudo-first-order rate constant of initial degradation. The pseudo-first-order rate constant (k_{app}) was calculated from the slope of the $\ln(C_o/C_t)$ versus irradiation time (t) shown in Figure 6(f). The rate constant of MB degradation was 0.00599 min^{-1}, 8.38072×10^{-4} min^{-1}, and 0.00138 min^{-1} in the solutions containing the M-H WO_3, C-H WO_3, and commercial WO_3, respectively.

4. Conclusions

In summary, WO_3 nanoplates were successfully synthesized by the citric acid-assisted conventional hydrothermal reaction at 200°C for 12 h. Phase, morphology, and optical properties of the products were investigated. The photocatalytic property of the C-H WO_3 was evaluated by identifying the degradation of MB dye under UV irradiation and compared with the M-H WO_3 and commercial WO_3. The results indicated that the M-H WO_3 nanoplates showed the highest efficiency for the degradation of MB dye at the rate of 90.07% under UV illumination within 360 min, corresponding to the BET surface area analysis.

Conflict of Interests

The authors declare that there is no conflict of interests regarding the publication of this paper.

Acknowledgments

The authors wish to thank the Thailand Research Fund (TRF) for providing financial support through the Royal Golden Jubilee Ph.D. Program and the TRF Research Grant BRG5380020; the National Nanotechnology Center (NANOTEC), National Science and Technology Development Agency (NSTDA), Thailand, through the project P-10-11345 for Research, Development and Engineering (RD & E); and the Thailand's Office of the Higher Education Commission through the National Research University (NRU) Project for Chiang Mai University (CMU), including the Graduate School of CMU through a general support.

References

[1] L. Li, J. Zhao, Y. Wang et al., "Oxalic acid mediated synthesis of $WO_3 \cdot H_2O$ nanoplates and self-assembled nanoflowers under mild conditions," *Journal of Solid State Chemistry*, vol. 184, no. 7, pp. 1661–1665, 2011.

[2] V. Hariharan, S. Radhakrishnan, M. Parthibavarman, R. Dhilipkumar, and C. Sekar, "Synthesis of polyethylene glycol (PEG) assisted tungsten oxide (WO_3) nanoparticles for l-dopa biosensing applications," *Talanta*, vol. 85, no. 4, pp. 2166–2174, 2011.

[3] J. Polleux, A. Gurlo, N. Barsan, U. Weimar, M. Antonietti, and M. Niederberger, "Template-free synthesis and assembly of single-crystalline tungsten oxide nanowires and their gas-sensing properties," *Angewandte Chemie International Edition*, vol. 45, no. 2, pp. 261–265, 2005.

[4] J. Shi, G. Hu, Y. Sun et al., "WO_3 nanocrystals: synthesis and application in highly sensitive detection of acetone," *Sensors and Actuators B: Chemical*, vol. 156, no. 2, pp. 820–824, 2011.

[5] X. Gao, X. Su, C. Yang et al., "Hydrothermal synthesis of WO_3 nanoplates as highly sensitive cyclohexene sensor and high-efficiency MB photocatalyst," *Sensors and Actuators B*, vol. 181, pp. 537–543, 2013.

[6] C. Dai, M. Liu, F. Chen, C. Wu, and M. Chang, "A nanowire WO_3 humidity sensor integrated with micro-heater and inverting amplifier circuit on chip manufactured using CMOS-MEMS technique," *Sensors and Actuators, B: Chemical*, vol. 123, no. 2, pp. 896–901, 2007.

[7] A. Danine, L. Cojocaru, C. Faure et al., "Room temperature UV treated WO_3 thin films for electrochromic devices on paper substrate," *Electrochimica Acta*, vol. 129, pp. 113–119, 2014.

[8] D. B. Hernandez-Uresti, D. Sánchez-Martínez, A. Martínez-delaCruz, S. Sepúlveda-Guzmán, and L. M. Torres- Martínez, "Characterization and photocatalytic properties of hexagonal and monoclinic WO_3 prepared via microwave-assisted hydrothermal synthesis," *Ceramics International*, vol. 40, no. 3, pp. 4767–4775, 2014.

[9] S. S. Thind, M. Tian, and A. Chen, "Direct growth and photoelectrochemical study of WO_3 nanostructured materials," *Electrochemistry Communications*, vol. 43, pp. 13–17, 2014.

[10] Z. Gu, T. Zhai, B. Gao et al., "Controllable assembly of WO_3 nanorods/nanowires into hierarchical nanostructures," *Journal of Physical Chemistry B*, vol. 110, no. 47, pp. 23829–23836, 2006.

[11] K. O. Rocha and S. M. Zanetti, "Structural and properties of nanocrystalline WO_3/TiO_2-based humidity sensors elements prepared by high energy activation," *Sensors and Actuators B: Chemical*, vol. 157, no. 2, pp. 654–661, 2011.

[12] K. Murugan, S. B. Chandrasekhar, and J. Joardar, "Nanostructured α/β-tungsten by reduction of WO_3 under microwave plasma," *International Journal of Refractory Metals and Hard Materials*, vol. 29, no. 1, pp. 128–133, 2011.

[13] J. Sungpanich, T. Thongtem, and S. Thongtem, "Large-scale synthesis of WO_3 nanoplates by a microwave-hydrothermal method," *Ceramics International*, vol. 38, no. 2, pp. 1051–1055, 2012.

[14] S. Komarneni, "Nanophase materials by hydrothermal, microwave-hydrothermal and microwave-solvothermal methods," *Current Science*, vol. 85, no. 12, pp. 1730–1734, 2003.

[15] L. Sun, X. Zhao, C. Jia et al., "Enhanced visible-light photocatalytic activity of g-C_3N_4-ZnWO4 by fabricating a heterojunction: investigation based on experimental and theoretical studies," *Journal of Materials Chemistry*, vol. 22, no. 44, pp. 23428–23438, 2012.

[16] S. Nishimoto, T. Mano, Y. Kameshima, and M. Miyake, "Photocatalytic water treatment over WO_3 under visible light irradiation combined with ozonation," *Chemical Physics Letters*, vol. 500, no. 1–3, pp. 86–89, 2010.

[17] W. Chu and Y. F. Rao, "Photocatalytic oxidation of monuron in the suspension of WO_3 under the irradiation of UV-visible light," *Chemosphere*, vol. 86, no. 11, pp. 1079–1086, 2012.

[18] N. A. Ramos-Delgadoa, M. A. Gracia-Pinillab, L. Maya-Treviño, L. Hinojosa-Reyesa, J. L. Guzman-Mara, and A. Hernández-Ramírez, "Solar photocatalytic activity of TiO_2 modified with WO_3 on thedegradation of an organophosphorus pesticide," *Journal of Hazardous Materials*, vol. 263, pp. 36–44, 2013.

[19] "Powder Diffraction File, JCPDS-ICDD," 12 Campus Boulevard, Newtown Square, Pa, USA, 2001.

[20] B. Ingham, S. V. Chong, and J. L. Tallon, "Layered tungsten oxide-based organic—Inorganic hybrid materials: an infrared and raman study," *Journal of Physical Chemistry B*, vol. 109, no. 11, pp. 4936–4940, 2005.

[21] H. S. Mansur, C. M. Sadahira, A. N. Souza, and A. A. P. Mansur, "FTIR spectroscopy characterization of poly (vinyl alcohol) hydrogel with different hydrolysis degree and chemically crosslinked with glutaraldehyde," *Materials Science and Engineering C*, vol. 28, no. 4, pp. 539–548, 2008.

[22] H. S. Mansur, R. L. Oréfice, and A. A. P. Mansur, "Characterization of poly(vinyl alcohol)/poly(ethylene glycol) hydrogels and PVA-derived hybrids by small-angle X-ray scattering and FTIR spectroscopy," *Polymer*, vol. 45, no. 21, pp. 7193–7202, 2004.

[23] S. Salmaoui, F. Sediri, and N. Gharbi, "Characterization of h-WO_3 nanorods synthesized by hydrothermal process," *Polyhedron*, vol. 29, no. 7, pp. 1771–1775, 2010.

[24] A. Kuzmin, J. Purans, E. Cazzanelli, C. Vinegoni, and G. Mariotto, "X-ray diffraction, extended x-ray absorption fine structure and Raman spectroscopy studies of WO_3 powders and (1-x)WO_3-y·xReO_2 mixtures," *Journal of Applied Physics*, vol. 84, no. 10, pp. 5515–5524, 1998.

[25] C. S. Rout, M. Hegde, and C. N. R. Rao, "H_2S sensors based on tungsten oxide nanostructures," *Sensors and Actuators B: Chemical*, vol. 128, no. 2, pp. 488–493, 2008.

[26] T. Siciliano, A. Tepore, G. Micocci, A. Serra, D. Manno, and E. Filippo, "WO_3 gas sensors prepared by thermal oxidization of tungsten," *Sensors and Actuators, B: Chemical*, vol. 133, no. 1, pp. 321–326, 2008.

[27] Y. S. Kim, "Thermal treatment effects on the material and gas-sensing properties of room-temperature tungsten oxide nanorod sensors," *Sensors and Actuators B*, vol. 137, no. 1, pp. 297–304, 2009.

[28] Y. Keereeta, T. Thongtem, and S. Thongtem, "Fabrication of $ZnWO_4$ nanofibers by a high direct voltage electrospinning process," *Journal of Alloys and Compounds*, vol. 509, no. 23, pp. 6689–6695, 2011.

[29] Y. Shen, D. Ding, and Y. Deng, "Fabrication and characterization of WO_3 flocky microspheres induced by ethanol," *Powder Technology*, vol. 211, no. 1, pp. 114–119, 2011.

[30] K. Lee, W. S. Seo, and J. T. Park, "Synthesis and optical properties of colloidal tungsten oxide nanorods," *Journal of the American Chemical Society*, vol. 125, no. 12, pp. 3408–3409, 2003.

[31] M. Lindner, J. Theurich, and D. W. Bahnemann, "Photocatalytic degradation of organic compounds: accelerating the process efficiency," *Water Science and Technology*, vol. 35, no. 4, pp. 79–86, 1997.

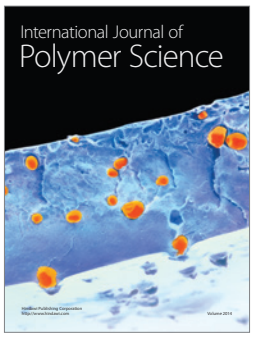


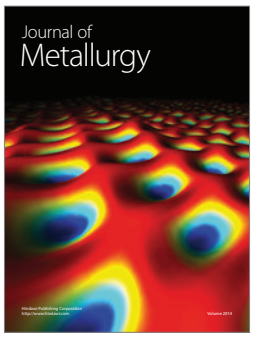




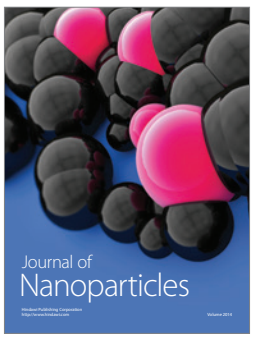


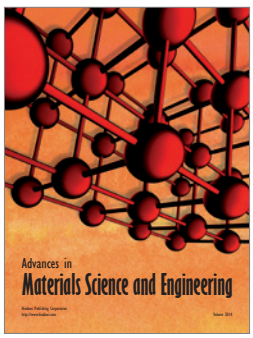




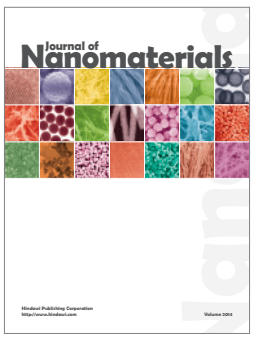














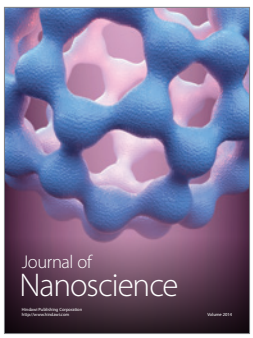












Hindawi
Submit your manuscripts at
http://www.hindawi.com

IOPscience iopscience.iop.org

Home Search Collections Journals About Contact us My IOPscience

Characterization of Cu_3SnS_4 Nanoparticles and Nanostructured Flowers Synthesized by a Microwave-Refluxing Method

This content has been downloaded from IOPscience. Please scroll down to see the full text.

2013 Jpn. J. Appl. Phys. 52 111201

(http://iopscience.iop.org/1347-4065/52/11R/111201)

View the table of contents for this issue, or go to the journal homepage for more

Download details:

IP Address: 202.28.248.41
This content was downloaded on 19/12/2013 at 08:53

Please note that terms and conditions apply.

Japanese Journal of Applied Physics **52** (2013) 111201 **REGULAR PAPER**
http://dx.doi.org/**10.7567/JJAP.52.111201**

Characterization of Cu_3SnS_4 Nanoparticles and Nanostructured Flowers Synthesized by a Microwave-Refluxing Method

Narongrit Tipcompor[1], Somchai Thongtem[2,3*], and Titipun Thongtem[1,3*]

[1]*Department of Chemistry, Faculty of Science, Chiang Mai University, Chiang Mai 50200, Thailand*
[2]*Department of Physics and Materials Science, Faculty of Science, Chiang Mai University, Chiang Mai 50200, Thailand*
[3]*Materials Science Research Center, Faculty of Science, Chiang Mai University, Chiang Mai 50200, Thailand*
E-mail: ttpthongtem@yahoo.com; schthongtem@yahoo.com

Received June 21, 2013; accepted August 23, 2013; published online October 30, 2013

Cu_3SnS_4 nanoparticles and nanostructured flowers were synthesized by 100, 300, 600, and 800 W microwave refluxing of the mixture containing 3 mmol $CuCl_2 \cdot 2H_2O$, 1 mmol $SnCl_2 \cdot 2H_2O$, and 4 mmol thiosemicarbazide ($NH_2NHCSNH_2$) in 50 ml ethylene glycol ($HOCH_2CH_2OH$). X-ray diffraction (XRD), selected area electron diffraction (SAED), X-ray photoelectron spectroscopy (XPS), scanning and transmission electron microscopy (SEM and TEM), Raman analysis, and photoluminescence (PL) spectrophotometry revealed the morphology transformation of pure tetragonal Cu_3SnS_4 with nanoparticles at 100 W into three-dimensional (3D) hierarchical flower-like structure at 800 W, including the presence of $2Cu^+$, Cu^{2+}, Sn^{4+}, and $4S^{2-}$ containing in the sulfide, the PL emission of the 3D hierarchical flower-like Cu_3SnS_4 at 366 nm, and the prominent Raman peak of Cu–Sn vibration at 319 cm^{-1}. In this research, a formation mechanism was also proposed according to the experimental results.
© 2013 The Japan Society of Applied Physics

1. Introduction

At present, I–IV–VI ternary semiconducting compounds, such as Cu–Sn–E (E = S and Se), have been very attractive, due to their mid-band-gap semiconductors and non-linear optical properties.[1)] For Cu, Sn, and S, they can form several sulfides, such as $CuSn_{3.75}S_8$, Cu_2SnS_3, $Cu_2Sn_3S_7$, Cu_3SnS_4, Cu_4SnS_4, and $Cu_4Sn_7S_{16}$.[2–4)] Among them, Cu_3SnS_4 (CTS) is one of a semiconducting material which has the potential to be used in solar cells and as a photocatalyst. Generally, optical band gap of CTS material is influenced by different morphologies and structures, crystalline degree, and different types and concentration of defects. Lin et al. have estimated optical band gap of the CTS nanocrystals to be 1.43 eV, the optimal value for solar energy converters.[5)] Furthermore, the optical band gap of three-dimensional (3D) hierarchical flower-like CTS microspheres was evaluated to be 1.38 eV by Chen et al.,[6)] who stated the potential application in solar energy conversion and photocatalysis. Optical properties of CTS sprayed thin film with 500 °C annealing were measured and the direct energy gap of the film was determined by Bouaziz et al. to be 1.22 eV.[7)] The energy band gap of tetragonal CTS with 500 °C sulfurization temperature was reported by Guan et al. to be 1.22 eV.[8)] Thin film of CTS was grown by sulfidation of Sn–Cu metallic precursors in a S_2 atmosphere at 520 °C to form orthorhombic CTS thin film with 1.60 eV band gap, reported by Fernandes et al.[9)] CTS thin film was prepared by a spray pyrolysis technique and followed by annealing at 550 °C in an atmosphere containing sulfur to form polycrystalline orthorhombic CTS thin film which was determined its direct energy gap of 1.8 eV by Chalapathi et al.[10)] The Cu–Sn–S precursor was sulfurized in sulfur containing atmosphere at 500 °C to form CTS thin film by Su et al., and its optical energy gap was determined to be 1.47 eV.[11)] The energy gap of orthorhombic (*Pmn*21) CTS with petrukite structure thin film, deposited by dc magnetron sputtering and followed by sulfurization in $N_2 + S_2$ vapor atmosphere at 520 °C, was determined to be 1.60 eV by Fernandes et al.[12)] Thus CTS is a very important semiconductor which attracts great attention of its promising optical, thermal and mechanical properties.[1)]

Microwave radiations (2.45 GHz) are coherent and polarized.[13)] They are able to couple with charged particles, and cause them to be heated up very rapidly. In general, materials are classified into three groups: reflectors (bulk metals and alloys), transmitters (fused-silica and fluoropolymers) and absorbers (inorganic materials, powdered metals, metal oxides and metal halides).[14)] Thus containers should appropriately be chosen. Microwave-assisted synthesis is a very interesting process for synthesizing of different materials. When microwave is applied to substances, at least one of their components is able to couple with the radiation. Comparing to a conventional method, it can accelerate the reaction rate, and consume lesser reaction time, especially materials with high dielectric constant. It is able to solve the problems of temperature and concentration gradients, including to provide uniform growth media. Due to a large amount of microwave energy passing through the solution, the vibrating electric field induces charged particles to vibrate accordingly. This process is very simple, fast, effective and environmentally benign.[15–17)] Microwave refluxing is a distillation process of which the system is heated by a microwave radiation. It involves the evaporation of liquid, condensation of vapor and return of condensate to its original syntem. It has been developed and widely used in industrial and laboratory distillation processes.[18)]

In this research, CTS with nanoparticles and flower-like clusters were synthesized by a microwave-assisted refluxing method. This success may lead to different applications in the near future.

2. Experiment

To synthesize CTS, 3 mmol $CuCl_2 \cdot 2H_2O$, 1 mmol $SnCl_2 \cdot 2H_2O$, and 4 mmol thiosemicarbazide (TBZ) were dissolved in 50 ml of ethylene glycol (EG). Each 50 ml solution was refluxed by 100, 300, 600, and 800 W microwave for 15, 30, and 60 min. Finally, black precipitates were synthesized, separated by filtration, washed with deionized water and ethanol, and dried at 70 °C for 12 h. The products were characterized by an X-ray diffractometer (XRD; Siemens D500) operating at 20 kV 15 mA and using Cu Kα line in combination with the database of JCPDS; a scanning

© 2013 The Japan Society of Applied Physics

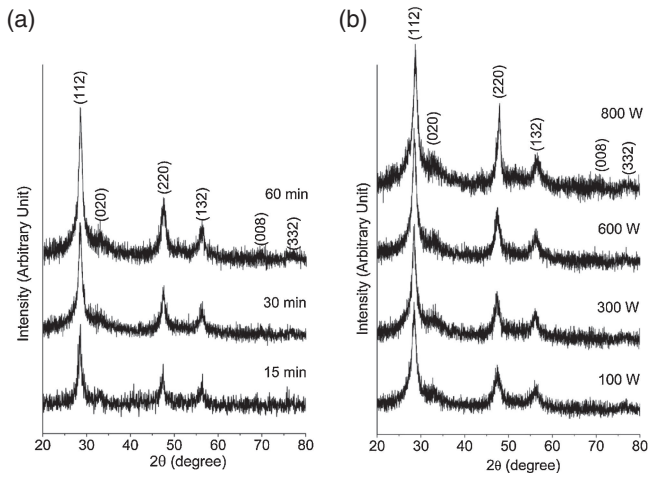


Fig. 1. XRD patterns of CTS synthesized by a microwave-assisted refluxing method in EG at (a) 800 W microwave for 15, 30, and 60 min; and (b) 100, 300, 600, and 800 W for 60 min.

electron microscope (SEM; JEOL JSM-6335F) operating at 15 kV; a transmission electron microscope (TEM; JEOL JEM-2010) and selected area electron diffraction (SAED) technique operating at 200 kV; an X-ray photoelectron spectrometer (XPS; Kratos Analytical Axis Ultra^{DLD}) operating at 15 kV 10 mA in a chamber with 5×10^{-9} Torr; a Raman spectrometer (Horiba Jobin Yvon T64000) using a 50 mW and 514.5 nm wavelength Ar green laser and a photoluminescence (PL) spectrometer (PerkinElmer LS 50B) using 300 nm excitation wavelength at room temperature.

3. Results and Discussion

3.1 XRD

XRD patterns [Fig. 1(a)] of the products synthesized by 800 W microwave refluxing of the starting agents dissolved in ethylene glycol. They were indexed and specified as tetragonal CTS (JCPDS No. 33-0501) without impurity detection. Its mineral name is known as kuramite.[5)] Upon reducing the lengths of microwave refluxing time from 60 to 30 and 15 min, the XRD peaks for the production in EG were broadened, and the crystalline degree of these pure products was lowered. To save the energy consumption, the refluxing power of microwave was gradually reduced step by step from 800 to 600, 300, and 100 W at a constant length of refluxing time for 60 min [Fig. 1(b)]. The products were still pure CTS phase, but the crystalline degree was lessened.

3.2 Electron microscopy

The SEM and TEM images of CTS synthesized by a 800 W microwave refluxing method for 15, 30, and 60 min are shown in Figs. 2(a)–2(e). For 15 min and 800 W microwave refluxing, the product was incomplete nanostructured flowers. They became complete flowers until the length of time was as long as 60 min. By fixing the length of time to be 60 min at different microwave powers (Fig. 3), the as-synthesized products with different morphologies were synthesized. At 100 W, the product was composed of a number of nanoparticles clustered together in group. By increasing the refluxing power of the microwave from 100 to 300, 600, and 800 W, the nanoparticles gradually transformed into incomplete flowers at 300 and 600 W, and into complete flower-like

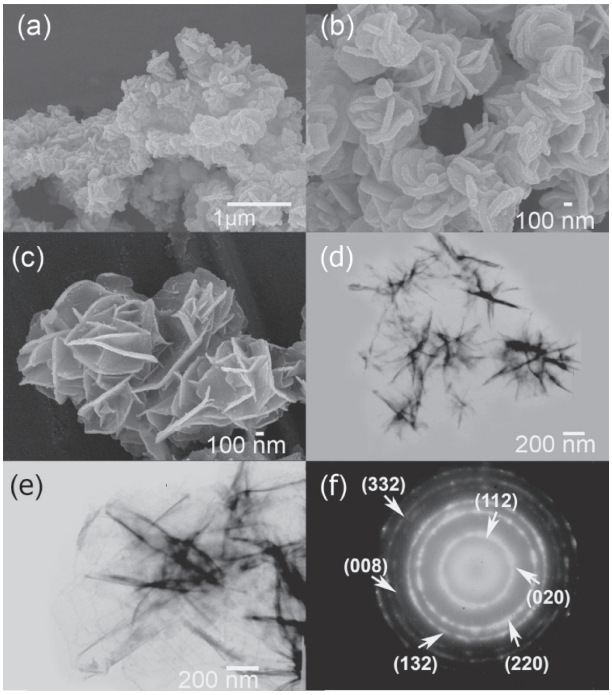


Fig. 2. (a–c) SEM images of CTS synthesized at 800 W microwave refluxing method in EG for 15, 30, and 60 min, respectively. (d, e) TEM images and (f) SAED pattern of CTS flowers synthesized by a 800 W microwave refluxing method for 60 min.

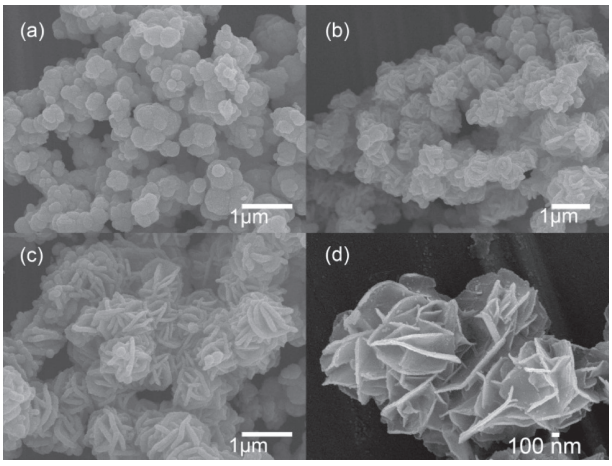


Fig. 3. SEM images of CTS synthesized by (a) 100, (b) 300, (c) 600, and (d) 800 W microwave refluxing method in EG for 60 min.

structure at 800 W. In this research, both powers of microwave and lengths of time have the influence to determine the product morphologies, including their crystalline degrees. A SAED pattern [Fig. 2(f)] of nanostructured flowers was diffuse and hollow, and was identified to correspond with polynanocrystals of tetagonal CTS (JCPDS No. 33-0501).

3.3 XPS

The XPS spectra of CTS nanostructured flowers (Fig. 4) revealed the presence of copper, tin and sulfur peaks. The Cu 2p core level spectrum indicates the observed binding energy (BE) for Cu $2p_{3/2}$ (932.4 eV) and $2p_{1/2}$ (952.4 eV), corresponding to the reported value for Cu^{+}. The Cu $2p_{3/2}$ satellite peak at 942.8 eV identified as Cu^{2+} was also detected. Obviously, there were both Cu^{2+} and Cu^{+} ions in

© 2013 The Japan Society of Applied Physics

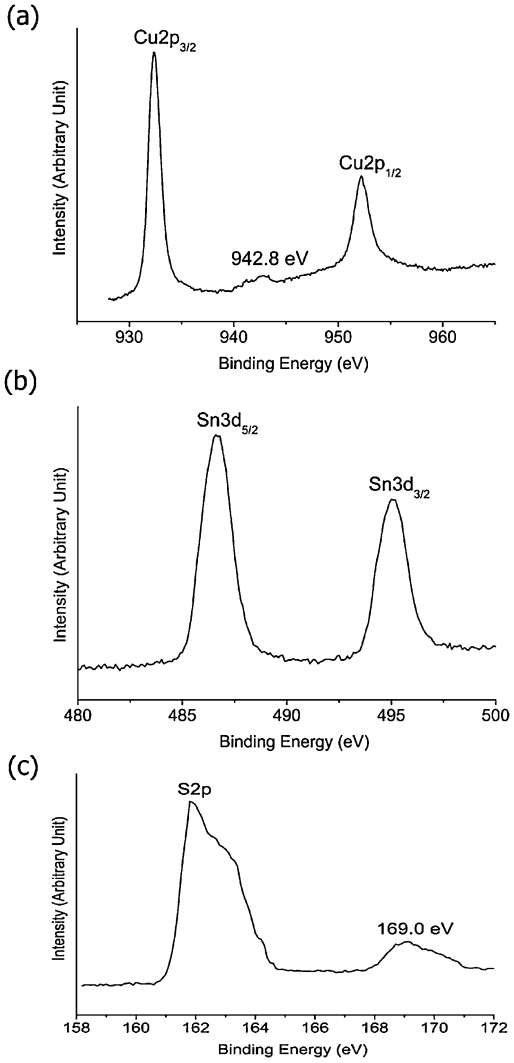


Fig. 4. (a) Cu 2p, (b) Sn 3d, and (c) S 2p core levels of nanostructured flower-like CTS synthesized by 800 W microwave refluxing for 60 min.

the as-synthesized CTS product. The photoelectron spectrum of Sn 3d core levels at 486.6 eV of Sn $3d_{5/2}$ and 495.1 eV of Sn $3d_{3/2}$ belongs to Sn^{4+}. No evidence of Sn^{2+} (binding energy at 485.2 eV) was detected in the spectrum. The S 2p core-level spectrum indicates the binding energy at 161.7 eV.[1,5,19–25] Furthermore, additional peak was detected at 169.0 eV and was likely to be from the oxidized parts of the product during the synthesis. The present analysis reveals that the CTS flowers were composed of $2Cu^{+}$, Cu^{2+}, Sn^{4+}, and $4S^{2-}$. The presence of both Cu(I) and Cu(II) in the complex charge balance CTS was also detected by Benedetto et al.[26,27] The kuramite CTS phase is a p-type semiconductor,[5] which exhibits a marked paramagnetism originated by the presence of Cu(II).[27] Its stoichiometric formula is written as $Cu(I)_2Cu(II)SnS_4$ with a random distribution of Cu(I), Cu(II), and Sn(IV) ions in the available tetrahedral sites.[27] In the present research, other minor peaks of C 1s (284.9 eV) and O 1s (531.4 eV) were also detected.[1,20–22] They belonged to the coated carbon to improve electrical conductivity for XPS analysis and the absorbed gaseous molecules in the characterized product. Based on the Cu 2p, Sn 3d, and S 2p core level peaks of CTS, the atomic ratio of Cu : Sn : S was determined to be 3.04 : 1.00 : 3.82 — very close to the stoichiometric ratio of the sulfide, and in accordance with the report of Yi et al.[28]

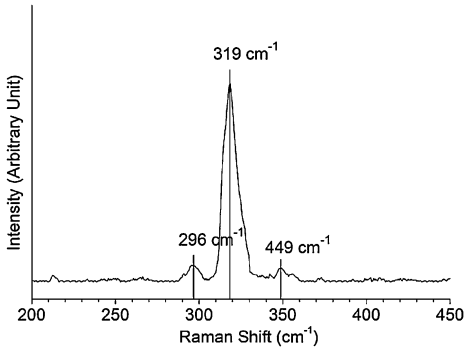


Fig. 5. Raman spectrum of CTS synthesized by 800 W microwave refluxing for 60 min.

3.4 Raman analysis

Figure 5 shows the Raman peaks of flower-like CTS synthesized by 800 W microwave refluxing for 60 min at 296, 319, and 449 cm^{-1}. The 319 cm^{-1} prominent Raman peak can be specified as Cu–Sn vibration analogy to other sulfide complexes.[4,8,9]

3.5 Proposed mechanism

To synthesize CTS by a microwave-assisted refluxing method, $CuCl_2 \cdot 2H_2O$, $SnCl_2 \cdot 2H_2O$, and TBZ with 3 : 1 : 4 molar ratio Cu : Sn : S were dissolved in ethylene glycol ($HOCH_2CH_2OH$). It is well known that TBZ ($NH_2NHCSNH_2$) is usually considered as a bidentate ligand of which sulfur and nitrogen atoms are in favorable positions to form five-membered rings and able to form complexes with transition metals.[29] In the present research, Cu(II) coordinated TBZ. Cu^{2+} ions were reduced to Cu^{+} ions by TBZ and the Cu^{+} ions further coordinated TBZ to form stable Cu(I)–TBZ complexes.[1] Cu^{2+} ions were reduced to Cu^{+} ions by EG as well.[30–33] According to the difference in the standard Gibbs free energy (ΔG^{o}): ΔG^{o} (Cu^{2+}/Cu^{+}) = −14.76 kJ; ΔG^{o} (Sn^{4+}/Sn^{2+}) = −28.95 kJ, Sn^{2+} ions could be slowly oxidized to Sn^{4+} by Cu^{2+} ions under a certain condition.[34] During stirring, Cu^{+}, Cu^{2+}, and Sn^{4+} ions formed complexes with TBZ. At this stage, free ions of Cu^{+}, Cu^{2+}, Sn^{4+}, and S^{2-} were very low, and the formation of CuS, Cu_2S, SnS, and SnS_2 was prohibited.

$$Cu^{2+}(aq) + e^{-} \rightarrow Cu^{+}(aq), \quad \Delta G^{o}(Cu^{2+}/Cu^{+}) = -14.76\,kJ \tag{1}$$

$$Sn^{4+}(aq) + 2e^{-} \rightarrow Sn^{2+}(aq), \quad \Delta G^{o}(Sn^{4+}/Sn^{2+}) = -28.95\,kJ \tag{2}$$

$$2Cu^{2+}(aq) + Sn^{2+}(aq) \rightarrow 2Cu^{+}(aq) + Sn^{4+}(aq), \quad \Delta G^{o}(\text{reaction}) = -570\,J \tag{3}$$

$$Cu(I)(aq) + TBZ \rightarrow Cu(I)\text{–}TBZ\ \text{complex} \tag{4}$$

$$Cu(II)(aq) + TBZ \rightarrow Cu(II)\text{–}TBZ\ \text{complex} \tag{5}$$

$$Sn(IV)(aq) + TBZ \rightarrow Sn(IV)\text{–}TBZ\ \text{complex} \tag{6}$$

During microwave refluxing, the complexes were decomposed several steps to form CTS. The decomposition proceeded with rather slow rate. The concentrations of the decomposed species were lower than that obtained by

© 2013 The Japan Society of Applied Physics

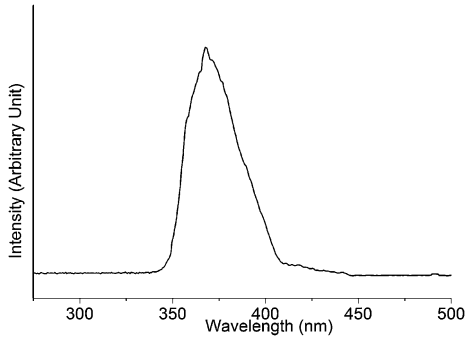


Fig. 6. PL emission of CTS synthesized by 800 W microwave refluxing for 60 min.

the direct ion-exchange reaction. Finally, CTS nuclei were synthesized in EG by the microwave-assisted refluxing method.

$$\text{Cu(I)–TBZ complex} + \text{Cu(II)–TBZ complex} + \text{Sn(IV)–TBZ complex} \rightarrow (Cu_3SnS_4)_n \rightarrow nCu_3SnS_4 \quad (7)$$

The nuclei grew to form nanoparticles which clustered together in groups at 100 W microwave power. Further, each of nanoparticles transformed into complete flowers at 800 W microwave power within 60 min.

3.6 PL emission

PL emission (Fig. 6) of CTS synthesized by 800 W microwave refluxing method in EG for 60 min was determined using 300 nm excitation wavelength at room temperature. The emission peak of the 3D-hierarchical flower-like CTS was detected at 366 nm wavelength (3.39 eV), due to the interband electron-hole recombination process. It should be noted that the transition between bands could involve electronic levels in the vicinity to the bottom of the lowest empty band and at the top of the highest occupied band.[23)] The emission was very close to the reports of Hu et al. who excited the CTS nanoshell tubes using 234 nm Xe light source and determined the PL emission of the CTS nanoshell tubes to be 345 nm,[1)] and of Xiong et al. who excited CTS nanorods using 264 nm and determined the PL emission of the CTS nanorods to be 319 nm of blue light.[23)] These results show that PL emissions of CTS were influenced by different morphologies of the products and excitation wavelengths.

4. Conclusions

Pure tetragonal CTS with nanoparticles and 3D-hierarchical flower-like structure were successfully synthesized by microwave refluxing of $CuCl_2 \cdot 2H_2O$, $SnCl_2 \cdot 2H_2O$, and TBZ in ethylene glycol. In this research, the CTS products were composed of $2Cu^+$ (BE = 932.4 and 952.4 eV), Cu^{2+} (BE = 942.8 eV), Sn^{4+} (BE = 486.6 and 495.1 eV) and $4S^{2-}$ (BE = 161.7 eV), including the PL emission at 366 nm for the 3D-hierarchical flower-like CTS, and the prominent Raman peak of Cu–Sn vibration at 319 cm^{-1}.

Acknowledgements

We wish to thank the Thailand Research Fund (TRF) for providing financial support through the Royal Golden Jubilee Ph. D. Program and the TRF Research Grant BRG5380020; the Thailand's Office of the Higher Education Commission through the National Research University (NRU) Project; and the National Nanotechnology Center (NANOTEC), National Science and Technology Development Agency (NSTDA), through the project P-10-11345; including the Graduate School of Chiang Mai University through a general support.

1) H. Hu, Z. Liu, B. Yang, X. Chen, and Y. Qian: J. Cryst. Growth **284** (2005) 226.
2) M. Bouaziz, J. Ouerfelli, S. K. Srivastava, J. C. Bernède, and M. Amlouk: Vacuum **85** (2011) 783.
3) M. Bouaziz, M. Amlouk, and S. Belgacem: Thin Solid Films **517** (2009) 2527.
4) A.-J. Cheng, M. Manno, A. Khare, C. Leighton, S. A. Campbell, and E. S. Aydil: J. Vac. Sci. Technol. A **29** (2011) 051203.
5) X. Lin, A. Steigert, M. Ch. Lux-Steiner, and A. Ennaoui: RSC Adv. **2** (2012) 9798.
6) F. Chen, J. Zai, M. Xu, and X. Qian: J. Mater. Chem. A **1** (2013) 4316.
7) M. Bouaziz, J. Ouerfelli, M. Amlouk, and S. Belgacem: Phys. Status Solidi A **204** (2007) 3354.
8) H. Guan, H. Shen, C. Gao, and X. He: J. Mater. Sci.: Mater. Electron. **24** (2013) 1490.
9) P. A. Fernandes, P. M. P. Salomé, and A. F. da Cunha: J. Phys. D **43** (2010) 215403.
10) U. Chalapathi, Y. B. Kishore Kumar, S. Uthanna, and V. S. Raja: AIP Conf. Proc. **1447** (2012) 649.
11) Z. Su, K. Sun, Z. Han, F. Liu, Y. Lai, J. Li, and Y. Liu: J. Mater. Chem. **22** (2012) 16346.
12) P. A. Fernandes, P. M. P. Salomé, and A. F. da Cunha: Phys. Status Solidi C **7** (2010) 901.
13) S. Bhunia and D. N. Bose: J. Cryst. Growth **186** (1998) 535.
14) J. W. Lekse, A. M. Pischera, and J. A. Aitken: Mater. Res. Bull. **42** (2007) 395.
15) P. Junploy, S. Thongtem, and T. Thongtem: Superlattices Microstruct. **57** (2013) 1.
16) C. Gabriel, S. Gabriel, E. H. Grant, B. S. J. Halstead, and D. M. P. Mingos: Chem. Soc. Rev. **27** (1998) 213.
17) K. J. Rao, B. Vaidhyanathan, M. Ganguli, and P. A. Ramakrishnan: Chem. Mater. **11** (1999) 882.
18) N. Tipcompor, S. Thongtem, and T. Thongtem: Ceram. Int. **39** (2013) S383.
19) J. Q. Hu, B. Deng, K. B. Tang, C. R. Wang, and Y. T. Qian: J. Mater. Res. **16** (2001) 3411.
20) M. X. Wang, L. S. Wang, G. H. Yue, X. Wang, P. X. Yan, and D. L. Peng: Mater. Chem. Phys. **115** (2009) 147.
21) Y.-H. A. Wang, N. Bao, and A. Gupta: Solid State Sci. **12** (2010) 387.
22) T. Kuzuya, K. Itoh, M. Ichidate, T. Wakamatsu, Y. Fukunaka, and K. Sumiyama: Electrochim. Acta **53** (2007) 213.
23) Y. Xiong, Y. Xie, G. Du, and H. Su: Inorg. Chem. **41** (2002) 2953.
24) M. Bouaziz, K. Boubaker, M. Amlouk, and S. Belgacem: J. Phase Equilibria Diffus. **31** (2010) 498.
25) X. Chen, X. Wang, C. An, J. Liu, and Y. Qian: J. Cryst. Growth **256** (2003) 368.
26) F. Di Benedetto, F. d'Acapito, I. Bencistà, A. De Luca, G. Fornaciai, S. Frizzera, M. Innocenti, G. Montegrossi, L. A. Pardi, and M. Romanelli: Phys. Status Solidi C (in press) [DOI: 10.1002/pssc.201200753].
27) F. Di Benedetto, D. Borrini, A. Caneschi, G. Fornaciai, M. Innocenti, A. Lavacchi, C. A. Massa, G. Montegrossi, W. Oberhauser, L. A. Pardi, and M. Romanelli: Phys. Chem. Miner. **38** (2011) 483.
28) L. Yi, D. Wang, and M. Gao: CrystEngComm **14** (2012) 401.
29) T. V. Koksharova, S. V. Kurando, and I. V. Stoyanova: Russ. J. Gen. Chem. **82** (2012) 1481.
30) A. Anžlovar, Z. C. Orel, and M. Žigon: J. Nanosci. Nanotechnol. **8** (2008) 3516.
31) R. S. Ningthoujam, N. S. Gajbhiye, and S. Sharma: Pramana—J. Phys. **72** (2009) 577.
32) G. Carotenuto, G. P. Pepe, and L. Nicolais: Eur. Phys. J. B **16** (2000) 11.
33) Z. C. Orel, E. Matijević, and D. V. Goia: J. Mater. Res. **18** (2003) 1017.
34) D. R. Gaskell: *Introduction to Metallurgical Thermodynamics* (McGraw-Hill, New York, 1981).

© 2013 The Japan Society of Applied Physics

Hindawi Publishing Corporation
Journal of Nanomaterials
Volume 2013, Article ID 970489, 6 pages
http://dx.doi.org/10.1155/2013/970489

Research Article

Characterization of Cubic $AgSbS_2$ Nanostructured Flowers Synthesized by Microwave-Assisted Refluxing Method

Narongrit Tipcompor,[1] Somchai Thongtem,[2,3] and Titipun Thongtem[1,3]

[1] *Department of Chemistry, Faculty of Science, Chiang Mai University, Chiang Mai 50200, Thailand*
[2] *Department of Physics and Materials Science, Faculty of Science, Chiang Mai University, Chiang Mai 50200, Thailand*
[3] *Materials Science Research Center, Faculty of Science, Chiang Mai University, Chiang Mai 50200, Thailand*

Correspondence should be addressed to Somchai Thongtem; schthongtem@yahoo.com
and Titipun Thongtem; ttpthongtem@yahoo.com

Received 29 April 2013; Revised 5 August 2013; Accepted 10 August 2013

Academic Editor: Sheng-Rui Jian

Copyright © 2013 Narongrit Tipcompor et al. This is an open access article distributed under the Creative Commons Attribution License, which permits unrestricted use, distribution, and reproduction in any medium, provided the original work is properly cited.

Cubic $AgSbS_2$ nanostructured flowers of nanorods were successfully synthesized by microwave-assisted refluxing of $AgNO_3$, $Sb(CH_3COO)_3$, and L-cysteine ($C_3H_7NO_2S$) dissolved in ethylene glycol at the pH of 4, characterized by X-ray diffraction (XRD) and electron microscopy (EM). The 1.89 eV direct energy gap was determined by UV-visible absorption, including two 688 and 857 nm emission wavelengths by photoluminescence (PL) spectroscopy. A possible formation mechanism of $AgSbS_2$ nanostructured flowers was also proposed according to the experimental results.

1. Introduction

Presently, silver antimony sulfide ($AgSbS_2$) is a very attractive material, due to its promising candidate for a number of applications: active recording films, micromechanical and optical memories, electrical switching and transmission in midinfrared [1–4]. $AgSbS_2$ crystallizes as two main crystal systems: monoclinic and cubic [5].

Microwave-assisted refluxing is a distillation process of which the system is heated by a microwave radiation. It involves the condensation of vapors and the return of this condensate to its original. It has been developed and widely used in industrial and laboratory distillations [6]. This process is very fast, simple, effective, and environmentally friendly. It can solve the problems of temperature and concentration gradients and provides uniform growth media.

To the best of our knowledge, there are not many reports on the synthesis of $AgSbS_2$: amorphous $AgSbS_2$ thin films by pulsed laser deposition [1], ternary $AgSbS_2$ thin films by direct fusion process [4], and $Ag(As_xSb_{1-x})S_2$ with x = 0–1 by solid state heating process [7]. Our motivation is to synthesize cubic $AgSbS_2$ nanostructured flowers of nanorods by microwave-assisted refluxing method. No one has ever succeeded in synthesizing them by a solution method.

2. Experimental Procedures

To synthesize $AgSbS_2$, 1 mmol $AgNO_3$, 1 mmol $Sb(CH_3COO)_3$, and 2 mmol L-cysteine ($C_3H_7NO_2S$, LC) (1 : 1 : 2 molar ratio Ag : Sb : S) were dissolved in 50 mL ethylene glycol ($C_2H_6O_2$, EG) and followed by pH adjusting to 0, 1, 2, 3, 4, 5, and 6 using HCl and NaOH. These solutions were processed by refluxing method irradiated with a 300 W microwave radiation for 10, 30, and 60 min. Finally, black precipitates were synthesized, separated by filtration, washed with deionized water and ethanol, and dried at 70°C for 12 h, for further characterization.

Crystalline phases of the as-synthesized nanostructured products were analyzed by an X-ray diffractometer (XRD, Philips X'Pert MPD) operating at 20 kV 15 mA and using Cu-K_α line in 2θ = 10–80 deg. An XRD pattern was also simulated in order to show the real existence of cubic $AgSbS_2$ phase in this research. The morphology investigation was carried out by a field emission scanning electron microscope

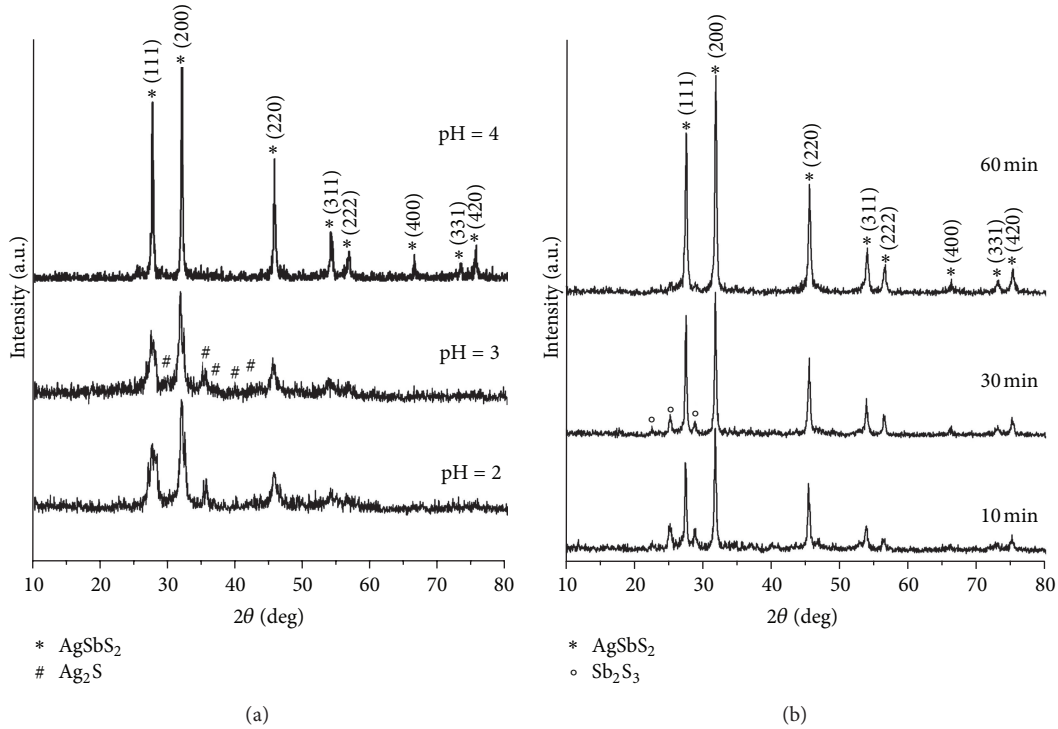


Figure 1: XRD patterns of cubic $AgSbS_2$ synthesized in the solutions (a) with the pH 4, 3, and 2 for 60 min and (b) with the pH 4 for 60, 30, and 10 min.

(FE-SEM, JEOL JSM-6335F) operating at 35 kV and a transmission electron microscope (TEM, JEOL JEM-2010), high-resolution transmission electron microscope (HRTEM), and selected area electron diffractometer (SAED) operating at 200 kV. Their optical properties were studied by a UV-visible spectrometer (Lambda 25 PerkinElmer) using a UV lamp with the resolution of 1 nm and a fluorescence spectrophotometer (LS50B PerkinElmer) using 300 nm excitation wavelength at room temperature.

3. Results and Discussion

At the pH 6 and 5, different phases were detected in the products. Upon further decreasing in the pH to 4, cubic $AgSbS_2$ (JCPDS number 17-0456) [5] was synthesized as the main product (Figure 1(a)). It was the only one cubic crystal system of the $AgSbS_2$ phase [5] with no impurity detection. At the pH 3, 2, 1, and 0, the patterns were specified as cubic $AgSbS_2$ mixed with Ag_2S (JCPDS number 09-0422) [5] impurities.

In the solution containing Ag^+, Sb^{3+}, and L-cysteine ($C_3H_7NO_2S$, LC) at the pH 6 and 5 (very close to the isoelectric point of LC), the solubility of LC was the lowest. The molecules often precipitated out of the solution [6] with the formation of different phases. At the pH 4, the H^+ ions formed bonds with oxygen ions of carboxylate groups, leaving sulfur ions of L-cysteine (LC) to form complex ions with Ag^+ and Sb^{3+} ions [8] at room temperature:

$$Ag^+ + uLC \longrightarrow [Ag(LC)_u]^+ \quad (1)$$

$$Sb^{3+} + vLC \longrightarrow [Sb(LC)_v]^{3+} \quad (2)$$

During microwave refluxing, these complex ions were decomposed with the formation of $(AgSbS_2)_n$:

$$n[Ag(LC)_u]^+ + n[Sb(LC)_v]^{3+} \longrightarrow (AgSbS_2)_n \quad (3)$$

Due to their stabilities, the decomposition proceeded with rather slow rates. The concentration of $(AgSbS_2)_n$ was lower than that synthesized by the direct ion-exchange reaction. Finally, $AgSbS_2$ was synthesized [9, 10]:

$$(AgSbS_2)_n \longrightarrow n(AgSbS_2) \quad (4)$$

Alternately, Ag^+ and Sb^{3+} formed complex ions with LC at room temperature:

$$Ag^+ + Sb^{3+} + xLC \longrightarrow [AgSb(LC)_x]^{4+} \quad (5)$$

Then the complex ions were decomposed by microwave refluxing to synthesize $AgSbS_2$:

$$n[AgSb(LC)_x]^{4+} \longrightarrow n(AgSbS_2) \quad (6)$$

At the pH 3, 2, 1, and 0, additional impurities were synthesized. At high acidic solutions, H^+ ions have much chance to form bonds with LC, leaving Ag^+ as free ions. During refluxing, S^{2-} ions were released from the LC and further reacted with Ag^+ ions to synthesize Ag_2S precipitates.

By reducing the refluxing time of the solution with the pH 4 from 60 min to 30 min and 10 min (Figure 1(b)), Sb_2S_3 (JCPDS number 02-0374) [5] precipitates were also detected caused by incomplete reaction.

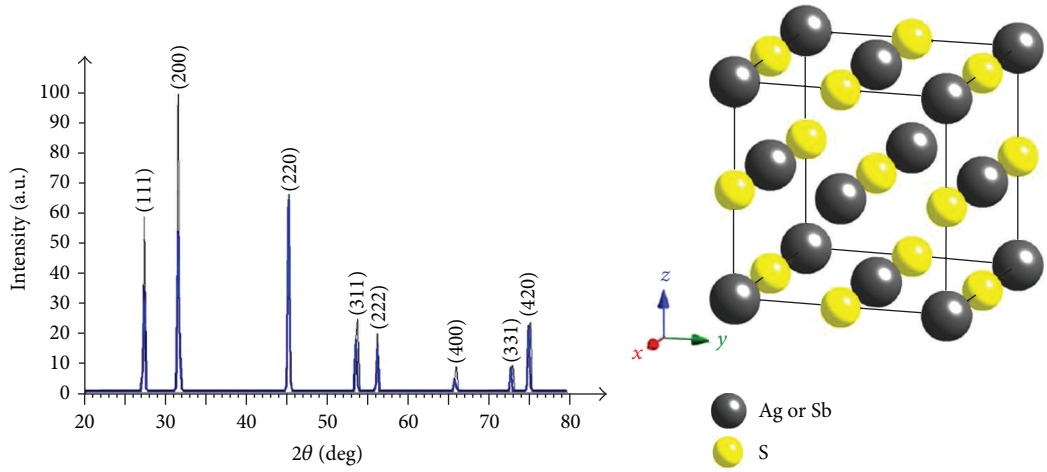


Figure 2: (a) XRD pattern and (b) unit cell of cubic $AgSbS_2$ obtained by simulation.

Table 1: Intensities and 2θ Bragg's angles for different crystallographic planes of simulated, JCPDS database and experimental XRD peaks of cubic $AgSbS_2$.

Plane	Simulation		JCPDS number 17-0456 [5]		Experiment	
	2θ (deg)	Intensity (%)	2θ (deg)	Intensity (%)	2θ (deg)	Intensity (%)
(111)	27.3	59.0	27.3	65.0	27.4	82.2
(200)	31.6	100.0	31.6	100.0	31.7	100.0
(220)	45.3	66.6	45.4	40.0	45.4	56.2
(311)	53.7	25.3	53.8	20.0	53.7	22.6
(222)	56.3	21.3	56.3	16.0	56.4	13.7
(400)	66.1	9.1	66.1	8.0	66.2	12.3
(331)	72.9	8.7	72.9	6.0	72.9	8.2
(420)	75.1	23.5	75.1	8.0	75.1	16.4

In order to show the real existence of cubic $AgSbS_2$ phase, its XRD pattern was simulated [11] and shown in Figure 2(a). The 2θ Bragg angles and peak intensities of the simulation, JCPDS database and experiment were summarized in Table 1. In this research, the experimental peaks were in good accordance with those of the simulation and the JCPDS database, including the intensities of the peaks that were controlled by different growth rates in different directions of unit cells. Simulated crystal structure [12] of $AgSbS_2$ is also shown in Figure 2(b). Its unit cell was cubic structure with Ag or Sb coordinates at (0, 0, 0) and S at (1/2, 1/2, 1/2), and vice versa. For each of $AgSbS_2$ unit cell, Ag or Sb atoms are located at each of the corners and the centers of all the cube faces, including S atoms located in between them. Ag and Sb atoms have the same probability to reside in any of the crystal lattice, and they both have the same occupancy as S atoms in the unit cell.

SEM and TEM images (Figures 3 and 4(a)) show nanostructured $AgSbS_2$ synthesized in the solutions with different pH values. At the pH 0, the product was composed of a number of nanoparticles oriented in different directions. Upon increasing of the pH from 0 to different values, they gradually transformed into different morphologies: clusters of nanoparticles (pH 1), mixed nanoparticles and incomplete nanostructured flowers (pH 2), incomplete nanostructured flowers (pH 3), nanostructured flowers of nanorods grown out of cores (pH 4), and facet irregular microparticles with different orientations (pH 6). These products have different morphologies, controlled by the nucleation and growth processes. At the pH 4 and 60 min, nanorods of flower-like clusters were characterized by HRTEM (Figures 4(b) and 4(c)). The nanorods appeared as rough surfaces with the detection of the (111) and (200) crystallographic planes at an angle of 54.7 degree, specified as single crystal.

To synthesize nanostructured flowers, $AgSbS_2$ molecules nucleated, followed by clustering of nuclei to form $AgSbS_2$ cores. A number of nanorods grew out of these cores to form $AgSbS_2$ flower-like clusters of nanorods (Figure 5). Due to the microwave-assisted refluxing process, the flower-like clusters were synthesized by the orientation growth, promoted by microwave refluxing. The atoms had more chance to arrange themselves in crystal lattice to form nanocrystalline flowers of nanorods. For the present research, microwave refluxing played a key role in the growth of flower-like crystals: decomposition of the complex ions, formation of $(AgSbS_2)_n$ nuclei, and orientation growth of $AgSbS_2$ crystals in the shape of flower-like clusters [9, 10].

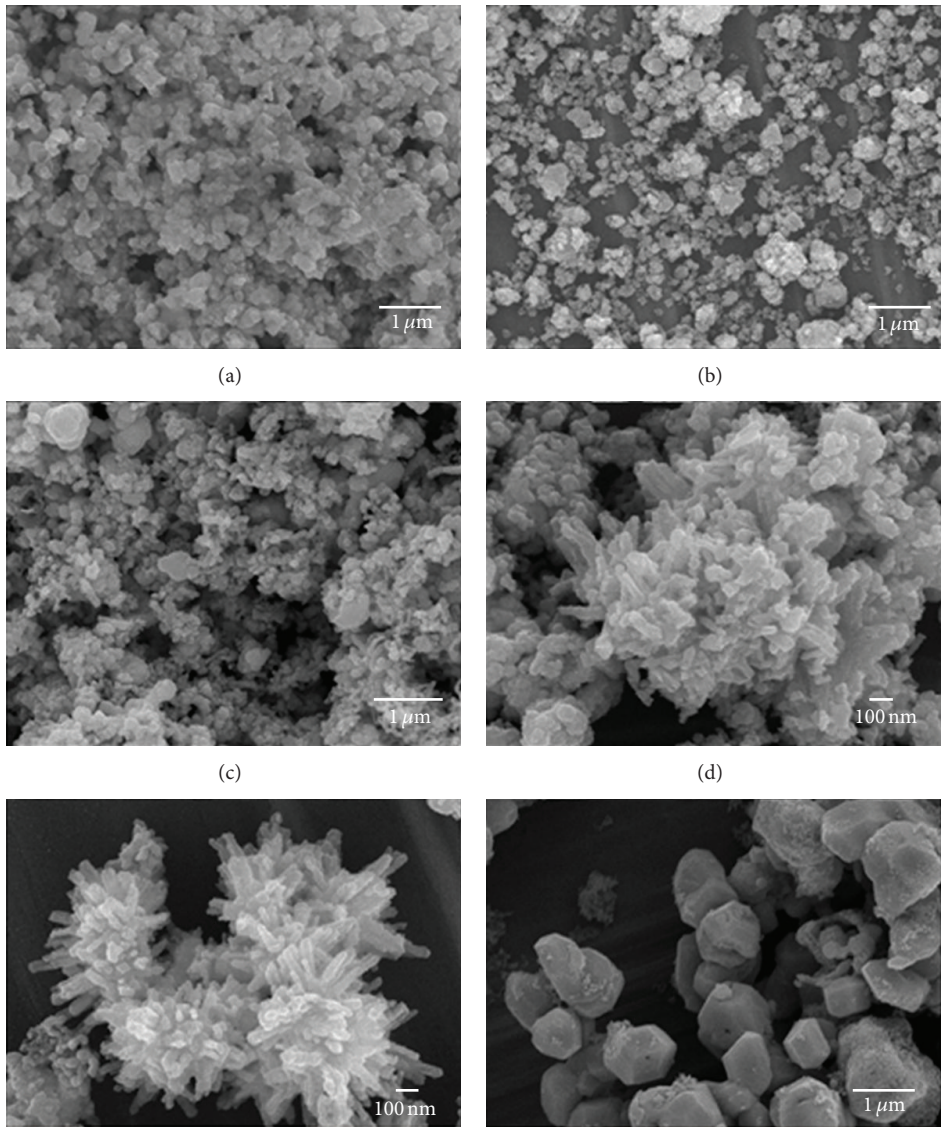


Figure 3: SEM images of the products synthesized in the solutions with the pH of ((a)–(f)) 0, 1, 2, 3, 4, and 6 for 60 min, respectively.

The SAED pattern (Figure 4(d)) appears as systematic spots corresponding to the (200), (202), and (002) crystallographic planes of a single crystalline nanorod of cubic $AgSbS_2$ (JCPDS number 17-0456) [5], with the [0–10] as zone axis. A simulated electron diffraction pattern (Figure 4(e)) [13] was in accordance with that obtained by the experiment, indicating that the interpreted pattern could exist in reality.

Figure 6(a) shows the photonic absorbance attenuating through $AgSbS_2$ nanostructured flowers of nanorods. It should be noted that the absorption was controlled by two photon energy ($h\nu$) ranges, the high and low energies. When photon energy is greater than the energy band gap (E_g), the absorption is linearly increased with the increase in the photon energy. The steep inclination of the linear portion of the curve was caused by the UV absorption for charged transition from the topmost occupied state of valence band to the bottommost unoccupied state of the conduction band. For the photon energy with less than E_g, the absorption curve was different from linearity, caused by the UV absorption for charged transition relating to defects. By extrapolating the linear portion curve of the $(\alpha h\nu)^2$ versus $h\nu$ plot to zero absorption ($\alpha = 0$), the direct energy gap (E_g) was determined to be 1.89 eV, very close to the 1.77–2 eV energy gap of $AgSbS_2$ thin films reported by Ibrahim [4].

Photoluminescence (PL) of $AgSbS_2$ nanostructured flowers (Figure 6(b)) was excited by 300 nm wavelength at room temperature. The emission was detected at 688 nm (1.8 eV) as main peak, including the minor peak at 857 nm, very close to the optical transmission of $AgSbS_2$ thin films for optical recording media reported by Wagner et al. [1]. The main emission peak was specified as the recombination of electrons and holes in trapped surface states residing in the forbidden

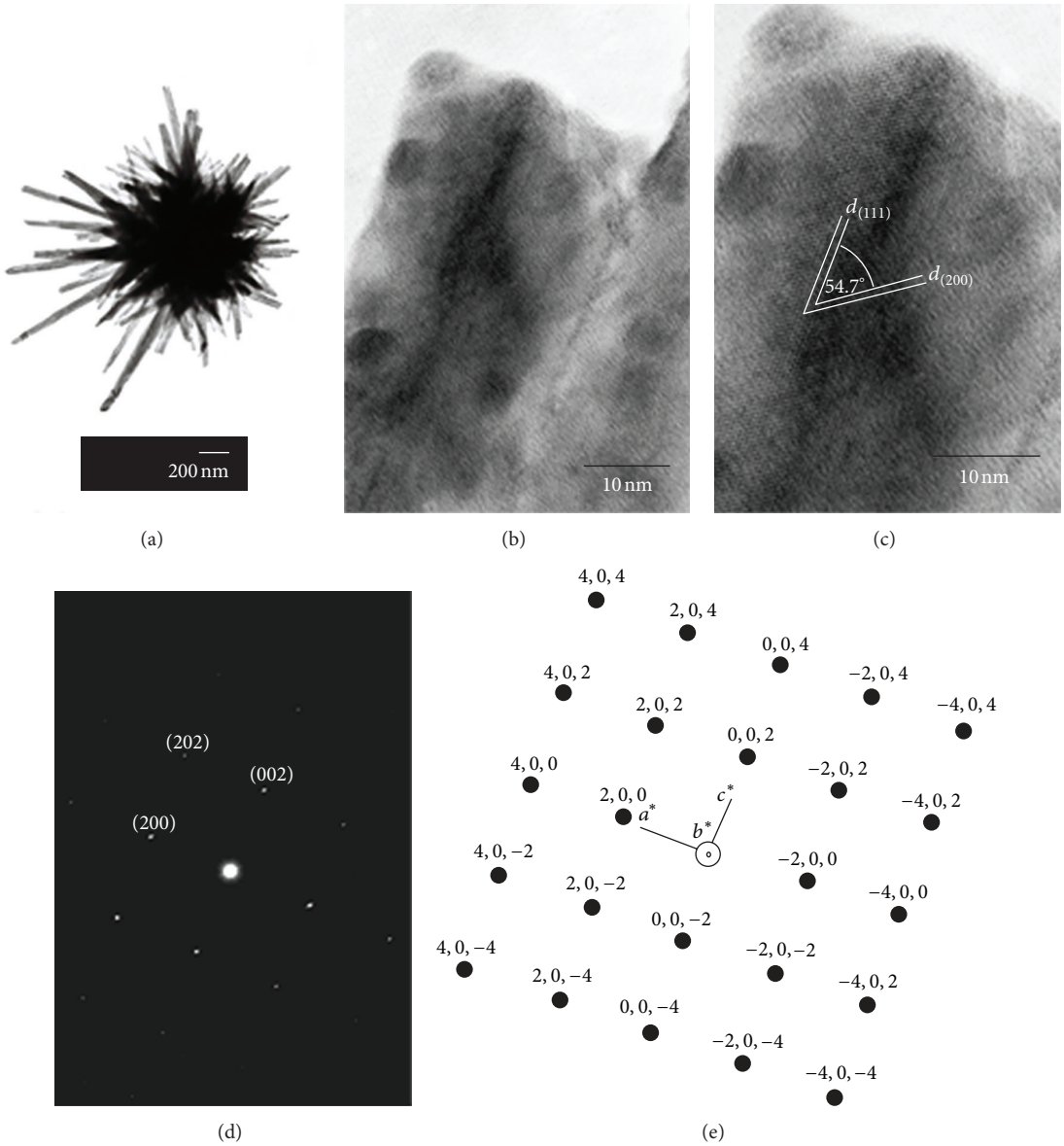


Figure 4: (a) TEM image, ((b), (c)) HRTEM images, and (d) SAED pattern of $AgSbS_2$ nanostructured flowers and (e) the simulated pattern of (d).

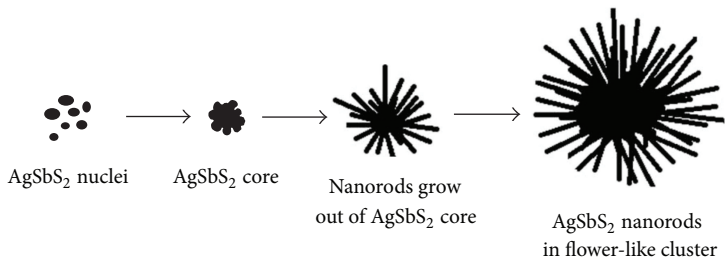


Figure 5: Schematic diagram for the formation of $AgSbS_2$ flower-like clusters of nanorods.

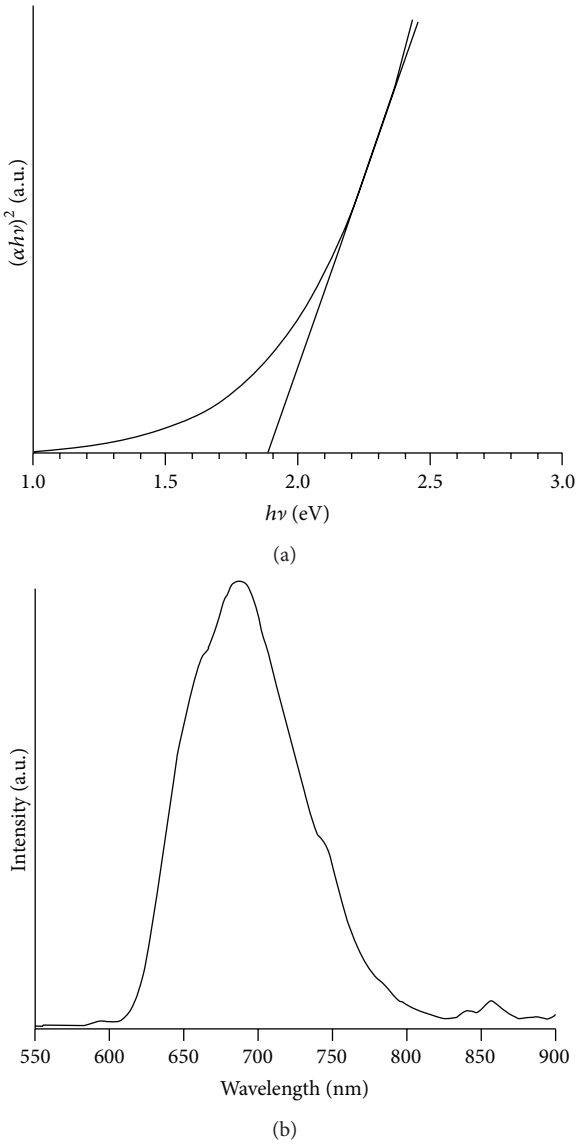


FIGURE 6: (a) The $(\alpha h\nu)^2$ and $h\nu$ plot and (b) photoluminescence of $AgSbS_2$ flower-like clusters of nanorods.

region [1], but for the shoulders, they were caused by the shallow levels of donors and acceptors between the valence and conduction bands [14]. Furthermore, PL emissions could be controlled by different morphologies of the products, including crystalline degree, temperature, different types and concentrations of defects, different shapes and sizes of the products, and excitation wavelengths.

4. Conclusions

$AgSbS_2$ nanostructured flowers were successfully synthesized by microwave-assisted refluxing of $AgNO_3$, $Sb(CH_3COO)_3$, and L-cysteine dissolved in ethylene glycol at the pH 4 for 60 min, according to the formation mechanism proposed in this report. Their direct energy gap was determined to be 1.89 eV, and their main and minor photoluminescence peaks were 688 and 857 nm, respectively.

Acknowledgments

The authors wish to thank the Thailand Research Fund (TRF) for providing financial support through the Royal Golden Jubilee Ph.D. Program and the TRF Research Grant BRG5380020 and the Thailand's Office of the Higher Education Commission through the National Research University (NRU) Project, including the Graduate School of Chiang Mai University through a general support.

References

[1] T. Wagner, J. Gutwirth, P. Nemec et al., "Amorphous chalcogenide $AgSbS_2$ films prepared by pulsed laser deposition," *Applied Physics A*, vol. 79, no. 4–6, pp. 1561–1562, 2004.

[2] J. Gutwirth, T. Wágner, P. Němec, S. O. Kasap, and M. Frumar, "Thermal and optical properties of $AgSbS_2$ thin films prepared by pulsed laser deposition (PLD)," *Journal of Non-Crystalline Solids*, vol. 354, no. 2-9, pp. 497–502, 2008.

[3] J. S. Sanghera, J. Heo, and J. D. Mackenzie, "Chalcohalide glasses," *Journal of Non-Crystalline Solids*, vol. 103, no. 2-3, pp. 155–178, 1988.

[4] A. M. Ibrahim, "Optical properties of ternary $AgSbS_2$ thin films," *Journal of Physics*, vol. 7, no. 29, article 019, pp. 5931–5938, 1995.

[5] "Powder Diffraction File," JCPDS-ICDD, 12 Campus Boulevard, Newtown Square, PA, 19073-3273, USA., 2001.

[6] http://en.wikipedia.org/.

[7] M. Razmara and R. Pattrick, "Synthesis, characterization, stability and structure of solid solutions between α-miargyrite ($AgSbS_2$)—smithite ($AgAsS_2$) and β-miargyrite—smithite," *Geopersia*, vol. 1, pp. 55–66, 2011.

[8] H. Gai, Y. Wu, L. Wu et al., "Solvothermal synthesis of CdS nanowires using L-cysteine as sulfur source and their characterization," *Applied Physics A*, vol. 91, no. 1, pp. 69–72, 2008.

[9] G. Shen, D. Chen, K. Tang, and Y. Qian, "Novel polyol route to AgBiS2 nanorods," *Journal of Crystal Growth*, vol. 252, no. 1-3, pp. 199–201, 2003.

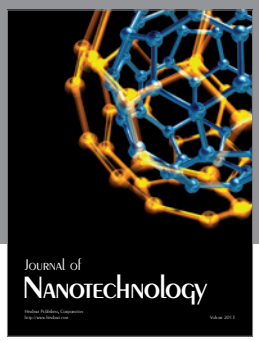
[10] D. Chen, G. Shen, K. Tang et al., "Microwave synthesis of $AgBiS_2$ dendrites in aqueous solution," *Inorganic Chemistry Communications*, vol. 6, no. 6, pp. 710–712, 2003.

[11] "CrystalDiffract Version 1. 2. 3," CrystalMaker Software Limited, Centre for Innovation & Enterprise, Oxford University Begbroke Science Park Woodstock Road, Begbroke, Oxfordshire, UK, 1994–2009.

[12] "CrystalMaker Version 2. 2. 0," CrystalMaker Software Limited, Centre for Innovation & Enterprise, Oxford University Begbroke Science Park, Sandy Lane, Yarnton, Oxfordshire, UK, 1994–2009.

[13] C. Boudias and D. Monceau, "CaRIne Crystallography 3. 1, DIVERGENT S.A," Centre de Transfert, Compiègne, France, 1989–1998.

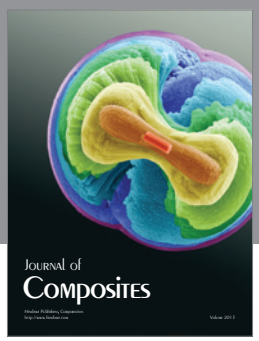
[14] H. Hu, Z. Liu, B. Yang, X. Chen, and Y. Qian, "Template-mediated growth of Cu_3SnS_4 nanoshell tubes," *Journal of Crystal Growth*, vol. 284, no. 1-2, pp. 226–234, 2005.

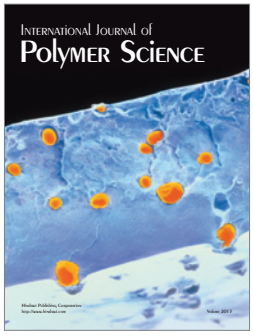


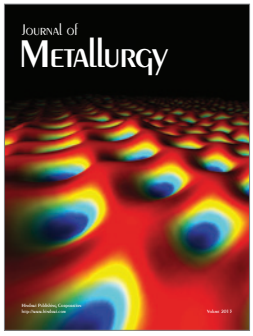




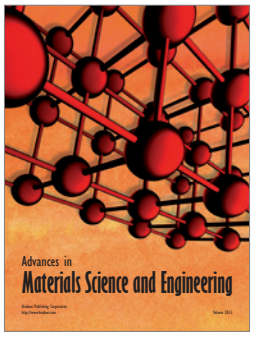


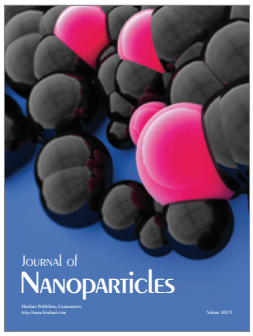




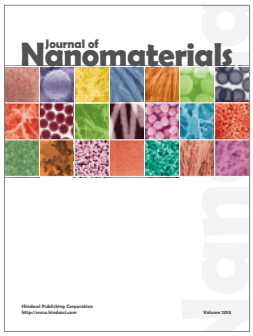




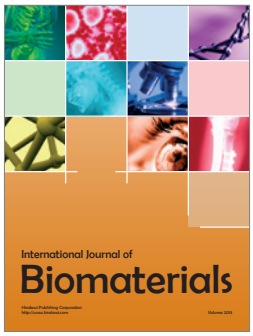












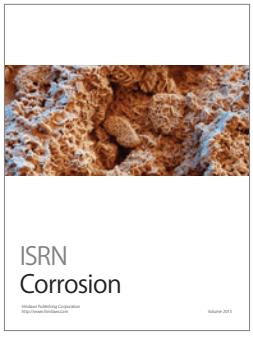
Hindawi

Submit your manuscripts at
http://www.hindawi.com











Materials Letters 101 (2013) 9–12

Contents lists available at SciVerse ScienceDirect

Materials Letters

journal homepage: www.elsevier.com/locate/matlet

Cyclic microwave-assisted synthesis of $CuFeS_2$ nanoparticles using biomolecules as sources of sulfur and complexing agent

Kamonwan Aup-Ngoen [a], Titipun Thongtem [b,c,*], Somchai Thongtem [a,c,**], Anukorn Phuruangrat [d]

[a] Department of Physics and Materials Science, Faculty of Science, Chiang Mai University, Chiang Mai 50200, Thailand
[b] Department of Chemistry, Faculty of Science, Chiang Mai University, Chiang Mai 50200, Thailand
[c] Materials Science Research Center, Faculty of Science, Chiang Mai University, Chiang Mai 50200, Thailand
[d] Department of Materials Science and Technology, Faculty of Science, Prince of Songkla University, Hat Yai, Songkhla 90112, Thailand

ARTICLE INFO

Article history:
Received 24 November 2012
Accepted 11 March 2013
Available online 21 March 2013

Keywords:
Electron microscopy
Nanocrystalline materials
Spectroscopy
X-ray techniques

ABSTRACT

Copper iron sulfide ($CuFeS_2$) nanoparticles were successfully synthesized by a 300 W cyclic microwave radiation, exposing onto ethylene glycol containing $Cu(CH_3COO)_2$, $FeCl_3 \cdot 6H_2O$ or $FeCl_2 \cdot 4H_2O$ and L-cysteine biomolecules. X-ray diffraction (XRD), field emission scanning electron microscopy (FE-SEM), transmission electron microscopy (TEM), Raman spectrometry and X-ray photoelectron spectroscopy (XPS) revealed the presence of pure tetragonal chalcopyrite $CuFeS_2$ nanoparticles with valence states of Cu^+, Fe^{3+} and S^{2-} and four Raman shifts at 215.0–218.6, 280.2–281.4, 394.4–394.9 and 472.2–473.4 cm^{-1}. A formation mechanism of the products was also proposed according to the experimental results.

© 2013 Elsevier B.V. All rights reserved.

1. Introduction

Chalcopyrite copper iron sulfide ($CuFeS_2$) is a I–III–VI_2 ternary compound known as an antiferromagnetic semiconductor, which has narrow band gap (0.5–0.6 eV), very high Néel temperature (550 °C) and innovative electrical, optical and magnetic properties [1–5]. It has potential applications for cathodes of lithium-ion batteries [6], solar cells [1] and thermoelectric devices [5]. Different methods have been investigated for the synthesis of $CuFeS_2$: nanorods and nanoparticles by hydrothermal synthesis [1,7], single crystalline nanowires and hexagonal plate-like chalcopyrite by the solvothermal process [2,6], spherical and pyramidal nanocrystals by thermal decomposition and reaction of metal-dithiocarbamate or acetylacetonate precursors with sulfur in an organic solvent mixture [3], and a combination of mechanical alloying and spark plasma sintering [5].

In this research, cyclic microwave radiation was used for the synthesis of $CuFeS_2$ nanoparticles using L-cysteine biomolecules as sources of sulfur and complexing agent. The process is more rapid and efficient than that achieved by a conventional one. Additionally, it can solve the problems of temperature and concentration gradients and provide uniform growth media.

2. Experiment

To synthesize $CuFeS_2$, 1 mmol $Cu(CH_3COO)_2$, 3 mmol $FeCl_3 \cdot 6H_2O$ or $FeCl_2 \cdot 4H_2O$ and 2 mmol $C_3H_7NO_2S$ (L-cysteine) were mixed in 40 ml ethylene glycol (EG) to form solutions which were processed by a 300 W cyclic microwave radiation (CMR) for 5–40 cycles. Each cycle, microwave radiation was on for 40 s every 40 s interval. In the end, the precipitates were separated, rinsed and dried at 70 °C for 24 h to form CA-1 and CA-2 products, where CA, 1 and 2 were for those synthesized using $Cu(CH_3COO)_2$, $FeCl_3 \cdot 6H_2O$ and $FeCl_2 \cdot 4H_2O$, respectively.

3. Results and discussion

XRD: The crystalline structure and chemical composition of the as-synthesized products were characterized by XRD of which the patterns (Fig. 1) were compared with the JCPDS database no. 01-0842 [8]. All diffraction peaks of CA-1 and CA-2 were readily indexed to be tetragonal chalcopyrite $CuFeS_2$. Their XRD peaks were similar in height and very sharp, implying that the products were composed of a number of particles with the same size and high crystalline degree.

SEM, TEM, EDX and SAED: An effect of different iron sources on morphologies was investigated by SEM and EDX (Fig. 2). The CA-1

* Corresponding author at: Department of Chemistry, Faculty of Science, Chiang Mai University, Chiang Mai 50200, Thailand. Tel.: +66 53943344; fax: +66 53892277.
** Corresponding author at: Department of Physics and Materials Science, Faculty of Science, Chiang Mai University, Chiang Mai 50200, Thailand. Tel.: +66 53941924; fax: +66 53943445.
E-mail addresses: ttpthongtem@yahoo.com (T. Thongtem), schthongtem@yahoo.com, sthongtem@hotmail.com (S. Thongtem).

0167-577X/$ - see front matter © 2013 Elsevier B.V. All rights reserved.
http://dx.doi.org/10.1016/j.matlet.2013.03.055

product contained 10–20 nm nanoparticles in clusters. Each cluster appeared as rough surface which was the proof of loosely packed nanoparticles grouping together [9]. For the CA-2 product, it was composed of nanoparticles in irregular clusters, in accordance with the above XRD analysis. EDX spectra of both products revealed the presence of Cu, Fe and S as fundamental elements, sputtered Au for conductivity improving, including C and O of polymer tape.

The nanoparticles were further investigated by TEM and SAED (Fig. 3). For 40 cycles, intensive contrast at dark edges surrounding small bright areas indicates that CA-1 was composed of a number of nanoparticles cluster together, which was not able to be detected by SEM. The product presents really fine nanoparticles.

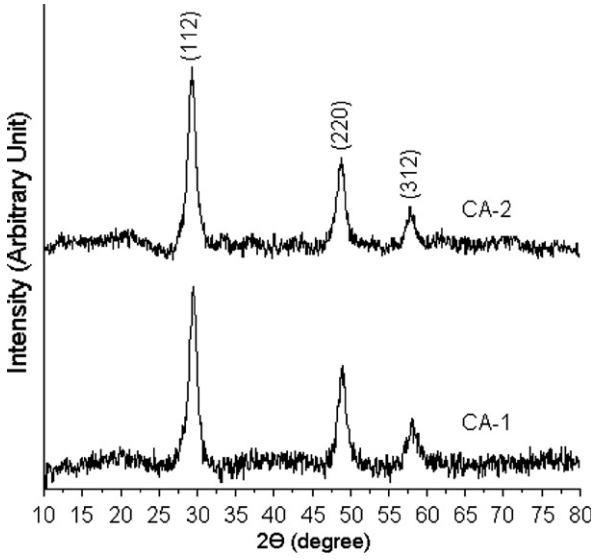


Fig. 1. XRD patterns of CA-1 and CA-2 synthesized for 40 cycles.

Upon decreasing the processing time from 40 cycles to 20 and 5 cycles, the products remained as clusters of nanoparticles with reducing their sizes in sequence. By changing the iron source from $FeCl_3 \cdot 6H_2O$ to $FeCl_2 \cdot 4H_2O$, clusters of nanoparticles were still detected. SAED patterns of these products were composed of diffuse and hollow concentric rings, specified as polynanocrystalline $CuFeS_2$ [8].

Raman and XPS spectra: Raman spectra of $CuFeS_2$ (Fig. 4) shows four Raman shifts at 215.0–218.6, 280.2–281.4 (A_1 modes), 394.4–394.9 (B_2 modes) and 472.2–473.4 (E modes) cm^{-1}, in accordance with the previous report [10]. A slight difference of Raman peaks was observed, caused by systematic downshift of Raman peaks of the CA-1 comparing with those of the CA-2. Band positions and relative intensities of the Raman peaks could slightly vary from one spectrum to another due to the orientation of crystal lattice and optical properties, including the presence of local impurities or defects inside [10,11].

XPS spectra of copper, iron and sulfur containing in CA-1 and CA-2 are shown in Fig. 5. The Cu2p core-level spectra show the analyzed binding energy (BE) of $Cu2p_{3/2}$ (932.3–932.5 eV) and $Cu2p_{1/2}$ (952.2–952.5 eV) peaks, corresponding to Cu^+. No $Cu2p_{3/2}$ satellite peak at 942 eV of Cu^{2+} was detected. For the Fe2p core-level spectra, BE of $Fe2p_{3/2}$ (711.3–711.5 eV) and $Fe2p_{1/2}$ (725.8–726.2 eV) were in good accordance with Fe^{3+}. The S2p core-level spectra reveal BE of $S2p_{3/2}$ (162.5–163.3 eV), corresponding to S^{2-} [2,3,12]. Furthermore, additional peaks were detected at 169.0–169.1 eV and were likely to be from the oxidized parts of the products during the synthesis. Other minor peaks of C1 s (284.5–285.3 eV) and O1 s (531.3–531.5 eV) were also detected [2]. They belonged to the coated carbon for conductivity improvement for XPS analysis and absorbed gaseous molecules.

Formation mechanism: Mixtures of $Cu(CH_3COO)_2$, $FeCl_3 \cdot 6H_2O$ and L-cysteine biomolecules in EG were processed by CMR to form $CuFeS_2$ with valence states of Cu^+, Fe^{3+} and S^{2-}. Possibly, $Cu(CH_3COO)_2$ was reduced by EG, a well-known reducing agent, by transforming Cu^{2+} into Cu^+ intermediate ions [13–16], which further combined with L-cysteine to form [Cu(L-cysteine) complexes]. Concurrently, Fe^{3+} formed [Fe(L-cysteine) complexes]

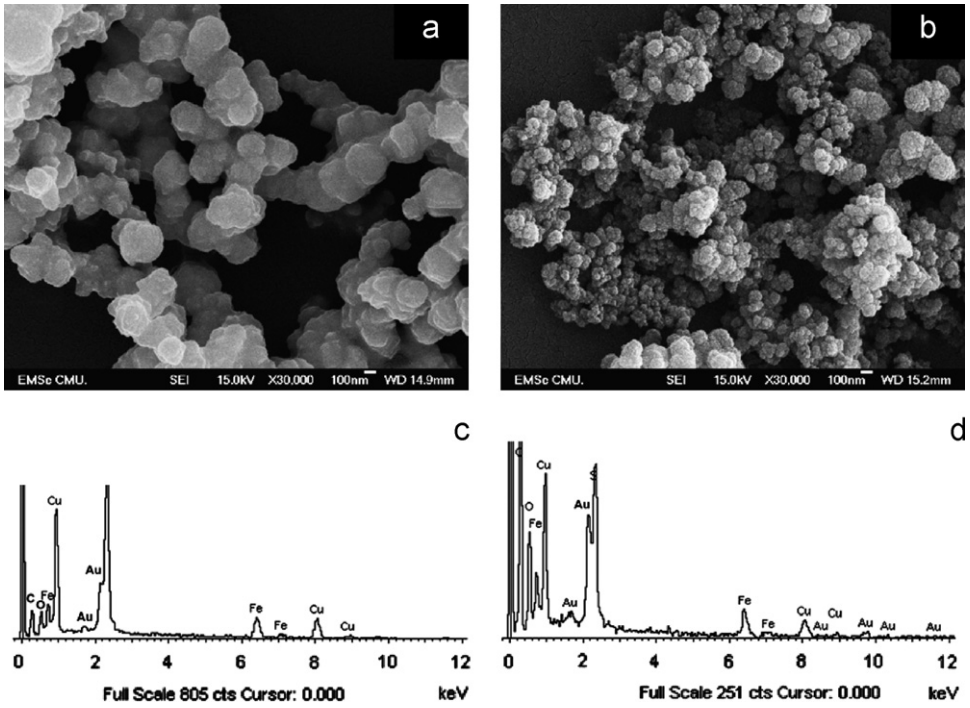


Fig. 2. SEM images and EDX spectra of (a,c) CA-1 and (b,d) CA-2 synthesized for 40 cycles.

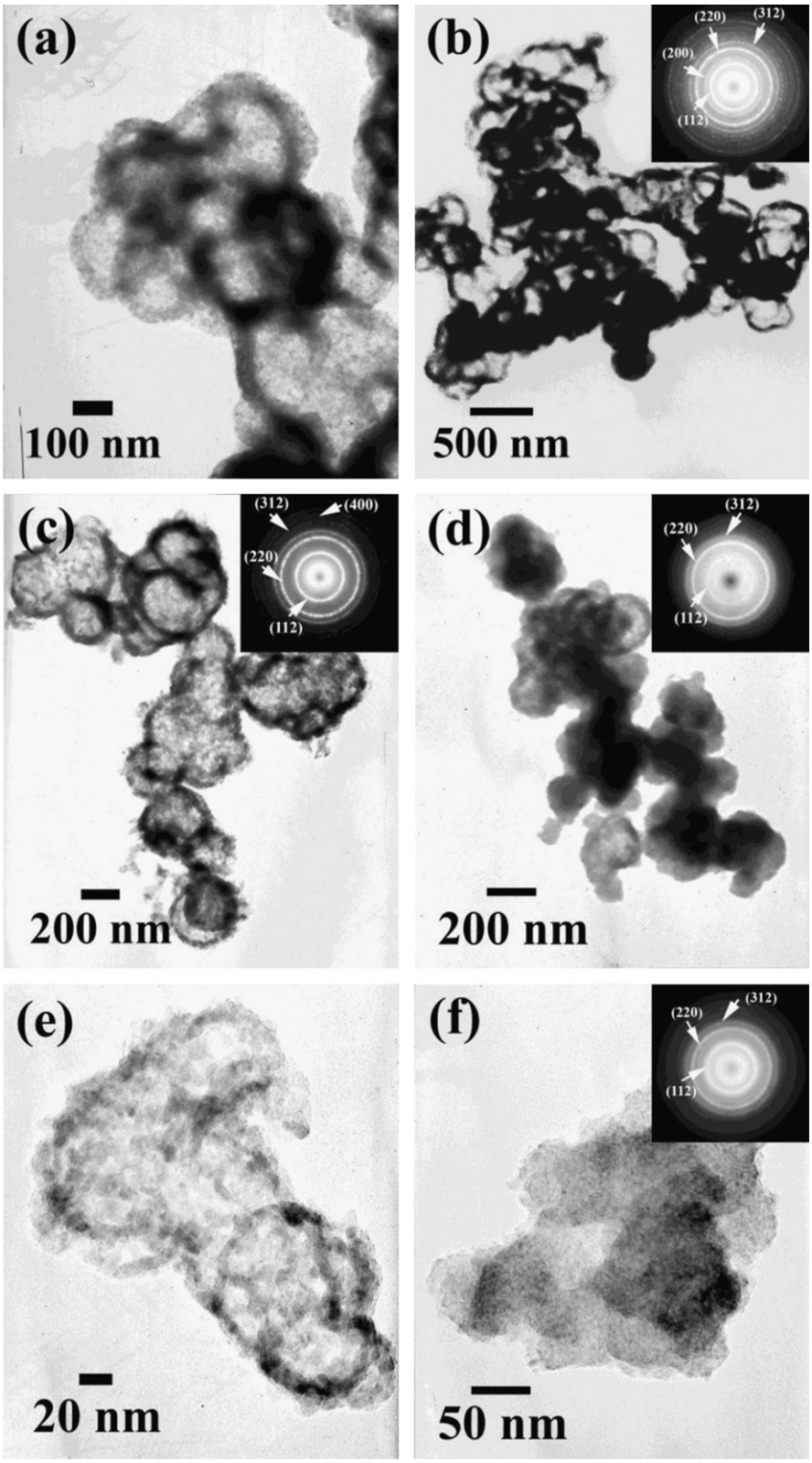


Fig. 3. TEM images and SAED patterns of (a–d) CA-1 synthesized for 40, 40, 20 and 5 cycles, including those of (e,f) CA-2 synthesized for 40 cycles, respectively.

with L-cysteine. During CMR, these complexes were combined and decomposed with the formation of $CuFeS_2$ nuclei. Alternately, [Cu–Fe(L-cysteine) complexes] could form with the subsequent formation of $CuFeS_2$ nuclei.

When $FeCl_2 \cdot 4H_2O$ was used instead of $FeCl_3 \cdot 6H_2O$, $CuFeS_2$ with valence states of Cu^+, Fe^{3+} and S^{2-} was also synthesized. Oxidation–reduction of Fe^{2+} and Cu^{2+} proceeded, including the formation of complexes and $CuFeS_2$ nuclei in sequence as above.

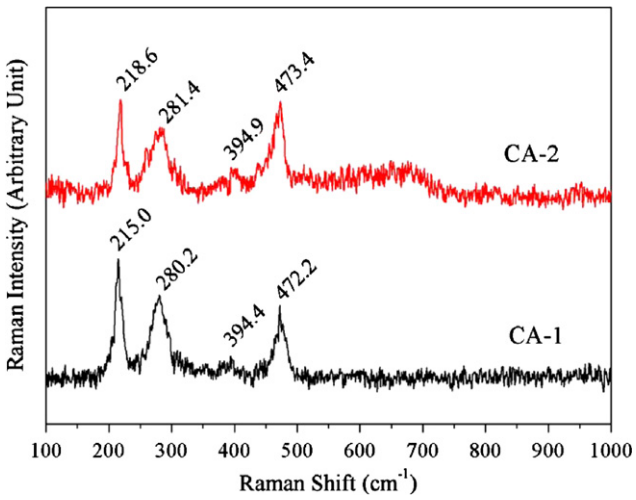


Fig. 4. Raman spectra of CA-1 and CA-2 synthesized for 40 cycles.

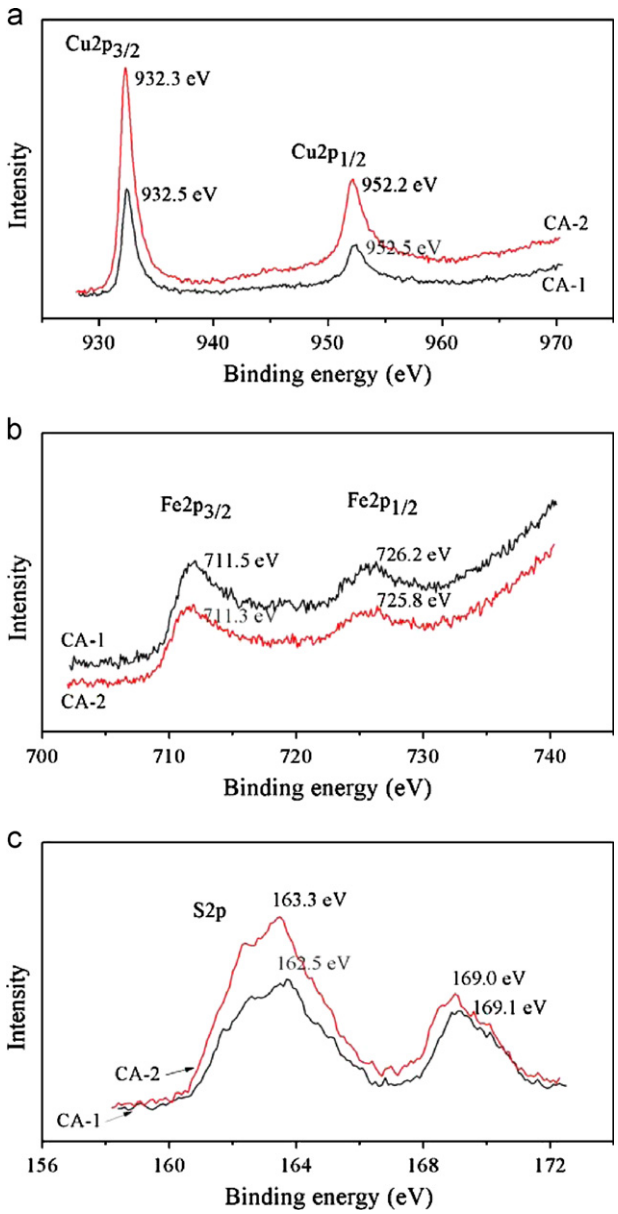


Fig. 5. XPS spectra of (a–c) Cu, Fe and S containing in CA-1 and CA-2 synthesized for 40 cycles, respectively.

The nuclei grew by forming $CuFeS_2$ nanoparticles and clustering in groups with reducing their surface energies.

4. Conclusions

Pure tetragonal $CuFeS_2$ nanoparticles were successfully synthesized by a 300 W CMR, exposing onto EG containing $Cu(CH_3COO)_2$, $FeCl_3 \cdot 6H_2O$ or $FeCl_2 \cdot 4H_2O$ and L-cysteine precursors for 5–40 cycles. Four Raman shifts were detected at 215.0–218.6, 280.2–281.4, 394.4–394.9 and 472.2–473.4 cm^{-1}, and BE of Cu^+ at 932.3–932.5 eV ($Cu2p_{3/2}$) and 952.2–952.5 eV ($Cu2p_{1/2}$), Fe^{3+} at 711.3–711.5 eV ($Fe2p_{3/2}$) and 725.8–726.2 eV ($Fe2p_{1/2}$), and S^{2-} at 162.5–163.3 eV ($S2p_{3/2}$). In this research, Fe-sources played the same role in crystalline degree and size distribution of the products.

Acknowledgments

We wish to thank the Thailand Research Fund for financial support through the research grant BRG5380020 and the Royal Golden Jubilee Ph.D. Program, and the Thailand's Office of the Higher Education Commission through the National Research University Project, including the Graduate School of Chiang Mai University through a general support.

References

[1] Chen KT, Chiang CJ, Ray D. Mater Lett 2013;95:172–4.
[2] Wang MX, Wang LS, Yue GH, Wang X, Yan PX, Peng DL. Mater Chem Phys 2009;115:147–50.
[3] Wang YHA, Bao N, Gupta A. Solid State Sci 2010;12:387–90.
[4] Disale SD, Garje SS. Appl Organomet Chem 2009;23:492–7.
[5] Li J, Tan Q, Li JF. J Alloys Compd 2013;551:143–9.
[6] Ding W, Wang X, Peng H, Hu L. Mater Chem Phys 2013;137:872–6.
[7] Hu J, Lu Q, Deng B, Tang K, Qian Y, Li Y, et al. Inorg Chem Commun 1999;2:569–71.
[8] Powder Diffract File, JCPDS-ICDD. 12 Campus Boulevard, Newtown Square, PA 19073-3273, USA; 2001.
[9] Zhang DE, Xie Q, Wang MY, Zhang XB, Li SZ, Han GQ, et al. Solid State Sci 2010;12:1529–33.
[10] Wang C, Xue S, Hu J, Tang K. Jpn J Appl Phys 2009;48:023003 3pp.
[11] White SN. Chem Geol 2009;259:240–52.
[12] Kuzuya T, Itoh K, Ichidate M, Wakamatsu T, Fukunaka Y, Sumiyama K. Electrochim Acta 2007;53:213–7.
[13] Anzlovar A, Orel ZC, Zigon M. J Nanosci Nanotechnol 2008;8:3516–25.
[14] Ningthoujam RS, Gajbhiye NS, Sharma S. Pramana-J Phys 2009;72:577–86.
[15] Carotenuto G, Pepe GP, Nicolais L. Eur Phys J B 2000;16:11–7.
[16] Orel ZC, Matijević E, Goia DV. J Mater Res 2003;18:1017–22.

Hindawi Publishing Corporation
Journal of Nanomaterials
Volume 2013, Article ID 208230, 4 pages
http://dx.doi.org/10.1155/2013/208230

Research Article

Photoluminescence of Hexagonal ZnO Nanorods Hydrothermally Grown on Zn Foils in KOH Solutions with Different Values of Basicity

Nuengruethai Ekthammathat,[1] Titipun Thongtem,[1,2] Anukorn Phuruangrat,[3] and Somchai Thongtem[2,4]

[1] *Department of Chemistry, Faculty of Science, Chiang Mai University, Chiang Mai 50200, Thailand*
[2] *Materials Science Research Center, Faculty of Science, Chiang Mai University, Chiang Mai 50200, Thailand*
[3] *Department of Materials Science and Technology, Faculty of Science, Prince of Songkla University, Hat Yai, Songkhla 90112, Thailand*
[4] *Department of Physics and Materials Science, Faculty of Science, Chiang Mai University, Chiang Mai 50200, Thailand*

Correspondence should be addressed to Titipun Thongtem; ttpthongtem@yahoo.com and
Anukorn Phuruangrat; phuruangrat@hotmail.com

Received 18 November 2012; Revised 19 February 2013; Accepted 25 February 2013

Academic Editor: Yun Zhao

Copyright © 2013 Nuengruethai Ekthammathat et al. This is an open access article distributed under the Creative Commons Attribution License, which permits unrestricted use, distribution, and reproduction in any medium, provided the original work is properly cited.

Aligned hexagonal ZnO nanorods on pure Zn foils were hydrothermally synthesized in 30 mL solutions containing 0.05–0.50 g KOH. The products were characterized by X-ray diffraction (XRD), scanning electron microscopy (SEM), transmission electron microscopy (TEM), and photoluminescence (PL) spectroscopy. In this research, wurtzite hexagonal ZnO nanorods grown along the [002] direction with green light emission at 541 nm caused by singly ionized oxygen vacancies inside were detected.

1. Introduction

One-dimensional (1D) semiconducting materials are able to be used for a number of potential applications in short wavelength optical, nanoelectronic, and optoelectronic devices due to their tunable electronic and optoelectronic properties controlled by morphologies and dimensions [1–3]. Compared to two-dimensional (2D), three-dimensional (3D), and zero-dimensional (0D) nanostructures, the 1D nanostructure has unique characteristic: large aspect ratio, single crystalline structure, and oriented growth [3]. Zinc oxide is an important low-cost II–VI basic semiconductor with 3.37 eV wide band gap and strong exciton binding energy of 60 meV at room temperature [4–7]. It possesses unique catalytic, electrical, optoelectronic, and photochemical properties—very interesting for a number of potential applications as room-temperature UV lasers, sensors, light-emitting diodes, optical switches, solar cells, and photocatalysis due to its low dielectric constant, high chemical stability, good photoelectric, and piezoelectric behaviors [4, 6, 8].

In the paper, hexagonal ZnO nanorods on Zn foils were hydrothermally synthesized in solutions containing 0.05–0.50 g KOH at 120°C. Their phase, morphology, and photoluminescence were investigated and discussed in more details.

2. Experimental Procedure

Reagents of the research were of analytical grade and used without further purification. The hexagonal prism ZnO nanorods were grown on Zn foils by the following. Several 10×10 mm square Zn foils with 0.25 mm thick were cleaned with deionized water and absolute alcohol in an ultrasound bath and put in 30 mL of 0.05, 0.10, 0.20, 0.30, 0.40, and 0.50 g KOH aqueous solutions, containing 1, 2, 4, 6, 8, and 10 times of KOH in sequence. All of the solutions and zinc foils were transferred into 50 mL Teflon-lined stainless steel autoclaves, which were tightly closed, heated at 120°C in a laboratory electric oven for 24 h, and naturally cooled to room temperature. In the end, the zinc foils were thoroughly rinsed by

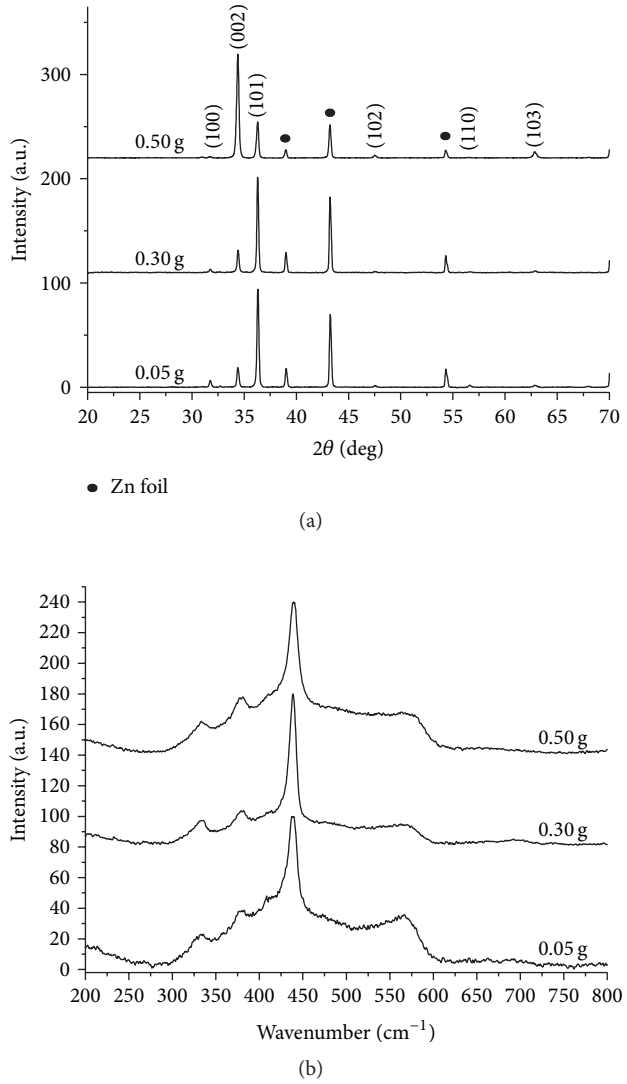


Figure 1: (a) XRD patterns and (b) Raman spectra of the as-synthesized ZnO in 30 mL solutions containing 1 (0.05 g), 6 (0.30 g) and 10 times (0.50 g) of KOH.

deionized water several times and alcohol, and dried at 70°C in an electric oven for 12 h for further characterization.

X-ray diffraction (XRD) operated on Philips X'Pert MPD X-ray diffractometer with Cu K_α radiation in the 2θ of 20–70 deg with a scanning rate of 0.02 deg per step and Raman spectroscopy on T64000 HORIBA Jobin Yvon at 50 mW Ar Laser with 514.5 nm wavelength were used to determine phase, crystalline degree, purity, and vibration modes. Their morphologies were characterized by scanning electron microscopy (SEM, JEOL JSM-6335F) with an accelerating voltage of 15 kV across the LaB_6 cathode. Their nanostructures and growth direction were further investigated by transmission electronic microscopy (TEM) and selected area electronic diffraction (SAED) on a JEOL JEM-2010 TEM at 200 kV with LaB_6 gun. At the end, optical properties of the products were analyzed by a LS50B *Perkin Elmer* fluorescence spectrometer in the wavelength range of 450–700 nm.

3. Results and Discussion

Figure 1(a) exhibits typical XRD patterns of the as-grown ZnO on Zn foils, revealing that all diffraction peaks were explicable in term of wurtzite ZnO structure with $a = b = 3.251$ Å and $c = 5.208$ Å (JCPDS No. 36-1451) [9]. Sharp diffraction peaks indicate good crystalline degree of the as-synthesized crystals without other impurities detection.

Degree of c orientation of the as-synthesized ZnO samples was explained by the relative texture coefficient (TC) [10, 11] of the (002) peak calculated using the formula

$$\mathrm{TC}_{002} = \frac{\left(I_{002}/I^0_{002}\right)}{\left[I_{002}/I^0_{002} + I_{100}/I^0_{100}\right]} \quad (1)$$

TC_{002} is the relative texture coefficient of the (002) over (100) diffraction peaks. I_{002} and I_{100} are the measured diffraction intensities of the (002) and (100) peaks, including the corresponding I^0_{002} and I^0_{100} values of the randomly oriented standard powder, respectively. For randomly crystallographic orientation, the texture coefficient of ZnO is 0.5. In the solution containing 0.50 g KOH, calculated TC_{002} was 0.86, which supported the preferential orientation of the as-synthesized ZnO nanorods grown along the [002] direction on the Zn foil.

Wurtzite ZnO structure belongs to C^4_{6v} ($P6_3mc$) space group with two formula units per primitive cell, and all atoms occupy the C^{3v} sites. Group theory of wurtzite ZnO structure predicts eight sets of phonon modes: $A_1 + E_1 + 2E_2$ (Raman active), $2B_2$ (Raman silent), and $A_1 + E_1$ (IR active). Moreover, the A_1 and E_1 symmetry are split into longitudinal (L) and transverse (T) optical (O) components due to the macroscopic electric fields associated with the LO phonons. Figure 1(b) shows Raman spectra of the as-synthesized ZnO nanorods. They show a dominant peak of typical characteristic of the wurtzite ZnO structure at 439 cm^{-1}, assigned to be the optical phonon E_{2H} mode. The weak peak at 332 cm^{-1} was assigned to be the second-order Raman scattering arising from the zone/zero boundary phonons E_{2H}–E_{2L} of multiphonon process, while the Raman peak at 379 cm^{-1} is attributed to A_1 symmetry with the TO mode. Furthermore, Raman spectra of ZnO samples at 567 cm^{-1} are a contribution of the E_1 (LO) mode which is directly associated with oxygen vacancies. The stronger E_1 (LO) mode indicates the presence of higher oxygen vacancies inside [5, 12–14].

SEM images as shown in Figure 2 were investigated on surfaces of Zn foils after hydrothermal treatment in 30 mL solutions containing 1 (0.05 g), 2 (0.10 g), 4 (0.20 g), 6 (0.30 g), 8 (0.40 g), and 10 times (0.50 g) of KOH. An interesting feature of the nanostructures grown on the bottom surfaces exhibited the presence of aligned nanorods of ZnO with the diameter ranging from 400 nm to 700 nm without the detection of other nanostructures. The lengths of the ZnO nanorods are in the range of several micrometers to even longer than 5–7 μm. These nanorods were enlarged and lengthened in sequence with an increase in the degree of basicity. The inset of Figure 2(f) demonstrates the hexagonal

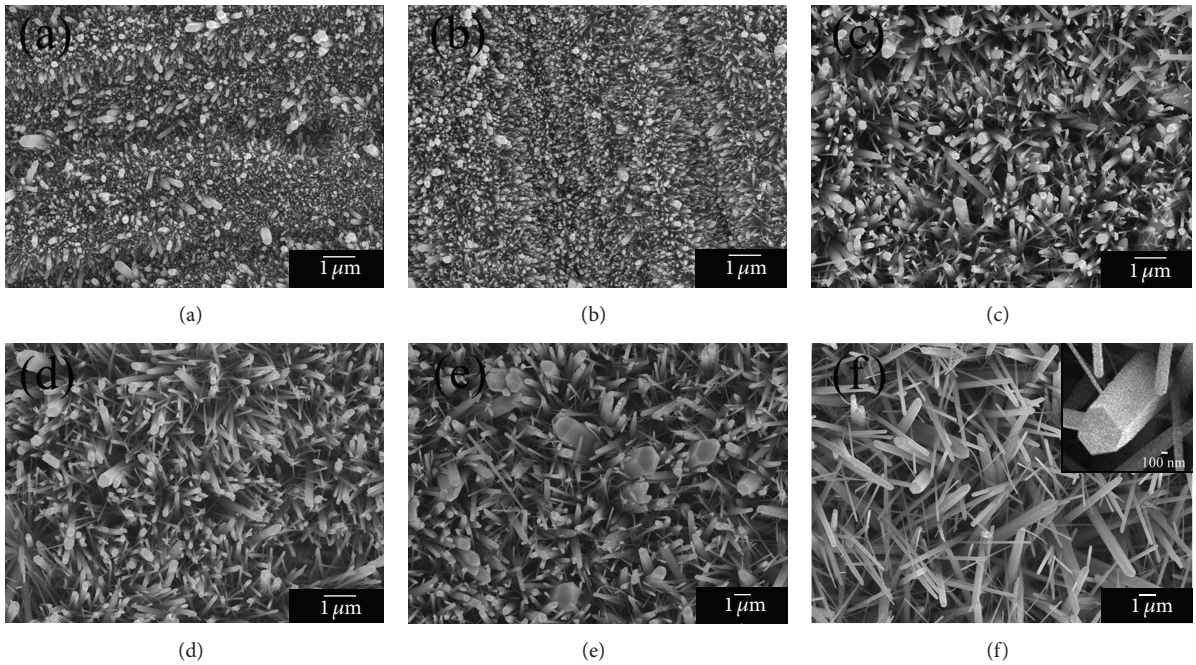


Figure 2: SEM images of the as-synthesized ZnO samples in 30 mL solutions containing (a) 1 (0.05 g), (b) 2 (0.10 g), (c) 4 (0.20 g), (d) 6 (0.30 g), (e) 8 (0.40 g), and (f) 10 times (0.50 g) of KOH.

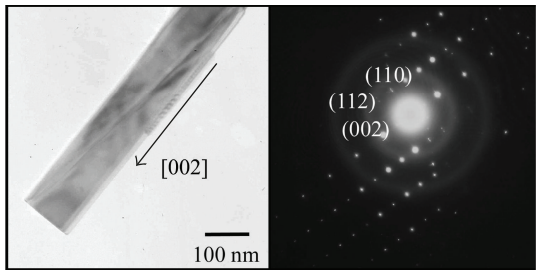


Figure 3: TEM image and SAED pattern of hexagonal ZnO nanorod in 30 mL solution containing 10 times (0.50 g) of KOH.

ZnO nanorod which was fully grown on Zn foil in the solution containing 0.50 g KOH.

The hexagonal ZnO nanorods were also characterized through TEM and SAED (Figure 3). TEM image reveals a single hexagonal ZnO nanorod with smooth surface and the preferred growth in the [002] direction. It shows the SAED pattern of bright spots corresponding to hexagonal wurtzite ZnO [9].

Based on the previous discussion, mechanism of the growth and morphology of ZnO nanostructure can be proposed as follows:

$$\mathrm{Zn} + 2\mathrm{H_2O} + 2\mathrm{OH^-} \longrightarrow \mathrm{Zn(OH)_4^{2-}} + \mathrm{H_2} \quad (2)$$

$$\mathrm{Zn(OH)_4^{2-}} \longrightarrow \mathrm{ZnO} + \mathrm{H_2O} + 2\mathrm{OH^-} \quad (3)$$

The formation of $\mathrm{Zn(OH)_4^{2-}}$ ions from $\mathrm{Zn^{2+}}$ and $\mathrm{OH^-}$ ions by a hydrothermal reaction is a key role in the formation of hexagonal wurtzite ZnO nanorods. The primary ZnO nanoparticles began to nucleate on Zn foil by the dissolution of Zn atoms into the solution and the cause of concentration gradient of $\mathrm{Zn^{2+}}$. The intrinsic electric fields of the polar ZnO lattice could be responsible for further growth of ZnO crystals, described as alternating planes of $\mathrm{Zn^{2+}}$ and $\mathrm{O^{2-}}$, stacked along the *c*-axis. The oppositely charged ions produced positively charged and negatively charged surfaces, resulting in polarization along the *c*-axis. The preferred *c*-axis orientation of ZnO nanostructure is driven by electrostatic interaction between the polar charges to minimize surface energy. Finally, ZnO nanorods grew on Zn foil as substrate [15].

The main emission of ZnO nanorods can be assigned as the recombination of free excitons. Other peaks probably originated from position of band-edge emission of ZnO of relatively large dimensions with different concentration of native defects [16]. It is well known that visible photoluminescence mainly originates from defect states of Zn interstitials, zinc vacancies, and oxygen vacancies [17]. Photoluminescence (PL) of ZnO nanorods grown on Zn foils was investigated using excitation wavelength of 214 nm at room temperature as shown in Figure 4. PL spectrum of hexagonal ZnO nanorods using 0.50 g KOH shows the highest strong green light emission at 541 nm, due to the singly ionized oxygen vacancies of ZnO, in accordance with other reports [16–18].

4. Conclusions

In summary, densely aligned hexagonal ZnO nanorods on Zn foils were synthesized by a 120°C and 24 h hydrothermal reaction. The XRD, SEM, and TEM analyses showed that the

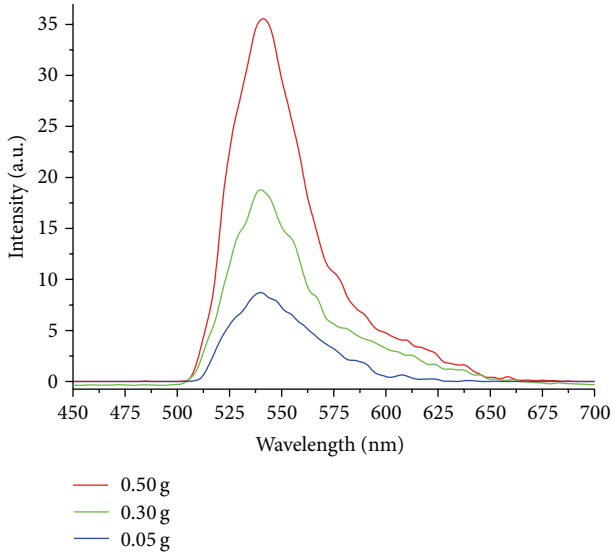


Figure 4: PL spectra of the as-synthesized ZnO in 30 mL solutions containing 1 (0.05 g), 6 (0.30 g), and 10 times (0.50 g) of KOH.

as-synthesized products were pure wurtzite ZnO nanorods with uniform hexagonal structure of 400–700 nm diameter and 5–7 μm long. Room temperature PL spectrum of the ZnO nanorods exhibited one strong green light emission at 541 nm due to the singly ionized oxygen vacancies inside.

Acknowledgments

The authors wish to thank the Thailand's Office of the Higher Education Commission for providing financial support through the National Research University (NRU) Project for Chiang Mai University (CMU) and the Human Resource Development Project in Science Achievement Scholarship of Thailand (SAST) and the Thailand Research Fund (TRF) for providing financial support through the TRF Research Grant BRG5380020, including the Graduate School of CMU through a general support.

References

[1] L. Z. Pei, H. S. Zhao, W. Tan, H. Y. Yu, Y. W. Chen, and Q. F. Zhang, "Single crystalline ZnO nanorods grown by a simple hydrothermal process," *Materials Characterization*, vol. 60, no. 9, pp. 1063–1067, 2009.

[2] Z. Li, X. Huang, J. Liu, Y. Li, and G. Li, "Morphology control and transition of ZnO nanorod arrays by a simple hydrothermal method," *Materials Letters*, vol. 62, no. 10-11, pp. 1503–1506, 2008.

[3] X. Wu, H. Chen, L. Gong, F. Qu, and Y. Zheng, "Low temperature growth and properties of ZnO nanorod arrays," *Advances in Natural Sciences*, vol. 2, Article ID 035006, 2011.

[4] H. Zhang, J. Feng, J. Wang, and M. Zhang, "Preparation of ZnO nanorods through wet chemical method," *Materials Letters*, vol. 61, no. 30, pp. 5202–5205, 2007.

[5] J. H. Yang, J. H. Zheng, H. J. Zhai, L. L. Yang, J. H. Lang, and M. Gao, "Growth mechanism and optical properties of ZnO nanosheets by the hydrothermal method on Si substrates," *Journal of Alloys and Compounds*, vol. 481, no. 1-2, pp. 628–631, 2009.

[6] X. Ren, D. Han, D. Chen, and F. Tang, "Large-scale synthesis of hexagonal cone-shaped ZnO nanoparticles with a simple route and their application to photocatalytic degradation," *Materials Research Bulletin*, vol. 42, no. 5, pp. 807–813, 2007.

[7] S. Suwanboon, R. Tanattha, and R. Tanakorn, "Fabrication and properties of nanocrystalline zinc oxide thin film prepared by sol-gel method," *Songklanakarin Journal of Science and Technology*, vol. 30, no. 1, pp. 65–69, 2008.

[8] D. Wang, C. Song, Z. Hu, W. Chen, and X. Fu, "Growth of ZnO prisms on self-source substrate," *Materials Letters*, vol. 61, no. 1, pp. 205–208, 2007.

[9] Powder Diffract, File, JCPDS Internat. Centre Diffract. Data, PA, 19073–3273, U.S.A, 2001.

[10] J. H. Park, P. Muralidharan, and D. K. Kim, "Solvothermally grown ZnO nanorod arrays on (101) and (002) single- and polycrystalline Zn metal substrates," *Materials Letters*, vol. 63, no. 12, pp. 1019–1022, 2009.

[11] F. Li, Z. Li, and F. J. Jin, "Structural and luminescent properties of ZnO nanorods," *Materials Letters*, vol. 61, no. 8-9, pp. 1876–1880, 2007.

[12] L. l. Yang, J. H. Yang, D. D. Wang et al., "Photoluminescence and Raman analysis of ZnO nanowires deposited on Si(100) via vapor-liquid-solid process," *Physica E*, vol. 40, no. 4, pp. 920–923, 2008.

[13] O. Lupan, L. Chow, L. K. Ono et al., "Synthesis and characterization of Ag- or Sb-doped ZnO nanorods by a facile hydrothermal route," *Journal of Physical Chemistry C*, vol. 114, no. 29, pp. 12401–12408, 2010.

[14] S. J. Chen, Y. C. Liu, Y. M. Lu, J. Y. Zhang, D. Z. Shen, and X. W. Fan, "Photoluminescence and Raman behaviors of ZnO nanostructures with different morphologies," *Journal of Crystal Growth*, vol. 289, no. 1, pp. 55–58, 2006.

[15] J. Y. Kim, H. Jeong, and D. J. Jang, "Hydrothermal fabrication of well-ordered ZnO nanowire arrays on Zn foil: room temperature ultraviolet nanolasers," *Journal of Nanoparticles Research*, vol. 13, no. 12, pp. 6699–6706, 2011.

[16] W. Li, Y. Sun, and J. Xu, "Controllable hydrothermal synthesis and properties of ZnO hierarchicalmicro/nanostructures," *Nano-Micro Letters*, vol. 4, no. 2, pp. 98–102, 2012.

[17] Y. J. Gao, W. C. Zhang, X. L. Wu et al., "Hydrothermal self-assembling of ZnO nanorods into sphere-like superstructures and their optical characteristics," *Applied Surface Science*, vol. 255, no. 5, pp. 1982–1987, 2008.

[18] G. Z. Wang, N. G. Ma, C. J. Deng et al., "Large-scale synthesis of aligned hexagonal ZnO nanorods using chemical vapor deposition," *Materials Letters*, vol. 58, no. 16, pp. 2195–2198, 2004.

Available online at www.sciencedirect.com

SciVerse ScienceDirect

Ceramics International 39 (2013) S563–S568

CERAMICS INTERNATIONAL

www.elsevier.com/locate/ceramint

Sonochemical synthesis, photocatalysis and photonic properties of 3% Ce-doped ZnO nanoneedles

Oranuch Yayapao[a], Somchai Thongtem[a,d,*], Anukorn Phuruangrat[b,**], Titipun Thongtem[c,d]

[a]Department of Physics and Materials Science, Faculty of Science, Chiang Mai University, Chiang Mai 50200, Thailand
[b]Department of Materials Science and Technology, Faculty of Science, Prince of Songkla University, Hat Yai, Songkhla 90112, Thailand
[c]Department of Chemistry, Faculty of Science, Chiang Mai University, Chiang Mai 50200, Thailand
[d]Materials Science Research Center, Faculty of Science, Chiang Mai University, Chiang Mai 50200, Thailand

Available online 24 October 2012

Abstract

ZnO nanostructured particles doped with 0–3% Ce were successfully synthesized by an ultrasonic solution method. Phase and morphology characterized by XRD, FTIR, SEM, TEM, HRTEM, SAED and EDX revealed the presence of hexagonal wurtzite ZnO nanoneedles with E_{2H} vibration at 426 cm^{-1}, composing of the corresponding elements and growing in the [0 0 1] direction. The 3% Ce-doped ZnO nanoneedles showed the 3.00 eV direct energy gap and 392.6 nm emission by UV–visible absorption and photoluminescence (PL) spectroscopy, including the most effective photocatalytic activity in the solution containing methylene blue.
© 2012 Elsevier Ltd and Techna Group S.r.l. All rights reserved.

Keywords: B. Electron microscopy; B. Spectroscopy; B. X-ray methods; E. Functional applications

1. Introduction

The II–VI semiconductors doped with rare-earth (RE) metals are very important for the present technology. They are promising for use as optoelectronic and luminescent devices: fluorescent lamps, cathode ray tube (CRT) phosphors and image intensifiers for X-ray screens [1]. RE atoms possessing special 4f shells are known as excellent candidates for luminescence centers of doped materials due to the transition of intra-4f or 4f–5d narrow emission line. The transitions play important roles in the absorption of RE atoms in the UV range. An energy transfer process from excited semiconductor host to doping lanthanide atoms promoted the doped nanocrystals to circumvent absorption of optically centers with remarkable improvement of luminescent properties [2,3].

Wurtzite ZnO (3.37 eV energy gap and 60 meV exciton binding energy at room temperature) is high electrochemical stability and non toxicity *n*-type oxide [2,4–7]. It is one of the most dominant UV-activated photocatalysts for air and water treatment due to its high photosensitivity and oxidation potential, and low cost. Lanthanide-doped ZnO nanocrystals are one of new classes of luminescent materials for advanced display and lighting applications [1,2]. Thus ZnO is a promising candidate for treatment of environmental pollution, solving the problem of energy depletion and suitably doped with luminescence centers.

In this research, we succeeded in doping Ce into wurtzite ZnO by sonochemistry. Phase, morphologies, UV–visible absorption and photoluminescence were studied, including the investigation of photocatalytic property of Ce-doped ZnO under the UV light.

2. Experimental details

To prepare 0–3% Ce-doped ZnO, 0.005 mol $Zn(NO_3)_2 \cdot 6H_2O$ and 0–3 mol% $Ce(NO_3)_3 \cdot 6H_2O$ were dissolved into 100 ml deionized water under vigorous stirring till complete dissolution. Subsequently, NH_4OH solution was slowly dropped into these solutions until the pH reaching at 9.5 and colorless solutions were achieved. Each of colorless solutions was sonicated in 35 kHz ultrasonic bath for 5 h.

*Corresponding author at: Chiang Mai University, Department of Physics and Materials Science, Faculty of Science, Chiang Mai 50200, Thailand. Tel.: +66 53 941924; fax: +66 53 943445.
**Corresponding author. Tel.: +66 74 288374; fax: +66 74 288395.
E-mail addresses: schthongtem@yahoo.com (S. Thongtem), phuruangrat@hotmail.com (A. Phuruangrat).

0272-8842/$ - see front matter © 2012 Elsevier Ltd and Techna Group S.r.l. All rights reserved.
http://dx.doi.org/10.1016/j.ceramint.2012.10.136

The precipitates were synthesized and collected for further characterization.

The photocatalytic activities of the as-synthesized samples were determined by measuring the degradation of methylene blue (MB) solution under UV light irradiation. The 500 mg photocatalyst was added to 100 ml 10^{-5} M MB aqueous solution. The solution was magnetically stirred for 60 min in the dark environment to establish adsorption/desorption equilibrium of MB on surfaces of the photocatalyst. Then the UV light was turned on to initiate the photocatalytic reaction.

3. Results and discussion

Fig. 1(a) shows XRD spectra of Ce-doped ZnO with different Ce^{3+} contents. For pure ZnO, the peaks were at 2θ of 32.11, 34.75, 36.59, 47.85 and 56.93 degree corresponding to the (1 0 0), (0 0 2), (1 0 1), (1 0 2) and (1 1 0) planes of hexagonal wurtzite ZnO of the JCPDS No. 36-1451 [8]. By doping Ce^{3+} in ZnO, only the ZnO peaks were still detected. No diffraction peaks of doping atoms or other phases were detected, indicating that the Ce^{3+} ions completely substituted for Zn^{2+} ions in ZnO

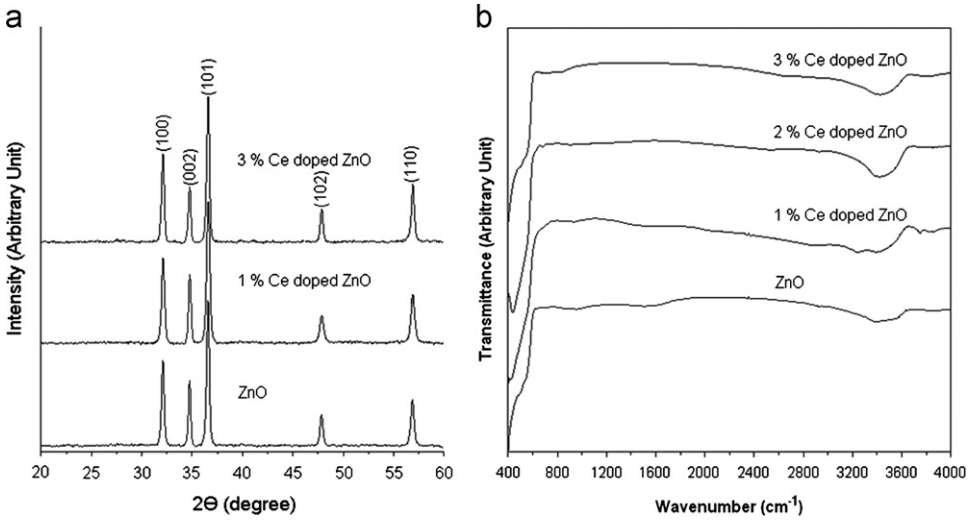


Fig. 1. (a) XRD and (b) FTIR spectra of ZnO with and without Ce doping.

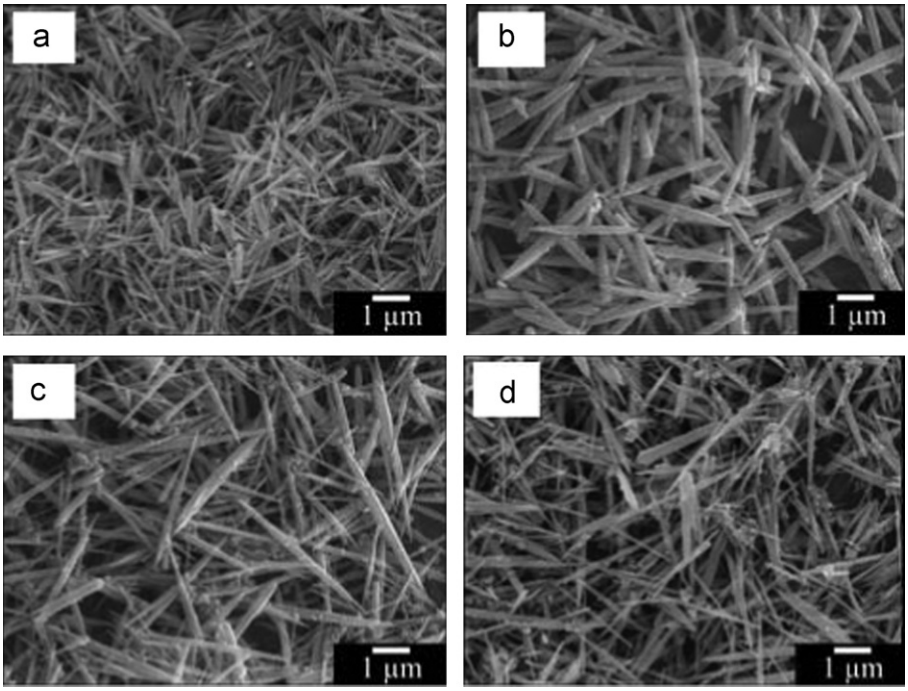


Fig. 2. SEM images of (a) undoped ZnO, and ((b)–(d)) 1, 2 and 3% Ce-doped ZnO, respectively.

lattice. Ce^{3+} concentration could be too low to be detected by XRD.

FTIR spectra (Fig. 1(b)) of the 0–3% Ce-doped ZnO, analyzed over the wave number of 400–4000 cm^{-1}, show strong bands at around 450–500 cm^{-1} with one broad band at 3300–3600 cm^{-1}. In this research, pure ZnO and 1–3% Ce-doped ZnO show the same strong absorption bands at 426 cm^{-1} with the shoulders at 565 cm^{-1}, assigned as E_{2H}

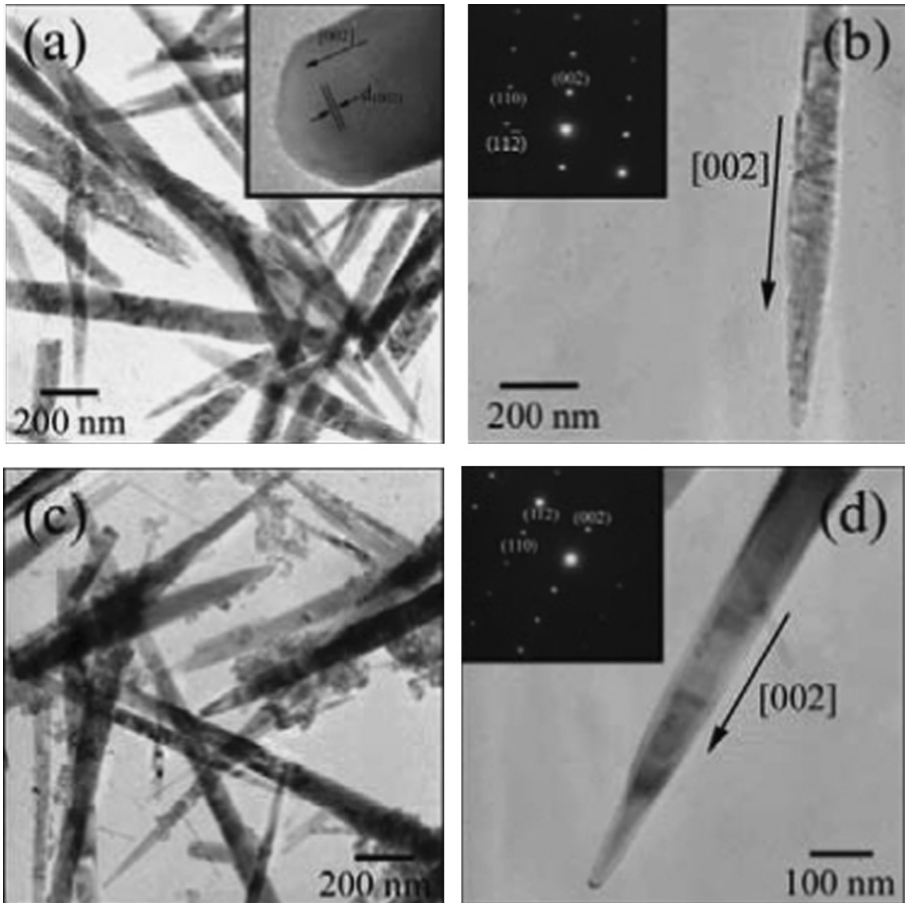


Fig. 3. TEM images, HRTEM images and SAED patterns of (a) and (b) pure ZnO and (c) and (d) 3% Ce-doped ZnO.

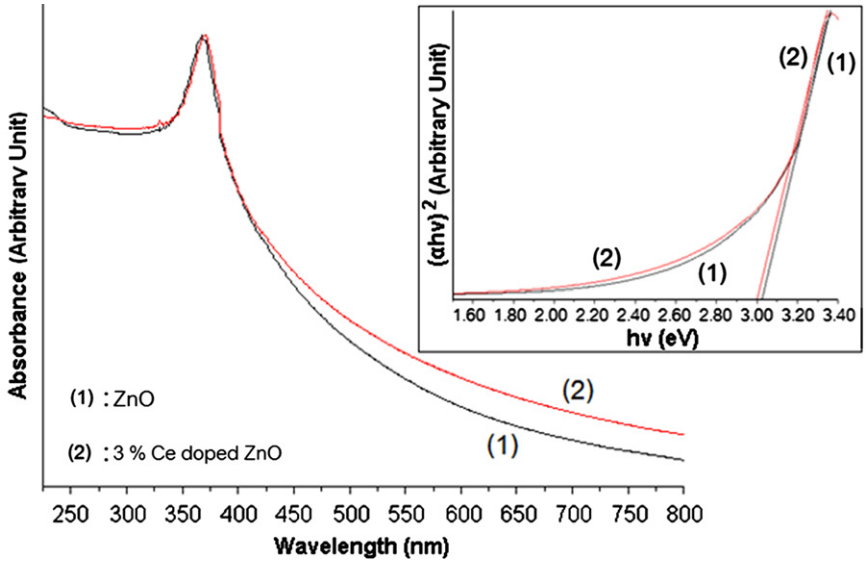


Fig. 4. UV–visible absorption and the $(\alpha h\nu)^2$ vs $h\nu$ plots of ZnO and 3% Ce-doped ZnO.

vibration and oxygen vacancies of wurtzite ZnO crystal, respectively [9]. For every two Ce^{3+} ions doped into ZnO crystal, one O^{2-} vacancy formed to maintain electroneutrality of the crystal. Considering the ionic radii of Zn^{2+} and Ce^{3+} [6,10,11], it was likely that Ce^{3+} partially substituted for Zn^{2+} in the ZnO crystal. An absorption bands at 3300–3600 cm^{-1} is the O–H stretching of adsorbed water on the sample surface.

Pure ZnO (Fig. 2(a)) was nanoneedle-like particles with sharp tips on both ends. A base width at the middle and tapered tips were 100 nm and 25 nm with 1 μm long. By doping with Ce (Fig. 2(b)–(d)), the morphology of 1–3% Ce-doped ZnO remained as nanoneedles, but their lengths were increased to 2–3 μm. The elemental distribution of 3% Ce-doped ZnO nanoneedles were characterized by EDX. Zn, O and Ce were shown on the elemental EDX-maps (result not shown), implying that Ce atoms were very distributive in the sample.

TEM and HRTEM images and SAED pattern (Fig. 3(a) and (b)) represent phase and morphology of pure ZnO nanoneedles with 800 nm long, uniform diameter and slightly rough surface. The HRTEM image was analyzed on edge part of a typical ZnO nanoneedle. The (0 0 2) fringe at right angle to the [0 0 1] growth direction with 2.61 Å apart were detected, in consistent with that of the bulk wurtzite ZnO crystal. Some defects were also detected. The SAED pattern shows a bright spot pattern of single crystal of hexagonal ZnO. Consider the 3% Ce-doped ZnO images and SAED pattern (Fig. 3(c) and (d)), they revealed the straight nanoneedles of single crystal with smooth surface and 80 nm in diameter. The *d*-spacing values measured from the SAED pattern with zone axis of [1–10] are 1.62 Å, 1.38 Å and 2.61 Å, well agree with the (1 1 0), (1 1 2) and (0 0 2) lattice planes of hexagonal ZnO phase, respectively. These indicated that 3% Ce-doped ZnO nanoneedles grew along the [0 0 1] direction.

Formation mechanism of ZnO nanoneedles proceeded in a sonochemical bath as follows. First, zinc nitrate, water and ammonium hydroxide absorbed ultrasound energy and followed by the dissociation process to form primary ions. Second, $[Zn(OH)_4]^{2-}$ complex ions formed and further decomposed to give ZnO molecules [12], which nucleated and grew as nanoneedles. Their preferential growth were along the [0 0 0 1] direction due to the intrinsic anisotropy in growth rate (v) with v[0 0 0 1] > v[0 1-1 0] > v[0 0 0 -1]. The structure of ZnO single crystal can be described as a number of alternating planes of coordinated Zn^{2+} and O^{2-} ions, the positively charged Zn-(0 0 0 1) and negatively charged O-(0 0 0 1) polar surfaces. Due to the decreasing in the concentration of ZnO_2^{2-} monomers by the rapid nucleation of ZnO, the absorption of OH^- on the positively charged plane dominated the competition of ZnO_2^{2-} growth units. Thus, the OH^- ions stabilized the surface charge of Zn-(0 0 0 1) to some degree, leading to the formation of nanoneedle-like ZnO along the [0 0 0 1] direction [13,14]. When the doping material was also mixed, Ce^{3+} ions diffused and resided in the ZnO nanoneedles.

UV absorption (Fig. 4) of undoped ZnO and 3% Ce-doped ZnO was investigated in 225–800 nm wavelength range. They presented well defined excitonic absorption peaks at 366 nm, corresponding to the band-to-band

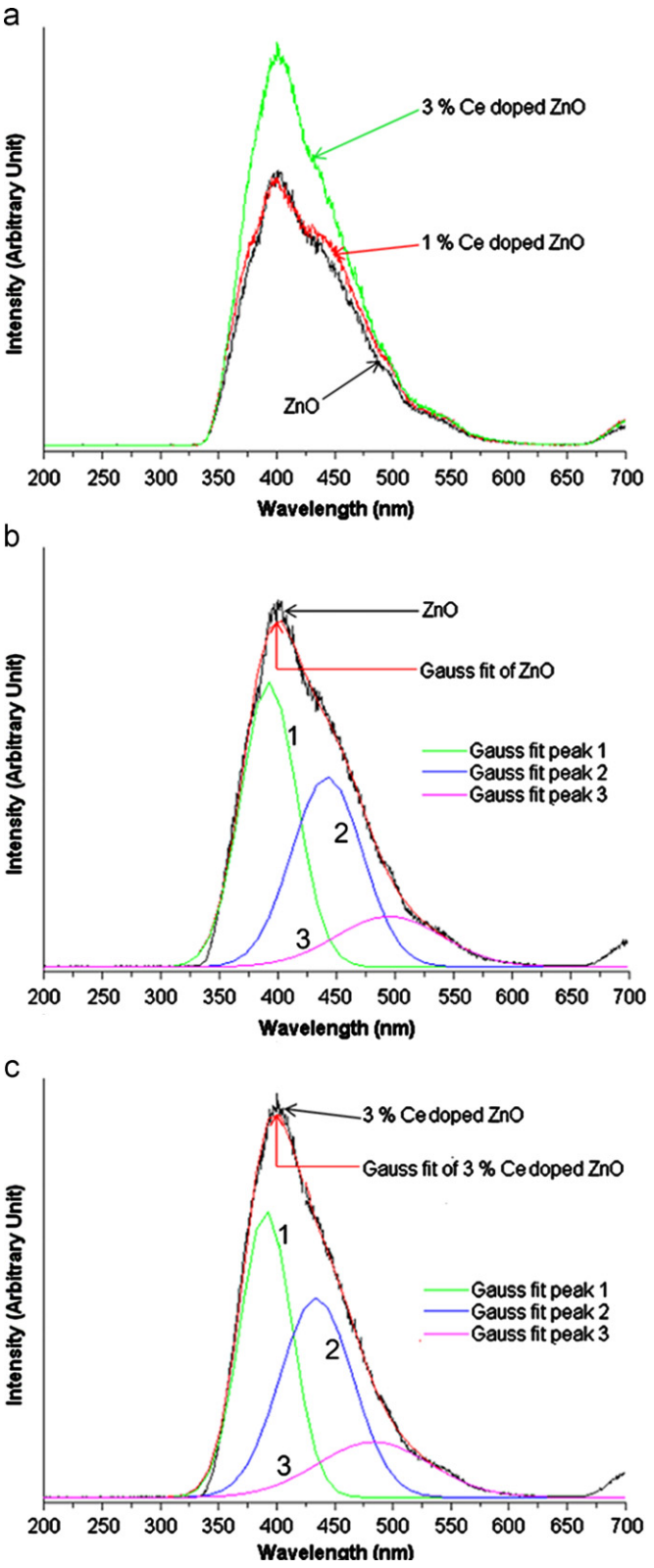


Fig. 5. (a) PL spectra of ZnO with and without Ce doping. Gaussian analysis of (b) ZnO and (c) 3% Ce-doped ZnO.

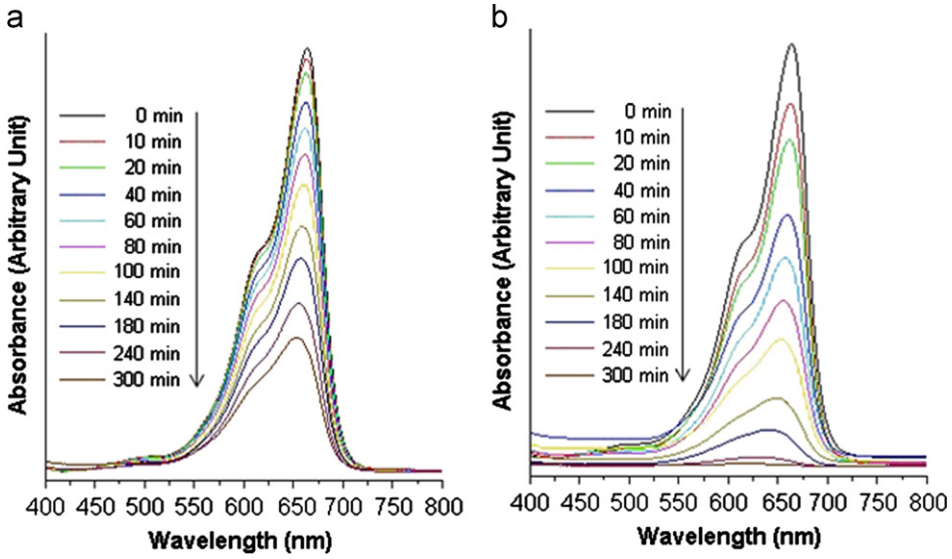


Fig. 6. UV–visible absorption of (a) pure ZnO and (b) 3% Ce-doped ZnO.

transition of ZnO [15], and at 370 nm of 3% Ce-doped ZnO with red shifted absorption as compared to that for ZnO. The direct energy gaps of undoped ZnO and 3% Ce-doped ZnO were determined to be 3.03 and 3.00 eV, respectively.

PL spectra (Fig. 5) of ZnO with and without Ce doping were studied using 318 nm excitation wavelength. They showed broad emissions in the wavelength range of 325–600 nm. The 3% Ce-doped ZnO showed higher emission intensity than any other products. Upon doing the Gaussian analysis for pure ZnO and 3% Ce-doped ZnO with the highest intensity, the spectra were disintegrated into three emission peaks at 393.1 nm, 442.9 nm and 495.6 nm for pure ZnO, and 392.6 nm, 433.7 nm and 482.2 nm for 3% Ce-doped ZnO-corresponding to the UV, blue and blue-green emissions, respectively [16,17]. The first was caused by the characteristic of near-band-edge emission of free exciton recombination process [18], but the second and third were possibly associated with oxygen vacancies [16] and other defects.

MB is adopted as a representative organic pollutant to evaluate the photocatalytic performance of the as-synthesized Ce-doped ZnO. UV–visible absorbance (Fig. 6) of undoped ZnO and 3% Ce-doped ZnO during photocatalysis for 0–300 min shows that the absorbance of MB for ZnO was gradually decreased, but that for 3% Ce-doped ZnO was decreased at much faster rate. Fig. 7 shows the MB degradation rate for ZnO with and without Ce doping under UV light for different lengths of time. Obviously, 3% Ce-doped ZnO shows the most effective in photocatalysis in these solutions. During the first 140 min, MB concentration was rapidly decreased to 32, 70 and 87% for ZnO, 1% Ce-doped ZnO and 3% Ce-doped ZnO, respectively. For 240 min, the MB degradation efficiency for 3% Ce-doped ZnO was higher than 98%, 1.97 times the degradation efficiency of ZnO (49.81%). The higher

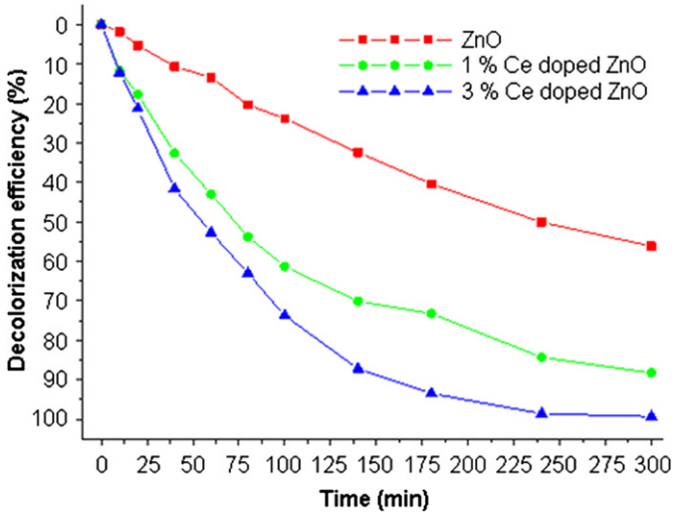


Fig. 7. Decolorization efficiencies of ZnO with and without Ce doping.

the concentration of oxygen defects on the surfaces of Ce-doped ZnO nanocrystals is, the stronger the photocatalytic activity will be. Finally, the experimental results presented in this article will be very useful for the research on other metallic/semiconducting catalysts with high catalytic activities.

4. Conclusions

Undoped ZnO and 1–3% Ce-doped ZnO nanoneedles were successfully synthesized in a controlled sonochemical process. The PL spectrum of 3% Ce-doped ZnO showed a strong emission at 392.6 nm with other two weak visible emissions. The facile, reproducible and effective route presented a useful method for the RE^{3+}-doped ZnO system. High crystalline quality and good optical properties of the

Ce-doped ZnO nanoneedles can lead the material to be a candidate for different applications in the future.

Acknowledgements

We wish to thank the Thailand Research Fund for financial support through the research grant BRG5380020, and the Thailand's Office of the Higher Education Commission through the National Research University Project for Chiang Mai University (CMU), including the Graduate School of CMU through the general support.

References

[1] J. Iqbal, X. Liu, H. Zhu, Z.B. Wu, Y. Zhang, D. Yu, R. Yu, Raman and highly ultraviolet red-shifted near band-edge properties of LaCe-co-doped ZnO nanoparticles, Acta Materialia 57 (2009) 4790–4796.

[2] Y.P. Du, Y.W. Zhang, L.D. Sun, C.H. Yan, Efficient energy transfer in monodisperse Eu-doped ZnO nanocrystals synthesized from metal acetylacetonates in high-boiling solvents, The Journal of Physical Chemistry C 112 (2008) 12234–12241.

[3] J. Flor, S.A.M. de Lima, M.R. Davolos, Effect of reaction time on the particle size of ZnO and ZnO:Ce obtained by a sol–gel method, Progress in Colloid and Polymer Science 128 (2004) 239–243.

[4] H.C. Gong, J.F. Zhong, S.M. Zhou, B. Zhang, Z.H. Li, Z.L. Du, Ce-induced single-crystalline hierarchical zinc oxide nanobrushes, Superlattices and Microstructures 44 (2008) 183–190.

[5] Z. Sofiani, B. Derkowska, P. Dalasiński, M. Wojdyła, S. Dabos-Seignon, M. Alaoui Lamrani, L. Dghoughi, W. Bała, M. Addou, B. Sahraoui, Optical properties of ZnO and ZnO:Ce layers grown by spray pyrolysis, Optics Communications 267 (2006) 433–439.

[6] D. Fangli, W. Ning, Z. Dongmei, S. Yingzhong, Preparation, characterization and infrared emissivity study of Ce-doped ZnO films, Journal of Rare Earths 28 (2010) 391–395.

[7] Y. Morinaga, K. Sakuragi, N. Fujimura, T. Ito, Effect of Ce doping on the growth of ZnO thin films, Journal of Crystal Growth 174 (1997) 691–695.

[8] Powder Diffract. File, JCPDS-ICDD, 12 Campus Boulevard, Newtown Square, PA 19073-3273, U.S.A. (2001).

[9] G. Xiong, U. Pal, J.G. Serrano, K.B. Ucer, R.T. Williams, Photoluminescence and FTIR study of ZnO nanoparticles: the impurity and defect perspective, Physica Status Solidi C Current Topics in Solid State Physics 3 (2006) 3577–3581.

[10] C. Ge, C. Xie, S. Cai, Preparation and gas-sensing properties of Ce-doped ZnO thin-film sensors by dip-coating, Materials Science and Engineering B 137 (2007) 53–58.

[11] J.E. Huheey, E.A. Keiter, R.L. Keiter, Inorganic Chemistry.: Principles of Structure and Reactivity, fourth ed., Harper Collins College Publ., NY 10022, U.S.A, 1993.

[12] P. Mishra, R.S. Yadav, A.C. Pandey, Growth mechanism and photoluminescence property of flower-like ZnO nanostructures synthesized by starch-assisted sonochemical method, Ultrasonics Sonochemistry 17 (2010) 560–565.

[13] B. Li, Y. Wang, Facile synthesis and enhanced photocatalytic performance of flower-like ZnO hierarchical microstructures, The Journal of Physical Chemistry C 114 (2010) 890–896.

[14] D. Wang, C. Song, Controllable synthesis of ZnO nanorod and prism arrays in a large area, The Journal of Physical Chemistry B 109 (2005) 12697–12700.

[15] H. Qin, W. Li, Y. Xia, T. He, Photocatalytic activity of heterostructures based on ZnO and N-doped ZnO, ACS Applied Materials & Interfaces 3 (2011) 3152–3156.

[16] Z. Zhu, D. Yang, H. Liu, Microwave-assisted hydrothermal synthesis of ZnO rod-assembled microspheres and their photocatalytic performances, Advanced Powder Technology 22 (2011) 493–497.

[17] C. Deng, H. Hu, G. Shao, C. Han, Facile template-free sonochemical fabrication of hollow ZnO spherical structures, Materials Letters 64 (2010) 852–855.

[18] J. Das, D. Khushalani, Nonhydrolytic route for synthesis of ZnO and its use as a recyclable photocatalyst, The Journal of Physical Chemistry C 114 (2010) 2544–2550.

Available online at www.sciencedirect.com

SciVerse ScienceDirect

Ceramics International 39 (2013) S383–S387

CERAMICS INTERNATIONAL

www.elsevier.com/locate/ceramint

Transformation of cubic $AgBiS_2$ from nanoparticles to nanostructured flowers by a microwave-refluxing method

Narongrit Tipcompor[a], Somchai Thongtem[b,c], Titipun Thongtem[a,c,*]

[a]Department of Chemistry, Faculty of Science, Chiang Mai University, Chiang Mai 50200, Thailand
[b]Department of Physics and Materials Science, Faculty of Science, Chiang Mai University, Chiang Mai 50200, Thailand
[c]Materials Science Research Center, Faculty of Science, Chiang Mai University, Chiang Mai 50200, Thailand

Available online 23 October 2012

Abstract

Cubic $AgBiS_2$ nanoparticles and flower-like clusters were successfully synthesized by microwave refluxing of CH_3COOAg, $Bi(NO_3)_3 \cdot 5H_2O$ and thiosemicarbazide ($NH_2NHCSNH_2$) in ethylene glycol. The phase was detected by X-ray diffraction (XRD) and selected area electron diffraction (SAED). The SAED pattern was also in accordance with that of the simulation. Scanning and transmission electron microscopy (SEM and TEM) revealed the gradual transformation of nanoparticles into flower-like clusters by increasing microwave power. Their UV–visible absorption and photoluminescence (PL) emission were detected by spectrometry. Possible formation mechanism of nanoparticles and nanostructured flowers was also proposed according to the experimental results.
© 2012 Elsevier Ltd and Techna Group S.r.l. All rights reserved.

Keywords: B. Electron microscopy; B. Spectroscopy; B. X-ray methods; E. Functional applications

1. Introduction

At present, I–V–VI ternary chalcogenides are very attractive materials, especially silver bismuth sulfide ($AgBiS_2$). It is a promising candidate for use as novel semiconductors [1] and has high potential for use as optoelectric and thermoelectric devices including optical recording media [2].

Microwave refluxing is a distillation process by microwave radiation involving the condensation of vapors and the return of the condensate (liquid produced by condensation of steam) to the original system. This process is very simple, fast, effective and environmentally benign. It can solve the problems of temperature and concentration gradients, and provides uniform growth media. It has been developed and widely used in industrial and laboratory distillations [3].

The motivation of doing this research is to synthesize $AgBiS_2$ crystals the shape and size of nanoparticles and flower-like clusters by a microwave-assisted refluxing method. The success in this synthesis may lead to different applications in the near future.

2. Experiment

In this research, 1 mmol CH_3COOAg, 1 mmol $Bi(NO_3)_3 \cdot 5H_2O$ and 2 mmol thiosemicarbazide ($NH_2NHCSNH_2$) with 1:1:2 M ratio Ag:Bi:S were dissolved in 50 ml of different solvents—ethylene glycol (EG), propylene glycol (PG), ethylene diamine (ED) and water. Each 50 ml solution was refluxed by 100, 300, 600 and 800 W microwave radiation for 20, 40 and 60 min. Finally, black precipitates were synthesized, separated by filtration, washed with de-ionized water and ethanol, and dried at 70 °C for 12 h.

The products were then characterized by different methods: X-ray diffractometer (XRD, SIEMENS D500, Germany) operating at 20 kV, 15 mA, and using Cu-K_α line in combination with the database of the Joint Committee on Powder Diffraction Standards (JCPDS) [4]; scanning electron microscope (SEM, JEOL JSM-6335F, Japan) operating at 15 kV; transmission electron microscope (TEM, JEOL JEM-2010, Japan) and selected area electron diffractometer (SAED) operating at 200 kV; UV–visible spectrometer (Lambda 25

*Corresponding author at: Department of Chemistry, Faculty of Science, Chiang Mai University, Chiang Mai 50200, Thailand. Tel.: +66 0 53 943344; fax: +66 0 53 892277.
E-mail address: ttpthongtem@yahoo.com (T. Thongtem).

0272-8842/$ - see front matter © 2012 Elsevier Ltd and Techna Group S.r.l. All rights reserved.
http://dx.doi.org/10.1016/j.ceramint.2012.10.099

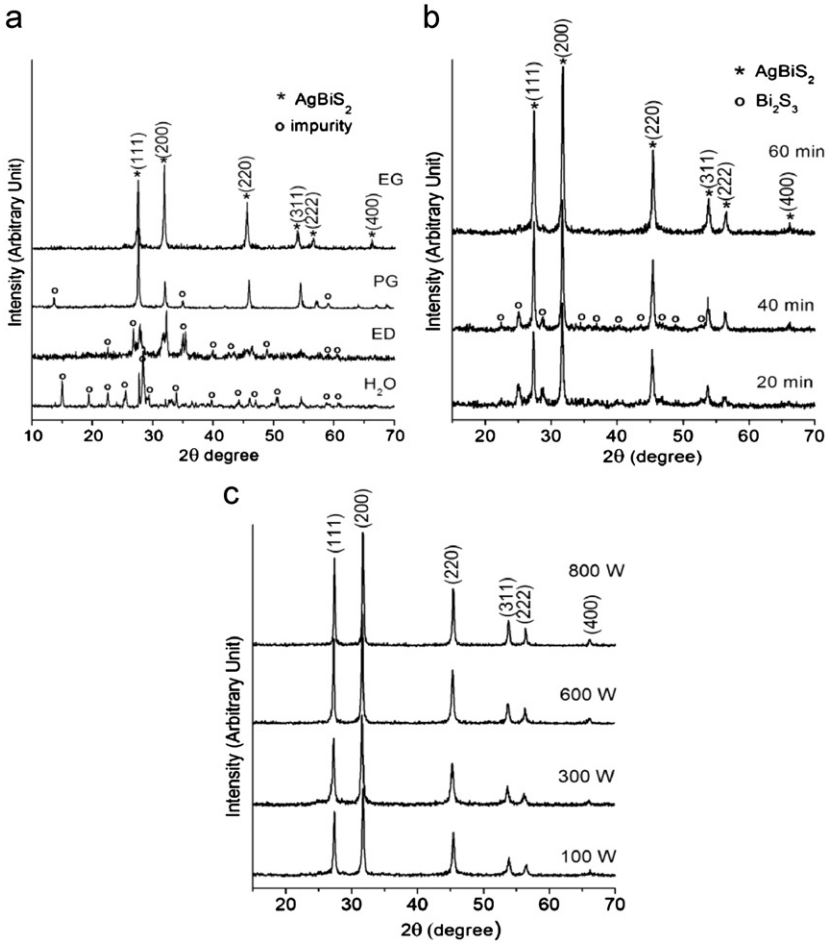


Fig. 1. XRD patterns of $AgBiS_2$ synthesized by a microwave-assisted refluxing method in (a) different solvents at 800 W microwave for 60 min, (b) EG at 800 W microwave for different lengths of time and (c) EG at different heating powers for 60 min.

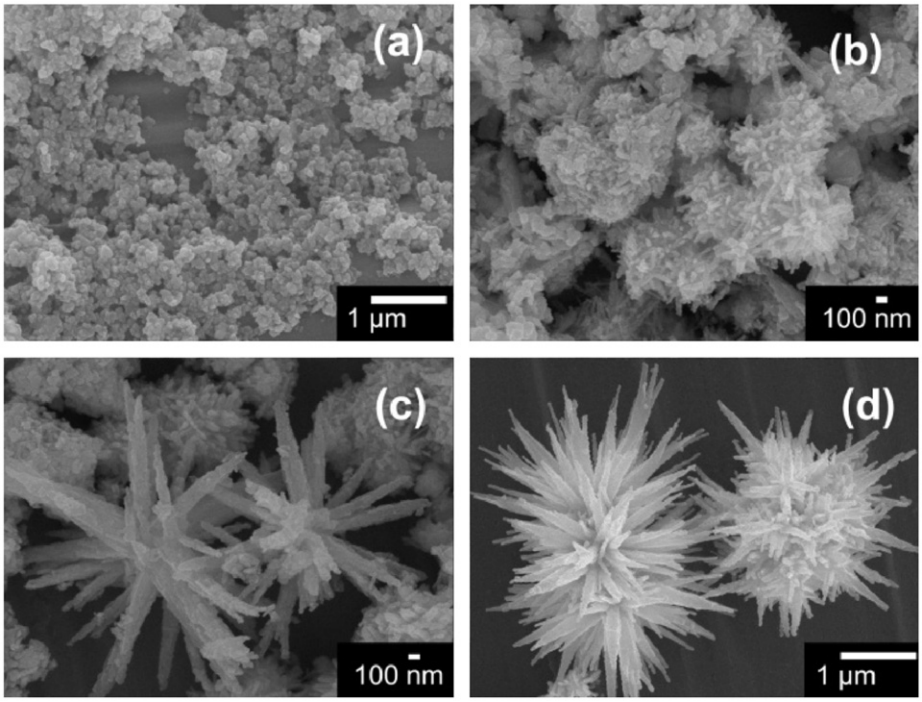


Fig. 2. SEM images of $AgBiS_2$ synthesized by (a–d) 100, 300, 600 and 800 W microwave refluxing method in EG for 60 min, respectively.

PerkinElmer, U.S.A.) using a UV lamp with the resolution of 1 nm; and photoluminescence (PL) spectrometer (LS 50B PerkinElmer, U.S.A.) using a 300 nm excitation wavelength at room temperature.

3. Results and discussion

3.1. XRD

XRD patterns (Fig. 1a) of the products synthesized by 800 W microwave refluxing of the starting agents dissolved in different solvents for 60 min. They were indexed and specified as cubic $AgBiS_2$ (JCPDS no. 04-0699) [4] without impurity detection only in the EG. Upon reducing the lengths of microwave refluxing time from 60 min to 40 and 20 min (Fig. 1b), the chemical reaction became incomplete and some Bi_2S_3 (JCPDS no. 06-0333) [4] residue was also detected.

To save the consumption of energy, the refluxing power of microwave was gradually reduced step by step from 800 W to 600, 300 and 100 W (Fig. 1c). The product was the still pure $AgBiS_2$ phase but the crystalline degree was lessened.

3.2. Electron microscopy

The as-synthesized products with different morphologies were characterized by SEM and TEM. At 100 W (Figs. 2a and 3a), the product was composed of a number of nanoparticles oriented in different directions. They are crystals with facets and angles. Their size distribution (Fig. 3c) is in the 30–100 nm range, with the average of 58.14 ± 11.87 nm. By increasing the refluxing power of the microwave, the products (Figs. 2b–d and 4a and b) gradually transformed into flower-like clusters at 800 W. SAED patterns of nanoparticles (Fig. 3b) and a petal of the flower-like cluster (Fig. 4c) were both indexed to correspond with polycrystalline and single crystalline $AgBiS_2$ [5], respectively. The interpreted pattern was also in accordance with that obtained by simulation (Fig. 4d).

3.3. Proposed mechanism

To synthesize $AgBiS_2$ by a microwave-assisted refluxing method, CH_3COOAg, $Bi(NO_3)_3 \cdot 5H_2O$ and thiosemicarbazide (TS) were dissolved in ethylene glycol (EG). Ag^+ and Bi^{3+} ions formed complexes with thiosemicarbazide during stirring. At this stage, free ions of Ag^+, Bi^{3+} and S^{2-} were very low. Thus, Ag_2S and Bi_2S_3 formations were prohibited.

During the microwave refluxing, the complexes were decomposed to synthesize $(AgBiS_2)_n$ nuclei. The decomposition proceeded with rather slow rates. Their concentration was lower than that obtained by the direct ion-exchange

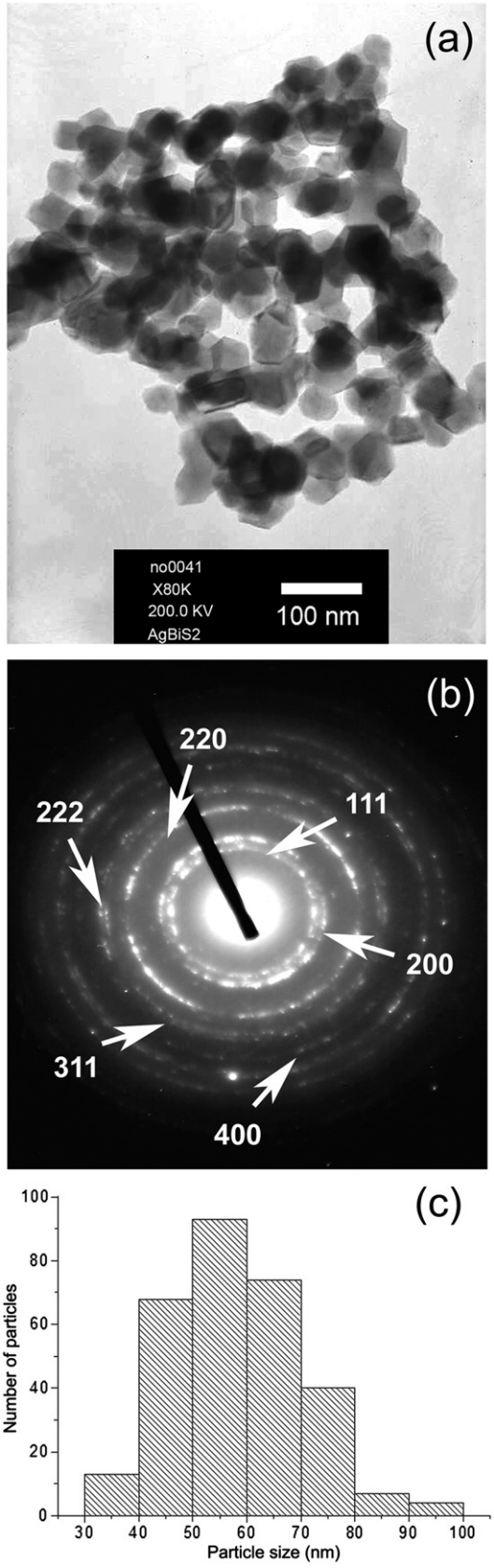


Fig. 3. (a) TEM image, (b) SAED pattern and (c) size distribution of $AgBiS_2$ nanoparticles synthesized by 100 W microwave refluxing method in EG for 60 min.

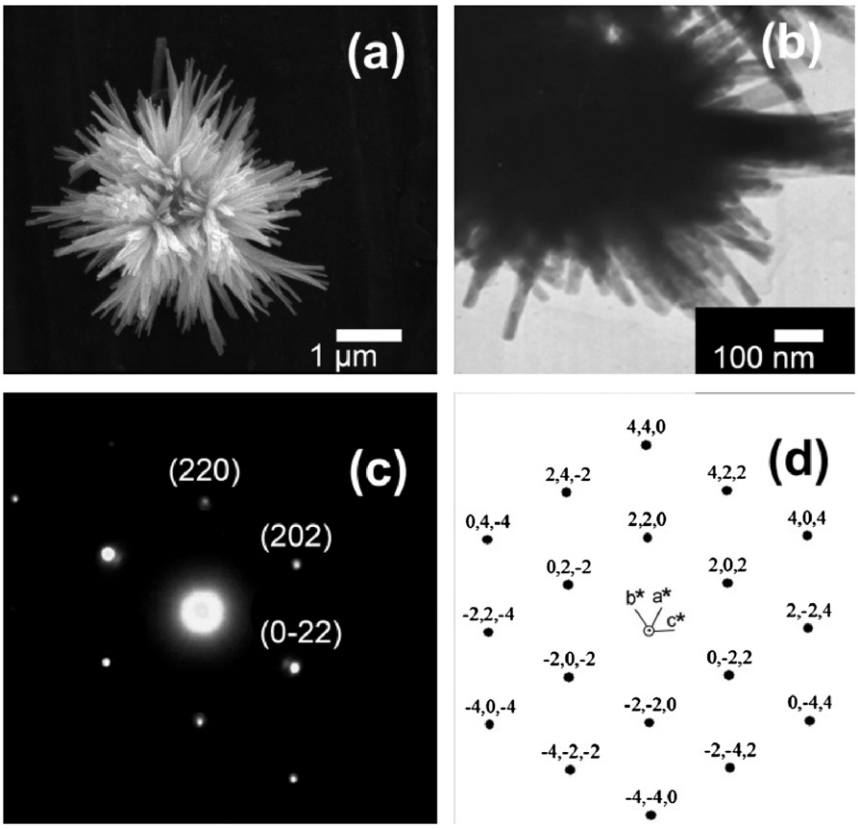


Fig. 4. (a, b) TEM images, (c) SAED pattern of a petal of $AgBiS_2$ flower synthesized by 800 W microwave refluxing method in EG for 60 min, and (d) its simulated pattern.

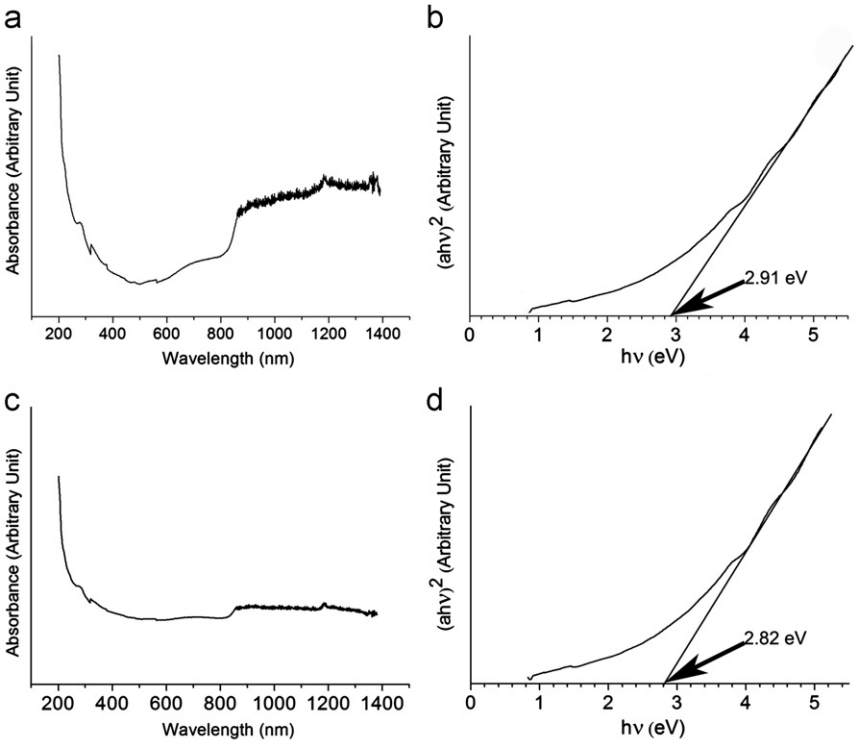


Fig. 5. UV–visible absorption and the $(\alpha h\nu)^2$ and $h\nu$ plots of $AgBiS_2$ (a, b) nanoparticles, and (c, d) flower-like clusters.

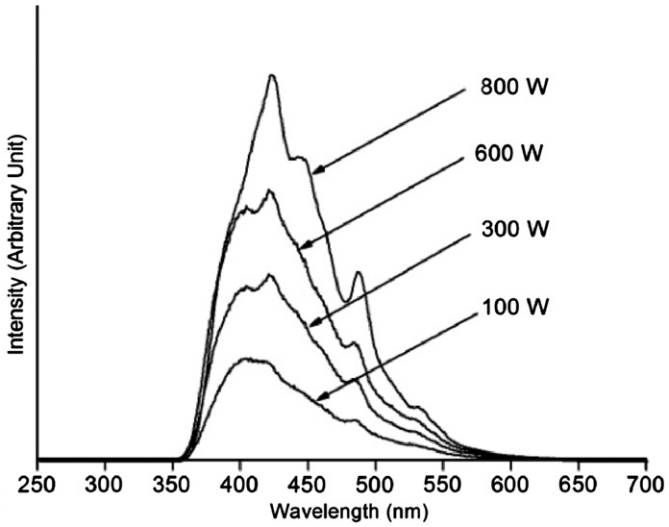


Fig. 6. PL emissions of $AgBiS_2$ synthesized by 100, 300, 600 and 800 W microwave refluxing in EG for 60 min.

reaction. Finally, $AgBiS_2$ nuclei were synthesized in EG by the microwave-assisted refluxing method.

$$Ag^+ + Bi^{3+} + TS \rightarrow Ag\text{–}Bi\text{–}TS \text{ complexes} \quad (1)$$

$$Ag\text{–}Bi\text{–}TS \text{ complexes} \rightarrow (AgBiS_2)_n \quad (2)$$

$$(AgBiS_2)_n \rightarrow n(AgBiS_2) \quad (3)$$

Alternately, Ag–TS and Bi–TS complexes could form and were decomposed to synthesize $AgBiS_2$ nuclei.

$$Ag^+ + TS \rightarrow Ag\text{–}TS \text{ complexes} \quad (4)$$

$$Bi^{3+} + TS \rightarrow Bi\text{–}TS \text{ complexes} \quad (5)$$

$$Ag\text{–}TS \text{ complexes} + Bi\text{–}TS \text{ complexes} \rightarrow n(AgBiS_2) \quad (6)$$

Due to the 100 W microwave refluxing, $AgBiS_2$ nanoparticles were synthesized by the orientation growth process. At higher refluxing power, the atoms were vibrated violently by a very strong force. Thus the nanoparticles gradually transformed into flower-like clusters at 800 W. In this research, the microwave refluxing played a key role in the decomposition of the complexes, formation of $(AgBiS_2)_n$ nuclei (nucleation), and the oriented growth of $AgBiS_2$ crystals [1,2].

3.4. Absorption and emission

UV–visible absorption (Fig. 5) of the as-synthesized nanoparticles and flower-like clusters indicated an exponential decreasing of optical absorption attenuated through the $AgBiS_2$ solids. Their allowed direct energy gaps were determined, by extrapolating linear portions of the curves to zero absorption, to be 2.91 eV for nanoparticles and 2.82 eV for flower-like clusters—in accordance with 2.88 eV of thin film reported by Ibrahim and Soliman [6].

PL emissions of different products (Fig. 6) were characterized using 300 nm excitation wavelength at room temperature. Their emission peaks were detected at the same wavelengths of 422.5 nm (2.93 eV) with two shoulders at 444.5 nm and 486.0 nm. The main emission peaks were specified as the recombination of electrons and holes in trapped surface states residing in the forbidden region [7,8]. But for the shoulders, they were caused by the shallow levels of donors and acceptors between the valence and conduction bands [9]. The present result corresponded to the 435 nm (2.85 eV) of $AgBiS_2$ nanostructured flowers and hexapod [10].

4. Conclusions

Pure cubic $AgBiS_2$ crystals the shape and size of nanoparticles and flower-like clusters were successfully synthesized by 100 W and 800 W microwave refluxing in ethylene glycol for 60 min. The phase was detected by XRD and SAED. SEM and TEM revealed the transformation of the as-synthesized nanoparticles at 100 W into flower-like clusters at 800 W. Their allowed direct energy gaps were determined to be 2.91 eV for nanoparticles and 2.82 eV for flower-like clusters, including their PL emission wavelengths were 422.5 nm.

Acknowledgments

We wish to thank the Thailand Research Fund (TRF) for providing financial support through the Royal Golden Jubilee Ph.D. Program and the TRF Research Grant BRG5380020, and the Thailand's Office of the Higher Education Commission through the National Research University Project, including the Graduate School of Chiang Mai University through the general support.

References

[1] D. Chen, G. Shen, K. Tang, X. Jiang, L. Huang, Y. Jin, Y. Qian, Microwave synthesis of $AgBiS_2$ dendrites in aqueous solution, Inorganic Chemistry Communications 6 (2003) 710–712.
[2] G. Shen, D. Chen, K. Tang, Y. Qian, Novel polyol route to $AgBiS_2$ nanorods, Journal of Crystal Growth 252 (2003) 199–201.
[3] 〈http://en.wikipedia.org〉 (accessed: 14 May 2012).
[4] Powder Diffraction File, JCPDS-ICDD, PA 19073-3273, 12 Campus Boulevard, Newtown Square, U.S.A., 2001.
[5] K.W. Andrews, D.J. Dyson, S.R. Keown, Interpretation of Electron Diffraction Patterns, Plenum Press, New York, 1971.
[6] A.M. Ibrahim, L.I. Soliman, Optical properties of $AgBiS_2$ thin films, Fizika A 5 (1996) 177–183.
[7] M.X. Wang, G.H. Yue, X.Y. Fan, P.X. Yan, Properties and characterization of Cu_3SbS_3 nanowires synthesized by solvothermal route, Journal of Crystal Growth 310 (2008) 3062–3066.
[8] G.H. Yue, X. Wang, L.S. Wang, W. Wang, D.L. Peng, Synthesis of single crystal $CuAlS_2$ nanowires via a low temperature direct polyol route, Physics Letters A 372 (2008) 5995–5998.
[9] G. Harichandran, N.P. Lalla, Facile synthesis of $CuAlS_2$ nanorods, Materials Letters 62 (2008) 1267–1269.
[10] T. Thongtem, J. Jaroenchaichana, S. Thongtem, Cyclic microwave-assisted synthesis of flower-like and hexapod silver bismuth sulfide, Materials Letters 63 (2009) 2163–2166.

Superlattices and Microstructures 57 (2013) 1–10

Contents lists available at SciVerse ScienceDirect

Superlattices and Microstructures

journal homepage: www.elsevier.com/locate/superlattices

Photoabsorption and photocatalysis of $SrSnO_3$ produced by a cyclic microwave radiation

Patcharanan Junploy [a], Somchai Thongtem [b,c,*], Titipun Thongtem [a,c,*]

[a] Department of Chemistry, Faculty of Science, Chiang Mai University, Chiang Mai 50200, Thailand
[b] Department of Physics and Materials Science, Faculty of Science, Chiang Mai University, Chiang Mai 50200, Thailand
[c] Materials Science Research Center, Faculty of Science, Chiang Mai University, Chiang Mai 50200, Thailand

ARTICLE INFO

Article history:
Received 15 November 2012
Received in revised form 30 January 2013
Accepted 31 January 2013
Available online 11 February 2013

Keywords:
Cyclic microwave radiation
Rod-like hexagonal $SrSn(OH)_6$ precursors
Rod-like orthorhombic $SrSnO_3$
Photocatalysis

ABSTRACT

Rod-like hexagonal $SrSn(OH)_6$ precursors were produced by a cyclic microwave radiation (CMR) of a template-free solution containing $SnCl_2{\cdot}2H_2O$ and $(CH_3CO_2)_2Sr$ at the pH 12.2, adjusted by NaOH solution. The rod-like hexagonal $SrSn(OH)_6$ precursors were calcined at 500 °C, 700 °C and 900 °C for 3 h following the thermogravimetric analysis. In the end, the perovskite orthorhombic $SrSnO_3$ products in the shape of rods with 530 cm^{-1} Sn–O stretching mode, characterized by X-ray diffraction, electron microscopy and Fourier transform infrared spectroscopy, were produced. UV–visible analysis of the best crystalline rod-like $SrSnO_3$ indicated an exponential decreasing of photonic absorption attenuated through the orthorhombic $SrSnO_3$ solid with 3.91 eV direct energy gap, including 85% decolorization efficiency under UV light for 320 min.

© 2013 Elsevier Ltd. All rights reserved.

1. Introduction

Perovskite alkaline earth stannate with $ASnO_3$ (A = Ca, Sr and Ba) general formulae has very interesting properties. One of them is $SrSnO_3$ that has been receiving much attention for different applications, such as components of ceramic dielectric materials, thermally capable capacitors and semiconducting sensors for humidity and gases [1,2]. It was synthesized by different methods: solid state reaction with heat treatment temperature above 1200 °C [3], hydrothermal method [4,5], combustion and coprecipitation methods [6] and polymeric precursor method [1].

* Corresponding authors. Addresses: Department of Physics and Materials Science, Faculty of Science, Chiang Mai University, Chiang Mai 50200, Thailand. Tel.: +66 (0)53 941924; fax: +66 (0)53 943445 (S. Thongtem), Department of Chemistry, Faculty of Science, Chiang Mai University, Chiang Mai 50200, Thailand. Tel.: +66 (0)53 943344; fax: +66 (0)53 892277 (T. Thongtem).
E-mail addresses: schthongtem@yahoo.com (S. Thongtem), ttpthongtem@yahoo.com (T. Thongtem).

0749-6036/$ - see front matter © 2013 Elsevier Ltd. All rights reserved.
http://dx.doi.org/10.1016/j.spmi.2013.01.008

In recent years, microwave radiation has been used for a number of applications in producing materials, including inorganic complexes, oxides, sulfides and others. The pulse radiation has shown to be very rapid growth in different applications to materials science and engineering due to its unique reaction effect, such as rapid volumetric heating and the consequent dramatic increase in reaction rate [7,8]. A solvent with high dielectric constant is rapidly heated up to high temperature by microwave radiation for a very short time. Water, a dielectric constant of 78.46 at 298 K and 1 atm [9], is excellent in coupling with the oscillating electric pulse, leading to molecular vibration. Thus, the microwave radiation has advantage of short reaction time such that the solution is able to attain high temperature very rapidly. It is more simple and efficient over other conventional methods. The as-produced products have small particle sizes, narrow size distribution and high purity [7].

In this research, a cyclic microwave radiation was used to produce rod-like hexagonal structured $SrSn(OH)_6$ precursors very rapidly without using any templates. The precursors were changed into pure perovskite orthorhombic rod-like structured $SrSnO_3$ by high temperature calcination. To the best of our knowledge, no data on the photocatalytic performance of rod-like structured $SrSnO_3$ for water treatment are available in literatures. Thus the performance is reported in this research.

2. Experiment

To synthesize rod-like $SrSnO_3$ products, each 0.005 mol of tin(II) chloride dihydrate ($SnCl_2{\cdot}2H_2O$) and strontium acetate ($(CH_3CO_2)_2Sr$) was separately dissolved in 40 ml de-ionized water with continuous stirring. Mixed these solutions together and adjusted the pH to 12.2 using 3 M NaOH with continuous stirring at room temperature for 1 h. At this stage, white suspension formed and separated by filtration, washed for several times by de-ionized water and absolute ethanol, and dried in air at 70 °C for 24 h.

The same solution was also irradiated using 180 W cyclic microwave radiation (CMR, 1 min on for every 1 min interval) for 30 cycles. In the end, white precipitates were produced, separated and dried by the same condition as above. The precipitates were divided into four parts. One was used as the reference, and each of the three remains was further calcined at 500 °C, 700 °C and 900 °C in an ambient atmosphere for 3 h to form white powders.

The above products were characterized by thermogravimetric analyzer (TGA, Shimadzu TGA-50) using a heating rate of 5 °C/min; X-ray diffractometer (XRD, Philips X' Pert MPD) operating at 20 kV, 15 mA with Cu Kα radiation (1.5405 Å) at a scanning rate of 0.02 °C/s in the 2θ range of 10–80 °C; Fourier transform infrared spectrometer (FTIR, Bruker Tensor 27) with KBr as a diluting agent and operated in the range of 4000–400 cm^{-1}; scanning electron microscope (SEM, JEOL JSM-6335F) operating at 15 kV; transmission electron microscope (TEM, JEOL JSM-2010) and selected area electron diffractometer (SAED) operating at 200 kV; and UV–visible spectrometer (Lambda 25 PerkinElmer) using a UV lamp with the resolution of 2.0 nm.

The photocatalytic activities of the as-produced rod-like $SrSnO_3$ were investigated through the degradation of methylene blue (MB) dye aqueous solutions. The 100 mg product was suspended in 100 ml 5.0×10^{-6} M MB solution, which was stirred for 1 h in the dark condition to establish an adsorption–desorption equilibrium of MB dye on the $SrSnO_3$ surfaces. Photocatalysis was initiated by two 18 W UV lamps for different lengths of time. Absorbance peaks at 663 nm wavelength, determined by UV–visible spectrometer, were assumed to be linearly dependent on the concentrations of MB before and after photocatalysis. Decolorization efficiency (%) was calculated by $\frac{I_o - I}{I_o} \times 100$, where I_o and I were the absorbance intensities of the solutions before and after photocatalysis, respectively.

3. Results and discussion

3.1. TGA

Mass losses of the $SrSn(OH)_6$ precursors (Fig. 1) produced by 180 W cyclic microwave radiation (CMR) were composed of two different steps with the total mass loss of 16.5% between room temperature (T_R) and 530 °C. At T_R–170 °C, the mass loss was 3.5% due to the evaporation of water and eth-

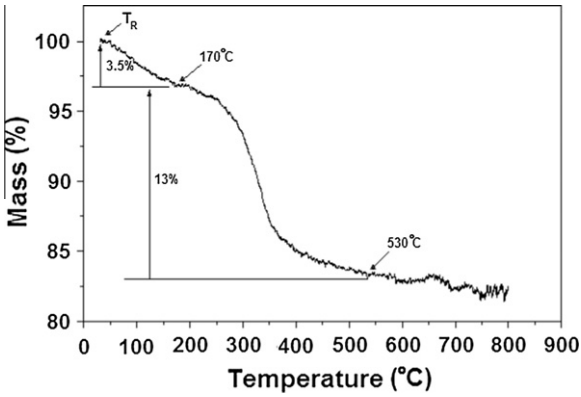


Fig. 1. TGA of the $SrSn(OH)_6$ precursors produced by 180 W CMR.

anol physically adsorbed on surfaces of the precursors. At 170–530 °C, the mass loss became faster due to the dehydration and dehydroxylation processes of precursor powder. Beyond the 530 °C, mass loss of the precursors tended to be terminated. When the molecular framework of the Sr–Sn–O–H precursors was broken, H_2O molecules were released from their grains, with the formation of $SrSnO_3$. It was likely that the $SrSn(OH)_6$ precursors had been completely transformed into $SrSnO_3$ [4,10] at this temperature.

3.2. XRD

Fig. 2a shows the XRD patterns of the suspensions produced by stirring at room temperature, before and after calcination at 900 °C for 3 h. XRD pattern of the product before high temperature calcination was indexed to correspond with hexagonal $SrSn(OH)_6$ (JCPDS No.09-0086) [11] as the major phase with some of tetragonal SnO_2 (JCPDS No. 21-1250) [11] as the minor one. Upon calcination the precursors in air at 900 °C for 3 h, they were transformed into perovskite orthorhombic $SrSnO_3$ phase (JCPDS No 77-1798) [11], with some tetragonal SnO_2 [11] residue. Small amount of the residue was mixed in the suspensions. Subsequently, they were sharpened and strengthened by the calcination process.

The same solution with the pH 12.2 was processed by a 180 W CMR for 30 cycles to form precipitates which were further calcined at high temperatures to produce powders (Fig. 2b). The precipitates without calcination were specified as hexagonal $SrSn(OH)_6$ [11] pure phase. These results confirm that the microwave pulse plays the role in forming the single phase by promoting the chemical reaction to be complete within a very short time. Upon calcination the precipitates in air at 500 °C, 700 °C and 900 °C for 3 h, their XRD patterns were specified to correspond with pure orthorhombic $SrSnO_3$ phase [11]. Along with the rise in calcination temperatures, their peaks became sharper and stronger and the crystalline degree increased step by step until reaching the best crystal at 900 °C and 3 h calcination. The analysis indicated that $SrSnO_3$ has an orthorhombic structure with Pbnm space group [11].

The degree of distortion from ideal cubic ABO_3 perovskite structure was estimated by the Goldschmidt tolerance factor (t) described as follows.

$$t = \frac{(r_A + r_O)}{\sqrt{2}(r_B + r_O)} \tag{1}$$

where r_A, r_B and r_O are the ionic radii of A, B and O. For $SrSnO_3$, the coordination number (CN) of Sr^{2+}, Sn^{4+} and O^{2-} are 12, 6 and 6, with the ionic radii of $r(Sr^{2+})$ = 1.44 Å, $r(Sn^{4+})$ = 0.74 Å and $r(O^{2-})$ = 1.40 Å [12], respectively. Calculated tolerance factor for $SrSnO_3$ was 0.94. The tolerance factor of $SrSnO_3$ is more deviated from unity due to the more distorted in the structure from the ideal cubic phase [13,14]. Thus $SrSnO_3$ transformed from cubic into orthorhombic structures by octahedral tilting distortion, fitted to the smaller ionic radius of Sr^{2+} cations to the cubo-octahedral cavity in the corner-

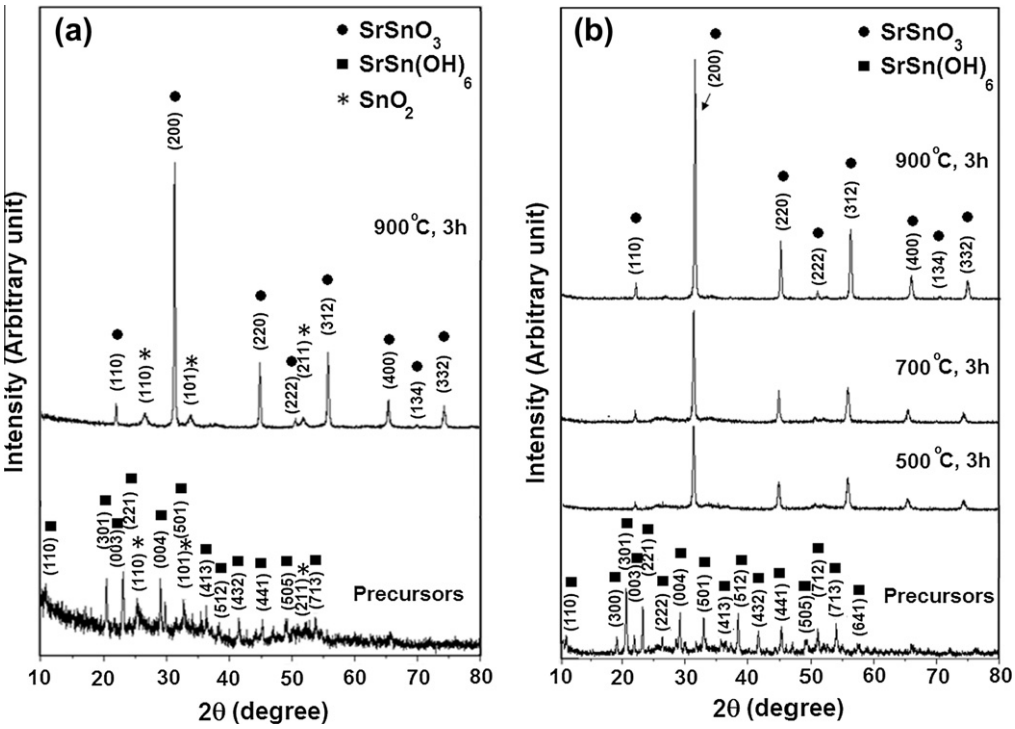


Fig. 2. XRD patterns of the products produced by (a) 1 h stirring at room temperature before and after calcination at 900 °C for 3 h, and (b) 180 W CMR for 30 cycles before and after calcination at 500 °C, 700 °C and 900 °C for 3 h.

sharing octahedral network. Some reports claimed that structure stability and phase transition of $SrSnO_3$ during the solid state reaction were varied with the temperatures [15,16]. In this research, there was no detection of phase transition, which might relate to the difference in defect formation containing in the products.

3.3. FTIR

Fig. 3 shows FTIR spectra of the $SrSn(OH)_6$ precursors produced by CMR before and after calcination in air at 500 °C, 700 °C and 900 °C for 3 h. The vibration bands in the range of 3600–3000 cm^{-1} and centered at 1459 cm^{-1} were assigned to be different types of O–H stretching and bending vibrations of water molecules adsorbed on the surfaces of $SrSn(OH)_6$ particles, respectively. Their intensities were significantly decreased by the high temperature calcination process in sequence until the best crystalline $SrSnO_3$ was completely produced at 900 °C. Those in the range of 1350–850 cm^{-1} were assigned to be the bending modes of different types of surface hydroxyl groups, which did not appear in the final product. The vibrations of the stannate group (SnO_3^{2-}) were detected as high intensity bands in the 400–300 and 700–600 cm^{-1} ranges, including the stretching vibration of the Sn–O bond at 530 cm^{-1} [1,4]. In this research, the calcined products were detected at 660 cm^{-1}, with some shoulders at 535 cm^{-1} and other bands starting at about 400 cm^{-1}.

3.4. SEM, TEM and SAED

Typical morphologies and phases of the as-produced products characterized by SEM, TEM and SAED are shown in Figs. 4–6. In this research, the precursors (Fig. 4a) produced by 1 h stirring at room

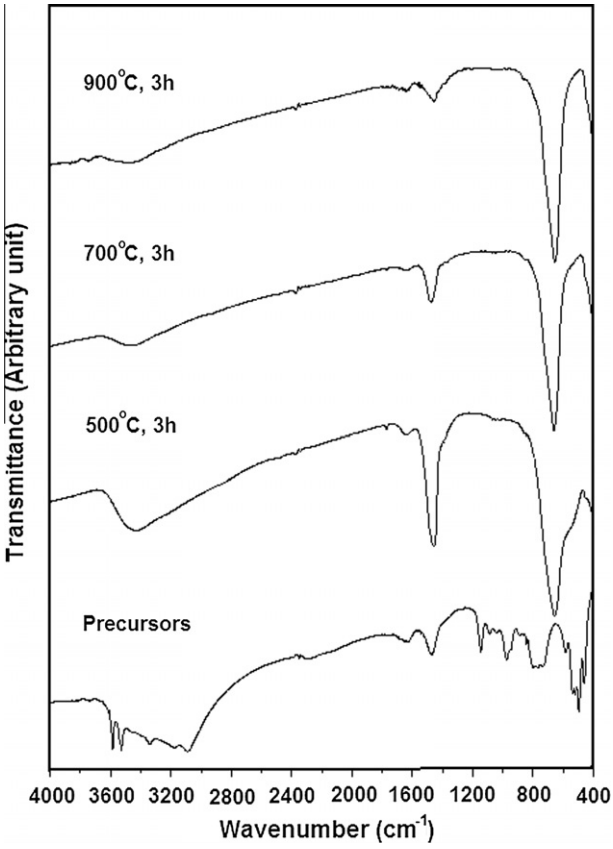


Fig. 3. FTIR spectra of the products produced by CMR before and after calcination in air at 500 °C, 700 °C and 900 °C for 3 h.

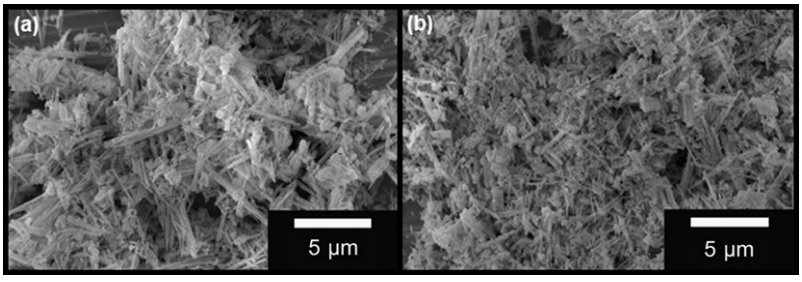


Fig. 4. SEM images of the products produced by 1 h stirring at room temperature (a) before and (b) after calcination at 900 °C for 3 h.

temperature shaped like rods with high degree of agglomeration. Upon calcination of the precursors (Fig. 4b) at 900 °C for 3 h, the particles still retained their rod-like precursor shape. Some impurities (Fig. 2a) were still to present in this product. Diameters of the rods after 900 °C calcination were smaller than those of the rod-like precursors produced by stirring at room temperature. To improve the purity and crystalline degree of the rod-like precursors, a CMR pulse was used to irradiate through

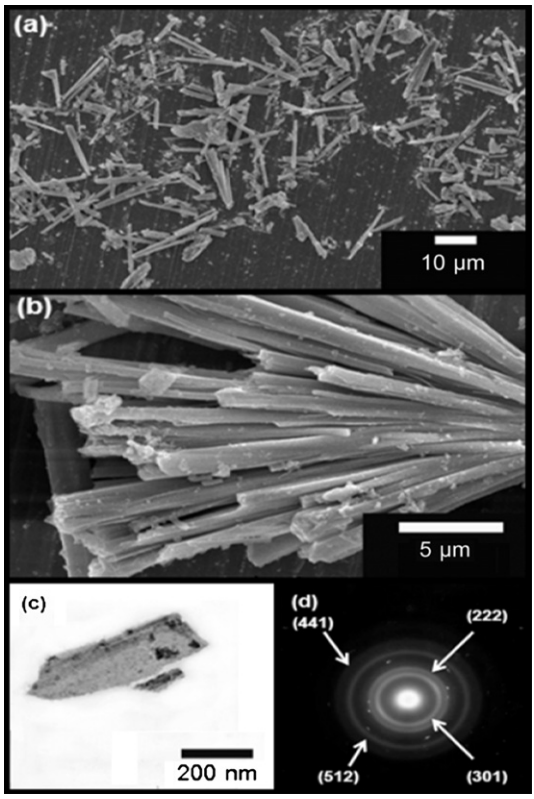


Fig. 5. (a, b) SEM images, (c) TEM image and (d) SAED pattern of the $SrSn(OH)_6$ rod-like precursors produced by CMR.

the 1 h stirred solution with the pH 12.2 to form white $SrSn(OH)_6$ precipitates. These white precipitates (Fig. 5a–c) after being irradiated by microwave radiation were still to be rod-like particles but slightly longer. At 500 °C, 700 °C and 900 °C, these final products were composed of $SrSnO_3$ single phase, specified by the above XRD analysis. At 900 °C, the rods (Fig. 6a–d) appeared as rough surfaces and piled up in bundles. Diameters of the rod-like products (Fig. 7): the precursors at T_R, and the products produced by calcination the precursors at 500 °C, 700 °C and 900 °C for 3 h, were determined in sequence as 0.745 ± 0.303 μm, 0.521 ± 0.184 μm, 0.442 ± 0.146 μm and 0.496 ± 0.160 μm, respectively. The diameters were very distributive, implying that they nucleated at different time and grew at different rates. The influence of calcination temperatures on the average diameters is shown in Fig. 8. The diameter was decreased with the increasing in the temperature due to the loss of hydroxyl group on the surface of rod-like $SrSn(OH)_6$ precursors as water molecules by transforming the rod-like precursors into the rod-like $SrSnO_3$ products. The diameters were decreased in sequence from T_R to 500 °C and 700 °C calcination, and increased again at 900 °C. For the 500 °C calcination product, the hydroxyl groups were not detected by XRD (Fig. 2b) but they were still detected by TGA (Fig. 1) and FTIR (Fig. 3). Diameters of the 700 °C calcination product were the smallest. At this stage, hydroxyl groups were completely released. Beyond 700 °C, they were gradually increased in size and were the biggest at 900 °C, due to the atomic arrangement and grain growth process. SAED pattern (Fig. 5d) of the precursors produced by CMR appears as diffuse and hollow concentric rings corresponding to nanostructured $SrSn(OH)_6$ [11] polycrystal. For the SAED pattern (Fig. 6e) of the rod-like $SrSnO_3$ produced by CMR combined with the 900 °C and 3 h calcination, it corresponds to single crystalline $SrSnO_3$ [11].

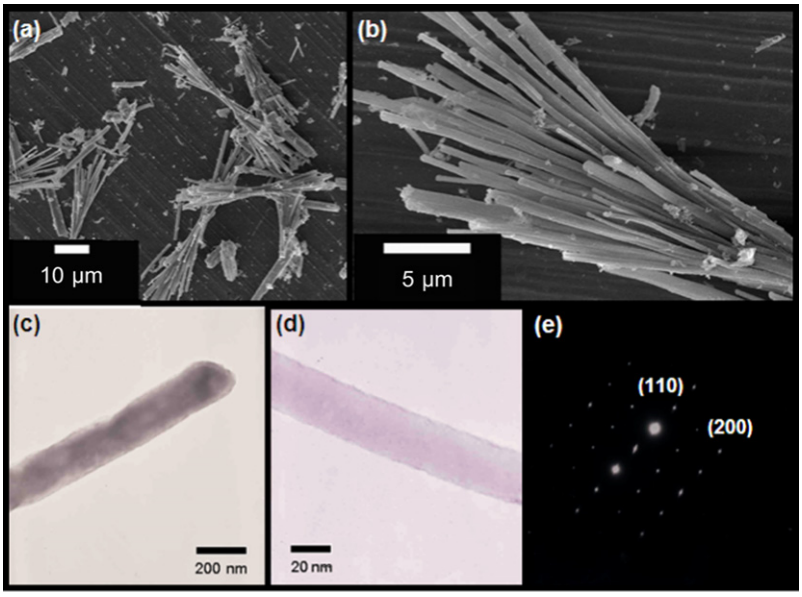


Fig. 6. (a and b) SEM images, (c and d) TEM images and (e) SAED pattern of the rod-like $SrSnO_3$ produced by the combinations of CMR and 900 °C calcination for 3 h.

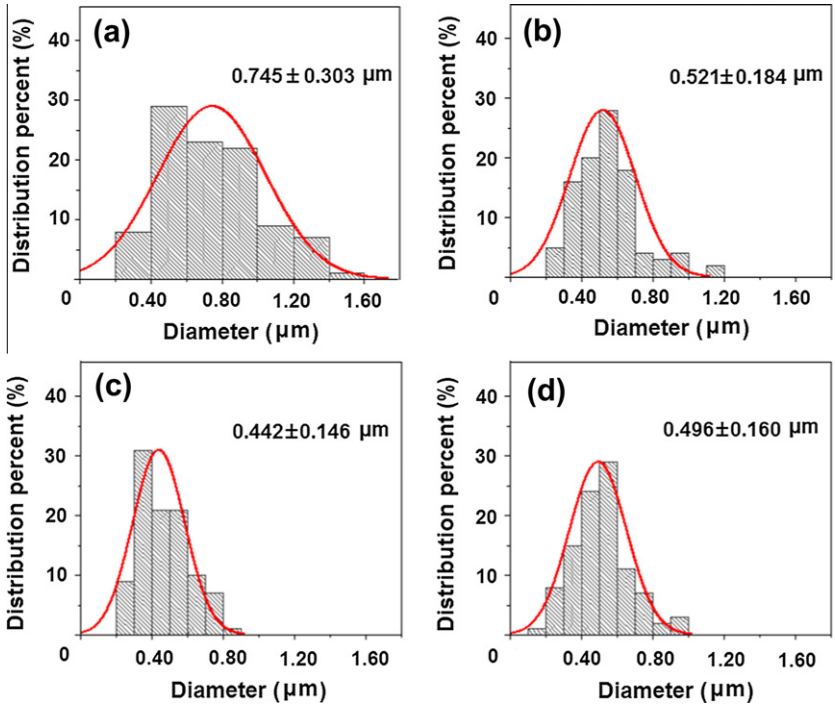


Fig. 7. Diameter distribution histograms of the products produced by CMR (a) before and (b–d) after calcination in air at 500 °C, 700 °C and 900 °C for 3 h, respectively.

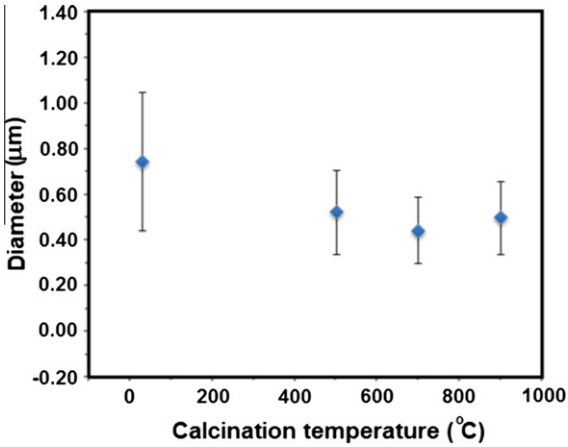


Fig. 8. Change of the average diameters of the rod-like products produced by CMR before and after calcination in air at 500 °C, 700 °C and 900 °C for 3 h.

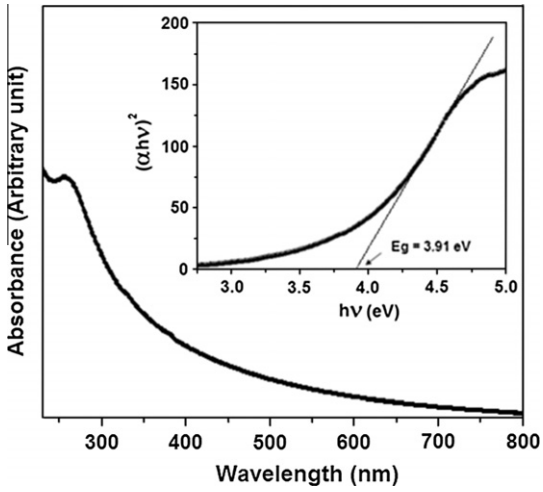


Fig. 9. The absorbance and the plot of $(\alpha h\nu)^2$ vs $h\nu$ of rod-like $SrSnO_3$ with 900 °C and 3 h calcination.

3.5. UV–visible absorption

Fig. 9 shows UV–visible absorption of rod-like $SrSnO_3$ produced by the CMR and followed by the 900 °C and 3 h calcination. The spectrum exhibited absorption near UV region due to the charge transition from O 2p to Sn 5s orbitals [5]. The relationship between absorption coefficient (α) and photon energy ($h\nu$) can be written as $(\alpha h\nu)^n = \alpha_o(h\nu - E_g)$, where ν is the frequency, h the Planck's constant, E_g the energy gap, α_o a constant (independent of photon energy), and $n = 2$ for direct transition or 1/2 for indirect transition [17]. The energy gap was determined by plotting the $(\alpha h\nu)^2$ versus equivalent energy of the photon frequency, called the Tauc plot (inset of Fig. 9). By extrapolating the linear part of the plot to zero absorbance, the extrapolated energy gap (E_g) for the direct transition is 3.91 eV, very close to those of the previous reports [5,13,17,18]. Some difference could be met, and it was influenced by the concentration of oxygen vacancies of $SrSnO_{3-\delta}$, existing on according to the equation:

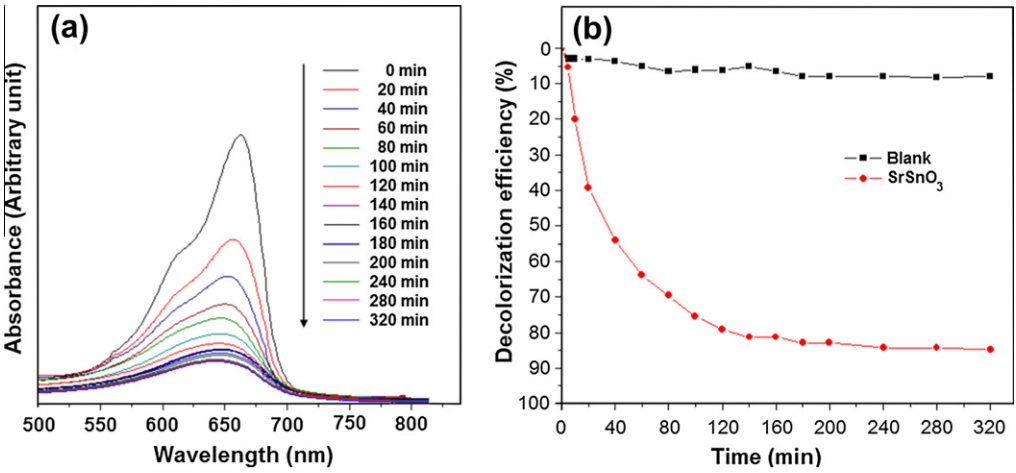


Fig. 10. (a) UV–visible absorption of MB dye in the solution containing rod-like $SrSnO_3$ with the best crystal irradiated with UV light for different lengths of time, and (b) decolorization efficiency of MB dye in the solution irradiated with UV light for different lengths of time, comparing to that of the blank.

$O_O \leftrightarrow 0.5O_2 + V_O'' + 2e^-$ [17]. During calcination at high temperature, very few of oxygen atoms could be released from crystal lattice of the $SrSnO_{3-\delta}$ solid as oxygen gas leaving their vacancies behind with electronic diffusion through the solid.

3.6. Photocatalysis

The rod-like $SrSnO_3$ with the best crystal was used for photocatalytic test. At the beginning, the color of MB dye solution was blue. The blue solution became decolorized by irradiation with UV light for different lengths of time. Each absorbance was determined from the UV–visible intensity at 663 nm wavelength (Fig. 10a) of the individual peak. Due to the performance of Fig. 10b, the rod-like $SrSnO_3$ is a candidate material used for photocatalysis for water treatment. The decolorization efficiency was 85% for 320 min with the solution color changed from blue to milky white, much more than that of the blank (7%). The photocatalytic reaction of the rod-like $SrSnO_3$ under UV light was proposed as follows. When MB dye solution was irradiated by UV light in the presence of $SrSnO_3$ catalyst, electrons in valence bands were excited and transferred into conduction bands to generate highly reactivity electron–hole pairs, by leaving holes in the valence bands behind. The adsorbed water molecules or hydroxyl ions reacted with holes in the valence bands to form ·OH radicals (H_2O or $OH^- + h^+ \rightarrow \cdot OH$) which were the highly potential radicals to oxidize or degrade the MB dye molecules. Concurrently, the adsorbed oxygen acted as electron acceptors on the surface of $SrSnO_3$ to generate $\cdot O_2^-$ superoxide ions ($O_2 + e^- \rightarrow \cdot O_2^-$) which could effectively decompose the organic molecules [19,20], making water more appropriate for a desired use.

4. Conclusions

In summary, the pure rod-like $SrSn(OH)_6$ precursors were produced through a facile cyclic microwave radiation (CMR) process without using any polymeric templates. This method is able to prevent agglomeration of the as-produced products, due to the vibrating pulse of microwave radiation. The production of rod-like $SrSnO_3$ was achieved by calcination the rod-like precursors in air at 500 °C, 700 °C and 900 °C for 3 h, with increasing in the crystalline degree in sequence. These highest crystalline $SrSnO_3$ rods have the potential for using as a photocatalytic material for water treatment.

Acknowledgements

We wish to thank the Thailand Research Fund (TRF) for providing financial support through the Royal Golden Jubilee Ph.D. Program and the TRF Research Grant BRG5380020, and the Thailand's Office of the Higher Education Commission through the National Research University Project, including the Graduate School of Chiang Mai University through a general support.

References

[1] M.C.F. Alves, M.R. Nascimento, S.J.G. Lima, P.S. Pizani, J.W.M. Espinosa, E. Longo, L.E.B. Soledade, A.G. Souza, I.M.G. Santos, Mater. Lett. 63 (2009) 118–120.
[2] J. Bohnemann, R. Libanori, M.L. Moreira, E. Longo, Chem. Eng. J. 155 (2009) 905–909.
[3] P.K. Bajpai, K. Ratre, M. Pastor, T.P. Sinha, Bull. Mater. Sci. 26 (2003) 461–464.
[4] L. Chao, Z. Youqi, F. Shaoming, W. Huanxin, G. Yanghai, B. Lei, C. Rongfeng, J. Phys. Chem. Solids 72 (2011) 869–874.
[5] D. Chen, J. Ye, Chem. Mater. 19 (2007) 4585–4591.
[6] S. Wang, M. Lu, G. Zhou, Y. Zhou, A. Zhang, Z. Yang, J. Alloys Compd. 432 (2007) 265–268.
[7] T. Ding, J.J. Zhu, Mater. Sci. Eng. B 100 (2003) 307–313.
[8] T. Thongtem, A. Phuruangrat, S. Thongtem, J. Phys. Chem. Solids 69 (2008) 1346–1349.
[9] M. Uematsu, E.U. Franck, J. Phys. Chem. Ref. Data 9 (1980) 1291–1306.
[10] Z. Jing, Mater. Sci. Eng. A 441 (2006) 176–180.
[11] Powder Diffract. File, JCPDS-ICDD, 12 Campus Boulevard, Newtown Square, PA 19073-3273, USA, 2001.
[12] P. Atkins, T. Overton, J. Rourke, M. Weller, F. Armstrong, Shriver and Atkins Inorg. Chem., 4th ed., Oxford University Press, Oxford, UK, 2006.
[13] W. Zhang, J. Tang, J. Ye, J. Mater. Res. 22 (2007) 1859–1871.
[14] D. Marrocchelli, S.R. Bishop, H.L. Tuller, G.W. Watson, B. Yildiz, Phys. Chem. Chem. Phys. 14 (2012) 12070–12074.
[15] M.C.F. Alves, S.C. Souza, M.R.S. Silva, E.C. Paris, S.J.G. Lima, R.M. Gomes, E. Longo, A.G. de Souza, I.M. Garcia dos Santos, J. Therm. Anal. Calorim. 97 (2009) 179–183.
[16] M.K. Singh, J.W. Hong, N.K. Karan, H.M. Jang, R.S. Katiyar, S.A.T. Redfern, J.F. Scott, J. Phys.: Condens. Matter. 22 (2010) 095901. 4pp.
[17] B. Bellal, B. Hadjarab, A. Bouguelia, M. Trari, Theore. Expt. Chem. 45 (2009) 172–179.
[18] W.F. Zhang, J. Tang, J. Ye, Chem. Phys. Lett. 418 (2006) 174–178.
[19] R.J. Tayade, T.S. Natarajan, H.C. Bajaj, Ind. Eng. Chem. Res. 48 (2009) 10262–10267.
[20] C.H. Wu, J.M. Chern, Ind. Eng. Chem. Res. 45 (2006) 6450–6457.

Superlattices and Microstructures 53 (2013) 195–203

Contents lists available at SciVerse ScienceDirect

Superlattices and Microstructures

journal homepage: www.elsevier.com/locate/superlattices

Characterization of ZnO flowers of hexagonal prisms with planar and hexagonal pyramid tips grown on Zn substrates by a hydrothermal process

Nuengruethai Ekthammathat [a], Titipun Thongtem [a,d,*], Anukorn Phuruangrat [b,*], Somchai Thongtem [c,d]

[a] Department of Chemistry, Faculty of Science, Chiang Mai University, Chiang Mai 50200, Thailand
[b] Department of Materials Science and Technology, Faculty of Science, Prince of Songkla University, Hat Yai, Songkhla 90112, Thailand
[c] Department of Physics and Materials Science, Faculty of Science, Chiang Mai University, Chiang Mai 50200, Thailand
[d] Materials Science Research Center, Faculty of Science, Chiang Mai University, Chiang Mai 50200, Thailand

ARTICLE INFO

Article history:
Received 20 June 2012
Received in revised form 14 October 2012
Accepted 15 October 2012
Available online 2 November 2012

Keywords:
ZnO flower-like structure
Hexagonal prisms
Hydrothermal method

ABSTRACT

Flower-like ZnO crystals on zinc substrates were synthesized by a simple hydrothermal method in different solutions containing 0.05, 0.10, 0.20, 0.30 and 0.40 g LiOH. X-ray diffraction (XRD), Fourier transform infrared (FTIR) spectroscopy, scanning electron microscopy (SEM), transmission electron microscopy (TEM) and selected area electron diffraction (SAED) showed that the products were wurtzite hexagonal ZnO flowers, composed of single crystalline hexagonal prisms grown along the [0001] direction with planar and hexagonal pyramid tips, including the Zn–O stretching vibration at 411.5 cm^{-1}. Photoluminescence (PL), excited by a 215 nm wavelength at room temperature, exhibited strong green emission at 543 nm.

© 2012 Elsevier Ltd. All rights reserved.

1. Introduction

Since the discovery of carbon nanotubes by Iijima in 1991, one dimensional (1D) nanomaterials, such as nanowires, nanotubes, nanorods and nanoribbons are very attractive for a number of worldwide researchers due to their unique physical, chemical and electron-transport properties, which are

* Corresponding authors. Address: Department of Chemistry, Faculty of Science, Chiang Mai University, Chiang Mai 50200, Thailand. Tel.: +66 (0)53 943344; fax: +66 (0)53 892277 (T. Thongtem), tel.: +66 (0)74 288374; fax: +66 (0)74 288395 (A. Phuruangrat).
E-mail addresses: ttpthongtem@yahoo.com (T. Thongtem), phuruangrat@hotmail.com (A. Phuruangrat).

0749-6036/$ - see front matter © 2012 Elsevier Ltd. All rights reserved.
http://dx.doi.org/10.1016/j.spmi.2012.10.013

different from those of their corresponding bulks. They have widely potential applications in devices and interconnected integration in nanoelectronics and molecular electronics [1–4]. Zinc oxide with a 3.37 eV direct band gap and a 60 meV large exciton binding energy is an important semiconducting and piezoelectric material, which has novel photoelectric and electronic properties as well as its promising functionalities: catalytic, electric, optoelectronic and piezoelectric properties, solar cells, lasers and other nanodevices [2,5–8]. Thus considerable efforts have been directed towards the production of well-aligned 1D nanostructured ZnO on substrates with specific optoelectronic and field-emission characteristics. These 1D nanorods were densely populated materials, and promoted rapid and effective diffusion of electrons through them for lasers and solar cells [9].

Physical and chemical methods such as vapor-phase approaches including pulsed laser deposition (PLD) [10], thermal evaporation [11–13] and chemical vapor deposition (CVD) [14,15] were used to synthesize the 1D metal oxide nanostructures deposited on substrates. These methods require high temperature and low pressure which are generally complex and expensive. Recently, hydrothermal route has been developed to synthesize ordered metal oxide nanostructures on substrates: ZnO [2,5,8], TiO_2 [16,17], Fe_3O_4 [18], CuO [19,20] and SnO_2 [21,22], by low temperature processing for controlling morphologies and phases and for scaling up production for commercial possibilities.

In this research, flower-like clusters of ZnO hexagonal prisms with planar and hexagonal pyramid tips were synthesized on zinc substrates by a hydrothermal method. The room temperature photoluminescence (PL) spectra of the flower-like ZnO nanostructures exhibited the sharp strong green emissions, which supports high potential optical applications.

2. Experimental procedure

All chemicals for this research were analytical grade and used without further purification. The ZnO hexagonal prisms with planar and hexagonal pyramid tips were fabricated on Zn substrates by a hydrothermal process at relatively low temperature. Test coupons of $15 \times 15 \times 0.25$ mm Zn foils as Zn source and substrates were carefully cleaned in an ultrasound bath containing deionized water and alcohol. The test coupons in the 20 ml aqueous solutions containing 0.05, 0.10, 0.20, 0.30 and 0.40 g LiOH as OH^- source were hydrothermally processed in 30 ml Teflon-lined stainless steel autoclaves at 120 °C for 1–24 h in an electric oven and cooled them down to room temperature. In the end, the coupons were thoroughly rinsed by deionized water several times and ethanol, dried in an electric oven at 70 °C under its atmospheric chamber for further characterization.

Crystalline phases and degree of the as-synthesized nanostructured samples were analyzed by X-ray diffractometer (XRD, Philips X'Pert MPD) operating at 20 kV 15 mA and using Cu Kα line in 2θ of 20–60°. The morphology investigation was carried out by field emission scanning electron microscope (FE-SEM, JEOL JSM-6335F) operating at 35 kV, including transmission electron microscope (TEM, JEOL JEM-2010) and selected area electron diffractometer (SAED) operating at 200 kV. Fourier transform infrared (FTIR, Bruker Tensor 27) spectrometer was carried out in the range of 400–1200 cm^{-1} at room temperature. The ZnO pellets with 1 cm in diameter for FTIR testing were prepared by 40 times dilution with KBr and pressed by 10 Torr pressure. Their optical properties were studied by a spectrophotometer (LS50B Perkin Elmer) using 215 nm excitation wavelength at room temperature.

3. Results and discussion

Crystal structure and phase of the as-synthesized ZnO grown on Zn substrates were characterized by XRD, as shown by the XRD patterns of Fig. 1. The XRD patterns corresponded with the (100), (002), (101), (102) and (110) planes at $2\theta = 31.77°$, 34.45°, 36.30°, 47.53° and 56.06° for wurtzite hexagonal ZnO structure of the JCPDS no 36-1451, and the (100) (101) and (102) planes at $2\theta = 39.03°$, 43.26° and 54.33° for hexagonal Zn structure of the JCPDS no 04-0831 [23]. No other characteristic peaks of impurities were detected in these samples. The spectra are very sharp, implying the high crystalline degree of the as-synthesized ZnO phase on Zn substrates. It should be noted that the relatively strong intensity peaks reflected and diffracted from the (101) and (002) crystallographic planes of wurtzite

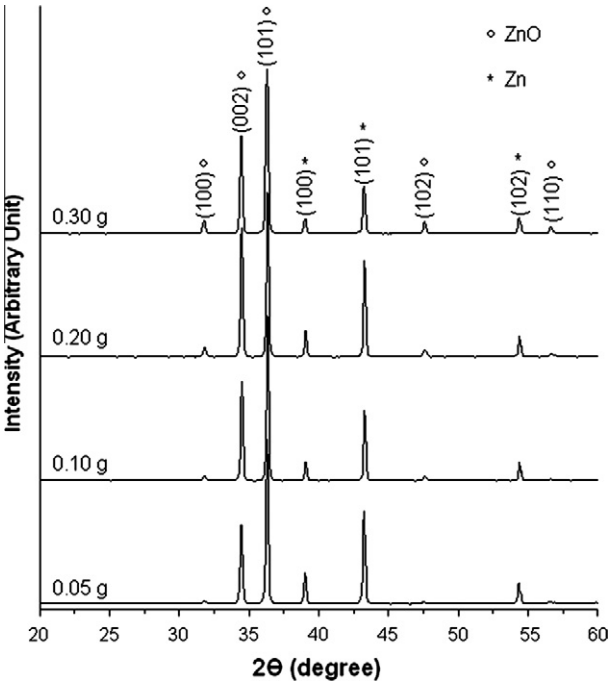


Fig. 1. XRD patterns of the as-synthesized ZnO phase on Zn substrates, hydrothermally synthesized in the solutions containing different contents of LiOH for 24 h.

hexagonal ZnO phase. Possibly, these ZnO unit cells preferentially grew along the [101] and [002] directions, in accordance with the XRD pattern reported by Pei et al. [24].

FTIR spectrum (Fig. 2) of the as-synthesized ZnO was recorded over the range of 400–1200 cm^{-1}. The main absorbance appeared at 411.5 cm^{-1} corresponding to the Zn–O stretching vibration of tetrahedral units [25], each of which was composed of four oxygen atoms with one zinc atom inside.

SEM images (Fig. 3) show the ZnO solid grown on Zn substrates by hydrothermal synthesis of the solution containing 0.10 g LiOH at 120 °C for different lengths of time. For 1 h, ZnO nanorod arrays were synthesized and uniformly covered the entire surface of zinc substrate. When the time was lengthened to 6 h, the ZnO solid was densely oriented hexagonal nanorods in large-scale uniform arrays with 50 nm in diameter grown on the Zn surface. By prolonging the reaction time to 18 h and 24 h, flower-like clusters of hexagonal prisms grown out of ZnO flower cores were more obviously detected. The ZnO individual hexagonal prism has 100 nm in diameter and 1–2 μm in length. High magnification SEM image (inserted in Fig. 3d) presents ZnO crystal shaped like a hexagonal prism with angles between the two adjacent edges of 120°. Each of them has planar tip on top. Obviously, the elongation of these crystals was the result of anisotropic growth of different crystal faces. The hexagonally prismatic shaped ZnO crystals originated by an axial growth of the hexagon normal to the (0001) crystallographic planes and directed along the *c*-axis of symmetry, including equatorial growth normal to the {10−10} family planes and radially pointed out of the *c*-axis [26,27]. Alternately, the individual ZnO hexagonal prism is surrounded by six ±(10−10), ±(1−100) and ±(01−10) prism planes with the acceleration of typical growth along the [0001] direction, leading to the formation of ZnO hexagonal prisms [26,28–30]. The solids appeared as high aspect ratio of hexagonal nanorods, identifying that the axial growth rate is faster than the equatorial growth rate [26].

Fig. 4 shows morphology development of the as-synthesized ZnO solids grown on Zn substrates by the 120 °C and 24 h hydrothermal reaction of the solutions containing different contents of LiOH. Clearly, the substrate was densely covered with ZnO hexagonal prisms of nanorods in the solution

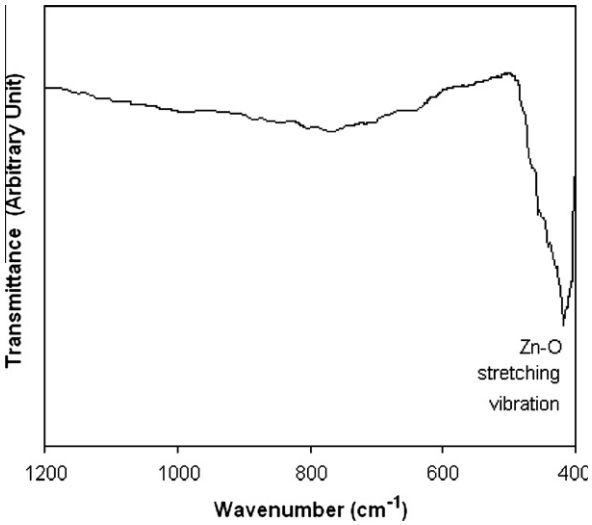


Fig. 2. FTIR spectrum of ZnO hydrothermally synthesized in the solution containing 0.30 g LiOH for 24 h.

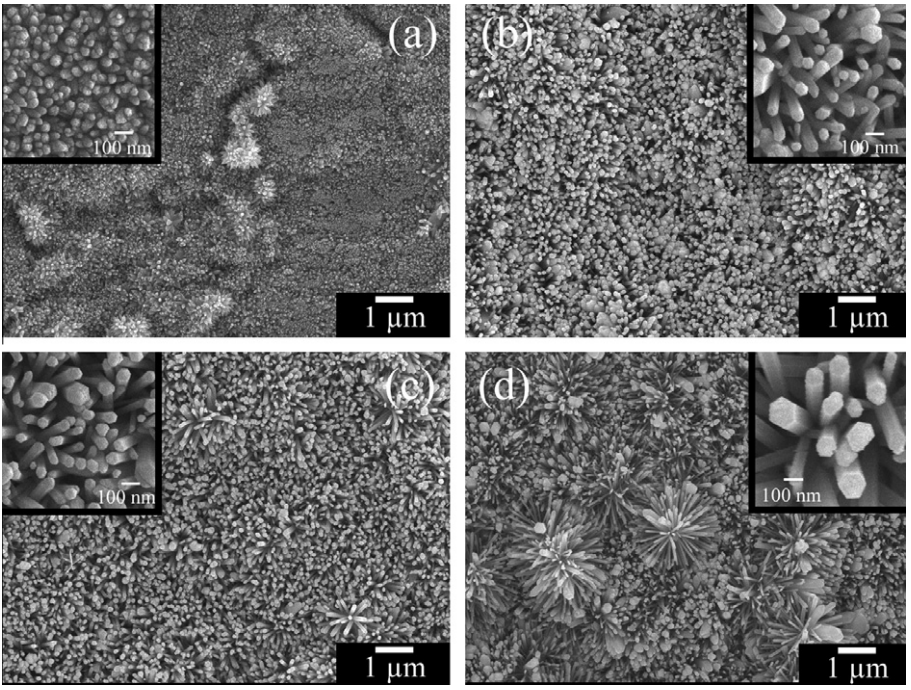


Fig. 3. SEM images of ZnO hydrothermally synthesized in the solution containing 0.10 g LiOH at 120 °C for (a–d) 1, 6, 18 and 24 h, respectively. High magnification images are shown as the insets.

containing 0.05 g LiOH. The ZnO nanorod arrays were about 1 μm long and 200 nm in diameters on average. At the current stage, ZnO flower-like clusters of nanorods shaped of hexagonal prism grown out of the ZnO cores were also detected on some areas of the substrate. Upon increasing the contents

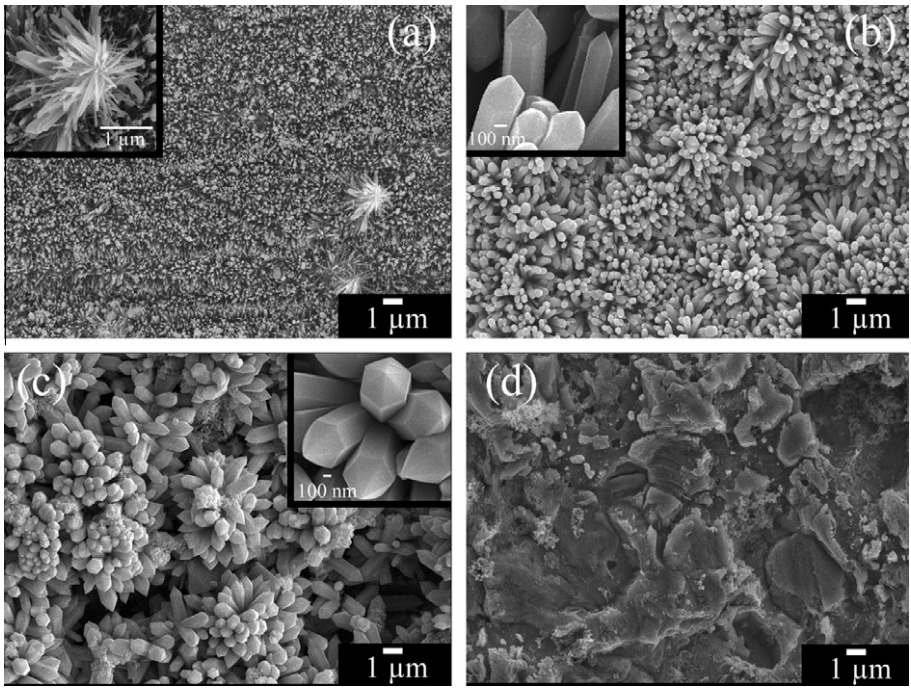


Fig. 4. SEM images of ZnO hydrothermally synthesized in the solutions containing (a–d) 0.05, 0.20, 0.30 and 0.40 g LiOH at 120 °C for 24 h, respectively. High magnification images are shown as the insets.

of LiOH from 0.05 g to 0.20 g and 0.30 g, the Zn substrates were fully covered with flower-like clusters of ZnO prisms. The top-view of these images was enlarged. They (inserted in Fig. 4b and c) appeared as ZnO hexagonal prisms of nanorods. These images indicated that an individual ZnO nanorod exhibits an obvious hexagonal prism with hexagonal pyramid-like sharp tip of well-defined crystallographic faces, pointing in different directions like a petal of flowers. In 0.40 g LiOH solution, the flower-like clusters were no longer synthesized and the Zn substrate was covered with irregular shape of ZnO agglomerates.

Further structural characterization of the ZnO flower-like hexagonal prism arrays with hexagonal pyramid sharp tips grown on the zinc substrates was studied by TEM. Typical TEM images (Fig. 5a and b) of ZnO hexagonal prisms with hexagonal pyramid sharp tips broken from a ZnO flower of hexagonal prisms present the assembly of several well-aligned nanorods with sharp tips, with their approximate lengths of 600 nm. Their diameters were 80 nm uniform along the entire lengths with very smooth surfaces. SAED pattern (Fig. 5c) of a single ZnO petal appeared as systematic bright spots, suggesting that the nanorod was single crystal. The pattern was identified as the $[-1\,1\,0]$ electron beam projection on the ZnO petal [31]. The simulated pattern (Fig. 5d) [32] with a^*, b^* and c^* lattice vectors in the $[1\,0\,0]$, $[0\,1\,0]$ and $[0\,0\,1]$ directions are in systematic arrays, and in good accordance with the result obtained by current interpretation. Thus the product was really proved to be wurtzite ZnO, with the preferential growth of the ZnO nanorod along the $[0\,0\,0\,1]$ direction [26,28,29]. To understand the characteristics of ZnO, it is necessary to study its growth mechanism. Wurtzite structured zinc oxide belongs to the P63mc space group with highly anisotropic structure along the *c*-axis. The $(0\,0\,0\,1)$ plane terminated with Zn and the $(0\,0\,0-1)$ plane with O. ZnO nanorods were easily synthesized by the nucleation and growth processes of the alternative arrangement of Zn and O atoms along the most favorable $[0\,0\,0\,1]$ direction [26,33].

Fig. 6 shows a schematic diagram for a possible growth mechanism of ZnO hexagonal prisms with planar and hexagonal pyramid tips on Zn substrates. In a typical alkaline solution of synthetic

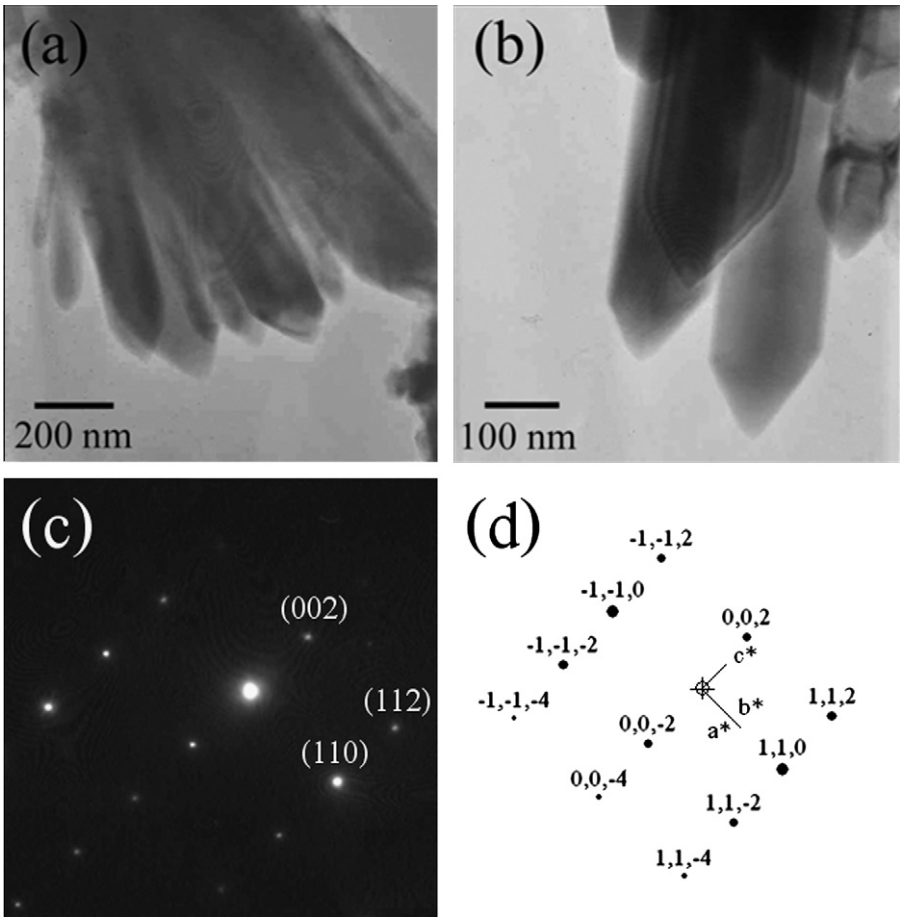


Fig. 5. (a, b) TEM images and (c) SAED pattern of hexagonal pyramid ZnO nanorods hydrothermally synthesized in the solution containing 0.30 g LiOH at 120 °C for 24 h, and (d) the simulation pattern of (c).

approach, $[Zn(OH)_4]^{2-}$ served as basic growth units for the formation of ZnO nuclei. In the present hydrothermal condition, Zn dissolved in the solution to form Zn^{2+} ions, which were further reacted with OH^- ions of LiOH to form $[Zn(OH)_4]^{2-}$. Subsequently, these $[Zn(OH)_4]^{2-}$ ions decomposed. ZnO molecular species were produced and nucleated as ZnO nuclei on Zn substrates. These ZnO nuclei grew to form hexagonal nanorod seeds. The hexagonal wurtzite ZnO with polar structure is hexagonal close packing of oxygen and zinc atoms in 3 m point group and P63mc space group with zinc atoms in tetrahedral sites. Thus, the crystal characteristics of wurtzite ZnO exhibit well defined crystallographic faces: (0001) base and nonpolar low symmetry (10−10) faces, with C_{6v} symmetry. In case of wurtzite ZnO polar crystal, each Zn^{2+} ion lies inside a tetrahedron of four oxygen ions. The Zn and O atoms are arranged alternatively along the *c*-axis such that the top face is the Zn-terminated (0001) plane and the bottom one the O-terminated (000−1) plane. The inherent asymmetry along the *c*-axis leads to the anisotropic growth of 1D ZnO crystallites. The formation of hexagonal prisms in the present study was attributed to the difference in growth rates of different crystal faces. The hydrothermal growth rates of different planes are as follows: (0001) > (10−11) > (10−10). The more rapid of the plane grows, the faster of its disappearance becomes. Therefore, the relative growth rate of these crystalline faces was determined the aspect ratio and final shape of the ZnO nanorods. The (0001) plane disappeared due to its most rapid growth rate leading to the sharp tip at the end of the *c*-axis. Growth rate of the (10−10) plane was at the slowest, therefore, the solids remained to form hexagonal prisms

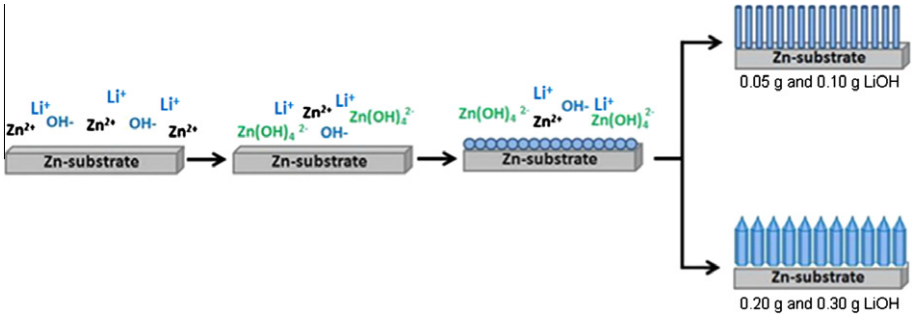


Fig. 6. Schematic diagram for a possible growth mechanism of ZnO hexagonal prisms with planar and hexagonal pyramid tips on Zn substrates.

with planar tips at lower pH (0.05 and 0.10 g LiOH), but the (10–11) plane remain to form hexagonal pyramid-like tips. However, the polar (0001) face is metastable and subjected to be etched at higher pH (0.20 and 0.30 g LiOH). Possibly, Zn atoms of the (0001) metastable polar face reacted with the OH^- ions, forming hydroxide species. The side faces of hexagonal prisms on the six ±[10−10], ±[1−100] and ±[01−10] symmetric directions were etched, remaining as hexagonal pyramid-like tips. Thus the one-dimensional growth continued to form hexagonal pyramid tips on top of ZnO nanorods [34,35].

The photoluminescence (PL) of ZnO was studied for its photonic applications. PL spectra (Fig. 7) of ZnO solids show the emission broad band at 505–625 nm in the visible range. They have the same strong green emission centered at 543 nm relating to different intrinsic defects originated during ZnO synthesis, but the exact mechanism is still ambiguous. There have been different proposed models to explain the emission from defects in ZnO crystal. The green emission at 542 nm originated from deep level associated with oxygen vacancies on outside walls of the ZnO nanorods [36,37]. Contrarily, the green emissions at 487 nm and 516 nm were believed to relate with oxygen vacancies, and the green–yellow emission at 574 nm to relate with oxygen vacancies [38]. In general, oxygen anions are so large that they are not able to reside in the interstitial sites of the ZnO solid synthesized by the 120 °C and 24 h hydrothermal method. The yellow–green emission at 573 nm is also known to be the presence of OH^- groups on the surface of ZnO nanorods, which were reduced by annealing the ZnO nanorods in oxygen atmosphere [39].

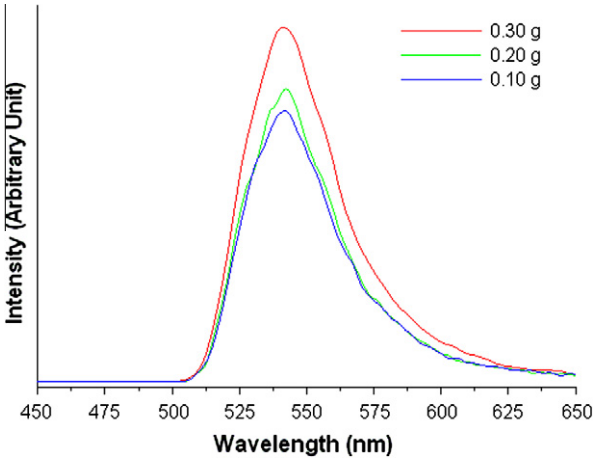


Fig. 7. PL spectra of ZnO hydrothermally synthesized in the solutions containing 0.10, 0.20 and 0.30 g of LiOH for 24 h.

4. Conclusions

Wurtzite ZnO solids were successfully synthesized on zinc substrates by a simple hydrothermal method at 120 °C for 24 h using 0.05–0.40 g LiOH. The phase, morphology and photoluminescence were characterized by X-ray diffraction, electron microscopy and spectrophotometry. In this research, the products were hexagonal wurtzite ZnO structure with the as-grown flower-like clusters composed of hexagonal prisms with planar and hexagonal pyramid tips on Zn substrates grown along the [0 0 0 1] direction. Photoluminescence spectra exhibited strong green emission at 543 nm due to the presence of oxygen vacancies in the solid.

Acknowledgments

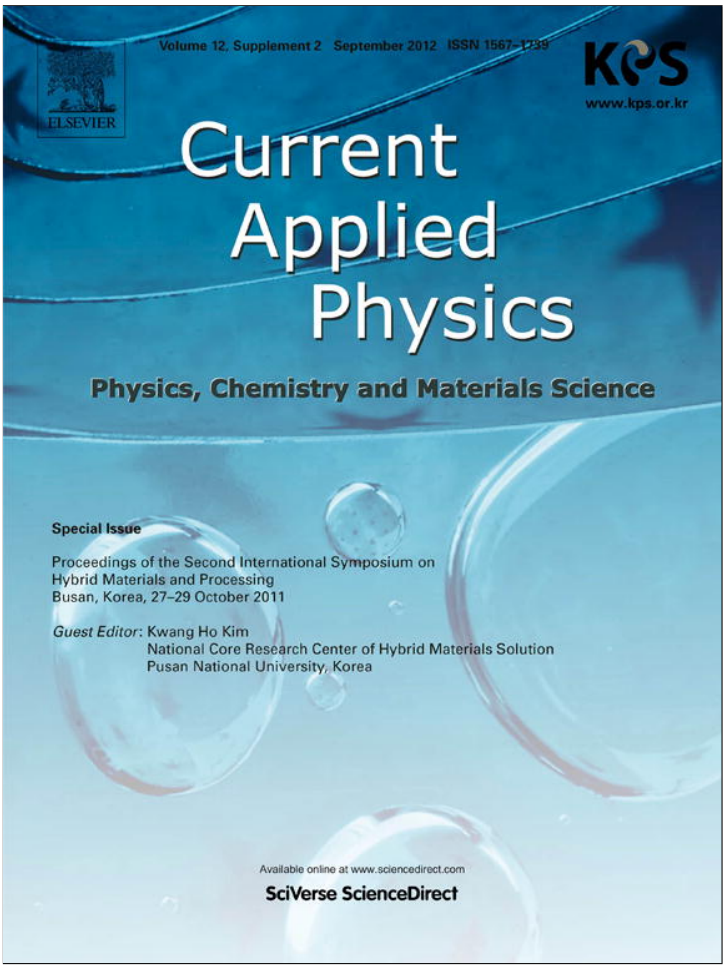
We wish to thank the Thailand's Office of the Higher Education Commission for providing financial support through the National Research University (NRU) Project for Chiang Mai University (CMU) and the Human Resource Development Project in Science Achievement Scholarship of Thailand (SAST), and the Thailand Research Fund (TRF) for providing financial support through the TRF Research Grant BRG5380020, including the Graduate School of CMU through the general support.

References

[1] S. Iijima, Helical microtubules of graphitic carbon, Nature 354 (1991) 56–58.
[2] Z. Li, X. Huang, J. Liu, Y. Li, G. Li, Morphology control and transition of ZnO nanorod arrays by a simple hydrothermal method, Mater. Lett. 62 (2008) 1503–1506.
[3] A. Phuruangrat, T. Thongtem, S. Thongtem, Characterisation of one-dimensional CdS nanorods synthesised by solvothermal method, J. Exp. Nanosci. 4 (2009) 47–54.
[4] T. Thongtem, C. Pilapong, J. Kavinchan, A. Phuruangrat, S. Thongtem, Microwave-assisted hydrothermal synthesis of Bi_2S_3 nanorods in flower-shaped bundles, J. Alloys Compd. 500 (2010) 195–199.
[5] C. Jia, X. Zhang, Y. Chen, Y. Su, Q. Zhou, M. Xin, Y. Lv, W. Kong, Liquid phase epitaxial growth and optical property of flower-like ZnO nanosheets on zinc foil, Appl. Surf. Sci. 254 (2008) 2331–2335.
[6] T. Thongtem, A. Phuruangrat, S. Thongtem, Characterization of nanostructured ZnO produced by microwave irradiation, Ceram. Int. 36 (2010) 257–262.
[7] A. Phuruangrat, T. Thongtem, S. Thongtem, Microwave-assisted synthesis of ZnO nanostructure flowers, Mater. Lett. 63 (2009) 1224–1226.
[8] Y. Tak, K. Yong, Controlled growth of well-aligned ZnO nanorod array using a novel solution method, J. Phys. Chem. B 109 (2005) 19263–19269.
[9] Z. Yang, C. Luan, W. Zhang, A. Liu, S. Tang, Fabrication and optical properties of ZnO nanostructured thin films via mechanical oscillation and hydrothermal method, Thin Solid Films 516 (2008) 5974–5980.
[10] K.A. Jeon, J.H. Kim, S.Y. Lee, Simple method for synthesis of silicon nanowire: pulsed laser deposition in furnace from p-Si wafer target, Prog. Solid State Chem. 33 (2005) 107–112.
[11] W. Lee, M.C. Jeong, J.M. Myoung, Catalyst-free growth of ZnO nanowires by metal-organic chemical vapor deposition (MOCVD) and thermal evaporation, Acta Mater. 52 (2004) 3949–3957.
[12] J.M. Wu, H.C. Shih, W.T. Wu, Y.K. Tseng, I.C. Chen, Thermal evaporation growth and the luminescence property of TiO_2 nanowires, J. Cryst. Growth 281 (2005) 384–390.
[13] S. Park, C. Hong, J. Kang, N. Cho, C. Lee, Growth of SnO_2 nanowires by thermal evaporation on Au-coated Si substrates, Curr. Appl. Phys. 9 (2009) S230–S233.
[14] F. Yu, D. Tang, K. Hai, Z. Luo, Y. Chen, X. He, Y. Peng, H. Yuan, D. Zhao, Y. Yang, Fabrication of SnO_2 one-dimensional nanosturctures with graded diameters by chemical vapor deposition method, J. Cryst. Growth 312 (2010) 220–225.
[15] R.R. Prabhakar, B. Varghese, W. Yuzhan, G. Xingyu, C.H. Sow, Carbon coated Nb_2O_5 nanowires as enhanced field emitters, Chem. Phys. Lett. 501 (2011) 431–436.
[16] F.D. Mai, W.L.W. Lee, J.L. Chang, S.C. Liu, C.W. Wu, C.C. Chen, Fabrication of porous TiO_2 film on Ti foil by hydrothermal process and its photocatalytic efficiency and mechanisms with ethyl violet dye, J. Hazard. Mater. 177 (2010) 864–875.
[17] Y. Su, S. Chen, N. Ma, X. Quan, H. Zhao, Photoelectrochemical characterization and application of direct-grown nanostructured anatase film via hydrothermal reactions, Separ. Purif. Technol. 68 (2009) 255–260.
[18] J. Chen, K. Huang, S. Liu, Hydrothermal preparation of a protective Fe_3O_4 film on Fe foil, Corr. Sci. 50 (2008) 1982–1986.
[19] Z.A. Jiang, J.T. Chen, J. Wang, R.F. Zhuo, D. Yan, F. Zhang, P.X. Yan, CuO nanosheets synthesized by hydrothermal process, Chin. Phys. Lett. 26 (2009) 086202.
[20] Y. Liu, Y. Chu, M. Li, L. Li, L. Dong, In situ synthesis and assembly of copper oxide nanocrystals on copper foil via a mild hydrothermal process, J. Mater. Chem. 16 (2006) 192–198.
[21] Q. Zhao, Z. Li, C. Wu, X. Bai, Y. Xie, Facile synthesis and optical property of SnO_2 flower-like architectures, J. Nanopart. Res. 8 (2006) 1065–1069.
[22] H.T. Chen, X.L. Wu, Y.Y. Zhang, J. Zhu, Y.C. Cheng, P.K. Chu, A novel hydrothermal route to synthesize solid SnO_2 nanospheres and their photoluminescence property, Appl. Phys. A 97 (2009) 581–585.
[23] Powder Diffract File, JCPDS-ICDD, 12 Campus Boulevard, Newtown Square, PA 19073-3273, USA, 2001.

[24] L.Z. Pei, H.S. Zhao, W. Tan, H.Y. Yu, Y.W. Chen, C.G. Fan, Q.F. Zhang, Hydrothermal oxidization preparation of ZnO nanorods on zinc substrate, Physica E 42 (2010) 1333–1337.
[25] S.K. Nandi, S. Chakraborty, M.K. Bera, C.K. Maiti, Structural and optical properties of ZnO films grown on silicon and their applications in MOS devices in conjunction with ZrO_2 as a gate dielectric, Bull. Mater. Sci. 30 (2007) 247–254.
[26] S.P. Garcia, S. Semancik, Controlling the morphology of zinc oxide nanorods crystallized from aqueous solutions: the effect of crystal growth modifiers on aspect ratio, Chem. Mater. 19 (2007) 4016–4022.
[27] C.X. Xu, G.P. Zhu, J. Kasim, S.T. Tan, Y. Yang, X. Li, Z.X. Shen, X.W. Sun, Spatial distribution of defect in ZnO nanodisks, Curr. Appl. Phys. 9 (2009) 573–576.
[28] C.X. Xu, X.W. Sun, Z.L. Dong, M.B. Yu, Zinc oxide nanodisk, Appl. Phys. Lett. 85 (2004) 3878–3880.
[29] M. Wang, S.H. Hahn, J.S. Kim, J.S. Chung, E.J. Kim, K.K. Koo, Solvent-controlled crystallization of zinc oxide nano(micro)disks, J. Cryst. Growth 310 (2008) 1213–1219.
[30] D. Chu, Y. Zeng, D. Jiang, Controlled growth and properties of Pb^{2+} doped ZnO nanodisks, Mater. Res. Bull. 42 (2007) 814–819.
[31] S. Jattukul, S. Thongtem, T. Thongtem, Morphology development of ZnO produced by sonothermal process, Ceram. Int. 37 (2011) 2055–2059.
[32] C. Boudias, D. Monceau, CaRIne Crystallography 3.1, DIVERGENT S.A., Centre de Transfert, 60200 Compiègne, France, 1989–1998.
[33] W. Peng, S. Qu, G. Cong, Z. Wang, Synthesis and structures of morphology-controlled ZnO nano- and microcrystals, Cryst. Growth Des. 6 (2006) 1518–1522.
[34] J.H. Yang, J.H. Zheng, H.J. Zhai, L.L. Yang, L. Liu, M. Gao, Solvothermal growth of highly oriented Wurtzite-structured ZnO nanotube arrays on zinc foil, Cryst. Res. Technol. 44 (2009) 619–623.
[35] D. Wang, C. Song, Controllable synthesis of ZnO nanorod and prism arrays in a large area, J. Phys. Chem. B 109 (2005) 12697–12700.
[36] H. Zhang, J. Feng, J. Wang, M. Zhang, Preparation of ZnO nanorods through wet chemical method, Mater. Lett. 61 (2007) 5202–5205.
[37] H. Gao, G. Fang, M. Wang, N. Liu, L. Yuan, C. Li, L. Ai, J. Zhang, C. Zhou, S. Wu, X. Zhao, The effect of growth conditions on the properties of ZnO nanorod dye-sensitized solar cells, Mater. Res. Bull. 43 (2008) 3345–3351.
[38] X. Wang, K. Huo, F. Zhang, Z. Hu, P.K. Chu, H. Tao, Q. Wu, Y. Hu, J. Zhu, Structural regulation and optical properties of one-dimensional ZnO nanomaterials in situ grown from and on brass substrates, J. Phys. Chem. C 113 (2009) 170–173.
[39] J. Lee, J. Chung, S. Lim, Improvement of optical properties of post-annealed ZnO nanorods, Physica E 42 (2010) 2143–2146.

Provided for non-commercial research and education use.
Not for reproduction, distribution or commercial use.



This article appeared in a journal published by Elsevier. The attached copy is furnished to the author for internal non-commercial research and education use, including for instruction at the authors institution and sharing with colleagues.

Other uses, including reproduction and distribution, or selling or licensing copies, or posting to personal, institutional or third party websites are prohibited.

In most cases authors are permitted to post their version of the article (e.g. in Word or Tex form) to their personal website or institutional repository. Authors requiring further information regarding Elsevier's archiving and manuscript policies are encouraged to visit:

http://www.elsevier.com/copyright

Author's personal copy

Current Applied Physics 12 (2012) S139–S143

Contents lists available at SciVerse ScienceDirect

Current Applied Physics

journal homepage: www.elsevier.com/locate/cap

Effects of solution pH and processing cycle on nanostructured $La_2(MoO_4)_3$ produced by cyclic microwave radiation

Yanee Keereeta [a], Titipun Thongtem [b,c,*], Somchai Thongtem [a,c,**]

[a] Department of Physics and Materials Science, Faculty of Science, Chiang Mai University, Chiang Mai 50200, Thailand
[b] Department of Chemistry, Faculty of Science, Chiang Mai University, Chiang Mai 50200, Thailand
[c] Materials Science Research Center, Faculty of Science, Chiang Mai University, Chiang Mai 50200, Thailand

ARTICLE INFO

Article history:
Received 9 December 2011
Received in revised form
3 February 2012
Accepted 16 February 2012
Available online 24 February 2012

Keywords:
Semiconductors
Scanning electron microscopy
Transmission electron microscopy
X-ray diffraction

ABSTRACT

$La_2(MoO_4)_3$ with different morphologies were successfully produced by a facile cyclic microwave radiation (CMR) processing of a 2:3 molar ratio lanthanum to molybdenum of $La(NO_3)_3{\cdot}6H_2O$ and $(NH_4)_6Mo_7O_{24}{\cdot}4H_2O$ in the solutions with different pH values adjusted by 2 M NaOH for different processing cycles. XRD, SEM, TEM, HRTEM and SAED showed that $La_2(MoO_4)_3$ microflowers of nanoflake-like petals could be produced by a 180 W CMR for 15 cycles in the solutions with the pH 7 and 8. The 904 and 887 cm^{-1} Raman symmetric stretching modes as well as the 320 cm^{-1} asymmetric bending modes were detected, and direct energy gaps of the UV–visible spectroscopy were 3.47 and 3.85 eV, respectively. The formation mechanism was also proposed in relation to the experimental results.

© 2012 Elsevier B.V. All rights reserved.

1. Introduction

Presently, chemists and materials scientists are paying much attention to study micro and nanostructured $La_2(MoO_4)_3$ materials, due to their novel morphologies, chemical and physical properties, including their potential applications for high-performance phosphors, catalysts, positive thermal expansion materials, and ionic conductors [1,2]. There have been several routes used to develop the materials: $La_2(MoO_4)_3$ phosphors with various Eu^{3+} concentrations by a facile co-precipitation process [1], positive thermal expansion lanthanum molybdate by rapid solidification with a CO_2 laser [2], monodisperse $La_2(MoO_4)_3$:Yb, Tm microarchitectures with uniform waxberry-like morphology by a facile surfactant-assisted hydrothermal route with SLS used as a structure directing agent [3], 3D flower-like $La_2(MoO_4)_3$:Eu microarchitectures by a facile hydrothermal process in the presence of AOT [4], uniform 3D $La_2(MoO_4)_3$ nanostructures with a pompon shape by a simple surfactant-free hydrothermal approach [5], and pomponlike $La_2(MoO_4)_3$ microstructures assembled with single-crystalline nanoflakes via a surfactant-assisted ultrasound route [6]. In the present research, $La_2(MoO_4)_3$ with different morphologies were produced by a facile cyclic microwave radiation (CMR) reaction, the environmentally benign rapid process, without using any surfactants or additives.

2. Experiment

To produce $La_2(MoO_4)_3$ with different morphologies, lanthanum nitrate hexahydrate ($La(NO_3)_3{\cdot}6H_2O$) and ammonium molybdate tetrahydrate ($(NH_4)_6Mo_7O_{24}{\cdot}4H_2O$) with 2:3 molar ratio La:Mo were separately dissolved in 15 ml de-ionized water, mixed, and followed by pH adjusting using 2 M NaOH. At the present stage, the mixtures turned into white colloid. Subsequently, they were processed by a 180 W cyclic microwave radiation (CMR) for 6, 9, 12, and 15 cycles. Each cycle was 20 s on for every 40 s interval. Frequency of the microwave radiation for the present research was 2,450 MHz. Finally, the products with and without processing by the CMR were washed with water and ethanol, and dried at 80 °C for 12 h. Phases, morphologies, structures, vibration modes and energy gaps of the products were characterized by X-ray diffraction (XRD, SIEMENS D500) operating at 20 kV and 15 mA, using K_α line from a copper target; scanning electron microscopy (SEM, JEOL JSM-6335F)

* Corresponding author. Department of Chemistry, Faculty of Science, Chiang Mai University, Chiang Mai 50200, Thailand. Tel.: +66 (0) 53 943344; fax: +66 (0) 53 892277.
** Corresponding author. Department of Physics and Materials Science, Faculty of Science, Chiang Mai University, Chiang Mai 50200, Thailand. Tel.: +66 (0) 53 941924; fax: +66 (0) 53 943445.
E-mail addresses: ttpthongtem@yahoo.com (T. Thongtem), schthongtem@yahoo.com (S. Thongtem).

1567-1739/$ – see front matter © 2012 Elsevier B.V. All rights reserved.
doi:10.1016/j.cap.2012.02.045

Author's personal copy

operating at 15 kV; transmission electron microscopy (TEM, JEOL JEM-2010), high resolution transmission electron microscopy (HRTEM) and selected area electron diffraction (SAED) operating at 200 kV; Raman spectroscopy (T64000 HORIBA Jobin Yvon) using a 50 mW and 514.5 nm wavelength Ar green laser; and UV–visible spectrometry (Lambda 25 Perkin–Elmer) using a UV lamp with the resolution of 1 nm.

3. Results and discussion

3.1. XRD

Crystallographic planes of XRD spectra produced in the solutions with different pH values by a 180 W CMR for 15 cycles (Fig. 1a) were indexed and compared with those of the JCPDS database nos: 01–0135, 45–0407, 23–1146, and 36–1481 for $(NH_4)_6Mo_7O_{24}\cdot 4H_2O$, $La_2(MoO_4)_3$, $La_2Mo_4O_{15}$ and $La(OH)_3$, respectively [7]. In the solution with the pH 2.78 (free of NaOH), the product was the mixture of $La_2(MoO_4)_3$, $La_2Mo_4O_{15}$, and $(NH_4)_6Mo_7O_{24}\cdot 4H_2O$. When 2 M NaOH was added to the solution until its pH was 5, the product contained $La_2(MoO_4)_3$ with some $(NH_4)_6Mo_7O_{24}\cdot 4H_2O$ residue. At the pH 7 and 8, the products were pure tetragonal $La_2(MoO_4)_3$ phase with no impurity detection. At the pH 9 and 10, additional $La(OH)_3$ was detected. Upon increasing the pH from 9 to 10, the intensity of $La(OH)_3$ peaks became higher but that of $La_2(MoO_4)_3$ was lower. For the present 180 W CMR and 15 cycles analysis, pure $La_2(MoO_4)_3$ was successfully produced in the solutions with the pH 7 and 8.

3.2. Raman analysis

To further ascertain the presence of $La_2(MoO_4)_3$, the products produced by the 180 W CMR and 15 cycles in the solutions with the pH of 7, 8 and 9 were characterized by Raman spectroscopy. Their Raman shifts (Fig. 1b) at 904 and 887 cm^{-1} corresponded to the symmetric stretching modes, and those at 821 and 782 cm^{-1} to the asymmetric stretching modes. The vibrations at 378 and 320 cm^{-1} were the symmetric and asymmetric bending modes of MoO_4^{2-} tetrahedrons, respectively. Below these wavenumber values, they were specified as the translation and lattice vibrations [2]. It should be noted that the Raman spectra contain prominent peaks at the same wavenumbers although the three products were produced at different pH values, which reflected their purity. Those produced in the pH 7 and 8 solutions were pure phase of $La_2(MoO_4)_3$, but that in the pH 9 solution was the mixed phases of $La_2(MoO_4)_3$ and $La(OH)_3$.

3.3. SEM, TEM, HRTEM and SAED

SEM, TEM and HRTEM images (Figs. 2–4) show the product morphologies, produced by the 180 W CMR in the solutions with different pH values and processing cycles. At the pH 2.78 (free of

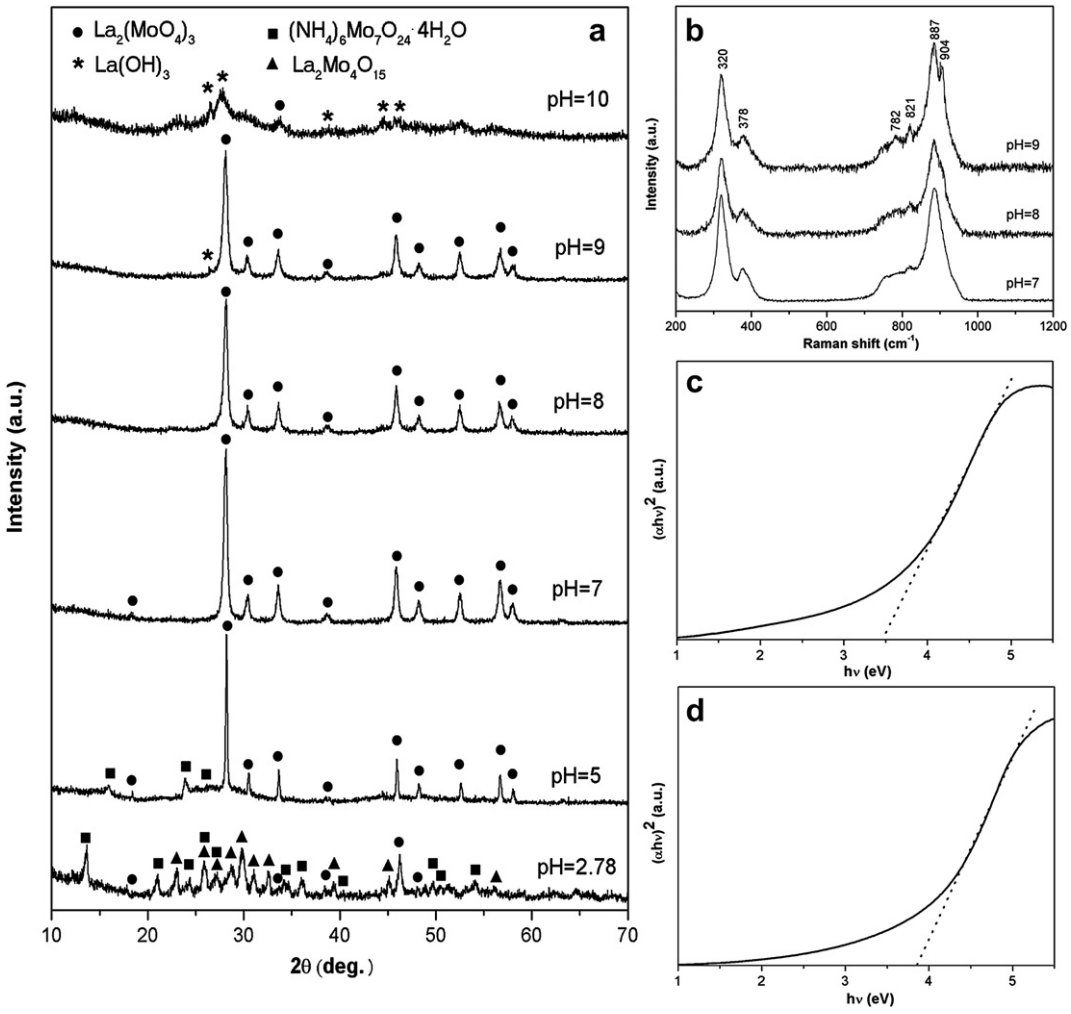


Fig. 1. (a, b) XRD and Raman spectra of the products produced in the solutions with different pH values, and (c, d) UV–visible absorption of $La_2(MoO_4)_3$ produced in the solutions of pH 7 and 8 by 180 W CMR for 15 cycles, respectively.

Author's personal copy

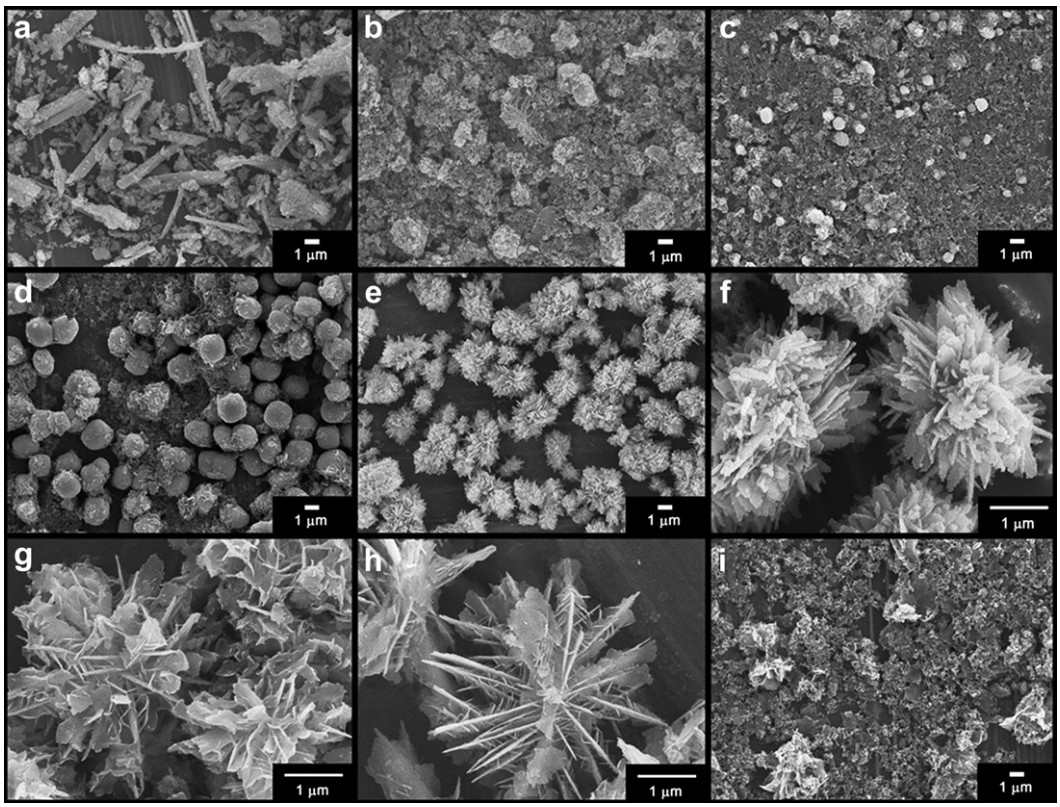


Fig. 2. SEM images of the products produced in the solutions with the pH of (a) 2.78, (b) 4, (c) 5, (d) 6, (e, f) 7, (g) 8, (h) 9, and (i) 10, by 180 W CMR for 15 cycles.

NaOH) and 15 cycle processing (Fig. 2a), the product was nanoparticles clustered together as irregular microparticles with different orientations. Upon increasing pH of the solution to 4, 5 and 6 (by adding 2 M NaOH) but keeping the processing cycle to be the same at 15 cycles (Fig. 2b–d), the products were developed in sequence: nanoparticles and microparticles, nanoparticles and round microparticles, and nanoparticles and larger round microparticles. At these states (pH 2.78, 4, 5 and 6), the products contained some impurities. At the pH 7 and 8, and 15 cycle processing (Figs. 2e–g, 3e & f, and 4a & d), the products (pure $La_2(MoO_4)_3$ phase) were microflowers of nanoflake-like petals. By increasing only the pH from 8 to 9 and 10 (Figs. 2h and i, and 4g & h), the products (mixed phases of $La_2(MoO_4)_3$ and $La(OH)_3$) were microflowers of nanoflake-like petals, and sponges, respectively. For comparison, the product produced in the solution of pH 7 without processing by the CMR (Fig. 3a) was composed of a number of nanoparticles with different orientations. In the present research, the effect of processing cycles was also studied. Upon processing by 180 W CMR of the solution with the pH 7 for 12 cycles (Fig. 3d), 9 cycles (Fig. 3c) and 6 cycles (Fig. 3b), the products were

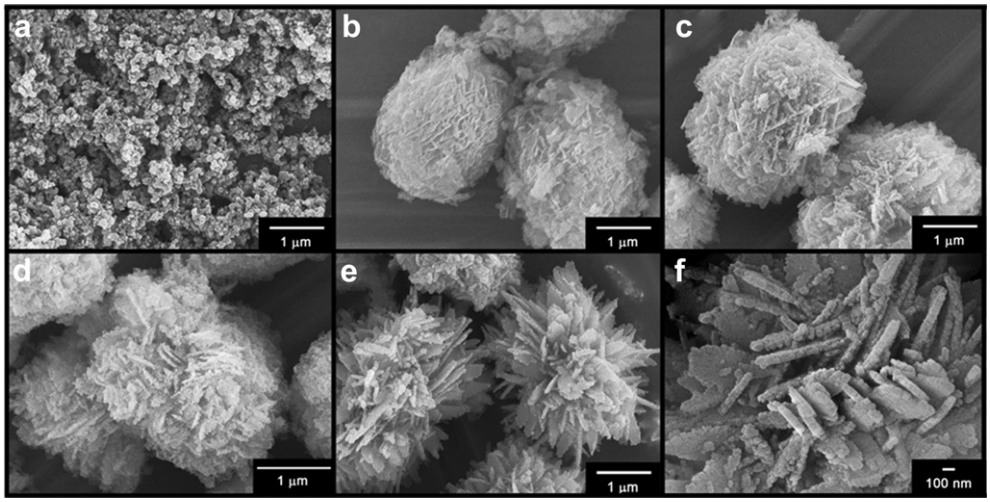


Fig. 3. SEM images of the products produced in the solutions with the pH 7: (a) before, (b–e) after processing by the 180 W CMR for 6, 9, 12 and 15 cycles, and (f) the enlarged image of (e), respectively.

Author's personal copy

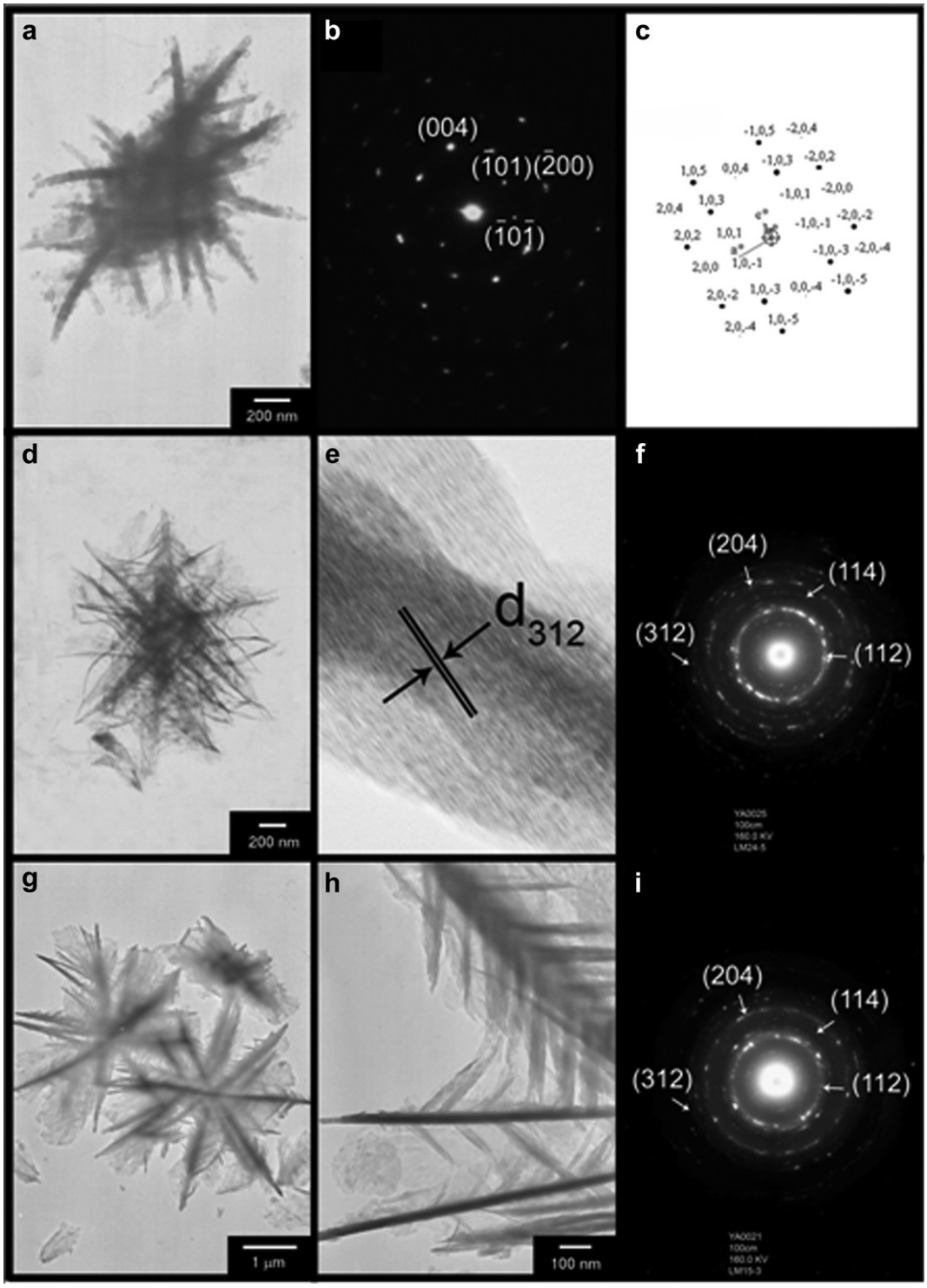


Fig. 4. TEM and HRTEM images, and SAED patterns of the products produced in the solutions with the pH of (a, b) 7, (d–f) 8, (g–i) 9 by 180 W CMR for 15 cycles, and (c) the simulated pattern of (b).

microparticles of nanoflakes, smaller microparticles of nanoflakes, and microparticles, respectively. The development of product morphologies by the solution pH and processing cycle was also summarized in Table 1. In order to present the crystalline product produced in the solution with the pH 8 by 180 W CMR for 15 cycles (Fig. 4d), the product was characterized by high resolution TEM, as shown in Fig. 4e. Its (312) lattice plane belonging to $La_2(MoO_4)_3$ phase was detected. This implied that the petal of the microflower was single crystal. A petal of the microflower produced in the solution with the pH 7 by 180 W CMR for 15 cycles (Fig. 4a), was characterized by SAED, as shown in Fig. 4b. The SAED pattern was indexed [8] and specified that the petal was $La_2(MoO_4)_3$ single crystal [7,8]. It was in accordance with its simulated pattern [9] (Fig. 4c), showing that the electron diffraction pattern could exist in reality. Other two microflowers produced in the solutions with the pH 8 and 9 by 180 W CMR for 15 cycles (Fig. 4d and g) were also

Author's personal copy

Table 1
Morphology development of the products produced by the 180 W CMR of the solutions with different pH values and processing cycles, as compared to the product without processing by the CMR.

pH	Cycles	Morphologies
2.78 (Free of NaOH)	15	Nanoparticles clustered together to be irregular microparticles with different orientations
4	15	Nanoparticles and microparticles
5	15	Nanoparticles and round microparticles
6	15	Nanoparticles and larger round microparticles
7	Without processing by CMR	Nanoparticles
7	15	Microflowers of nanoflake-like petals
8	15	Microflowers of nanoflake-like petals
9	15	Microflowers of nanoflake-like petals
10	15	Sponges
7	12	Microparticles of nanoflakes
7	9	Smaller microparticles of nanoflakes
7	6	Microparticles

characterized by SAED, as shown in Fig. 4f and i. These two SAED patterns were indexed [8] to correspond with the (112), (114), (204) and (312) crystallographic planes of $La_2(MoO_4)_3$ polycrystalline [7,8] microflowers. Also, these two patterns were composed of diffuse and hollow concentric rings, which were the indication of nanostructured microflowers.

3.4. Formation mechanism

When $La(NO_3)_3\cdot 6H_2O$ and $(NH_4)_6Mo_7O_{24}\cdot 4H_2O$ solutions were mixed with and without NaOH adding, a number of nuclei were produced. Concurrently, they clustered together to form nanoparticles (white colloid). Upon processing the mixtures by a 180 W cyclic microwave radiation for 15 cycles, larger nanoparticles were produced. At the pH 2.78 (free of NaOH), some nanoparticles clustered together to be irregular microparticles of mixed phases. When 2 M NaOH was added to the solutions until their pH values were 4, 5 and 6 in sequence, the products were the mixtures of nanoparticles and microparticles with the increasing in the content of microparticles and the degree of purity. The basicity of the solutions were further increased until at the pH values of 7, 8 and 9, these products became microflowers of nanoflake-like petals. The microflowers were pure phase of $La_2(MoO_4)_3$ only those produced in the solutions with the pH 7 and 8. In the solution with the pH 9, some $La(OH)_3$ impurity was also produced, due to the excess of hydroxyl ions. In the pH 10 solution, the product was sponges of mixed phases of $La_2(MoO_4)_3$ and $La(OH)_3$. Upon increasing the basicity from the pH 9 to 10, the content of the first constituent became lowered and that of the second one was raised up. It should be noted that OH^- ions not only controlled the purity of the products but also functioned as a template in directing the product morphologies. By decreasing the processing times of the pH 7 mixtures from 15 cycles to 12, 9, and 6 cycles, the products gradually turned into microparticles of nanoflakes, smaller microparticles of nanoflakes, and microparticles, respectively. During the CMR process, $La_2(MoO_4)_3$ was produced by the reaction.

$$14La^{3+} + 3Mo_7O_{24}^{6-} + 12H_2O \rightarrow 7La_2(MoO_4)_3 + 24H^+$$

3.5. UV–visible spectroscopy

UV–visible absorption of pure $La_2(MoO_4)_3$ microflowers with nanoflake-like petals produced in the solutions with the pH 7 and 8 by 180 W CMR for 15 cycles was characterized by a UV–visible spectrophotometer, as shown in Fig. 1c and d. For the photon energy ($h\nu$) of more than energy gap (E_g), the relationship between the square absorbance and the photon energy for direct interband transitions was linearly increased with the increasing of photon energy. The inclination of the linear portion of the curve was caused by the UV absorption for charged transition from the topmost occupied state of valence band to the bottommost unoccupied state of the conduction band. For the photon energy with less than energy gap, the absorption curve became different from linearity, caused by the UV absorption for charged transition relating to defects [10,11]. The direct energy gaps of the $La_2(MoO_4)_3$ microflowers produced in the solutions with the pH 7 and 8 were determined to be 3.47 and 3.85 eV, respectively, a promising material for high-performance phosphor.

4. Conclusions

$La_2(MoO_4)_3$ with different morphologies were successfully produced by facile CMR processing of the solutions containing $La(NO_3)_3\cdot 6H_2O$ and $(NH_4)_6Mo_7O_{24}\cdot 4H_2O$ with different pH values and processing cycles. In the present research, $La_2(MoO_4)_3$ microflowers produced in the solutions with the pH 7 and 8 presented their direct energy gaps of 3.47 and 3.85 eV, respectively.

Acknowledgments

We wish to thank the National Nanotechnology Center (NANOTEC), National Science and Technology Development Agency (NSTDA), Thailand, for providing financial support through the project P-10-11345, the Thailand's Office of the Higher Education Commission through the National Research University (NRU) Project, and the Thailand Research Fund (TRF) through the Royal Golden Jubilee Ph.D. Program and the TRF Research Grant, including the Graduate School of Chiang Mai University through the general support.

References

[1] Y. Tian, B. Chen, R. Hua, J. Sun, L. Cheng, H. Zhong, X. Li, J. Zhang, Y. Zheng, T. Yu, L. Huang, H. Yu, Optical transition, electron-phonon coupling and fluorescent quenching of $La_2(MoO_4)_3$:Eu^{3+} phosphor, J. Appl. Phys. 109 (2011) 053511-1–053511-6.
[2] E.J. Liang, H.L. Huo, Z. Wang, M.J. Chao, J.P. Wang, Rapid synthesis of $A_2(MoO_4)_3$ (A = Y^{3+} and La^{3+}) with a CO_2 laser, Solid State Sci. 11 (2009) 139–143.
[3] Zh. Chen, W. Bu, N. Zhang, J. Shi, Controlled construction of monodisperse $La_2(MoO_4)_3$:Yb, Tm, microarchitectures with upconversion luminescent property, J. Phys. Chem. C 112 (2008) 4378–4383.
[4] N. Zhang, W. Bu, Y. Xu, D. Jiang, J. Shi, Self-assembled flowerlike europium-doped lanthanide molybdate microarchitectures and their photoluminescence properties, J. Phys. Chem. C 111 (2007) 5014–5019.
[5] W. Bu, Y. Xu, N. Zhang, H. Chen, Z. Hua, J. Shi, Controlled construction of uniform pompon-shaped microarchitectures self-assembled from single-crystalline lanthanum molybdate nanoflakes, Langmuir 23 (2007) 9002–9007.
[6] Y. Ding, Ch. Li, R. Guo, Facile fabrication of pomponlike microarchitectures of lanthanum molybdate via an ultrasound route, Ultrason. Sonochem. 17 (2010) 46–54.
[7] Powder Diffraction File, JCPDS-ICDD, 12 Campus Boulevard, Newtown square, U.S.A, 2001, PA 19073–3273.
[8] K.W. Andrews, D.J. Dyson, S.R. Keown, Interpreting Electron Diffraction Patterns, Plenum Press, New York, 1971.
[9] C. Boudias, D. Monceau, CaRIne Crystallography 3.1, DIVERGENT S.A., Centre de Transfert, 60200 Compiègne, France, 1989.
[10] J. Kavinchan, T. Thongtem, S. Thongtem, Cyclic microwave assisted synthesis of Sb_2S_3 dumb-bells using polyvinylpyrrolidone as a template and splitting agent, Mater. Lett. 64 (2010) 2388–2391.
[11] Y. Keereeta, T. Thongtem, S. Thongtem, Fabrication of $ZnWO_4$ nanofibers by a high direct voltage electrospinning process, J. Alloys Compd. 509 (2011) 6689–6695.

Materials Letters 87 (2012) 153–156

Contents lists available at SciVerse ScienceDirect

Materials Letters

journal homepage: www.elsevier.com/locate/matlet

Characterization of $SrCO_3$ and $BaCO_3$ nanoparticles synthesized by cyclic microwave radiation

Narongrit Tipcompor [a], Titipun Thongtem [a,d,*], Anukorn Phuruangrat [b,**], Somchai Thongtem [c,d]

[a] Department of Chemistry, Faculty of Science, Chiang Mai University, Chiang Mai 50200, Thailand
[b] Department of Materials Science and Technology, Faculty of Science, Prince of Songkla University, Hat Yai, Songkhla 90112, Thailand
[c] Department of Physics and Materials Science, Faculty of Science, Chiang Mai University, Chiang Mai 50200, Thailand
[d] Materials Science Research Center, Faculty of Science, Chiang Mai University, Chiang Mai 50200, Thailand

ARTICLE INFO

Article history:
Received 5 July 2012
Accepted 1 August 2012
Available online 9 August 2012

Keywords:
Nanoparticles
Electron microscopy
FTIR
X-ray techniques

ABSTRACT

Uniform strontium carbonate ($SrCO_3$) and barium carbonate ($BaCO_3$) nanoparticles were successfully synthesized using alkaline earth metal nitrate ($M(NO_3)_2$ with $M^{2+}=Sr^{2+}$ and Ba^{2+}) and sodium carbonate (Na_2CO_3) in ethylene glycol by a cyclic microwave radiation. The products were characterized by X-ray powder diffraction (XRD), Fourier transform infrared (FTIR) spectroscopy, transmission electron microscopy (TEM) and selected area electron diffraction (SAED). In this research, the products were orthorhombic $SrCO_3$ and $BaCO_3$ phase with nanoparticles over the ranges of 20–50 nm for $SrCO_3$ and 40–100 nm for $BaCO_3$, including the detection of asymmetric C–O stretching, symmetric C–O stretching, out of plane bending and in plane bending vibrations at 1463, 1071, 862 and 708 cm^{-1} for $SrCO_3$, and 1439, 1059, 858 and 692 cm^{-1} for $BaCO_3$, respectively.

© 2012 Elsevier B.V. All rights reserved.

1. Introduction

Recently, strontium carbonate ($SrCO_3$) and barium carbonate ($BaCO_3$) have been found to be very important materials for ceramic industries [1–4]. $SrCO_3$ is a reagent for the production of color television glass tubes and ferrite magnets for DC motors. It is widely used in the production of iridescent glasses, pigments, driers, paints, fireworks and pyrotechnics. $BaCO_3$ has a more thermodynamically stable crystal modification among the heavy metal carbonates. It has attracted attention due to its close relationship with aragonite and applications in many ceramic and glass industries. It is also highly utilized precursors for the synthesis of magnetic ferrites and ferroelectric materials. Related biomimetic approaches for $BaCO_3$ crystallization include influence of urease, presence of polyelectrolytes and double hydrophilic block copolymers as crystal modifiers [1–7].

Microwave radiation represents a major breakthrough as a method for synthesizing both chemicals. There is a dramatic change in the way chemical synthesis is performed and the way it is perceived in science and technology. Conventional heating has been recognized as a time-consuming method. In concert with rapidly expanding applications, microwave synthesis can be effectively applied to any reactions, because of its properties for short-time consumption, improvement in yield and production of clean products. Microwave-assisted synthesis creates completely new possibilities in forming chemicals. Microwave energy can directly transmit to reactants, and accelerate reaction that is unable to be done by the conventional method. It is well known to interact with dielectric materials, liquids and solids, leading to be generally known as dielectric heating. Electric dipoles of the materials respond to an external applied electric field. Especially for liquids, the reorientation leads to the generation of heat as new process in synthesizing materials [8,9]. In 2006, Ma et al. [10] reported the synthesis of $BaCO_3$ nanorods by a microwave radiation of $Ba(NO_3)_2$ and $(NH_4)_2CO_3$ in the presence of NaOH or hexamethylenetetramine ($(CH_2)_6N_4$) in ethylene glycol. Two years later, he and his co-researchers [11] reported the synthesis of one-dimensional $SrCO_3$ nanostructures assembled from nanocrystals by a microwave-assisted aqueous solution method. They showed that the heating time played an important role in its size and morphology. Zhang et al. [12] had much success in synthesizing $BaCO_3$ crystals with higher-order superstructures by a rapid microwave-assisted route in an aqueous system containing sodium dodecyl sulfate (SDS), $BaCl_2 \cdot 2H_2O$ and $NaHCO_3$ as starting reagents. They also studied the influence of the microwave heating powers, length of time, content of SDS, initial concentration of reactants, pH values and type of surfactants on its morphology.

In this research, the novelty synthesis of uniform $SrCO_3$ and $BaCO_3$ nanoparticles by a cyclic microwave radiation (CMR) was

* Corresponding author at: Department of Chemistry, Faculty of Science, Chiang Mai University, Chiang Mai 50200, Thailand. Tel.: +66 53 943344; fax: +66 53 892277.
** Corresponding author. Tel.: +66 74 288374; fax: +66 74 288395.
E-mail addresses: ttpthongtem@yahoo.com (T. Thongtem), phuruangrat@hotmail.com (A. Phuruangrat).

0167-577X/$ - see front matter © 2012 Elsevier B.V. All rights reserved.
http://dx.doi.org/10.1016/j.matlet.2012.08.002

reported and compared with those synthesized by precipitation at room temperature (PRT) without using a heating source.

2. Experiment

To synthesize uniform $SrCO_3$ and $BaCO_3$ nanoparticles, each 0.005 mol of $M(NO_3)_2$ ($M^{2+}=Sr^{2+}$ and Ba^{2+}) and Na_2CO_3 as starting materials was mixed in 50 ml ethylene glycol (EG) with 30 min stirring at room temperature. The solutions were transferred into 125 ml flasks, each of which was put in a domestic microwave oven (2.45 GHz) at a time. They were heated by a CMR at 20% of 180 W for 20 min. Each cycle, the microwave oven was on for 24 s every 96 s interval. At the conclusion, white precipitates were synthesized. Concurrently, the same solutions as the above were stirred for 24 h at room temperature without the use of the microwave radiation until white precipitates were achieved. All the products were washed with distilled water and absolute ethanol, dried in air at 80 °C for 24 h, and collected for further characterization by X-ray powder diffraction (XRD), transmission electron microscopy (TEM), selected area electron diffraction (SAED) and Fourier transform infrared (FTIR) spectroscopy.

3. Results and discussion

For solution method at room temperature, $SrCO_3$ and $BaCO_3$ precipitated by direct reaction of the alkaline earth metal nitrate salts ($Sr(NO_3)_2$ and $Ba(NO_3)_2$) and Na_2CO_3. Sr^{2+} and Ba^{2+} cations, the electron pair acceptors (Lewis acid), reacted with CO_3^{2-} anions, the electron pair donors (Lewis base). Reaction between these two species led to covalent bonding between them, by donation of electron-pairs of the highest occupied molecular orbitals (HOMO) in valence bands of Lewis base to the lowest unoccupied molecular orbitals (LUMO) conduction bands of Lewis acid to form Lewis addition compounds, or more commonly Lewis adducts. When $M(NO_3)_2$ and Na_2CO_3 were dissolved in EG, stirred at room temperature for 24 h, $SrCO_3$ and $BaCO_3$ white precipitates were synthesized. Additionally, the solutions were stirred for 30 min instead of 24 h, and heated by 180 W cyclic microwave radiation for 20 min. The mixtures of the alkaline earth metal nitrate salts and sodium carbonate were combined to form $SrCO_3$ and $BaCO_3$ white precipitated nanoparticles. This research revealed that the microwave radiation as an external energy was able to accelerate the kinetics (rates) and thermodynamics for the formation of $SrCO_3$ and $BaCO_3$ nanoparticles.

Fig. 1 shows XRD patterns of $SrCO_3$ and $BaCO_3$ nanoparticles synthesized by PRT and CMR. All diffraction peaks were specified as orthorhombic $SrCO_3$ and $BaCO_3$, comparing to the JCPDS nos. 05-0418 ($a=5.1070$ Å, $b=8.4140$ Å and $c=6.0290$ Å and $\alpha=\beta=\gamma=90^\circ$) for $SrCO_3$ and 05-0378 ($a=5.3140$ Å, $b=8.9040$ Å and $c=6.4300$ Å and $\alpha=\beta=\gamma=90^\circ$) for $BaCO_3$ [13]. Diffraction intensities of the products formed by CMR were higher than those formed by PRT, which reflected the better crystalline degree formed by CMR. All diffraction peaks of $BaCO_3$ were at lower Bragg angles than the same diffraction peaks of $SrCO_3$ due to the difference of ionic radii of the alkaline earth metals ($Sr^{2+}=0.125$ nm and $Ba^{2+}=0.142$ nm) [14].

Particle sizes of the products synthesized by CMR were calculated by Scherrer formula [14,15]

$$L=\frac{k\lambda}{B\cos\theta} \quad (1)$$

where λ is the wavelength of Cu Kα radiation (0.15418 nm [1]), θ the Bragg angles of the (111) peaks of the XRD patterns, L the average crystallite sizes of $SrCO_3$ and $BaCO_3$, k the constant (0.89), and B the full widths at half maximum of the (111) peaks. They were 10.94 nm for $SrCO_3$ and 15.29 nm for $BaCO_3$. The particle size of the first was smaller than that of the second, in accordance with the lesser ionic radius and atomic mass of the first as compared to the greater ionic radius and atomic mass of the second.

The real particle sizes (Fig. 2) of $SrCO_3$ and $BaCO_3$ were characterized by TEM. The products formed by CMR were composed of dispersed round nanoparticles with the sizes of 20–50 nm for $SrCO_3$ and 40–100 nm for $BaCO_3$. The dispersion was influenced by the microwave vibration during processing. Comparing $SrCO_3$ and $BaCO_3$ formed by PRT, the products clustered together as irregular nanoparticles with larger particle-sizes. The SAED patterns (insets of Fig. 2a and b) of the products synthesized by CMR appear as diffuse and hollow concentric rings of bright spots, belonging to the polynanocrystals. They corresponded with the (111), (002), (112), (221), (132) and (113) planes of both $SrCO_3$ and $BaCO_3$ JCPDS database [13].

FTIR spectra (Fig. 3) of $SrCO_3$ and $BaCO_3$ were recorded over the 400–4000 cm^{-1} wavenumbers. Considering the free planar CO_3^{2-} complex ions, they have D_{3h} symmetry. The absorption bands were caused by the vibrations in CO_3^{2-} at 400–1800 cm^{-1}, due to the asymmetric C–O stretching, symmetric C–O stretching, out of plane bending and in plane bending vibrations at 1463, 1071, 862 and 708 cm^{-1} for $SrCO_3$, and 1439, 1059, 858 and 692 cm^{-1} for $BaCO_3$, respectively [2,16,17]. The O–H stretching and bending vibrations of residual water contained in $SrCO_3$ were detected at 3448 and 1637 cm^{-1}, and in $BaCO_3$ at 3457 and

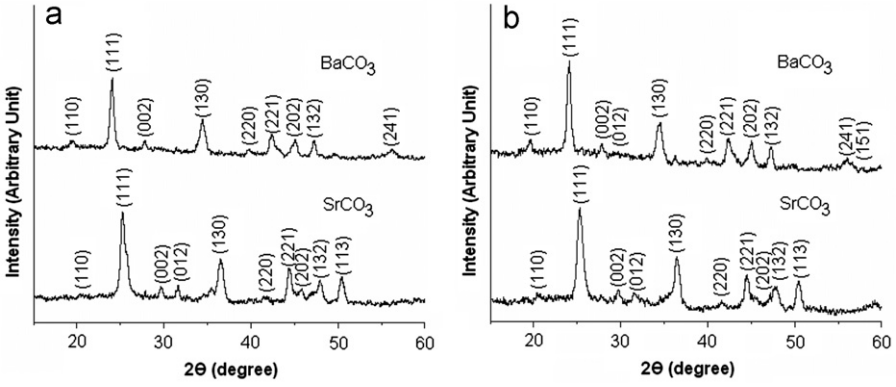


Fig. 1. XRD patterns of $SrCO_3$ and $BaCO_3$ precipitated in the solutions by (a) PRT and (b) CMR.

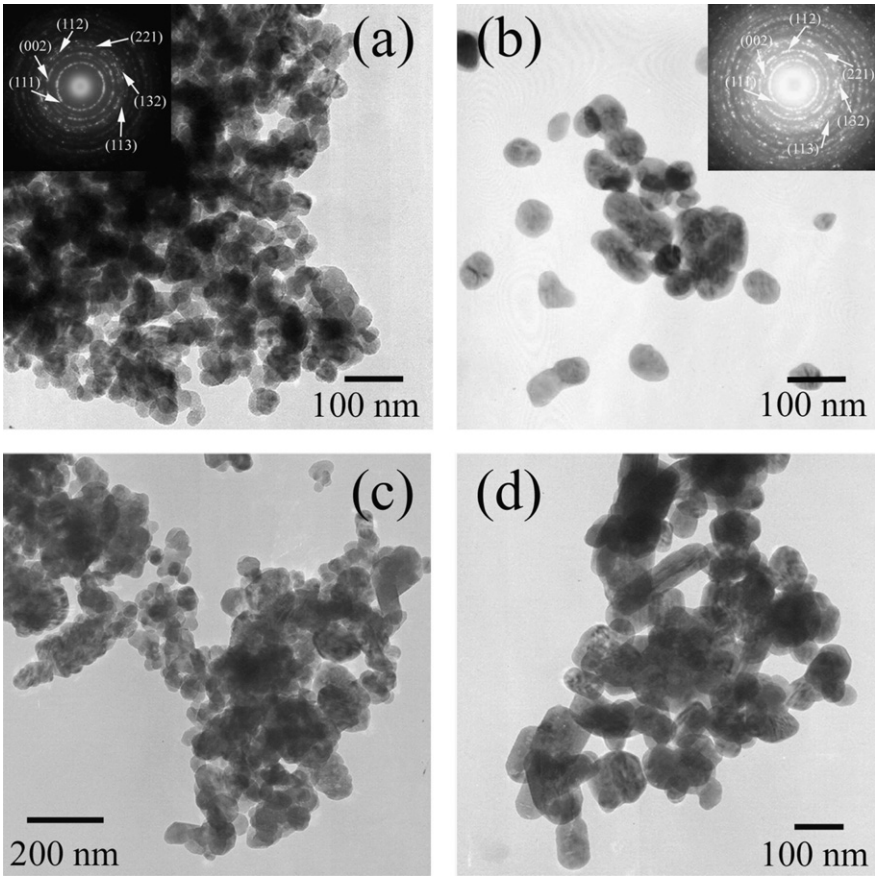


Fig. 2. TEM images and SAED patterns of (a) $SrCO_3$ and (b) $BaCO_3$ synthesized by CMR, and (c) $SrCO_3$ and (d) $BaCO_3$ synthesized by PRT.

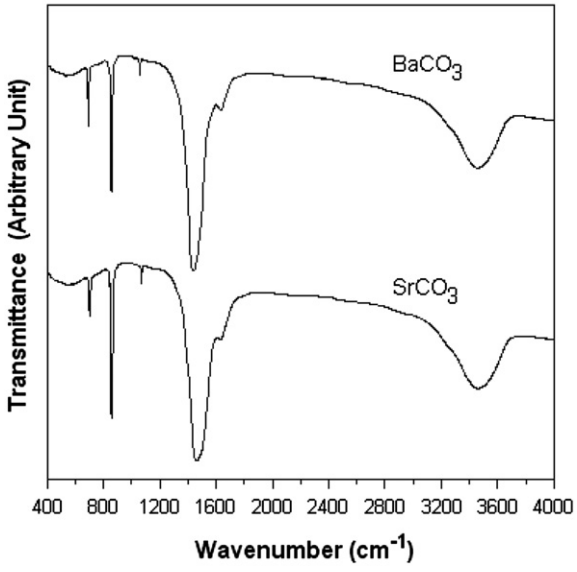


Fig. 3. FTIR spectra of $SrCO_3$ and $BaCO_3$ synthesized by CMR.

1642 cm^{-1}, respectively. It should be noted that the vibrations were shifted from the higher wavenumbers for $SrCO_3$ to the lower ones for $BaCO_3$, due to the difference of bonding of the CO_3^{2-} complex ions influenced by the change of efficient masses of the vibrating groups. There was no detection of the EG peaks in these FTIR spectra, indicating that the EG solvent was not included in these products.

4. Conclusions

Uniform $SrCO_3$ and $BaCO_3$ nanocrystals were successfully synthesized by a cyclic microwave radiation. The alkaline earth metal carbonates with orthorhombic structures were composed of round nanoparticles, and provided the evidence of the asymmetric C–O stretching, symmetric C–O stretching, out of plane bending and in plane bending vibrations of CO_3^{2-} complex ions.

Acknowledgments

We wish to thank the Thailand Research Fund (TRF) for providing financial support through the Royal Golden Jubilee Ph.D. Program and the TRF Research Grant BRG5380020, and the Thailand's Office of the Higher Education Commission through the National Research University (NRU) Project for Chiang Mai University (CMU), including the Graduate School of CMU through the general support.

References

[1] Shi L, Du F. Mater Lett 2007;61:3262–4.
[2] Shi L, Du F. Mater Res Bull 2007;42:1550–5.
[3] Ma MG, Zhu YJ, Zhu JF, Xu ZL. Mater Lett 2007;61:5133–6.
[4] Ma MG, Zhu YJ, Cheng GF, Huang YH. Mater Lett 2008;62:3110–3.
[5] Du J, Liu Z, Li Z, Han B, Huang Y, Zhang J. Micropor Mesopor Mater 2005;83:145–9.
[6] Alavi MA, Morsali A. Ultrason Sonochem 2008;15:833–8.
[7] Li L, Chu Y, Liu Y, Dong L, Huo L, Yang F. Mater Lett 2006;60:2138–42.
[8] Palchik O, Zhu J, Gedanken A. J Mater Chem 2000;10:1251–4.
[9] Hayes BL. Microwave Synthesis, Chemistry at the Speed of Light. PO Box 200, Matthews, NC 28105, USA: CEM Publishing; 2002.
[10] Ma MG, Zhu YJ, Zhu JF, Cheng GF. Chem Lett 2006;35:1138–9.

[11] Ma MG, Zhu YJ. Mater Lett 2008;62:2512–5.
[12] Zhang H, Hong J, Ni Y, Zhou Y. CrystEngComm 2008;10:1031–6.
[13] Powder Diffract. File, JCPDS-ICDD, 12 Campus Boulevard, Newtown Square, PA 19073-3273, USA; 2001.
[14] Phuruangrat A, Thongtem T, Thongtem S. J Ceram Soc Jpn 2008;116:605–9.
[15] Suwanboon S, Tanattha R, Tanakorn R. Songklanakarin. J Sci Technol 2008;30:65–9.
[16] Thongtem T, Tipcompor N, Phuruangrat A, Thongtem S. Mater Lett 2010;64:510–2.
[17] Wu S, Cao H, Yin S, Zhang X, Chernow V. Inorg Chem 2009;48:10326–9.

Materials Letters 80 (2012) 114–116

Contents lists available at SciVerse ScienceDirect

Materials Letters

journal homepage: www.elsevier.com/locate/matlet

Characterization and photonic absorption of hierarchical tree-like CdS nanostructure synthesized by solvothermal method

Anukorn Phuruangrat [a,*], Titipun Thongtem [b], Somchai Thongtem [c,**]

[a] Department of Materials Science and Technology, Faculty of Science, Prince of Songkla University, Hat Yai, Songkhla 90112, Thailand
[b] Department of Chemistry, Faculty of Science, Chiang Mai University, Chiang Mai 50200, Thailand
[c] Department of Physics and Materials Science, Faculty of Science, Chiang Mai University, Chiang Mai 50200, Thailand

ARTICLE INFO

Article history:
Received 2 March 2012
Accepted 19 April 2012
Available online 26 April 2012

Keywords:
Electron microscopy
Spectroscopy
X-ray techniques

ABSTRACT

Hierarchical tree-like wurtzite CdS nanostructure was successfully synthesized by the 200 °C and 24 h solvothermal reaction of cadmium nitrate and thiourea as starting materials in 1:1 volume ratio of diethylenetriamine and ethylenediamine as a mixed solvent. Phase and morphology of the as-synthesized CdS product were characterized by X-ray diffraction (XRD), Raman spectroscopy and transmission electron microscopy (TEM), including its photonic absorption by UV–visible spectroscopy. XRD spectrum and TEM image showed hexagonal wurtzite CdS structure with a 1–2 μm prototypical cluster, composed of a number of limbed nanorods. Its Raman spectrum was specified as the first-order (1LO) and second-order (2LO) longitudinal optical phonon modes at 298 and 599 cm^{-1}. UV–visible spectrum shows an absorption peak centered at around 489 nm, assigned as the excitonic transition, blue shifted comparing to its bulk.

© 2012 Elsevier B.V. All rights reserved.

1. Introduction

Among the II–VI semiconducting materials, cadmium sulfide (CdS) with 2.42 eV direct band gap at room temperature has received much attention for a number of researchers, due to its excellent properties for luminescence and photochemistry. It has a wide variety of applications, such as light-emitting diodes, solar cells and optoelectronic devices [1,2]. Over the past decade, different morphologies were produced, including nanorods [1], microflowers [2], nanostructured mutipods [3], nanowires [4,5], nanotubes [6] and nanoribbons [7,8]. They were successfully synthesized by both physical and chemical processes: solvothermal/hydrothermal [1–4], dc electrochemical deposition [5], chemical vapor deposition (CVD) [6,7] and microwave radiation [8]. Among them, the solvothermal route, reaction of precursors in a closed system in the presence of an organic solvent at a temperature higher than the boiling temperature of the solvent, is one of the most effective synthetic methods for synthesizing nanostructured CdS [1] controlled by a variety of parameters. In this work, a hierarchical tree-like CdS nanostructure was synthesized by a facile solvothermal method and its optical property was also studied.

2. Experiment

To synthesize hierarchical tree-like wurtzite CdS nanostructure, each 0.005 mol of cadmium nitrate ($Cd(NO_3)_2$) and thiourea (NH_2CSNH_2) was dissolved in 50 ml of 1:1 volume ratio of diethylenetriamine and ethylenediamine mixture under 30 min stirring at room temperature. Subsequently, the solution was solvothermally processed at 200 °C for 24 h, and left cool down to room temperature. At the conclusion, orange precipitate was synthesized, separated by filtration, washed with de-ionized water and absolute ethanol, and dried at 70 °C for 12 h, for further characterization by X-ray diffraction (XRD), Raman spectrometry, transmission electron microscopy (TEM) with equipped energy dispersive X-ray (EDX) spectroscopy and UV–visible spectroscopy.

3. Results and discussion

XRD spectrum (Fig. 1) of the as-synthesized CdS product was indexed using Bragg's law for diffraction, and specified as wurtzite hexagonal CdS structure with P63mc space group, comparing to the JCPDS database no. 41-1049 [9]. No other characteristic peaks of impurities were detected, showing that the product was pure phase. The spectrum shows sharp and narrow diffraction peaks with different intensities, indicating that the as-synthesized CdS product was good crystalline. The (002) diffraction peak was higher than the others, implying that the product has a preferred ordering orientation growth along the *c*-axis. Calculated lattice parameters for wurtzite hexagonal CdS structure using Bragg's law for diffraction and plane-

* Corresponding author. Tel.: +66 74 288 374; fax: +66 74 288 395.
** Corresponding author. Tel.: +66 53 941 924; fax: +66 53 943 445.
E-mail addresses: phuruangrat@hotmail.com (A. Phuruangrat), schthongtem@yahoo.com (S. Thongtem).

0167-577X/$ – see front matter © 2012 Elsevier B.V. All rights reserved.
doi:10.1016/j.matlet.2012.04.089

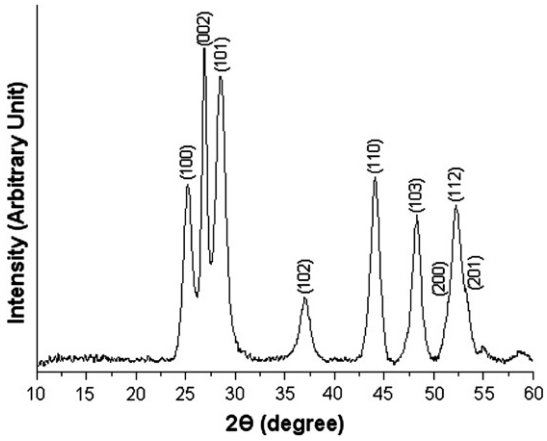


Fig. 1. XRD spectrum of the as-synthesized CdS product.

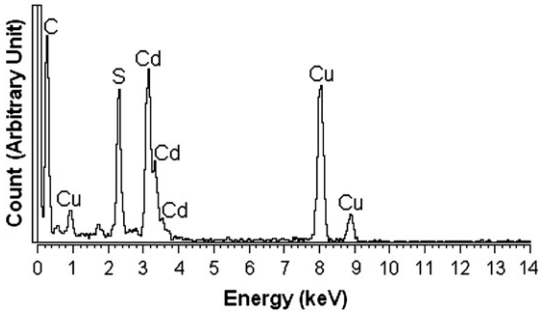


Fig. 3. EDX spectrum of a hierarchical tree-like CdS nanostructure.

spacing equation [10] were a = b = 0.413 nm and c = 0.669 nm, in accordance with those of the JCPDS database.

The *c*-orientation degree of the as-synthesized CdS product was explained by a relative texture coefficient (TC) [3] of the (002) peak calculated using the formula,

$$TC002 = \frac{(I002/I^o002)}{[I002/I^o002 + I100/I^o100]}, \quad (1)$$

where TC_{002} is the relative texture coefficient of the (002) over (100) diffraction peaks. I_{002} and I_{100} are the diffraction intensities of the (002) and (100) experimental peaks, including I^o_{002} and I^o_{100} the corresponding intensities of the randomly oriented CdS powder of the JCPDS database, respectively. Texture coefficient of random crystallographic orientation wurtzite CdS structure is 0.5. In the present research, the calculated TC_{002} is 0.55, which supports the preferential orientation of the as-synthesized CdS product grew along the [001] direction.

Fig. 2 shows TEM images of the as-synthesized CdS product of a hierarchical tree-like CdS nanostructure with 1–2 μm prototypical cluster, composing of a number of limbed nanorods. At high magnification, the branches were composed of small nanorods with 20–30 nm in diameter and 100–200 nm in length, growing out of hierarchical tree-like CdS nanostructured trunks. HRTEM image (inset of Fig. 2c) revealed that the hierarchical tree-like CdS nanostructured nanorods grew out along the [001] direction. Qualitative and quantitative analyses of the as-synthesized CdS product were characterized by EDX. It presents three L_α, $L_{\beta1}$ and $L_{\beta2}$ lines of Cd at 3.13, 3.32 and 3.53 keV, and a $K_{\alpha1,2}$ line of S at 2.31 keV (Fig. 3). The molar ratio of Cd:S was 0.98:1 in good accordance with the stoichiometric CdS phase. The $K_{\alpha1,2}$ and K_β lines of Cu at 8.04 and 8.91 keV as well as C-$K_{\alpha1,2}$ line at 0.28 keV of Cu grid with C film coated on top were also detected [11].

Hexagonal wurtzite structured CdS belongs to a C^4_{6V} space group. According to factor group analysis, its Raman active modes are $1A_1 + 1E_1 + 2E_2$ (E_2^H and E_2^L). Only the $2B_2$ modes are silent. Phonon polarization of the A_1 branch is in the *z* direction, and those of the doubly degenerate E_1 and E_2 are in the *xy* plane. The wurtzite structure is noncentrosymmetric, thus both A_1 and E_1 modes split into longitudinal optical (LO) and transverse optical (TO) components [12]. Raman spectroscopy of hierarchical tree-like CdS nanostructure was at 298 and 599 cm^{-1} wavenumbers, assigned as the first (1LO) and second (2LO) longitudinal optical phonon modes [4,12], comparing to the characteristic Raman spectrum of bulk CdS at 297.5 and 599 cm^{-1} corresponding to the 1LO and 2LO reported by Singh et al. [13]. The 1LO Raman wavenumber of the hierarchical tree-like CdS nanostructure was blue shifted due to the phonon confinement in the transverse direction and the transition of elementary excitons in the longitudinal direction and strain effect [13].

Energy level and band gap of CdS were calculated and reported by Ge et al.[2]. For this material, S3p character is the highest occupied molecular orbital level, and Cd3d + S3p hybrid is the lowest unoccupied molecular orbital level. Upon photoexcitation, charged particles transferred from the S3p orbital to the empty Cd3d + S3p hybrid, including the formation of photogenerated electron–hole pairs. The optical absorbance spectrum of hierarchical tree-like CdS nanostructure (Fig. 4) showed strong absorption edge at 489 nm. Obviously, blue shift to a shorter wavelength was detected, comparing to its CdS bulk (515 nm) – caused by the quantum confinement effect [14,15]. Fig. 4 shows UV–visible absorption of hierarchical tree-like wurtzite CdS nanostructure. Its band gap was determined at zero absorbance to be 3.93 eV [16]. In the present research, band gap and maximum absorption of hierarchical tree-like CdS nanostructure are blue shifted comparing to bulk CdS (2.42 eV) [8].

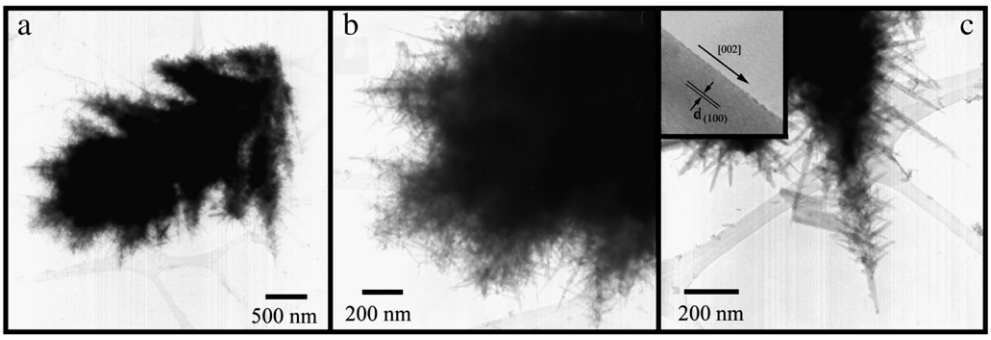


Fig. 2. TEM images at different magnifications of hierarchical tree-like wurtzite CdS nanostructure.

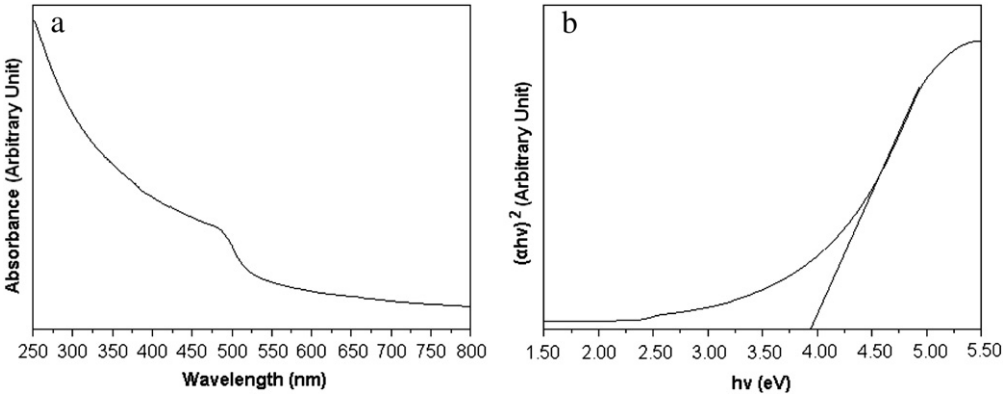


Fig. 4. (a) UV–visible spectrum and (b) $(\alpha h\nu)^2$ vs hν curve of the hierarchical tree-like wurtzite CdS nanostructure.

4. Conclusions

Hexagonal wurtzite CdS nanostructure was successfully synthesized by the 200 °C and 24 h solvothermal method. XRD and TEM analyses revealed that the product was hierarchical tree-like CdS nanostructure with a 1–2 μm prototypical cluster, composed of a number of limbed nanorods. UV–visible absorption spectrum was blue shift at 489 nm, assigned as the exitonic absorption comparing to its bulk.

Acknowledgements

We wish to thank Prince of Songkla University for providing financial support through the contract number SCI540660S, the National Nanotechnology Center (NANOTEC), National Science and Technology Development Agency through the project P-10-11345, and the Thailand Research Fund (TRF) through the TRF Research Grant.

References

[1] Dalvand P, Mohammadi MR, Fray DJ. Mater Lett 2011;65:1291–4.
[2] Ge M, Cui Y, Liu L, Zhou Zh. Appl Surf Sci 2011;257:6595–600.
[3] Phuruangrat A, Thongtem T, Thongtem S. Chalcogenide Lett 2010;7:605–8.
[4] Phuruangrat A, Thongtem T, Thongtem S. Curr Appl Phys 2009;9:S201–4.
[5] Mondal SP, Dhar A, Ray SK. Mater Sci Semicond Process 2007;10:185–93.
[6] Shen XP, Yuan AH, Wang F, Hong JM, Xu Zh. Solid State Commun 2005;133:19–22.
[7] Wang Y, Wang GZ, Yau MY, To CY, Ng DHL. Chem Phys Lett 2005;407:510–5.
[8] Zhu JJ, Wang H, Zhu JM, Wang J. Mater Sci Eng B 2002;94:136–40.
[9] Powder Diffract. File. 12 Campus Boulevard, Newtown Square, PA 19073-3273, USA: JCPDS-ICDD; 2001.
[10] Suryanarayana C, Norton MG. X-ray Diffract., A Pract. Appro. New York: Plenum Press; 1998.
[11] Oxford Instruments Analytical, Halifax Rd, High Wycombe Bucks HP12 3SE, UK.
[12] Phuruangrat A, Thongtem T, Thongtem S. Mater Lett 2009;63:1538–41.
[13] Singh V, Chauhan Pr. Chalcogenide Lett 2009;6:421–6.
[14] Yang XH, Wu QSh, Li L, Ding YP, Zhang GX. Colloids Surf A 2005;264:172–8.
[15] Maleki M, Mirdamadi Sh, Ghasemzadeh R, Ghamsari MS. Mater Lett 2008;62:1993–5.
[16] Suwanboon S, Chukamnerd S, Anglong U. Songklanakarin J Sci Technol 2007;29:1563–70.

Available online at www.sciencedirect.com

SciVerse ScienceDirect

Ceramics International 38 (2012) 4075–4079

CERAMICS INTERNATIONAL

www.elsevier.com/locate/ceramint

Template-free synthesis of neodymium hydroxide nanorods by microwave-assisted hydrothermal process, and of neodymium oxide nanorods by thermal decomposition

Anukorn Phuruangrat [a,*], Somchai Thongtem [b], Titipun Thongtem [c,**]

[a] Department of Materials Science and Technology, Faculty of Science, Prince of Songkla University, Hat Yai, Songkhla 90112, Thailand
[b] Department of Physics and Materials Science, Faculty of Science, Chiang Mai University, Chiang Mai 50200, Thailand
[c] Department of Chemistry, Faculty of Science, Chiang Mai University, Chiang Mai 50200, Thailand

Received 8 May 2011; received in revised form 21 January 2012; accepted 24 January 2012
Available online 1 February 2012

Abstract

Based on the 150 °C and 1 h microwave-assisted hydrothermal reaction of $Nd(NO_3)_3$ dissolved in deionized water with pH 10 adjusted by concentrated NH_4OH solution, the phase and morphology of the product, characterized by XRD, SEM and TEM analyses, were specified as hexagonal $Nd(OH)_3$ nanorods 50 nm in diameter and 700 nm long, growing along the [0 0 1] direction. TGA analysis showed the evaporation of adsorbed water and dehydration of $Nd(OH)_3$ to synthesize the final pure Nd_2O_3 product. With 500 °C and 2 h calcination of the $Nd(OH)_3$ self-template precursor, Nd_2O_3 nanorods were synthesized, retaining both the morphology and growth direction of the precursor.
© 2012 Elsevier Ltd and Techna Group S.r.l. All rights reserved.

Keywords: A. Microwave processing; A. Calcination; B. Electron microscopy; B. X-ray methods; Nanorods

1. Introduction

Since the discovery of carbon nanotubes (CNTs), a new structured carbon, in 1991 [1], one-dimensional (1D) nanostructures such as nanorods, nanowires, nanobelts and nanotubes have been promising materials for various electronic, optoelectronic, magnetic and photonic devices due to their unique physical and chemical properties – quite different from those of the corresponding bulk materials [2–4]. Rare earth oxides have been used in a number of scientific areas, such as ceramic industries, and as catalysts for dehydrogenation, hydrogenation and esterification reactions, arising from their 4f electrons [2,5–9]. Among these, neodymium oxide (Nd_2O_3) has been widely used in luminescent materials for photonic applications, as a catalyst for the synthesis of ammonia and the oxidative coupling of methane, and as a protective coating [7,10]. Therefore, the preparation and characterization of Nd_2O_3 nanorods have attracted much interest in recent years. There are many reports on the synthesis of rare earth oxides with different morphologies, i.e. the synthesis of: uniform nanorods, nanowires and nanoplates of rare earth oxides (M_2O_3, M = Pr, Nd, Sm, Eu, Gd, Tb and Dy) by microwave irradiation [5]; Nd_2O_3 nanowires through a sol–gel process assisted by a porous anodic aluminum oxide (AAO) template [6]; rare earth oxide nanoparticles of Sm and Nd by hydrogen plasma-metal reaction [7]; $Ln(OH)_3$ (Ln = La, Pr, Nd, Sm, Eu and Gd) by a simple wet chemical method [8]; Nd_2O_3 nanopowders by sol–gel auto-combustion [9]; Nd_2O_3 nanoparticles by a tartrate route [10]; and Nd_2O_3 nanoparticles [11] and rod-like Eu:Gd_2O_3 phosphor [12] via a hydrothermal route.

In the present research, we report the template-free synthesis of $Nd(OH)_3$ nanorods by the 150 °C and 1 h microwave-assisted hydrothermal (MH) reaction of $Nd(NO_3)_3$ solution with pH 10 adjusted by concentrated NH_4OH solution – a novel, facile, fast and environmentally benign low-temperature process. Subsequently, the $Nd(OH)_3$ nanorod self-template precursor was further calcined at 450 and 500 °C for 2 h to form Nd_2O_3 nanorods. This success may lead to large-scale synthesis applicable for a number of industries.

* Corresponding author. Tel.: +66 (0)74 288 374; fax: +66 (0)74 288 395.
** Corresponding author. Tel.: +66 (0)53 943 344; fax: +66 (0)53 892 277.
E-mail addresses: phuruangrat@hotmail.com (A. Phuruangrat), ttpthongtem@yahoo.com (T. Thongtem).

0272-8842/$36.00 © 2012 Elsevier Ltd and Techna Group S.r.l. All rights reserved.
doi:10.1016/j.ceramint.2012.01.065

2. Experimental procedure

Neodymium (III) nitrate ($Nd(NO_3)_3$) and ammonium hydroxide (NH_4OH) were purchased from Sigma–Aldrich Co., and used without further purification. In a typical synthesis, 50 ml of aqueous 0.01 M $Nd(NO_3)_3$ was adjusted the pH to 10 by concentrated NH_4OH solution. It was transferred into a 100 ml Teflon-lined stainless-steel autoclave, which was filled with deionized water up to 80% total capacity. The system was heated by 0–100% 300 W microwave from room temperature to 150 °C for 20 min, held at this temperature for 1 h, and left cool down to room temperature. The resulting product was filtered, washed with distilled water and absolute ethanol, and dried at 80 °C for 12 h. Then the filtered product, the self-template precursor, was further calcined at the rate of 5 °C min^{-1} to 450, 500 and 550 °C and held at each of these temperatures for 2 h in ambient atmosphere to synthesize the final powders.

The weight loss (less), purified phase, structure and morphology of the as-synthesized products were characterized by a Shimadzu Scientific Instruments TGA-50 Thermogravimetric (TGA) analyzer under a stream of nitrogen at a heating rate of 10 °C min^{-1}, a Bruker AXS D8 Advance Powder X-ray diffractometer (XRD) with K_α line from a copper target, a JEOL JSM-6335F field emission scanning electron microscope (FE-SEM) operating at 15 kV accelerating voltage with Au sputtering on the samples, and a JEOL JEM-2100F transmission electron microscope (TEM) and high resolution transmission electron microscope (HRTEM) including selective area electron diffractometer (SAED) operating at the accelerating voltage of 200 kV.

3. Results and discussion

Fig. 1 shows the thermogravimetric analysis (TGA) curve of the $Nd(OH)_3$ precursor. It shows continuous weight loss over a range of 50–650 °C, with a total weight loss of 15.44%. Theoretically, $Nd(OH)_3$ decomposes to form Nd_2O_3 and H_2O:

$$2Nd(OH)_3 \rightarrow Nd_2O_3 + 3H_2O \quad (1)$$

Under the molar conservation of the (1) reaction, the calculated weight loss is 13.84%, lower than that from TGA analysis. The precursor might absorb some moisture (water vapor) from the ambient atmosphere, which would evaporate during TGA analysis. The weight loss of the $Nd(OH)_3$ precursor was classified into three steps. First, weight loss in the temperature range of 50–270 °C was specified as the decomposition of adsorbed residual water on the surface of $Nd(OH)_3$. Second, weight loss at the temperature range 270–430 °C was due to the dehydration of $Nd(OH)_3$ to form NdOOH. Third, weight loss at 430–650 °C corresponded to the well-defined NdOOH dehydration into a hexagonal Nd_2O_3 structure [12–14]. In the present research, the TGA weight loss (Table 1) was very close to the theoretical value calculated from the molar conservation of products and reactants of the (2) and (3) chemical reactions [12]. The dehydration of $Nd(OH)_3$ to form Nd_2O_3 can be written as follows:

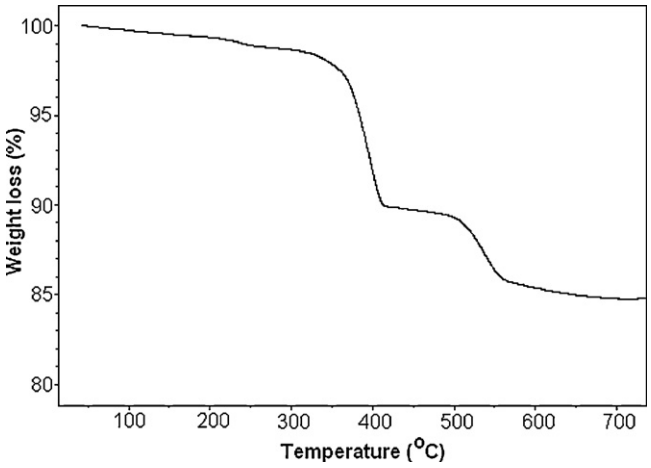


Fig. 1. TGA curve of $Nd(OH)_3$ precursor synthesized by the 150 °C and 1 h MH process.

$$2Nd(OH)_3 \rightarrow 2NdOOH + 2H_2O \quad \text{at} 270-430\,^\circ C \quad (2)$$

$$2NdOOH \rightarrow Nd_2O_3 + H_2O \quad \text{at} 430-650\,^\circ C \quad (3)$$

The different phases of the products were analyzed by X-ray diffraction, as shown in Fig. 2. All diffraction peaks of the as-synthesized precursor were indexed as pure phase of hexagonal $Nd(OH)_3$, JCPDS No. 70-0214 [14]. Its diffraction peaks were at 2θ of 16.06, 27.90, 28.94, 32.34, 37.13, 40.59, 48.65, 49.26, 50.01, 57.11, 65.55, 71.73 and 79.42°, which were assigned as the (1 0 0), (1 1 0), (1 0 1), (2 0 0), (1 1 1), (2 0 1), (0 0 2), (3 0 0), (2 1 1), (1 1 2), (1 3 1), (3 0 2) and (2 3 1) planes, respectively. Upon calcination at 450, 500 and 550 °C for 2 h, the peaks were at 2θ of 26.88, 29.82, 30.80, 40.52, 47.44, 53.54, 57.00, 57.67, 61.89, 64.14, 68.76, 74.29 and 77.83°, specified as the (1 0 0), (0 0 2), (0 1 1), (0 1 2), (1 1 0), (1 0 3), (1 1 2), (2 0 1), (0 0 4), (2 0 2), (0 1 4), (0 2 3) and (1 2 1) planes of pure hexagonal Nd_2O_3 phase, in accordance with JCPDS No. 75-2255 [14]. Atomic diffusion became more violent with an increase in calcination temperature.

In microwave-assisted hydrothermal (MH) synthesis, the final morphology of the product was controlled by surface chemistry, resulting in either oriented or random attachment of particles. During the MH process, Nd^{3+} ions reacted with

Table 1
Weight loss of $Nd(OH)_3$ precursor characterized by TGA at 50–650 °C.

Temperature range (°C)	Reaction	TGA weight loss (%)	Theoretical weight loss (%)
50–270	Dehydration of water on $Nd(OH)_3$ surface	1.23	–
270–430	$2Nd(OH)_3 \rightarrow 2NdOOH + 2H_2O$	8.91	9.23
430–650	$2NdOOH \rightarrow Nd_2O_3 + H_2O$	5.30	4.61

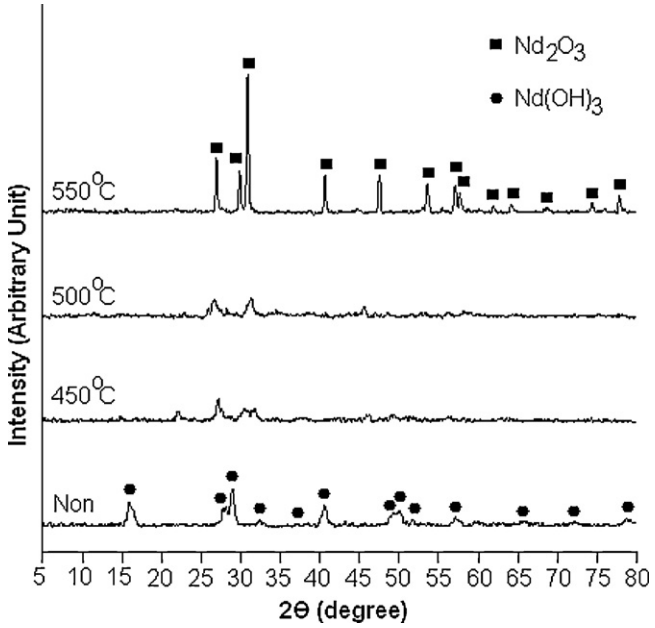


Fig. 2. XRD patterns of $Nd(OH)_3$ precursor, and Nd_2O_3 synthesized by the 450, 500 and 550 °C calcination of its precursor for 2 h.

hydroxyl ions of NH_4OH to form $Nd(OH)_3$ nanorods:

$$Nd^{3+} + 3OH^- \rightarrow Nd(OH)_3 \quad (4)$$

In general, the morphology of the product was determined by the rates of nucleation and crystal growth, which were controlled by the inherent crystal structure and chemical potential of the precursor solution [15,16]. When the rate of nucleation was greater than that of crystal growth, the crystal size as well as its aspect ratio would be small. In contrast, fast crystal growth would lead to a large crystal with a high aspect ratio along the preferential direction [15]. At a high concentration of hydroxyl ions, the reaction of Nd^{3+} and OH^- to form $Nd(OH)_3$ was very fast, and the aggregation of particles led to the formation of nanorods. The concentrations of Nd^{3+} and OH^- were high enough to form $Nd(OH)_3$ in the shape of nanorods. Further calcination of $Nd(OH)_3$ nanorods in a furnace at 450–550 °C led to the dehydration process, with the formation of Nd_2O_3 by the following reaction:

$$2Nd(OH)_3 \rightarrow Nd_2O_3 + 3H_2O \quad (5)$$

Under the optimum conversion condition (500 °C and 2 h), the final geometry of Nd_2O_3 nanorods was predetermined by the shape and size of the $Nd(OH)_3$ nanorods, functioning as self-template precursors.

Morphologies of the products were characterized by SEM, as shown in Fig. 3. Fig. 3a shows $Nd(OH)_3$ nanorods 700 nm long and 50 nm in diameter. The growth of $Nd(OH)_3$ nanorods was reliable in the reaction system without any catalyst, template or surfactant. The anisotropic growth of $Nd(OH)_3$ was mainly controlled by the inherent crystal structure and chemical potential of the solution [16]. For the crystal structure of $Nd(OH)_3$, all of the positive Nd^{3+} cations reside on the (0 0 1) face, with most of their dangling bonds coordinated with OH^- anions, alternately stacking along the [0 0 1] direction. Compared with the (1 1 0) and (1 0 0) planes, they have fewer ions with weaker polarity than the (0 0 1) plane. This characteristic structure promotes the highest density of Nd^{3+} and OH^- ions along the [0 0 1] direction,

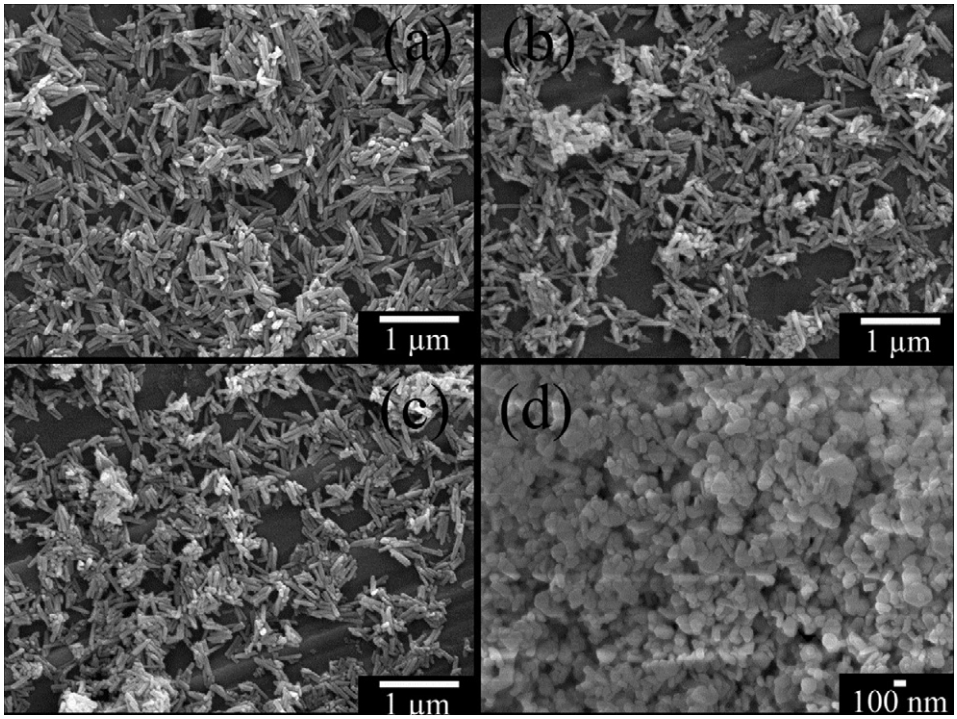


Fig. 3. SEM images of (a) $Nd(OH)_3$ nanorods synthesized by the 150 °C and 1 h MH process and (b–d) Nd_2O_3 synthesized by the 450, 500 and 550 °C calcination of $Nd(OH)_3$ precursor for 2 h, respectively.

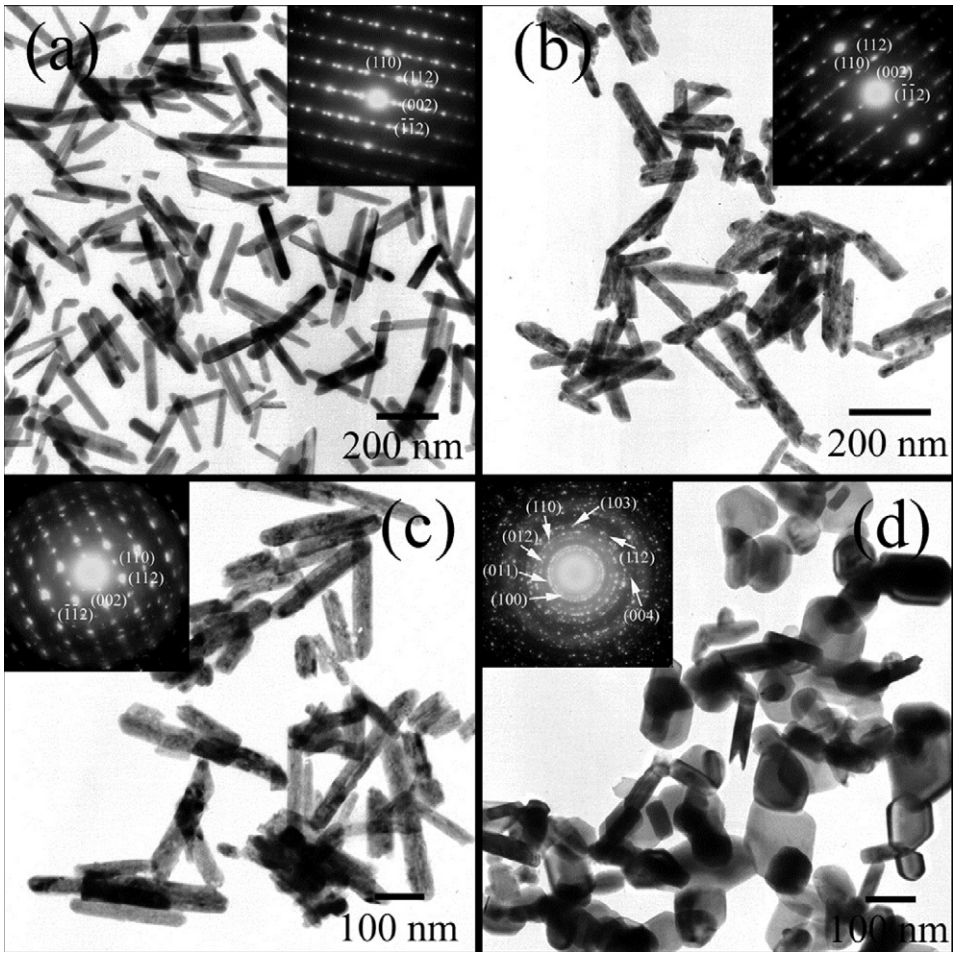


Fig. 4. TEM images and SAED patterns of (a) $Nd(OH)_3$ nanorods synthesized by the 150 °C and 1 h MH process and (b–d) Nd_2O_3 synthesized by the 450, 500 and 550 °C calcination of $Nd(OH)_3$ precursor for 2 h, respectively.

which leads the (0 0 1) face to have the highest chemical potential and the most activity in relation to the surrounding growth conditions. Thus, the final crystal morphology is cooperative with the internal crystal structure and external reaction conditions [8]. It should be noted that calcination temperature was an important factor in determining the average particle size of the product. The particle size of Nd_2O_3 was increased with increasing calcination temperature. The degree of crystallinity was also increased. SEM analysis shows nanorod shapes with an estimated size of ∼70 nm in diameter and ∼500 nm in length from calcination at 450 and 500 °C for 2 h. Upon increasing the calcination temperature to 550 °C, but keeping the length of time at 2 h, they changed to nanoparticles with their sizes range of 80–200 nm.

TEM images of $Nd(OH)_3$ and Nd_2O_3 are shown in Fig. 4. The $Nd(OH)_3$ crystallites, synthesized by the microwave-assisted hydrothermal process, displayed uniform nanorods 20–40 nm in diameter and 200–400 nm in length (Fig. 4a). The morphology was almost the same when the $Nd(OH)_3$ precursor was calcined at either 450 °C or 500 °C for 2 h. But for 550 °C and 2 h calcination, the product became nanoparticles with an average size of 100 nm. At these stages, water evaporated and atomic diffusion proceeded. Selected area electron diffraction (SAED) patterns (insets of Fig. 4a–c) of the individual products corresponded to the (1 1 0), (1 1 2), (0 0 2) and (−1 −1 2) planes with [2 –2 0] as the zone axis, and were specified as $Nd(OH)_3$ and Nd_2O_3 single crystals [14] in accordance with the above XRD analysis. It should be noted that the planes of $Nd(OH)_3$ and Nd_2O_3 single crystals were the same, but their 2θ Bragg's angles were different. At 550 °C for 2 h, the SAED pattern (inset of Fig. 4d) was composed of concentric rings of bright spots, characterized as polycrystal. The interpreted pattern corresponded to the (1 0 0), (0 1 1), (0 1 2), (1 1 0), (1 0 3), (1 1 2) and (0 0 4) planes of Nd_2O_3 [14]. Fig. 5 shows typical HRTEM images of $Nd(OH)_3$ and Nd_2O_3 nanorods. Clearly, Fig. 5a reveals only d-spacing of the (1 1 0) and (2 0 0) planes, with a lattice spacing of about 0.321 and 0.278 nm for an individual $Nd(OH)_3$ nanorod. The HRTEM result suggested that the $Nd(OH)_3$ nanorod grew along the [0 0 1] direction, making angles of about 60° and 0° with the (1 1 0) and (2 0 0) lattice planes, respectively. Fig. 5b shows the 0.332 nm interplanar space, corresponding to d-spacing of the (1 0 0) plane of an individual Nd_2O_3 nanorod, parallel with its [0 0 1] growth direction.

4. Conclusions

Uniform Nd_2O_3 nanorods were successfully synthesized by the 500 °C and 2 h calcination of a $Nd(OH)_3$ nanorod precursor,

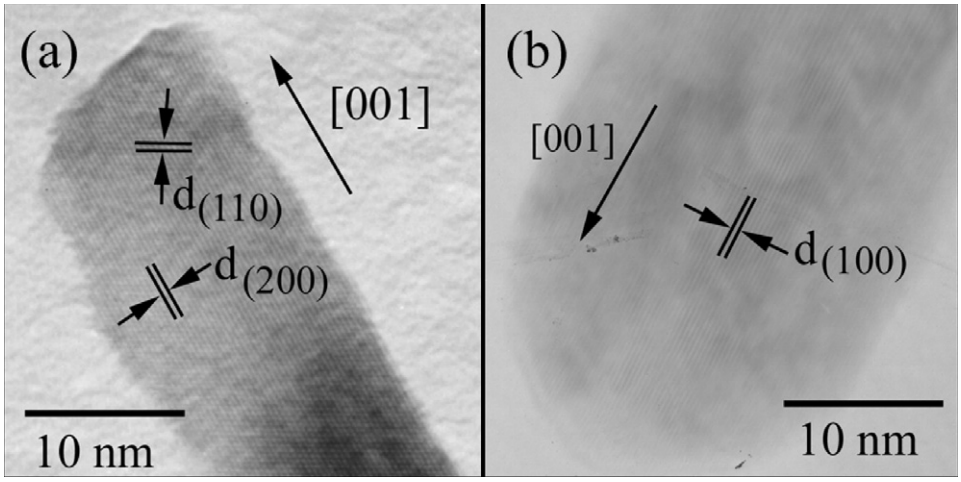


Fig. 5. HRTEM images of (a) $Nd(OH)_3$ nanorod synthesized by the 150 °C and 1 h MH process and (b) Nd_2O_3 nanorod synthesized by the 500 °C and 2 h calcination of $Nd(OH)_3$ nanorod precursor.

which was synthesized by a one-step MH method at 150 °C for 1 h. Based on the experimental results, the final morphology of the one-dimensional (1D) Nd_2O_3 nanostructure was controlled by the morphology of the $Nd(OH)_3$ self-template nanorod and the calcination temperature. A possible growth mechanism of $Nd(OH)_3$ 1D nanorods was proposed, in which the growth was promoted by the highest number of Nd^{3+} and OH^- ions along the [0 0 1] direction.

Acknowledgments

We wish to thank the National Nanotechnology Center (NANOTEC), National Science and Technology Development Agency, for providing financial support through the project P-10-11345, the Thailand's Office of the Higher Education Commission through the National Research University (NRU) Project, and the Thailand Research Fund through the TRF Research Grant.

References

[1] S. Iijima, Helical microtubules of graphitic carbon, Nature 354 (1991) 56–58.
[2] N. Zhang, R. Yi, L. Zhou, G. Gao, R. Shi, G. Qiu, X. Liu, Lanthanide hydroxide nanorods and their thermal decomposition to lanthanide oxide nanorods, Mater. Chem. Phys. 114 (2009) 160–167.
[3] X. Wang, Y. Li, Solution-based synthetic strategies for 1D nanostructures, Inorg. Chem. 45 (2006) 7522–7534.
[4] H. Guan, Y. Zhang, Hydrothermal synthesis and characterization of hexagonal and monoclinic neodymium orthophosphate single-crystal nanowires, J. Solid State Chem. 177 (2004) 781–785.
[5] A.B. Panda, G. Glaspell, M.S. El-Shall, Microwave synthesis and optical properties of uniform nanorods and nanoplates of rare earth oxides, J. Phys. Chem. C 111 (2007) 1861–1864.
[6] X. Qu, J. Dai, J. Tian, X. Huang, Z. Liu, Z. Shen, P. Wang, Syntheses of Nd_2O_3 nanowires through sol–gel process assisted with porous anodic aluminum oxide (AAO) template, J. Alloys Compd. 469 (2009) 332–335.
[7] T. Liu, Y. Zhang, H. Shao, X. Li, Synthesis and characteristics of Sm_2O_3 and Nd_2O_3 nanoparticles, Langmuir 19 (2003) 7569–7572.
[8] L. Qian, Y. Gui, S. Guo, Q. Gong, X. Qian, Controlled synthesis of light rare-earth hydroxide nanorods via a simple solution route, J. Phys. Chem. Solids 70 (2009) 688–693.
[9] W. Yang, Y. Qi, Y. Ma, X. Li, X. Guo, J. Gao, M. Chen, Synthesis of Nd_2O_3 nanopowders by sol–gel auto-combustion and their catalytic esterification activity, Mater. Chem. Phys. 84 (2004) 52–57.
[10] B. Zhaorigetu, G. Ridi, L. Min, Preparation of Nd_2O_3 nanoparticles by tartrate route, J. Alloys Compd. 427 (2007) 235–237.
[11] L. Kępiński, M. Zawadzki, W. Mišta, Hydrothermal synthesis of precursors of neodymium oxide nanoparticles, Solid State Sci. 6 (2004) 1327–1336.
[12] C. Chang, F. Kimura, T. Kimura, H. Wada, Preparation and characterization of rod-like Eu:Gd_2O_3 phosphor through a hydrothermal routine, Mater. Lett. 59 (2005) 1037–1041.
[13] T. Thongtem, A. Phuruangrat, D.J. Ham, J.S. Lee, S. Thongtem, Controlled Gd_2O_3 nanorods and nanotubes by the annealing of $Gd(OH)_3$ nanorod and nanotube precursors and self-templates produced by a microwave-assisted hydrothermal process, CrystEngComm 12 (2010) 2962–2966.
[14] Powder Diffract. File, JCPDS-ICDD, 12 Campus Boulevard, Newtown Square, PA 19073-3273, U.S.A., 2001.
[15] W.B. Hu, D.T. Tian, Y.Z. Mi, G.H. Nie, Y.M. Zhao, Z.L. Liu, K.L. Yao, Synthesis and characterization of In_2O_3 nanocube via a solvothermal-calcination route, Mater. Chem. Phys. 118 (2009) 277–280.
[16] X. Wang, Y. Li, Synthesis and characterization of lanthanide hydroxide single-crystal nanowires, Angew. Chem. Int. Ed. 41 (2002) 4790–4793.

Hindawi Publishing Corporation
Journal of Nanomaterials
Volume 2012, Article ID 930763, 5 pages
doi:10.1155/2012/930763

Research Article

Characterization of Orthorhombic α-MoO_3 Microplates Produced by a Microwave Plasma Process

Arrak Klinbumrung,[1] Titipun Thongtem,[2,3] and Somchai Thongtem[1,3]

[1] *Department of Physics and Materials Science, Faculty of Science, Chiang Mai University, Chiang Mai 50200, Thailand*
[2] *Department of Chemistry, Faculty of Science, Chiang Mai University, Chiang Mai 50200, Thailand*
[3] *Materials Science Research Center, Faculty of Science, Chiang Mai University, Chiang Mai 50200, Thailand*

Correspondence should be addressed to Somchai Thongtem, schthongtem@yahoo.com

Received 1 October 2011; Accepted 8 November 2011

Academic Editor: William W. Yu

Copyright © 2012 Arrak Klinbumrung et al. This is an open access article distributed under the Creative Commons Attribution License, which permits unrestricted use, distribution, and reproduction in any medium, provided the original work is properly cited.

Orthorhombic α-MoO_3 microplates were produced from $(NH_4)_6Mo_7O_{24}\cdot 4H_2O$ solid powder by a 900 W microwave plasma for 40, 50, and 60 min. Phase, morphologies, and vibration modes were characterized by X-ray diffraction (XRD), selected area electron diffraction (SAED), scanning electron microscopy (SEM), and Raman and Fourier transform infrared (FTIR) spectroscopy. Sixty min processing resulted in the best crystallization of the α-MoO_3 phase, with photoluminescence (PL) in a wavelength range of 430–440 nm.

1. Introduction

Basically, molybdenum oxides are classified into two types: the thermodynamically stable orthorhombic α-MoO_3 phase, and the metastable monoclinic β-MoO_3 phase with ReO_3-type structure. Orthorhombic α-MoO_3 phase is a promising oxide, with structural anisotropy [1]. It is a wide bandgap n-type semiconductor, which is very attractive for different technological applications such as photochromic materials (changing from colorless to blue by UV irradiation) [2–4], smart windows [5], self-developing photography [2], conductive gas sensors [3], lubricants [6], and catalysts [7]. Orthorhombic α-MoO_3 was composed of MoO_6 octahedral corner-sharing chains, with edge sharing of two similar chains to form layers bonded by the weak van der Waals attraction [2]. Different methods were used to produce the oxide, which led to achieving products with different properties: evaporation of Mo foil by IR in 1 atm synthetic air to produce a uniformly semitransparent film on alumina substrate [3], direct oxidation of a Mo spiral coil in ambient atmosphere to produce film on Si (001) substrate [8], flash evaporation of molybdenum oxide powder on silica glass substrate, and (111)-oriented silicon wafer in vacuum [9], precipitation [10], and hydrothermal method [11].

In the present research, α-MoO_3 microplates were produced by exposing a solid powder to microwave plasma. This very simple and rapid process, which is also benign to the environment, may lead to large-scale industrial production.

2. Experiment

To produce MoO_3, $(NH_4)_6Mo_7O_{24}\cdot 4H_2O$ powder was used as a starting material without further purification. Each 0.5 g powder was loaded into three 14 mm I.D. $\times$ 100 mm long silica boats. Each was placed in a horizontal quart tube, which was tightly closed and evacuated until its absolute pressure was 3.7 ± 0.1 kPa. The powder was heated in batches by a 900 W microwave plasma; each batch was irradiated for 5 min. After the processing of each batch, the powder was thoroughly mixed and repeatedly heated for a total of 40, 50, or 60 min. During processing, the horizontal quart tube was continuously evacuated to drain the evolved gases out of the system.

The products were characterized using X-ray diffractometer (XRD, SIEMENS D500) operating at 20 kV, 15 mA, and using Cu-K_α line, in combination with the database of the Joint Committee on Powder Diffraction Standards

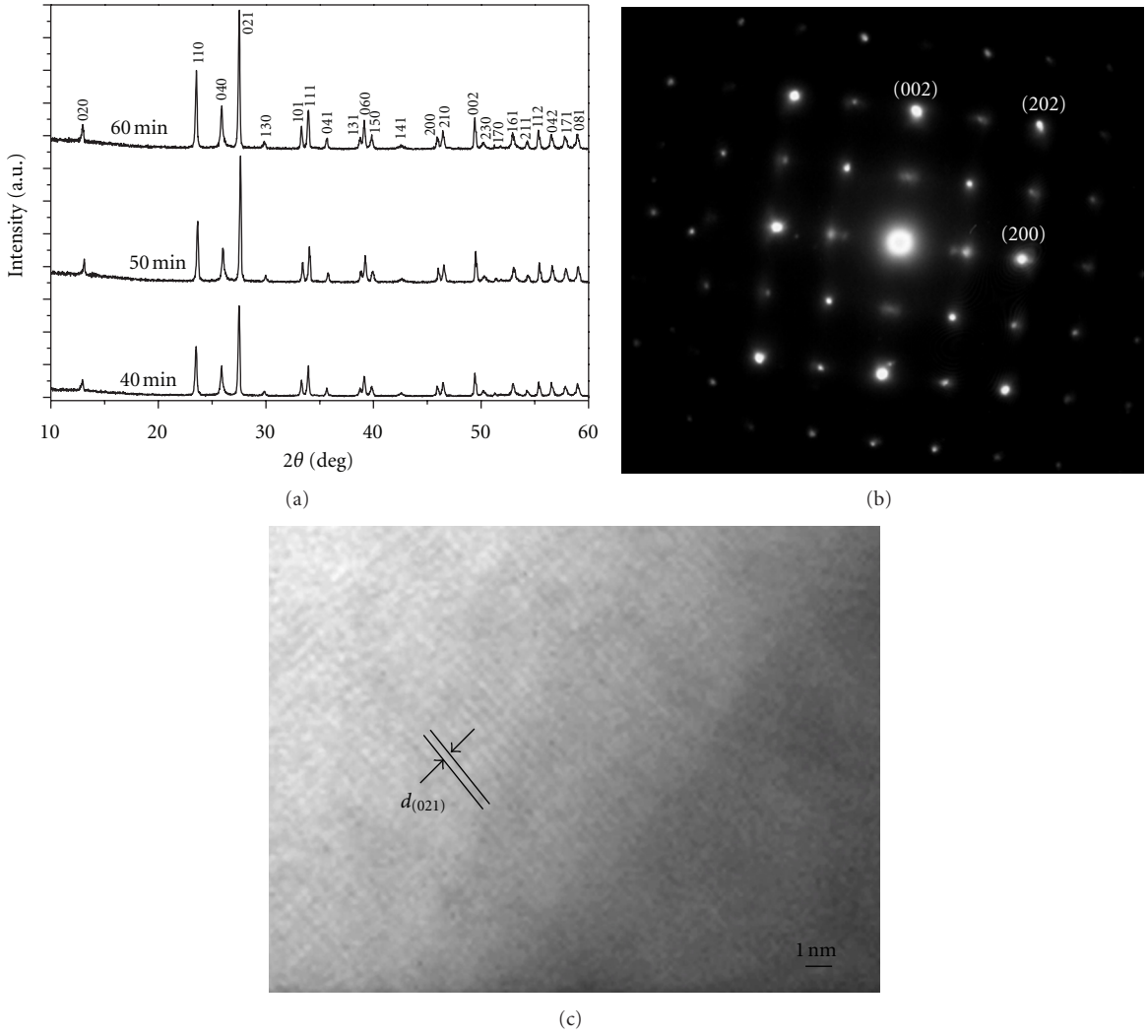


FIGURE 1: (a) XRD patterns of α-MoO_3 processed for 40, 50, and 60 min. (b, c) SAED pattern and HRTEM image of α-MoO_3 processed for 60 min.

(JCPDS) [12]; scanning electron microscope (SEM, JEOL JSM-6335F) operating at 15 kV, transmission electron microscope (TEM, JEOL JEM-2010), and selected area electron diffractometer (SAED) operating at 200 kV; Fourier transform infrared spectrometer (FTIR, Bruker Tensor 27) with KBr as a diluting agent and operated in the range of 2000–400 cm^{-1}, Raman spectrometer (T64000 HORIBA Jobin Yvon) using a 50 mW and 514.5 nm wavelength Ar green laser, and photoluminescence (PL) spectrometer (LS 50B PerkinElmer) using a 380 nm excitation wavelength at room temperature.

3. Results and Discussion

3.1. XRD, SAED, and HRTEM. XRD patterns of the products processed for 40, 50, and 60 min are shown in Figure 1(a). Their peaks were specified as orthorhombic MoO_3 of JCPDS database number 05–0508 [12], with no impurity detection. The (020) peaks at 2θ of 12.8° were clearly detected, and they indicated the presence of orthorhombic phase instead of monoclinic [13]. It should be noted that their intensities were slightly increased with the increase of processing time. The XRD peaks for 60 min processing time were the strongest, reflecting the product with the best degree of crystallinity. During processing, $(NH_4)_6Mo_7O_{24}\cdot 4H_2O$ decomposed as follows:

$$(NH_4)_6Mo_7O_{24}\cdot 4H_2O(s) \longrightarrow 7MoO_3(s) + 6NH_3(g) + 7H_2O(g) \quad (1)$$

$MoO_3(s)$ was left as the final solid products. Two gases (NH_3 and H_2O) diffused out of the system, and evacuated out of the horizontal quart tube. It should be noted that some reactant could remain, and was mixed with the final product if the processing time was less than 40 min. Longer processing times resulted in greater purification of the final product.

Calculated lattice parameters (Å) using the plane spacing equation for orthorhombic phase [14] were a = 3.96, b =

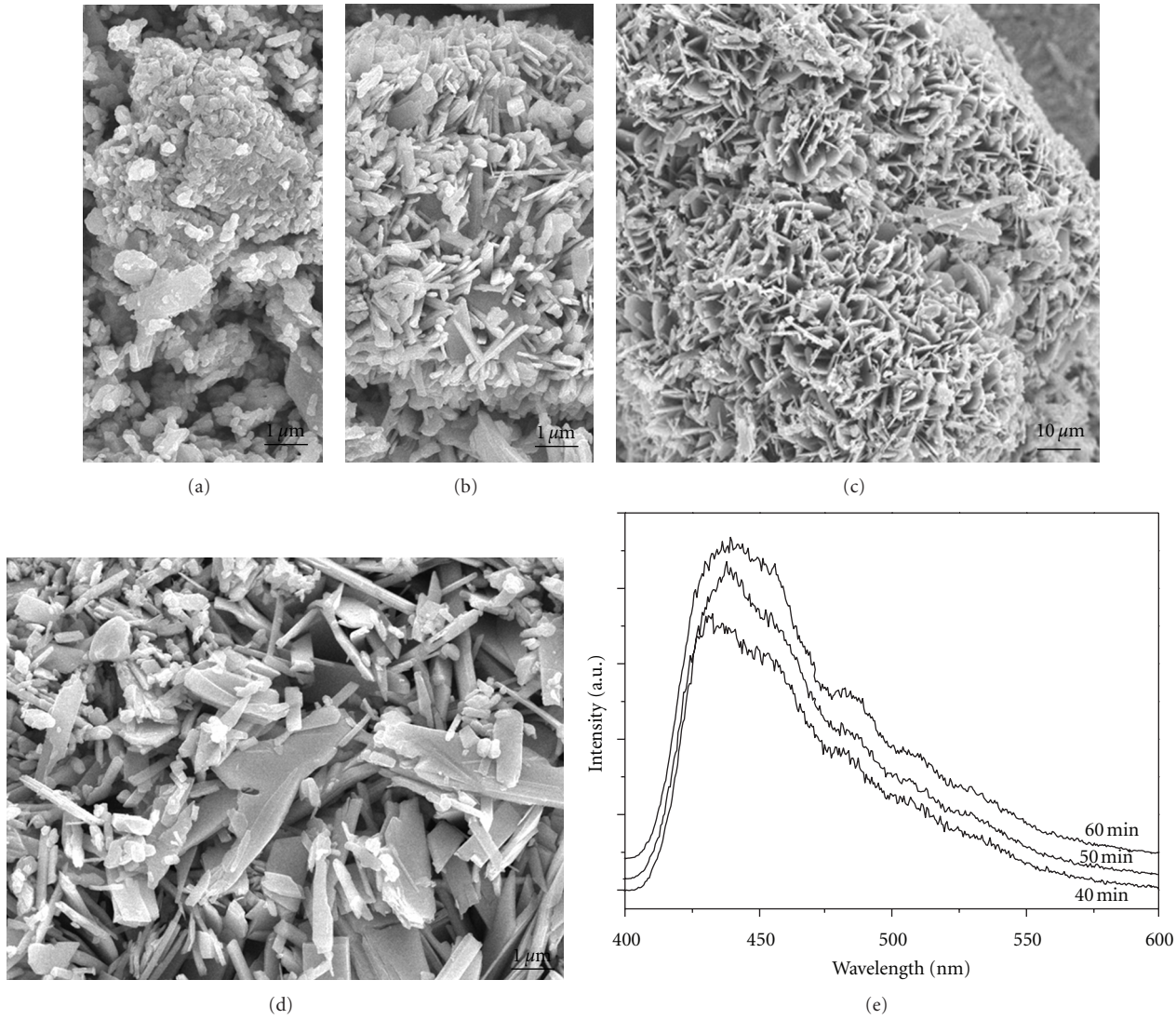


Figure 2: SEM images of α-MoO_3 processed for (a) 40 min, (b) 50 min, and (c, d) 60 min, and (e) PL emissions of α-MoO_3 processed for 40, 50, and 60 min.

13.86, and c = 3.70, in accordance with those of the JCPDS database [12]. Figure 1(b) shows the SAED pattern of a single crystal processed for 60 min. It was indexed [15] to correspond with the (002), (202), and (200) crystallographic planes, which were specified as orthorhombic α-MoO_3 [2, 12, 16]. In the present analysis, an electron beam was sent to the crystal along the (010) direction. The (021) crystallographic plane with 0.33 nm spacing was detected by HRTEM (Figure 1(c)), implying that the product was crystalline in nature. These last two analyses were in accordance with that of the above XRD.

3.2. SEM. SEM images of MoO_3 crystals processed for 40, 50, and 60 min are shown in Figures 2(a)–2(d). Clusters of spheres ranging from 100 nm to a few hundred nm, as well as a small fraction of plates, were produced by 40 min processing. When the processing time was 50 min, more plates—about 100 nm thick and a few μm long—were produced, growing perpendicular to the cluster surface. Sixty min processing resulted in a further increase in the number of plates produced, as well as their sizes: 100–200 nm thick and a few μm long. During processing, some plates could be broken due to the internal stress developed inside.

3.3. Raman and FTIR Analyses. Raman spectra (Figure 3(a)) of MoO_3 crystals processed for 40, 50 and 60 min were studied in the range of 150–1050 cm^{-1}. During the analysis, a low-intensity laser was used to avoid crystallization. The product of 60 min processing was a highly ordered crystalline structure, and its Raman peaks were the highest. The heights were reduced when the processing time was shortened. In the present research, 12 typical Raman peaks were detected. The peaks at 990 cm^{-1} were specified as the Mo=O asymmetric stretching modes of terminal (unshared) oxygen [16]. The strongest peaks were at 813 cm^{-1}, and were specified as the doubly connected bridge-oxygen Mo_2–O stretching modes

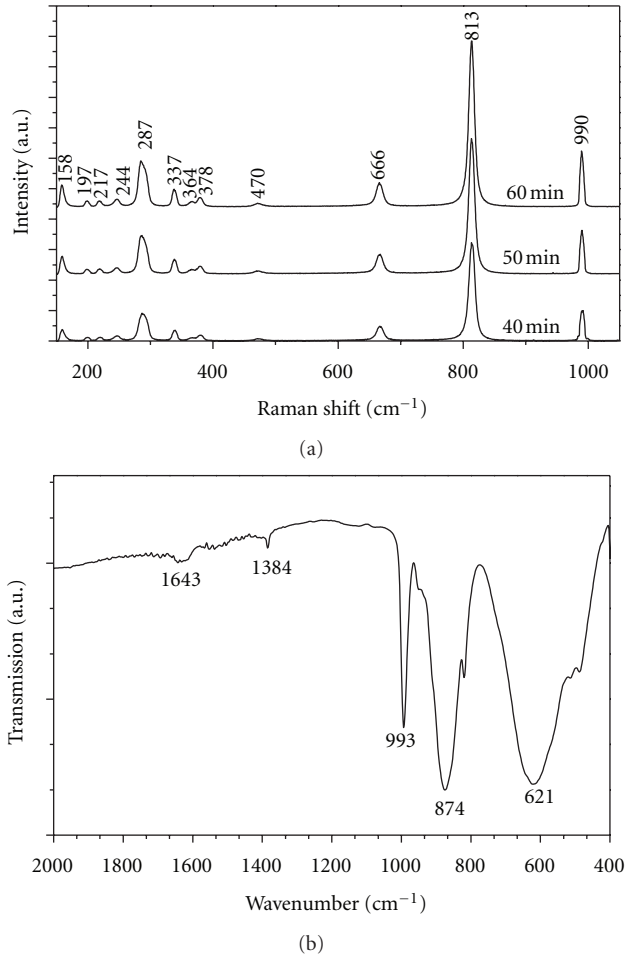


Figure 3: (a) Raman analysis of α-MoO_3 processed for 40, 50, and 60 min. (b) FTIR spectrum of α-MoO_3 processed for 60 min.

[2] of doubly coordinated oxygen, caused by corner-shared oxygen atoms in common to two MoO_6 octahedrons [16]. The peaks at 666 cm^{-1} were the Mo_3–O stretching modes of triply coordinated bridge-oxygen, caused by edge-shared oxygen atoms in common to three octahedrons [2, 16]. Their remains were the O–Mo–O asymmetric stretching/bending modes at 470 cm^{-1}, O–Mo–O scissoring modes at 378 and 364 cm^{-1}, O–Mo–O bending modes at 337 cm^{-1}, O=Mo=O wagging modes at 287 cm^{-1}, O=Mo=O twisting modes at 244 cm^{-1}, R_c modes at 217 cm^{-1}, O=Mo=O twisting modes at 197 cm^{-1}, and T_b modes at 158 cm^{-1} [16]. Sometimes the Raman peaks were positively/negatively shifted, due to the increase or decrease in the vibration constant of the products [2]. In the present research, the vibrations were the same values, although the processing time and degree of crystallinity were different.

Figure 3(b) shows the FTIR spectrum of α-MoO_3 over the 400–2000 cm^{-1} range. Three strong vibrations were detected at 621, 874 and 993 cm^{-1}, associated respectively with the stretching mode of oxygen linked with three metal atoms, the stretching mode of oxygen in the Mo–O–Mo units, and the MoO stretching mode—the specification of a layered orthorhombic α-MoO_3 phase [17]. Two weak vibrations were also detected at 1384 and 1643 cm^{-1}, associated with the vibration mode of the Mo–OH bond and the bending mode of adsorbed water, respectively [17, 18].

3.4. PL Emission. PL emission of orthorhombic α-MoO_3 processed for 40, 50, and 60 min was studied using 380 nm excitation wavelength at room temperature. The PL spectra (Figure 2(e)) presented broad peaks over the 400–600 nm range with a strong indigo emission centered at 430–440 nm—in accordance with the report of Song et al. [4]. These emissions were caused by the band-to-band transition. In the present research, very weak shoulders, caused by the electron-hole recombination between the conduction band and the sublevel of adsorbed oxygen acceptors, were also detected; these were able to be reduced by calcination at high temperatures [4]. The luminescence intensity increased with the increase of processing times, in accordance with the improvement of the degree of crystallinity characterized by the above XRD analysis.

4. Conclusions

Orthorhombic α-MoO_3 was successfully produced by a 900 W microwave plasma process for 40, 50, and 60 min. The product processed for 60 min was α-MoO_3 microplates with three main Raman peaks (666, 813, and 990 cm^{-1}), three main FTIR vibration modes (621, 874, and 993 cm^{-1}), and 430–440 nm indigo emission—a promising material for different applications.

Acknowledgments

The authors wish to thank the National Nanotechnology Center (NANOTEC), National Science and Technology Development Agency, Thailand, for providing financial support through the project code: P-10-11345, the Thailand's Office of the Higher Education Commission through the National Research University Project, and the Strategic Scholarships for Thai Ph.D. Program, and the Thailand Research Fund (TRF) through the TRF Basic Research Grant, including the Graduate School of Chiang Mai University through the general support.

References

[1] X. W. Lou and H. C. Zeng, "Hydrothermal synthesis of α-MoO_3 nanorods via acidification of ammonium heptamolybdate tetrahydrate," *Chemistry of Materials*, vol. 14, no. 11, pp. 4781–4789, 2002.

[2] T. He and J. Yao, "Photochromism of molybdenum oxide," *Journal of Photochemistry and Photobiology C*, vol. 4, no. 2, pp. 125–143, 2003.

[3] E. Comini, L. Yubao, Y. Brando, and G. Sberveglieri, "Gas sensing properties of MoO_3 nanorods to CO and CH_3OH," *Chemical Physics Letters*, vol. 407, no. 4–6, pp. 368–371, 2005.

[4] J. Song, X. Ni, D. Zhang, and H. Zheng, "Fabrication and photoluminescence properties of hexagonal MoO_3 rods," *Solid State Sciences*, vol. 8, no. 10, pp. 1164–1167, 2006.

[5] T. He, Y. Ma, Y. Cao, Y. Yin, W. Yang, and J. Yao, "Enhanced visible-light coloration and its mechanism of MoO_3 thin films by Au nanoparticles," *Applied Surface Science*, vol. 180, no. 3-4, pp. 336–340, 2001.

[6] J. Wang, K. C. Rose, and C. M. Lieber, "Load-independent friction: MoO_3 nanocrystal lubricants," *Journal of Physical Chemistry B*, vol. 103, no. 40, pp. 8405–8409, 1999.

[7] K. R. Reddy, K. Ramesh, K. K. Seela, V. V. Rao, and K. V. R. Chary, "Alkylation of phenol with methanol over molybdenum oxide supported on NaY zeolite," *Catalysis Communications*, vol. 4, no. 3, pp. 112–117, 2003.

[8] Y. Zhao, J. Liu, Y. Zhou et al., "Preparation of MoO_3 nanostructures and their optical properties," *Journal of Physics Condensed Matter*, vol. 15, no. 35, pp. L547–L552, 2003.

[9] C. Julien, A. Khelfa, O. M. Hussain, and G. A. Nazri, "Synthesis and characterization of flash-evaporated MoO_3 thin films," *Journal of Crystal Growth*, vol. 156, no. 3, pp. 235–244, 1995.

[10] H. X. Bai, X. H. Liu, and Y. C. Zhang, "Synthesis of MoO_3 nanoplates from a metallorganic molecular precursor," *Materials Letters*, vol. 63, no. 1, pp. 100–102, 2009.

[11] T. Xia, Q. Li, X. Liu, J. Meng, and X. Cao, "Morphology-controllable synthesis and characterization of single-crystal molybdenum trioxide," *Journal of Physical Chemistry B*, vol. 110, no. 5, pp. 2006–2012, 2006.

[12] Powder Diffract, File, JCPDS-ICDD, 12 Campus Boulevard, Newtown Square, P.A. 19073-3273, USA, 2001.

[13] T. Mizushima, K. Fukushima, H. Ohkita, and N. Kakuta, "Synthesis of β-MoO_3 through evaporation of HNO_3-added molybdic acid solution and its catalytic performance in partial oxidation of methanol," *Applied Catalysis A*, vol. 326, no. 1, pp. 106–112, 2007.

[14] C. Suryanarayana and M. G. Norton, *X-Ray Diffract*, Plenum Press, New York, NY, USA, 1998.

[15] K. W. Andrews, D. J. Dyson, and S. R. Keown, *Interpreting Electron Diffraction Patterns*, Plenum Press, New York, NY, USA, 1971.

[16] T. Siciliano, A. Tepore, E. Filippo, G. Micocci, and M. Tepore, "Characteristics of molybdenum trioxide nanobelts prepared by thermal evaporation technique," *Materials Chemistry and Physics*, vol. 114, no. 2-3, pp. 687–691, 2009.

[17] G. S. Zakharova, C. Täschner, V. L. Volkov et al., "$MoO_{3-\delta}$ nanorods: synthesis, characterization and magnetic properties," *Solid State Sciences*, vol. 9, no. 11, pp. 1028–1032, 2007.

[18] M. Dhanasankar, K. K. Purushothaman, and G. Muralidharan, "Effect of temperature of annealing on optical, structural and electrochromic properties of sol-gel dip coated molybdenum oxide films," *Applied Surface Science*, vol. 257, no. 6, pp. 2074–2079, 2011.

Composition Comments

1. We reduced the font size of some labels in Figure 1. Please check.

Author(s) Name(s)

It is very important to confirm the author(s) last and first names in order to be displayed correctly on our website as well as in the indexing databases:

Author 1

Last Name: Klinbumrung

First Name: Arrak

Author 2

Last Name: Thongtem

First Name: Titipun

Author 3

Last Name: Thongtem

First Name: Somchai

Powder Technology 221 (2012) 383–386

Contents lists available at SciVerse ScienceDirect

Powder Technology

journal homepage: www.elsevier.com/locate/powtec

Solvothermal synthesis of CdS nanorods using poly(vinyl butyral-co-vinyl alcohol-co-vinyl acetate) as a capping agent in ethylenediamine solvent

Anukorn Phuruangrat [a,*], Titipun Thongtem [b,**], Somchai Thongtem [c]

[a] Department of Materials Science and Technology, Faculty of Science, Prince of Songkla University, Hat Yai, Songkhla 90112, Thailand
[b] Department of Chemistry, Faculty of Science, Chiang Mai University, Chiang Mai 50200, Thailand
[c] Department of Physics and Materials Science, Faculty of Science, Chiang Mai University, Chiang Mai 50200, Thailand

ARTICLE INFO

Article history:
Received 16 May 2011
Received in revised form 16 January 2012
Accepted 21 January 2012
Available online 28 January 2012

Keywords:
CdS nanorods
Solvothermal synthesis
X-ray diffraction
Electron microscopy
Spectroscopy

ABSTRACT

One-dimension (1D) cadmium sulfide (CdS) nanorods were successfully synthesized using cadmium nitrate ($Cd(NO_3)_2$) and thiourea (NH_2CSNH_2) as starting materials and poly(vinyl butyral-co-vinyl alcohol-co-vinyl acetate) as a capping agent in ethylenediamine as a solvent by solvothermal reaction at 200 °C for 24 and 72 h. The phase, morphology, atomic vibration and optical property of the products were characterized by X-ray diffraction (XRD), scanning electron microscopy (SEM), transmission electron microscopy (TEM), Raman spectroscopy and UV–visible spectroscopy. In the present research, the products were wurtzite hexagonal CdS nanorods growing along the [001] direction, with the 1LO and 2LO vibration modes at 298 and 597 cm^{-1} and the absorption peak centered at 486 nm.

© 2012 Elsevier B.V. All rights reserved.

1. Introduction

One-dimensional (1D) nanostructured materials, such as nanowires, nanorods and nanotubes, which have anisotropic geometries and unique physical properties are highly potential application for a number of technologies [1–3]. CdS, one of the most advantaged direct band-gap II–VI semiconductors, has stimulated intensive interest due to its wide applications in photoelectronic conversion for solar cells, optoelectronics, light-emitting diodes and photocatalyst. It is one of the most important materials with a wide band gap of 2.5 eV for the bulk hexagonal wurtzite structure, and 3.53 eV for bulk cubic zinc blende structure [4–7]. It has been synthesized by both physical and chemical methods, including solvothermal [6], cyclic microwave radiation [7], electrochemical synthesis [8] and chemical vapor deposition [9].

Previously, 1D CdS was synthesized by solvothermal method using polymer-added solutions such as polyvinyl alcohol (PVA) [10], polyethylene glycol (PEG) [11] and polyvinyl pyrrolidone (PVP) [12] to improve the length and diameter. For the present research, 1D CdS nanostructure was synthesized by solvothermal method using ethylenediamine as a solvent and poly(vinyl butyral-co-vinyl alcohol-co-vinyl acetate) as a capping agent, and compared with the non-capping solvothermal condition.

2. Experimental procedure

To synthesize CdS nanostructure, 0.005 mol of $Cd(NO_3)_2$ and NH_2CSNH_2 as cadmium and sulfur sources each was mixed in 50 ml ethylenediamine (en), and followed by 0.5 g poly(vinyl butyral-co-vinyl alcohol-co-vinyl acetate) as a capping polymer adding. The mixture solution was transferred in a Teflon container and put in a home-made stainless steel autoclave, which was tightly closed, heated in an electric oven at 200 °C for 24 h, and cooled to room temperature. The 200 °C solvothermal processes were also done for two more solutions with and without polymer adding for 72 and 24 h, respectively. Finally, yellow precipitates were produced, collected, washed with distilled water and absolute ethanol for several times and dried at 80 °C for 24 h.

The products were analyzed by X-ray diffractometer (XRD, SIEMENS D500) operating at 20 kV 15 mA, and using Cu-K_α line of a copper target with the scanning angle 2θ ranging from 15 to 60°. Raman spectrometer (T64000 HORIBA Jobin Yvon) was operated by a 50 mW and 514.5 nm wavelength Ar green laser. SEM images were taken through a scanning electron microscope (SEM, JEOL JSM-6335F) operating at 15 kV, equipped with an energy dispersive X-ray analyzer (EDX, Oxford Instruments). TEM and HRTEM images of the products were taken on a transmission electron microscope (TEM, JEOL JEM-2010) using LaB_6 electron gun with an accelerating voltage of 200 kV. The samples used for TEM analysis were prepared by sonicating of dried products in absolute ethanol for 15 min and followed by putting 3–5 drops of the suspensions on carbon-coated copper grids. A room temperature absorption spectrum was carried out

* Corresponding author. Tel.: +66 74 288374; fax: +66 74 288395.
** Corresponding author. Tel.: +66 53 943344; fax: +66 53 892277.
E-mail addresses: phuruangrat@hotmail.com (A. Phuruangrat), ttpthongtem@yahoo.com (T. Thongtem).

0032-5910/$ – see front matter © 2012 Elsevier B.V. All rights reserved.
doi:10.1016/j.powtec.2012.01.033

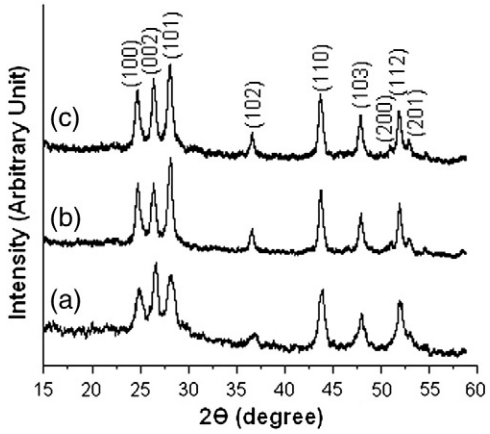


Fig. 1. XRD patterns of CdS synthesized by the 200 °C solvothermal reaction of different solutions and lengths of time: (a) polymer-free for 24 h, (b) polymer-added for 24 h and (c) polymer-added for 72 h.

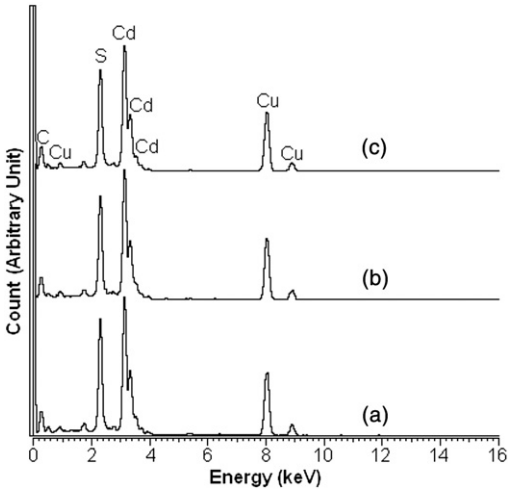


Fig. 3. EDX spectra of CdS synthesized by the 200 °C solvothermal reaction of different solutions and lengths of time: (a) polymer-free for 24 h, (b) polymer-added for 24 h and (c) polymer-added for 72 h.

on a Perkin Elmer Lambda 25 UV–visible spectrometer with the resolution of 1 nm in the wavelength range of 250–800 nm.

3. Results and discussion

XRD patterns of the as-synthesized samples prepared by solvothermal method at different conditions are shown in Fig. 1. All the diffraction peaks can be indexed to be hexagonal CdS phase, in agreement with the JCPDS no. 41-1049 [13] ($a = b = 4.1409$ Å and $c = 6.7198$ Å). No impurities such as CdO, S, and $Cd(OH)_2$ were detected. In the present research, the products were very high purity. The lattice parameters of hexagonal CdS structure of polymer-added at 200 °C for 72 h were calculated using plane-spacing equation for hexagonal structure and Bragg's law for diffraction [14]. They were $a = b = 4.1395$ Å and $c = 6.7356$ Å and were very close to the standard values. It should be noted that the c/a ratio and intensity percent of the (002) plane of the experiment were higher than those of the standard, implying that the product has preferential growth along the c axis.

The degree of c-orientation of CdS nanorods was illustrated by the relative texture coefficient [15–17], given by

$$TC_{002} = \frac{(I_{002}/I^{\circ}_{002})}{[I_{002}/I^{\circ}_{002} + I_{101}/I^{\circ}_{101}]}$$

where TC_{002} was the relative texture coefficient for diffraction peaks of (002) over (101). I_{002} and I_{101} were the experimental diffraction intensities of the (002) and (101) peaks, including I°_{002} and I°_{101} were the corresponding values of the standard measured from the randomly oriented particles. The texture coefficient of CdS with random crystallographic orientations is 0.5. TC_{002} of CdS with polymer-added at 200 °C for 72 h was 0.53, showing the product growth along the c-axis with low c-orientation.

Morphologies of the products were investigated by scanning electron microscopy (SEM) and transmission electron microscopy (TEM). SEM images of the products are showed in Fig. 2. It should be noted that the as-synthesized CdS sample for polymer-free at 200 °C for 24 h was spherical nanoparticles with the size of 20 nm approximately. For the solvothermal reaction at 200 °C for 24 h of the polymer-added solution, morphologies of the as-synthesized CdS sample became nanorods with the length of 100–200 nm and diameter of 20–50 nm approximately, and a little amount of spherical nanoparticles. The whole CdS nanorods were synthesized by prolonging the solvothermal reaction time to 72 h. Their length and diameter were 1000 nm and 20–60 nm, respectively. It can be concluded that the poly(vinyl butyral-co-vinyl alcohol-co-vinyl acetate) and reaction time have the influence on the formation and elongation of 1D CdS nanorods. The qualitative and quantitative analyses of the as-prepared CdS samples were analyzed by EDX (Fig. 3), which revealed the presence of only Cd and S as the elementary components of the products. The molar ratios of Cd to S obtained from the peak areas were very close to that of the stoichiometric CdS of 1:1 by mole. The Cu and C peaks of the copper stubs and carbon tapes were also detected.

TEM images of the products are showed in Fig 4. The TEM image and SAED pattern of CdS for polymer-free (Fig. 4a) presented mixed-morphologies of nanoparticles and nanorods with the ring pattern, confirming the product of different orientation particles. These rings were indexed to be the (100), (002), (101), (102), (110), (103) and (200) planes, corresponding to those of the standard [13]. When the polymer was added to the solution at 200 °C 24 h (Fig. 4b), CdS

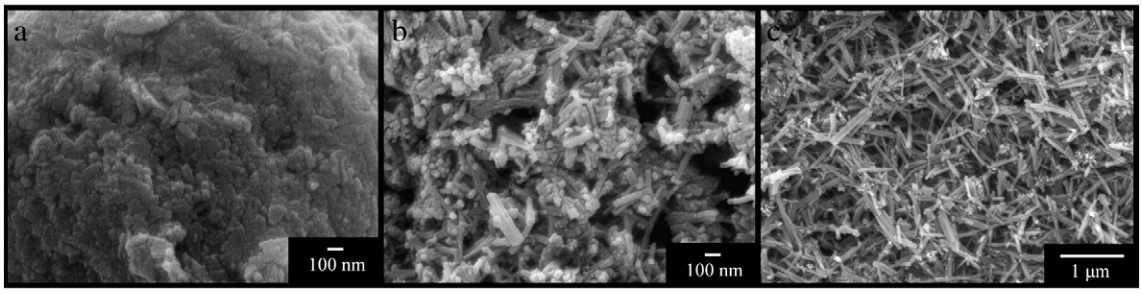


Fig. 2. SEM images of CdS synthesized by the 200 °C solvothermal reaction of different solutions and lengths of time: (a) polymer-free for 24 h, (b) polymer-added for 24 h and (c) polymer-added for 72 h.

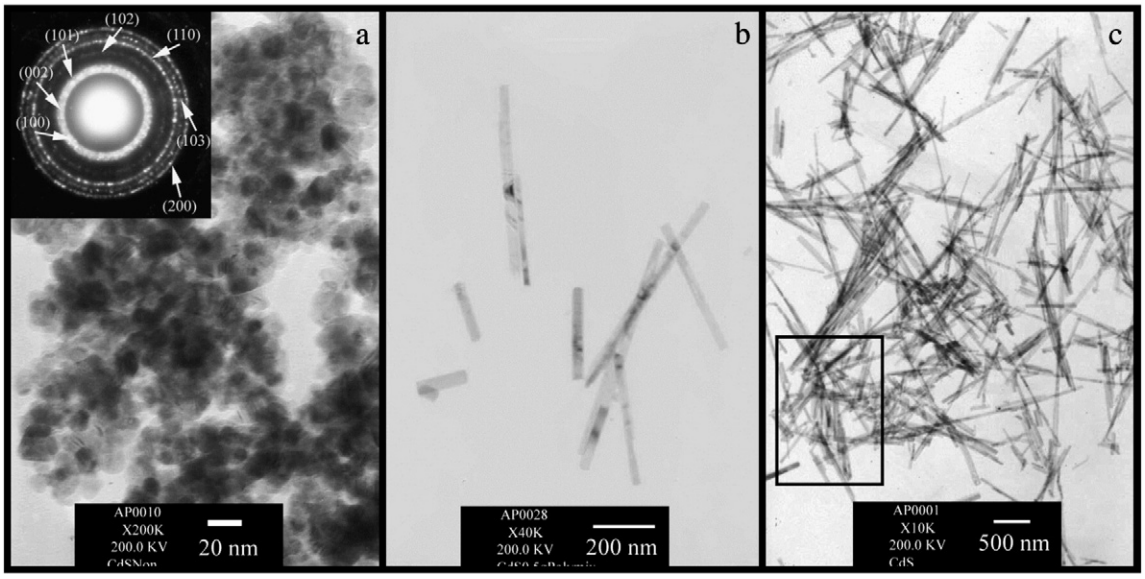


Fig. 4. TEM images and SAED pattern of CdS synthesized by the 200 °C solvothermal reaction of different solutions and lengths of time: (a) polymer-free for 24 h, (b) polymer-added for 24 h and (c) polymer-added for 72 h.

nanorods with the diameter around 20 nm and the length around 120–700 nm were detected. Their lengths were increased to 3000 nm by prolonging the reaction time to 72 h (Fig. 4c).

Fig. 5 shows a transmission electron microscopic (TEM) image on a rectangle area of Fig 4c, selected area electron diffraction (SAED) patterns, and high resolution transmission electron microscopic (HRTEM) images of CdS nanorods with polymer-added at 200 °C for 72 h. Fig. 5b–d shows SAED patterns on the area numbers of 1, 2 and 3 of Fig 5a. They were identified as the [−110] zone axis of hexagonal CdS structure. The electron diffraction pattern was simulated by CaRIne program [18] with the [−110] as zone axis of hexagonal CdS structure (Fig. 5e), which confirmed the product phase detected by SAED. Finally, HRTEM images of Fig 5f–h were taken on the area numbers of 1, 2 and 4, respectively. Their lattice plane spaces were

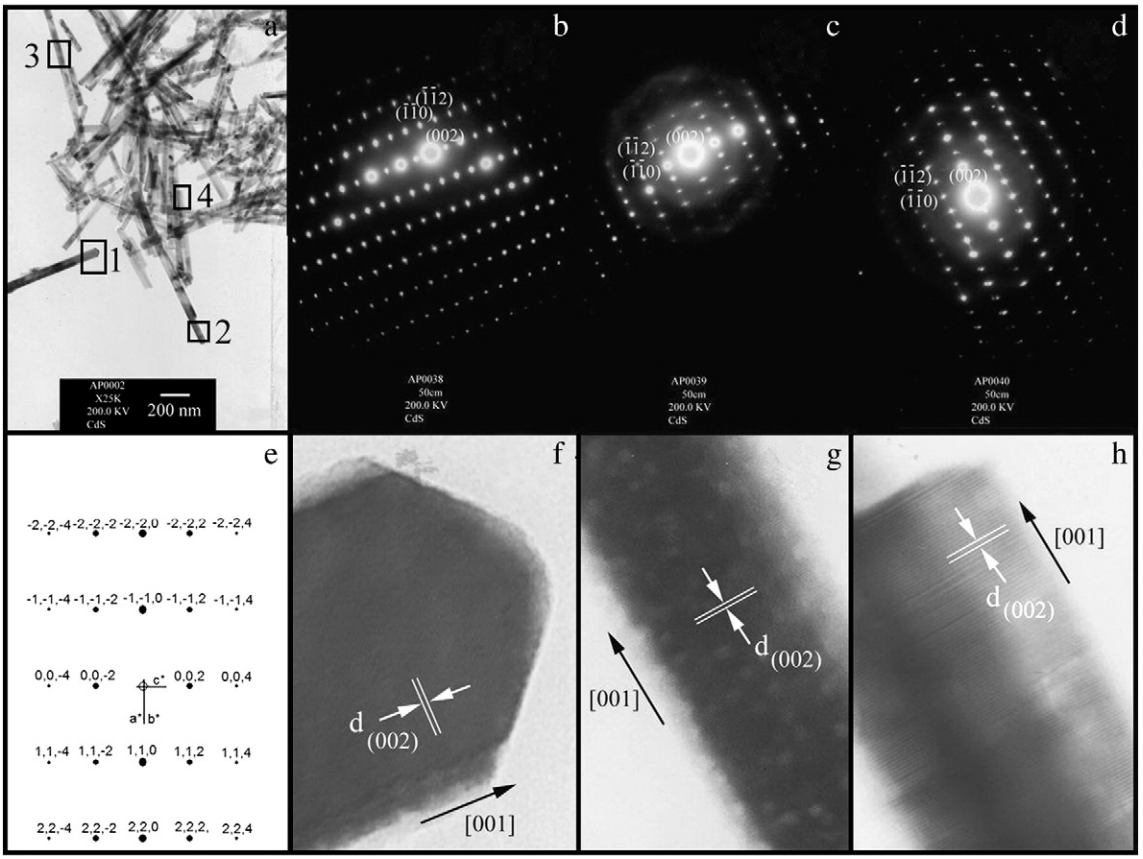


Fig. 5. (a) TEM image of CdS nanorods solvothermally synthesized in the polymer-added solution at 200 °C for 72 h. SAED patterns and HRTEM images on different areas of (a): (b and f) on 1, (c and g) on 2, (d) on 3, and (h) on 4. (e) Electron diffraction pattern simulation for the [−110] zone axis.

calculated to be the same of 3.42 Å, corresponding to the space of the (002) plane of wurtzite CdS. These indicated that the product was CdS nanorods with their growth along the [001] direction.

The hexagonal wurtzite CdS has C^4_{6v} space group. The $1A_1 + 1E_1 + 2E_2$ (E_{2H} and E_{2L}) modes are Raman active and the $2B_2$ modes are silent. For the A_1 branch, phonon polarization is in the z direction. The doubly degenerate E_1 and E_2 branches are polarized in the x–y plane. Because the wurtzite structure is noncentrosymmetric, both A_1 and E_1 modes split into longitudinal optical (LO) and transverse optical (TO) components [1]. Raman spectra of the products (Fig. 6) show at the same position of 1LO and 2LO of A_1 modes at 298 and 597 cm^{-1}, which were polarized in the x–z face and strongly couple to the excitons along the c axis [5,19]. Intensity of the 1LO was stronger than that of the 2LO. Intensity ratio of $I_{1LO/2LO}$ decreased from 3.13 for CdS polymer-free at 200 °C for 24 h to 2.11 for CdS polymer-added CdS at 200 °C for 24 h, and 1.72 for CdS polymer-added at 200 °C for 72 h. The exciton-LO phonon coupling in the 1D nanostructured semiconductor was greatly strengthened, caused by the phonon confinement in the transverse direction and the transition of the elementary excitation particles (carriers, excitons and phonons) in the longitudinal direction [19].

In the present research, ethylenediamine (en), a strongly bidentate ligand, coordinated with Cd^{2+} and reacted with thiourea to synthesize CdS nanorods in the en solution containing the capping polymer.

$$Cd^{2+} + 2en \rightarrow Cd(en)_2^{2+}$$

$$NH_2CSNH_2 + H_2O \rightarrow NH_2CONH_2 + H_2S$$

$$Cd(en)_m^{2+} + S^{2-} \leftrightarrow CdS(en)_m \leftrightarrow CdS(en)_{m-n} + n(en).$$

Due to the relatively weak attraction of Cd^{2+} and en ($\log\beta = 10.09$, β is a constant of the $Cd(en)_2^{2+}$ complex ions) and the slow release rate of S^{2-} ions to bond with the complex, the reaction rate was relatively slow [20]. The last reaction proceeded for several steps. Finally, hexagonal CdS nuclei were synthesized. During growing of the nuclei, the capping polymer adsorbed on their side walls, causing the lateral growth to be terminated. The tips were uncovered, and axial growth proceeded in the [001] direction (Fig. 5f–h) via the diffusion process. Hence, CdS nanorods were synthesized [21].

The optical characterization of CdS nanorods was investigated by UV–visible spectroscopy as shown in Fig. 7. The spectrum of CdS nanorods shows an absorption peak centered at around 486 nm with its band gap (E_g) of 2.55 eV due to the excitation of CdS. It should be noted that the absorption peak was blue-shift (27 nm) to the shorter wavelength, comparing to the bulk CdS ($E_g = 2.42$ eV, 513 nm), due to the quantum confinement effect of the small diameter of CdS nanorods [11,22].

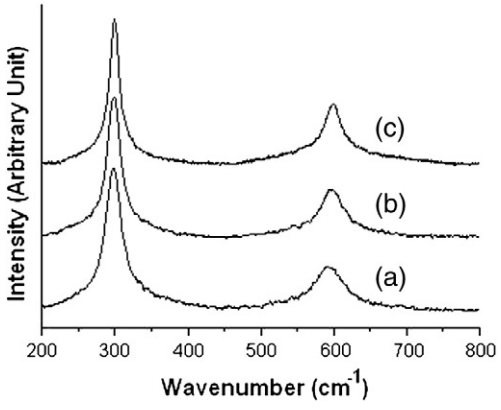


Fig. 6. Raman spectra of CdS synthesized by the 200 °C solvothermal reaction of different solutions and lengths of time: (a) polymer-free for 24 h, (b) polymer-added for 24 h and (c) polymer-added for 72 h.

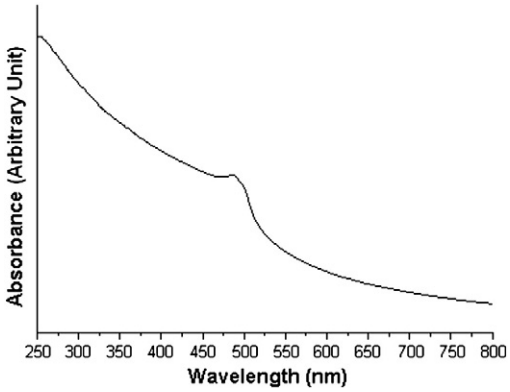


Fig. 7. UV–visible absorption spectrum of CdS nanorods solvothermally synthesized in the polymer-added solution at 200 °C for 72 h.

4. Conclusions

Cadmium sulfide nanorods were synthesized by solvothermal reaction of the mixture of cadmium nitrate, thiourea and poly(vinyl butyral-co-vinyl alcohol-co-vinyl acetate) in ethylenediamine at 200 °C for 72 h. The results indicated that the capping agent and length of reaction time played an important role in the 1D growth of CdS nanorods.

Acknowledgments

We are very grateful to the Prince of Songkla University for providing financial support through the contract number SCI540660S; the Thailand's Office of the Higher Education Commission through the National Research University (NRU) Project for Chiang Mai University; and the Thailand Research Fund (TRF) through the TRF Research Grant.

References

[1] H.M. Fan, X.F. Fan, Z.H. Ni, Z.X. Shen, Y.P. Feng, B.S. Zou, J. Phys, Chem. C 112 (2008) 1865–1870.
[2] S.M. Lee, S.N. Cho, J. Cheon, Adv. Mater. 15 (2003) 441–444.
[3] D. Chen, G. Shen, K. Tang, X. Liu, Y. Qian, G. Zhou, J. Cryst, Growth 253 (2003) 512–516.
[4] L. Zeiri, I. Patla, S. Acharya, Y. Golan, S. Efrima, J. Phys, Chem. C 111 (2007) (1848) 11843–11848.
[5] H. Cao, G. Wang, S. Zhang, X. Zhang, D. Rabinovich, Inorg. Chem. 45 (2006) 5103–5108.
[6] T. Thongtem, A. Phuruangrat, S. Thongtem, Mater. Lett. 61 (2007) 3235–3238.
[7] T. Thongtem, A. Phuruangrat, S. Thongtem, J. Phys, Chem. Solids 69 (2008) 1346–1349.
[8] D. Mo, J. Liu, H.J. Yao, J.L. Duan, M.D. Hou, Y.M. Sun, Y.F. Chen, Z.H. Xue, L. Zhang, J. Cryst, Growth 310 (2008) 612–616.
[9] S.M. Zhou, Mater. Lett. 61 (2007) 119–122.
[10] A. Phuruangrat, T. Thongtem, S. Thongtem, J. Exper. Nanosci. 4 (2009) 47–54.
[11] H. Gai, Y. Wu, Z. Wang, L. Wu, Y. Shi, M. Jing, K. Zou, Polymer Bull. 61 (2008) 435–441.
[12] W. Qingqing, Z. Gaoling, H. Gaorong, Mater. Lett. 59 (2005) 2625–2629.
[13] Powder Diffract. File, JCPDS-ICDD, 12 Campus Boulevard, Newtown Square, PA 19073–3273, U.S.A. 2001.
[14] C. Suryanarayana and M.G. Norton, X-ray Diffract., A Pract. Appro., Plenum Press, New York, 1998.
[15] H.Z. Zhang, X.C. Sun, R.M. Wang, D.P. Yu, J. Cryst, Growth 269 (2004) 464–471.
[16] F. Li, Z. Li, F.J. Jin, Mater. Lett. 61 (2007) 1876–1880.
[17] P. Che, J. Meng, L. Guo, J. Lumin. 122–123 (2007) 168–171.
[18] C. Boudias and D. Monceau, CaRIne Crystallography 3.1, DIVERGENT S.A., Centre de Transfert, 60200 Compiègne, France, 1989–1998.
[19] A. Pan, R. Liu, Q. Yang, Y. Zhu, G. Yang, B. Zou, K. Chen, J. Phys, Chem. B 109 (2005) 24268–24272.
[20] M. Maleki, Sh. Mirdamadi, R. Ghasemzadeh, M.S. Ghamsari, Mater. Lett. 62 (2008) 1993–1995.
[21] T. Thongtem, C. Pilapong, S. Thongtem, Curr. Appl. Phys. 9 (2009) 1272–1277.
[22] S. Yan, D. Hu, J. Wu, J. Qian, Y. Wang, Z. Xiao, Solid State Sci. 12 (2010) 1507–1510.

Appl Phys A (2012) 107:249–254
DOI 10.1007/s00339-012-6771-3

Applied Physics A
Materials Science & Processing

Hydrothermal synthesis and electrochemical properties of α-MoO_3 nanobelts used as cathode materials for Li-ion batteries

Anukorn Phuruangrat · Jun Song Chen · Xiong Wen Lou · Oranuch Yayapao · Somchai Thongtem · Titipun Thongtem

Received: 30 August 2011 / Accepted: 4 January 2012 / Published online: 25 January 2012
© Springer-Verlag 2012

Abstract Uniform α-MoO_3 nanobelts were successfully synthesized by the hydrothermal process at 180°C for 20 h of the acidic solutions with different pH values of 0–0.75, adjusted using HCl (conc.). XRD and SEM results revealed that the pH of the precursor solutions played an important role in the phase, impurities, and morphology of the products. At the pH = 0, the perfect α-MoO_3 nanobelts with a few tens of microns long were synthesized. By the TEM characterization, orthorhombic MoO_3 has a distinctive layered structure along the [010] direction, consisting of distorted MoO_6 octahedrons connected by common corners along the [100] direction and common edges along the [001] direction. The electrochemical measurement showed that the α-MoO_3 nanobelts have high specific charge capacity.

A. Phuruangrat (✉)
Department of Materials Science and Technology, Faculty of Science, Prince of Songkla University, Hat Yai, Songkhla 90112, Thailand
e-mail: phuruangrat@hotmail.com
Fax: +66-74-288395

J.S. Chen · X.W. Lou
Division of Bioengineering, School of Chemical and Biomedical Engineering, Nanyang Technological University, 70 Nanyang Drive, Singapore 637457, Singapore

O. Yayapao · T. Thongtem (✉)
Department of Chemistry, Faculty of Science, Chiang Mai University, Chiang Mai 50200, Thailand
e-mail: ttpthongtem@yahoo.com
Fax: +66-53-892277

S. Thongtem
Department of Physics and Materials Science, Faculty of Science, Chiang Mai University, Chiang Mai 50200, Thailand

S. Thongtem · T. Thongtem
Materials Science Research Center, Faculty of Science, Chiang Mai University, Chiang Mai 50200, Thailand

1 Introduction

Lithium ion batteries are used in a wide range of portable electronic devices, including mobile phones, laptop computers, and video cameras [1, 2]. It is well known that the electrochemical properties of lithium-ion batteries strongly depend on the synthetic conditions, such as starting materials, test temperatures, lengths of times, and cooling rate [3]. To improve the capability of batteries to get high power density, utilization of nanostructured materials with small particle size and large surface area is considered, in order to reduce diffusion distance of ions [1, 2], including to increase electrochemical activity and charge/discharge efficiency [4]. It was demonstrated that the rate capabilities of nanostructured electrodes were improved, comparing to their bulk counterparts. The improvement of rate capability is associated with large surface area and short diffusion path length in the nanostructured materials [1, 5]. Especially, one-dimensional nanomaterials have attracted great interest because of their unique physicochemical properties, arising from their high surface area, novel size effects, and significantly enhanced kinetics [6]. The high surface-to-volume ratio and excellent surface activities of 1D nanostructured materials have showed the great interest in their development for the improvement of electrochemical performance for the next generation of power sources [7].

Orthorhombic molybdenum trioxide (α-MoO_3) is built up of asymmetrical MoO_6 octahedrons, interconnected through corner linking along the [100] direction and edge sharing along the [001] direction to form double layers parallel to the (010) plane [8]. Intercalated species such as H^+

and Li^+ invariably assumed to be in interstitial sites within the gaps between zigzag chains and unique layers, bonded by the van der Waals force of attraction, parallel to the (010) plane structure of α-MoO_3 to formed molybdenum bronzes (A_xMoO_3, A = H, Li, Mg, etc.) proceeded via chemical reactions with solids, as well as electrochemically aqueous and nonaqueous media [9, 10]. The intercalation of MoO_3 is generally accompanied by pronounced change in coloration and the reversible extent. The oxide has attracted interest for a number of applications, including secondary batteries and electrochromic devices [9]. In this research, we reported the synthesis of MoO_3 nanobelts by hydrothermal method for use as cathode materials in Li-ion batteries.

2 Experiment

All chemical reagents were analytical grade, purchased from Fisher Scientific Inc. and used without further purification. To synthesize a precursor solution, 9.00 g of commercial MoO_3 was dissolved in 50 ml 35% H_2O_2 with continuous stirring in ice bath for 1 h and kept in a refrigerator for 1 week. Then the precursor solution was heated in hot bath at 80°C for 1 h to decompose H_2O_2. Finally, the orange precursor solution was mixed with deionized water to achieve 250 ml solution and put in a dark box.

To synthesize MoO_3 nanobelts, pH of each 10 ml of the mixtures was adjusted to be different values using HCl (conc.) and stirred for 30 min. They were transferred into 50 ml lab-made Teflon-lined stainless steel autoclaves. The autoclaves were tightly closed and separately heated at 180°C for 20 h in an electric oven. At the completion of the reaction, light-blue precipitates were synthesized, separated by filtration, washed with distilled water to remove possibly remaining ions and ethanol, dried at 80°C in an electric oven for 24 h, and collected for further analyses.

Phase and morphology of the as-synthesized α-MoO_3 nanobelts were characterized by X-ray diffractometer (XRD) of Philips X'Pert MPD using a 1.5405 Å Cu-K_α radiation at 45 kV and 35 mA with a scanning rate of 0.04 deg/s, ranging from 10 to 60 deg. FTIR spectrum was recorded on Perkin Elmer RX Spectrophotometer with KBr as a diluting agent and operated in the range of 400–4,000 cm^{-1} with the resolution of 4 cm^{-1}. Raman spectroscopy, T64000 HORIBA Jobin Yvon, was operated using 50-mW Ar laser with 514.5-nm wavelength. The morphology of the α-MoO_3 nanobelts was investigated by a field emission scanning electron microscopy (FE-SEM), JEOL JSM-6445F using LaB_6 as electron gun with sample coating by gold sputtering. Transmission electron microscopy (TEM) and selected area electron diffraction (SAED) were performed on a JEOL JEM-2100F at 200 kV. A sample for TEM analysis was prepared by sonicating of dry α-MoO_3 nanobelts in ethanol for 15 min and followed by depositing of 3–5 drops of the sample suspension onto a carbon film coated on a copper grid.

The lithium intercalation/deintercalation test was carried out using two-electrode Swagelok-type cell with pure lithium as the counter and reference electrodes at room temperature. The working electrode was a mixture of active material (α-MoO_3 nanobelts), Super P^{TM} Li carbon black, and polyvinylidene difluoride (PVDF) organic binder with a weight ratio of 70:20:10. The electrolyte used for the test was 1 M $LiPF_6$ in a 50:50 w/w mixture of ethylene carbonate and diethyl carbonate. A cell was assembled in an Ar-filled glove box with the moisture and oxygen contents maintained below 1 ppm. Cyclic voltammogram (CV) and electrochemical charge/discharge measurement were performed using a CHI 660 C electrochemical workstation and a NEWARE battery tester, respectively. The cell was charged and discharged at 100 and 400 mA g^{-1} current densities, and the voltage window was fixed between 0.05 and 3.5 V.

3 Results and discussion

Typical XRD patterns over the 2θ of 10–60 deg range of the as-synthesized MoO_3 samples by hydrothermal reaction at 180°C for 20 h of solutions with three pH values are shown in Fig. 1. At the pH = 1, the XRD peaks were not able to be identified the product phase. But for higher acidity with the pH of 0–0.75, all the diffraction peaks were indexed as pure orthorhombic α-MoO_3 of the JCPDS No. 05-0508 [11], with no other impurity detection. It should be noted that the XRD intensity of MoO_3 at pH = 0 shows higher intensity than those of others, indicating the best crystalline product.

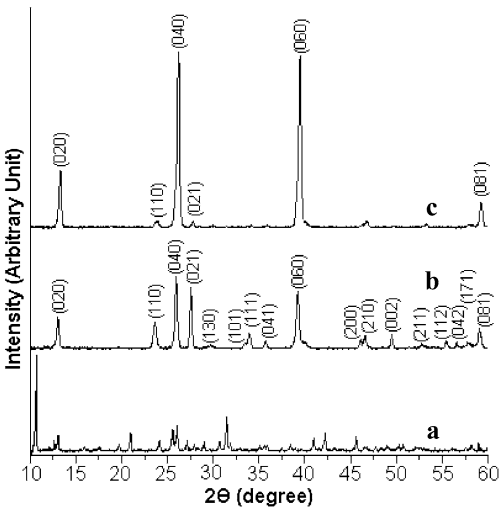


Fig. 1 XRD patterns of α-MoO_3 nanostructure synthesized by the 180°C and 20 h hydrothermal reaction of the solutions with the adjusted pH of (**a**)–(**c**) 1, 0.5, and 0 by HCl (conc.)

The present analysis indicated that pH of the solution played an important role in controlling the purity of the orthorhombic α-MoO_3 phase and its crystalline degree. The high and sharp diffraction peaks revealed not only the presence of α-MoO_3 but also an indication of the well-crystallized phase synthesized by the process. Comparing with the standard XRD pattern, the stronger intensity of the diffraction peaks of $(0k0)$ with $k = 2, 4, 6$ indicates an anisotropic growth in the b axis of the as-synthesized α-MoO_3 phase [12, 13].

Group theory calculation predicted the following irreducible representation at the center of Brillouin zone optical vibration modes of molybdenum trioxide with D_{2h}^{16}(Pbnm) space group as follows:

$$\Gamma = 8A_g + 8B_{1g} + 4B_{2g} + 4B_{3g} + 4A_u + 3B_{1u} + 7B_{2u} + 7B_{3u} \quad (1)$$

where A_g, B_{1g}, B_{2g}, and B_{3g} are Raman-active modes, A_u is an inactive mode, and B_{1u}, B_{2u}, and B_{3u} are infrared-active modes [11, 14–16]. Figure 2a shows a typical Raman spectrum of the MoO_3 nanobelts with the twelve peaks at 99, 129, 160, 198, 220, 246, 292, 339, 377, 666, 815, and 991 cm^{-1} in the wavenumber range of 50–1100 cm^{-1}. The vibration modes, belonging to a highly ordered structure, were very sharp. The peaks at 99 and 129 cm^{-1} were assigned as the B_{2g} with T_a, and B_{3g} with T_c vibration modes, respectively [17]. That at 160 cm^{-1} was the A_g/B_{1g} [17] of the $\delta(O_2Mo_2)_n$ vibration mode [14]. The stronger 198 cm^{-1} peak was assigned as the B_{2g} mode due to the O=Mo=O twisting. Two other weaker peaks at 220 and 246 cm^{-1} were as A_g with R_c vibration mode, and B_{3g} with O=Mo=O twisting mode, respectively [17, 18]. Other peak at 292 cm^{-1} could be assigned as the wagging mode for the double bond O=Mo=O, due to the hydration process [18]. The 339 and 377 cm^{-1} peaks were assigned to be the A_g/B_{1g} mode with the δ O–Mo–O bending, and B_{1g} mode with the δ O–Mo–O scissoring [17]. The 666 cm^{-1} peak was assigned as the B_{2g}/B_{3g} mode with the ν_{as} O–Mo–O asymmetric stretching of triply coordinated oxygen due to the edge-sharing oxygen of the common three octahedrons [17, 18]. The 815 cm^{-1} peak corresponded to the A_g mode with the ν_{as} Mo=O asymmetric stretching [17] for the doubly coordinated oxygen due to the corner-sharing oxygen of the common two octahedrons [18]. The 991 cm^{-1} peak was specified as the A_g mode with the ν_{as} Mo=O asymmetric stretching [17] for the terminal unshared oxygen [18]. The vibration peaks were in good accordance with those reported in literatures for the orthorhombic α-MoO_3 crystalline phase [17–19].

The FTIR spectrum of the as-synthesized α-MoO_3 made as a pellet by KBr mixing was recorded in the wavenumber range of 400–4000 cm^{-1} as shown in Fig. 3. The absorption band at 555 cm^{-1} was attributed to the Mo–O–Mo bending with O shared by three Mo [20] inside octahedrons.

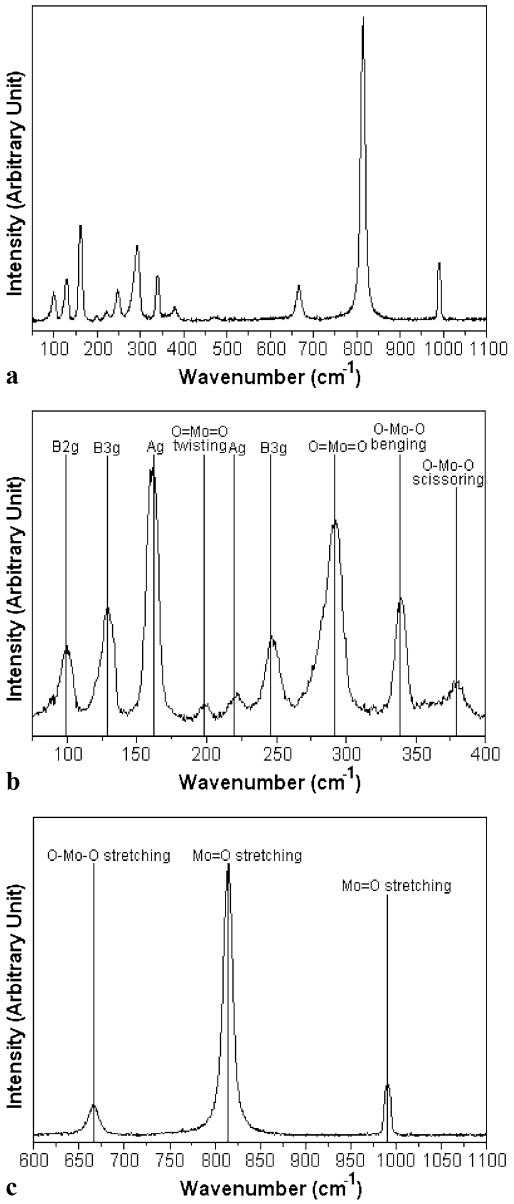


Fig. 2 (**a**) Raman spectrum of α-MoO_3 nanostructure synthesized by the 180°C and 20 h hydrothermal reaction of the solution with the pH = 0. (**b**) and (**c**) are enlarged images of (**a**)

Those at 818 and 875 cm^{-1} were attributed to the vibrations of the Mo–O bridging bonds inside the octahedrons [21]. An intensive band at 997 cm^{-1} was related to the terminal Mo=O bond for crystalline α-MoO_3 [20, 21]. These bands are typical characteristic of crystalline MoO_3, consisting of MoO_6 octahedrons packed as layers [8, 20, 21]. In addition, the bands at 3400 and 1630 cm^{-1} were the indication of hydroxyl groups adsorbed on the octahedral layer surface [20].

SEM images of the products synthesized at 180°C for 20 h in the pH range of 0–1 are showed in Fig. 4. At pH = 1, the product was composed of both nano- and microrods of the impure phases, mixed with one or more impuri-

ties. When the pH of the precursor solution was further reduced by HCl adding to 0.75–0, the α-MoO_3 nanobelts were synthesized. It should be noted that the length of α-MoO_3 nanobelts were controlled by the pH of precursor solutions. Their lengths were from 5 μm to a few tens of microns by increasing the acidity of the precursor solutions. Low magnification SEM image (Fig. 4f) revealed that the product was consisted of large quantity of uniform nanobelts, synthesized at pH = 0. In the present research, it can be concluded that pH of the precursor solutions played the key role in the phase, impurities and morphology of the nanostructured products.

Further characterization of the α-MoO_3 nanobelts was performed by TEM as shown in Fig. 5a. Clearly, the morphology of α-MoO_3 appeared as nanobelts. They were a few tens of microns long and several tens of nanometers wide with smooth facets enclosing their surfaces with sharp edges and oval tips/ends. The SAED patterns (Fig. 5b–d), recorded from three different α-MoO_3 nanobelts, were further indexed [22, 23] as the (100), (101), and (001) planes with [0–10] as zone axis. They were confirmed that these nanobelts were orthorhombic MoO_3 [11] consisting of distorted MoO_6 octahedrons connected by common corners along the [100] direction (a-axis) and common edges along the [001] direction (c-axis) with distinctive layered structure parallel to the (010) plane [8, 12]. Bonding along the [100] direction differs greatly from that along the [001] direction, resulting in the difference of chemical reactivity. The interaction of layers along the [010] direction is the weak van der Waals bonding. In contrast, the interconnection along the [001] direction is by strong covalent bonding. Due to the release of more energy to create strong covalent bond of the nanobelts along the [001] direction, these promote their growth along the [001] direction, with the termination along the [100] and [010] directions. In view of energy, the growth of α-MoO_3 nanobelts was preferential along the c axis [12, 24], enclosed by six faces of the (100) top and bottom each, two (010) sides, and two (001) ends (inset of Fig. 5a).

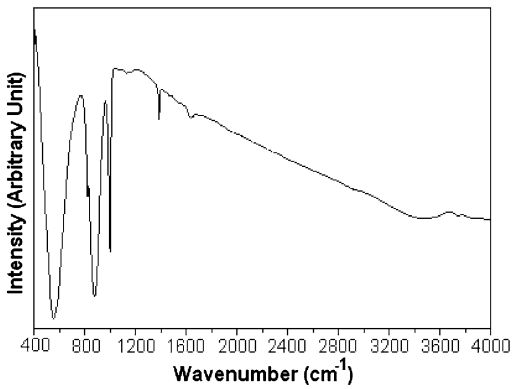


Fig. 3 FTIR spectrum of α-MoO_3 nanostructure synthesized by the 180°C and 20 h hydrothermal reaction of the solution with pH = 0

Possible formation mechanism of α-MoO_3 nanobelts was proposed and discussed. When commercial MoO_3 powder was dissolved in H_2O_2, the peroxomolybdate solution was synthesized:

$$2MoO_3 + 8H_2O_2 \rightarrow 2MoO_2(OH)(OOH) + 6H_2O + 3O_2 \quad (2)$$

During hydrothermal reaction, $MoO_2(OH)(OOH)$ precursors were decomposed by releasing of water and oxygen molecules to form MoO_3 crystal:

$$MoO_2(OH)(OOH) \rightarrow MoO_3 + H_2O + 0.5O_2 \quad (3)$$

At the same time, MoO_6 octahedrons with corner sharing along the [100] direction and edge sharing along the [001] direction including zigzag chains and unique layers parallel to the (010) plane were formed [10, 12].

The electrochemical properties of the as-synthesized α-MoO_3 (Fig. 6) were studied and shown as the cyclic voltammograms recorded at a scanning rate of 0.5 mV/s over the

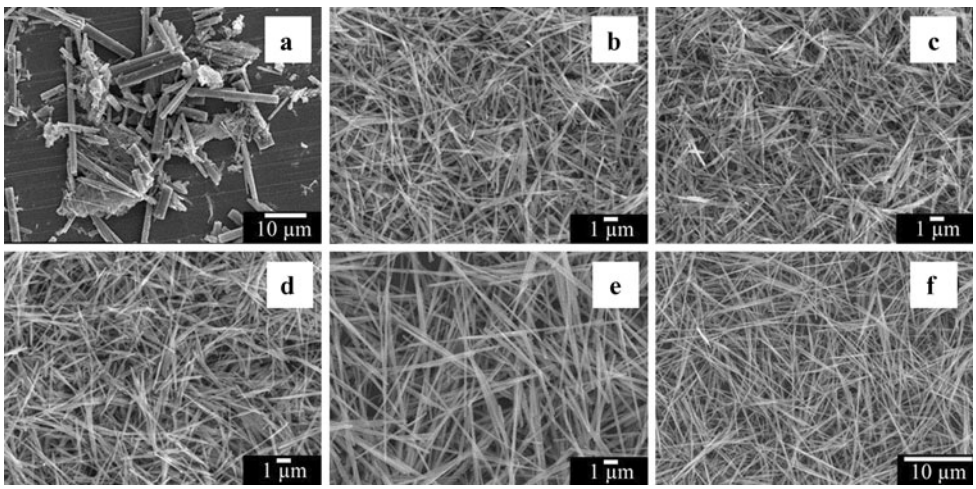


Fig. 4 SEM images of α-MoO_3 nanostructure synthesized by the 180°C and 20 h hydrothermal reaction of the solutions with the pH of (**a**) 1, (**b**) 0.75, (**c**) 0.5, (**d**) 0.25, and (**e**), (**f**) 0

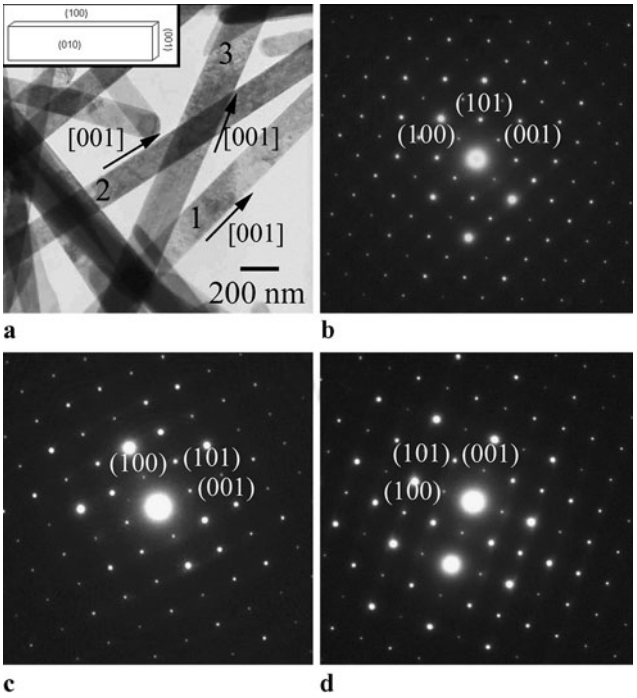


Fig. 5 TEM image and SEAD patterns of α-MoO_3 nanobelts synthesized by the 180°C and 20 h hydrothermal reaction of the solution with pH = 0

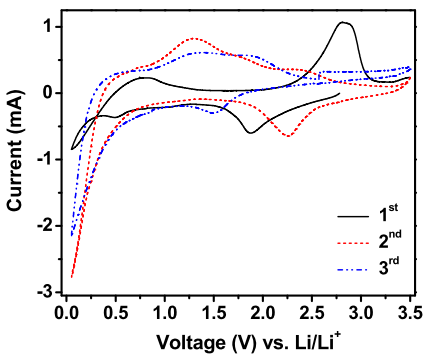


Fig. 6 Three cyclic voltammograms of α-MoO_3 nanobelts synthesized by the 180°C and 20 h hydrothermal reaction of the solution with pH = 0

voltage range of 0.05–3.5 V vs Li/Li^+. The cathodic and anodic peaks of the 1st cycle respectively appeared at 2.85 and 1.86 V, which were attributed to the lithium-ion intercalation into the α-MoO_3 nanobelt electrode and the deintercalation process, as shown by the following:

$$xLi^+ + xe^- + [Mo^{VI}]O_3 \leftrightarrow Li_x[Mo^{(VI-x)}]O_3 \leftrightarrow Li_x[Mo^{VI}_{1-x}Mo^{V}_{x}]O_3 \quad (4)$$

Intercalation/deintercalation of electrons and charge balancing lithium cations led to the formation of $Li_x[Mo^{VI}_{1-x}Mo^{V}_{x}]O_3$. The orthorhombic MoO_3 phase was ready to be intercalated by Li^+ cations to form

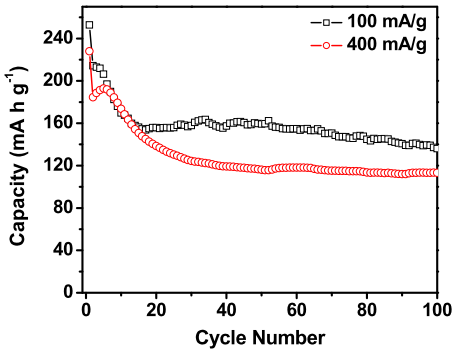


Fig. 7 Cyclic performance of α-MoO_3 nanobelts for charge–discharge current density of 100 and 400 mA g^{-1} (vs Li/Li^+)

$Li_x[Mo^{VI}_{1-x}Mo^{V}_{x}]O_3$, where x could be as large as 1.5, with the reduction of oxidation states of Mo from Mo^{VI} to Mo^{V} [8, 10]. Due to the layered structure of α-MoO_3 nanobelts, Li^+ cations could be intercalated into/deintercalated out of the structure with easily. Cyclically, the peak potential shifted considerably, and the quantity of inserted Li^+ ions decreased. For the 2nd and 3rd cycles, the cathodic and anodic peaks were different from those of the first, because the prior inserted Li^+ ions of single-crystalline MoO_3 nanobelts played an important role in hindering the new Li^+ ions from being inserted into their interiors, which led to a slow and shallow lithiation/intercalation. Furthermore, the passive film formation on the working electrode could result in the irreversible capacity even after the first cycle. Possible formation of Li_2O at the solid-electrolyte interface (SEI) and electrolytic decomposition/reduction, the intercalation/deintercalation process through the subsequent cycles, and the destruction of α-MoO_3 nanostructure as well as the increase in electrical resistance of working electrode influenced the change of the performance of the irreversible capacity of the cyclic process [1, 6, 7].

Figure 7 shows the capacity-cycle number of α-MoO_3 nanobelts as a cathode material for charge–discharge current density of 100 and 400 mA g^{-1}. The present material has high specific capacities of 252 and 227 mA h g^{-1} for the initiation of charge–discharge process, respectively. Its capacities were decreased to 158 and 124 mA h g^{-1} after 30 cycles due to the irreversible capacity associated with the decomposition of the electrolytic solution and the solid-electrolyte interface (SEI) formation [25–27]. They were constant at 160 and 119 mA h g^{-1} afterwards. Upon further processing to 100 cycles, the capacity losses were 11.4 and 4.8% of the corresponding values at 30 cycles, demonstrating a good cyclic stability.

4 Conclusions

In summary, α-MoO_3 nanobelts with the width up to several tens of nanometers and a few tens of microns long

were synthesized by hydrothermal method without the use of templates or catalysts. XRD, SEM, and TEM analyses show orthorhombic single-crystalline structure with preferential growing along the [001] direction. At the initiation of charge–discharge process, the electrochemical measurement showed high specific capacities of 252 and 227 mA h g^{-1} for the current densities of 100 and 400 mA g^{-1}. The nanobelts showed a good stability although the process achieved at 100 cycles.

Acknowledgements We wish to thank the National Nanotechnology Center (NANOTEC), National Science and Technology Development Agency for providing financial support through the project P-10-11345, the Thailand's Office of the Higher Education Commission through the National Research University (NRU) Project, and the Thailand Research Fund through the TRF Research Grant.

References

1. L.C. Yang, Q.S. Gao, Y. Tang, Y.P. Wu, R. Holze, J. Power Sources **179**, 357–360 (2008)
2. H. Habazaki, M. Kiriu, H. Konno, Electrochem. Commun. **8**, 1275–1279 (2006)
3. W.T. Jeong, J.H. Joo, K.S. Lee, J. Alloys Compd. **358**, 294–301 (2003)
4. A. Phuruangrat, T. Thongtem, S. Thongtem, Mater. Lett. **61**, 3805–3808 (2007)
5. M.G. Kim, J. Cho, Adv. Funct. Mater. **19**, 1497–1514 (2009)
6. Y. Cai, S. Liu, X. Yin, Q. Hao, M. Zhang, T. Wang, Physica E **43**, 70–75 (2010)
7. M.S. Park, G.X. Wang, Y.M. Kang, D. Wexler, S.X. Dou, H.K. Liu, Angew. Chem., Int. Ed. **46**, 750–753 (2007)
8. Ch.V.S. Reddy, E.H. Walker Jr., C. Wen, S. Mho, J. Power Sources **183**, 330–333 (2008)
9. J.W. Bullard III, R.L. Smith, Solid State Ion. **160**, 335–349 (2003)
10. L. Zheng, Y. Xu, D. Jin, Y. Xie, Chem. Mater. **21**, 5681–5690 (2009)
11. Powder Diffract. File, JCPDS-ICDD, 12 Campus Boulevard, Newtown Square, PA 19073-3273, USA (2001)
12. S. Wang, Y. Zhang, X. Ma, W. Wang, X. Li, Z. Zhang, Y. Qian, Solid State Commun. **136**, 283–287 (2005)
13. Q.P. Ding, H.B. Huang, J.H. Duan, J.F. Gong, S.G. Yang, X.N. Zhao, Y.W. Du, J. Cryst. Growth **294**, 304–308 (2006)
14. D. Liu, W.W. Lei, J. Hao, D.D. Liu, B.B. Liu, X. Wang, X.H. Chen, Q.L. Cui, G.T. Zou, J. Liu, S. Jiang, J. Appl. Phys. **105**, 023513 (2009)
15. X. Chen, W. Lei, D. Liu, J. Hao, Q. Cui, G. Zou, J. Phys. Chem. C **113**, 21582–21585 (2009)
16. S. Phadungdhitidhada, P. Mangkorntong, S. Choopun, N. Mangkorntong, Ceram. Int. **34**, 1121–1125 (2008)
17. T. Siciliano, A. Tepore, E. Filippo, G. Micocci, M. Tepore, Mater. Chem. Phys. **114**, 687–691 (2009)
18. K. Kalantar-zadeh, J. Tang, M. Wang, K.L. Wang, A. Shailos, K. Galatsis, R. Kojima, V. Strong, A. Lech, W. Wlodarski, R.B. Kaner, Nanoscale **2**, 429–433 (2010)
19. J.V. Silveira, J.A. Batista, G.D. Saraiva, J.M. Filho, A.G.S. Filho, S. Hue, X. Wang, Vib. Spectrosc. **54**, 179–183 (2010)
20. T. Xia, Q. Li, X. Liu, J. Meng, X. Cao, J. Phys. Chem. B **110**, 2006–2012 (2006)
21. I.B. Troitskaia, T.A. Gavrilova, S.A. Gromilov, D.V. Sheglov, V.V. Atuchin, R.S. Vemuri, C.V. Ramana, Mater. Sci. Eng. B **174**, 159–163 (2010)
22. K.W. Andrews, D.J. Dyson, S.R. Keown, *Interpretation of Electron Diffraction Patterns* (Plenum, New York, 1971)
23. Y. Keereeta, T. Thongtem, S. Thongtem, J. Alloys Compd. **509**, 6689–6695 (2011)
24. G. Wei, W. Qin, D. Zhang, G. Wang, R. Kim, K. Zheng, L. Wang, J. Alloys Compd. **481**, 417–421 (2009)
25. M.S. Park, Y.M. Kang, G.X. Wang, S.X. Dou, H.K. Liu, Adv. Funct. Mater. **18**, 455–461 (2008)
26. L. Mai, B. Hu, Y. Qi, Y. Dai, W. Chen, Int. J. Electrochem. Sci. **3**, 216–222 (2008)
27. T.M. McEvoy, K.J. Stevenson, J.T. Hupp, X. Dang, Langmuir **19**, 4316–4326 (2003)

Applied Surface Science 258 (2012) 4971–4976

Contents lists available at SciVerse ScienceDirect

Applied Surface Science

journal homepage: www.elsevier.com/locate/apsusc

Photoemission and energy gap of $MgWO_4$ particles connecting as nanofibers synthesized by electrospinning–calcination combinations

Surangkana Wannapop [a], Titipun Thongtem [b,c,*], Somchai Thongtem [a,c,**]

[a] Department of Physics and Materials Science, Faculty of Science, Chiang Mai University, Chiang Mai 50200, Thailand
[b] Department of Chemistry, Faculty of Science, Chiang Mai University, Chiang Mai 50200, Thailand
[c] Materials Science Research Center, Faculty of Science, Chiang Mai University, Chiang Mai 50200, Thailand

ARTICLE INFO

Article history:
Received 4 November 2011
Received in revised form 10 January 2012
Accepted 23 January 2012
Available online 1 February 2012

Keywords:
$MgWO_4$ nanofibers
Electrospinning
Indirect band gap

ABSTRACT

Mixtures of magnesium acetate tetrahydrate ($(CH_3COO)_2Mg{\cdot}4H_2O$), ammonium tungstate tetrahydrate ($(NH_4)_6W_7O_{24}{\cdot}4H_2O$), and poly(vinyl alcohol) with the molecular weight of 72,000 were electrospun through a +15 kV direct voltage to form fibers on ground flat aluminum foils. The electrospun fibers of 1.5, 3.0, and 4.5 mmol of each starting material containing 1.3 g poly(vinyl alcohol) were further calcined at 500–700 °C for 3 h constant length of time. At 500 and 600 °C calcination, both monoclinic and anorthic phases of $MgWO_4$ particles with different sizes connecting as fibrous assemblies were detected. Upon increasing the calcination temperature to 700 °C, only monoclinic phase of facet nanoparticles interconnecting along the fibrous axes with 4.19 eV indirect band gap and 461 nm photoemission was synthesized. In the present research, formation of $MgWO_4$ molecules as well as nucleation and growth of nanoparticles was also proposed.

© 2012 Elsevier B.V. All rights reserved.

1. Introduction

Two majorities of AWO_4 (A^{2+} = divalent cations) naturally crystallized on Earth are tetragonal scheelite ($I4_1/a$ space group) with large cationic radii (>0.099 nm: Ba, Ca, Sr, Pb, Eu), and monoclinic wolframite ($P2/c$ space group) with small cationic radii (<0.077 nm: Co, Cd, Fe, Mn, Mg, Ni, Zn). For the first, each W^{6+} ion is surrounded by four O^{2-} ions forming $(WO_4)^{2-}$ tetrahedral unit. But for the second, each W^{6+} ion is surrounded by six O^{2-} ions forming $(WO_6)^{6-}$ octahedral complex [1–6]. $MgWO_4$ is a semiconducting material, containing both light (Mg and O) and heavy (W) elements. It is very interesting for different technological applications: luminescence, scintillation [7,8], tunable microwave applications [9] and tunable solid state lasers [10]. Thus the study of photonic absorption and emission of $MgWO_4$ particles interconnecting as fiber-like assemblies became increasingly attractive for a number of applications.

Basically, electrospinning equipment is composed of three components: a direct current (d.c.) power supply, a long hollow needle and an electrical conducting screen. During electrospinning, a drop of polymeric solution at the tip of the hollow needle is charged by a positive d.c. high voltage. The mutual positive charge repulsion on the polymeric droplet is created. When the applied d.c. voltage is increased, the liquid droplet is stretched to be a conical shape, known as Taylor cone. Upon further increasing the d.c. voltage until it is sufficiently high, the repulsive force overcomes the surface tension of the polymeric liquid, and the jet of liquid is ejected out of the Taylor cone. Meanwhile, the liquid jet evaporates and solidifies, leaving behind the polymeric fibers deposited on the ground conducting screen [11,12].

There are several parameters playing the role in electrospun fibers: (a) variable parameters of electrospinning equipment (applied voltage at the needle tips as well as electric field inside fibers, pressure used to push the liquid out of the hollow needles, and a distance between the needle tip and ground conducting screen), (b) solution properties (viscosity, surface tension, elasticity and conductivity) and (c) ambient parameters (temperature, humidity and wind blow). These can play the role in the surface morphologies of electrospun fibers, fibrous diameter, number of beads including their shape and size, and defects (pores) on fibers [11,12]. Inclination (vertical or horizontal) of the hollow needle also has the influence on electrospun fibers.

To the best of our knowledge, no $MgWO_4$ nanofibers have ever been synthesized by electrospinning and high temperature calcination. It is therefore for us to use the mixture of inorganic and organic salts dissolving in poly(vinyl alcohol) (PVA) to synthesize inorganic–polymeric fibers, which would transform into nanofibers by subsequent calcination at high temperature. This success may

* Corresponding author at: Department of Chemistry, Faculty of Science, Chiang Mai University, Chiang Mai 50200, Thailand. Tel.: +66 53 943344; fax: +66 53 892277.
** Corresponding author at: Department of Physics and Materials Science, Faculty of Science, Chiang Mai University, Chiang Mai 50200, Thailand. Tel.: +66 53 941924; fax: +66 53 943445.
E-mail addresses: ttpthongtem@yahoo.com, ttpthongtem@gmail.com (T. Thongtem), schthongtem@yahoo.com (S. Thongtem).

0169-4332/$ – see front matter © 2012 Elsevier B.V. All rights reserved.
doi:10.1016/j.apsusc.2012.01.133

Table 1
Product codes of the present research.

Product code	$(CH_3COO)_2Mg{\cdot}4H_2O$ (mmol)	$(NH_4)_6W_7O_{24}{\cdot}4H_2O$ (mmol)	PVA (g)	Calcination temperature (°C)/time (h)
P1	1.5	1.5	0.9	None
P2	1.5	1.5	1.1	None
P3	1.5	1.5	1.3	None
P3C1	1.5	1.5	1.3	500/3
P4	3.0	3.0	1.3	None
P4C1	3.0	3.0	1.3	500/3
P5	4.5	4.5	1.3	None
P5C1	4.5	4.5	1.3	500/3
P5C2	4.5	4.5	1.3	600/3
P5C3	4.5	4.5	1.3	700/3

lead to new industrial process by direct high voltage electrospinning.

2. Experiment

Different contents of magnesium acetate tetrahydrate ($(CH_3COO)_2Mg{\cdot}4H_2O$), ammonium (meta) tungstate tetrahydrate ($(NH_4)_6W_7O_{24}{\cdot}4H_2O$), and poly(vinyl alcohol) (PVA, 72,000 MW) were thoroughly mixed by dissolving in 30 ml deionized water each with 30 min stirring. Each of these mixtures was electrospun through a horizontal plastic syringe, biased with a +15 kV direct voltage to form fibers on a ground flat aluminum foil placed 15 cm apart. The fibers were also calcined at 500, 600, and 700 °C for 3 h constant length of time, and left them cool down to room

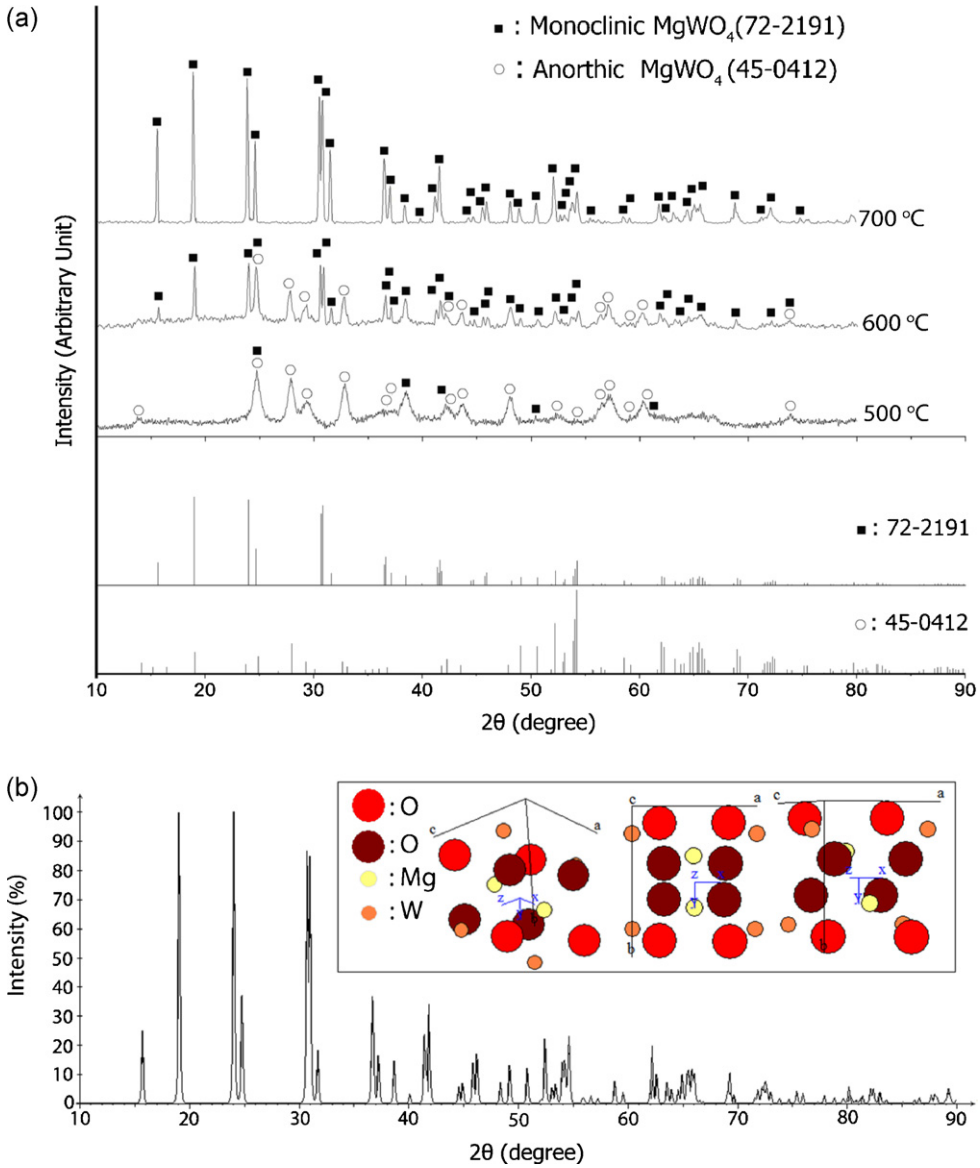


Fig. 1. (a) XRD spectra of the P5C1, P5C2 and P5C3 products, compared with the anorthic and monoclinic $MgWO_4$ phases. (b) Simulated XRD pattern and crystal structure of monoclinic $MgWO_4$.

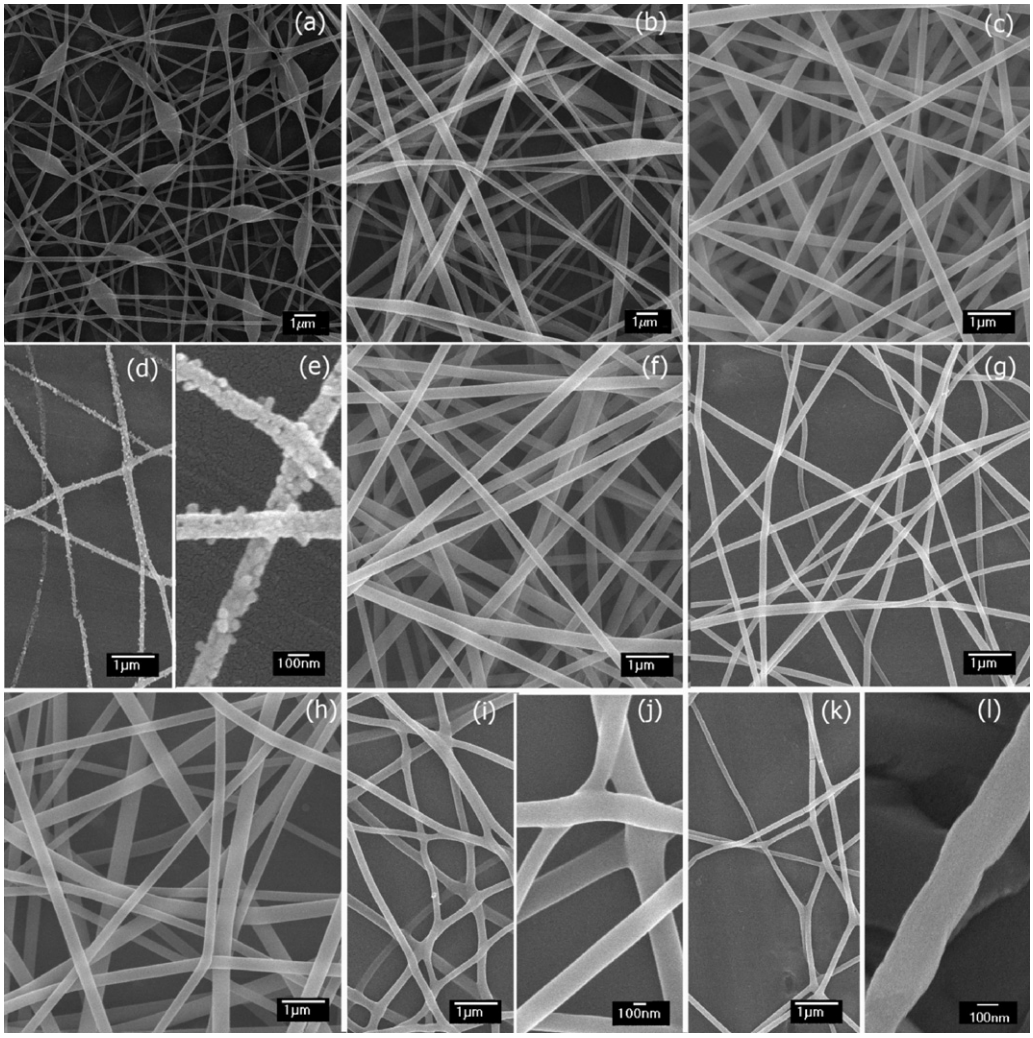


Fig. 2. SEM images of the (a) P1, (b) P2, (c) P3, (d and e) P3C1, (f) P4, (g) P4C1, (h) P5, (i and j) P5C1, (k) P5C2 and (l) P5C3 products.

temperature. The products synthesized from different contents of the starting materials with and without subsequent calcination at high temperatures were summarized and encoded (Table 1). These products were further characterized by X-ray diffractometer (XRD, SIEMENS D500) operating at 20 kV 15 mA, and using Cu-K_α line, in combination with the database of the Joint Committee on Powder Diffraction Standards (JCPDS) [13]; scanning electron microscope (SEM, JEOL JSM-6335F) operating at 15 kV; transmission electron microscope (TEM, JEOL JEM-2010), high resolution transmission electron microscope (HRTEM) and selected area electron diffractometer (SAED) operating at 200 kV; atomic force microscope (AFM, NanoScope IIIa, MMAFML N, Veeco) with silicon tip driven at a frequency of 200–300 kHz tapping mode; UV–visible spectrometer (Lambda 25 PerkinElmer) using a UV lamp with the resolution of 1 nm; and photoluminescence (PL) spectrometer (LS 50B PerkinElmer) using a 290 nm excitation wavelength at room temperature.

3. Results and discussion

3.1. XRD

XRD spectra (Fig. 1a) of the P5C1, P5C2 and P5C3 products show that chemical reactions of the starting materials were completed. $MgWO_4$ with anorthic (JCPDS no. 45-0412) and monoclinic (JCPDS no. 72-2191) [13] were successfully synthesized. During electrospinning by a +15 kV direct voltage, $(CH_3COO)_2Mg{\cdot}4H_2O$ reacted with $(NH_4)_6W_7O_{24}{\cdot}4H_2O$ to synthesize $MgWO_4$ molecules, blended in the PVA template.

$$7Mg^{2+} + (W_7O_{24})^{6-} + 4H_2O \rightarrow 7MgWO_4 + 8H^+ \quad (1)$$

$(CH_3COO)_2Mg{\cdot}4H_2O$ and $(NH_4)_6W_7O_{24}{\cdot}4H_2O$ could remain in the template but their concentrations were too low to be detected by XRD. By calcination at 500 °C for 3 h, PVA evaporated and decomposed. The PVA was no longer detected at 494 °C and above [14]. At the same time, the $(CH_3COO)_2Mg{\cdot}4H_2O$ and $(NH_4)_6W_7O_{24}{\cdot}4H_2O$ residues combined to form $MgWO_4$ molecules, which nucleated and grew to be particles (mixed phases) with different orientations. Upon increasing of the calcination temperature to 600 °C, the anorthic phase became lessened, with the greater extent of the monoclinic one. At 700 °C and 3 h calcination, only the monoclinic crystal structure was detected, and the product was the best crystal – the atoms resided in perfect crystal lattice. Its calculated lattice parameters [15] (Table 2) were very close to those of the standard values [13], which supported the presence of $MgWO_4$ with monoclinic crystal system. By using the Scherrer formula [15], crystallite sizes of the P5C1, P5C2 and P5C3 products were calculated and summarized in Table 2. Crystallite sizes of both anorthic and monoclinic phases were increased

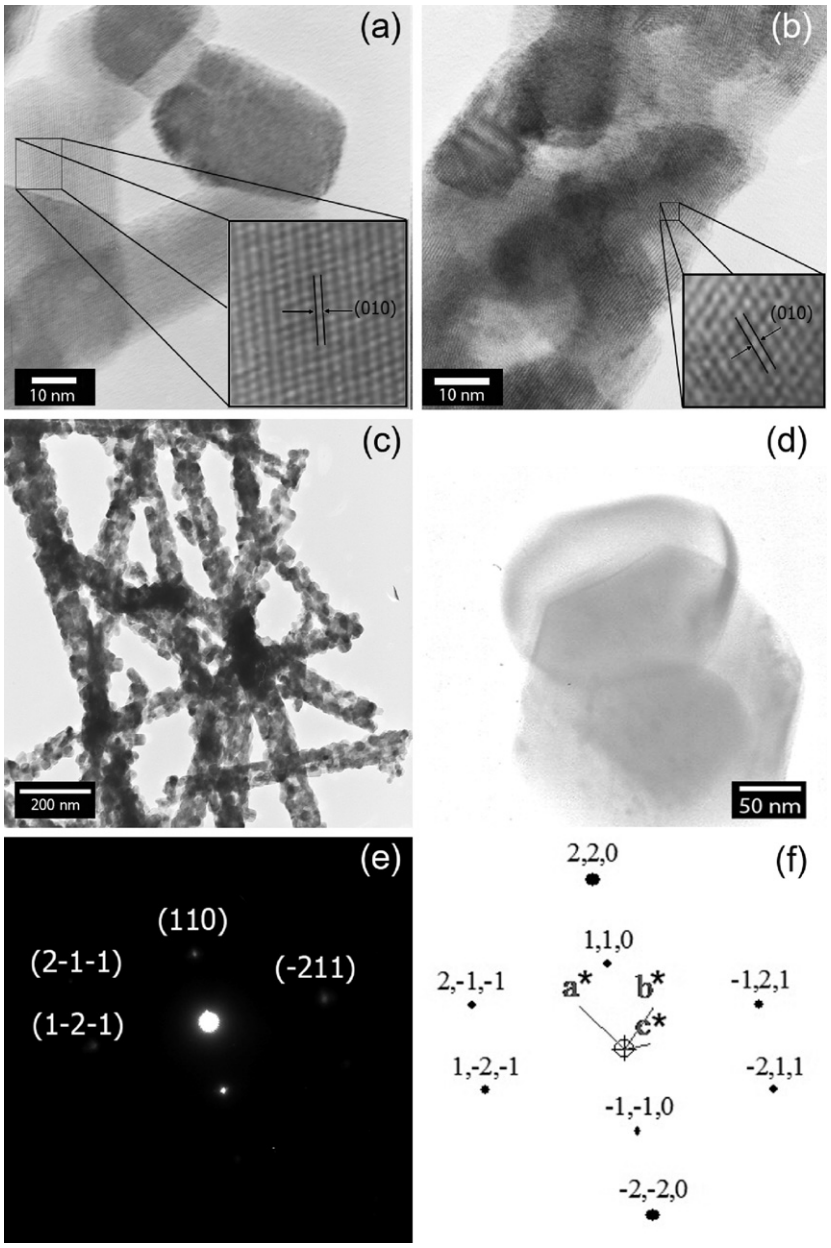


Fig. 3. TEM and HRTEM images, and SAED and simulated patterns of the (a) P3C1, (b and c) P5C1 and (d–f) P5C3 products.

with the increasing in the calcination temperatures, but the rate of increasing for the first was slower than that for the second. It should be noted that the anorthic crystallites were smaller than the monoclinic ones.

XRD pattern of monoclinic $MgWO_4$ was simulated [16] as shown in Fig. 1b. In the present research, the 2θ Bragg's angles and peak intensities of the experiment, simulation and JCPDS database were in good accordance. Simulated crystal structure of monoclinic $MgWO_4$ (inset of Fig. 1b) was explained as network of interconnecting zigzag chains of alternate MgO_6 and WO_6 distorted octahedrons running along the [0 0 1] direction, with Mg ions in the O ion polyhedrons [10].

Table 2
Lattice parameters and crystallite sizes of the P5C1, P5C2 and P5C3 products.

Product	Lattice parameter (nm)			Crystallite size (nm)	
	a	*b*	*c*	Anorthic	Monoclinic
P5C1	–	–	–	15.0	23.0
P5C2	–	–	–	29.6	68.8
P5C3	0.465	0.564	0.490	–	69.8

3.2. SEM, TEM, HRTEM, SAED and AFM

SEM, TEM and HRTEM images (Figs. 2 and 3a–d) show external surfaces of the products electrospun from different contents of the starting materials, before and after calcination at 500, 600, and 700 °C for 3 h constant length of time. Before calcination, some beads were detected on the P1 and P2 products (Fig. 2a and b) but no longer detected on the P3 product (Fig. 2c). Upon increasing the amount of PVA, the beads became lessened. Finally, they were no longer detected. These showed that the increase of viscosity of the mixtures played the role in the absence of beads on the electrospun fibers. The mixture of 1.5 mmol $(CH_3COO)_2Mg{\cdot}4H_2O$), 1.5 mmol $(NH_4)_6W_7O_{24}{\cdot}4H_2O$ and 1.3 g PVA has the viscosity and density high enough to form the bead-free electrospun fibers. By

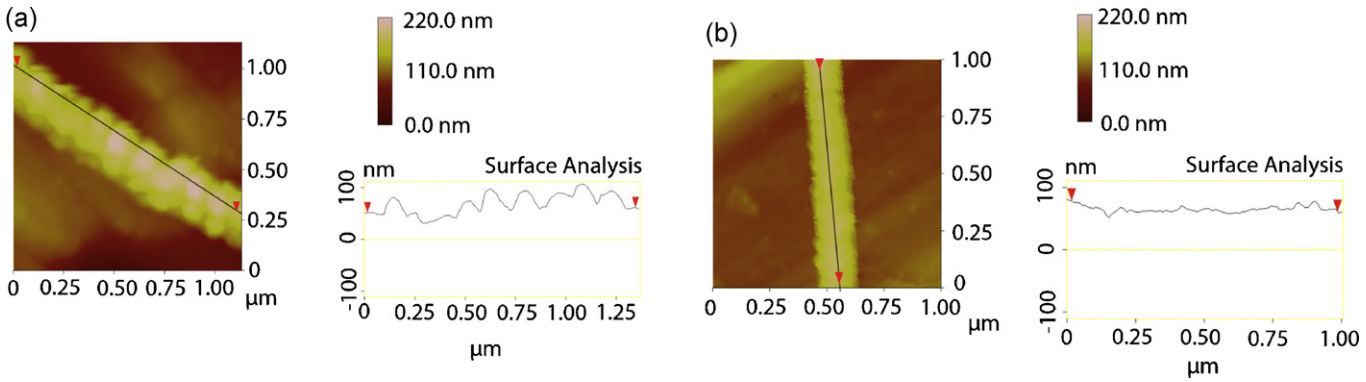


Fig. 4. AFM images and surface roughness of the (a) P4C1 and (b) P5C1 products.

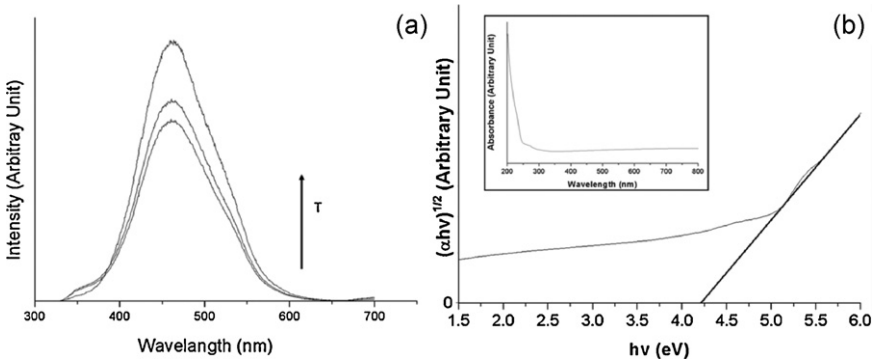


Fig. 5. (a) PL emission of the P5C1, P5C2 and P5C3 products, and (b) UV–visible absorption of the P5C3 product.

increasing the amount of the starting materials but keeping the amount of PVA constant at 1.3 g, the products were still to be bead-free electrospun fibers (Fig. 2f and h). $MgWO_4$ molecules and nanoparticles in the fibers became denser, proved by the P3C1, P4C1 and P5C1 products (Figs. 2d, e, g, i, j, and 3a–c). Surfaces of the fibers were roughened. The products were composed of interconnecting of facet nanoparticles along the fibrous axes. Upon increasing the calcination temperature of the P5C1 product from 500 °C to 600 °C (P5C2) and 700 °C (P5C3) (Figs. 2k, l, and 3d), both the nanoparticles and fibers were enlarged. A number of the (0 1 0) crystallographic planes of typical nanoparticles of the P3C1 and P5C1 products (insets of Fig. 3a and b) were detected by HRTEM – revealing the presence of crystalline $MgWO_4$ in the fibers. A SAED pattern of the P5C3 product (Fig. 3e) corresponded to the database of the monoclinic $MgWO_4$ [13], and the pattern obtained by simulation (Fig. 3f) [16].

AFM images and surface roughness of the P4C1 and P5C1 products are shown in Fig. 4. After 500 °C and 3 h calcination, the fibers were very rough and uneven, which reflected on their surface energy. Root mean square (RMS) values and maximum heights were 19.671 nm and 60.275 nm for the first, and 4.761 nm and 27.421 nm for the second, respectively. Each of these products contained particles with different sizes connecting as fiber-like assembly – in accordance with the above SEM and TEM analyses.

3.3. PL emission and UV–visible absorption

By using 290 nm excitation wavelength, PL emissions (Fig. 5a) of the P5C1, P5C2 and P5C3 products were detected at 461 nm – in accordance with the report of Danevich et al. [8]. The different emission was caused by the distorted $(WO_6)^{6-}$ octahedrons, Jahn–Teller effect, and the perturbation of $(WO_4)^{2-}$ tetrahedrons induced by defects [17].

UV–visible absorption (Fig. 5b) of P5C3 indicated an exponential decreasing of photonic absorption attenuated through the product. Its indirect E_g was determined, by extrapolating linear portion of the curve to zero absorption, to be 4.19 eV – very close to that reported by Lacomba-Perales et al. [1], and Kim et al. [18]. Particle-sizes and morphologies could play the role in the absorbance characteristics [19,20], having the influence on the energy gap.

4. Conclusions

The mixture of 4.5 mmol $(CH_3COO)_2Mg{\cdot}4H_2O$, 4.5 mmol $(NH_4)_6W_7O_{24}{\cdot}4H_2O$ and 1.3 g PVA was electrospun through a +15 kV direct voltage to form $MgWO_4$–PVA fibers, which were followed by 700 °C calcination for 3 h to form interconnecting facet nanoparticles of $MgWO_4$ along the fibrous axes with 4.19 eV indirect band gap and 461 nm PL emission – the promising nanofibers for a variety of applications.

Acknowledgements

We wish to thank the National Nanotechnology Center (NANOTEC), National Science and Technology Development Agency, Thailand, for providing financial support through the project code: P-10-11345; the Thailand's Office of the Higher Education Commission through the National Research University Project, and the Strategic Scholarships for Frontier Research Network of the Joint Ph.D. Research Program; and the Thailand Research Fund (TRF) through the TRF Research Grant, including the Graduate School of Chiang Mai University through the general support.

References

[1] R. Lacomba-Perales, J. Ruiz-Fuertes, D. Errandonea, D. Martínez-García, A. Segura, Optical absorption of divalent metal tungstates: correlation between the band-gap energy and the cation ionic radius, EPL 83 (2008), 37002 (5pp).

[2] Z. Lou, M. Cocivera, Cathodoluminescence of $CaWO_4$ and $SrWO_4$ thin films prepared by spray pyrolysis, Mater. Res. Bull. 37 (2002) 1573–1582.

[3] S.H. Yu, B. Liu, M.S. Mo, J.H. Huang, X.M. Liu, Y.T. Qian, General synthesis of single-crystal tungstate nanorods/nanowires: a facile, low-temperature solution approach, Adv. Funct. Mater. 13 (2003) 639–647.

[4] A. Golubović, R. Gajić, Z. Dohčević-Mitrović, S. Nikolić, Nd induced changes in IR spectra of $CaWO_4$ single crystals, J. Alloys Compd. 415 (2006) 16–22.

[5] X. Wang, H. Xu, H. Wang, H. Yan, Morphology-controlled $BaWO_4$ powders via a template-free precipitation technique, J. Cryst. Growth 284 (2005) 254–261.

[6] J.T. Kloprogge, M.L. Weier, L.V. Duong, R.L. Frost, Microwave-assisted synthesis and characterisation of divalent metal tungstate nanocrystalline minerals: ferberite, hübnerite, sanmartinite, scheelite and stolzite, Mater. Chem. Phys. 88 (2004) 438–443.

[7] V.B. Mikhailik, H. Kraus, V. Kapustyanyk, M. Panasyuk, Y. Prots, V. Tsybulskyi, L. Vasylechko, Structure, luminescence and scintillation properties of the $MgWO_4$–$MgMoO_4$ system, J. Phys.: Condens. Matter 20 (2008) 365219 (8 pp).

[8] F.A. Danevich, D.M. Chernyak, A.M. Dubovik, B.V. Grinyov, S. Henry, H. Kraus, V.M. Kudovbenko, V.B. Mikhailik, L.L. Nagornaya, R.B. Podviyanuk, O.G. Polischuk, I.A. Tupitsyna, Y.Y. Vostretsov, $MgWO_4$ – a new crystal scintillator, Nucl. Instrum. Methods Phys. Res. A 608 (2009) 107–115.

[9] M. Zhang, J. Zhai, J. Zhang, H. Jiang, X. Yao, Effect of $MgWO_4$ content on properties of $Ba_{0.5}Sr_{0.5}TiO_3$ composite ceramics for tunable microwave applications, Mater. Res. Bull. 46 (2011) 1102–1106.

[10] E. Cavalli, A. Belletti, M.G. Brik, Optical spectra and energy levels of the Cr^{3+} ions in MWO_4 (M = Mg, Zn, Cd) and $MgMoO_4$ crystals, J. Phys. Chem. Solids 69 (2008) 29–34.

[11] J.M. Deitzel, J. Kleinmeyer, D. Harris, N.C.B. Tan, The effect of processing variables on the morphology of electrospun nanofibers and textiles, Polymer 42 (2001) 261–272.

[12] Z.M. Huang, Y.Z. Zhang, M. Kotaki, S. Ramakrishna, A review on polymer nanofibers by electrospinning and their applications in nanocomposites, Compos. Sci. Technol. 63 (2003) 2223–2253.

[13] Powder Diffract. File, JCPDS-ICDD, 12 Campus Boulevard, Newtown Square, PA 19073-3273, USA, 2001.

[14] S. Wannapop, T. Thongtem, S. Thongtem, Characterization of $SrWO_4$–PVA and $SrWO_4$ spiders' webs synthesized by electrospinning, Ceram. Int. 37 (2011) 3499–3507.

[15] C. Suryanarayana, M.G. Norton, X-ray Diffraction: A Practical Approach, Plenum Press, New York, 1998.

[16] C. Boudias, D. Monceau, CaRIne Crystallography 3.1, Divergent S.A., Centre de Transfert, 60200 Compiègne, France, 1989–1998.

[17] V.B. Mikhailik, H. Kraus, D. Wahl, H. Ehrenberg, M.S. Mykhaylyk, Optical and luminescence studies of $ZnMoO_4$ using vacuum ultraviolet synchrotron radiation, Nucl. Instrum. Methods Phys. Res. A 562 (2006) 513–516.

[18] D.W. Kim, I.S. Cho, S.S. Shin, S. Lee, T.H. Noh, D.H. Kim, H.S. Jung, K.S. Hong, Electronic band structures and photovoltaic properties of MWO_4 (M = Zn, Mg, Ca, Sr) compounds, J. Solid State Chem. 184 (2011) 2103–2107.

[19] M. Hojamberdiev, G. Zhu, Y. Xu, Template-free synthesis of $ZnWO_4$ powders via hydrothermal process in a wide pH range, Mater. Res. Bull. 45 (2010) 1934–1940.

[20] Y. Keereeta, T. Thongtem, S. Thongtem, Fabrication of $ZnWO_4$ nanofibers by a high direct voltage electrospinning process, J. Alloys Compd. 509 (2011) 6689–6695.

Journal of Alloys and Compounds 516 (2012) 172–178

Contents lists available at SciVerse ScienceDirect

Journal of Alloys and Compounds

journal homepage: www.elsevier.com/locate/jallcom

Free-polymer controlling morphology of α-MoO_3 nanobelts by a facile hydrothermal synthesis, their electrochemistry for hydrogen evolution reactions and optical properties

Hathai Sinaim [a], Dong Jin Ham [b], Jae Sung Lee [b], Anukorn Phuruangrat [c,*], Somchai Thongtem [d,e], Titipun Thongtem [a,e,**]

[a] Department of Chemistry, Faculty of Science, Chiang Mai University, Chiang Mai 50200, Thailand
[b] Eco-friendly Catalysis and Energy Laboratory (NRL), Department of Chemical Engineering, School of Environmental Science and Engineering, Pohang University of Science and Technology, San 31, Hyoja-dong, Pohang 790-784, Republic of Korea
[c] Department of Materials Science and Technology, Faculty of Science, Prince of Songkla University, Hat Yai, Songkhla 90112, Thailand
[d] Department of Physics and Materials Science, Faculty of Science, Chiang Mai University, Chiang Mai 50200, Thailand
[e] Materials Science Research Center, Faculty of Science, Chiang Mai University, Chiang Mai 50200, Thailand

ARTICLE INFO

Article history:
Received 1 January 2011
Received in revised form 4 December 2011
Accepted 11 December 2011
Available online 19 December 2011

Keywords:
Hydrothermal synthesis
α-MoO_3 nanobelts
Hydrogen evolution reactions
Optical properties

ABSTRACT

Orthorhombic molybdenum oxide (α-MoO_3) nanobelts were successfully synthesized by the 100–180 °C and 2–20 h hydrothermal reactions of $(NH_4)_6Mo_7O_{24}{\cdot}4H_2O$ solutions containing 15 ml 2 M acid (HNO_3, H_2SO_4 or HCl) with no surfactant and template adding. These products were characterized by X-ray diffraction (XRD), Fourier transform infrared (FTIR) and Raman spectroscopy, and electron microscopy (EM). In the present research, the product synthesized by the 180 °C and 20 h hydrothermal reaction of the solution containing HNO_3 was α-MoO_3 nanobelts with >10 μm long and <200 nm wide. Electrochemistry for hydrogen evolution reactions (HER) and optical properties of the as-synthesized α-MoO_3 nanobelts were characterized by linear sweep voltammetry (LSV) and Tafel plot, including UV–vis and photoluminescence (PL) spectroscopy. These imply that α-MoO_3 nanobelts show satisfied performance for HER, with the 3.75 eV direct allowed band gap (E_g) due to the charged transition of $O_{2p} \rightarrow Mo_{4d}$, including the emission of 437 nm wavelength at room temperature.

© 2011 Elsevier B.V. All rights reserved.

1. Introduction

Over the past decades, scientists and engineers have focused on the fabrication of one-dimensional (1-D) inorganic nanomaterials such as nanowires, nanobelts and nanotubes because these materials exhibit novel chemical and physical properties comparing to their corresponding bulks, owing to the reduced size and large surface area to volume ratio [1].

Among layer inorganic materials, molybdenum oxide (MoO_3) with very interesting catalytic, photochromic and electrochromic properties has been widely used as catalytic material, sensors, smart windows, lubricants and electrochemical storages [1–3]. MoO_3 has two basic structures: the thermodynamically stable orthorhombic MoO_3 (α-type), and the metastable monoclinic MoO_3 (β-type) with ReO_3-type structure. The most important characteristic of α-MoO_3 is its structural anisotropy, considered as a layered structure. Each layer is composed of two sub-layers, formed by corner sharing of octahedrons along the [1 0 0] direction, with edge sharing of octahedrons along the [0 0 1] direction. Alternating stacks of these layered sheets, bound by the van der Waals interaction along the [0 1 0] direction, lead to the formation of α-MoO_3. One might take the benefit of an intrinsic structural anisotropy of α-MoO_3 for tuning its properties by interlayer structural modification and annealing [3,4]. Moreover, α-MoO_3 is a wide band gap (2.6 eV) n-type semiconductor [5], and has been used as a catalyst for hydrogen evolution reaction (HER) [6].

There are a number of reports on the synthesis of 1D MoO_3 nanomaterial which shows a better of both chemical and physical properties than other morphologies. Among them, α-MoO_3 nanorods are promising cathodes in reversible lithium ion batteries. MoO_3 nanobelt films are excellent field emitters. MoO_3 nanorods have been found to be a valuable candidate for use as gas sensors owing to its sensitivity to nitrogen dioxide and anhydrous

* Corresponding author. Tel.: +66 074 288 374; fax: +66 074 288 395.
** Corresponding author at: Department of Chemistry, Faculty of Science, Chiang Mai University, Chiang Mai 50200, Thailand. Tel. +66 053 943 344; fax +66 053 892 277.
E-mail addresses: phuruangrat@hotmail.com (A. Phuruangrat), ttpthongtem@yahoo.com (T. Thongtem).

0925-8388/$ – see front matter © 2011 Elsevier B.V. All rights reserved.
doi:10.1016/j.jallcom.2011.12.024

ammonia, including carbon monoxide and methanol at a working temperature of 200 °C and 40% relative humidity [7].

Nanostructured materials can be synthesized by both physical and chemical methods: solid-state reaction and wet chemical method. Nevertheless, the products obtained from solid-state reactions are irregular morphologies, large particle-sized distribution and non-homogeneous phase. On the other hand, advanced wet chemical method has been succeeded in synthesizing highly purified metal oxides and superconductors with multiple cationic compositions [8]. They include sonochemistry [2], microwave-assisted hydrothermal synthesis [6], spray pyrolysis [9], and hydrothermal reaction [10]. These methods are able to synthesize better crystal quality at lower growth temperature than the solid state route.

In the present research, α-MoO_3 nanostructure was synthesized using a facile hydrothermal process. The influences of different reaction temperatures, holding reaction time and type of acids on phase, morphology and formation mechanism of α-MoO_3 nanostructures were studied. The electrochemistry for hydrogen evolution reaction (HER) and optical properties of the products were also investigated.

2. Experimental

2.1. Synthesis of α-MoO_3 nanobelts

All chemicals with analytical grade, purchased from Fisher Scientific Inc., were used without further purification. First, 0.005 mole ammonium heptamolybdate tetrahydrate ($(NH_4)_6Mo_7O_{24}{\cdot}4H_2O$) was dissolved in 20 ml deionized water with 30 min continuous stirring at room temperature. Second, 15 ml 2 M acid (HNO_3, H_2SO_4 or HCl) was added to this colorless solution, and followed by 30 min stirring. Third, these three mixtures were independently transferred into three lab-made Teflon-lined stainless steel autoclaves to 50 ml capacity. The autoclaves were tightly closed and heated at 100–180 °C for 2–20 h in an electric oven. Finally, light-blue precipitates were synthesized, separated by filtration, washed with distilled water for removal of ionic remains in the final products and followed with ethanol to facilitate water evaporation, and dried at 80 °C in an electric oven for 24 h. Phase, morphology and vibration modes, including electrochemical and optical properties of the products were characterized by a variety of techniques.

2.2. Physical, electrochemical and optical properties of α-MoO_3 nanobelts

The as-synthesized α-MoO_3 nanobelts were characterized by X-ray diffractometer (XRD) on Philips X'Pert MPD using a CuK_α radiation at 45 kV and 35 mA with a scanning rate of 0.04°/s ranging from 10 to 60°. The XRD raw data were interpreted using X'Pert HighScore software. The morphology of the α-MoO_3 nanobelts was investigated by a low vacuum scanning electron microscopy (LV-SEM), JEOL, JSM-5910LV with W as an electron gun. The samples used for LV-SEM were sonicated in ethanol, each of which was subsequently dropped on stubs. Leave them dried in an ambient atmosphere for 24 h, and coat them by gold sputtering. Transmission electron microscopy (TEM) and selected area electron diffraction (SAED) were performed by a JEOL, JEM-2100F at 200 kV. The samples used for TEM analysis were prepared by sonicating of dried products in ethanol for 15 min and depositing 3–5 drops of the suspensions onto carbon foils supported on copper grids. FTIR spectra were recorded on Perkin Elmer Spectrum RX FTIR spectrophotometer with KBr as a diluting agent and operated in the range of 400–4000 cm^{-1} with the resolution of 4 cm^{-1}. Raman spectroscopy, T64000 HORIBA JOBIN YVON, was operated using 30 mW He–Ne laser with 632.8 nm wavelength.

The hydrogen evolution reaction (HER) was tested by a Princeton Applied Research (PAR) for linear sweep potential from −0.20 to 0.20 V (vs RHE) with a scanning rate of 50 mV s^{-1}, using a glassy carbon, Pt wire and Ag/AgCl (3 M NaCl) as working, counter and reference electrodes, respectively, in 1 M H_2SO_4 solution as electrolyte. Working electrode was prepared as explained in the previous reports [6,11].

Absorption property of the as-synthesized α-MoO_3 nanobelts was studied in colloid solutions on Perkin Elmer, Lambda-25 UV–visible (UV–vis) spectrometer in 250–800 nm wavelength range. Photoluminescent (PL) property was investigated by LS50B Perkin Elmer fluorescence spectrophotometer using 337 nm excitation wavelength at room temperature. Each sample for photonic testing was prepared by dissolving 0.02 g product in 100 ml ethanol and followed by 10 min sonication.

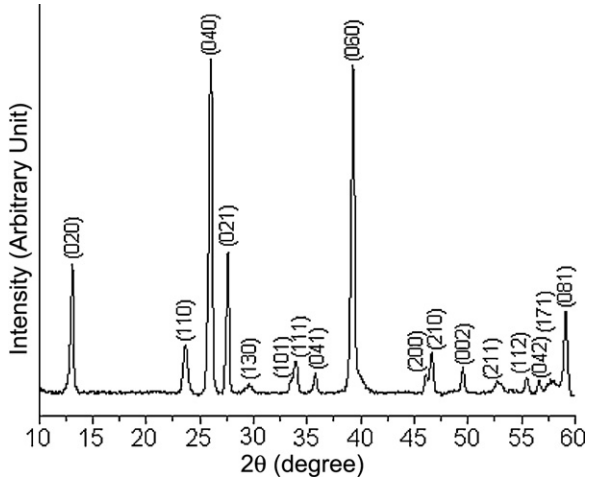


Fig. 1. XRD pattern of α-MoO_3 nanostructure synthesized by hydrothermal reaction at 180 °C for 20 h.

3. Results and discussion

3.1. Characterization of α-MoO_3 nanobelts

The as-synthesized MoO_3 product was characterized by XRD in order to identify the phase and structure of the product. Fig. 1 shows XRD pattern of the MoO_3 product synthesized by hydrothermal method under 180 °C for 20 h using $(NH_4)_6Mo_7O_{24}{\cdot}4H_2O$ as molybdenum source and followed by 15 ml 2 M HNO_3 addition. All the diffraction peaks of the product were identified to correspond with orthorhombic MoO_3 (α-MoO_3) of the JCPDS No. 05-0508 [12]. It should be noted that the intensities in the family (0 k 0) planes with k = 2, 4, and 6 were higher than those of the standard which revealed a layered crystal structure or a highly anisotropic growth of the oxide [10,13]. Considering MoO_3, it is an orthorhombic structure, composed of highly distorted MoO_6 octahedrons which are interconnected with the edges in the [0 0 1] direction and interlinked with the corners in the [1 0 0] direction, leading to a so called double-layer planar structure. Each of these double layers is zigzag bonded together by the van der Waals force to make the product appear as stratified structure [14,15]. Therefore, the increasing in the intensities of the (0 2 0), (0 4 0) and (0 6 0) planes implies that the unit cells of layer-structured α-MoO_3 crystal are highly anisotropic growth along the b axis.

Fig. 2 shows the low and high magnification SEM images of α-MoO_3. At low magnification (Fig. 2a), the product is completely uniform α-MoO_3 nanobelts with no detection of any other morphologies. Their lengths are >10 μm, and their widths are <200 nm. The α-MoO_3 nanobelts hydrothermally synthesized by other researchers are compared in Table 1. The present research is at an advantage in synthesizing these α-MoO_3 nanobelts without using any polymers in controlling the structure. The high magnification SEM image (Fig. 2b) shows that the surfaces of α-MoO_3 nanobelts are smooth and even. A typical nanobelt is 100–120 nm thick.

FTIR spectrum (Fig. 3a) shows the vibrational interaction between molybdenum and oxygen atoms of α-MoO_3 nanobelts. The sharp band at 996 cm^{-1} is assigned as the terminal oxygen symmetric stretching vibration of Mo═O belonging to the layered structured α-MoO_3 phase [14,16,17]. The vibration band at 882 cm^{-1} corresponds to the bridge oxygen asymmetric stretching vibration of Mo—O—Mo [13,14,16,17], and at 570 cm^{-1} to the symmetric stretching vibration of O atoms linked to three Mo atoms [13,14,16].

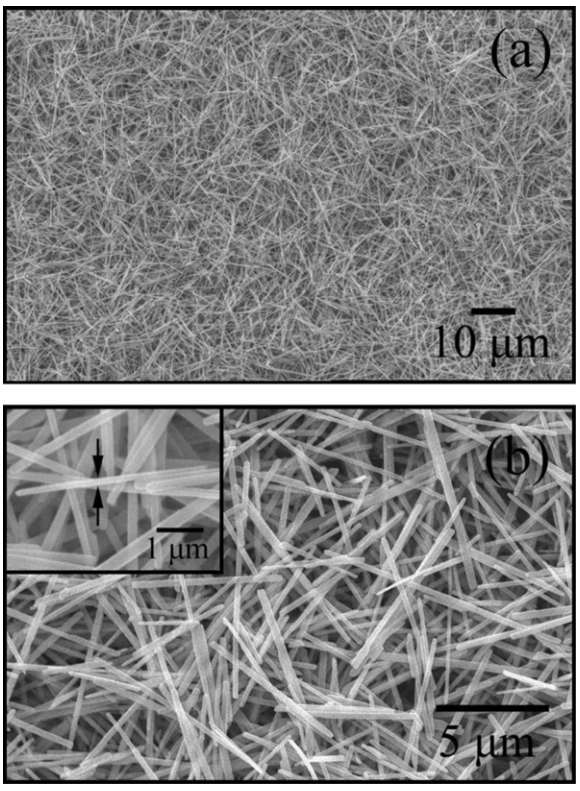


Fig. 2. SEM images at (a) low and (b) high magnifications of α-MoO_3 nanobelts synthesized by hydrothermal reaction at 180 °C for 20 h.

The α-MoO_3 is a layer structure with ABA stacking, which contains edge- and corner-linked octahedrons. The Mo^{6+} ions occupy in octahedral interstices within the lattice of O^{2-} ions. Layered α-MoO_3 structure is composed of one Mo atom and three nonequivalent types of O atoms, namely, O_1, O_2, and O_3. The Mo—O_1 is the shortest bond with 1.67 Å apart. In the *c* axis, there are two equal Mo—O_2 bonds with 1.95 Å long, and the third bond is in the *b* axis with 2.33 Å long. Along the *a* axis, there are two Mo—O_3 bonds with 1.73 and 2.23 Å long [18]. Group theory predicted the following irreducible representation at the center (Γ) of Brillouin zone. Optical vibrational modes of molybdenum oxide with $D_{2h}{}^{16}$ (Pbnm) space group are given as follows.

$$\Gamma = 8A_g + 8B_{1g} + 4B_{2g} + 4B_{3g} + 4A_u + 3B_{1u} + 7B_{2u} + 7B_{3u} \quad (1)$$

where A_g, B_{1g}, B_{2g}, and B_{3g} are Raman-active modes. A_u is an inactive mode, and B_{1u}, B_{2u} and B_{3u} are infrared-active modes [18,19]. The Raman spectrum of α-MoO_3 operated using 632.8 nm wavelength of He–Ne laser at 50–1100 cm^{-1} is shown in Fig. 3b. Roughly speaking, the Raman spectrum of α-MoO_3 was classified into stretching, deformation and lattice modes at 1000–600, 400–200, and below 200 cm^{-1}, respectively [18,20]. The peak at 159 cm^{-1} is the A_g/B_{1g} mode, corresponding to the δ $(O_2Mo_2)_n$ polyhedrons along with the chain axis. Its intensity was strongly increased by the polarization along the *c* axis. The peaks at 82, 98, 116, and 127 cm^{-1} were specified as the A_g, B_{2g}, B_{2g} and B_{3g}, corresponding to the T_a, T_a, T_c and T_c translation of rigid MoO_4 chain modes, respectively. Between 400 and 200 cm^{-1} vibrations are the 245 (B_{3g}, δ O_2—Mo—O_2 scissoring), 292 (B_{3g}, δ O_1=Mo=O_1 wagging), 338 (A_g/B_{1g}, δ O_3—Mo—O_3 bending), and 379 cm^{-1} (B_{1g}, δ O_2=Mo=O_2 scissoring) peaks. The peak at 471 cm^{-1} is the A_g mode which corresponds to the ν_{as} Mo—O_2—Mo stretching and bending vibration. The 664 cm^{-1} peak is the B_{2g}/B_{3g} mode, corresponding to the ν_{as} Mo—O_2—Mo stretching. Those at 816 and 992 cm^{-1} are the A_g modes. They are specified as the ν_s Mo—O_3—Mo stretching of which bonding aligns along the *a* axis, and ν_{as} Mo=O_1 stretching of which bonding aligns along the *b* axis [18–24]. Different Raman vibration modes of the present α-MoO_3 nanobelts and those of other reports are compared in Table 2.

TEM image of α-MoO_3 (Fig. 4a) shows uniform nanobelts with 100–200 nm wide and several μm long. Their surfaces are very smooth and even. The selected area electron diffraction (SAED) patterns (Fig. 4b–d) were recorded perpendicular to the growth direction of the three nanobelts of Fig. 4a. They appear as bright spots of electron diffraction patterns which indicate the single crystalline nanobelts with high crystallinity. All SAED patterns were indexed to correspond with the (0 0 1), (1 0 1) and (1 0 0) planes with the electron beams in the [0 1 0], [0 1 0], and [0–10] directions of the individual α-MoO_3 nanobelts as compared to those of the JCPDS standard No. 05-0508 [12]. They were suggested that the product was α-MoO_3 nanobelts growing along the [0 0 1] direction [10]. The α-MoO_3 nanobelt structure model (inset of Fig. 4a) grows along the *c* axis, with the ±(1 0 0) top and bottom, ±(0 1 0) side, and ±(0 0 1) end surfaces [10]. In general, α-MoO_3 is composed of distorted MoO_6 octahedrons with sharing corners along the [1 0 0] direction (*a*-axis), and zigzag edges along the [0 0 1] direction (*c*-axis) to form layers. Each of the layers is bound together by the weak van der Waals attraction along the *b*-axis to form the pronounced nanomaterial with large surface area to volume ratio [16,19].

In contrast, the interaction along the *c* axis is strong covalent bond, implying that more energy was released during their growth along the [0 0 1] direction. The energy release was in favor with the growth of α-MoO_3 unit cells along the *b* axis. The XRD peaks of the (0 *k* 0) planes were higher than those of the corresponding standard, since the (0 1 0) plane retained in the final product, as the consequence of fast growing rate [6,10].

The formation mechanism of α-MoO_3 nanobelts from isopolymolybdate $(Mo_7O_{24})^{6-}$ anions under hydrothermal treatment was reported by Lou and Zeng [4] as follows.

$$Mo_7O_{24}{}^{6-} + 6H^+ \rightarrow 7MoO_3 + 3H_2O \quad (2)$$

The $Mo_7O_{24}{}^{6-}$ anions were obtained by dissolving of $(NH_4)_6Mo_7O_{24}{\cdot}4H_2O$ as starting material in a solution containing HNO_3. The overall equilibrium would shift the hydrothermal reaction to the right, although several intermediate steps may proceed. Thus other compounds/phases may exist. However, Xia et al. [25] suggested the growth of 1-D α-MoO_3 nanostructure by electroneutral and dehydration reactions as follows.

$$Mo_7O_{24}{}^{6-} + 6H^+ + 11H_2O \rightarrow 7MoO_3{\cdot}2H_2O \quad (3)$$

Table 1
The 1D α-MoO_3 nanostructure synthesized by hydrothermal reactions.

Researchers	Mo source	Polymer	Temperature (°C)	Time (h)	Morphology	Length (μm)	Width (nm)
Wang et al. [10]	$(NH_4)_6Mo_7O_{24}{\cdot}4H_2O$	CTAB	180	20	Nanobelts	>5	100–200
Reddy et al. [13]	$(NH_4)_6Mo_7O_{24}{\cdot}4H_2O$	PVP	180	360	Nanorods	6	5–100
Reddy et al. [16]	$(NH_4)_6Mo_7O_{24}{\cdot}4H_2O$	PEG	180	96	Nanobelts	1–5	100–600
Mohan et al. [17]	$(NH_4)_6Mo_7O_{24}{\cdot}4H_2O$	PEG	180	48	Nanobelts	<0.32	70–180
Ours	$(NH_4)_6Mo_7O_{24}{\cdot}4H_2O$	Free	180	20	Nanobelts	>10	<200

CTAB, cetyltrimethyl ammonium bromide; PVP, polyvinylpyrrolidone; PEG, polyethylene glycol.

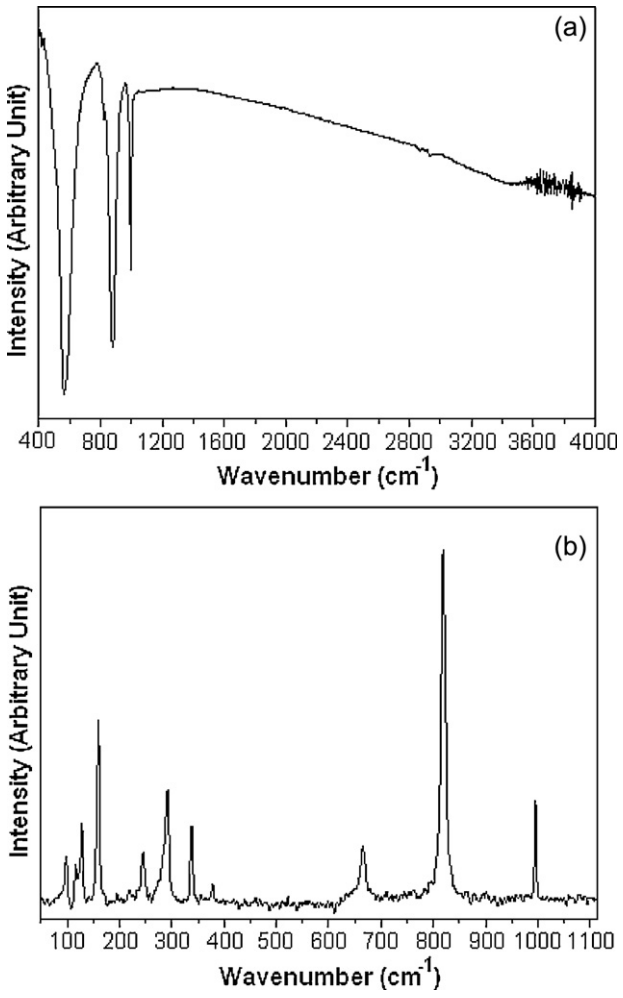


Fig. 3. (a) FTIR and (b) Raman spectra of α-MoO_3 nanobelts synthesized by hydrothermal reaction at 180 °C for 20 h.

At high temperature, water was released by two steps as follows.

$$MoO_3{\cdot}2H_2O \rightarrow \alpha\text{-}MoO_3{\cdot}H_2O + H_2O \quad (4)$$

$$\alpha\text{-}MoO_3{\cdot}H_2O \rightarrow \alpha\text{-}MoO_3 + H_2O \quad (5)$$

The crystal structure of $MoO_3{\cdot}2H_2O$ is monoclinic symmetry and does not display any one-dimensional chain structure. α-$MoO_3{\cdot}H_2O$ exhibits Mo—O—Mo chains running along the [0 0 1] direction. There is the maximum intensity of one-dimensional growth due to the presence of two different sorts of chains along the *a* and *c* axes of orthorhombic α-MoO_3 [25].

3.2. The effect of reaction temperature, holding time and type of acids on the formation of α-MoO_3 nanobelts

The effect of reaction temperature, holding time and type of acids was studied during the formation of α-MoO_3 nanobelts. Figs. S1 and S2 of the Supporting Information show the XRD patterns and SEM images of α-MoO_3 nanobelts, which were synthesized by hydrothermal reactions at 100–180 °C for 20 h. XRD analysis proved that the product at 100 °C for 20 h was composed of mixed phase of hexagonal MoO_3 (h-MoO_3) and orthorhombic α-MoO_3, corresponding to the JCPDS No. 21-0569 for h-MoO_3, and 05-0508 for orthorhombic α-MoO_3 [12]. The h-MoO_3 phase became lessened when the reaction hydrothermal temperature was increased. Pure α-MoO_3 was synthesized at 140 °C and above, with no detection of any other impurities. The α-MoO_3 nanobelts were agglomerated as nanobelt bundles at 100–160 °C for 20 h. They were separated into individual uniform nanobelts at 180 °C for 20 h. Figs. S3 and S4 of the Supporting Information show the XRD patterns and SEM images of α-MoO_3 nanobelts synthesized by the hydrothermal reactions at a constant temperature of 180 °C for 2–20 h. When the reaction time was decreased from 20 h to 5 h, the product remained as pure α-MoO_3 phase. Upon reducing the length of time to 2 h, the mixture of h-MoO_3 and α-MoO_3 as minor and major phases was detected. At this stage (180 °C, 2 h), the agglomerated bundle of nanobelts was synthesized. For longer time (5–10 h), individual of α-MoO_3 nanobelts was synthesized, but composed of a mixture of nano- and micro-belts. At 180 °C for 20 h, uniform α-MoO_3 nanobelts were synthesized and detected.

When either HCl or H_2SO_4 instead of HNO_3 was used, the XRD patterns (Fig. S5 of the Supporting Information) remained the same, excluding intensities of the diffraction peaks. The XRD patterns also corresponded to the pure phase of α-MoO_3, but all intensities of the diffraction peaks of α-MoO_3 for using of HCl and H_2SO_4 became lessened – lowering the degree of crystallinity. The products synthesized in the HCl and H_2SO_4 acidic solutions, shown by SEM images (Fig. S6 of the Supporting Information), are short agglomerated α-MoO_3 nanobelts. These proved that the reaction hydrothermal temperature, holding reaction time and type of acids are the key factors used to control pure phase and uniform α-MoO_3 nanobelts. In general, the nanomaterials with high crystallinity

Table 2
Raman vibration modes of α-MoO_3 nanostructures.

Raman vibration modes	Assignment	Wavenumber (cm^{-1})					
		Ours	Ref. [18]	Ref. [21]	Ref. [22]	Ref. [23]	Ref. [24]
A_g	T_a Translation of rigid MoO_4 chain (T_a)	82	–	89	82	82	83
B_{2g}	T_a Translation of rigid MoO_4 chain (T_a)	98	–	100	–	98	98
B_{2g}	T_c Translation of rigid MoO_4 chain (T_c)	116	116	116	115	114	116
B_{3g}	T_c Translation of rigid MoO_4 chain (T_c)	127	130	129	129	128	128
A_g/B_{1g}	$\delta\,(O_2Mo_2)_n$	159	157	159	158	157	156
B_{2g}	$\delta\,O_2$—Mo—O_2 scissoring	196	198	197	198	197	198
A_g	$\delta\,O_2$—Mo—O_2 scissoring	218	217	216	216	216	218
B_{3g}	$\delta\,O_2$—Mo—O_2 scissoring	245	246	247	246	244	246
B_{2g}	$\delta\,O_1$=Mo=O_1 wagging	283	284	285	284	282	286
B_{3g}	$\delta\,O_1$=Mo=O_1 wagging	292	291	293	–	–	291
A_g/B_{1g}	$\delta\,O_3$—Mo—O_3 bending	338	338	334	336	336	338
A_g	$\delta\,O_2$=Mo=O_2 scissoring	365	365	366	365	365	366
B_{1g}	$\delta\,O_2$=Mo=O_2 scissoring	379	378	376	379	377	380
A_g	ν_{as} Mo—O_2—Mo bending	471	471	473	–	469	472
B_{2g}/B_{3g}	ν_{as} Mo—O_2—Mo stretching	664	667	667	666	666	666
A_g	ν_s Mo—O_3—Mo stretching	816	817	823	819	818	820
A_g	ν_{as} Mo=O_1 stretching	992	996	996	996	994	996

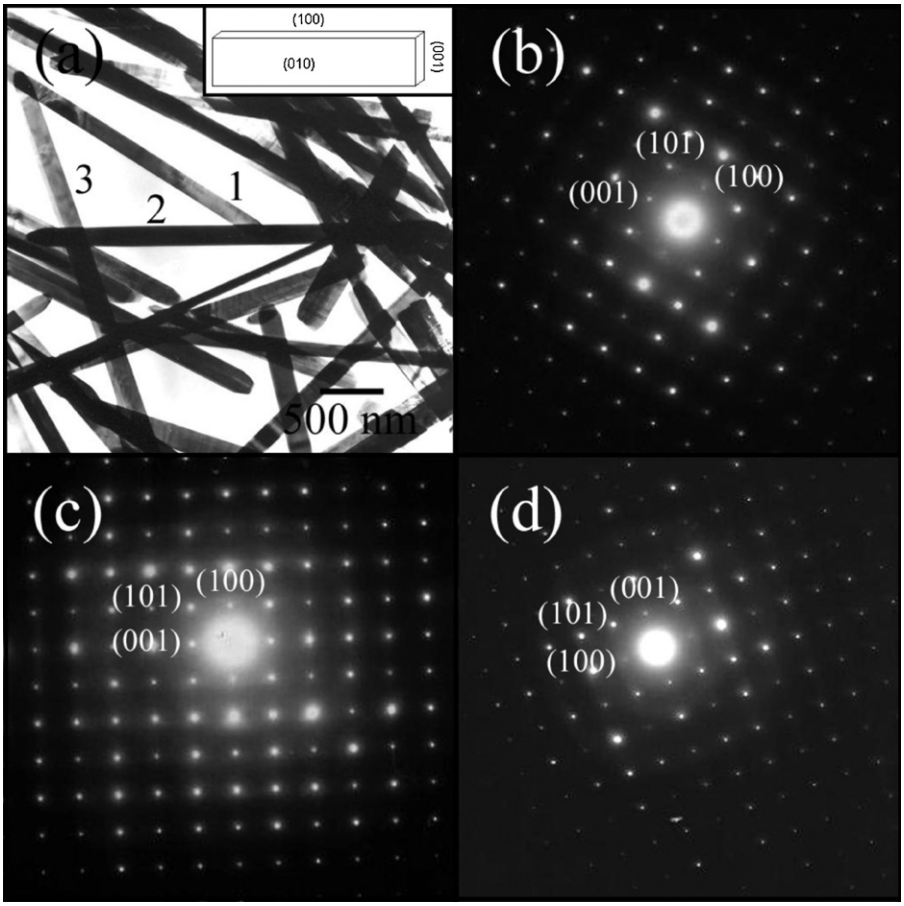


Fig. 4. (a) TEM image and structure model (inset) of α-MoO_3 nanobelts synthesized by hydrothermal reaction at 180 °C for 20 h, and (b–d) SAED patterns on the 1, 2 and 3 nanobelts of (a).

and uniform morphology have the potential to improve the electrochemical and photoluminescent properties. Therefore, the best condition for the synthesis of uniform α-MoO_3 nanobelts with high crystallinity in this research is the 180 °C and 20 h hydrothermal processing of the solution containing 15 ml 2 M HNO_3.

3.3. Electrochemical property of α-MoO_3 nanobelts

α-MoO_3 is a material with tunnel structure for using in electrochromic applications, constituted by $[MoO_6]^{6-}$ octahedrons with sharing edges and corners, resulting in zigzag chains and unique layers binding along the [0 1 0] direction. Consider three phases of MoO_3, monoclinic (β-MoO_3) is metastable. At 140 °C and above, h-MoO_3 (hexagonal) would transformed into orthorhombic α-MoO_3 – the most thermodynamically stable phase [10,14]. Smaller ions such as H^+ and Li^+ can be intercalated in its layer structure [16,17,26–28]. The hydrogen evolution reaction (HER) in 1 M H_2SO_4 with α-MoO_3 nanobelts as a catalyst can be explained as follows [11].

$$xH^+ + xe^- + MoO_3 \rightarrow H_xMoO_3 \quad \text{cathodic reaction} \tag{6}$$

$$H_xMoO_3 \rightarrow 0.5xH_2 + MoO_3 \quad \text{anodic reaction} \tag{7}$$

where x is the stoichiometric parameter which varied between 0 and 1. When a voltage (cathodic reaction) was applied, H^+ ions migrated in the layered $[MoO_6]^{6-}$ octahedrons along the (0 1 0) plane of α-MoO_3, with electron trapping on some Mo^{6+}, forming Mo^{5+}. Coloration was attributed to the intervalence charged transition between Mo^{6+} and the newly formed Mo^{5+}. The intercalated

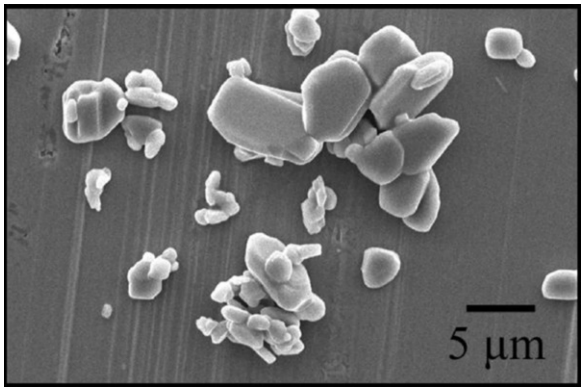


Fig. 5. SEM image of commercial MoO_3 microparticles.

H_xMoO_3 is known as the molybdenum bronze [28]. At the anodic reaction, it led to the oxidation of Mo(V) with the evolution of H_2 gas [6,11]. The HER of α-MoO_3 nanobelts was investigated by linear sweep voltammetry (LSV) and Tafel plot comparing to the commercial MoO_3 microparticles with the particle size of 2–5 μm (Fig. 5).

Fig. 6 shows the LSV curves of pure glassy carbon electrode (black/top), commercial MoO_3 microparticles (blue/middle), and α-MoO_3 nanobelts (green/bottom). The pure glassy carbon electrode shows no actively electrochemical reaction. When the surfaces of glassy carbon electrodes were coated by commercial MoO_3 microparticles

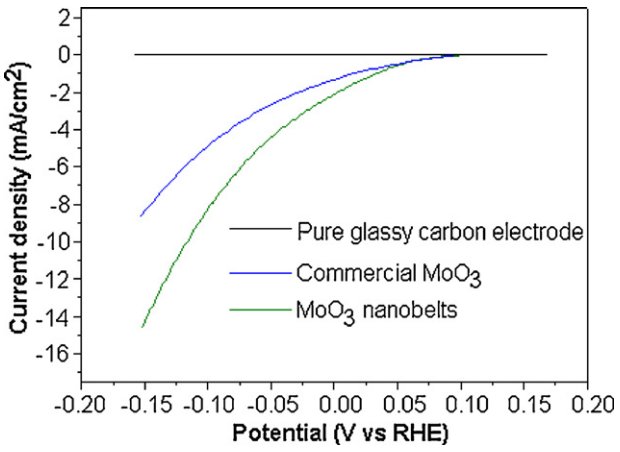


Fig. 6. LSV curves of HER testing for pure glassy carbon, and carbon electrodes coated with α-MoO_3 nanobelts and commercial MoO_3 microparticles.

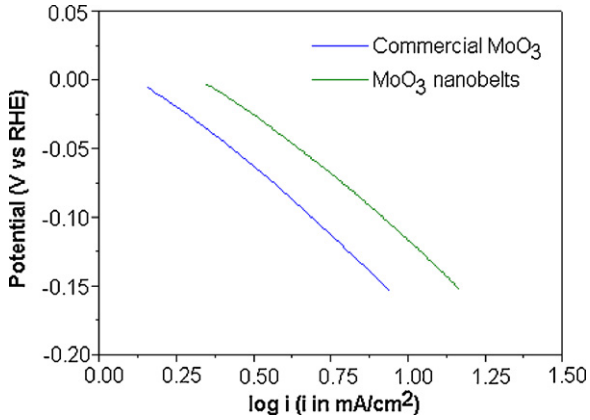


Fig. 7. Tafel plots of α-MoO_3 nanobelts and commercial MoO_3 microparticles.

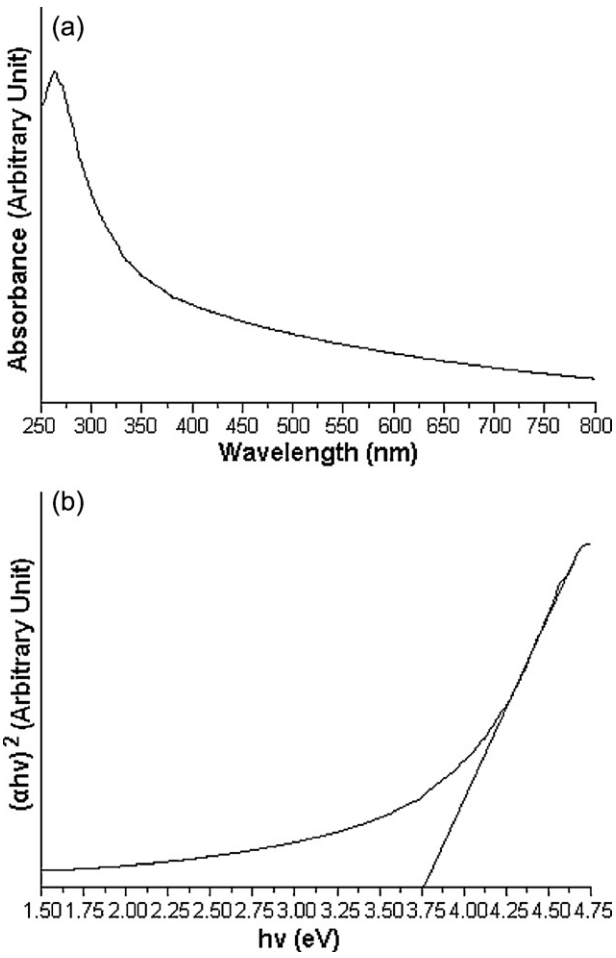


Fig. 8. (a) UV–vis absorbance, and (b) the $(\alpha h\nu)^2$ vs $h\nu$ plot of α-MoO_3 nanobelts.

and α-MoO_3 nanobelts, they showed the current density of −2.68, −4.89 and −8.33 mA/cm^2, and −4.54, −8.25 and −14.41 mA/cm^2 at −0.05, −0.10 and −0.15 V, respectively. The electrocatalytic activity of α-MoO_3 nanobelts is ~1.70 times higher than that of the commercial MoO_3 microparticles. (For interpretation of the references to color in this text, the reader is referred to the web version of this article.)

Tafel plots as shown in Fig. 7 were calculated from LSV data at low over-potential region from −0.005 to −0.035 V (vs RHE). Comparing Tafel plots between α-MoO_3 nanobelts (green/right) and commercial MoO_3 microparticles (blue/left), the exchange current density (I_o) of α-MoO_3 nanobelts (2.10 mA/cm^2) was higher than that of the commercial MoO_3 microparticles (1.34 mA/cm^2). The high exchange current density (I_o) of α-MoO_3 nanobelts implied that lower intrinsic electric resistance originated from the vectorial electron transfer along the crystal growth direction. This phenomenon has been apparently detected in 1-D nanostructure which preserved the high aspect ratio to their unique textural properties. Owing to the vectorial electron transfer, α-MoO_3 nanobelts could provide facile electron pathway, and the enhanced electrochemical activity was detected. Furthermore, the Tafel slope and onset potential of α-MoO_3 nanobelts were −131 mV/dec and +0.096 V vs RHE, respectively. They were higher than the −138 mV/dec and +0.094 V vs RHE of the commercial MoO_3 microparticles. More positive onset potential of α-MoO_3 nanobelts could turn out to be a more active electrocatalyst than the commercial MoO_3 microparticles. Lower Tafel slope has been related with the large number of electrons participating in HER. The number of electrons of α-MoO_3 nanobelts and commercial MoO_3 microparticles was 0.9 and 0.85, respectively. Consequently, these electrochemical results have provided that 1-D structured α-MoO_3 nanobelts as electrocatalyst could be a better performance than general 0-D particles for HER. The electrochemical data for HER was also summarized in Table 3. (For interpretation of the references to color in this text, the reader is referred to the web version of this article.)

3.4. Optical property of α-MoO_3 nanobelts

The optical absorption spectrum of α-MoO_3 nanobelts (Fig. 8a) exhibited the strong absorption centered at ~262 nm in the UV region, due to the charged transfer in the $[MoO_6]^{6-}$ octahedrons [29]. The direct band gap (E_g) was calculated from the relation between the absorption coefficient and photon energy given by

$$\alpha h\nu = (h\nu - E_g)^n \quad (8)$$

where α, h, ν, and E_g are the absorbance, Planck constant, photon frequency, and photonic band gap, respectively. The parameter n is a constant associated with the different types of electronic transition: $n = 1/2$, 2, 3/2 or 3 for direct allowed, indirect allowed, direct forbidden and indirect forbidden transitions, respectively [29–31]. Fig. 8b shows the plot of $(\alpha h\nu)^2$ vs $h\nu$. By extrapolating the linear portion of the curve to zero absorbance, the direct E_g of α-MoO_3 nanobelts was determined to be 3.75 eV, larger than that of its bulk state (2.9 eV) [32], due to the quantum size effect [33]. The gap is increased with the decrease in the particle sizes and increase in the surface area to volume ratios. Morphologies, crystalline degree and structural order–disorder can play the role in the gap [34] as

Table 3
Electrocatalytic HER properties of commercial MoO_3 microparticles and α-MoO_3 nanobelts.

Electrocatalyst	Specific activity at −0.05 V (mA/cm^2)	Specific activity at −0.10 V (mA/cm^2)	Specific activity at −0.15 V (mA/cm^2)	Onset potential (V vs RHE)	Tafel slope[a] (mV/dec)	I_o (mA/cm^2)
MoO_3 microparticles	−2.68	−4.89	−8.33	+0.094	−138	1.34
α-MoO_3 nanobelts	−4.54	−8.25	−14.41	+0.096	−131	2.10

[a] In the low overpotential region from −0.005 V to −0.035 V (vs RHE).

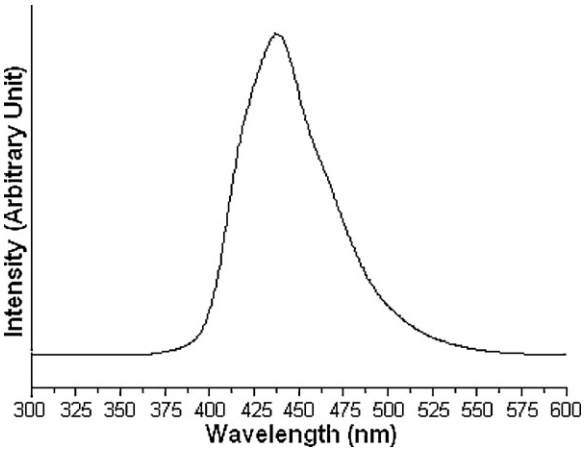


Fig. 9. PL emission of α-MoO_3 nanobelts at room temperature.

well. The direct allowed E_g for the absorbance of α-MoO_3 nanobelts was caused by the charged transition from the uppermost valence band of O_{2p} to the lowest conduction band of Mo_{4d} ($O_{2p} \rightarrow Mo_{4d}$) of α-$MoO_3$ [35].

Fig. 9 is a photoluminescence spectrum of α-MoO_3 nanobelts excited by 337 nm wavelength at room temperature. It shows a broad peak at 375–550 nm with the maximum emission peak at 437 nm, corresponding to the report of Song et al. [36], due to the charged transition from the lowest conduction band to the uppermost valence band of α-MoO_3 nanobelts.

4. Conclusions

In summary, α-MoO_3 nanobelts with >10 μm long and <200 nm wide were successfully synthesized under hydrothermal reaction at 180 °C for 20 h in controlling agent solution. In the present research, α-MoO_3 nanobelts grew along the *c* axis, with the ±(1 0 0) top and bottom and ±(0 1 0) side surfaces. Comparing HER of α-MoO_3 nanobelts and that of the commercial MoO_3 microparticles, the first showed the better performance electrochemical HER activity, including the 3.75 eV energy gap caused by the $O_{2p} \rightarrow Mo_{4d}$ charged transition, and the 437 nm emission peak excited by 337 nm wavelength at room temperature.

Acknowledgements

We wish to thank the National Nanotechnology Center (NANOTEC), National Science and Technology Development Agency, for providing financial support through the project code: P-10-11345, the Thailand's Office of the Higher Education Commission through the National Research University (NRU) Project, and the Thailand Research Fund (TRF) through the TRF Research Grant, including Graduate School of Chiang Mai University through the general support.

Appendix A. Supplementary data

Supplementary data associated with this article can be found, in the online version, at doi:10.1016/j.jallcom.2011.12.024.

References

[1] R.Q. Song, A.W. Xu, B. Deng, Y.P. Fang, J. Phys. Chem. B 109 (2005) 22758–22766.
[2] S.R. Dhage, M.S. Hassan, O.B. Yang, Mater. Chem. Phys. 114 (2009) 511–514.
[3] L. Mai, B. Hu, W. Chen, Y. Qi, Ch. Lao, R. Yang, Y. Dai, Zh.L. Wang, Adv. Mater. 19 (2007) 3712–3716.
[4] X.W. Lou, H.Ch. Zeng, Chem. Mater. 14 (2002) 4781–4789.
[5] G. Wei, W. Qin, D. Zhang, G. Wang, R.y. Kim, K. Zheng, L. Wang, J. Alloys Compd. 481 (2009) 417–421.
[6] A. Phuruangrat, D.J. Ham, S. Thongtem, J.S. Lee, Electrochem. Commun. 11 (2009) 1740–1743.
[7] G.S. Zakharova, C. Täschner, V.L. Volkov, I. Hellmann, R. Klingeler, A. Leonhardt, B. Büchner, Solid State Sci. 9 (2007) 1028–1032.
[8] J.H. Ryu, J.W. Yoon, K.B. Shim, Solid State Commun. 133 (2005) 657–661.
[9] S.S. Mahajan, S.H. Mujawar, P.S. Shinde, A.I. Inamdar, P.S. Patil, Sol. Energy Mater. Sol. Cells 93 (2009) 183–187.
[10] Sh. Wang, Y. Zhang, X. Ma, W. Wang, X. Li, Z. Zhang, Y. Qian, Solid State Commun. 136 (2005) 283–287.
[11] A. Phuruangrat, D.J. Ham, S.J. Hong, S. Thongtem, J.S. Lee, J. Mater. Chem. 20 (2010) 1683–1690.
[12] Powder Diffract. File, JCPDS-ICDD, 12 Campus Boulevard, Newtown Square, PA 19073-3273, U.S.A., 2001.
[13] Ch.V.S. Reddy, E.H. Walker Jr., S.A. Wicker Sr., Q.L. Williams, R.R. Kalluru, J. Solid State Electrochem. 13 (2009) 1945–1949.
[14] L. Cheng, M. Shao, X. Wang, H. Hu, Chem. Eur. J. 15 (2009) 2310–2316.
[15] M.B. Rahmani, S.H. Keshmiri, J. Yu, A.Z. Sadek, L. Al-Mashat, A. Moafi, K. Latham, Y.X. Li, W. Wlodarski, K. Kalantar-zadeh, Sens. Actuators B 145 (2010) 13–19.
[16] Ch.V.S. Reddy, E.H. Walker Jr., Ch. Wen, S. Mho, J. Power Sources 183 (2008) 330–333.
[17] V.M. Mohan, H. Bin, W. Chen, J. Solid State Electrochem. 14 (2010) 1769–1775.
[18] D. Liu, W.W. Lei, J. Hao, D.D. Liu, B.B. Liu, X. Wang, X.H. Chen, Q.L. Cui, G.T. Zou, J. Liu, S. Jiang, J. Appl. Phys. 105 (2009) 023513-1–023513-7.
[19] X. Chen, W. Lei, D. Liu, J. Hao, Q. Cui, G. Zou, J. Phys. Chem. C 113 (2009) 21582–21585.
[20] S. Phadungdhitidhada, P. Mangkorntong, S. Choopun, N. Mangkorntong, Ceram. Int. 34 (2008) 1121–1125.
[21] M. Dieterle, G. Weinberg, G. Mestl, Phys. Chem. Chem. Phys. 4 (2002) 812–821.
[22] T. Siciliano, A. Tepore, E. Filippo, G. Micocci, M. Tepore, Mater. Chem. Phys. 114 (2009) 687–691.
[23] L.G. Pereira, L.E.B. Soledade, J.M. Ferreira, S.J.G. Lima, V.J. Fernandes Jr., A.S. Araújo, C.A. Paskocimas, E. Longo, M.R.C. Santos, A.G. Souza, I.M.G. Santos, J. Alloys Compd. 459 (2008) 377–385.
[24] L. Seguin, M. Figlarz, R. Cavagnat, J.C. Lassègues, Spectrochim. Acta Part A 51 (1995) 1323–1344.
[25] T. Xia, Q. Li, X. Liu, J. Meng, X. Cao, J. Phys. Chem. B 110 (2006) 2006–2012.
[26] X.K. Hu, Y.T. Qian, Z.T. Song, J.R. Huang, R. Cao, J.Q. Xiao, Chem. Mater. 20 (2008) 1527–1533.
[27] L. Zheng, Y. Xu, D. Jin, Y. Xie, Chem. Mater. 21 (2009) 5681–5690.
[28] J. Chen, H. Yang, L. Chang, W. Fu, Y. Zeng, H. Zhu, G. Zou, Front. Phys. China 1 (2007) 92–95.
[29] Y. Keereeta, T. Thongtem, S. Thongtem, J. Alloys Compd. 509 (2011) 6689–6695.
[30] T. Thongtem, S. Jattukul, Ch. Pilapong, S. Thongtem, Curr. Appl. Phys. 12 (2012) 23–30.
[31] S. Suwanboon, R. Tanattha, R. Tanakorn, Songklanakarin J. Sci. Technol. 30 (2008) 65–69.
[32] Y. Zhao, J. Liu, Y. Zhou, Z. Zhang, Y. Xu, H. Naramoto, S. Yamamoto, J. Phys.: Condens. Matter 15 (2003) L547–L552.
[33] T. Thongtem, A. Phuruangrat, S. Thongtem, Appl. Surf. Sci. 254 (2008) 7581–7585.
[34] T. Thongtem, A. Phuruangrat, S. Thongtem, Mater. Lett. 61 (2007) 3235–3238.
[35] M. Itoh, K. Hayakawa, Sh. Oishi, J. Phys.: Condens. Matter 13 (2001) 6853–6864.
[36] J. Song, X. Ni, D. Zhang, H. Zheng, Solid State Sci. 8 (2006) 1164–1167.

Materials Letters 72 (2012) 104–106

Contents lists available at SciVerse ScienceDirect

Materials Letters

journal homepage: www.elsevier.com/locate/matlet

Controlling morphologies of Bi_2S_3 nanostructures synthesized by glycolthermal method

Anukorn Phuruangrat [a,*], Somchai Thongtem [b], Titipun Thongtem [c,**]

[a] Department of Materials Science and Technology, Faculty of Science, Prince of Songkla University, Hat Yai, Songkhla 90112, Thailand
[b] Department of Physics and Materials Science, Faculty of Science, Chiang Mai University, Chiang Mai 50200, Thailand
[c] Department of Chemistry, Faculty of Science, Chiang Mai University, Chiang Mai 50200, Thailand

ARTICLE INFO

Article history:
Received 14 September 2011
Accepted 22 December 2011
Available online 29 December 2011

Keywords:
Semiconductors
X-ray techniques
Electron microscopy

ABSTRACT

Single crystalline orthorhombic Bi_2S_3 nanostructures with different morphologies were synthesized by the 180 °C and 12 h glycolthermal reactions, using ethylene glycol, propylene glycol and polyethylene glycol with different molecular weights as solvents. The as-synthesized products were characterized by X-ray diffraction (XRD), transmission electron microscopy (TEM), high resolution transmission electron microscopy (HRTEM), and selected area electron diffraction (SAED). In the present research, different solvents played the role in the product morphologies. A formation mechanism of Bi_2S_3 nanostructures was also proposed.

© 2011 Elsevier B.V. All rights reserved.

1. Introduction

Generally, nanostructured materials exhibit novel properties, comparing to their bulks due to their quantum confinement effect and number of free electrons. Much effort has been dedicated to achieve in controlling over the morphologies [1–3]. Among them, ceria nanospindles as a catalyst for oxidation of CO were synthesized via a simple template-free solvothermal treatment [4], large-scale synthesis of single-crystalline and uniform CeO_2 nanorods by a precipitation method [5], and CeO_2 nanoplates, nanotubes, and nanorods by CTAB assisted hydrothermal synthesis, including the study of their morphologies on the oxidation of CO [6].

Over the past decades, chalcogenide semiconductors (A_2X_3, A = Sb, Bi, As, and X = S, Se, Te) have received considerable attention due to their wide applications in television cameras with photoconducting targets, thermoelectric devices, optoelectronic devices, and IR spectroscopy photovoltaic converters, including their unique thermal, mechanical, electron transport, phonon transport, optical and non-linear optical properties [2,3,7]. Particularly, Bi_2S_3 is a low direct band gap (1.3–1.7 eV) layered semiconductor that crystallizes in orthorhombic system with a promising candidate for a number of applications. It has large absorption coefficient, and is an ideal candidate for solar cells and photodetectors in the visible region, including thermoelectric applications [2,7–10].

Glycols such as ethylene glycol, 1,2-propadiol and polyethylene glycol with different molecular weights (MWs) are novel solvents for synthesizing nanostructured materials with different morphologies [11–15]. In this research, the synthesis of Bi_2S_3 with different morphologies by glycolthermal method using ethylene glycol (EG), propylene glycol (PG), polyethylene glycol (PEG) with different MWs as solvents was reported.

2. Experiment

All chemicals with analytical grade were used without further purification. In this experiment, 0.01 mol $Bi(NO_3)_3 \cdot 5H_2O$ and 0.015 mol L-cysteine were dissolved in 75 ml of different glycol solvents including EG, PG and PEG with different MWs of 200, 300, 400 and 600 under 1 h vigorous stirring. PEG with MW of 200 was encoded as PEG-200, and similarly for others. Each solution was loaded into an 80 ml Teflon-lined stainless-steel autoclave. The autoclaves were tightly closed and put in an oven at 180 °C for 12 h. At the conclusion, deep gray precipitates were synthesized, repeatedly washed with distilled water and absolute ethanol, and dried in vacuum at 60 °C for 4 h for further characterization.

3. Results and discussion

XRD patterns (Fig. 1) of the as-synthesized products in different glycols were indexed as pure orthorhombic Bi_2S_3 with Pbnm space group (JCPDS database no. 17-0320) [16] with its calculated lattice parameters [17] of 11.1300, 11.260 and 3.960 Å. Strong sharp reflection peaks indicated that well-crystallized products were synthesized through the glycolthermal process.

* Corresponding author. Tel.: +66 74 288374; fax: +66 74 288395.
** Corresponding author. Tel.: +66 53 943344; fax: +66 53 892277.
E-mail addresses: phuruangrat@hotmail.com (A. Phuruangrat), ttpthongtem@yahoo.com (T. Thongtem).

0167-577X/$ – see front matter © 2011 Elsevier B.V. All rights reserved.
doi:10.1016/j.matlet.2011.12.085

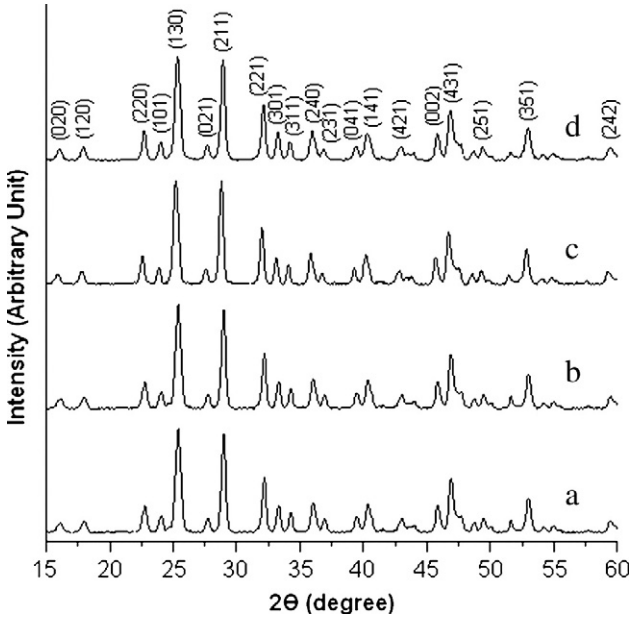


Fig. 1. XRD patterns of Bi_2S_3 nanostructures synthesized in (a–d) EG, PG, PEG-300, and PEG-600, respectively.

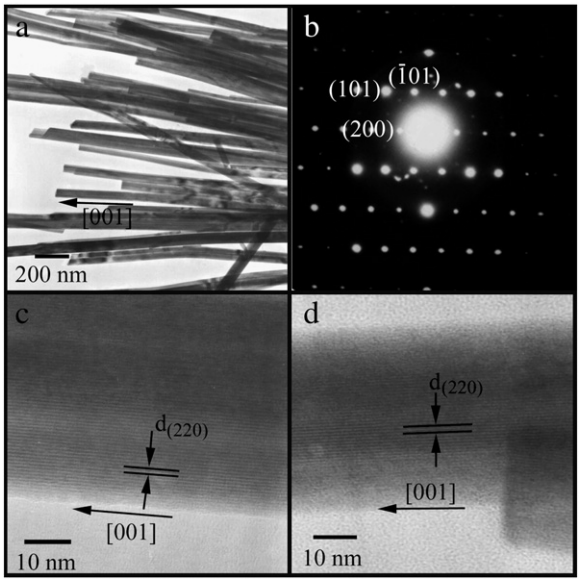


Fig. 3. TEM and HRTEM images, and SAED pattern of Bi_2S_3 nanowires synthesized in PG.

TEM images (Fig. 2a–f) of Bi_2S_3 nanostructures synthesized in different solvents revealed different product morphologies. A large number of Bi_2S_3 nanorods and nanowires were synthesized in EG and PG, respectively. They were well segregated with 50 nm diameter and 200–1200 nm long for nanorods, and 50 nm diameter and as long as 4 μm for nanowires. It should be noted that no individual nanorods and nanowires were synthesized in other glycols, showing that EG and PG have the advantage in forming the segregated nanorods and nanowires. TEM image of the as-synthesized Bi_2S_3 in PEG-200 indicates that the product was a cluster of typical straw-sheaves, composed of high agglomeration of numerous nanorods with radial radiation out of their center. Each straw-sheaf was approximately 4 μm long. In this research, nanostructured microflowers composed of petals with different shapes and sizes were synthesized in PEG-300, PEG-400 and PEG-600. Spherical Bi_3S_2 microflowers synthesized in PEG-300 were clearly detected. A number of nanoneedles radially radiated from a common point to build up microflowers. Bi_2S_3 architecture synthesized in PEG-400 was composed of well-aligned nanorods pointed out of a common center to form 4 μm microflower. Upon increasing the MW of PEG to 600, a typical TEM image presents Bi_2S_3 microflowers of nanorods, growing out of centers. Each microflower consisted of nanorods with 20—50 nm diameter and several hundred nanometers long. In conclusion, different solvents played the key role in the formation of Bi_2S_3 nanostructures with different morphologies.

Bi_2S_3 nanowires were further characterized by TEM, SAED and HRTEM (Fig. 3). Bi_2S_3 long uniform nanowires with 35 nm diameter growing along the c axis were detected. The HRTEM image, recorded on two different nanowires, revealed the presence of single crystalline nanowires with 3.96 Å lattice spacing of the (220) planes of orthorhombic Bi_2S_3 [16]. Due to lowest excess energy of the (001) planes than others [18], the nanowires preferentially grew along the [001] direction—in accordance with the previous report [19].

Bi_2S_3 microflower (Fig. 4a and b) shows an individual Bi_2S_3 flower-like structure with perfect geometry, assembled by tens of

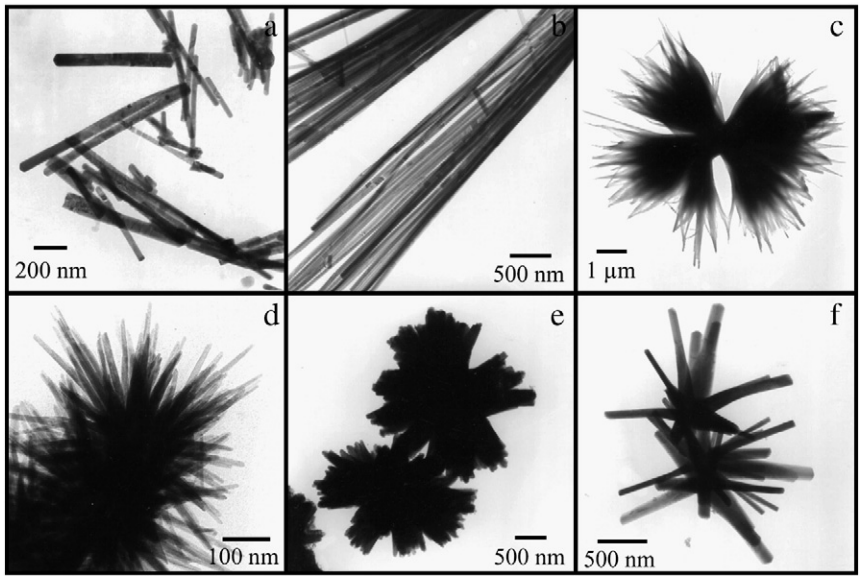


Fig. 2. TEM images of Bi_2S_3 nanostructures synthesized in (a–f) EG, PG, PEG-200, PEG-300, PEG-400 and PEG-600, respectively.

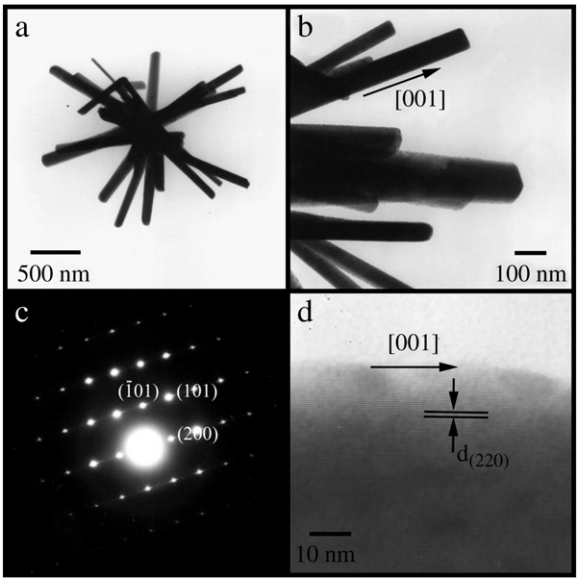


Fig. 4. TEM and HRTEM images, and SAED pattern of Bi_2S_3 nanowires synthesized in PEG-600.

uniform nanorods with 0.75–1 μm long and 40–80 nm diameter. SAED pattern (Fig. 4c) was indexed through the [010] electron beam direction and specified as orthorhombic Bi_2S_3 [16]. HRTEM image (Fig. 4d) of the individual Bi_2S_3 nanorod clearly presents 3.96 Å lattice spacing of orthorhombic Bi_2S_3 [16]. The Bi_2S_3 nanorod building up the flower-like structure was single crystal composed of the (220) parallel planes, and has the preferred growth along the [001] direction.

Basing on the above, a formation mechanism of Bi_2S_3 with different morphologies was proposed. Although the exact mechanism is still unclear, the interaction between Bi^{3+} and S^{2-} ions assumingly played a significant role in the formation of Bi_2S_3 nanostructures. Two paths were possible. (1) Initially, Bi^{3+} ions were solvated by glycol molecules. Afterwards S^{2-} ions synthesized from L-cysteine through the hydrolysis reaction might attack the Bi^{3+} ions, inducing the formation of bond between Bi^{3+} and S^{2-}. (2) Alternately, Bi^{3+} ions might react with L-cysteine to form complexes. Subsequently, the complexes glycolthermally decomposed to form Bi_2S_3 molecules. During processing, Bi_2S_3 molecules of these two paths gradually nucleated, and provided as seeds for crystalline growing. Concurrently different templates (EG, PG, PEG-200, PEG-300, PEG-400 and PEG-600) modeled the growing Bi_2S_3 nuclei to be perfect nanorods, nanowires, straw-sheaves of nanorods, and microflowers of nanorods [1–3,20].

4. Conclusions

Nanorods, nanowires, straw-sheaves and microflowers of nanostructured orthorhombic Bi_2S_3 were synthesized by the 180 °C and 12 h glycolthermal reactions, and were found to be controlled by different solvents: EG, PG and PEG with different MWs.

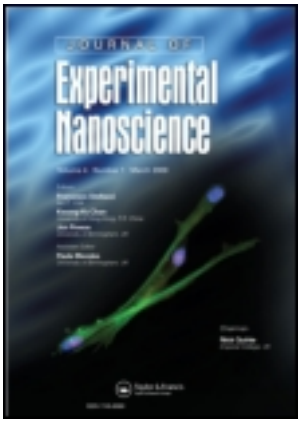
Acknowledgements

We wish to thank the National Nanotechnology Center (NANOTEC), National Science and Technology Development Agency, for providing financial support through the project code: P-10-11345, and the Thailand Research Fund through the TRF research grant.

References

[1] Tang C, Wang C, Su F, Zang C, Yang Y, Zong Z, et al. Solid State Sci 2010;12:1352–6.
[2] Thongtem T, Pilapong C, Kavinchan J, Phuruangrat A, Thongtem S. J Alloy Compd 2010;500:195–9.
[3] Zhu G, Liu P. Cryst Res Technol 2009;44:713–20.
[4] Zhang D, Niu F, Yan T, Shi L, Du X, Fang J. Appl Surf Sci 2011;257:10161–7.
[5] Pan C, Zhang D, Shi L, Fang J. Eur J Inorg Chem 2008;2008:2429–36.
[6] Pan C, Zhang D, Shi L. J Solid State Chem 2008;181:1298–306.
[7] Lu J, Han Q, Yang X, Lu L, Wang X. Mater Lett 2007;61:3425–8.
[8] Begum A, Hussain A, Rahman A. Mater Sci Appl 2011;2:163–8.
[9] Yu Y, Sun WT. Mater Lett 2009;63:1917–20.
[10] Tang CJ, Zhang YX, Dou XC, Li GH. J Cryst Growth 2010;312:692–7.
[11] Zhang D, Yan T, Shi L, Pan C, Zhang J. Appl Surf Sci 2009;255:5789–94.
[12] Phuruangrat A, Ekthammathat N, Thongtem T, Thongtem S. J Alloy Compd 2011;509:10150–4.
[13] Zhang D, Fu H, Shi L, Pan C, Li Q, Chu Y, et al. Inorg Chem 2007;46:2446–51.
[14] Phuruangrat A, Thongtem T, Thongtem S. Appl Surf Sci 2008;254:7553–8.
[15] Thongtem T, Phuruangrat A, Thongtem S. J Ceram Proc Res 2008;9:189–91.
[16] Powder Diffract. File, JCPDS-ICDD, 12 Campus Boulevard, Newtown Square, PA 19073-3273, U.S.A. 2001.
[17] Suryanarayana C, Norton MG. X-ray Diffract. NY: Plenum Press; 1998.
[18] Phuruangrat A, Thongtem T, Thongtem S. Mater Lett 2009;63:1538–41.
[19] Wang Y, Chen J, Wang P, Chen L, Chen YB, Wu LM. J Phys Chem C 2009;113:16009–14.
[20] Wu J, Qin F, Cheng G, Li H, Zhang J, Xie Y, et al. J Alloy Compd 2011;509:2116–26.

This article was downloaded by: [UNSW Library]
On: 05 February 2013, At: 22:11
Publisher: Taylor & Francis
Informa Ltd Registered in England and Wales Registered Number: 1072954 Registered office: Mortimer House, 37-41 Mortimer Street, London W1T 3JH, UK



Journal of Experimental Nanoscience
Publication details, including instructions for authors and subscription information:
http://www.tandfonline.com/loi/tjen20

Microwave-assisted synthesis and characterisation of uniform $LaPO_4$ nanorods

Nuengruethai Ekthammathat [a], Titipun Thongtem [a], Anukorn Phuruangrat [b] & Somchai Thongtem [c]

[a] Department of Chemistry and Center for Innovation in Chemistry, Faculty of Science, Chiang Mai University, Chiang Mai 50200, Thailand

[b] Department of Materials Science and Technology, Faculty of Science, Prince of Songkla University, Hat Yai, Songkhla 90112, Thailand

[c] Department of Physics and Materials Science, Faculty of Science, Chiang Mai University, Chiang Mai 50200, Thailand

Version of record first published: 21 Jun 2012.

To cite this article: Nuengruethai Ekthammathat , Titipun Thongtem , Anukorn Phuruangrat & Somchai Thongtem (2012): Microwave-assisted synthesis and characterisation of uniform $LaPO_4$ nanorods, Journal of Experimental Nanoscience, 7:6, 616-623

To link to this article: http://dx.doi.org/10.1080/17458080.2011.551896

PLEASE SCROLL DOWN FOR ARTICLE

Full terms and conditions of use: http://www.tandfonline.com/page/terms-and-conditions

This article may be used for research, teaching, and private study purposes. Any substantial or systematic reproduction, redistribution, reselling, loan, sub-licensing, systematic supply, or distribution in any form to anyone is expressly forbidden.

The publisher does not give any warranty express or implied or make any representation that the contents will be complete or accurate or up to date. The accuracy of any instructions, formulae, and drug doses should be independently verified with primary sources. The publisher shall not be liable for any loss, actions, claims, proceedings,

demand, or costs or damages whatsoever or howsoever caused arising directly or indirectly in connection with or arising out of the use of this material.

Downloaded by [UNSW Library] at 22:11 05 February 2013

Journal of Experimental Nanoscience
Vol. 7, No. 6, October–November 2012, 616–623

Taylor & Francis
Taylor & Francis Group

Microwave-assisted synthesis and characterisation of uniform $LaPO_4$ nanorods

Nuengruethai Ekthammathat[a], Titipun Thongtem[a]*, Anukorn Phuruangrat[b]* and Somchai Thongtem[c]

[a]*Department of Chemistry and Center for Innovation in Chemistry, Faculty of Science, Chiang Mai University, Chiang Mai 50200, Thailand;* [b]*Department of Materials Science and Technology, Faculty of Science, Prince of Songkla University, Hat Yai, Songkhla 90112, Thailand;* [c]*Department of Physics and Materials Science, Faculty of Science, Chiang Mai University, Chiang Mai 50200, Thailand*

(*Received 25 September 2010; final version received 23 December 2010*)

Lanthanum phosphate ($LaPO_4$) phosphor materials with one-dimensional (1D) nanorods and nanoparticles were successfully synthesised from $LaCl_3 \cdot 7H_2O$ and $Na_3PO_4 \cdot 12H_2O$ with pH adjusted at the range 1–6 using 37% HNO_3 by the microwave radiation at 180 W for 60 min. X-ray diffraction patterns indicated that the as-synthesised products were hexagonal $LaPO_4$ nanostructures. Scanning electron microscopy and transmission electron microscopy analyses showed that these products were nanoparticles, short and long nanorods, controlled by pH of the precursor solutions. Asymmetric stretching and bending vibrations of the PO_4^{3-} groups were detected using Fourier transform-infrared spectroscopy. A possible formation mechanism of $LaPO_4$ phosphor materials with 1D nanorods and nanoparticles was also proposed according to the experimental results.

Keywords: $LaPO_4$; 1D nanorods; nanoparticles; microwave-assisted synthesis

Downloaded by [UNSW Library] at 22:11 05 February 2013

1. Introduction

In recent years, scientists and researchers have focused on doing research on the properties of one-dimensional (1D) nanomaterials, including nanorods, nanowires, nanobelts and nanotubes for use as phosphor materials, which have more efficient novel luminescent properties, due to their quantum size effect [1–3]. In comparison with 0D structures, the space anisotropy of a 1D structure provided a better model system to study the dependence of electronic transport, optical and mechanical properties on size confinement and dimensionality [4,5]. Their properties were controlled by the morphology and size which can be controlled by several parameters including temperature, holding reaction time, template/surfactant added, pH value, synthesised methods, starting materials and many others [6,7].

*Corresponding author. Emails: ttpthongtem@yahoo.com (T. Thongtem); phuruangrat@hotmail.com (A. Phuruangrat)

ISSN 1745–8080 print/ISSN 1745–8099 online
© 2012 Taylor & Francis
http://dx.doi.org/10.1080/17458080.2011.551896
http://www.tandfonline.com

Downloaded by [UNSW Library] at 22:11 05 February 2013

Lanthanide orthophosphate ($LnPO_4$) nanomaterials including lanthanum phosphate ($LaPO_4$), $CePO_4$, $EuPO_4$ and $GdPO_4$ belong to the group of phosphor materials, which are very interesting for researchers due to their unique chemical and physical properties [1,2]. They have a variety of potentially beneficial properties such as very high thermal stability ($\sim$2300°C), low solubility ($K_{sp} = 10^{-25} - 10^{-27}$) in water, high refractive index ($n \approx 1.5$) and high concentration of lasing ions ($\sim 1.8 \times 10^{21}$ ions cm^{-3}). Because of these unique properties, $LnPO_4$ is capable of being used in various applications, such as luminescent or laser materials, magnets, ceramics, catalysts, proton conductors, moisture sensors, heat-resistant materials, hosts for radioactive nuclear waste, green ($^5D_4$–$^7F_5$ of Tb^{3+} at 543 nm) phosphor (for Tb^{3+} co-activated by bulk $LaPO_4$) in fluorescent lamps, scintillators for X-ray and gamma-ray detection in medical science, biochemical probes and medical diagnostics [8]. Among them, $LaPO_4$, with a unique 4f shell of La^{3+} ions, has been widely used in optoelectronic devices high-performance luminescent devices, magnets, catalysts, time-resolved fluorescence labels for biological detection and other functional materials [1,8,9].

There are a number of reports on the synthesis of $LaPO_4$ nanomaterials by various methods, such as liquid phase reaction [10], sonochemical method [11], precipitation [12], solvothermal/hydrothermal method [9,13] and solid–liquid reaction [14], but they are not advantageous due to the high-temperature consumption and long-reaction time. In the past decades, microwave radiation has been considered as a new candidate, and is capable of being applied for the synthesis of nanomaterials such as YVO_4 [15], ZnO [16], CeO_2 [17] and $PbWO_4$ [18]. The microwave method consumes low power and has short-reaction time, and is able to produce highly purified products with controlled morphologies, compared to others [19].

In this research, hexagonal $LaPO_4$ nanorods have been synthesised by microwave radiation method at the precursor pH range of 1–6. The products were characterised by X-ray diffraction (XRD), scanning electron microscopy (SEM) and transmission electron microscopy (TEM) and Fourier transform-infrared spectrometry (FT-IR).

2. Experiment

To synthesise $LaPO_4$ nanostructures, chemical-grade reagents purchased from Merck Company, $LaCl_3 \cdot 7H_2O$, $Na_3PO_4 \cdot 12H_2O$ and 37% HNO_3, were used without further purification.

Each 0.003 mole of $LaCl_3 \cdot 7H_2O$ and $Na_3PO_4 \cdot 12H_2O$ was dissolved in 80 mL deionised (DI) water with vigorous stirring for 15 min, and followed by the addition of 37% HNO_3 to the precursor solutions for adjusting the pH to be in the range 1–6. Each of these solutions was continuously heated by a microwave oven (Electrolux, EMS 2820, 2.45 GHz) at 180 W and 60 min at a time, and naturally cooled down to room temperature. Finally, white precipitates were produced, filtered, washed with DI water and 95% ethanol several times and dried at 80°C for 12 h. The final products were collected for further characterisation.

Phase, morphologies and vibration modes of the products were characterised by XRD (Philips X'Pert MPD) using Cu-Kα line ($\lambda = 1.54056$ Å), and scanned at 2θ angle ranging from 10° to 60° with a scanning rate of 0.04° per step. The XRD data were analysed by X'Pert HighScore Plus program in combination with The Joint Committee on Powder

Diffraction Standards (JCPDS). Field emission scanning electron microscopy (FE-SEM, JEOL JSM-6335F) and TEM (JEOL JEM-2010) were operated at 15.0 and 200 kV with LaB_6 electron gun. FT-IR spectroscopy analysis (Perkin Elmer RX spectrophotometer) of the products with 40 times concentration diluted by KBr was performed over 400–4000 cm^{-1} range with 4 cm^{-1} resolution.

3. Results and discussion

Phase and crystalline structure of $LaPO_4$ synthesised by microwave radiation method with pH adjusted to be in the range 1–6 by the addition of 37% HNO_3 were investigated by XRD, as shown in Figure 1. These patterns were identified as purified hexagonal $LaPO_4$ phase, compared to the JCPDS No. 04-0635 ($a = b = 7.0420$ Å and $c = 6.4490$ Å) [20]. When the precursor pH values were lowered from 6 to 1, the XRD peaks became sharper, proving that the product crystal has improved. Therefore, it can be concluded that hexagonal $LaPO_4$ crystalline was influenced by the precursor pH. Lattice parameters of hexagonal $LaPO_4$ nanostructures were calculated from the equation of plane spacing for the hexagonal structure in combination with the Bragg's law for diffraction, as shown below.

$$\frac{1}{d^2} = \frac{4}{3a^2}(h^2 + hk + k^2) + \frac{1}{c^2}l^2 \tag{1}$$

$$\lambda = 2\mathrm{d}\sin\theta, \tag{2}$$

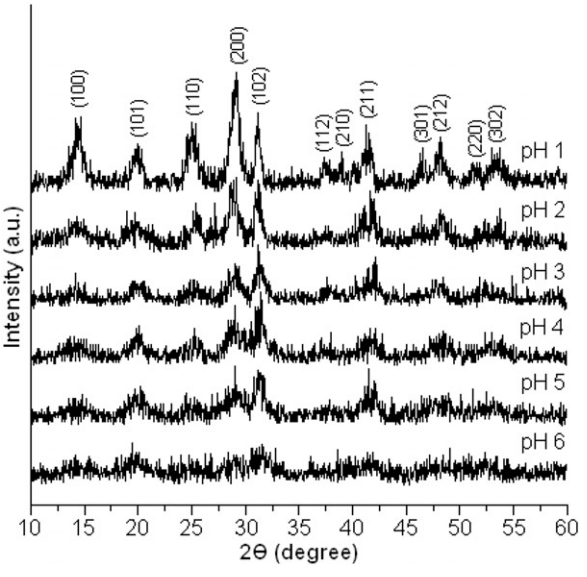


Figure 1. XRD patterns of $LaPO_4$ synthesised in the solutions with different pH values by microwave radiation at 180 W for 60 min.

Downloaded by [UNSW Library] at 22:11 05 February 2013

where a and c are the lattice parameters, h, k and l the Miller indices, d the plane spacing and θ the Bragg's angle [21]. The calculated lattice parameters of the hexagonal $LaPO_4$ nanomaterials (pH = 1) are $a = b = 7.0859$ Å and $c = 6.5016$ Å, very close to those of the JCPDS standard values [20].

Consider the lanthanide phosphate compounds such as $CePO_4$, $LaPO_4$ and $GdPO_4$. Their different modes were originated from the vibration in the tetrahedral PO_4^{3-} units. The selection rule for the isolated PO_4^{3-} tetrahedrons shows different vibration modes as $A_1(R) + E(R) + 2F_2(IR + R)$. The $\nu_1(A_1)$ and $\nu_2(E)$ corresponding to the symmetric stretching and bending modes are Raman active. The $\nu_3(F_2)$ and $\nu_4(F_2)$ are the asymmetric stretching and bending modes, specified as Raman and IR doubly active. The symmetry of PO_4^{3-} ions in the lanthanide phosphate compounds decreases from T_d to C_1. Thus, the non-IR modes become IR active [22]. FT-IR spectra of $LaPO_4$ synthesised by the microwave-assisted synthesis at the pH levels of 1, 3 and 5 were recorded in the range 400–4000 cm^{-1} as shown in Figure 2. The broad bands at 3440 cm^{-1} and 1644 cm^{-1} were, respectively, assigned to be the O–H stretching and bending modes of absorbed water containing in the products. The other peaks at 1046, 614 and 540 cm^{-1} were seen in the vibrations in PO_4^{3-} of $LaPO_4$. The mode at 1046 cm^{-1} was ascribed as the asymmetric stretching vibration of P–O bonds. Those centred at 614 and 540 cm^{-1} were the P–O bending vibrations of the PO_4^{3-} groups [7,9,22]. There were no other functional groups, detected in these products.

The morphologies of $LaPO_4$ nanostructures were characterised by SEM and TEM. From SEM analysis (Figure 3), it is observed that the morphologies of the as-synthesised $LaPO_4$ products have different shapes (nanoparticles and nanorods), depending on the precursor pH of the system. At the pH range of 4–6, there were agglomerates of nanoparticles with size less than 50 nm. When the precursor pH was lowered to 3, the $LaPO_4$ nanoparticles arranged themselves and diffused to form short nanorods.

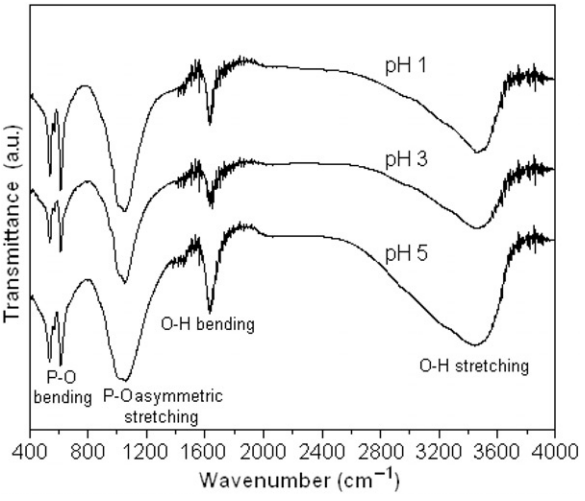


Figure 2. FTIR spectra of $LaPO_4$ synthesised in the solutions with pH values of 1, 3 and 5 by microwave radiation at 180 W for 60 min.

Downloaded by [UNSW Library] at 22:11 05 February 2013

Finally, the short nanorods (~200 nm) and long nanorods (~600 nm) were, respectively, produced at the pH values of 2 and 1, under the microwave radiation. These results confirmed that pH is the key factor to control the $LaPO_4$ morphologies, by changing from nanoparticles to 1D nanorods, due to the increase in the H^+ concentration of the solutions. The effect of pH on different morphologies of $LaPO_4$ nanostructures is illustrated in Figure 4.

The uniform shape of $LaPO_4$ nanorods was characterised by TEM, as shown in Figure 5. It indicates the true morphology of $LaPO_4$ at the pH values 1 and 2, showing that both these products are nanorods with different lengths and diameters. The $LaPO_4$ nanorods are 100–200 nm long with 10–12 nm diameter for pH value 2, and 600–1000 nm long, with 20–40 nm diameter for pH value 1 – in accordance with those of the SEM analysis. The lattice plane and growth direction of $LaPO_4$ nanorods were analysed by high-resolution transmission electron microscope (HRTEM), as shown in Figure 5(c) and (d). It shows lattice fringes, of which a number of planes are parallel to the $LaPO_4$ nanorods. These planes are 4.42 Å apart, corresponding to the (1 0 1) plane of hexagonal $LaPO_4$ structure (JCPDS No. 04-0635) [20]. This analysis demonstrated that the hexagonal $LaPO_4$ nanorods grew along the [−1 0 1] direction.

A possible formation mechanism of $LaPO_4$ phosphor nanomaterials is simply explained as follows:

$$PO_4^{3-} + nH^+ \rightarrow H_nPO_4^{(3-n)-} \tag{3}$$

$$La^{3+} + H_nPO_4^{(3-n)-} \rightarrow LaPO_4\ (\text{white precipitates}) + nH^+. \tag{4}$$

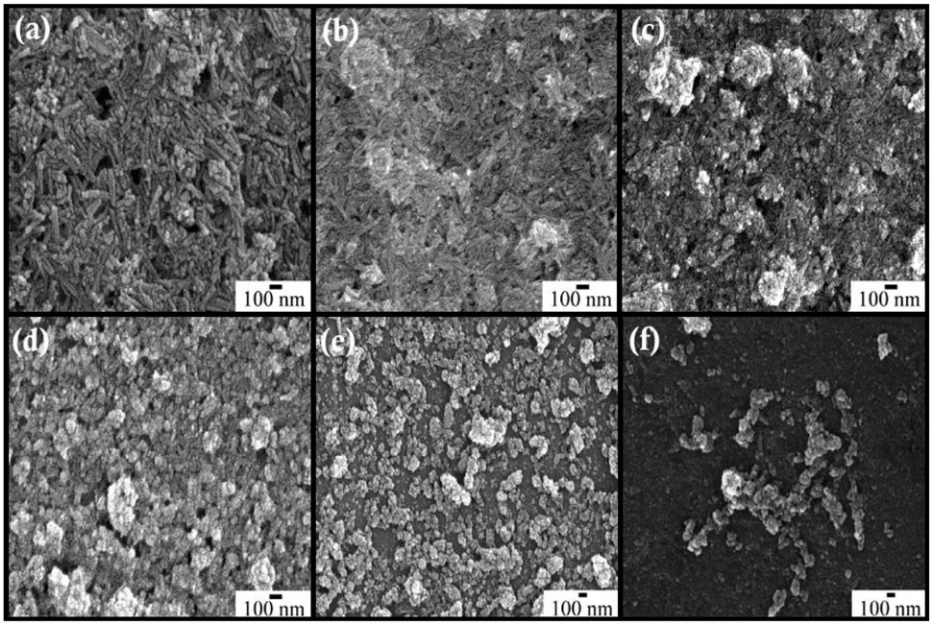


Figure 3. SEM images of $LaPO_4$ synthesised in the solutions with pH values of (a)–(f) 1, 2, 3, 4, 5 and 6 by microwave radiation at 180 W for 60 min, respectively.

Downloaded by [UNSW Library] at 22:11 05 February 2013

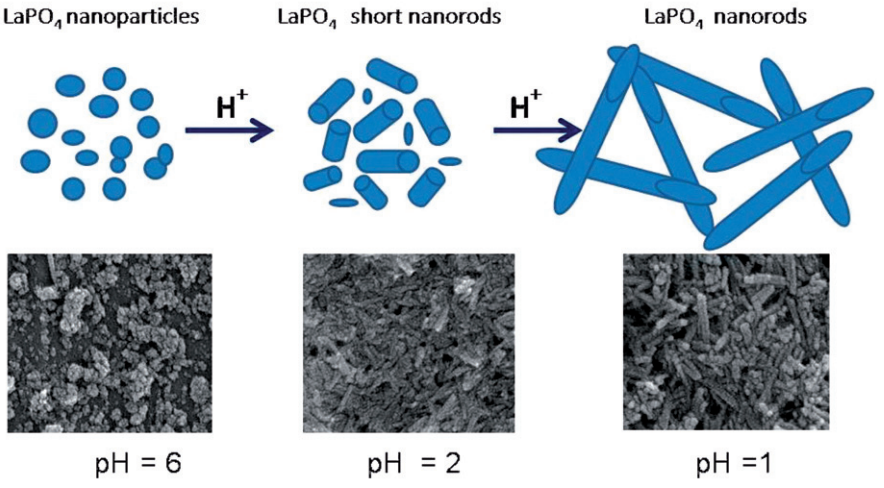


Figure 4. Schematic diagram for the formation of $LaPO_4$ products.

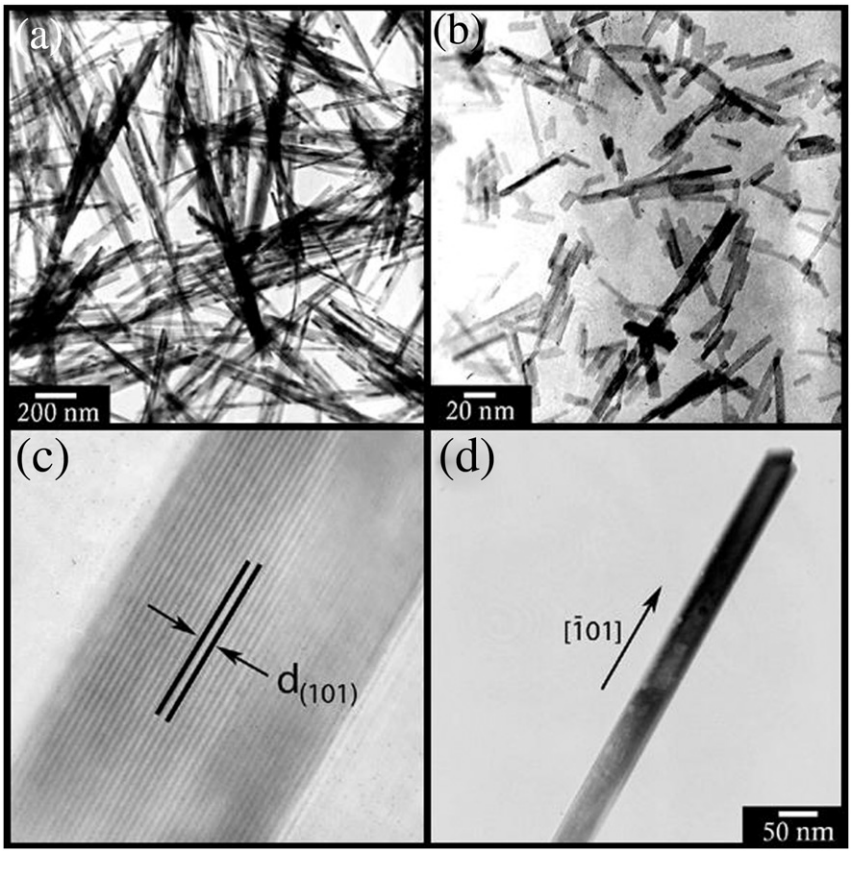


Figure 5. TEM and HRTEM images of $LaPO_4$ synthesised in the solutions with the pH of (a), (c) and (d) 1, and (b) 2, by microwave radiation at 180 W for 60 min.

Downloaded by [UNSW Library] at 22:11 05 February 2013

In this research, $LaCl_3 \cdot 7H_2O$ and $Na_3PO_4 \cdot 12H_2O$ dissolved in DI water with the addition of HNO_3 (conc.). Thus, H^+ ions reacted with PO_4^{3-} ions to form $H_nPO_4^{(3-n)-}$, which subsequently reacted with La^{3+} to produce $LaPO_4$ white precipitates by the microwave radiation at 180 W for 60 min. The products have different morphologies for different pH values of the solutions. These implied that H^+ ions induced the system to be at the highest chemical potential and led the product to grow in 1D $LaPO_4$ nanorods at pH value of 1 – in accordance with the report of Zhang and Guan [23]. Compared to the facile solution-precipitation process reported by Wang et al. [24], $LaPO_4$ products with different morphologies were synthesised. The effect of the precursor pH on the different morphologies was explained above. In this research, microwave radiation as a heating source has more advantages than the conventional heating method, due to the rapid volumetric heating, resulting in higher reaction rate and selectivity, reduction in reaction time often by orders of magnitude, and increasing yields of the products [18]. It is a candidate for the synthesis of nanomaterials.

Downloaded by [UNSW Library] at 22:11 05 February 2013

4. Conclusion

Hexagonal $LaPO_4$ nanorods were successfully synthesised from $LaCl_3 \cdot 7H_2O$ and $Na_3PO_4 \cdot 12H_2O$ in DI water at pH level 1 by the 180-W and 60-min microwave radiation. This method is simple and inexpensive, with short-reaction time and can be applied for the synthesis of other nanomaterials.

Acknowledgements

The research was supported by the National Nanotechnology Center (NANOTEC), a member of National Science and Technology Development Agency (NSTDA), Ministry of Science and Technology; Thailand Research Fund (TRF); and Center for Innovation in Chemistry (PERCH-CIC), Commission on Higher Education (CHE), Ministry of Education, Thailand.

References

[1] L. Qian, W. Du, Q. Gong, and X. Qian, *Controlled synthesis of light rare earth phosphate nanowires via a simple solution route*, Mater. Chem. Phys. 114 (2009), pp. 479–484.

[2] Y.S. Zhao, H. Fu, A. Peng, Y. Ma, D. Xiao, and J. Yao, *Low-dimensional nanomaterials based on small organic molecules: Preparation and optoelectronic properties*, Adv. Mater. 20 (2008), pp. 2859–2876.

[3] X. Liu, Q. Wang, Z Gao, J. Sun, and J. Shen, *Fabrication of lanthanide phosphate nanocrystals with well-controlled morphologies by layer-by-layer adsorption and reaction method at room temperature*, Cryst. Growth Des. 9 (2009), pp. 3707–3713.

[4] L. Yu, H. Song, Z. Liu, L. Yang, and S.L.Z. Zheng, *Electronic transition and energy transfer processes in $LaPO_4$-Ce^{3+}/Tb^{3+} nanowires*, J. Phys. Chem. B 109 (2005), pp. 11450–11455.

[5] L. Yu, H. Song, S. Lu, Z. Liu, and L. Yang, *Influence of shape anisotropy on photoluminescence characteristics in $LaPO_4$:Eu nanowires*, Chem. Phys. Lett. 399 (2004), pp. 384–388.

[6] Z.G. Yan and C.H. Yan, *Controlled synthesis of rare earth nanostructures*, J. Mater. Chem. 18 (2008), pp. 5046–5059.

[7] L. Ma, W.X. Chen, Y.F. Zheng, and Z.D. Xu, *Hydrothermal growth and morphology evolution of $CePO_4$ aggregates by a complexing method*, Mater. Res. Bull. 43 (2008), pp. 2840–2849.

[8] C.R. Patra, G. Alexandra, S. Patra, D.S. Jacob, A. Gedanken, A. Landau, and Y. Gofer, *Microwave approach for the synthesis of rhabdophane-type lanthanide orthophosphate (Ln = La, Ce, Nd, Sm, Eu, Gd and Tb) nanorods under solvothermal conditions*, New J. Chem. 29 (2005), pp. 733–739.

[9] P. Yang, Z. Quan, C. Li, Z. Hou, W. Wang, and J. Lin, *Solvothermal synthesis and luminescent properties of monodisperse $LaPO_4$:Ln (Ln = Eu^{3+}, Ce^{3+}, Tb^{3+}) particles*, J. Solid State Chem. 182 (2009), pp. 1045–1054.

[10] H.K. Jung, J.S. OH, S. Seok, and T.H. Lee, *Preparation and luminescence properties of $LaPO_4$:Er, Yb nanoparticles*, J. Lumin. 114 (2005), pp. 307–313.

[11] C. Yu, M. Yu, C. Li, X. Liu, J. Yang, P. Yang, and J. Lin, *Facile sonochemical synthesis and photoluminescent properties of lanthanide orthophosphate nanoparticles*, J. Solid State Chem. 182 (2009), pp. 339–347.

[12] R. Wang, W. Pan, J. Chen, M. Fang, and J. Meng, *Effect of $LaPO_4$ content on the microstructure and machinability of $Al_2O_3/LaPO_4$ composites*, Mater. Lett. 57 (2002), pp. 822–827.

[13] W.T. Yao and S.H. Yu, *Recent advances in hydrothermal syntheses of low dimensional nanoarchitectures*, Int. J. Nanotechnology 4 (2007), pp. 129–162.

[14] W. Ruigang, P. Wei, C. Jian, F. Minghao, C. Zhenzhu, and L. Yongming, *Synthesis and sintering of $LaPO_4$ powder and its application*, Mater. Chem. Phys. 79 (2003), pp. 30–36.

[15] W.J. Park, M.K. Jung, T. Masaki, S.J. Im, and D.H. Yoon, *Characterization of YVO_4:Eu^{3+}, Sm^{3+} red phosphor quick synthesized by microwave rapid heating method*, Mater. Sci. Eng. B 146 (2008), pp. 95–98.

[16] S. Cho, S.H. Jung, and K.H. Lee, *Morphology-controlled growth of ZnO nanostructures using microwave irradiation: From basic to complex structures*, J. Phys. Chem. C 112 (2008), pp. 12769–12776.

[17] C.S. Riccardi, R.C. Linma, M.L. dos Santos, P.R. Bueno, J.A. Varela, and E. Longo, *Preparation of CeO_2 by a simple microwave–hydrothermal method*, Solid State Ionics 180 (2009), pp. 288–291.

[18] G. Wang and C. Hao, *Fast synthesis and morphology control of lead tungstate microcrystals via a microwave-assisted method*, Mater. Res. Bull. 44 (2009), pp. 418–421.

[19] C.O. Kappe, D. Dallinger, and S.S. Murphree, *Practical microwave synthesis for organic chemists: Strategies, instruments, and protocols*, WILEY-VCH Verlag GmbH & Co. KGaA, Weinheim, 2009, pp. 1–9.

[20] Powder Diffract File, JCPDS-ICDD, 12 Campus Boulevard, Newtown Square, PA 19073-3273, USA, 2001.

[21] C. Suryanarayana and M.G. Norton, *X-ray Diffraction, A Practical Approach*, Plenum Press, New York, 1998.

[22] K. Wang, J. Zhang, J. Wang, C. Fang, W. Yu, X. Zhao, and H. Xu, *Growth defects and infrared spectra analysis of $CePO_4$ single crystals*, J. Appl. Cryst. 38 (2005), pp. 675–677.

[23] Y. Zhang and H. Guan, *Hydrothermal synthesis and characterization of hexagonal and monoclinic $CePO_4$ single-crystal nanowires*, J. Cryst. Growth 256 (2003), pp. 156–161.

[24] Z. Chai, L. Gao, C. Wang, H. Zhang, R. Zheng, P.A. Webley, and H. Wang, *Synthesis of mesoporous $LaPO_4$ nanostructures with controllable morphologies*, New J. Chem. 33 (2009), pp. 1657–1662.

Downloaded by [UNSW Library] at 22:11 05 February 2013

Materials Letters 68 (2012) 265–268

Contents lists available at SciVerse ScienceDirect

Materials Letters

journal homepage: www.elsevier.com/locate/matlet

Characterization of $ZnMoO_4$ nanofibers synthesized by electrospinning–calcination combinations

Yanee Keereeta [a], Titipun Thongtem [b,*], Somchai Thongtem [a]

[a] Department of Physics and Materials Science, Faculty of Science, Chiang Mai University, Chiang Mai 50200, Thailand
[b] Department of Chemistry, Faculty of Science, Chiang Mai University, Chiang Mai 50200, Thailand

ARTICLE INFO

Article history:
Received 13 September 2011
Accepted 27 October 2011
Available online 29 October 2011

Keywords:
Electron microscopy
Semiconductors
Spectroscopy
X-ray techniques

ABSTRACT

$ZnMoO_4$ nanofibers were synthesized by electrospinning–calcination combinations. In the present research, anorthic structured $ZnMoO_4$ was detected by X-ray diffraction (XRD) and confirmed by simulation and selected area electron diffraction (SAED). Morphology was confirmed by scanning and transmission electron microscopy (SEM, TEM) and atomic force microscopy (AFM). Vibrations were detected by Fourier transform infrared (FTIR) and Raman spectroscopy. By using photoluminescence (PL) and UV–visible spectroscopy, the PL emission was found to be in the same range as the indirect energy gap (E_g). A formation mechanism was proposed according to the experimental results.

© 2011 Elsevier B.V. All rights reserved.

1. Introduction

$ZnMoO_4$, a semiconducting material, exists as anorthic and monoclinic structures [1]. It contains non-heavy elements and Mo as high as 42.58 wt.%. It is nontoxic, and also is very attractive for its properties of luminescence, scintillation and photocatalysis, and for its use in battery electrodes and drug delivery systems [2–6]. Previously, $ZnMoO_4$ with rhombus sheet or flower-like structure, α-$ZnMoO_4$, and needle-like $ZnMoO_4{\cdot}0.8H_2O$ were successfully synthesized by simple hydrothermal crystallization reactions of $(NH_4)_6Mo_7O_{24}{\cdot}4H_2O$ and $Zn(NO_3)_2{\cdot}6H_2O$ solutions containing citric acid [4]. $AMoO_4$ with scheelite (A = Ca, Sr, Ba) and wolframite (A = Mg, Mn, Zn) structures were synthesized by conventional mixed oxide calcination method [2]; nanocrystalline wolframite-structured $MMoO_4$ (M = Ni, Zn) phosphors by a modified citrate complex route assisted by microwave irradiation [3]; $ZnMoO_4$ hollow microspheres by yeast-directed hydrothermal synthesis of $Zn(AC)_2$ and Na_2MoO_4 in aqueous solution [5]; and $ZnBO_4$ (B = W, Mo) single crystals by the Czochralski method [6]. In the present research, anorthic $ZnMoO_4$ nanofibers were successfully synthesized by electrospinning–calcination combinations. To the best of our knowledge, no $ZnMoO_4$ nanofibers have ever been synthesized by the present processes. This success may lead to large-scale production in the near future.

2. Experiment

To synthesize $ZnMoO_4$ nanofibers, 0.003 mol $Zn(CH_3COO)_2{\cdot}2H_2O$, 0.003 mol $(NH_4)_6Mo_7O_{24}{\cdot}4H_2O$, and 1.5 g poly (vinyl alcohol) (PVA) with the molar mass of 72,000 g/mol were dissolved in 30 ml deionized water, and vigorously stirred at 80 °C for 30 min. The mixture was electrospun through a horizontal hollow needle, biased with +15 kV direct voltage to synthesize a fibrous web on a grounded aluminum foil. These fibers were subsequently calcined at 300, 400, 519, and 600 °C for 3, 6, and 9 h, for further different analyses. For convenience, $ZnMoO_4$-PVA fibers before calcination were symbolized as PBF. The fibers after calcination at 400 °C for 3 h were as P4003, at 519 °C for 3 h as P5193, and similarly for other products.

3. Results and discussion

3.1. Phase analysis

A comparison of XRD patterns (Fig. 1a) to those of JCPDS No. 35–0765 [1] revealed that they corresponded to anorthic (triclinic [7]) structured $ZnMoO_4$ with P-1 space group. Some PVA seemed to remain in the P4003 product. The PVA peak at 2θ of 22.5° [8] could be covered by the peaks of $ZnMoO_4$; but for the P5193, P5196 and P5199, no PVA was in existence on the products [8]. The nanofibers were the best crystal quality, with their atoms residing in a perfect crystal lattice. The lengths of calcination time did not have strong influence on the degree of crystallinity. Calculated crystal axes (8.3600, 9.7000 and 6.9690 Å) and angles (106.880, 102.010 and 96.859°) [9] were in accordance with those of the JCPDS database [1]. XRD patterns of purified $ZnMoO_4$ were compared with that obtained by simulation

* Corresponding author. Tel.: +66 53 943344; fax: +66 53 892277.
E-mail addresses: ttpthongtem@yahoo.com, ttpthongtem@gmail.com (T. Thongtem).

0167-577X/$ – see front matter © 2011 Elsevier B.V. All rights reserved.
doi:10.1016/j.matlet.2011.10.097

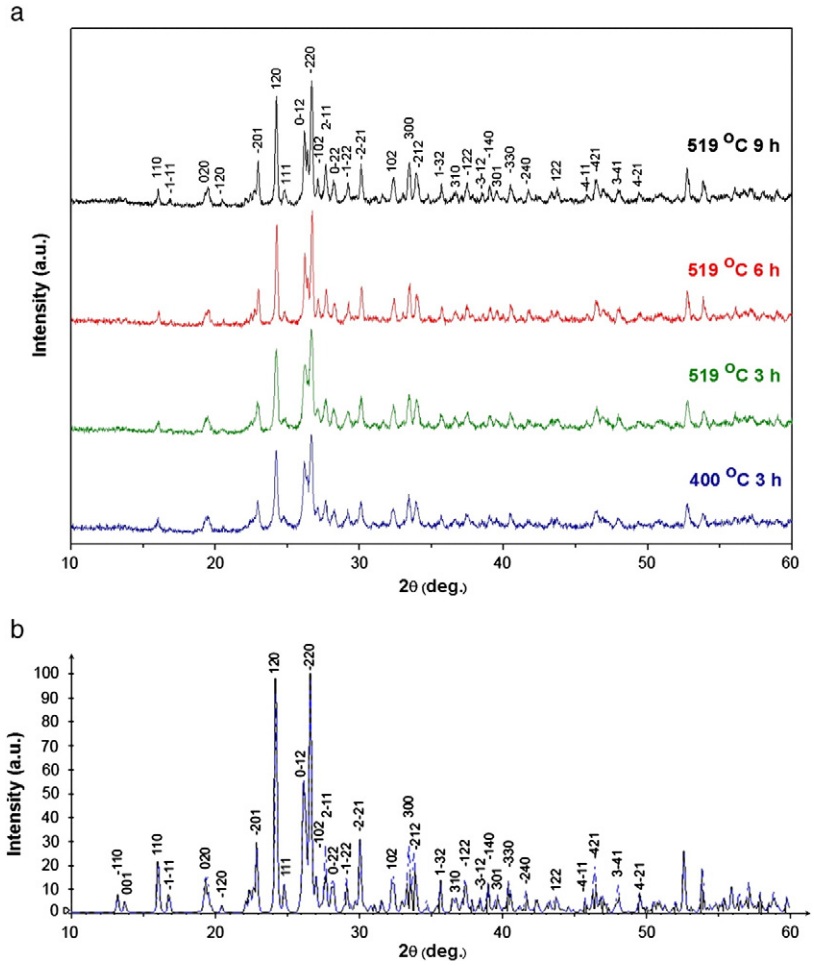


Fig. 1. (a) XRD patterns of P4003, P5193, P5196 and P5199. (b) The simulated pattern.

(Fig. 1b) [10]. The 2θ Bragg angles and peak intensities of the experiment, simulation, and JCPDS database were in good accordance.

The simulated structure (Fig. 2a) contained three non-equivalent units of MoO_4 tetrahedrons with different Mo–O bond lengths. Zn^{2+} ions occupied sites with five- and six-fold coordination. The SAED pattern (Fig. 2b) was indexed [11] and specified as $ZnMoO_4$ [1].

3.2. Morphologies

Before calcination (Figs. 2c, d and 3a), the product was composed of fibers with smooth surfaces; diameters were in the 110–230 nm range. $ZnMoO_4$ nuclei blended in the fibers were unable to be detected. Upon calcination at 300, 400 and 519 °C for 3 h (Figs. 2e-g and 3b-d), the fibers became less thick due to the evaporation of PVA. Some PVA was still left on the fibers at 300 and 400 °C, but was no longer left at 519 °C [8]. At these stages, $ZnMoO_4$ nuclei also grew into nanoparticles. The rate of particle growth became faster at higher temperature. At 300, 400 and 519 °C for 3 h, the evaporation rate of PVA was faster than the growth rate of particles. Thus, at 519 °C and 3 h (Figs. 2e-g and 3d), the fibers were the smallest (nanofibers). At a constant temperature of 519 °C (Fig. 3e and f), the nanofibers were also enlarged with prolonged times (6 and 9 h). The nanofibers seemed to be constant at 100 nm diameter. At 600 °C and 3 h (Fig. 3g), the fibers were the largest. Sometimes the fibers were broken, caused by the internal stress developed inside. On close inspection of a nanofiber of P5193 (Fig. 2g and h), the product was found to consist of faceted nanoparticles. Characterization on a rectangle of Fig. 2h showed that the particle was composed of a number of parallel strips (Fig. 2i), corresponding to the $(\bar{2}02)$ crystallographic planes.

3.3. Formation mechanism

$Zn(CH_3COO)_2{\cdot}2H_2O$, $(NH_4)_6Mo_7O_{24}{\cdot}4H_2O$ and PVA mixture was electrospun through +15 kV to heat up the as-spun fibers. $ZnMoO_4$ molecules were synthesized, nucleated, blended in PVA template, and deposited as fibers on aluminum foil.

$$7Zn^{2+} + Mo_7O_{24}^{6-} + 4H_2O \rightarrow 7ZnMoO_4 + 8H^+$$

At high-temperature calcination, PVA and residual water evaporated and decomposed. $ZnMoO_4$ nuclei grew to form nanoparticles, and arranged themselves in lines like nanofibers. In the present research, the reactants could be left inside the fibers after electrospinning. Thus, $ZnMoO_4$ molecules formed, nucleated, and grew into nanoparticles by high-temperature calcination.

3.4. Vibration modes

Fig. 3h shows FTIR spectra of different products; the major vibrations of PVA were clearly detected. But no $ZnMoO_4$ was detected in the PBF. Upon calcination at different conditions, PVA evaporated and decomposed. Some trace PVA was still detected in the P4003; however it was no longer detected in the P5193, P5196 and P5199, and the vibrations at 750–960 cm^{-1} became strengthened. Those at 957 cm^{-1} were specified as the ν_1 stretching of Mo–O in bridging Mo–O–Mo linkages. The vibrations at 870 cm^{-1} corresponded to the ν_1 stretching of $(MoO_4)^{2-}$tetrahedrons, and those at 754 cm^{-1} to the ν_3 stretching of Mo–O [12,13].

Raman vibrations (Fig. 3i) of $ZnMoO_4$-PVA fibers after calcination at different conditions showed the strongest intensity at 965 cm^{-1},

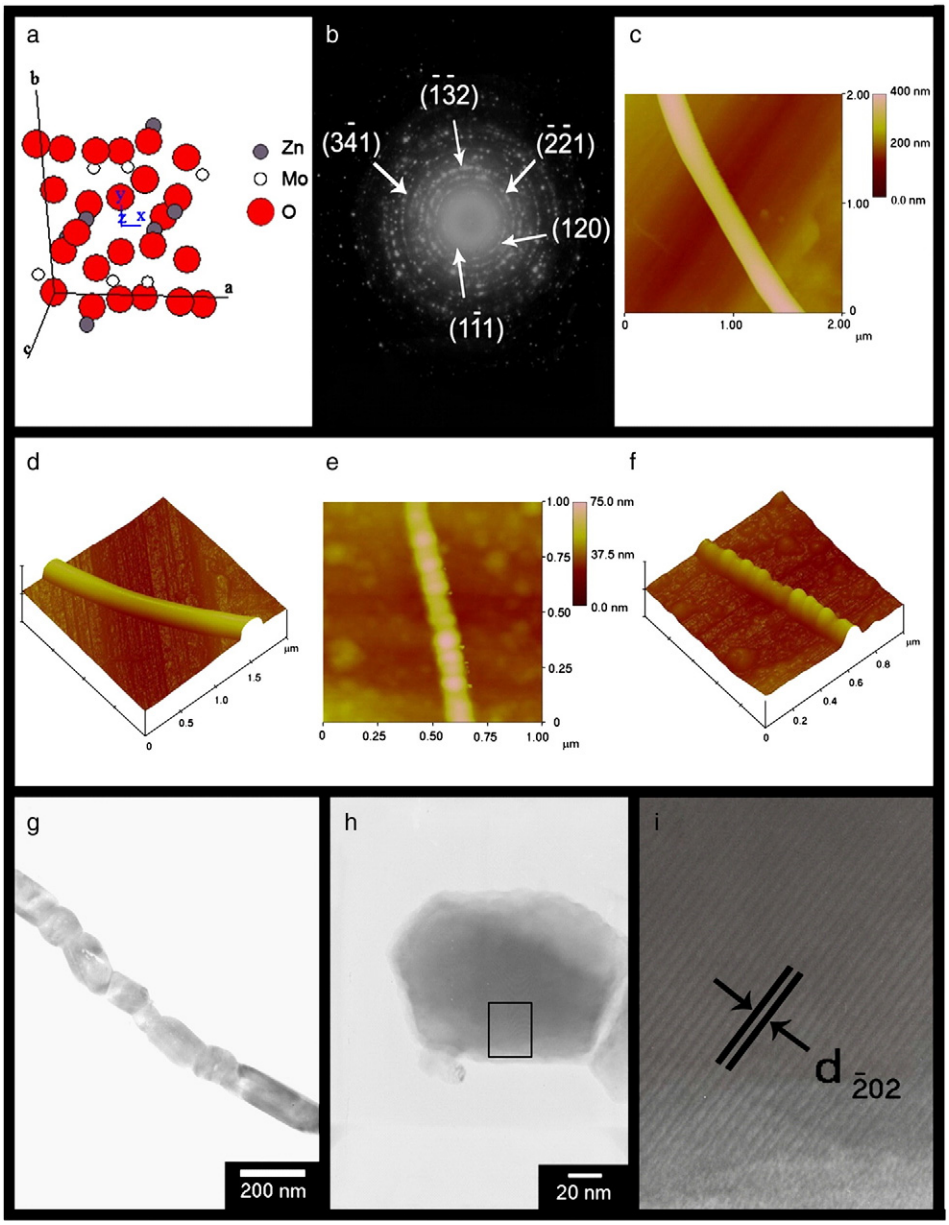


Fig. 2. (a) Crystal structure of $ZnMoO_4$ obtained by simulation, and (b) SAED pattern of P5193. AFM, TEM and HRTEM images of (c, d) PBF, and (e–i) P5193.

corresponding to previous reports [13–15]. Mo – O – Mo bridging between MoO_4 units was not detected, indicating the presence of isolated MoO_4 tetrahedrons. The crystals contained both ZnO_5 and ZnO_6 polyhedrons, deformed by the Jahn–Teller effect. Commonly, there was single-corner sharing of ZnO_5/ZnO_6 and MoO_4, with a number of Zn – O – Zn and Zn – O – Mo linkages inside, leading to the sharp peaks caused by Mo^{6+} bonding of isolated MoO_4 tetrahedrons [7,14].

3.5. Absorption and emission

UV–visible absorption (Fig. 3j) of the P5193 indicated an exponential decreasing of the photonic absorbance (α) attenuated through the product. Its indirect E_g was determined (by extrapolating the linear portion of the curve to zero absorption) to be 3.3 eV — very close to that for $xMoO_3$-(1-x)ZnO [12], but less than that estimated for perfect $ZnMoO_4$ [16].

By using a 240 nm excitation wavelength, PL emissions (Fig. 3k) of the P5193 were detected at 371 nm (3.34 eV) and 390 nm (3.18 eV) due to the transitions between Mo_{4d} and O_{2p} states — in accordance with other reports [3,7]. The different emission was caused by the non-equivalent MoO_4 units, Jahn–Teller effect, and the perturbation of MoO_4 induced by defects [7]. In the present research, the PL emission was in the same range as the indirect E_g, relating to the indirect transition in the nanofibers.

4. Conclusions

$ZnMoO_4$-PVA fibers were successfully synthesized by electrospinning of $Zn(CH_3COO)_2 \cdot 2H_2O$, $(NH_4)_6Mo_7O_{24} \cdot 4H_2O$, and PVA mixture. To form $ZnMoO_4$ nanofibers, the as-spun fibers were subsequently calcined at 519 °C for 3, 6 and 9 h. The PL emission of the P5193 was in the same range as the 3.3 eV indirect E_g — a promising value for scintillation and luminescence.

Acknowledgements

We wish to thank the National Nanotechnology Center (NANOTEC), National Science and Technology Development Agency, for providing

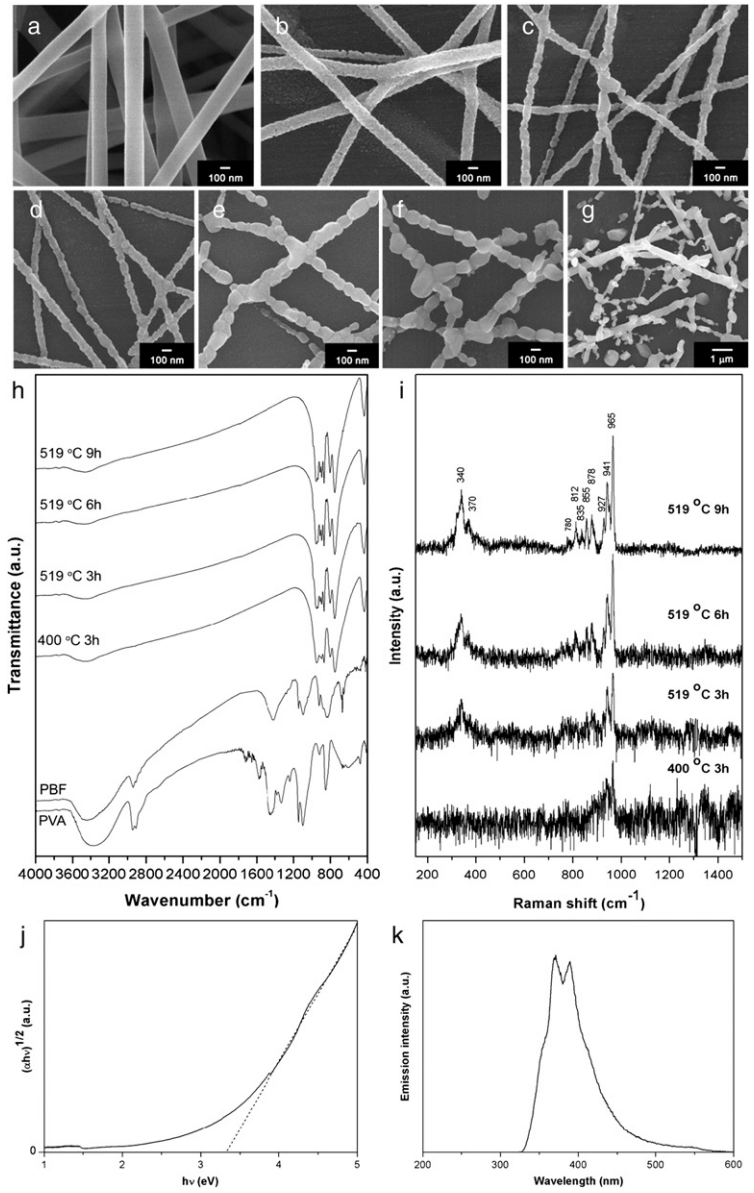


Fig. 3. (a–g) SEM images of PBF, P3003, P4003, P5193, P5196, P5199 and P6003, (h, i) FTIR and Raman spectra of PVA, PBF, P4003, P5193, P5196 and P5199, and (j, k) UV-visible absorption and PL emission of P5193, respectively.

financial support through the project code: P-10-11345, and the Thailand Research Fund (TRF) through the RGJ-Ph.D. Program, and the TRF Basic Research Grant, including Graduate School of Chiang Mai University through the general support.

References

[1] Powder Diffract. File, JCPDS-ICDD, 12 Campus Boulevard, Newtown Square, PA 19073–3273, U.S.A. 2001.
[2] Choi GK, Kim JR, Yoon SH, Hong KS. Microwave dielectric properties of scheelite (A = Ca, Sr, Ba) and wolframite (A = Mg, Zn, Mn) $AMoO_4$ compounds. J Eur Ceram Soc 2007;27:3063–7.
[3] Ryu JH, Koo SM, Yoon JW, Lim CS, Shim KB. Synthesis of nanocrystalline $MMoO_4$ (M = Ni, Zn) phosphors via a citrate complex route assisted by microwave irradiation and their photoluminescence. Mater Lett 2006;60:1702–5.
[4] Zhang G, Yu S, Yang Y, Jiang W, Zhang S, Huang B. Synthesis, morphology and phase transition of the zinc molybdates $ZnMoO_4 \cdot 0.8H_2O$/α-$ZnMoO_4$/$ZnMoO_4$ by hydrothermal method. J Cryst Growth 2010;312:1866–74.
[5] Li Y, Weisheng G, Bo B, Kaijie G. Yeast-directed hydrothermal synthesis of $ZnMoO_4$ hollow microspheres and its photocatalytic degradation of auramine O. 2009 Internat Conf Energy Environm Tech. IEEE; 2009, doi:10.1109/ICEET.2009.631.
[6] Dubovik AM, Vostretsov YY, Grinyov BV, Danevich FA, Kraus H, Nagornaya LL, et al. Research and development of $ZnBO_4$ (B = W, Mo) crystal scintillators for dark matter and double beta decay searching. Acta Phys Pol A 2010;117:15–9.
[7] Mikhailik VB, Kraus H, Wahl D, Ehrenberg H, Mykhaylyk MS. Optical and luminescence studies of $ZnMoO_4$ using vacuum ultraviolet synchrotron radiation. Nucl Instrum Methods Phys Res A 2006;562:513–6.
[8] Keereeta Y, Thongtem T, Thongtem S. Fabrication of $ZnWO_4$ nanofibers by a high direct voltage electrospinning process. J Alloys Compd 2011;509:6689–95.
[9] Suryanarayana C, Norton MG. X-ray Diffract. NY: Plenum Press; 1998.
[10] Boudias C, Monceau D. CaRIne Crystallography 3.1. Centre de Transfert, 60200 Compiègne, France: DIVERGENT S.A.; 1989–1998.
[11] Andrews KW, Dyson DJ, Keown SR. Interpret Electr Diffract Patterns. NY: Plenum Press; 1971.
[12] Bhattacharya S, Kar T, Bar AK, Roy D, Graca MPF, Valente MA. Structural behaviors and optical properties of semiconducting zinc-molybdate glass nanocomposites. Sci Adv Mater 2011;3:284–8.
[13] Šubčík J, Koudelka L, Mošner P, Montagne L, Revel B, Gregora I. Structure and properties of MoO_3-containing zinc borophosphate glasses. J Non-Cryst Solids 2009;355:970–5.
[14] Aleksandrov L, Komatsu T, Iordanova R, Dimitriev Y. Structure study of MoO_3-ZnO-B_2O_3 glasses by Raman spectroscopy and formation of α-$ZnMoO_4$ nanocrystals. Opt Mater 2011;33:839–45.
[15] Basiev TT, Sobol AA, Voronko YK, Zverev PG. Spontaneous Raman spectroscopy of tungstate and molybdate crystals for Raman lasers. Opt Mater 2000;15:205–16.
[16] Spassky DA, Vasil'ev AN, Kamenskikh IA, Mikhailin VV, Savon AE, Hizhnyi YA, et al. Electronic structure and luminescence mechanisms in $ZnMoO_4$ crystals. J Phys 2011;23:365501–10.

Journal of Alloys and Compounds 509 (2011) 6689–6695

Contents lists available at ScienceDirect

Journal of Alloys and Compounds

journal homepage: www.elsevier.com/locate/jallcom

Fabrication of $ZnWO_4$ nanofibers by a high direct voltage electrospinning process

Yanee Keereeta [a], Titipun Thongtem [b,c,*], Somchai Thongtem [a,c]

[a] Department of Physics and Materials Science, Faculty of Science, Chiang Mai University, Chiang Mai 50200, Thailand
[b] Department of Chemistry, Faculty of Science, Chiang Mai University, Chiang Mai 50200, Thailand
[c] Materials Science Research Center, Faculty of Science, Chiang Mai University, Chiang Mai 50200, Thailand

ARTICLE INFO

Article history:
Received 25 February 2011
Received in revised form 21 March 2011
Accepted 24 March 2011
Available online 31 March 2011

Keywords:
Semiconductors
Nanofabrications
Luminescence
Scanning electron microscopy
X-ray diffraction

ABSTRACT

Mixtures of zinc acetate dihydrate, ammonium metatungstate hydrate, and 5 wt%, 6 wt%, and 7 wt% of poly (vinyl alcohol) (PVA) were electrospun by a +15 kV direct voltage to produce fibers. In the present research, the electrospun fibers of 6 wt% PVA were further calcined at 400–600 °C for 3 h. The sanmartinite monoclinic structured $ZnWO_4$ was detected by X-ray diffractometer (XRD) and selected area electron diffraction (SAED), weight loss by thermogravimetric analyser (TGA), morphology and particle size by scanning and transmission electron microscopes (SEM, TEM) and atomic force microscope (AFM), including their vibration modes by Fourier transform infrared spectrometer (FTIR) and Raman spectrometer. The 4.42 eV direct energy gap (E_g) and 460 nm emission wavelength, caused by the electronic transition of $(WO_6)^{2-}$ octahedrons, were determined by UV–visible absorption and photoluminescence (PL) spectrometers. A possible formation mechanism of $ZnWO_4$ nanofibers was also proposed according to the experimental results.

© 2011 Elsevier B.V. All rights reserved.

1. Introduction

Recently, nanostructured materials such as nanowires, nanorods, nanotubes and nanofibers have received considerable attention for a variety of applications [1]; especially, nanofibers or non-woven textiles [2]. They have attractive properties and novel potential applications for using as solar cells, electromagnetic shielding materials, non-wetting textiles, medical prosthesis, and liquid crystal devices [3,4]. A possible process used to produce nanofibrous inorganic materials is by electrospinning, which is now becoming increasingly popular [5] even for the industrial scale production. It is able to produce continuous polymer fibers with diameters of micro- and nano-scale through the action of an external electric field imposed in a polymer solution or melt [2]. By using the inorganic material and polymer mixtures as the starting precursors, the inorganic material–polymer electrospun fibers can be produced easily. When diameters of the electrospun fibers are lessened from micrometers to sub-micrometers or nanometers, there appear some amazing characteristics such as very large surface area to volume ratio, flexibility in surface functionality, and superior mechanical performance [4]. Subsequently, inorganic nanofibers can be produced by the calcination of inorganic material–polymer electrospun fibers obtained by electrospinning of the sol–gel solution [6].

Among different semiconducting materials, $ZnWO_4$ has excellent properties and strong potential application in various fields such as photoluminescence [7–9], Raman laser converters [7], photocatalyst [7], and scintillator material [7,10]. $ZnWO_4$ belongs to the monoclinic sanmartinite-type structure with $P2/c$ space group [11]. In the past decade, nanosized $ZnWO_4$ has been produced by several processes such as co-precipitation [7], Czochralski technique [12], hydrothermal method [8,13–15], microwave-assisted synthesis [16], and polymerized complex method [17].

To produce non-woven fibers by the electrospinning process, a positive high direct voltage is applied to a liquid droplet, ejected out of the tip of a hollow needle. The droplet is charged and stretched – known as Taylor cone. If the molecular cohesion of the liquid – such as polymeric solution or melt, and the direct voltage are sufficiently high, a very long thin charged liquid jet will be formed. During flying, the jet dries and solidifies – caused by the external electric field inside. Finally, the fiber is produced, and deposited on a grounded collector [4].

In the present research, $ZnWO_4$–PVA electrospun fibers were firstly produced by the lab-made electrospinning equipment. They are very novel and promising material for a variety of applications. These electrospun fibers were subsequently calcined at high temperature to form $ZnWO_4$ nanofibers. To the best of our knowledge, there are no $ZnWO_4$ nanofibers have ever been produced by the present process. It is therefore for us to use the mixture of inorganic materials and polymer to produce the inorganic material–polymer

* Corresponding author at: Department of Chemistry, Faculty of Science, Chiang Mai University, Chiang Mai 50200, Thailand. Tel.: +66 0 53 943344; fax: +66 0 53 892277.
E-mail address: ttpthongtem@yahoo.com (T. Thongtem).

0925-8388/$ – see front matter © 2011 Elsevier B.V. All rights reserved.
doi:10.1016/j.jallcom.2011.03.140

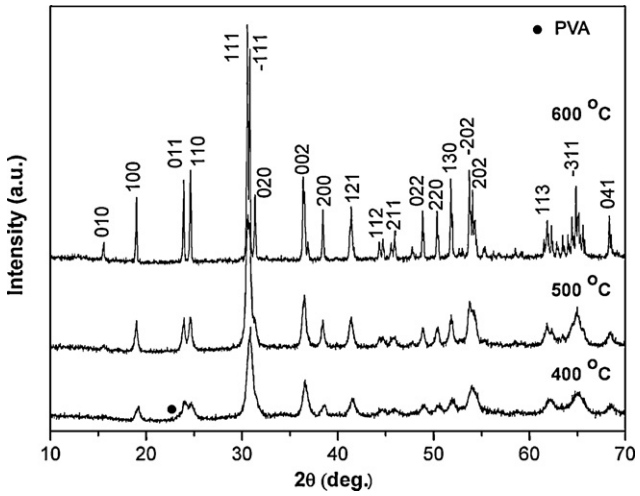


Fig. 1. XRD patterns of the electrospun fibers after calcination at 400 °C, 500 °C, and 600 °C for 3 h.

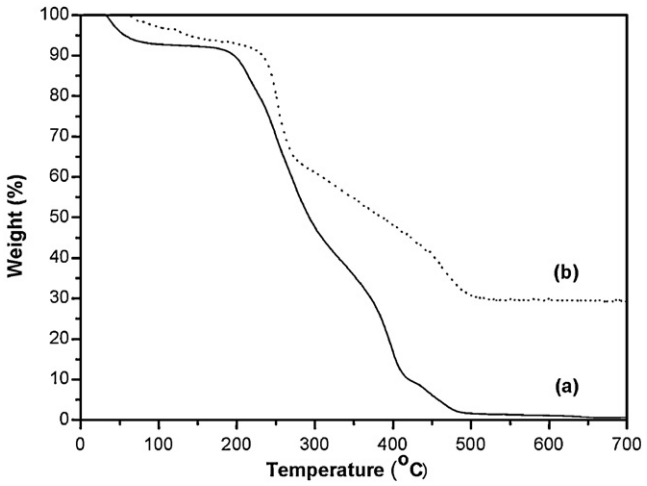


Fig. 2. TGA curves of (a) PVA, and (b) $ZnWO_4$–PVA electrospun fibers produced from 6 wt% PVA solution.

electrospun fibers, which would transform into nanofibrous inorganic material by subsequent calcination at high temperature. Moreover, the success in producing the solid nanofibrous material may lead to new industrial process under the action of an external electric field.

2. Experimental procedure

Basing on the conventional sol–gel process – 1:1 molar ratio of Zn:W of zinc acetate dihydrate ($Zn(CH_3COO)_2{\cdot}2H_2O$, 99.0%) and ammonium metatungstate hydrate ($H_{26}N_6O_{40}W_{12}{\cdot}H_2O$, 99.0%) was dissolved in 10 ml deionized water, and stirred for 10 min. Then 20 ml aqueous solutions of 5 wt%, 6 wt%, and 7 wt% poly (vinyl alcohol) (PVA, 125,000 MW) were added to the precursor solutions, with 30 min vigorous stirring in a 80 °C water bath. Each of the solution mixtures was loaded into a plastic syringe on a horizontal platform. A piece of flat aluminum foil was vertically placed 15 cm away for collecting the fibers. Electrospinning was done by ejecting a jet of inorganic material–polymeric solution out of the long hollow needle, and a +15 kV of d.c. power supply was simultaneously applied at the needle tip. Finally a dense web of electrospun fibers was collected on the grounded aluminum foil. The fibers produced from 6 wt% PVA solution was calcined by increasing from room temperature (T_R) at a rate of 5 °C/min until reaching 400 °C, 500 °C, and 600 °C, held at each of these temperatures for 3 h, and left the system to cool down to room temperature. The products were characterized using thermogravimetric analyser (TGA, Shimadzu TGA-50 analyzer, Japan) using a heating rate of 5 °C/min; X-ray diffractometer (XRD, SIEMENS D500, Germany) operating at 20 kV, 15 mA, and using Cu-Kα line, in combination with the database of the Joint Committee on Powder Diffraction Standards (JCPDS) [11]; scanning electron microscope (SEM, JEOL JSM-6335F, Japan) operating at 15 kV; transmission electron microscope (TEM, JEOL JEM-2010, Japan), high resolution transmission electron microscope (HRTEM) and selected area electron diffractometer (SAED) operating at 200 kV; atomic force microscope (AFM, NanoScope IIIa, MMAFML N, Veeco, USA) with silicon tip driven at a frequency of 200–300 kHz tapping mode; Fourier transform infrared spectrometer (FTIR, Bruker Tensor 27, Germany) with KBr as a diluting agent and operated in the range of 4000–400 cm^{-1}; Raman spectrometer (T64000 HORIBA Jobin Yvon, USA) using a 50 mW and 514.5 nm wavelength Ar green laser; UV–visible spectrometer (Lambda 25 PerkinElmer, USA) using a UV lamp with the resolution of 1 nm; and photoluminescence (PL) spectrometer (LS 50B PerkinElmer, USA) using a 280 nm excitation wavelength at room temperature.

3. Results and discussion

3.1. XRD

XRD patterns of the electrospun fibers after calcination at 400 °C, 500 °C and 600 °C are presented in Fig. 1. Comparing to the JCPDS database no. 15-0774 [11], they corresponded to sanmartinite structured $ZnWO_4$ with monoclinic crystal system and $P2/c$ space group. In the present study, temperature was found to have influence on the crystallinity and purity of $ZnWO_4$ fibers; especially, the relatively high temperature calcination. At 400 °C, XRD revealed that the product was not perfectly pure $ZnWO_4$. It contained some residual PVA at 2θ of approximately 22.5° [18]. Upon increasing the calcination temperatures to be 500 °C and 600 °C, the spectra became sharper and the XRD intensities were stronger. The crystalline degree of the products was much improved. No PVA was detected by the XRD. At 600 °C calcination, the product was the best pure crystal. Its degree of crystallinity was the highest, and the atoms resided in the perfect crystal lattice. By using the Scherrer formula [19], the crystallite sizes obtained by 400 °C, 500 °C, and 600 °C calcination for 3 h were 16 nm, 30 nm, and 105 nm, respectively.

3.2. TGA

Fig. 2 shows the thermal behavior of PVA and $ZnWO_4$–PVA electrospun fibers characterized by TGA analyzer with a heating rate of 5 °C/min. The weight loss of pure PVA exhibited the degradation process as follows. The first weight loss was 10.5%, due to the evaporation of loosely bound water at 32–200 °C. The second was the large amount of weight loss for 79.3%, predominantly caused by the decomposition of PVA structure at 200–420 °C. The third was 8.3%, by the breaking of PVA backbone at 420–490 °C. The weight loss tended to terminate upon further heating to above 490 °C [20]. When the $ZnWO_4$–PVA electrospun fibers were characterized, their weight losses were divided into three different steps. The first weight loss in the temperature range of 32–226 °C was 11.2%, and associated with water evaporation. The second weight loss of 45.7% at 226–420 °C was caused by the decomposition of PVA. The final weight loss of 15.5% in the temperature range of 420–519 °C was likely to be the oxidation and decomposition of the PVA main chain. These last two steps were attributed to the loss of PVA and organic compound blended in the fibers. At a temperature above 519 °C, there was no significant change in their weight. Thus, pure crystalline $ZnWO_4$ fibers were assumed to be produced at a temperature of 519 °C and above, very close to the reports of Zhao et al. (486 °C) [10], and Ryu et al. (550 °C) [17]. Comparing between PVA and $ZnWO_4$–PVA electrospun fibers, their weight and weight loss percents of each steps were different, mainly caused by the evaporation and decomposition of water and PVA.

3.3. SEM, TEM, AFM, and SAED

Fig. 3a–c shows SEM images of the electrospun fibers produced from the solutions of 5 wt%, 6 wt% and 7 wt% PVA. These products were composed of fibers shaped like a web of spiders,

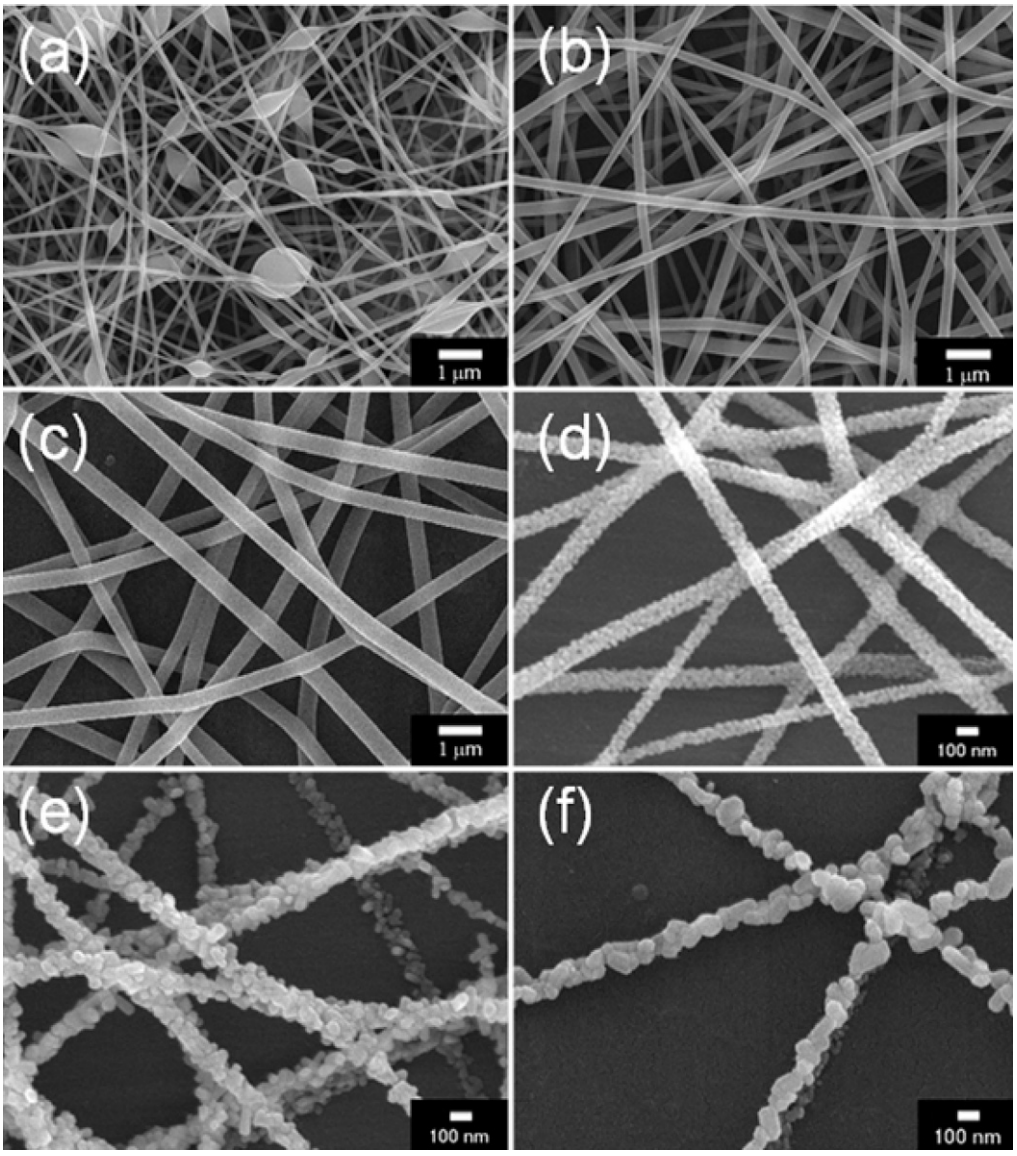


Fig. 3. SEM images of the electrospun fibers using different PVA contents of (a–c) 5 wt%, 6 wt%, and 7 wt%, and (d–f) the electrospun fibers of (b) after calcination at 400 °C, 500 °C, and 600 °C for 3 h, respectively.

with their smooth surfaces. The as-electrospun nuclei blended in the fibers were not detected by SEM. For 5 wt% PVA, some beads were also detected. When the content of PVA was increased from 5 wt% to 7 wt%, diameters of the fibers were also increased and the beads were no longer detected. This implies that the electrospun beaded fibers were influenced by the stability of the jet of inorganic material–polymeric solutions, and PVA contents. It should be noted that at low PVA content, the web was composed of fibers and beads. At sufficiently high PVA content, it was exactly right to eject the inorganic material–polymeric solution through the syringe out of the long hollow needle [21], and the product was composed of the bead-free fibers. The diameters of the fibers of Fig. 3b were in the range of 100–250 nm. When they were calcined at 400 °C, 500 °C and 600 °C for 3 h as shown in Fig. 3d–f, the fibers became thinner with their surfaces roughened. These were caused by the evaporation of PVA and volatile components. The nuclei grew up, due to the high temperature calcination indicating that these products were composed of a number of solid nanoparticles joined together in lines shaped like fibers. Upon increasing the calcination temperature, the evaporation rate of PVA and the crystalline degree of inorganic material became higher. At 600 °C, PVA was completely decomposed, and the polycrystalline fibers were produced. At this stage, the diameters of the fibers were in the range of 50–100 nm. The nanoparticles grew up to be larger particles with the average diameter of 100 nm.

Typical TEM and HRTEM images of electrospun fibers after calcination at 500 °C and 600 °C for 3 h are shown in Fig. 4a–c. The results confirmed that the fibers with 500 °C calcination were composed of a number of nanoparticles with average diameter of 50 nm. The corresponding SAED pattern (Fig. 4d) was indexed [22] and specified as $ZnWO_4$ (JCPDS database no. 15-0774) [11]. The (1 3 0) lattice planes (Fig. 4b) were also detected as clear and coherent parallel stripes, composing the crystalline structured $ZnWO_4$. The analysis implies that each of the nanoparticles is single crystal. Upon increasing the calcination temperature from 500 °C to 600 °C, the average size of crystalline particles was increased by 1.5 times of the precursor or about 75 nm in diameter joined together to form fiber-like assembly. Fig. 4e and f shows SAED and simulated patterns of its single crystal. This SAED pattern was indexed [22] and specified as $ZnWO_4$ (JCPDS database no. 15-0774) [11]. It was also in

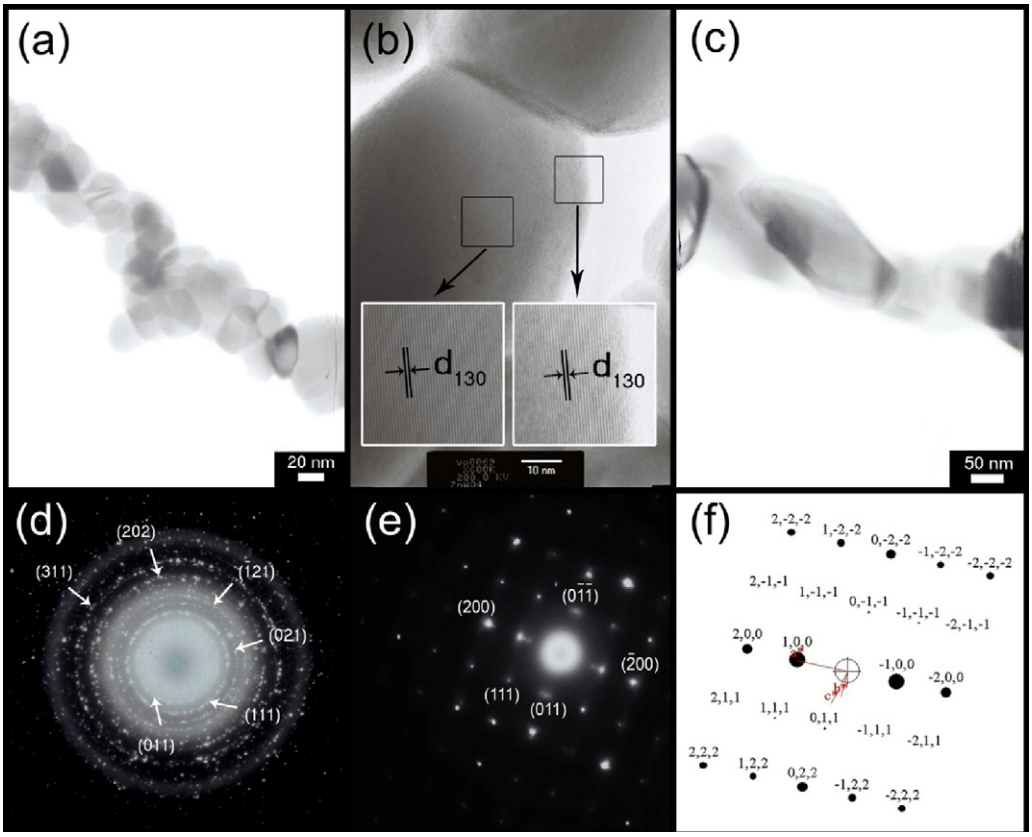


Fig. 4. TEM and HRTEM images, and SAED and simulated patterns of the electrospun fibers after calcination at (a, b and d) 500 °C, and (c, e and f) 600 °C for 3 h.

accordance with that obtained by the simulation [23]. This product was really proved to be monoclinic sanmartinite-type structured $ZnWO_4$.

External morphologies of the electrospun fibers with their corresponding height profiles before (A), and after (B and C) calcination at 500 °C are shown in Fig. 5. In the present research, the as-spun fiber appeared as smooth and even surface, with 250 nm diameter. After calcination at 500 °C, the fiber became thinner. Its surface was roughened and uneven. This product contained different sized particles, connected as fiber-like assembly in accordance with the above SEM and TEM analyses.

3.4. FTIR

To explain the structure of the products in more detail, they were characterized by FTIR in the range between 4000 and 400 cm^{-1}. The FTIR spectra (Fig. 6) were provided further insight into the structure of PVA (*MW* = 125,000), and $ZnWO_4$–PVA electrospun fibers with and without calcination at 400 °C, 500 °C and 600 °C. Obviously, the major vibrational modes associated with poly (vinyl alcohol) were the following. The O—H stretching of alcohol and residual water was detected at 3600–3200 cm^{-1}. The vibrational mode at 2943 cm^{-1} corresponds to the C—H stretching of alkyl groups. The C=O stretching mode was detected at 1721 cm^{-1}, CH_2 bending mode at 1448 cm^{-1}, and C—O stretching mode of carboxyl at 1098 cm^{-1} [24,25]. When the $ZnWO_4$–PVA as-spun fibers were characterized by FTIR, additional six modes were detected at 1000–450 cm^{-1}. They were the stretching and bending modes of Zn—O—W (880, 826 cm^{-1}), W—O in $(WO_6)^{2-}$ octahedrons (709, 660 cm^{-1}), and Zn—O (540, 475 cm^{-1}), respectively [10,17]. Once, the $ZnWO_4$–PVA electrospun fibers were calcined at high temperature, the PVA began to evaporate and decompose. At higher temperatures, the evaporation rates were faster and the PVA spectra became lessened. Until at 600 °C calcination, the vibrational modes of PVA were no longer detected, and those of $ZnWO_4$ were the strongest.

3.5. Raman analysis

The Raman spectra of $ZnWO_4$–PVA electrospun fibers with 400 °C, 500 °C, and 600 °C calcination are shown in Fig. 7. It should be noted that the Raman peaks of the electrospun fibers with 400 °C calcination were broadened, caused by the dispersion of the crystallite sizes and relaxation of the $ZnWO_4$ particles [7]. When the calcination temperatures were increased to be 500 °C and 600 °C, the $ZnWO_4$ crystals were improved and its crystalline degree was increased. These promoted the atoms to concurrently vibrate at the same mode and the intensity increased in the strength. The spectra show the peaks at 195 cm^{-1} which was interpreted as $\nu(A_g)$ involving the Zn^{2+} cations. The peaks at 277 cm^{-1} were specified as $\nu_{def}(A_g)$ of the cationic sublattices. Those at 344 and 409 cm^{-1} were assigned as $r(B_g)$ and $\delta(A_g)$ deformation modes, and at 783 cm^{-1} and 901 cm^{-1} as antisymmetric B_g and symmetric A_g modes of the terminal WO_2 groups, including at 515 and 547 cm^{-1} as $\nu_{sym}(B_g)$ and $\nu_{sym}(A_g)$, and at 678 and 710 cm^{-1} as $\nu_{as}(A_g)$ and $\nu_{as}(B_g)$ modes of the $(W_2O_4)_n$ chains, reported by Kloprogge et al. [16], respectively. These last two vibrations were reported as B_g and A_g internal stretching modes, reported by Errandonea et al. [26] and Siriwong et al. [27]. The Raman spectra were also used to prove the crystalline $ZnWO_4$.

3.6. Formation mechanism

A possible formation mechanism of $ZnWO_4$–PVA electrospun fibers produced by electrospinning was proposed according to the above results as follows. The mixture solution of zinc acetate dihy-

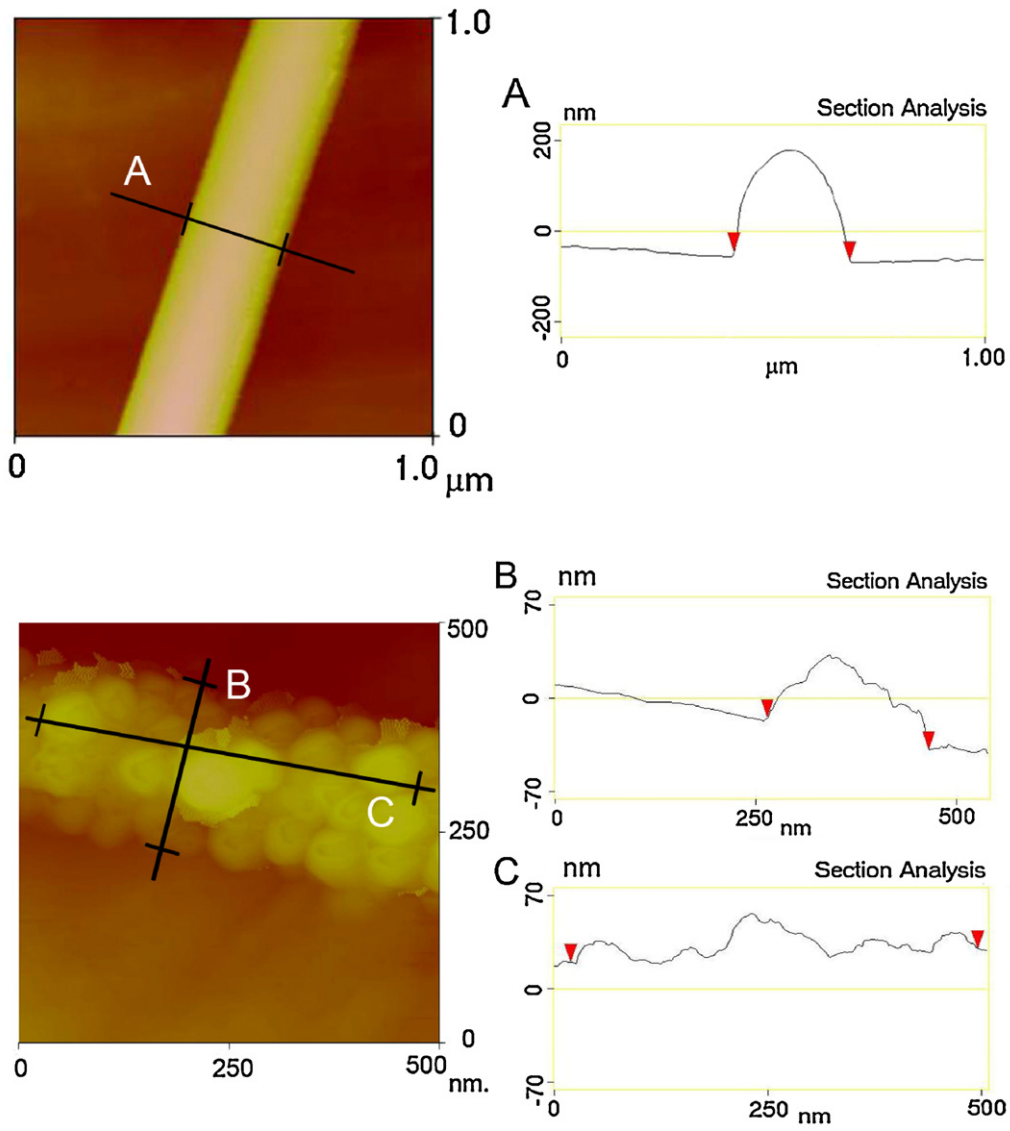


Fig. 5. AFM images and height profiles of the electrospun fibers before (A), and after (B and C) calcination at 500 °C for 3 h.

drate, ammonium metatungstate hydrate and PVA was ejected out of a hollow needle as a non-woven fiber. Concurrently, a high direct voltage was supplied to the needle tip. The external electric field (**E**) developed inside the fiber, axially pointed towards the grounded collector. Thus the fiber was heated up. Zinc acetate dihydrate reacted with ammonium metatungstate hydrate to produce $ZnWO_4$ molecules, which nucleated and blended in PVA template.

$$12Zn(CH_3COO)_2 \cdot 2H_2O + H_{26}N_6O_{40}W_{12} \cdot H_2O + 31H_2O \rightarrow 12ZnWO_4 + 48CO_2 + 105H_2 + 3N_2 \quad (1)$$

At this stage, $ZnWO_4$–PVA electrospun product shaped like fibers formed and deposited as a web of fibers on a grounded aluminum foil (Figs. 3a–c, and 5 (left top)). Upon calcination at 400–600 °C, PVA and residual water evaporated and decomposed. $ZnWO_4$ nuclei grew to form nanoparticles (Figs. 3d–f, 4a–c, and 5 (left bottom)). The rates of evaporation and decomposition increased with the increasing in the calcination temperature. At 600 °C, PVA and water were no longer detected (Figs. 1, 4e and 6e). A number of the nanoparticles joined together in line shaped like a web of nanofibers.

3.7. UV–visible absorption

UV–visible absorption of $ZnWO_4$–PVA electrospun fibers after calcination at 600 °C is shown in Fig. 8, which indicated an exponential decreasing of the photonic absorbance attenuated through the material. For crystalline semiconductors, the UV absorption near band edge follows the equation.

$$\alpha h\nu = (h\nu - E_g)^n \quad (2)$$

where α, h, ν, and E_g are the absorbance, Planck constant, photon frequency, and photonic energy band gap, respectively. The parameter n is a pure number associated with the different types of electronic transitions: $n = 1/2$, 2, 3/2 or 3 for direct-allowed, indirect-allowed, direct-forbidden and indirect-forbidden transitions, respectively [10,15,28,29]. It should be noted that the absorption was controlled by two photon energy ($h\nu$) ranges – the high and low energies. When the photon energy is greater than the energy band gap (E_g), absorption is linearly increased with the increasing of photon energy. The steep inclination of the linear portion of the curve was caused by the UV absorption for charged transition from the topmost occupied state of valence band to the bottommost unoccupied state of the conduction band. For the pho-

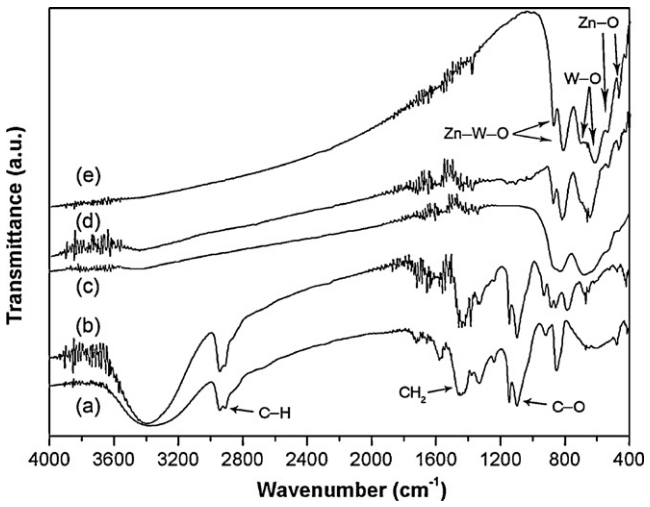


Fig. 6. FTIR spectra of (a) PVA, and (b–e) $ZnWO_4$–PVA electrospun fibers before and after calcination at 400 °C, 500 °C, and 600 °C for 3 h, respectively.

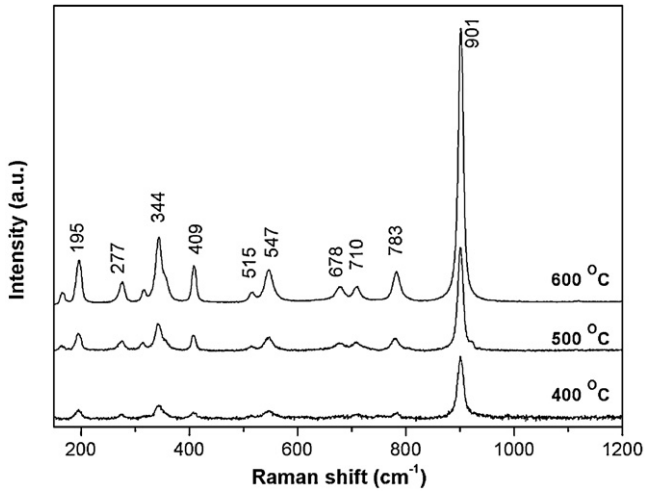


Fig. 7. Raman spectra of $ZnWO_4$–PVA electrospun fibers after calcination at 400 °C, 500 °C, and 600 °C for 3 h.

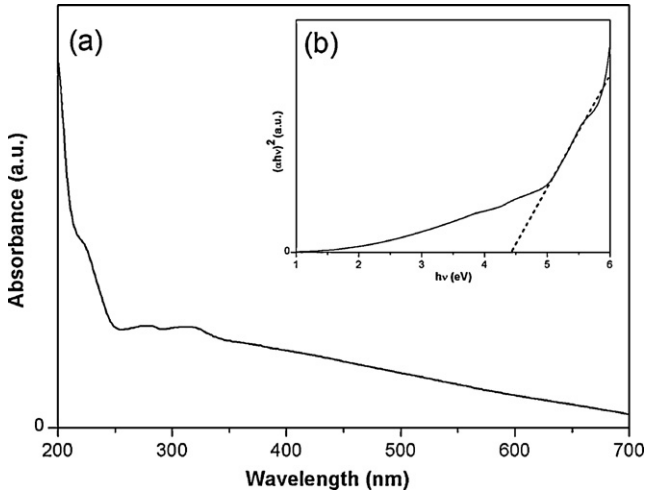


Fig. 8. UV–visible absorption of $ZnWO_4$–PVA electrospun fibers after calcination at 600 °C for 3 h.

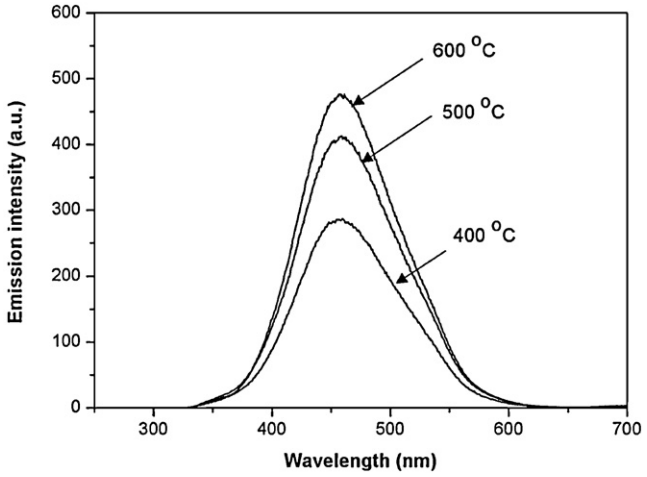


Fig. 9. PL emission of $ZnWO_4$–PVA electrospun fibers after calcination at 400 °C, 500 °C, and 600 °C for 3 h.

ton energy with less than E_g, the absorption curve became different from linearity, which was caused by the UV absorption for charged transition relating to defect levels. Its direct energy gap was determined by extrapolating the linear portion curve of the $(\alpha h\nu)^2$ vs $h\nu$ plot to $\alpha = 0$ (zero absorption). For the present work, direct energy gap was 4.42 eV – very close to those of 3.9–4.4 eV reported by Lacomba-Perales et al. [30], and 4.01 eV reported by Zhao et al. [10]. For tungstates, the top occupied states of valence band correspond to O_{2p}, and the lowest unoccupied states of conduction band to W_{5d} [27]. For bivalent metal tungstates, the hybridization of the valence states of the metal with O_{2p} and W_{5d} states played an important role in determining the energy band gap. A wide band gap was achieved for those of the tungstates with the s states of the bivalent cations hybridized with the O_{2p} and W_{5d} states, while a narrow band gap was caused by the p, d, and f states hybridization. As for a wide band gap of $ZnWO_4$, the s states hybridization seemed to be taken into account in the electronic transition. The transition of excitons (electron–hole pairs) between the O_{2p} and W_{5d} orbitals of pure WO_3 was induced by photonic absorption – the O_{2p} orbitals constituted the valence band, and the W_{5d} orbitals the conduction band. For transition metal tungstates – $ZnWO_4$ excluded, the valence orbitals of the transition metal cations ($Co^{II}(3d^7)$, $Ni^{II}(3d^8)$, $Cu^{II}(3d^9)$) hybridized with the W_{5d} orbitals to make the constitution of the conduction band different. For $Zn^{II}(3d^{10})$, the only possibility is to form the conduction band composed of Zn_{3s} and W_{5d} states, in order to enlarge the energy band gap (E_g) [28]. However, particle-sizes and morphologies were found to play the role in the absorbance characteristics [15], which have the influence on the energy gap as well.

3.8. PL emission

The optical property of $ZnWO_4$ nanofibers with calcination at high temperatures was studied using 280 nm excitation wavelength, and the results are shown in Fig. 9. In this research, the emission peaks presented broad bands over the 350–600 nm range with a strong blue emission peaks centered at the same wavelengths of 460 nm in accordance with the report of Chen et al. [31]. The transitions were caused by the hybridization of the W_{5d} and O_{2p} states with very strong tendency for self-trapping of the $(WO_6)^{2-}$ octahedral structure of $ZnWO_4$, in response to this PL emission [15]. The luminescence intensity was increased with the increasing of the calcination temperature, in accordance with the improvement of crystalline degree characterized by the above XRD analysis.

4. Conclusions

A solution of zinc acetate dihydrate and ammonium metatungstate hydrate with 1:1 molar ratio of Zn:W was prepared and further mixed with 5 wt%, 6 wt%, and 7 wt% PVA, to form three mixtures. By using the +15 kV direct voltage, these mixtures were electrospun to form the webs of $ZnWO_4$–PVA fibers on the ground aluminum foils. In the present research, the electrospun fibers of 6 wt% PVA were further calcined at 400–600 °C for 3 h to form $ZnWO_4$ nanofibers. At 600 °C, the product was $ZnWO_4$ nanoparticles joined together in line shaped like a web of spiders with their direct energy gap of 4.42 eV caused by the hybridization of Zn_{3s} and W_{5d} states, and luminescence at 460 nm (blue) by the transition of the $(WO_6)^{2-}$ octahedrons – one of the promising materials for a variety of applications.

Acknowledgements

We wish to thank the Thailand's Office of the Higher Education Commission for providing financial support through the National Research University (NRU) Project, and the Thailand Research Fund (TRF) through the TRF Advanced Research Scholar and the Royal Golden Jubilee Ph.D. Program.

References

[1] Z.W. Fu, J. Ma, Q.Z. Qin, Nanostructured $LiCoO_2$ and $LiMn_2O_4$ fibers fabricated by a high frequency electrospinning, Solid State Ionics 176 (2005) 1635–1640.
[2] J.M. Deitzel, J. Kleinmeyer, D. Harris, N.C.B. Tan, The effect of processing variables on the morphology of electrospun nanofibers and textiles, Polymer 42 (2001) 261–272.
[3] J. Lyons, C. Li, F. Ko, Melt-electrospinning part I: processing parameters and geometric properties, Polymer 45 (2004) 7597–7603.
[4] Z.M. Huang, Y.Z. Zhang, M. Kotaki, S. Ramakrishna, A review on polymer nanofibers by electrospinning and their applications in nanocomposites, Compos. Sci. Technol. 63 (2003) 2223–2253.
[5] P.K. Panda, S. Ramakrishna, Electrospinning of alumina nanofibers using different precursors, J. Mater. Sci. 42 (2007) 2189–2193.
[6] J.Y. Li, H. Dai, Q. Li, X.H. Zhong, X.F. Ma, J. Meng, X.Q. Cao, Lanthanum zirconate nanofibers with high sintering-resistance, Mater. Sci. Eng. B 133 (2006) 209–212.
[7] A. Kalinko, A. Kuzmin, Raman and photoluminescence spectroscopy of zinc tungstate powders, J. Lumin. 129 (2009) 1144–1147.
[8] G. Huang, C. Zhang, Y. Zhu, $ZnWO_4$ photocatalyst with high activity for degradation of organic contaminants, J. Alloys Compd. 432 (2007) 269–276.
[9] R.P. Jia, G.X. Zhang, Q.S. Wu, Y.P. Ding, $ZnWO_4$-TiO_2 composite nanofilms: Preparation, morphology, structure and photoluminescent enhancement, Mater. Lett. 61 (2007) 1793–1797.
[10] X. Zhao, W. Yao, Y. Wu, S. Zhang, H. Yang, Y. Zhu, Fabrication and photoelectrochemical properties of porous $ZnWO_4$ film, J. Solid State Chem. 179 (2006) 2562–2570.
[11] Powder Diffract. File, JCPDS-ICDD, 12 Campus Boulevard, Newtown Square, PA 19073-3273, USA, 2001.
[12] A. Kornylo, A. Jankowska-Frydel, B. Kuklinski, M. Grinberg, N. Krutiak, Z. Moroz, M. Pashkowsky, Spectroscopic properties of $ZnWO_4$ single crystal doped with Fe and Li impurities, Radiat. Meas. 38 (2004) 707–710.
[13] H. Fu, J. Lin, L. Zhang, Y. Zhu, Photocatalytic activities of a novel $ZnWO_4$ catalyst prepared by a hydrothermal process, Appl. Catal. A 306 (2006) 58–67.
[14] F.S. Wen, X. Zhao, H. Huo, J.S. Chen, E. Shu-Lin, J.H. Zhang, Hydrothermal synthesis and photoluminescent properties of $ZnWO_4$ and Eu^{3+}-doped $ZnWO_4$, Mater. Lett. 55 (2002) 152–157.
[15] M. Hojamberdiev, G. Zhu, Y. Xu, Template-free synthesis of $ZnWO_4$ powders via hydrothermal process in a wide pH range, Mater. Res. Bull. 45 (2010) 1934–1940.
[16] J.T. Kloprogge, M.L. Weier, L.V. Duong, R.L. Frost, Microwave-assisted synthesis and characterisation of divalent metal tungstate nanocrystalline minerals: ferberite, hübnerite, sanmartinite, scheelite and stolzite, Mater. Chem. Phys. 88 (2004) 438–443.
[17] J.H. Ryu, C.S. Lim, K.H. Auh, Synthesis of $ZnWO_4$ nanocrystalline powders, by the polymerized complex method, Mater. Lett. 57 (2003) 1550–1554.
[18] K. Pal, A.K. Banthia, D.K. Majumdar, Preparation and characterization of polyvinyl alcohol–gelatin hydrogel membranes for biomedical applications, AAPS PharmSciTech 8 (2007), doi:10.1208/pt080121, Art. No. 21.
[19] C. Suryanarayana, M.G. Norton, X-ray Diffraction: A Practical Approach, Plenum Press, New York, 1998.
[20] E.A. El-hefian, M.M. Nasef, A.H. Yahaya, The preparation and characterization of chitosan/poly (vinyl alcohol) blended films, E-J. Chem. 7 (2010) 1212–1219.
[21] B. Ding, H.Y. Kim, S.C. Lee, D.R. Lee, K.J. Choi, Preparation and characterization of nanoscaled poly (vinyl alcohol) fibers via electrospinning, Fibers Polym. 3 (2002) 73–79.
[22] K.W. Andrews, D.J. Dyson, S.R. Keown, Interpretation of Electron Diffraction Patterns, Plenum Press, New York, 1971.
[23] C. Boudias, D. Monceau, CaRIne Crystallography 3.1, DIVERGENT S.A., Centre de Transfert, 60200 Compiègne, France, 1989–1998.
[24] H.S. Mansur, R.L. Oréfice, A.A.P. Mansur, Characterization of poly (vinyl alcohol)/poly (ethylene glycol) hydrogels and PVA-derived hybrids by small-angle X-ray scattering and FTIR spectroscopy, Polymer 45 (2004) 7193–7202.
[25] H.S. Mansur, C.M. Sadahira, A.N. Souza, A.A.P. Mansur, FTIR spectroscopy characterization of poly (vinyl alcohol) hydrogel with different hydrolysis degree and chemically crosslinked with glutaraldehyde, Mater. Sci. Eng. C 28 (2008) 539–548.
[26] D. Errandonea, F.J. Manjón, N. Garro, P. Rodríguez-Hernández, S. Radescu, A. Mujica, A. Muñoz, C.Y. Tu, Combined Raman scattering and ab initio investigation of pressure-induced structural phase transitions in the scintillator $ZnWO_4$, Phys. Rev. B 78 (2008) 054116–54121.
[27] P. Siriwong, T. Thongtem, A. Phuruangrat, S. Thongtem, Hydrothermal synthesis, characterization, and optical properties of wolframite $ZnWO_4$ nanorods, CrystEngComm 13 (2011) 1564–1569.
[28] T Montini, V. Gombac, A. Hameed, L. Felisari, G. Adami, P. Fornasiero, Synthesis, characterization and photocatalytic performance of transition metal tungstates, Chem. Phys. Lett. 498 (2010) 113–119.
[29] O. Yayapao, T. Thongtem, A. Phuruangrat, S. Thongtem, CTAB-assisted hydrothermal synthesis of tungsten oxide microflowers, J. Alloys Compd. 509 (2011) 2294–2299.
[30] R. Lacomba-Perales, J. Ruiz-Fuertes, D. Errandonea, D. Martínez-García, A. Segura, Optical absorption of divalent metal tungstates: correlation between the band-gap energy and the cation ionic radius, Europhys. Lett. 83 (2008), doi:10.1209/0295-5075/83/37002, Art. No. 37002.
[31] S.J. Chen, J.H. Zhou, X.T. Chen, J. Li, L.H. Li, J.M. Hong, Z. Xue, X.Z. You, Fabrication of nanocrystalline $ZnWO_4$ with different morphologies and sizes via hydrothermal route, Chem. Phys. Lett. 375 (2003) 185–190.

ChalcogenideLetters Vol. 8, No. 1, January 2011, p. 1 – 7

CHARACTERIZATION OF NANOSTRUCTURED CdTe SYNTHESIZED BY SOLID STATE MICROWAVE-PLASMA PROCESS

WONCHAI PROMNOPAS[a,c], TITIPUN THONGTEM[b,c], SOMCHAI THONGTEM[a,c,*]
[a]*Department of Physics and Materials Science, Faculty of Science, Chiang Mai University, Chiang Mai 50200, Thailand*
[b]*Department of Chemistry, Faculty of Science, Chiang Mai University, Chiang Mai 50200, Thailand*
[c]*Materials Science Research Center, Faculty of Science, Chiang Mai University, Chiang Mai 50200, Thailand*

Purified cubic CdTe nanocrystals were synthesized from 1:1 molar ratio of Cd:Te using 900 W microwave plasma. The phase was detected using X-ray diffraction (XRD), which are in accordance with those of the simulation, and selected area electron diffraction (SAED). Raman spectroscopic, scanning electron microscopic (SEM) and focused ion beam (FIB) techniques showed that the products were nanocrystals with fundamental transverse optical (1TO) and longitudinal optical (1LO) vibrations at 140 cm^{-1} and 169 cm^{-1}, respectively. Its direct energy gap (E_g) was determined to be 1.6 eV.

(Received January 5, 2011; accepted January 23, 2011)

Keywords: Nanostructured CdTe; X-ray diffraction; Raman spectroscopy; Focused ion beam technique; UV-visible absorption

1. Introduction

CdTe is one of the II–VI semiconducting materials, which has a direct band gap of 1.5 eV at room temperature [1]. It is widely used as photovoltaic detectors, photo-electrochemical cells [1], space charge limited diodes, infrared (IR) detectors [2], and high efficiency solar cells [3]. There are a number of processes used to synthesize this material – tetrapod nanocrystals by a facile one-pot synthetic method [4], nanocrystals in tri-octylphosphine-dodecylamine mixture [5], nanocrystals in aqueous solution [6], nanoparticles in aqueous solution by colloidal method [7], thin film by thermal evaporation and close spaced sublimation [1,2,8,9], thin film by spray deposition in the presence of electric field [10], thin film by sintering [3], thin film by pulsed laser deposition [11], thin film by chemical solution method [12], thin film by electrochemical method [13], and epilayer by vapor phase epitaxy [14].

Microwave radiation (2,450 MHz) is coherent and polarized [15]. When this radiation is supplied to chemicals, one or more of the components is capable of coupling with it. This can lead to higher heating rate than that achieved by conventional method. The entire volume of materials is internally heated up. Microwave radiation can solve the problems of temperature and concentration gradients. By focusing large amount of microwave radiation into the system, the vibrating electric field applied a force on charged particles which vibrated accordingly. Vibrations of the reactants have the influence on the reaction to proceed with efficiency. Subsequently, pure products were synthesized [15,16].

In the present research, nanostructured CdTe was synthesized by solid state microwave-plasma process. This process is rapid, done in closed system, and safe for lives. The synthesized

*Corresponding author: schthongtem@yahoo.com

product is also pure, although it was synthesized by solid state reaction process. The product was then characterized using different techniques.

2. Experimental

To synthesize CdTe nanocrystals, Cd and Te powders (purum, analytical grade, Fluka) were used without further purification. Solid mixture of 1:1 molar ratio Cd:Te was thoroughly mixed, loaded into silica tubes (11 mm I.D. x 100 mm long), and placed in a horizontal (H) quartz tube. The tube was tightly closed and evacuated to 3.9±0.2 kPa absolute pressure for removal of air. Subsequently, argon was gradually fed into this H tube. The procedure was repeated three times. Finally, argon in the H tube was evacuated to a constant value of 3.9±0.2 kPa absolute pressure. The solid mixture was heated in a manner of batch run by a 2,450 MHz microwave with 900 W output power to produce plasma. Each batch, the solids were heated for 10 min, left to cool down in vacuum to room temperature, and thoroughly mixed. The process was repeated under the same condition until at the completion of 10, 20 and 30 min. The products were then analyzed using X-ray powder diffractometer (XRD) with a 1.5418 Å wavelength of Cu-K_α line, scanning electron microscope (SEM) operated at 15 kV, focused ion beam (FIB) technique operated at 30 kV, and selected area electron diffractometer (SAED) operated at 200 kV, Raman spectrometer using 30 mW He-Ne laser with 632.8 nm (red) wavelength, and UV-visible spectrometer operated at the 300-850 nm wavelength range with the 0.5 $nm.sec^{-1}$ scanning rate.

3. Results and discussion

XRD spectra of the products synthesized for different lengths of time are shown in Fig. 1. The XRD spectra were interpreted as CdTe cubic structure with F-43m space group, comparing to the JCPDS database no 15-0770 [17]. Their diffraction peaks corresponding to the (111), (220), (311), (400), and (331) planes are at 2θ = 23.84, 39.36, 46.48, 56.84, and 62.48 deg, respectively. By increasing the length of time to 30 min, the product's crystalline degree was the highest. The reactants have more chance to form new product (CdTe), and the atoms have more chance to arrange themselves in their crystal lattices. Its lattice parameter (a) was calculated using Bragg's law for diffraction and the plane-spacing equation for cubic structure [18], and is summarized in Table 1. This parameter is 0.6496±0.0020 nm, which is very close to that of the JCPDS database no 15-0770 (a = 0.6481 nm) - confirming the detection of cubic lattice structured CdTe.

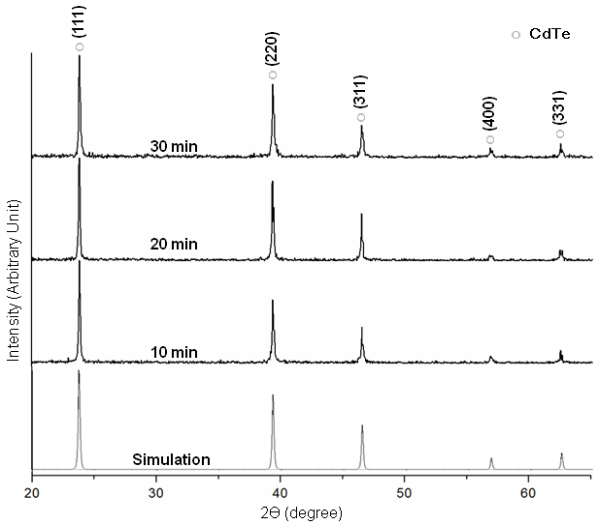


Fig. 1. XRD spectra of cubic structured CdTe synthesized by the solid state microwave-plasma process for 10 min, 20 min, and 30 min, including its simulation.

An XRD diffraction pattern of CdTe was also simulated using the CaRIne program [19] in combination with the calculated lattice parameter, and is shown in Fig. 1. The 2θ Bragg's angles and diffraction intensities of different peaks of the experiment, simulation and JCPDS database no 15-0770 [17] are shown in Table 1. Both 2θ Bragg's angles and diffraction intensities of different peaks obtained from the experiment, simulation and JCPDS database are in good accordance.

Table 1. The 2θ Bragg's angles (deg) and diffraction intensities (%) of nanostructured CdTe obtained from the 30 min experiment, simulation and JCPDS database no 15-0770, including its calculated lattice parameter (a, nm) for different crystallographic planes.

Plane	Experiment		Simulation		JCPDS database		a
	2θ	Intensity	2θ	Intensity	2θ	Intensity	
(111)	23.84	100	23.78	100	23.76	100	0.6522
(220)	39.36	71.65	39.32	75.3	39.31	60	0.6500
(311)	46.48	32.08	46.48	44.7	46.43	30	0.6478
(400)	56.84	10.16	56.83	11.4	56.82	6	0.6507
(331)	62.48	14.43	62.47	16.4	62.35	10	0.6473
							0.6496±0.0020

Fig. 2 shows SAED patterns of nanostructured CdTe synthesized by the 900 W microwave plasma for 10 and 30 min. The patterns appear as white concentric rings, characterized as polycrystals. These rings are diffuse and hollow showing that the product was composed of a number of nanosized crystals. At the present stage, the electron beam reflected and diffracted from polycrystals to form the concentric rings. Interplanar spaces (d) were calculated using their diffraction ring diameters [20], and compared with those of the JCPDS database no 15-0770 [17]. They both correspond to the (111), (220), (311), (400), and (331) crystallographic planes of the products and were specified as cubic CdTe.

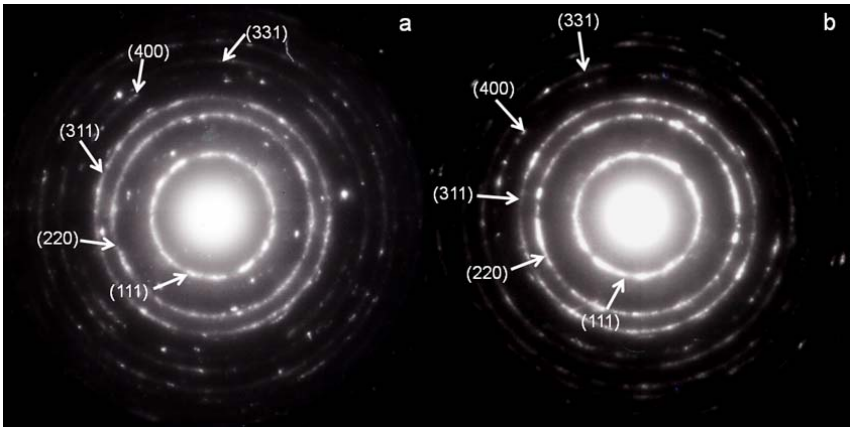


Fig. 2. SAED patterns of nanostructured CdTe, synthesized by 900 W microwave plasma for (a) 10 min, and (b) 30 min.

Morphology of the product (Fig. 3), synthesized by 900 W microwave plasma for 10 and 30 min, was investigated by SEM and FIB. Both of them show that the product was composed of a number of nanoparticles gathering together in the shape of spheres, aligning in different orientations. These spheres were larger with increasing the length of time. It should be noted that the detections of nanostructured CdTe by SEM and FIB are in good accordance with the interpretation of the SAED, explained above.

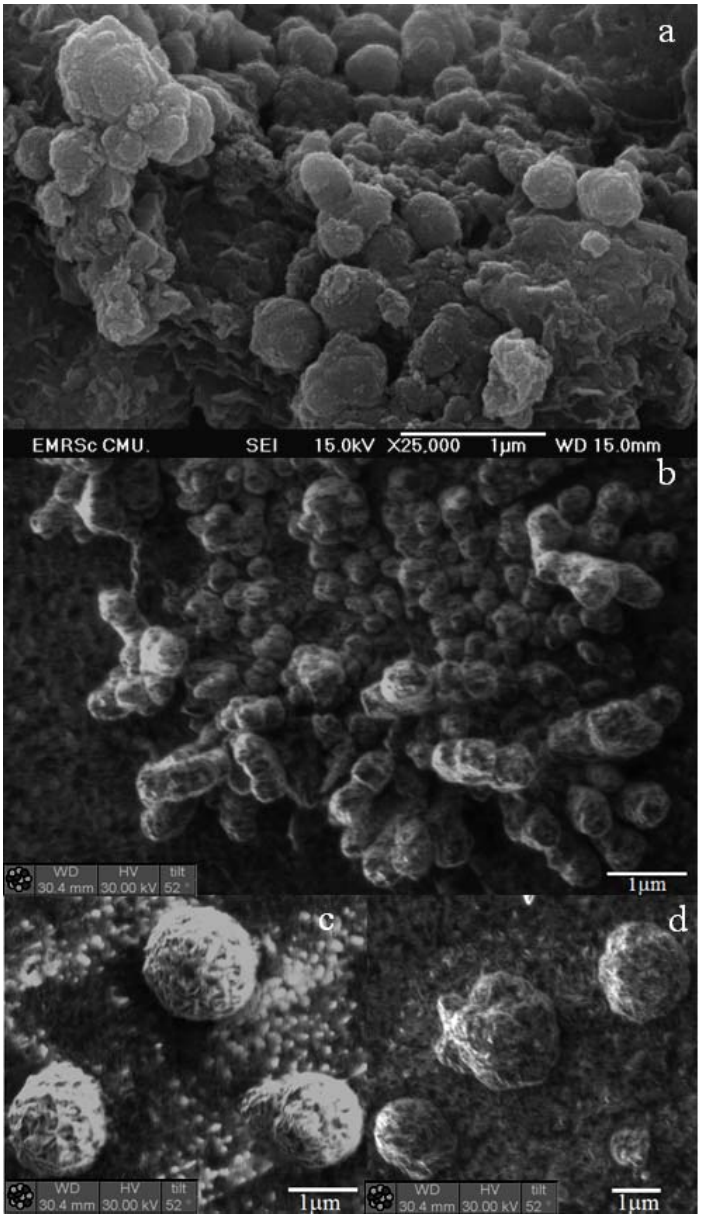


Fig. 3. SEM and FIB images of nanostructured CdTe synthesized by 900 W microwave plasma for (a, b) 10 min, and (c, d) 30 min.

The presence of cubic CdTe can be analyzed using a Raman spectrometer. For this case, test specimens are non-destructive and can be re-used for other purposes. The Raman shifts (Fig. 4) show the vibration modes of CdTe, corresponding to the fundamental transverse optical (1TO) and longitudinal optical (1LO) vibrations at 140 cm^{-1} and 169 cm^{-1}, respectively. They are in good accordance with those obtained by Dutta et al. who specified the 1TO, and 1LO Raman shifts of CdTe at 141, and 166 cm^{-1} [21], and by Campos et al. at 141, and 167 cm^{-1} [22], respectively. Other peaks at 120 cm^{-1} were caused by the residual Te [22], although the Te peaks were not detected by XRD measurement – its concentration could be too low to be detected by the XRD analysis. By increasing the length of time, this 120 cm^{-1} peak became lower – implying that the Te content became lessened. It should be noted that the 140 cm^{-1} peak was influenced not only by the vibration of cubic CdTe, but also the residual Te [22]. Comparing to the XRD results, the 140 cm^{-1} peak was dominantly influenced by the vibration of nanostructured CdTe.

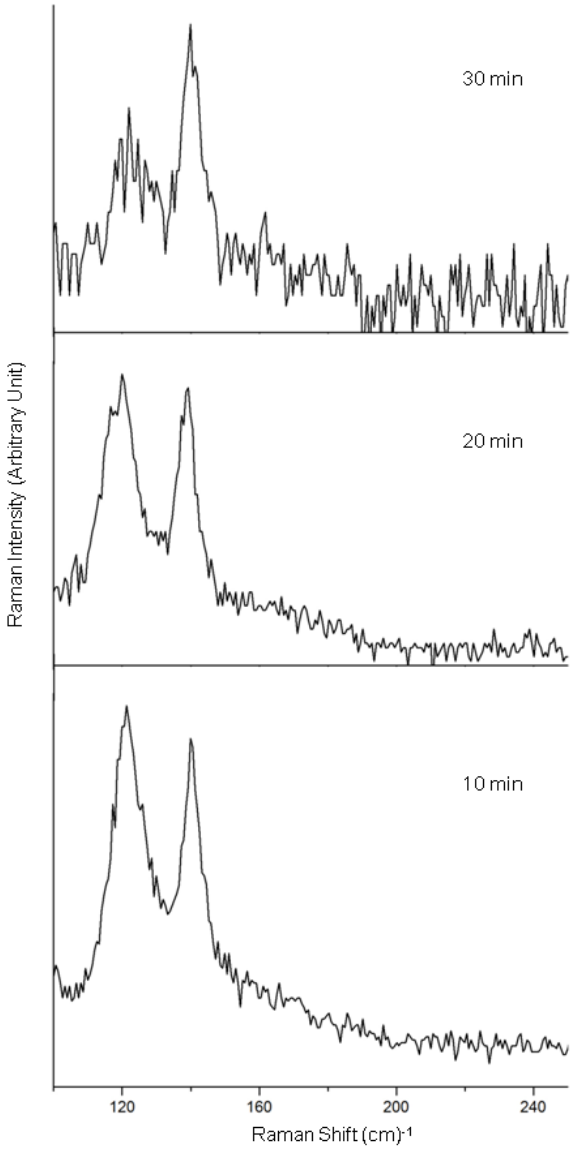


Fig. 4. Raman shifts of nanostructured CdTe, synthesized by 900 W microwave plasma for 10 min, 20 min, and 30 min.

The UV-visible spectrum of nanostructured CdTe, synthesized by 900 W microwave plasma for 30 min, was investigated using UV-visible spectrometer at room temperature. Its direct energy band gap (E_g) was calculated from the $(\alpha h\nu)^2$ vs $h\nu$ plot (Fig. 5), where α, h and ν are the absorbance, Planck constant and frequency [23], respectively. The absorbance increases with increasing photon energy ($h\nu$). The direct band gap of the semiconducting nanostructured CdTe was determined by extrapolating the broken line to the photon energy axis at $\alpha = 0$, which gives the energy band gap of CdTe to be 1.6 eV. This value is in accordance with 1.64 eV of the as-deposited CdTe film determined by Kokate et al. [23], and 1.6 eV of the cubic CdTe film by Pandey et al. [11]. These energy band gaps are also influenced by film thickness, particle-size, and degree of crystallinity [2].

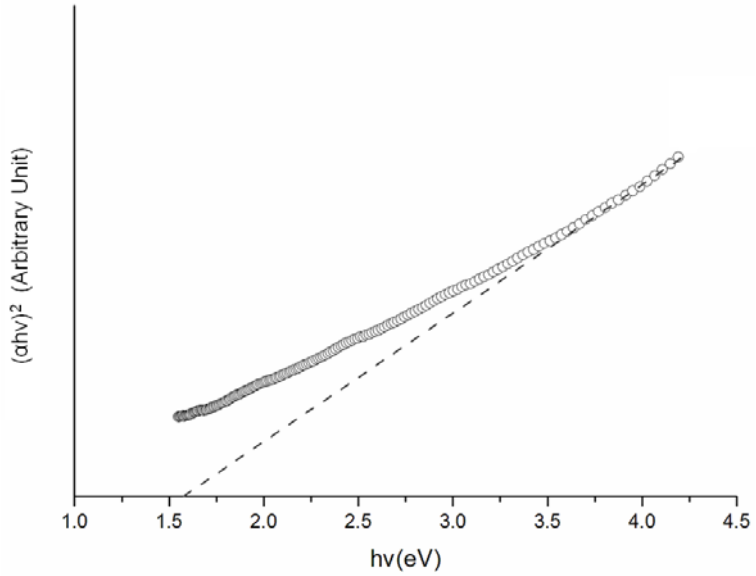


Fig. 5. The $(\alpha hv)^2$ and hv plot of nanostructured CdTe, synthesized by 900 W microwave plasma for 30 min.

4. Conclusions

Purified cubic CdTe nanocrystals were successfully synthesized by the solid state microwave plasma process. Its 1TO and 1LO modes were respectively detected at 140 cm^{-1} and 169 cm^{-1}, including the determined direct band gap (E_g) of 1.6 eV.

Acknowledgements

The research was supported by the Thailand's Office of the Higher Education Commission under the National Research University Project, and Strategic Scholarship for Frontier Research Network for Thai Ph.D. Program, and the Thailand Research Fund (TRF), Bangkok, Thailand.

References

[1] S. Lalitha, S.Zh. Karazhanov, P. Ravindran, S. Senthilarasu, R. Sathyamoorthy, J. Janabergenov, Physica B **387**, 227 (2007).
[2] R. Sathyamoorthy, Sa.K. Narayandass, D. Mangalaraj, Solar Energy Mater. Solar Cells **76**, 339 (2003).
[3] S. Kumar, S.K. Sharma, T.P. Sharma, M. Husain, J. Phys. Chem. Solids 61, 1809 (2000).
[4] H. Lee, S.W. Yoon, J.P. Ahn, Y.D. Suh, J.S. Lee, H. Lim, D. Kim, Solar Energy Mater. Solar Cells **93**, 779 (2009).
[5] S.F. Wuister, F. van Driel, A. Meijerink, J. Lumines. 102-103, 327 (2003).
[6] A.S. Susha, A.M. Javier, W.J. Parak, A.L. Rogach, Coll. Surf. A 281, 40 (2006).
[7] J.H. Kim, H. Kim, K. Cho, S. Kim, Solid State Comm. 136, 220 (2005).
[8] S. Chandramohan, R. Sathyamoorthy, P. Sudhagar, D. Kanjilal, D. Kabiraj, K. Asokan, Thin Solid Films **516**, 5508 (2008).
[9] M.E. Hernández-Torres, R. Silva-González, G. Casarrubias-Segura, J.M. Gracia-Jiménez, Solar Energy Mater. Solar Cells **90**, 2241 (2006).
[10] V.V. Ison, A.R. Rao, V. Dutta, Solar Energy Mater. Solar Cells 93, 1507 (2009).
[11] S.K. Pandey, U. Tiwari, R. Raman, Ch. Prakash, V. Krishna, V. Dutta, K. Zimik, Thin Solid Films **473**, 54 (2005).

[12] M. Sotelo-Lerma, R.A. Zingaro, S.J. Castillo, J. Organomet. Chem. **623**, 81 (2001).
[13] X. Mathew, J.P. Enriquez, Solar Energy Mater. Solar Cells **63**, 347 (2000).
[14] N.V. Sochinskii, M. Abellán, J. Rodríguez-Fernández, E. Diéguez, J. Franc, P. Hlidek, P. Praus, V. Babentsov, Superlatt. Microstruct. **45**, 228 (2009).
[15] S. Bhunia, D.N. Bose, J. Cryst. Growth **186**, 535 (1998).
[16] C. Gabriel, S. Gabriel, E.H. Grant, B.S.J. Halstead, D.M.P. Mingos, Chem. Soc. Rev. **27**, 213 (1998).
[17] Powder Diffract. File, JCPDS Internat. Centre Diffract. Data, PA 19073-3273, U.S.A. (2001).
[18] C. Suryanarayana, M.G. Norton, X-ray Diffract, A Practical Approach, Plenum Press, New York (1998).
[19] C. Boudias, D. Monceau, CaRIne Crystallography 3.1, DIVERGENT S.A., Centre de Transfert, 60200 Compiègne, France, (1989-1998).
[20] K.W. Andrews, D.J. Dyson, S.R. Keown, Interpret. Electr. Diffract. Patter., 2nd ed, Plenum Press, NY, (1971).
[21] V.V. Ison, A.R. Rao, V. Dutta, Solid State Sci. **11**, 2003 (2009).
[22] C.E.M. Campos, K. Ersching, J.C. de Lima, T.A. Grandi, H. Höhn, P.S. Pizani, J. Alloys Compd. **466**, 80 (2008).
[23] A.V. Kokate, M.R. Asabe, P.P. Hankare, B.K. Chougule, J. Phys. Chem. Solids **68**, 53 (2007).

Materials Letters 65 (2011) 442–445

Contents lists available at ScienceDirect

Materials Letters

journal homepage: www.elsevier.com/locate/matlet

Cyclic microwave-assisted synthesis of Cu_3BiS_3 dendrites using L-cysteine as a sulfur source and complexing agent

Kamonwan Aup-Ngoen [a], Somchai Thongtem [a,*], Titipun Thongtem [b]

[a] Department of Physics and Materials Science, Faculty of Science, Chiang Mai University, Chiang Mai 50200, Thailand
[b] Department of Chemistry, Faculty of Science, Chiang Mai University, Chiang Mai 50200, Thailand

ARTICLE INFO

Article history:
Received 27 August 2010
Accepted 7 October 2010
Available online xxxx

Keywords:
Characterization methods
Luminescence
Nanomaterials
Solar energy materials
X-ray techniques

ABSTRACT

Nanostructured Cu_3BiS_3 dendrites were successfully synthesized from CuCl, $BiCl_3$ and L-cysteine in ethylene glycol (EG), using cyclic microwave radiation (CMR). The phase was detected by X-ray diffraction (XRD) and selected area electron diffraction (SAED), and was in accordance with that obtained by the simulation. Scanning and transmission electron microscopic (SEM and TEM) techniques revealed the gradual transformation of nanoparticles to nanostructured dendrites, due to the increase of microwave power. Photoluminescence of Cu_3BiS_3 dendrites was a blue emission centered at 367 nm.

© 2010 Elsevier B.V. All rights reserved.

1. Introduction

Due to the linear and non-linear properties of I-V-VI ternary compounds, a number of studies have been devoted to the technological applications of these semiconducting materials. They have a high potential for use as optoelectronic and thermoelectric devices, including optical recording media [1]. Copper bismuth sulfide (Cu_3BiS_3), with the mineral name wittichenite [2], is one of the promising materials for use as p-type semiconductors [3,4], and as solar absorbers in photovoltaic devices [5]. It can be synthesized by different methods: powders in the polyacrylic acid matrix [3]; nanorods via a simple ethanol-thermal route [4]; thin films by reactive sputter deposition on hot substrates [5]; nanocrystallines by a hydrothermal decomposition process [6]; and others.

Microwaving is a process used for the synthesis of nanostructured materials. It can solve the problems of temperature and concentration gradients, and provides uniform growth media. By focusing microwave radiation into solutions, the vibrating electric field applies a force on dissolving species to induce vibrations with different modes. The processing is more rapid and efficient than that achieved by a conventional one, even at a low microwave power [7,8]. To avoid over-boiling, CMR was used instead of continuous.

Our motivation was to synthesize novel Cu_3BiS_3 dendritic crystals using a genetically coded amino acid (L-cysteine) by CMR. No one has ever succeeded in synthesizing Cu_3BiS_3 dendrites by this process.

2. Experiment

To synthesize nanostructured Cu_3BiS_3 dendrites, 3 mmol CuCl and 1 mmol $BiCl_3$ were dissolved in 30 ml EG to form a solution. Then 3 mmol L-cysteine ($C_3H_7NO_2S$) was added with 30 min continuous stirring. Samples of the solution were irradiated using 300–700 W CMR (30 s on for every 30 s interval) for 40 cycles. Finally, precipitates were synthesized, separated by filtration, washed with de-ionized water and absolute ethanol, and dried at 70 °C for 24 h, for further characterization.

3. Results and discussion

Fig. 1 shows XRD patterns of the products synthesized by 300–700 W CMR. At 300 W, the XRD pattern was composed of rather broad peaks, specifying that the product's degree of crystallinity was quite low. Comparing the XRD pattern to the JCPDS database (nos. 43-1479 and 02-1272) [2], this product was proved to be orthorhombic Cu_3BiS_3 mixed with Cu_2S impurity. The strongest intensity peak at 31.3° was found to correspond with the (131) crystallographic plane of the Cu_3BiS_3 phase, which was specified as the main product. When the microwave power was increased, the XRD pattern became sharper. At 700 W, the pattern was composed of the sharpest peaks. At this stage, the degree of crystallinity was the highest — implying that the atoms had arranged themselves in the best order. By increasing microwave power, the impurities were lessened as well. Until microwaving at powers of 600 and 700 W, the products were pure single-phase orthorhombic Cu_3BiS_3.

SEM and TEM images show nanostructured Cu_3BiS_3 synthesized using different microwave powers. At 300 W, the product (Fig. 2a)

* Corresponding author. Tel.: +66 53941922; fax: +66 53943445.
E-mail address: schthongtem@yahoo.com (S. Thongtem).

0167-577X/$ – see front matter © 2010 Elsevier B.V. All rights reserved.
doi:10.1016/j.matlet.2010.10.047

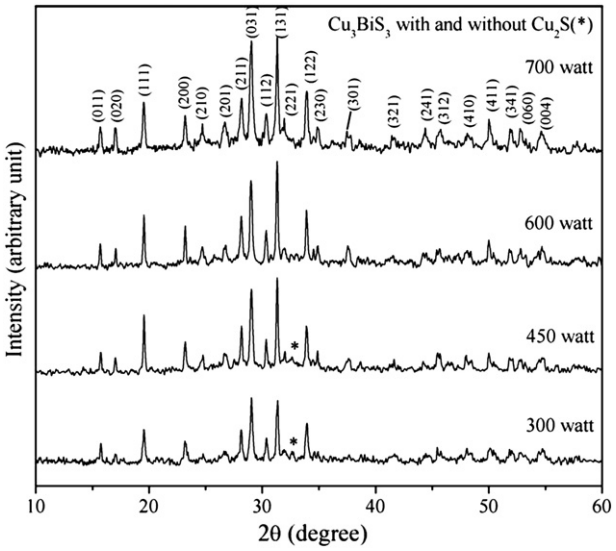


Fig. 1. XRD patterns of Cu_3BiS_3 synthesized at different microwave powers.

was composed of a number of nanoparticles with different orientations. By increasing the powers from 300 W to 450 and 600 W (Fig. 2b, c,and Fig. 3a,c), some of the products were gradually transformed into dendrites. At these stages, the products were mixtures of nanoparticles and dendrites. It should be noted that their morphologies shown on SEM images are in three dimensions, but those on TEM images are in two dimensions. At 700 W (Figs. 2d and 3e), the whole product consisted of dendrites with different orientations. This phenomenon proved that microwave radiation at higher powers has a strong influence on vibrating atoms to form a crystal lattice, and that orthorhombic Cu_3BiS_3 unit cells were able to arrange themselves to fit with both nanoparticles and dendrites. When a dendrite, produced at 700 W, was characterized using HRTEM (Fig. 3f,g), a number of the (011) planes 5.6 Å apart were detected — implying that the dendrite was single crystal. SAED patterns of the whole products, synthesized using 450, 600, and 700 W (Fig. 3b,d,and h), appear as concentric rings of bright spots of polycrystals; but that of a dendrite synthesized at 700 W (Fig. 3i) was composed of systematic spots of diffraction electrons from a single crystal. The patterns for both polycrystals and single crystal were interpreted [9], and specified as orthorhombic Cu_3BiS_3 [2], with the electron beam for the interpretation of Fig. 3i in the [4-3-5] direction. No Cu_2S impurity was detected in the SAED pattern of the product synthesized at 450 W, due to the very low Cu_2S concentration in this host. An electron diffraction pattern (Fig. 3j) was also simulated [10], using the [4-3-5] direction as a zone axis. It appears as a systematic array of spots, corresponding to that obtained by the interpretation of Fig. 3i — showing that this electron diffraction pattern of the product could exist in reality.

In this research, CuCl and $BiCl_3$ were dissolved in EG to form a solution. L-cysteine, a genetically coded amino acid, was used as a sulfur source and complexing agent. By adding L-cysteine to the solution, Cu^+ and Bi^{3+} ions coordinated with it to form complexes.

$$Cu^+ + \text{L-cysteine} \xrightarrow{\textit{coordination}} [\text{Cu(L-cysteine)complexes}]$$

$$Bi^{3+} + \text{L-cysteine} \xrightarrow{\textit{coordination}} [\text{Bi(L-cysteine)complexes}]$$

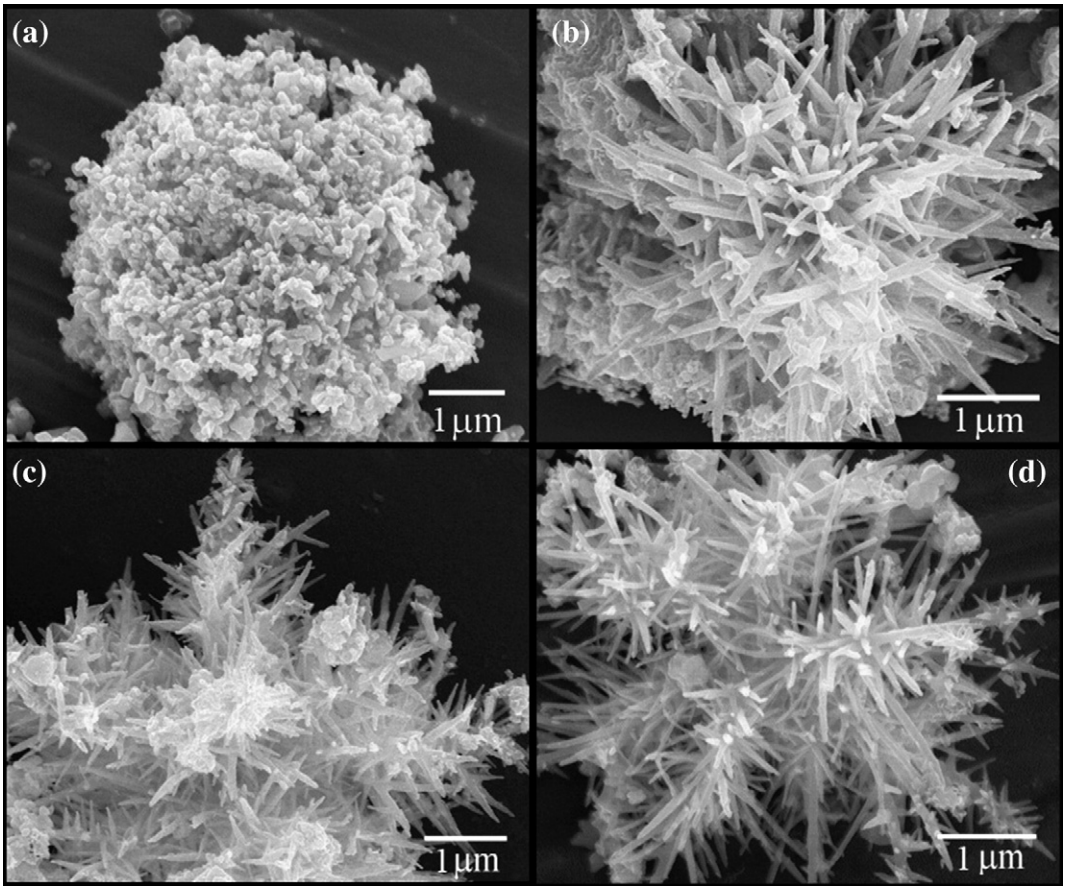


Fig. 2. SEM images of Cu_3BiS_3 synthesized at (a–d) 300, 450, 600, and 700 W, respectively.

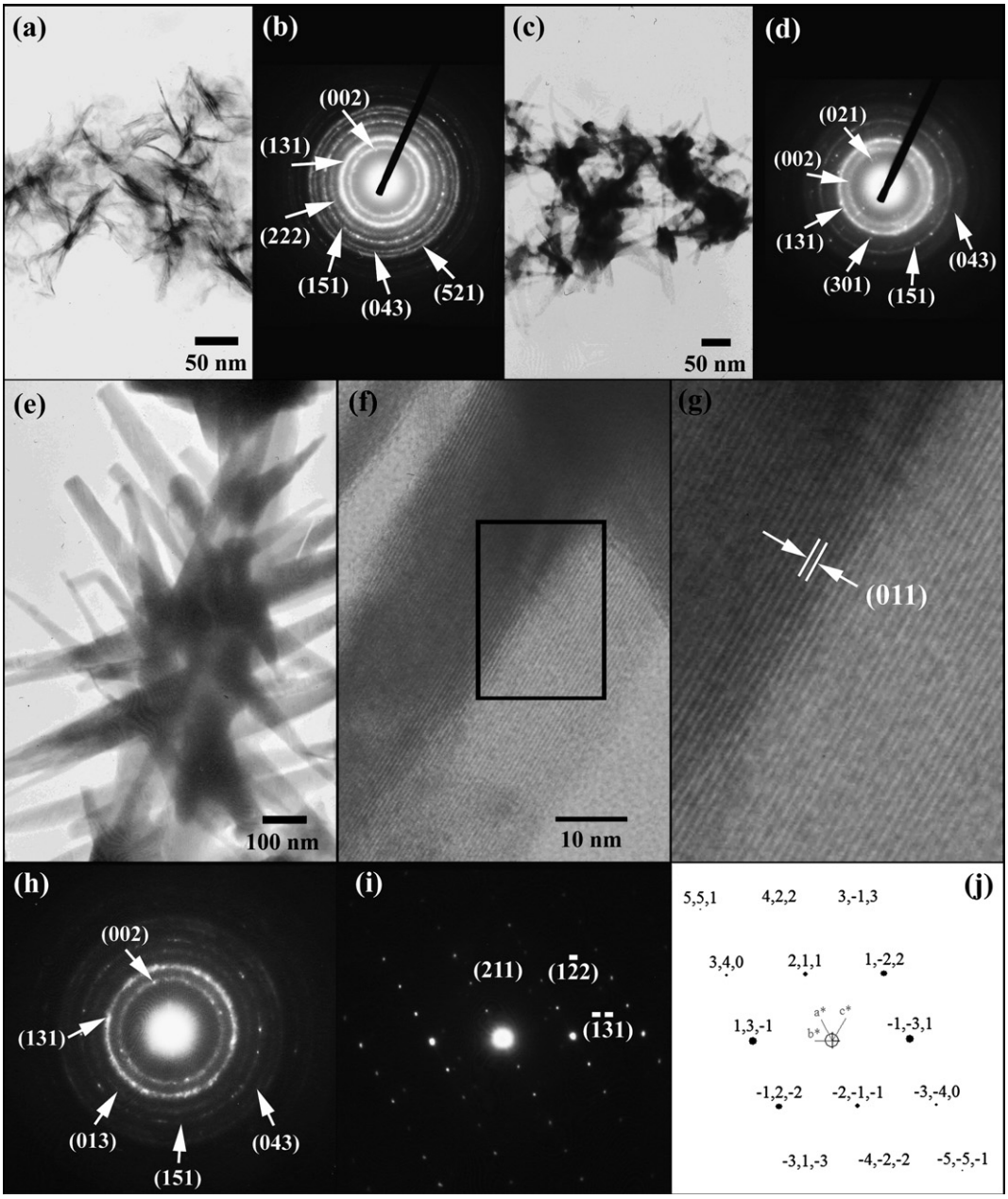


Fig. 3. TEM and HRTEM images, and SAED patterns of Cu_3BiS_3 synthesized at (a, b) 450 W, (c, d) 600 W, and (e–i) 700 W. (j) Simulated pattern of (i).

Under 700 W CMR, these complexes decomposed, and Cu_3BiS_3 nuclei were synthesized very rapidly. At this stage, the number of free ions was very low. Thus, Cu_2S and Bi_2S_3 formations were inhibited [1,11,12].

$$[\mathrm{Cu(L-cysteine)complexes}] + [\mathrm{Bi(L-cysteine)complexes}] \xrightarrow{\textit{decomposition}} \mathrm{Cu_3BiS_3(nuclei)}$$

Concurrently, [Cu–Bi(L-cysteine) complexes] could possibly form by the reaction

$$\mathrm{Cu^{+} + Bi^{3+} + L-cysteine} \xrightarrow{\textit{coordination}} \mathrm{[Cu-Bi(L-cysteine)complexes].}$$

These complexes were then decomposed by CMR.

$$\mathrm{[Cu-Bi(L-cysteine)complexes]} \xrightarrow{\textit{decomposition}} \mathrm{Cu_3BiS_3(nuclei).}$$

These nuclei grew to synthesize Cu_3BiS_3 dendrites. Dendritic growth was promoted by the strong atomic vibrations. Thus these atoms had more chances to arrange themselves in perfect order to form dendritic crystals. In the present research, CMR played a key role in the growth of Cu_3BiS_3 crystals: both in the decomposition of the complexes, and in the nucleation and growth of Cu_3BiS_3. By using CMR, the process is rapid and homogenous, providing a uniform growth environment; thus crystalline dendrites were rapidly synthesized. At 300 W CMR, the nucleation rate of Cu_3BiS_3 was slower; Cu_2S at a very low concentration thus had a better chance to nucleate as a second phase contained in this nanoparticle product.

Photoluminescence (PL) of Cu_3BiS_3 dendrites was studied at room temperature, using 300 nm excitation wavelength from a xenon laser. The spectrum (Fig. 4) was blue emission centered at 367 nm, with the shoulder at 412 nm (caused by some defects that originated during the synthesis process). These Cu_3BiS_3 dendrites were I-V-VI ternary promising materials for use in solar energy converters and optical nanodevices.

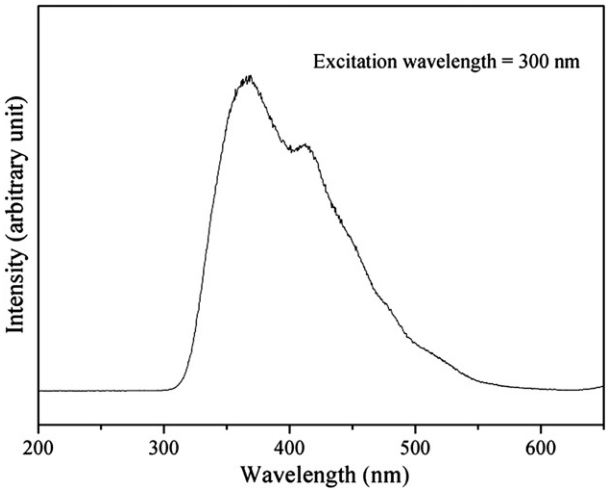


Fig. 4. PL emission of Cu_3BiS_3 dendrites synthesized at 700 W.

4. Conclusions

Nanostructured Cu_3BiS_3 dendrites were successfully synthesized by CMR. The phase was detected using XRD and SAED. SEM and TEM images showed that, with increasing microwave power, nanoparticles were gradually transformed into dendritic single crystals composed of a number of (011) parallel crystallographic planes. PL emission of the Cu_3BiS_3 dendrites was blue emission centered at 367 nm.

Acknowledgements

This research was supported by the Thailand Research Fund (TRF), and the National Nanotechnology Center (NANOTEC), a member of National Science and Technology Development Agency (NSTDA), Ministry of Science and Technology, Thailand.

References

[1] Jiasong Z, Weidong X, Huaidong J, Wen C, Lijun L, Xinyu Y, et al. L Mater Lett 2010;64:1499–502.
[2] Powder Diffract File, JCPDS-ICDD, 12 Campus Boulevard, Newtown Square, PA 19073-3273, U.S.A. 2001.
[3] Hu H, Gomez-Daza O, Nair PK. J Mater Res 1998;13:2453–6.
[4] Chen D, Shen G, Tang K, Liu X, Qian Y, Zhou G. J Cryst Growth 2003;253:512–6.
[5] Gerein NJ, Haber JA. Chem Mater 2006;18:6297–302.
[6] Hu J, Deng B, Wang C, Tang K, Qian Y. Mater Chem Phys 2003;78:650–4.
[7] Wang G, Hao C. Mater Res Bull 2009;44:418–21.
[8] Sczancoski JC, Cavalcante LS, Joya MR, Espinosa JWM, Pizani PS, Varela JA. J Colloid Interf Sci 2009;330:227–36.
[9] Andrews KW, Dyson DJ, Keown SR. Interpret Electr Diffract Pattern. 2nd ed. Plenum Press: New York; 1971.
[10] Boudias C, Monceau D. CaRIne Crystallography 3.1, DIVERGENT S.A. 60200 Compiègne, France: Centre de Transfert; 1989–1998.
[11] Thongtem T, Jaroenchaichana J, Thongtem S. Mater Lett 2009;63:2163–6.
[12] Chen D, Shen G, Tang K, Jiang X, Huang L, Jin Y, et al. Inorg Chem Commun 2003;6:710–2.

Journal of Alloys and Compounds 509 (2011) 2294–2299

Contents lists available at ScienceDirect

Journal of Alloys and Compounds

journal homepage: www.elsevier.com/locate/jallcom

CTAB-assisted hydrothermal synthesis of tungsten oxide microflowers

Oranuch Yayapao[a], Titipun Thongtem[a,*], Anukorn Phuruangrat[b,*], Somchai Thongtem[c]

[a] Department of Chemistry and Center for Innovation in Chemistry, Faculty of Science, Chiang Mai University, Chiang Mai 50200, Thailand
[b] Department of Materials Science and Technology, Faculty of Science, Prince of Songkla University, Hat Yai, Songkhla 90112, Thailand
[c] Department of Physics and Materials Science, Faculty of Science, Chiang Mai University, Chiang Mai 50200, Thailand

ARTICLE INFO

Article history:
Received 6 September 2010
Received in revised form 25 October 2010
Accepted 28 October 2010
Available online 10 November 2010

Keywords:
Hydrothermal reaction
o-WO_3 microflowers
Optical properties

ABSTRACT

Orthorhombic tungsten oxide (o-WO_3) was synthesized by 200 °C, 24 h hydrothermal reactions of ammonium metatungstate hydrate solutions containing different volumes of 1 M HCl and cetyltrimethylammonium bromide (CTAB) cationic surfactant. The as-synthesized products were characterized by X-ray powder diffraction (XRD), Fourier transform infrared (FTIR) and Raman spectroscopy, and scanning and transmission electron microscopy (SEM, TEM), including UV–visible and photoluminescent (PL) spectroscopy. These analyses showed that their phases and morphologies were controlled by the acidity of the solutions. In 7.50 ml 1 M HCl-added solution, the product was o-WO_3 microflowers, with microsquare layers growing out of their cores. FTIR and Raman vibrations of W=O, O–W–O, and W–O–W stretching modes were detected, and showed typical crystalline WO_3. Their optical properties showed a maximum absorption at 275 nm in the UV region and a maximum emission peak at 375 nm. The possible formation mechanism of o-WO_3 microflowers was also proposed according the experimental results.

© 2010 Elsevier B.V. All rights reserved.

1. Introduction

Presently, many chemists and materials scientists are paying close attention to the study of nanostructured oxides – including zero-dimensional (0D) quantum dots, one-dimensional (1D) nanowires and nanorods, and two-dimensional (2D) nanosheets and nanodisks – because these materials have novel physical and chemical properties which are different from their corresponding bulks [1–3]. Among the different oxides with nanostructures, tungsten oxide (WO_3) has received wide attention owing to its unique photochromic and electrochromic properties. It is considered to be a promising material for multiple potential applications, including semiconductors for gas sensors, electrodes for secondary batteries, solar energy converters, and photocatalysts [3–6]. A number of synthetic methods have been developed for WO_3 such as a hydrothermal/solvothermal route [2,3,5,7], thermal processing [4], electric heating in vacuum [6], and physical/chemical vapor deposition process [8,9]. Among these, synthesis under hydrothermal conditions is a low-temperature, environmentally benign and low-cost route for preparation of nanosized oxide materials, and is becoming an increasingly attractive method [10].

In the present research, orthorhombic tungsten oxide (o-WO_3) microflowers were synthesized using a CTAB-assisted hydrothermal method. The as-synthesized o-WO_3 products were further characterized by X-ray powder diffraction (XRD), Fourier transform infrared (FTIR) and Raman spectroscopy, and scanning and transmission electron microscopy (SEM, TEM), including UV–visible (UV–vis) and photoluminescent (PL) spectroscopy.

2. Experiment

A 1.38 g of ammonium metatungstate hydrate ($(NH_4)_6H_2W_{12}O_{40}\cdot xH_2O$) was dissolved in 20 ml deionized water; 0–7.50 ml 1 M HCl was subsequently added to form H_2WO_4 with 30 min continuous stirring. CTAB surfactant (0.36 g) was added to each solution with an additional 30 min of continuous stirring. The mixtures were transferred into homemade, Teflon-lined, stainless steel autoclaves. These were tightly closed, heated at 200 °C for 24 h, and naturally cooled to room temperature. Finally, light-green precipitates were synthesized, separated by filtration, washed with deionized water and ethanol, and dried at 70 °C for 12 h.

The products were characterized and recorded on a Philips X'Pert MPD X-ray diffractometer (XRD) equipped with a graphitic monochromator of Cu Kα radiation (λ = 0.1542 nm), using a scanning rate of 0.02°/s over the 2θ range of 10–60°. FTIR spectra were recorded on PerkinElmer Spectrum RX FTIR Spectrometer with KBr as a diluting agent and operated in the range of 400–4,000 cm^{-1} with the resolution of 4 cm^{-1}. Raman vibrations of the products were detected by a HORIBA JOBIN YVON T64000 Raman spectrometer with 50 mW and 514.5 nm wavelength Ar laser. Field-emission scanning electron microscopic (FE-SEM) images were taken by a JEOL JSM-6335F operated at 15.0 kV beam energy. Transmission electron microscopic (TEM) images, and selected area electron diffraction (SAED) pattern were taken on a JEOL JEM-2010, employing at an accelerating voltage of 200 kV. UV–visible and photoluminescent spectra were carried out by a Lambda 25 spectrometer using UV lamp with the resolution of 1 nm, and LS50B Fluorescence Spectrometer, PerkinElmer, at 450 W Xe-lamp with the 0.2 nm resolution and 200 nm excitation wavelength at room temperature.

* Corresponding authors. Tel.: +66 0 53 943344; fax: +66 053 892277.
E-mail addresses: ttpthongtem@yahoo.com (T. Thongtem), phuruangrat@hotmail.com (A. Phuruangrat).

0925-8388/$ – see front matter © 2010 Elsevier B.V. All rights reserved.
doi:10.1016/j.jallcom.2010.10.204

3. Results and discussion

Fig. 1 shows the XRD patterns of the products synthesized by 200 °C, 24 h hydrothermal reactions using $(NH_4)_6H_2W_{12}O_{40}{\cdot}xH_2O$ and CTAB as a tungsten source and surfactant, with 0–7.50 ml 1 M HCl added. In the HCl-free solution, the product was an amorphous phase. When 2.50 ml 1 M HCl was added to the solution, both orthorhombic $WO_3{\cdot}0.33H_2O$ (JCPDS No. 35-0270) and WO_3 phases (JCPDS No. 20-1324) [11] were detected. These products became pure orthorhombic WO_3 (o-WO_3) in the 5.00 ml and 7.50 ml 1 M HCl-added precursor solutions. The analysis implies that HCl has an influence on the synthesis of pure o-WO_3 phase.

SEM images (Fig. 2a and b) show o-WO_3 in the shape of ~8 μm microseeds in numerous square layers in the 5.00 ml 1 M HCl-added solution. By increasing 1 M HCl from 5.00 ml to 7.50 ml, these microsquare layers grew out of the microseed cores to form microflower-like particles (Fig. 2c and d), composed of 2–3 μm × 100–300 nm × 100–300 nm petals with very smooth surfaces.

In general, o-WO_3 has a distorted ReO_3-type structure consisting of a three-dimensional network of WO_6 octahedrons linked by their oxygen corners [5,12]. The vibrations are in the infrared (IR) range, and are classified into three regions: 600–900, 200–400 and <200 cm^{-1}, corresponding to O–W–O stretching and bending modes, and lattice vibration, respectively [13]. In this research, the products (Fig. 3) were further characterized by FTIR spectroscopy in the range of 400–4000 cm^{-1}, and the vibrations compared to those of CTAB. Some bands were detected at 2800–3020 cm^{-1}, which can be attributed to the CTAB surfactant. The FTIR spectrum of CTAB shows two intense bands at 2918 and 2846 cm^{-1}, corresponding to the asymmetric and symmetric stretching vibrations of C–CH_2 in the methylene chains. The sharp bands at 1450–1500 cm^{-1} were specified as the deformation of –CH_2– and –CH_3, and the weak band at 3011 cm^{-1} as the C–CH_3 asymmetric stretching and N–CH_3 symmetric stretching vibrations of the solid surfactant [14–17]. In case of the as-synthesized products, broad bands between 590

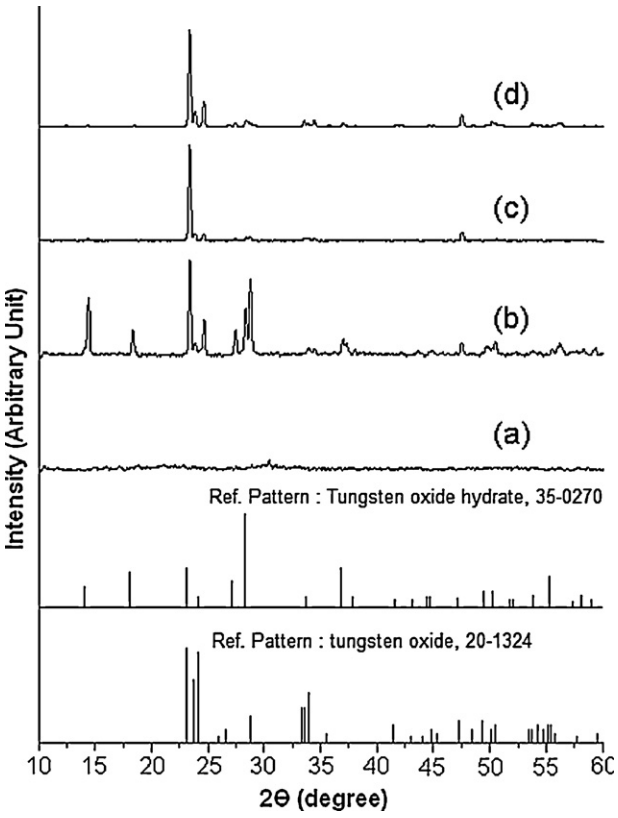


Fig. 1. XRD patterns of the products synthesized by the hydrothermal reaction at 200 °C for 24 h in the respective solutions containing (a–d) 0.00 ml, 2.50 ml, 5.00 ml, and 7.50 ml of 1 M HCl, as compared to the JCPDS standard patterns of orthorhombic WO_3 $0.33H_2O$ and WO_3 [11].

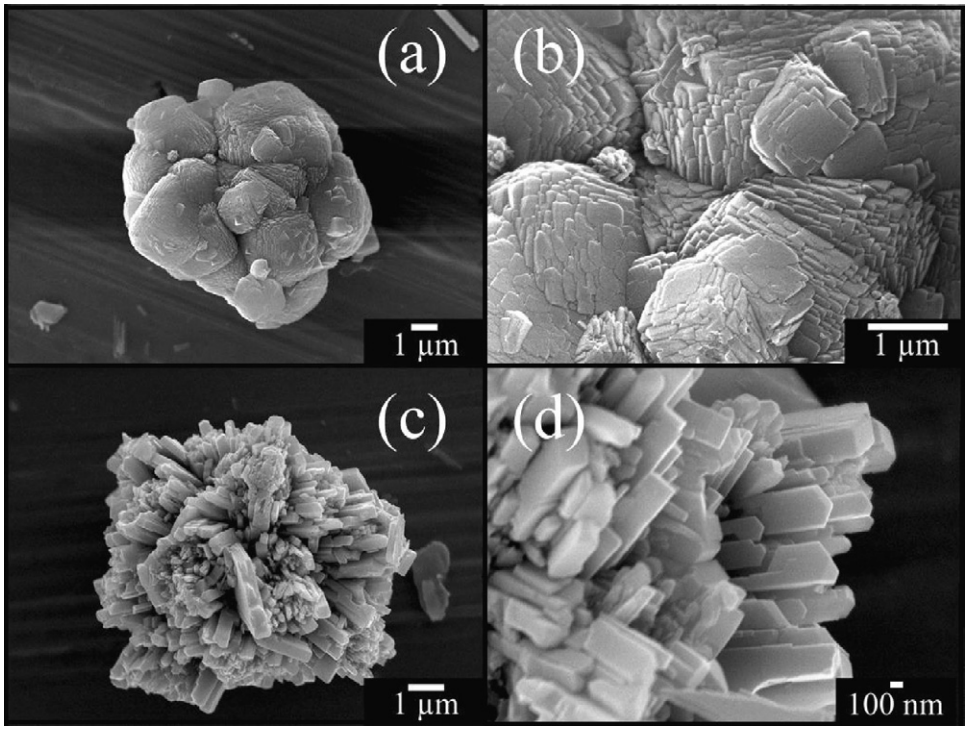


Fig. 2. SEM images of o-WO_3 synthesized by the hydrothermal reaction at 200 °C for 24 h in the solutions containing (a, b) 5.00 ml, and (c, d) 7.50 ml of 1 M HCl.

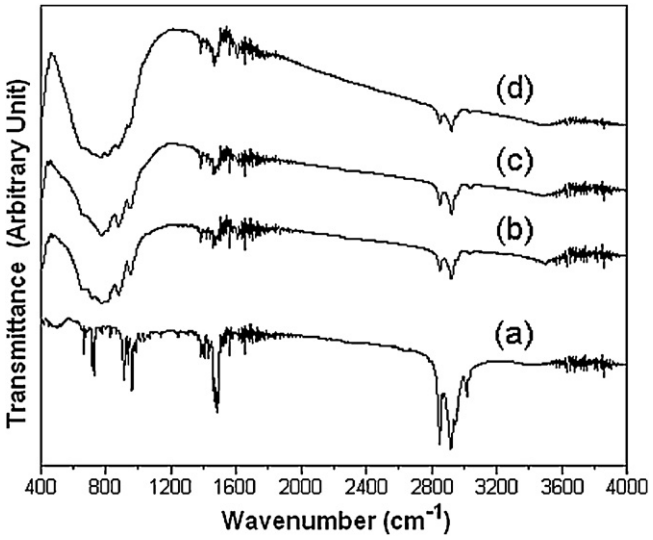


Fig. 3. FTIR spectra of (a) CTAB, and (b–d) the products synthesized by the hydrothermal reaction at 200 °C for 24 h in the solutions containing 2.50 ml, 5.00 ml, and 7.50 ml of 1 M HCl, respectively.

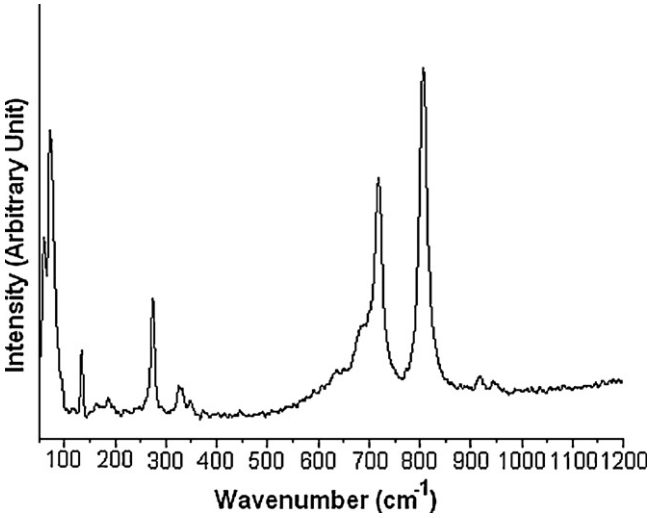


Fig. 4. Raman spectrum of o-WO_3 microflowers, synthesized by the hydrothermal reaction at 200 °C for 24 h in the solution containing 7.50 ml 1 M HCl.

and 949 cm^{-1} were detected. They are attributed to the stretching of short W=O bonds, while the bands at 817 and 728 cm^{-1} were assigned to be the O–W–O stretching modes. The vibrational bands centered at 659 and 590 cm^{-1} were attributed to the W–O–W stretching modes [5]. The asymmetric and symmetric stretching vibrations of CH_2 in the methylene chains of the incorporated CTAB were also detected at the same wavenumbers as those of the solid surfactant – implying that no intermolecular interaction was enhanced due to the capping effect, and the conformation of methylene chains remained unchanged. Their intensities are weakened, because CTAB was not completely removed by washing with deionized water and ethanol, and remained as the adsorbed head groups on the surfaces of these products – as was also found in previous reports [14,15,17].

The Raman spectrum of the as-synthesized WO_3 microflowers over the range of 50–1200 cm^{-1} is shown in Fig. 4. Generally, the 950–1050 cm^{-1} Raman wavenumbers of the transition metal oxide are assigned to be the symmetric stretching modes of metal and oxygen bonds (short terminal W=O, ν_s(W=O) terminal bands), and 750–950 cm^{-1} bands were either the antisymmetric stretching of W–O–W bonds (ν_{as}(W–O–W)) or symmetric stretching of –O–W–O– bonds (ν_s(–O–W–O–)). The Raman spectrum of the as-synthesized WO_3 microflowers detected vibrational peaks at 806, 718, 686, 326, 274, 134, 76 and 60 cm^{-1}. The two main intense peaks at 806 and 718 cm^{-1}, and the shoulder at 686 cm^{-1}, are typical Raman peaks of crystalline WO_3, which correspond to the stretching and bending vibrations of the bridging tungsten and oxygen atoms. They are assigned to be the W–O stretching (ν), W–O bending (δ) and O–W–O deformation (γ) modes, respectively. Two peaks at 326 and 274 cm^{-1} are assigned to be the bending δ(O–W–O) vibrations. Those below 200 cm^{-1} modes were attributed to the lattice vibrations. All these peaks are in good accordance with those of other reports [1,5,12,18,19].

Detailed morphology of the as-synthesized o-WO_3 structure was proved by TEM images (Fig. 5), which show the product shape to be microflowers 6–8 μm in diameter; these are composed of a large number of petals with lengths up to several micrometers. Some petals were released from the microflower cores by ultrasonic vibrations during preparation of the samples for TEM analysis. Fig. 6a and b presents high-magnification TEM images with the *x*-axis of Fig. 5b tilted. These o-WO_3 petals are straight and smooth, with uniform dimension along their axial direction. The selected area electron diffraction patterns (Fig. 6c and d) were indexed and specified as orthorhombic WO_3 phase (JCPDS No. 20-1324) [11],

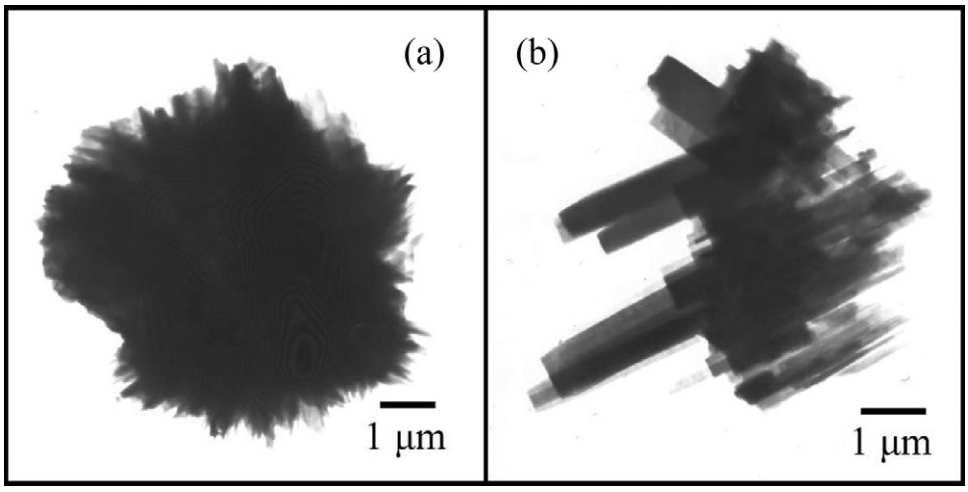


Fig. 5. TEM images of o-WO_3 microflowers, synthesized by the hydrothermal reaction at 200 °C for 24 h in the solution containing 7.50 ml 1 M HCl.

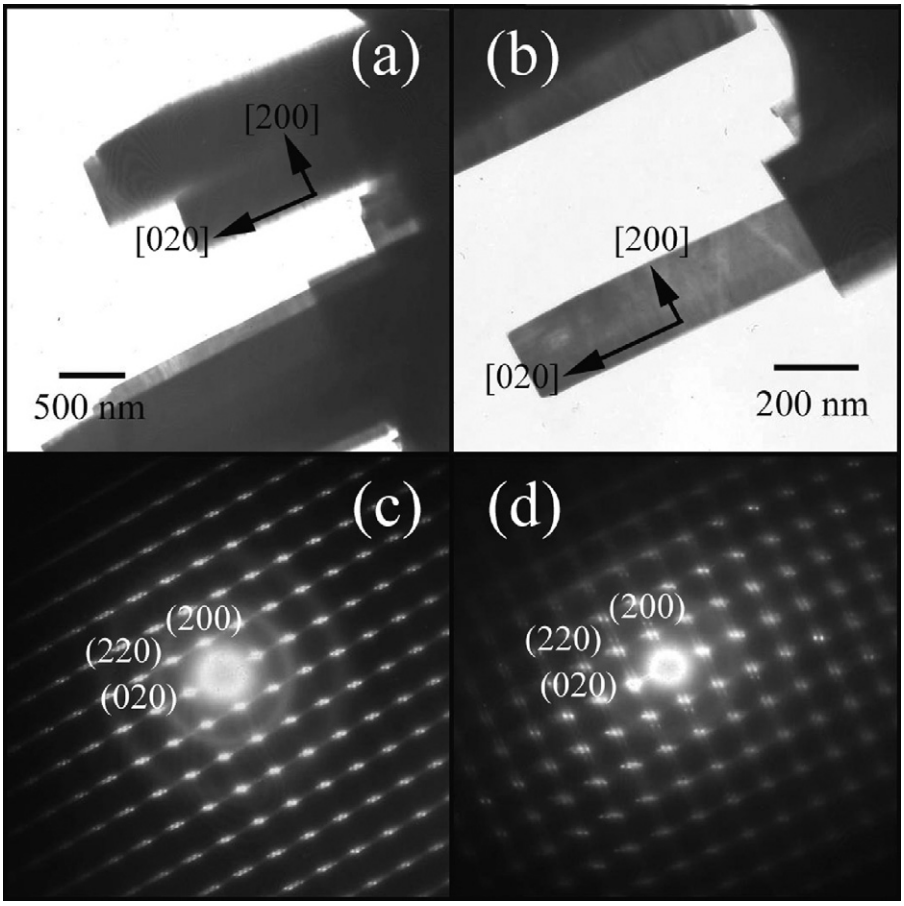


Fig. 6. (a, b) High magnification TEM images, and (c, d) SAED patterns of o-WO_3 microflowers of Fig. 5(b).

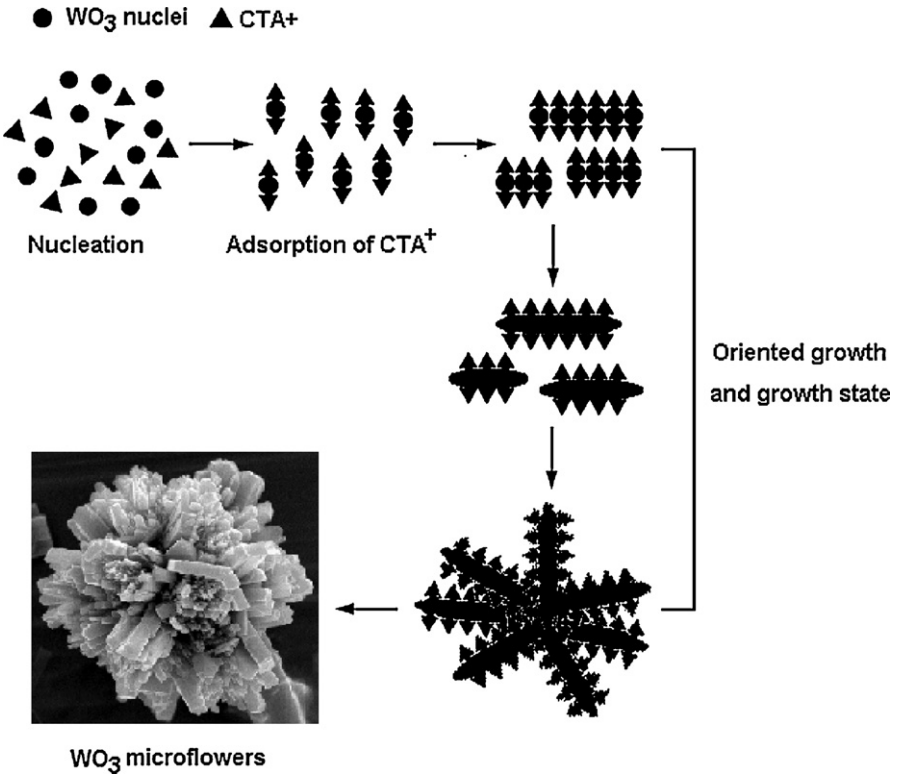


Fig. 7. Schematic diagram for the formation of o-WO_3 microflowers.

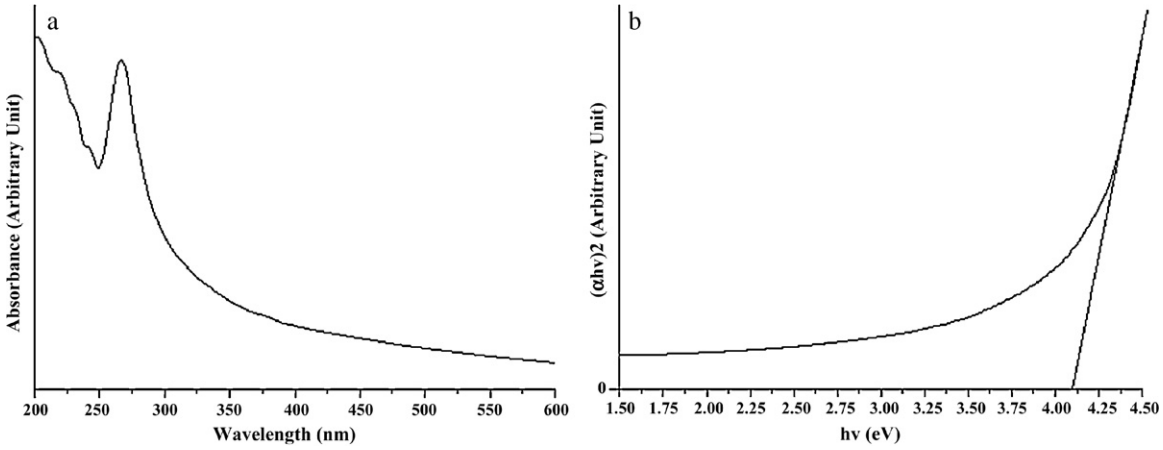


Fig. 8. (a) UV–visible spectrum, and (b) the $(\alpha h\nu)^2$ versus $h\nu$ plot of o-WO_3 microflowers, synthesized by the hydrothermal reaction at 200 °C for 24 h in the solution containing 7.50 ml 1 M HCl.

in accordance with the XRD analysis. They show the (0 2 0), (2 2 0) and (2 0 0) diffraction planes with the electron beam in the [0 0 −1] direction. It should be noted that the growth direction of the petals is normal to the (0 2 0) plane of the microsquare layers – implying that the o-WO_3 microsquare layers are aligned along the [0 2 0] direction.

The formation of o-WO_3 microflowers can be explained by polycondensation, electroneutral and dehydration reactions from the polyoxotungstate anions, as shown below:

$$H_2W_{12}O_{40}{}^{6-} + 6H^+ + (8+n)H_2O \rightarrow 12H_2WO_4 \cdot nH_2O \quad (1)$$

$$H_2WO_4 \cdot nH_2O \rightarrow \text{o-}WO_3(\text{nuclei}) + (n+1)H_2O \quad (2)$$

$$\text{o-}WO_3(\text{nuclei}) \rightarrow WO_3(\text{microflowers}) \quad (3)$$

When $(NH_4)_6H_2W_{12}O_{40}{\cdot}xH_2O$ was dissolved in deionized water, followed by the addition of HCl, the colorless solution of $H_2W_{12}O_{40}{}^{6-}$ anions changed to $H_2WO_4{\cdot}nH_2O$ yellow precursor precipitates. Upon the 200 °C hydrothermal reaction, $H_2WO_4{\cdot}nH_2O$ was further decomposed to produce o-WO_3 (nuclei) [20–22], containing in microsquare layers of $[WO_6]^{6-}$ octahedrons [5,12] lying in the [2 0 0] direction. At this stage, CTAB – which is a positively charged cationic surfactant (CTA^+) with a long hydrophobic tail [14,23,24] – was attracted by the four negatively charged oxygen atoms in the planar surface of $[WO_6]^{6-}$, due to the stereochemical effect. The $[CTA\text{–}WO_6]^{2-}$ bonds orientated parallel to the [0 2 0] direction inhibited growth in the [2 0 0] and [0 0 2] directions because of the CTA^+ hydrophobic tails [21,23]. The $[CTA\text{–}WO_6]^{2-}$ petals grew out from cores to form o-WO_3 microflowers, and the CTAB molecules were washed out, as shown in Fig. 7.

UV–vis absorbance for o-WO_3 microflowers (Fig. 8a) shows an absorption band in the 200–450 nm range and a strong band at 275 nm, attributed to the high UV spectrum [25]; this might be a consequence of the confined nature of electrons in the [0 1 0] direction [1]. No absorption band in the visible range was detected. This result is in accordance with those reported by Nataraj and co-workers [18], and Xu and co-workers [25]. The direct band gap (E_g) of o-WO_3 microflowers was determined by Eq. (4):

$$\alpha h\nu = (h\nu - E_g)^n \quad (4)$$

where α, h, ν, and E_g are the absorbance, Planck constant, photon frequency, and optical band gap, respectively. The parameter n is a pure number associated with the different types of electronic transitions: $n = 1/2, 2, 3/2$ or 3 for direct–allowed, indirect–allowed, direct–forbidden and indirect–forbidden transitions, respectively [26]. Its direct energy gap was determined by extrapolation of the linear portion of the curve (Fig. 8b) to $\alpha = 0$, corresponding to 4.10 eV. It should be noted that the change of absorption was controlled by two photon energy ($h\nu$) ranges – the high and low energies. When the photon energy is greater than the energy band gap (E_g), absorption was linearly increased with the increasing of photon energy. But for the photon energy with less than E_g, the absorption became different from the linearity, due to the dominant photonic absorption relating to defect levels between the valence and conduction bands of the product.

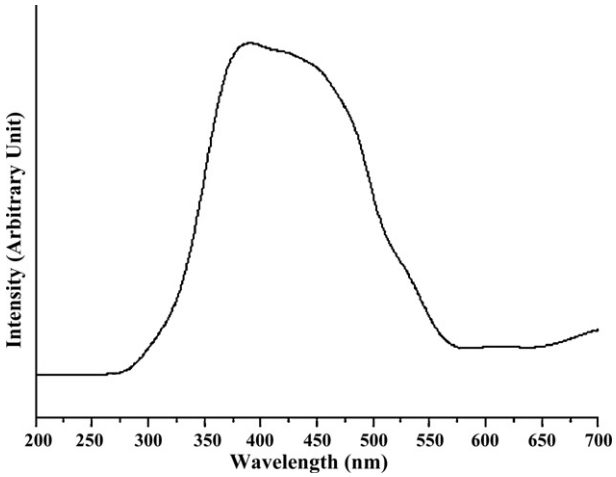


Fig. 9. PL spectrum of o-WO_3 microflowers.

The PL spectrum (Fig. 9) of the as-synthesized o-WO_3 microflowers was recorded using 200 nm excitation wavelength at room temperature. The emission peak presents a broad band at 275–575 nm with a maximum emission at 375 nm in the violet region by Gaussian curve fitting, due to the electronic transition of WO_3. This PL emission is in accordance with the report of Lee and co-workers [27].

4. Conclusions

In summary, o-WO_3 microflowers composing of long petals (E_g = 4.10 eV) were successfully synthesized by the CTAB-assisted hydrothermal reaction at 200 °C for 24 h. Their microsquare layers grew along the [0 2 0] direction to form the petals. UV spectrum shows a maximum absorption at 275 nm, and PL emission at 375 nm.

Acknowledgements

This research was supported by the National Nanotechnology Center (NANOTEC), a member of National Science and Technology Development Agency (NSTDA); Ministry of Science and Technology; Thailand Research Fund (TRF); and Center for Innovation in Chemistry (PERCH-CIC), Commission on Higher Education (CHE), Ministry of Education, Thailand.

References

[1] A. Wolcott, T.R. Kuykendall, W. Chen, S. Chen, J.Z. Zhang, J. Phys. Chem. B 110 (2006) 25288–25296.
[2] A. Yan, C. Xie, D. Zeng, S. Cai, M. Hu, Mater. Res. Bull. 45 (2010) 1541–1547.
[3] Z. Gu, Y. Ma, W. Yang, G. Zhang, J. Yao, Chem. Commun. (2005) 3597–3599.
[4] S. Sun, Y. Zhao, Y. Xia, Z. Zou, G. Min, Y. Zhu, Nanotechnology 19 (2008) 305709.
[5] S. Salmaoui, F. Sediri, N. Gharbi, Polyhedron 29 (2010) 1771–1775.
[6] D.Z. Guo, K. Yu-Zhang, A. Gloter, G.M. Zhang, Z.Q. Xue, J. Mater. Res. 19 (2004) 3665–3670.
[7] Y. Bi, D. Li, H. Nie, Mater. Chem. Phys. 123 (2010) 225–230.
[8] Y.B. Li, Y. Bando, D. Golberg, K. Kurashima, Chem. Phys. Lett. 367 (2003) 214–218.
[9] P. Tägtström, U. Jansson, Thin Solid Films 352 (1999) 107–113.
[10] Y. Li, X. Su, J. Jian, J. Wang, Ceram. Int. 36 (2010) 1917–1920.
[11] Powder Diffract File, JCPDS-ICDD, 12 Campus Boulevard, Newtown Square, PA, U.S.A.
[12] I.M. Szilágyi, J. Madarász, G. Pokol, P. Király, G. Tárkányi, S. Saukko, J. Mizsei, A.L. Tóth, A. Szabó, K. Varga-Josepovits, Chem. Mater. 20 (2008) 4116–4125.
[13] C. Guéry, C. Choquet, F. Dujeancourt, J.M. Tarascon, J.C. Lassègues, J. Solid State Electrochem. 1 (1997) 199–207.
[14] Z.M. Sui, X. Chen, L.Y. Wang, L.M. Xu, W.C. Zhuang, Y.C. Chai, C.J. Yang, Physica E 33 (2006) 308–314.
[15] H. Kavas, Z. Durmus, M. Şenel, S. Kazan, A. Baykal, M.S. Toprak, Polyhedron 29 (2010) 1375–1380.
[16] G. Wang, Q. Mu, T. Chen, Y. Wang, J. Alloys Compd. 493 (2010) 202–207.
[17] Y.D. Wang, S. Zhang, C.L. Ma, H.D. Li, J. Lumin. 126 (2007) 661–664.
[18] S. Rajagopal, D. Nataraj, D. Mangalaraj, Y. Djaoued, J. Robichaud, O.Y. Khyzhun, Nanoscale Res. Lett. 4 (2009) 1335–1342.
[19] J. Díaz-Reyes, R.J. Delgado-Macuil, V. Dorantes-García, A. Pérez-Benítez, J.A. Balderas-López, J.A. Ariza-Ortega, Mater. Sci. Eng. B 174 (2010) 182–186.
[20] E.V. Timofeeva, G.A. Tsirlina, O.A. Petrii, Russ. J. Electrochem. 39 (2003) 716–726.
[21] A. Phuruangrat, D.J. Ham, S. Thongtem, J.S. Lee, Electrochem. Commun. 11 (2009) 1740–1743.
[22] Z. Jiao, X.W. Sun, J. Wang, L. Ke, H.V. Demir, J. Phys. D: Appl. Phys. 43 (2010) 285501.
[23] X.M. Sun, X. Chen, Z.X. Deng, Y.D. Li, Mater. Chem. Phys. 78 (2002) 99–104.
[24] T. Thongtem, S. Kaowphong, S. Thongtem, Appl. Surf. Sci. 254 (2008) 7765–7769.
[25] Q. Xiang, G.F. Meng, H.B. Zhao, Y. Zhang, H. Li, W.J. Ma, J.Q. Xu, J. Phys. Chem. C 114 (2010) 2049–2055.
[26] J.C. Sczancoski, L.S. Cavalcante, N.L. Marana, R.O. da Silva, R.L. Tranquilin, M.R. Joya, P.S. Pizani, J.A. Varela, J.R. Sambrano, M.S. Li, E. Longo, J. Andrés, Curr. Appl. Phys. 10 (2010) 614–624.
[27] J. Wang, P.S. Lee, J. Ma, J. Cryst. Growth 311 (2009) 316–319.

Journal of Physics and Chemistry of Solids 72 (2011) 176–180

Contents lists available at ScienceDirect

Journal of Physics and Chemistry of Solids

journal homepage: www.elsevier.com/locate/jpcs

Microwave-assisted synthesis and optical property of $CdMoO_4$ nanoparticles

Anukorn Phuruangrat [a,*], Nuengruethai Ekthammathat [b], Titipun Thongtem [b,*], Somchai Thongtem [c]

[a] Department of Materials Science and Technology, Faculty of Science, Prince of Songkla University, Hat Yai, Songkhla 90112, Thailand
[b] Department of Chemistry, Faculty of Science, Chiang Mai University, Chiang Mai 50200, Thailand
[c] Department of Physics and Materials Science, Faculty of Science, Chiang Mai University, Chiang Mai 50200, Thailand

ARTICLE INFO

Article history:
Received 20 January 2010
Received in revised form
21 November 2010
Accepted 5 December 2010
Available online 10 December 2010

Keywords:
A. Semiconductors
C. Electron microscopy
C. Raman spectroscopy
C. X-ray diffraction
D. Optical properties

ABSTRACT

Microwave-assisted synthesis is a novel method used to synthesize $CdMoO_4$ nanoparticles in propylene glycol. The effects of reaction time and microwave power on phase, morphologies, and optical properties of $CdMoO_4$ nanoparticles were studied, using X-ray diffraction (XRD), Raman spectroscopy, Fourier transform infrared spectroscopy (FTIR), transmission electron microscopy (TEM), and UV–visible spectroscopy. The present analyses proved that these crystalline powders were scheelite-type tetragonal structured $CdMoO_4$, with the crystallite size of 14–20 nm, and 4.51–4.73 eV band gaps, controlled by the synthetic conditions.

© 2010 Elsevier Ltd. All rights reserved.

1. Introduction

Metal molybdates and tungstates have two types of structures, depending on the size of bivalent cations—scheelite (ionic radius >0.99 Å—Ca, Sr, Ba, and Pb) and wolframite (ionic radius <0.77 Å—Mg, Mn, Fe, Co, Ni, and Zn) [1–3]. They have attracted considerable interest for a number of researchers, due to their promising technological importance in a wide range of applications, including photoluminescence, scintillating materials, humidity sensors, photoelectric devices, photonic crystals, light weight filler materials, photocatalysts, and chemical reactors [1–6].

Cadmium molybdate ($CdMoO_4$) is one of the metallic molybdate compounds with a scheelite structure, and has a body-center orthorhombic primitive cell with C_{4h}^6 space group. Each site of Cd and Mo is surrounded by eight oxygen (octahedron) and four equivalent oxygen (tetrahedron) sites, respectively. The calculation of the electronic structure shows that the Cd_{4d} state localizes at the bottom region of the O_{2p} valence band, and the Cd_{5s} state has a significant contribution to the bottom of the conduction band, composed of the Mo_{4d} state [7]. $CdMoO_4$ is an interesting material owing to its excellent optical and chemical properties, electronic excitation at VUV synchrotron radiation, pressure-induced phase transformations, and ^{111}Cd and ^{113}Cd spin-lattice relaxation. As a wide band gap semiconductor of 3.25 eV, $CdMoO_4$ is expected to be a photocatalyst under UV radiation [5–8].

Recently, there have been some reports on the synthesis of $CaMoO_4$. For example, Jiang et al. [1] reported the synthesis of $CdMoO_4$ nanoparticles with good crystallization at 90 °C for 20 h by a hydrothermal method. It showed the emission peak at 390 nm, using 330 nm excitation wavelength. Liu and Tan [7] synthesized $CdMoO_4$ nanorods by hydrothermal method at a relatively low temperature, and tested on the electrochemical properties for use as a cathode material of lithium rechargeable batteries. Ren et al. [9] showed that the photoluminescence properties of $CdMoO_4$ nanoparticles were controlled by its shape and size, determined by the pH of the solutions. There are some reports on the synthesis of $CdMoO_4$ hollow microspheres composed of nanoparticles by a facile aqueous reaction process without using templates and other additives by Zhen et al. [4], Zhou et al. [6], and Wang et al. [8]. Compared to the large amount synthesis using microwave radiation, this method has been considered to be a good process for preparation of other metal molybdates and tungstates [2,10–12], due to the convenience of morphology and size controlling, simple and one step synthesis, uniform composition and phase, and large scale synthesis for industrial application.

In the present research, the microwave-assisted synthesis of highly crystalline $CdMoO_4$ nanocrystals with particle size smaller than 50 nm was firstly reported. The effects of reaction time and microwave power on phase, morphologies, and optical properties of $CdMoO_4$ nanoparticles were studied, and compared with those of the co-precipitation method.

2. Experiment

The analytical grade chemicals, such as cadmium (II) nitrate tetrahydrate ($Cd(NO_3)_2 \cdot 4H_2O$, 99.99%), sodium molybdate dihydrate

* Corresponding authors. Tel.: +66 0 53 943344; fax: +66 0 53 892277.
E-mail addresses: phuruangrat@hotmail.com (A. Phuruangrat), ttpthongtem@yahoo.com (T. Thongtem).

0022-3697/$ - see front matter © 2010 Elsevier Ltd. All rights reserved.
doi:10.1016/j.jpcs.2010.12.003

($Na_2MoO_4 \cdot 2H_2O$, $\geq 99.5\%$), and propylene glycol ($C_3H_8O_2$, 99.99%) were bought from Sigma-Aldrich, and used without further purification.

To synthesize $CdMoO_4$ nanoparticles, each 0.005 mole of $Cd(NO_3)_2 \cdot 4H_2O$ and $Na_2MoO_4 \cdot 2H_2O$ was separately dissolved in 15.00 ml propylene glycol, mixed, and stirred for 30 min. Then the solution was transferred to a microwave oven and heated at 20% (each cycle—the microwave was on for 24 s and off for 96 s) of 180–600 W for 20–60 min. On completion of the reaction, white powders were produced, collected, and washed with distilled water and absolute ethanol, and dried in air at 80 °C for 24 h.

The products were characterized and recorded on a Philips X'Pert MPD X-ray diffractometer (XRD) equipped with a graphitic monochromator with CuKα radiation ($\lambda = 0.154056$ nm), using a scanning rate of 0.02°/s over the 2θ range of 15–60°. FTIR spectra were recorded on a Perkin Elmer Spectrum RX FTIR spectrometer with KBr as a diluting agent and operated in the range of 400–4000 cm^{-1} with the resolution of 4 cm^{-1}. Raman vibrations of the products were detected by a HORIBA JOBIN YVON T64000 Raman spectrometer with 50 mW and 514.5 nm wavelength Ar laser. Transmission electron microscopic (TEM) images and selected area electron diffraction (SAED) patterns were taken on a JEOL JEM-2010, employed at an accelerating voltage of 200 kV. UV–visible spectra were carried out using a Lambda 25 spectrometer using UV lamp with the resolution of 1 nm.

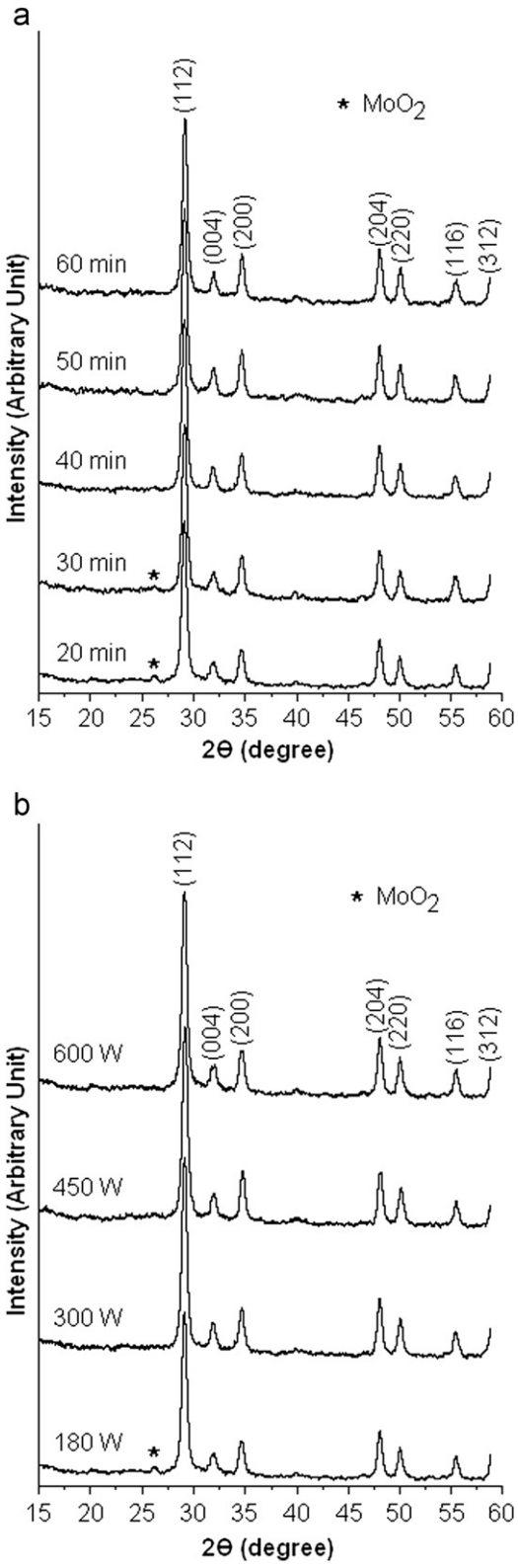


Fig. 1. XRD patterns of $CdMoO_4$ synthesized using microwave radiation at (a) 180 W for 20–60 min and (b) 180–600 W for 20 min.

3. Results and discussion

$CdMoO_4$ has scheelite structure with lattice constants of $a = 5.1550$ Å and $c = 11.1940$ Å and has $I4_1/a$ or C_{4h}^6 space group. This structure has eight symmetry elements, and a body-centered orthorhombic ($a \neq b \neq c$, $\alpha = \beta = \gamma = 90°$) primitive cell that includes two formula units of $CdMoO_4$. Each Mo site is surrounded by four equivalent O sites at a bond length of 1.75 Å to form $[MoO_4]^{2-}$ anions in approximately tetrahedral symmetry. Each Cd site is surrounded by eight O sites at bond lengths of 2.40 and 2.44 Å in approximately octahedral symmetry. $CdMoO_4$ has strong covalent bonds of Mo–O in $[MoO_4]^{2-}$ molecular ionic units and weak coupling between $[MoO_4]^{2-}$ anions and Cd^{2+} cations [7,11–15].

Fig. 1 shows the XRD patterns of the products synthesized at different microwave radiation powers and lengths of reaction time. For the microwave radiation at 180 W for 20 and 30 min, the products were composed of tetragonal $CdMoO_4$ and MoO_2, compared to the JCPDS nos. 07-0209 for $CdMoO_4$ ($a = b = 5.1550$ Å, $c = 11.1940$ Å, and $\alpha = \beta = \gamma = 90°$), and 01-0615 for MoO_2 [16] as the main phase and impurity, respectively. On using 180 W microwave radiation and the reaction times of 40, 50, and 60 min or increasing the microwave radiation power from 180 to 300, 450, and 600 W with the reaction time remaining at 20 min, the products became the only pure tetragonal $CdMoO_4$ phase with no detection of any impurity. The XRD peaks became stronger and shaper with the increase in the microwave radiation power and length of reaction time, indicating that the crystalline degree of the tetragonal $CdMoO_4$ phase became higher. At 600 W and 20 min, lattice parameters were calculated using the

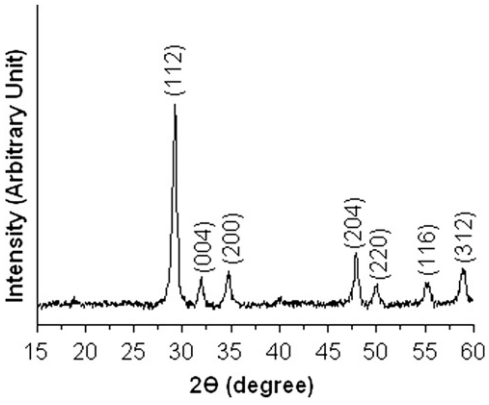


Fig. 2. XRD pattern of $CdMoO_4$ synthesized by co-precipitation method at room temperature for 48 h.

plane spacing equation of tetragonal structure [17] and Bragg's law for diffraction. They were $a=b=5.1619$ Å, and $c=11.1952$ Å, in accordance with those of the JCPDS database no. 07-0209 [16].

Approximate crystallite sizes (L) of $CdMoO_4$ nanocrystals synthesized under different conditions were calculated from the Scherrer formula [17]

$$L=\frac{\lambda k}{B\cos\theta} \quad (1)$$

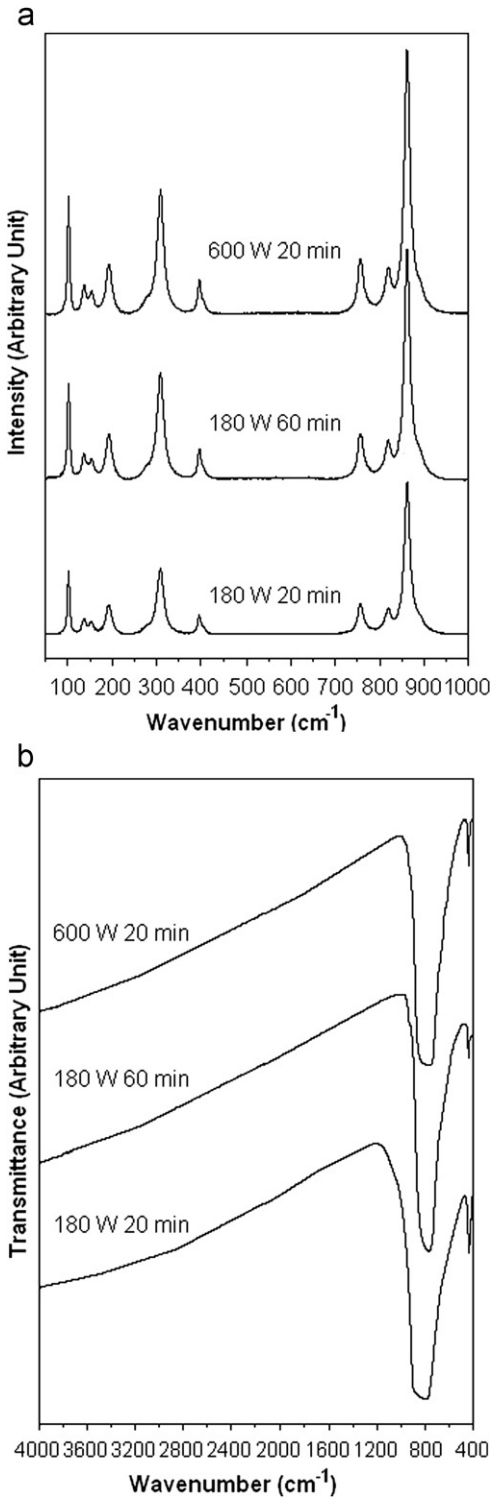


Fig. 3. (a) Raman and (b) FTIR spectra of $CdMoO_4$ synthesized using microwave radiation at 180 W for 20 min, 180 W for 60 min, and 600 W for 20 min.

where λ, θ, k, and B are the wavelength of CuKα radiation (1.54056 Å), Bragg angles of the (1 1 2) planes, a constant (0.89), and full widths at half maximum of the (1 1 2) peaks, respectively. Calculated crystallite sizes of $CdMoO_4$ nanocrystals synthesized under microwave radiation power of 180 W for 20, 30, 40, 50, and 60 min are 15.00, 15.24, 15.52, 15.55, and 15.60 nm, and under microwave radiation powers of 300, 450, and 600 W for 20 min are 15.55, 16.18, and 20.20 nm, respectively. The crystallite size increases are 4% by increasing the length of time from 20 to 60 min with the microwave power remaining at 180 W, and 35% by increasing the microwave power from 180 to 600 W with the length of time remaining at 20 min. These analyses implied that microwave radiation power and length of reaction time played a role in the phase, crystalline degree, and crystallite sizes of $CdMoO_4$ nanoparticles. The microwave power had a stronger influence on them than the length of reaction time.

Compared to the non-microwave radiation method, $Cd(NO_3)_2\cdot 4H_2O$ and $Na_2MoO_4\cdot 2H_2O$ as cadmium and molybdate sources were mixed in 30.00 ml propylene glycol. On stirring for 24 h, the colorless solution changed into a white colloidal solution. The experiment was continued with stirring until 48 h completion, and white precipitates were synthesized. After washing and drying, they were characterized by XRD (Fig. 2). The product was identified to be pure tetragonal $CdMoO_4$ phase, compared to the JCPDS no. 07-0209 [16], but the intensity peaks became lessened. These results proved that the microwave radiation played a role in accelerating the crystalline degree of $CdMoO_4$ powders.

In lattice space, scheelite compounds ($CaMoO_4$, $CaWO_4$, $SrMoO_4$, $SrWO_4$, etc.) correspond to S_4 symmetry. A group theoretical analysis of the scheelite structure yields 26 lattice modes at the Γ point of the Brillouin zone—$3A_g+5A_u+5B_g+3B_u+5E_g+5E_u$. The 13 g modes are Raman active, and the 13 u modes are infrared active ($4A_u$ and $4E_u$), acoustic ($1A_u$ and $1E_u$), and silent ($3B_u$). The Raman active phonon modes can be classified into two types of vibrations, the internal and external modes (rotation and translation) with respect to (w.r.t.) the $[MoO_4]^{2-}$ tetrahedrons. Among them, seven modes are internal stretching vibrations of $\nu_1(A_g)$, $\nu_3(B_g)$, and $\nu_3(E_g)$, and bending of $\nu_2(A_g)$, $\nu_2(B_g)$, $\nu_4(B_g)$, and $\nu_4(E_g)$. The six remaining are external modes—three rotations, two translations, and an unidentified mode. The internal modes correspond to normal vibrations of the $[MoO_4]^{2-}$ tetrahedrons, while the external modes involve motions of the metallic atoms (e.g. Ca, Sr, Ba, Cd, etc.) w.r.t. $[MoO_4]^{2-}$ tetrahedrons [10–12,15,18–20]. It is expected that the frequencies and wavenumbers of the internal stretching modes are higher than those of the external ones, because the internal covalent bonding within the $[MoO_4]^{2-}$ tetrahedrons is stronger than the external lattice binding. Fig. 3a shows the Raman spectra of $CdMoO_4$ produced by the microwave radiation method under different conditions. They show strong Raman peaks that indicate a strong interaction between the ions, which mainly arise from the stretching and bending vibrations of the shorter metal–oxygen bonds within the anionic groups. All Raman spectra were identified as $\nu_1(A_g)$, $\nu_3(B_g)$, $\nu_3(E_g)$, $\nu_4(E_g, B_g)$, and $\nu_2(A_g, B_g)$ at 862, 820, 755, 396, and 309 cm^{-1}, respectively. Three rotation and two translation modes of $[MoO_4]^{2-}$ units were detected at 280, 192, 153, 135, and 102 cm^{-1}, respectively. These results are in accordance with those reported in the literature [15,20] (Table 1), although their wavenumber vibration modes were not exactly the same values, due to the difference in geometries, particle sizes, and nature of the products.

For T_d-symmetry, the scheelite structure has four vibrations, specified as $\nu_1(A_1)$, $\nu_2(E)$, $\nu_3(F_2)$ and $\nu_4(F_2)$. In lattice space, its IR spectrum is in accordance with the S_4 symmetry. The correlations of the $T_d \leftrightarrow S_4$ symmetries are $A_1 \leftrightarrow A$, $E \leftrightarrow A+B$, and $F_2 \leftrightarrow B+E$. There was no detection of the ν_1 mode. Only the ν_2, ν_3, and ν_4 modes were detected. Fig. 3b shows the FTIR spectra of $CdMoO_4$ produced by microwave radiation method under different conditions. For the

present analysis, a strong transmittance mode specified as Mo–O anti-symmetric stretching vibration (ν_3) of $[MoO_4]^{2-}$ tetrahedrons was detected at 743–895 cm^{-1}, and an additional weak peak of the Mo–O bending mode (ν_4) at 423 cm^{-1}. These results are in accordance with those previously reported [10–12].

TEM images of the $CdMoO_4$ nanocrystallines obtained from different conditions under microwave radiation method are shown in Fig. 4 and their SAED patterns were inserted inside. At 180 W for 20 min, the product was composed of clusters of spherical nanoparticles with average particle size and standard deviation of 14.16 ± 2.18 nm. By increasing the reaction time from 20 to 60 min or microwave power from 180 to 600 W, the products are perfectly and homogeneously spherical nanoparticles with average particle size of 15.19 ± 1.95 nm at 180 W for 60 min, and 19.99 ± 2.72 nm at 600 W for 20 min. Obviously, the increase in the particle size of $CdMoO_4$ nanoparticles was by increasing the microwave power and reaction time of the microwave radiation synthetic process. Their SAED patterns show bright fully concentric rings of poly-nanocrystalline $CdMoO_4$—corresponding to the (1 1 2), (0 0 4), (2 0 0), (2 1 1), (2 0 4), (2 2 0), (1 1 6), and (3 1 2) planes. It should be noted that the particle sizes of tetragonal $CdMoO_4$ crystallites can be controlled under the microwave radiation process by varying the microwave power and reaction time.

The direct band gap energy (E_g) of $CdMoO_4$ nanoparticles was calculated by the Wood and Tauc method [19]. The optical band gap is associated with the absorbance and photon energy by the

Table 1
Raman vibration modes of $CdMoO_4$ obtained from this work and those reported in literature. (S=strong, M=medium, W=weak, V=very, R=rotation, and T=translation).

Vibration mode	Raman intensity	Wavenumber (cm^{-1})		
		This work	Daturi et al. [15]	Jayaraman et al. [20]
$\nu_1(A_g)$	VS	862	863	867
$\nu_3(B_g)$	W	820	822	825
$\nu_3(E_g)$	W	755	759	761
$\nu_4(E_g, B_g)$	M	396	402	399
	M		396	401
$\nu_2(A_g, B_g)$	M	309	308	309
R	VW	280	277	282
R	M	192	189	193
R	VW	153	173	154
T	M	135	150	137
	M	102	135	107
T	S	102	101	103

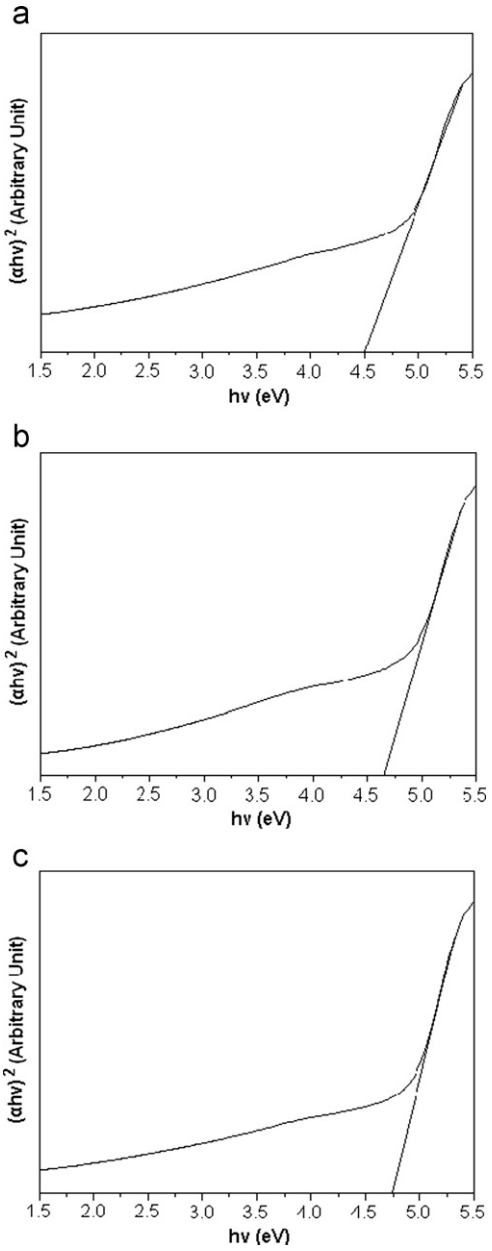


Fig. 5. $(\alpha h\nu)^2$ and $h\nu$ plots of $CdMoO_4$ nanoparticles synthesized at (a) 180 W for 20 min, (b) 180 W for 60 min, and (c) 600 W for 20 min.

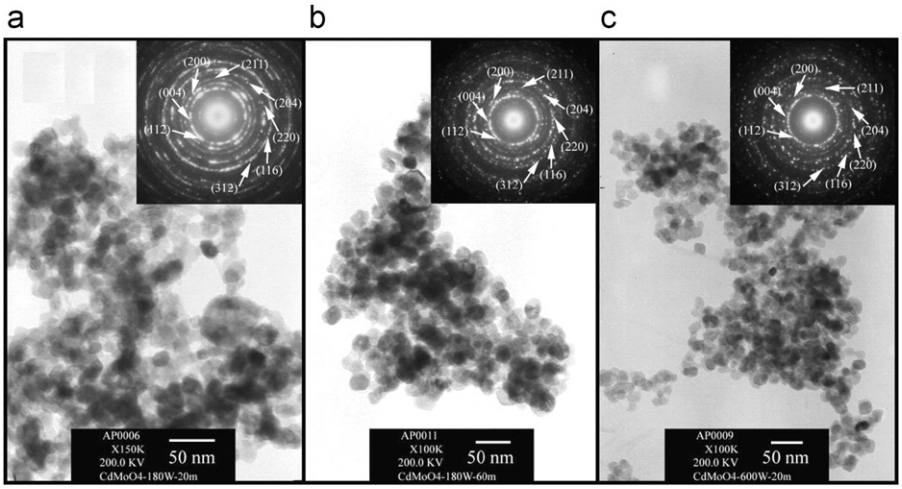


Fig. 4. TEM images and SAED patterns of $CdMoO_4$ synthesized using microwave radiation at (a) 180 W for 20 min, (b) 180 W for 60 min, and (c) 600 W for 20 min.

following equation:

$$\alpha h\nu \propto (h\nu - E_g)^{1/2} \quad (2)$$

where α, h, ν, and E_g are the absorbance, Planck constant, frequency, and optical band gap. The plots of $(\alpha h\nu)^2$ and $h\nu$ of $CdMoO_4$ nanoparticles at 180 W for 20 min, 180 W for 60 min, and 600 W for 20 min are shown in Fig. 5. E_g of $CdMoO_4$ nanoparticles was evaluated by extrapolating the linear portions of the curves to the zero absorbance. The energy band gaps are 4.51, 4.65, and 4.73 eV for 180 W for 20 min, 180 W for 60 min, and 600 W for 20 min, respectively. In fact, the energy band gap is influenced by several factors, such as bond distortion, degree of structural order–disorder, and defects of the crystal [18].

4. Conclusions

$CdMoO_4$ nanoparticles were synthesized by the microwave radiation method under different conditions. XRD patterns, TEM images, and UV–visible absorbance revealed that these crystalline powders had a scheelite-type tetragonal structure with $I4_1/a$ space group, the particle size range of 14–20 nm, and 4.51–4.73 eV band gaps. Raman spectra showed the vibration as $\nu_1(A_g)$, $\nu_3(B_g)$, $\nu_3(E_g)$, $\nu_4(E_g, B_g)$, and $\nu_2(A_g, B_g)$ at 862, 820, 755, 396, and 309 cm^{-1}, with three rotation and two translation modes at 280, 192, 153, 135, and 102 cm^{-1}, respectively. The FTIR analysis shows a strong transmittance mode specified as Mo–O anti-symmetric stretching vibration (ν_3) and Mo–O bending mode (ν_4) of $[MoO_4]^{2-}$ tetrahedrons at 743–895 and 423 cm^{-1}, respectively.

Acknowledgements

This research was supported by the National Nanotechnology Center (NANOTEC), a member of National Science and Technology Development Agency (NSTDA), Ministry of Science and Technology, and the Thailand Research Fund (TRF), Bangkok, Thailand.

References

[1] X. Jiang, J. Ma, B. Lin, Y. Ren, J. Liu, X. Zhu, J. Tao, J. Am. Ceram. Soc. 90 (2007) 977–979.
[2] A. Phuruangrat, T. Thongtem, S. Thongtem, J. Phys. Chem. Solids 70 (2009) 955–959.
[3] X. Wu, J. Du, H. Li, M. Zhang, B. Xi, H. Fan, Y. Zhu, Y. Qian, J. Solid State Chem. 180 (2007) 3288–3295.
[4] L. Zhen, W.S. Wang, C.Y. Xu, W.Z. Shao, M.M. Ye, Z.L. Chen, Scripta Mater. 58 (2008) 461–464.
[5] W.S. Wang, L. Zhen, C.Y. Xu, W.Z. Shao, Cryst. Growth Des. 9 (2009) 1558–1568.
[6] L. Zhou, W. Wang, H. Xu, S. Sun, Cryst. Growth Des. 8 (2008) 3595–3601.
[7] H. Liu, L. Tan, Ionics 16 (2010) 57–60.
[8] W.S. Wang, L. Zhen, C.Y. Xu, B.Y. Zhang, W.Z. Shao, J. Phys. Chem. B 110 (2006) 23154–23158.
[9] Y. Ren, J. Ma, Y. Wang, X. Zhu, B. Lin, J. Liu, X. Jiang, J. Tao, J. Am. Ceram. Soc. 90 (2007) 1251–1254.
[10] T. Thongtem, A. Phuruangrat, S. Thongtem, Mater. Lett. 62 (2008) 454–457.
[11] A. Phuruangrat, T. Thongtem, S. Thongtem, J. Alloys Compd. 481 (2009) 568–572.
[12] A. Phuruangrat, T. Thongtem, S. Thongtem, J. Cryst. Growth 311 (2009) 4076–4081.
[13] M. Fujita, M. Itoh, T. Katagiri, D. Iri, M. Kitaura, V.B. Mikhailik, Phys. Rev. B 77 (2008) 155118-1–155118-7.
[14] Y. Abraham, N.A.W. Holzwarth, R.T. Williams, Phys. Rev. B 62 (2000) 1733–1741.
[15] M. Daturi, G. Busca, M.M. Borel, A. Leclaire, P. Piaggio, J. Phys. Chem. B 101 (1997) 4358–4369.
[16] Powder Diffraction File, JCPDS-ICDD, 12 Campus Boulevard, Newtown Square, PA 19073-3273, U.S.A., 2001.
[17] C. Suryanarayana, M.G. Norton, X-ray Diffraction: a Practical Approach, Plenum Press, NY, 1998.
[18] J.C. Sczancoski, L.S. Cavalcante, M.R. Joya, J.W.M. Espinosa, P.S. Pizani, J.A. Varela, E. Longo, J. Colloid Interface Sci. 330 (2009) 227–236.
[19] J.C. Sczancoski, L.S. Cavalcante, M.R. Joya, J.A. Varela, P.S. Pizani, E. Longo, Chem. Eng. J. 140 (2008) 632–637.
[20] A. Jayaraman, S.Y. Wang, S.K. Sharma, Phys. Rev. B 52 (1995) 9886–9889.

Int.J.Nano.Dim 1(2): 111-118, autumn 2010
ISSN: 2008-8868

Contents list available at **IJND**

International Journal of Nano Dimension

Journal homepage : **www.IJND.ir**

Preparation and characterization of nano-crystalline $LiNi_{0.5}Co_{0.5}VO_4$ by tartate precursor combustion method

A. Phuruangrat[1,*], T. Thongtem[2], S. Thongtem[3]

[1]*Department of Materials Science and Technology, Faculty of Science,Prince of Songkla University, Hat Yai, Songkhla 90112, Thailand*
[2]*Department of Chemistry, Faculty of Science, Chiang Mai University,Chiang Mai 50200, Thailand*
[3]*Department of Physics and Materials Science, Faculty of Science,Chiang Mai University, Chiang Mai 50200, Thailand*

Received: 11 October 2010; Accepted: 27 October 2010

Abstract

$LiNi_{0.5}Co_{0.5}VO_4$ has been successfully synthesized by tartate precursor combustion method using Li_2CO_3, $Co(NO_3)_2.6H_2O$, $Ni(NO_3)_2.6H_2O$ and NH_4VO_3 as a starting materials in deionized water with the subsequent calcination at 450-600 ^oC for 12 h. The combustion and decomposition of tartate precursor were studied by TGA and compared with tartaric acid. It found weight loss at 50-450 ^oC. The product showed a inverse spinel $LiNi_{0.5}Co_{0.5}VO_4$ which confirmed by PXRD. The crystal and particle sizes improved when calcination temperature was increased. Raman and FITR were studied the vibration of product. They detected V-O stretching in VO_4 tetrahedron, Li-O bending in LiO_6 octahedron and Li-O-M (M = Ni and Co) stretching. The TEM showed morphologies that composed nano-particle of $LiNi_{0.5}Co_{0.5}VO_4$.

Keywords*: Lithium ion batteries, $LiNi_{0.5}Co_{0.5}VO_4$, Polymerization complex , Cathode material*

1. Introduction

In recent years, the research on lithium ion secondary batteries has been done to increase the density energy, life cycle and safety of the batteries. One way to increase their density energies is usage of high voltage cathode materials [1-2]. Among of them, the inverse spinel structure transition metal oxides cathode as $LiNiVO_4$, $LiNi_{0.5}Co_{0.5}VO_4$ and $LiCoVO_4$ can display very well even at a voltage as high as 4.3-4.8 V. Chu et al. [3] reported that the inverse spinel $LiNi_{0.5}Co_{0.5}VO_4$ has voltage as high as 4.8 V. It is the new candidate cathodes material for Li-ion secondary batteries. Solid state reaction is widely used to prepare cathode materials but it is a

* Corresponding author: Anukorn Phuruangrat
Chiang Mai University, Chiang Mai 50200,
Thailand
Tel +66-53-943-341
Email phuruangrat@hotmail.com

Dsadvantage method because of high calcination, bigger particle sizes, impurity and long reaction time [4-5]. Thus, cathode materials were synthesized by solid state reaction due to lower efficiency of electrochemical properties. Therefore, the wet chemical route such as sol-gel [6], polymerization [2], precipitate [7] and hydrothermal [8] is the way to synthesized good physical and chemical properties of cathode material. They are advantage because they have the ability to control homogeneity, particle sizes and economy [4-8]. In this paper present tartate precursor combustion method to synthesized nanopowders $LiNi_{0.5}Co_{0.5}VO_4$ at low temperature.

2. Materials and methods

$LiNi_{0.5}Co_{0.5}VO_4$ was prepared by using Li_2CO_3, $Ni(NO_3)_2.6H_2O$, $Co(NO_3)_2.6H_2O$ and NH_4VO_3 in molar ratio 0.5:0.5:0.5:1.0 (the molar ratio of Li:Ni:Co:V = 1.0:0.5:0.5:1.0). Each of them were dissolved in deionized water, sequentially mixed them together at room temperature. Then, the solution was adjusted at pH 5 by using HNO_3. A saturated tartaric acid solution was slowly added, and heated at 80 ^oC under magnetic stirring until it became a gelatin (precursor). The precursor was calcined at 450-600 ^oC for 12 h. The flow chart in this synthesis was shown in Figure 1.

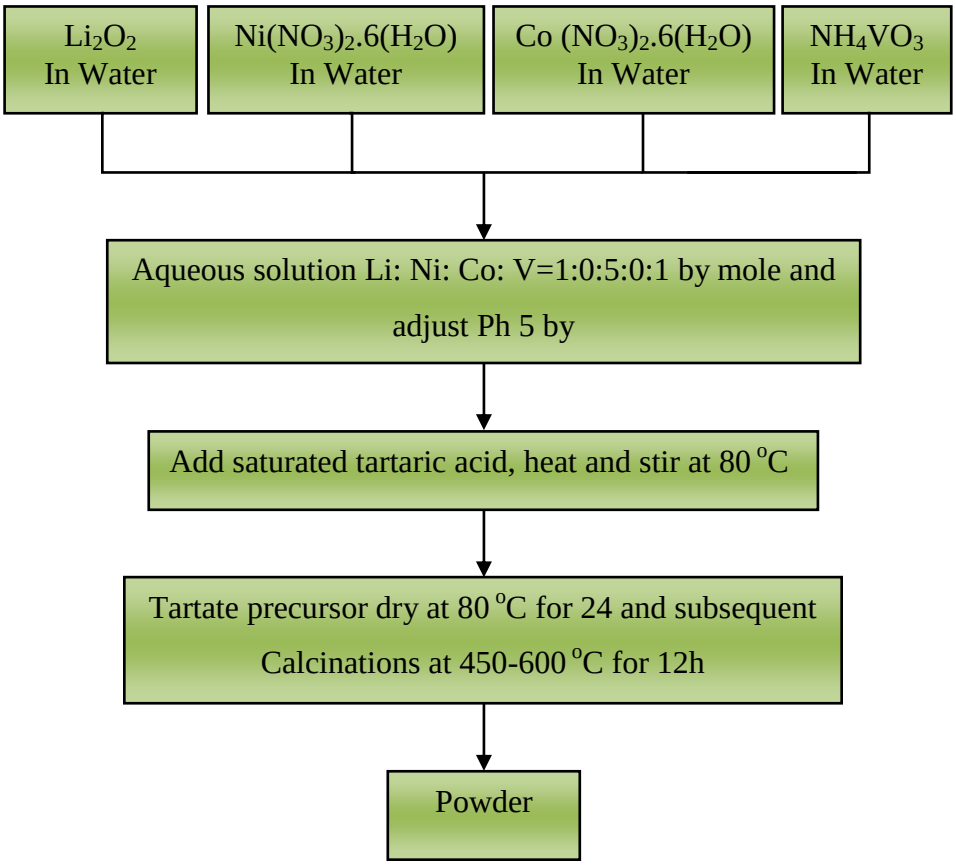


Fig.1. Synthesis process of $LiNi_{0.5}Co_{0.5}VO_4$

The product was analyzed by TGA-7 Perkin Elmer thermogravimetric analyzer (TGA) with the heating rate of 10 ^{o}C/min in a nitrogen atmosphere. The D-500 Siemens powder X-ray diffraction (PXRD) was carried out using Cu K_{α} radiation with the scanning angle range 2Θ from 10 to 60°, a graphitic monochromatized and a Ni filter. Fourier transform infrared spectroscopy (FTIR) was recoded using by TORNOR 27 OPUS with KBr as diluted agent. Raman spectroscopy (HORIBA JOBIN YVON T64000) was operated using 50 mW Ar Laser with λ = 514.5 nm. Transmission Electron Microscopy (JEOL, JEM-2010), Selected Area Electron Diffraction Pattern (SADP) and Energy Dispersive X-ray Spectroscopy (EDX, Oxford instruments INCA) were operated at 200 kV and 15 kV, respectively.

3. Results and discussion

Tartate precursor was analyzed using TGA at temperature range 50-600 ^{o}C in N_2 atmosphere as shown in Figure 2. Its weight loss is in the temperature rang 50-450 ^{o}C. First step, the adsorbed and lattice water in precursor were evaporated at temperature range 50-195 ^{o}C. The second step is the decomposition of residual tartaric acid and tartate of lithium, nickel, cobalt and vanadium at 195-290 ^{o}C when compared the pure tartaric acid. The third is decomposition and combustion of residual starting materials and other organic compounds at 290-450 ^{o}C. After 450 ^{o}C, the weight loss of tartate precursor is almost constant. The total weight loss during the thermal analysis is 70 % by weight.

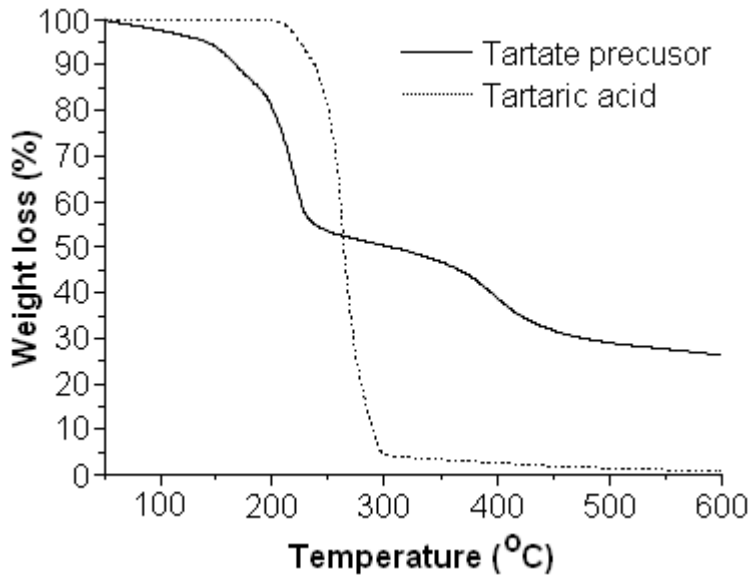


Fig. 2. TGA analysis of nanopowder at temperature range 50-600 ^{o}C in N_2 atmosphere

The XRD patterns of $LiNi_{0.5}Co_{0.5}VO_4$ at different calcination temperatures are showed in Figure 3 and are identical to the JCPDS standards of $LiNiVO_4$ (38-1395) and $LiCoVO_4$ (38-1396) [9]. No impurities such as NiO, CoO, and Co_3O_4 were detected.

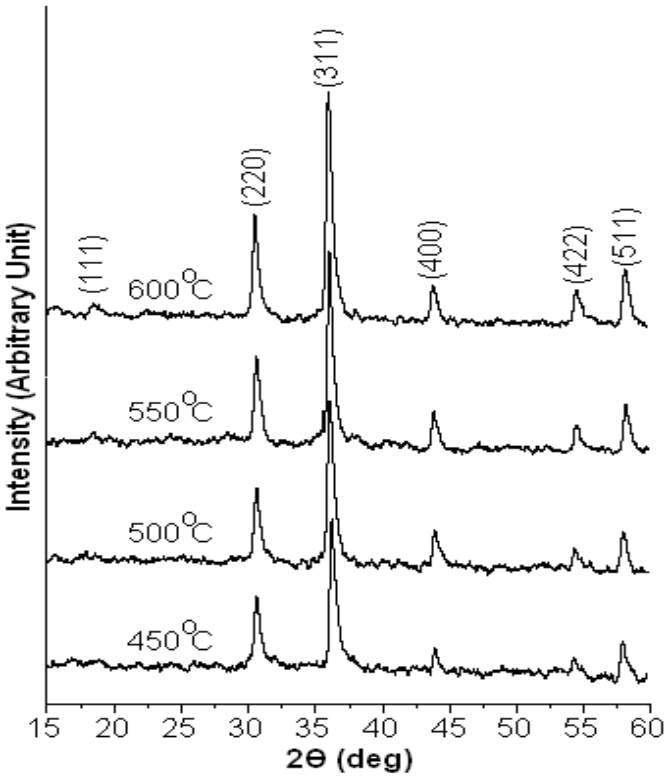


Fig. 3. The XRD patterns of $LiNi_{0.5}Co_{0.5}VO_4$ at difference calcinations temperatures

The diffraction peaks of product correspond to (111), (220), (311), (400), (422) and (511), respectively. They are dominated the (311) peak at 2θ = 36.10. The 2θ position of (311) plane of $LiNi_{0.5}Co_{0.5}VO_4$ is between the (311) peaks of $LiNiVO_4$ and $LiCoVO_4$. The XRD patterns displayed weak (111) and strong (220) peaks. It indicates the predominant inverse spinel structure. That presently, vanadium atoms are in the tetrahedrally coordinated 8a site leading to the higher (220) and lower (111) peaks and the metal ions (Li, Ni and Co atoms) are random in equally octahedron site. At calcination temperature 450–600 °C for 12 h, the spectra become sharper and the intensities are stronger. The degree of crystallinity increases with an increase in the calcination temperature. The degree of crystallinity for inverse spinel structure transition metal oxides cathode was determined from the intensity ratio $I_{(200)}/I_{(311)} = 0.5$. It found that the intensities ratio $I_{(220)}/I_{(311)}$ of $LiNi_{0.5}Co_{0.5}VO_4$ for calcination temperature at 600 ^oC for 12 h is 0.48 which showed high crystalline product[2]. The calcination temperature can play the role in improving crystal and grain size of the products. These correspond to the increase in XRD intensities with the increase in the calcinations temperature [1].

The lattice constant (a) of $LiNi_{0.5}Co_{0.5}VO_4$ was calculated from the relation between the plane spacing equation of cubic structure and Bragg's law as shown in Equation 1 [10].

(Eq. 1)

$$a=\frac{\lambda}{2\sin\theta}\sqrt{h^2+k^2+l^2}$$

Where, λ is the wavelength of Cu K_α , θ is the Bragg angle and hkl is Miller indices of lattice plane. At calcination temperature 600 ^oC for 12 h, it is 8.2436 Å. The lattice constant of $LiNi_{0.5}Co_{0.5}VO_4$ is between those of $LiNiVO_4$ and $LiCoVO_4$. It could be seen that nearly the cell constant of $LiNi_{0.5}Co_{0.5}VO_4$ (a = 8.2492 Å) when calculated form lattice constants of $LiNiVO_4$ and $LiCoVO_4$ [11].

For inverse spinel structure transition metal oxides as $LiNiVO_4$, $LiNi_{0.5}Co_{0.5}VO_4$ and $LiCoVO_4$ have F_{d3m} (O^7_h) symmetry of which five modes are Raman active ($A_{1g} + E_g + 3F_{2g}$) and four modes are inferred active ($4F_{1u}$) [12]. Raman spectra (Figure 4) was observed in the 700-850 cm^{-1} can be attributed to the stretching vibration of VO_4 tetrahedron. $LiNi_{0.5}Co_{0.5}VO_4$ has strong frequency band at 801.16 cm^{-1} corresponds to the stretching mode of VO_4 tetrahedron with an A_{1g} symmetry, whereas the band stretching at 314.90 cm^{-1} corresponds to the bending mode of VO_4 tetrahedron with an E_g symmetry. The two stretching frequencies band at 256.23 and 411.81 cm^{-1} are the vibration of LiO_6 octahedron. The stretching vibration of Li-O-M (M = Ni and Co) was detected at 470.22 cm^{-1}.

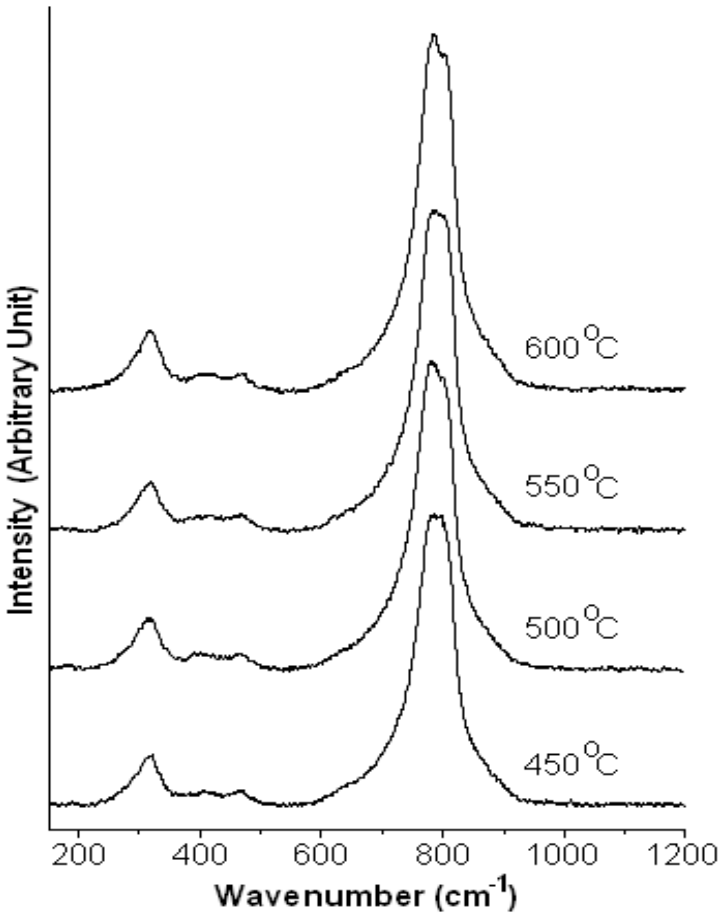


Fig.4. Raman spectra of nanopowder

FTIR spectra of $LiNi_{0.5}Co_{0.5}VO_4$ is showed in Figure 5. The asymmetric stretching vibration of VO_4 tetrahedron was showed the broad band at 810-850 cm^{-1} and weak band around 900 cm^{-1} assigned to be the symmetric stretching mode in the symmetric stretching mode of VO_4 tetrahedrons.

In addition, oxygen atom in the VO_4 tetrahedron can from bond with Li and Co or Ni atom which can lead to some asymmetry. Hence the broad band around 810-850 cm^{-1} are tentatively assigned to be the asymmetrical stretching mode in the distorted VO_4 unit [2, 6]. If can be considered that all Li atoms are accommodated in octahedron LiO_6 environments, then Raman- and IR-active modes are normally spit into (A+2B). LiO_6 octahedrons have vibrations in IR modes observed at 410 cm^{-1} corresponding to v (Li-O) [1,4].

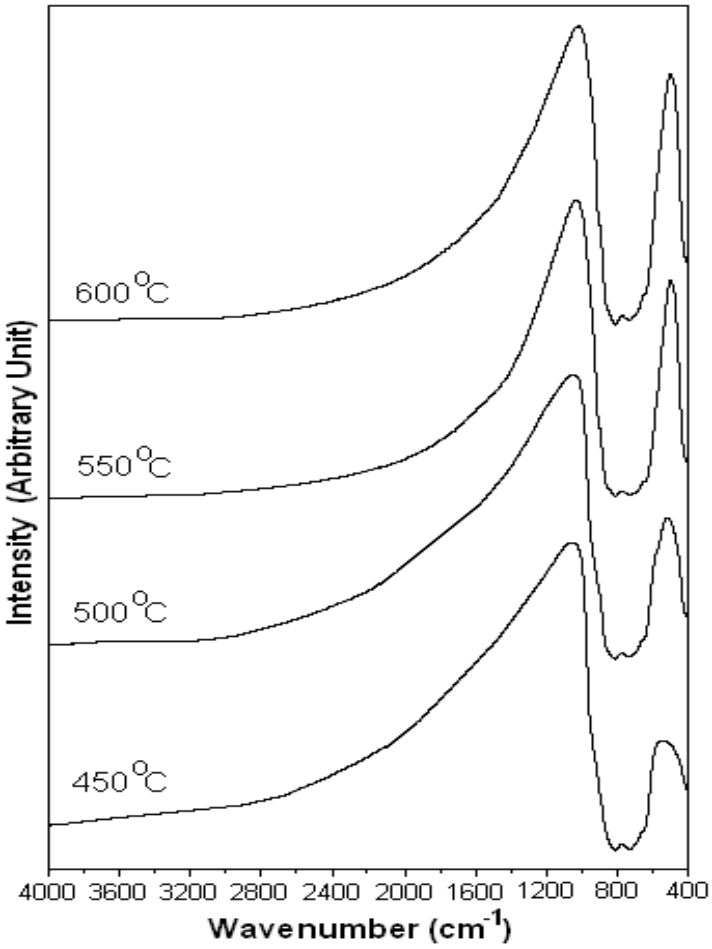


Fig. 5. FTIR spectra of $LiNi_{0.5}Co_{0.5}VO_4$

TEM images and SAED patterns of $LiNi_{0.50}Co_{0.50}VO_4$ with 450-600 °C calcination temperature for 12 h are shown in Figure 6. At 450 °C for 12 h, the grain size is 20-80 nm. When increased calcination temperature to 600°C, the grain size is 200-700 nm due to the effect of calcination temperature which corresponded the XRD patterns. Their SAED patterns show a. ring patterns which indicated that polycrystalline $LiNi_{0.50}Co_{0.50}VO_4$. The diffraction planes are (111), (220), (311), (400), (422), (511) and (533), respectively.

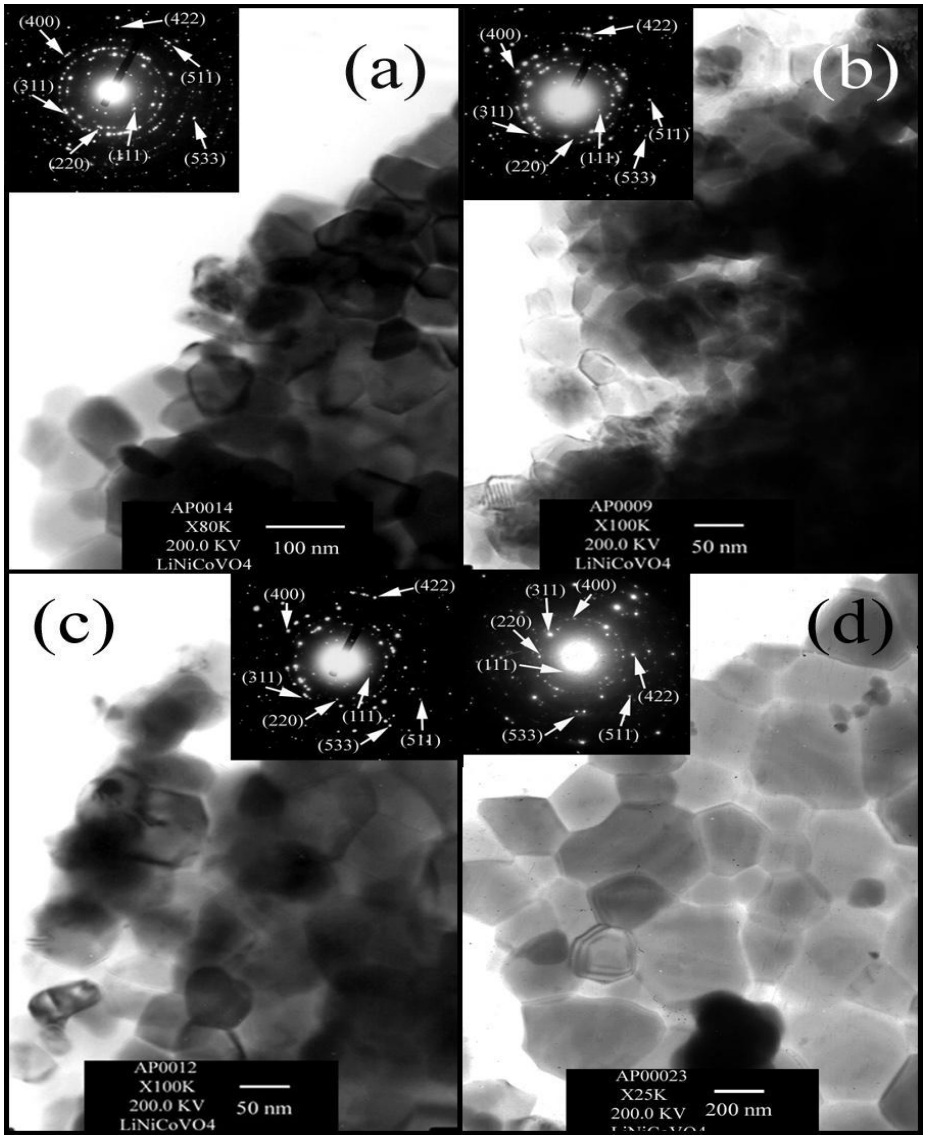


Fig. 6. TEM images and SAED patterns of $LiNi_{0.50}Co_{0.50}VO_4$ with 450-600 ^oC calcination temperature for 12 h

4. Conclusion

$LiNi_{0.5}Co_{0.5}VO_4$ was synthesized by tartate precursor combustion method. TGA show the weight loss tartate precursor at 50-450 ^oC in N_2 atmosphere. The phase and morphologies were studied by XRD, SAED and TEM. XRD pattern and TEM images show that the $LiNi_{0.5}Co_{0.5}VO_4$ started to form at 450 ^oC and its particle sizes is 20-80 nm which has relatively larger specific surface and more favorable for lithium-ion migration as the cathode materials. When increase temperature calcination, it lead to improve the crystalline and grain size of products.

Acknowledgements

We are grateful to the Thailand Research Fund, Bangkok for financially supporting the research, Graduate School of Chiang Mai University for general funding.

References

[1] Liu , J.R., Wang , M., Lin , X., Yin , D.C., Huang , W.D. (2002) . Citric acid complex method of preparing inverse spinel $LiNiVO_4$ cathode material for lithium batteries. *J. Power Source* , 108 ,113-116.

[2] Phuruangrat , A., Thongtem , T., Thongtem , S. (2007) . Preparation and characterization of nano-crystalline $LiCoVO_4$ and $LiNiVO_4$ used as cathodes for lithium ion batteries. *J. Ceram. Process. Res*, 8 ,450-452.

[3] Chu , P.P., Huang , D.L., Fey , G.T.K. (2000) . Solid-state 7Li NMR studies of inverse spinel $LiNi_xCo_{1-x}VO_4$ cathode materials. *J. Power Source*, 90 , 95-102.

[4] Vivekanandhan , S., Venkateswarlu , M., Satyanarayana , N. (2004) . Glycerol-assisted gel combustion synthesis of nano-crystalline $LiNiVO_4$ powders for secondary lithium batteries. *Mater. Lett*, 58 ,1218-1222.

[5] Chen , W., Mai , L.Q., Xu , Q., Zhu , Q.Y., Yang , H.P. (2003) . Novel soft solution synthesis and characterization of submicromic $LiCoVO_4$. *Mat. Sci. Eng. B*, 100, 221-224.

[6] Mai , L.Q., Chen , W., Xu , Q., Zhu , Q.Y., Han , C.H., Guo , W.L. (2003), Influence of surface modification on structure and electrochemical performance of $LiNi_{0.5}Co_{0.5}VO_4$. *Solid State Ionics*, 161, 205-208.

[7] Fey , G.T.K., Chen , K.S.(1999).Synthesis, characterization, and cell performance of $LiNiVO_4$ cathode materials prepared by a new solution precipitation method. *J. Power Source*, 81-82 ,467-471.

[8] Thongtem , T., Phuruangrat , A., Thongtem , S. (2006) . Analyses of nano-crystalline $LiCoVO_4$ prepared by solvothermal reaction. *Mater. Lett* , 60 , 3776-3781.

[9] Powder Diffract. File, JCPDS Internat. Centre for Diffract Data, U.S.A., (2001).

[10] Suryanrayana , C., Norton , M.G. X-ray Diffraction A Practical Approach, *Plenum Press*, New York .(1998). 97-236.

[11] Liu , Y., Xu , Y., Li , J.P., Zhang , B., Wu , D., Sun , Y.H. (2006) . Synthesis of CdS_xSe_{1-x} nanorods via a solvothermal route. *Mater. Res. Bull* , 41 , 99-109.

[12] Fey , G.T.K., Huang , L.D. (1999) . Synthesis, characterization and cell performance of inverse spinel electrode materials for lithium secondary batteries. *Electrochim. Acta* , 45 ,295-314.

Materials Science-Poland, *Vol. 28*, *No. 2*, *2010*

Synthesis of nanocrystalline metal molybdates using cyclic microwave radiation

A. PHURUANGRAT[1], T. THONGTEM[2*], S. THONGTEM[1]

[1]Department of Physics and Materials Science, Faculty of Science, Chiang Mai University, Chiang Mai 50200, Thailand

[2]Department of Chemistry, Faculty of Science, Chiang Mai University, Chiang Mai 50200, Thailand

Nanocrystalline compounds $MMoO_4$ (M = Ca, Sr and Ba) were synthesized in propylene glycol using cyclic microwave radiation. XRD, TEM, SAED and EDX analyses revealed the presence of nanocrystallites of the phases containing the corresponding alkaline earth metals, Mo and O. The calculated lattice parameters and the crystallite sizes both increased with the increase in the atomic masses and the ionic radii of the divalent metals. Six different vibrations were detected using Raman spectroscopy, and very strong Mo–O stretching mode of $[MoO_4]^{2-}$ tetrahedrons was observed using FTIR.

Keywords: *alkaline earth metal molybdate; cyclic microwave-assisted synthesis; scheelite structure*

1. Introduction

Nanomaterials have very unusual physical and chemical properties, different from their bulks [1, 2]. Metal molybdates $MMoO_4$ (M = Ca, Sr and Ba, ionic radii of divalent metals > 0.1 nm) with scheelite structure [3] are very suitable for use as luminescent materials, optical fibres, scintillators and catalysts [4, 5].

A variety of methods are used to synthesize nanosized metal molybdates such as hydrothermal processing [5], reverse microemulsion [6], reverse micelles with solvothermal method [7], the molten salt method [8] and solid state reactions [9]. Recently, the microwave-assisted route has been applied as a novel way to synthesize nanomaterials. The process requires a short reaction time. The products have a narrow particle size distribution and high purity compared with those synthesized by the conventional method [2]. Previously, metal molybdates were synthesized via a citrate complex route assisted by microwave radiation, followed by high temperature calcination [4]. For the present research, purified nanocrystalline $MMoO_4$ (M = Ca, Sr and Ba) were synthesized using cyclic microwave radiation without any further calcination at high temperatures.

*Corresponding author, e-mail: ttpthongtem@yahoo.com

2. Experimental

0.005 mol of each $M(NO_3)_2$ (M = Ca, Sr and Ba) and Na_2MoO_4 was separately dissolved in 15 cm^3 propylene glycol (PG). The corresponding solutions were mixed and stirred for 30 min. The mixtures were heated at 600 W cyclic microwave radiation. Every 100 s, the microwave was switched on for 15 s and switched off for 85 s. The cyclic process was terminated after 30 min had elapsed. Finally, white precipitates were produced. They were washed with distilled water and absolute ethanol, and dried in air at 80 °C for 24 h.

The final products were characterized using an X-ray diffractometer (D-500 Siemens) with CuK_α radiation, a graphite monochrome and Ni filter with 2θ scanning angle ranging from 15° to 60°, Fourier transform infrared spectrometer (Bruker Tensor 27) with the spectral resolution of 4 cm^{-1} with KBr as a diluting agent, Raman spectrometer (Horiba Jobin Yvon T64000) using 50 mW Ar laser (λ = 514.5 nm) with the spectral resolution of 5 cm^{-1}, and a transmission electron microscope (Jeol, Jem-2010) operating at 200 kV with an energy dispersive X-ray analyzer (Oxford Instruments, INCA).

3. Results and discussion

XRD spectra of $MMoO_4$ (M = Ca, Sr and Ba) are shown in Fig 1. The phases were identified by comparing their spectra with those of the JCPDS standard, PDF numbers: 85-0585 ($CaMoO_4$), 86-0586 ($SrMoO_4$) and 29-0193 ($BaMoO_4$) [10].

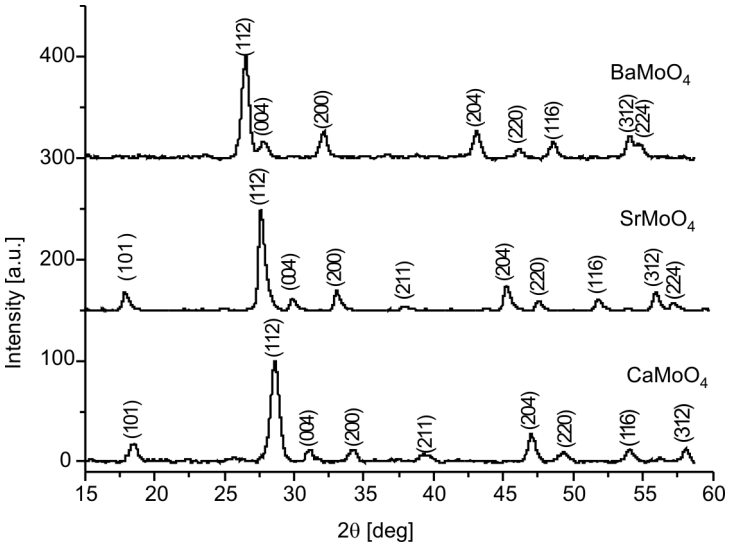


Fig. 1. XRD spectra of $CaMoO_4$, $SrMoO_4$ and $BaMoO_4$

No characteristic peaks of impurities were detected. The molybdates have tetragonal scheelite structure ($a = b \neq c$ and $\alpha = \beta = \gamma = 90°$) with $I4_1/a$ space group [6, 10]. Their lattice parameters were calculated from the equation of plane spacing for the tetragonal structure and Bragg's law for diffraction [11]. They are a = 0.5221 nm, c = 1.1417 nm for $CaMoO_4$, a = 0.5417 nm, c = 1.2004 nm for $SrMoO_4$, and a = 0.5610 nm, c = 1.2766 nm for $BaMoO_4$. The calculated parameters are very close to those of the JCPDS standard [10]. Increase in the lattice parameters was related to the atomic masses and ionic radii of alkaline earth metals (Ca^{2+} – 0.112 nm, Sr^{2+} – 0.125 nm, Ba^{2+} – 0.142 nm) [3], which imply the difference of charge densities in MO_8 polyhedral environment of the scheelite structure [12].

The crystallite sizes of $MMoO_4$ (M = Ca, Sr and Ba) were calculated from the (112) peaks of XRD spectra and by applying Scherrer's formula, $B = \lambda k/L\cos\theta$, where λ, θ, L, k and B are the wavelength of CuK_α radiation, the Bragg angle, the average crystallite size, a constant (0.89), and the full width at half maximum of (112) peak in radians, respectively [11]. The calculated crystallite sizes of $CaMoO_4$, $SrMoO_4$ and $BaMoO_4$ are 14.48, 15.83 and 18.00 nm, respectively. They all increased with the increase in the ionic radii and the atomic masses of the alkaline earth metals.

It is proposed that the most likely reaction occurring in the synthesis of the nanocrystalline molybdates via the cyclic microwave radiation process is:

$$M(NO_3)_2 + Na_2MoO_4 \rightarrow MMoO_4 + 2NaNO_3$$

PG and microwave radiation influence the fabrication of uniform nanosized particles, which can be explained as follows. PG has a high boiling point (187 °C) [13], thus the problem of overheating by microwave radiation can be overcome. At 25 °C, PG has a high permanent dipole moment (2.50 D) and a high electric permittivity (30.2) [14] which enables coupling with the electric field leading to the molecular vibration of PG. The solution may be rapidly heated to a high temperature and due to the microwave vibration (2.45 GHz) [15], nucleation and growth proceed in uniform environment. Finally, nanosized particles are synthesized.

Alkaline earth metal molybdates contain $[MoO_4]^{2-}$ tetrahedrons. 26 various vibrations in the lattice space ($3A_g + 5A_u + 5B_g + 3B_u + 5E_g + 5E_u$) were determined by the group theory calculations [3,16]. $3A_g$, $5B_g$ and $5E_g$ vibrations are Raman active. Only $4A_u$ and $4E_u$ of the $5A_u$ and $5E_u$ vibrations are infrared active, and the remaining ones ($1A_u$ and $1E_u$) are acoustic vibrations. $3B_u$ vibrations are silent modes [3, 17]. Raman spectra (Fig. 2) show six vibrations at 875, 845, 792, 392, 322 and 204 cm^{-1} for $CaMoO_4$, 883, 842, 794, 368, 327 and 181 cm^{-1} for $SrMoO_4$, and 887, 834, 788, 359, 327 and 192 cm^{-1} for $BaMoO_4$. They correspond to $\nu_1(A_g)$, $\nu_3(B_g)$, $\nu_3(E_g)$, $\nu_4(B_g)$, $\nu_2(A_g)$ and $\nu_{\text{free rotation}}(A_g)$ modes, respectively [18].

FTIR spectra of the molybdates are shown in Fig 3. For T_d symmetry, $\nu_3(F_2)$ and $\nu_4(F_2)$ modes are infrared active. They correspond to stretching and bending modes, respectively [19, 20]. Very strong Mo–O stretching vibration in $[MoO_4]^{2-}$ tetrahedrons was detected at 783–955 cm^{-1} and weak Mo–O bending vibration was evident at 422 cm^{-1}.

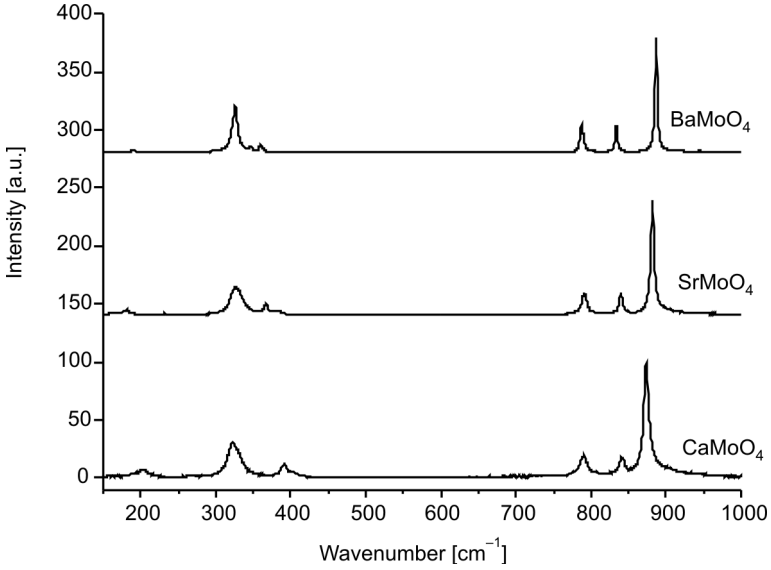


Fig. 2. Raman spectra of $CaMoO_4$, $SrMoO_4$ and $BaMoO_4$

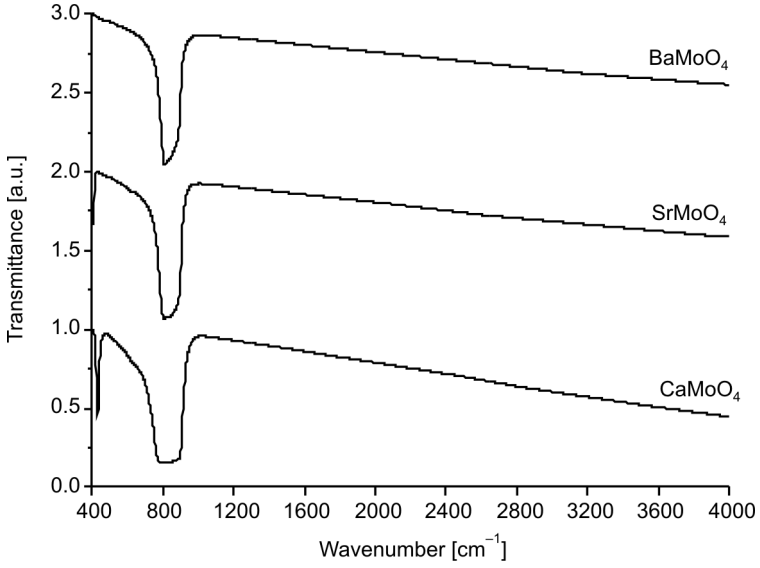


Fig. 3. FTIR spectra of $CaMoO_4$, $SrMoO_4$ and $BaMoO_4$

TEM images and SAED patterns of metal molybdates are shown in Fig 4. The products were composed of a number of round nanosized particles. Their average sizes were estimated from 500 particles seen on TEM images. Their distribution curves (Fig. 5) are narrow. The particle sizes are 20 ± 5 nm for $CaMoO_4$, 21 ± 5 nm for $SrMoO_4$, and 22 ± 5 nm for $BaMoO_4$.

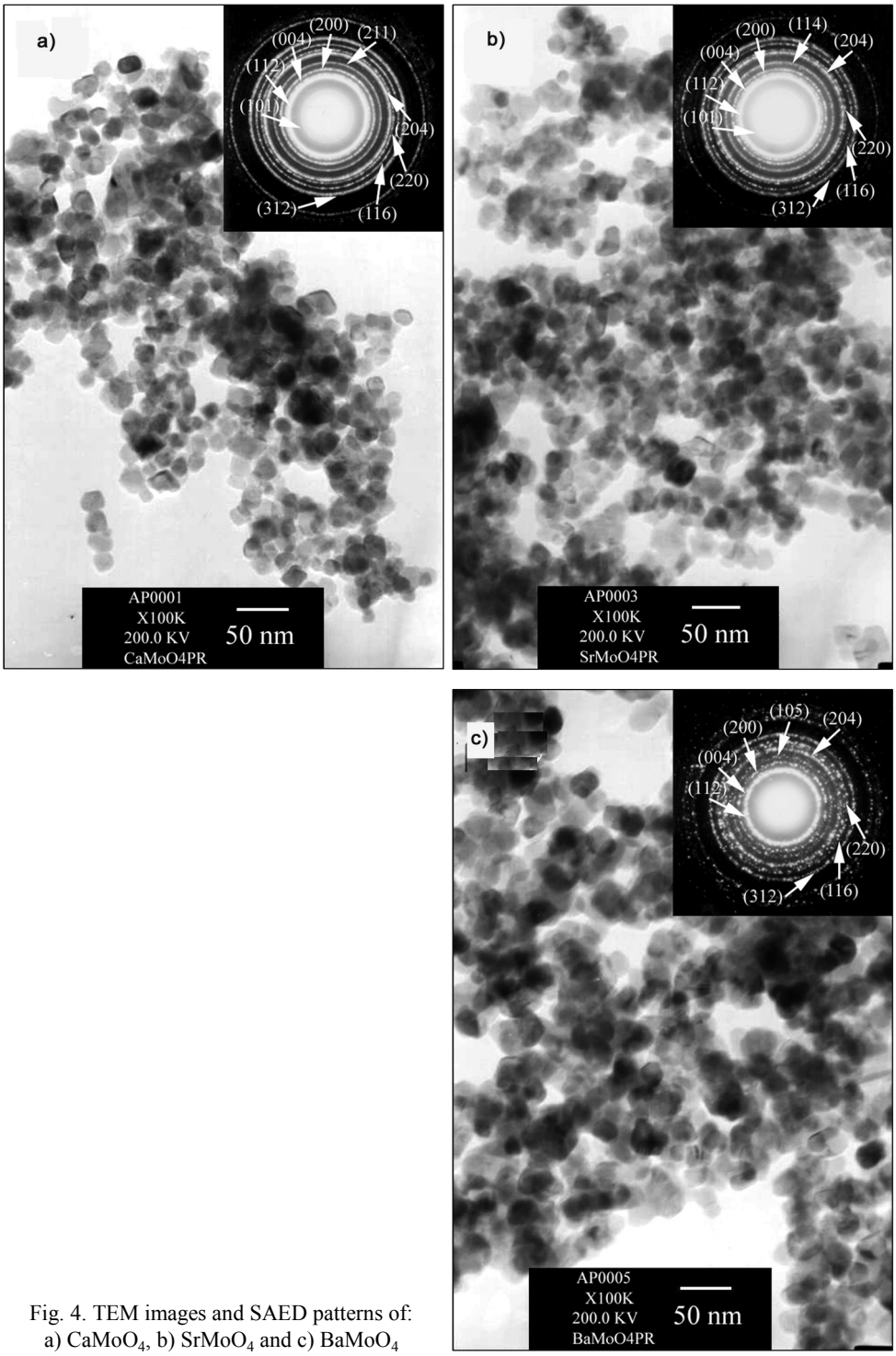


Fig. 4. TEM images and SAED patterns of: a) $CaMoO_4$, b) $SrMoO_4$ and c) $BaMoO_4$

Narrow particle size distributions and homogeneous particles favour good luminescent properties [21]. The products contain less contaminations, or fewer dead layers on the phosphor surface [21]. SAED patterns show a number of bright spots: the brightness of some of them is continuous, whereas for others they are at random. The spots are so close that they form fully concentric rings. These indicate that the molybdates consist of nanosized polycrystals with different orientations. Interplanar spaces were calculated from the diameters of the rings [22, 23], and compared with those of the JCPDS standard [10]. Crystallographic planes were indexed on the patterns. The products are specified as $MMoO_4$ (M = Ca, Sr and Ba).

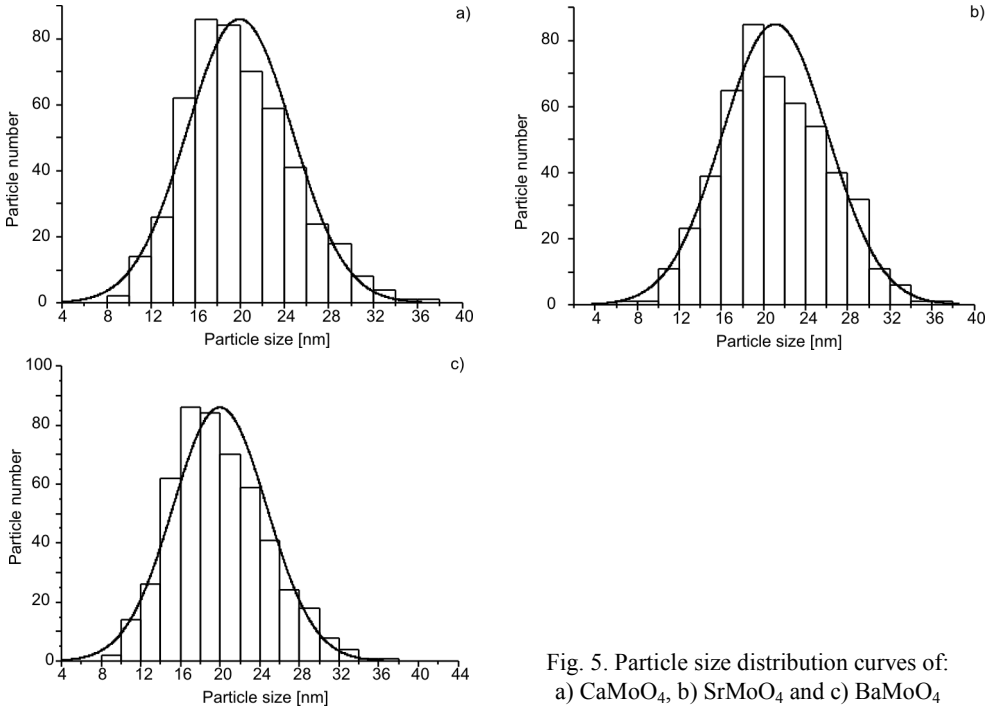


Fig. 5. Particle size distribution curves of: a) $CaMoO_4$, b) $SrMoO_4$ and c) $BaMoO_4$

EDX analyses of $CaMoO_4$, $SrMoO_4$ and $BaMoO_4$ (results not shown) revealed Ca peaks at 3.69 keV (K_α) and 4.01 keV (K_β), Sr peaks at 1.81 keV (L_α), 14.14 keV (K_α) and 15.84 keV (K_β), and Ba peaks at 4.47 keV (L_α), 4.83 keV ($L_{\beta1}$), and 5.16 keV ($L_{\beta2}$). O peaks of the three molybdates were detected at 0.53 keV (K_α), and Mo peaks were detected at 2.29 keV (L_α), 17.45 keV (K_α) and 19.61 keV (K_β) [24]. Elemental analysis shows that the M:Mo:O atomic ratios are very close to those of the corresponding stoichiometric molybdates. Cu of copper grids and C layers were also detected.

4. Conclusions

Nanocrystalline compounds $MMoO_4$ (M = Ca, Sr and Ba) were successfully synthesized from $M(NO_3)_2$ and Na_2MoO_4 in propylene glycol, by applying cyclic micro-

wave radiation. XRD, SAED and EDX analyses revealed the presence of nanocrystalline $MMoO_4$ containing the corresponding alkaline earth metals, Mo and O. The products were composed of a number of round nanosized particles, according to TEM analysis. Their size distributions are very narrow. Six vibrations were detected using Raman spectroscopy. FTIR data revealed very strong Mo–O stretching vibrations in $[MoO_4]^{2-}$ tetrahedrons, which were detected in the 783–955 cm^{-1} range. FTIR data also confirmed weak Mo–O bending at 422 cm^{-1}.

Acknowledgements

The authors are extremely grateful to the Thailand Research Fund and the National Research Council of Thailand for supporting the research, and the Graduate School of Chiang Mai University for general funding.

References

[1] ZHAO Y., LIAO X.H., HONG J.M., ZHU J.J., Mater. Chem. Phys., 87 (2004), 149.
[2] LIAO X.H., CHEN N.Y., XU S., YANG S.B., ZHU J.J., J. Cryst. Growth, 252 (2003), 593.
[3] BASIEV T.T., SOBOL A.A., VORONKO Y.K., ZVEREV P.G., Opt. Mater., 15 (2000), 205.
[4] RYU J.H., YOON J.W., SHIM K.B., J. Alloy. Comp., 413 (2006), 144.
[5] ZHANG Y., YANG F., YANG J., TANG Y., YUAN P., Solid State Commun., 133 (2005), 759.
[6] LI Z., DU J., ZHANG J., MU T., GAO Y., HAN B., CHEN J., CHEN J., Mater. Lett., 59 (2005), 64.
[7] ZHANG C., SHEN E., WANG E., KANG Z., GAO L., HU C., XU L., Mater. Chem. Phys., 96 (2006), 240.
[8] WANG Y., MA J., TAO J., ZHU X., ZHOU J., ZHAO Z., XIE L., TIAN H., Ceram. Int., 33 (2007), 693.
[9] PARHI P., SINGH S.S., RAY A.R., RAMANAN A., Bull. Mater. Sci., 29 (2006), 115.
[10] Powder Diffract. File, JCPDS Int. Centre Diffr. Data, U.S.A. (2001).
[11] SURYANARAYANA C., NORTON M.G., *X-ray Diffraction. A Practical Approach*, Plenum Press, New York, (1998).
[12] ERRANDONEA D., PELLICER-PORRES J., MANJON F.J., SEGURA A., FERRER-ROCA CH., KUMAR R.S., TSCHAUNER O., RODRÍGUEZ-HERNÁNDEZ P., LÓPEZ-SOLANO J., RADESCU S., MUJICA A., MUÑOZ A., AQUILANTI G., Phys. Rev. B, 72 (2005), 174106.
[13] ANDREESCU D., MATIJEVIĆ E., GOIA D.V., Colloid. Surf. A, 291 (2006), 93.
[14] SENGWA R.J., J. Mol. Liq., 108 (2003), 47.
[15] CHEN D., TANG K., SHEN G., SHENG J., FANG Z., LIU X., ZHENG H., QIAN Y., Mater. Chem. Phys., 82 (2003), 206.
[16] PORTO S.P.S., SCOTT J.F., Phys. Rev. 157 (1967), 716.
[17] GOLUBOVIĆ A., GAJIĆ R., DOHČEVIĆ-MITROVIĆ Z., NIKOLIĆ S., J. Alloys Comp., 415 (2006), 16.
[18] CHEN D., TANG K., LI F., ZHENG H., Cryst. Growth Design, 6 (2006), 247.
[19] DE AZEVEDO MARQUES A.P., DE MELO D.M.A., PASKOCIMAS C.A., PIZANI P.S., JOYA M.R., LEITE E.R., LONGO E., J. Solid State Chem., 179 (2006), 671.
[20] CLARK G.M., DOYLE W.P., Spectrochim. Acta, 22 (1966), 1441.
[21] RYU J.H., YOON J.W., LIM C.S., OH W.C., SHIM K.B., J. Alloy. Comp., 390 (2005), 245.
[22] THONGTEM T., PHURUANGRAT A., THONGTEM S., J. Mater. Sci., 42 (2007), 9316.
[23] THONGTEM T., KAOWPHONG S.AND THONGTEM S., J. Mater. Sci., 42 (2007), 3923.
[24] *X-ray Absorption and Emission Energy*, Oxford Instrum. Analyt., Halifax Rd., High Wycombe Bucks HP12 3SE, U.K.

Received 7 October 2007
Revised 2 December 2007

Journal of Alloys and Compounds 500 (2010) 195–199

Contents lists available at ScienceDirect

Journal of Alloys and Compounds

journal homepage: www.elsevier.com/locate/jallcom

Microwave-assisted hydrothermal synthesis of Bi_2S_3 nanorods in flower-shaped bundles

Titipun Thongtem[a,*], Chalermchai Pilapong[a], Jutarat Kavinchan[a], Anukorn Phuruangrat[b,*], Somchai Thongtem[b]

[a] Department of Chemistry, Faculty of Science, Chiang Mai University, Chiang Mai 50200, Thailand
[b] Department of Physics and Materials Science, Faculty of Science, Chiang Mai University, Chiang Mai 50200, Thailand

ARTICLE INFO

Article history:
Received 18 January 2010
Received in revised form 22 March 2010
Accepted 31 March 2010
Available online 8 April 2010

Keywords:
Semiconductors
Chemical synthesis
Luminescence
Scanning electron microscopy
Transmission electron microscopy
X-ray diffraction

ABSTRACT

Bi_2S_3 nanorods in flower-shaped bundles were successfully synthesized from the decomposition of Bi–thiourea complexes under the microwave-assisted hydrothermal process. X-ray powder diffraction (XRD) patterns and field emission scanning electron microscopy (FE-SEM) show that Bi_2S_3 has the orthorhombic phase and appears as nanorods in flower-shaped bundles. A transmission electron microscopic (TEM) study reveals the independent single Bi_2S_3 nanorods with their growth along the [0 0 1] direction. A possible formation mechanism of Bi_2S_3 nanorods in flower-shaped bundles is also proposed and discussed. Their UV–vis spectrum shows the absorbance at 596 nm, with its direct energy band gap of 1.82 eV.

© 2010 Elsevier B.V. All rights reserved.

1. Introduction

In recent years, the fabrication of nanomaterials and nanodevices has been widely and deeply researched due to the novel properties comparing to their normal counterparts, and strong dependence on their characteristics such as shape, size and crystallinity [1,2]. Among them, one-dimensional (1D) nanostructures possess unique physical, chemical, and electron-transport properties, different from those of bulky and isotropic materials [2–4].

Binary metal chalcogenides of $A_2^{V}X_3^{VI}$ (A = As, Sb, Bi; X = S, Se, Te) semiconductors have a number of applications including photoconducting targets of television cameras, electronic and optoelectronic devices, thermoelectric devices, and infrared (IR) spectroscopy [2,4–6]. Bismuth sulfide (Bi_2S_3) has a 1.3 eV direct band gap, and is suitable for application in photovoltaic materials, photodiode arrays, sensors and IR spectroscopy photovoltaic converters, thermoelectric cooling technologies based on the Peltier effect [2,3,5,7–10]. The convention hydrothermal (CH) method has been widely used to synthesize the Bi_2S_3 nanomaterials [1–7]. It was able to control the morphologies: nanorods, nanowires, agglomerated particles and urchinlike [1–8].

Herein, an economical method to synthesize Bi_2S_3 nanorods in flower-shaped bundles by microwave-assisted hydrothermal (MH) method is reported. This method is simple, fast and inexpensive, as compared to the convention hydrothermal (CH) one.

2. Experimental procedure

The analytical grade chemicals: bismuth nitrate pentahydrate ($Bi(NO_3)_3{\cdot}5H_2O$), thiourea (NH_2CSNH_2) and polyvinylpyrrolidone (PVP) were used without further purification. To synthesize Bi_2S_3 flower-like structure, 0.005 mole $Bi(NO_3)_3{\cdot}5H_2O$ and 0.001 mole NH_2CSNH_2 were dissolved in 60 ml distilled water, and followed by 0.5 ml 37% HNO_3 and 0.5 g PVP adding, respectively. The mixture was stirred for 30 min at room temperature and put into a 100 ml Teflon-lined autoclave, which was tightly closed, heated up to 200 °C by a 300 W microwave radiation, held at this temperature for 1 h, and then naturally cooled to room temperature. After the microwave-assisted hydrothermal process, the product was filtered, washed with distilled water and absolute ethanol for several times, and dried at 80 °C for 24 h. This process was also repeated by using the convention hydrothermal method, heated by an electric oven, at 200 °C for 24 h.

The products were analyzed using an X-ray diffractometer (D8 Advance, Bruker Ltd., Germany) with Cu Kα radiation in the 2θ range from 5° to 80°. The Raman spectra was recorded on HORIBA JOBIN YVON T64000 Raman spectrometer using 50 mW Ar Laser with $\lambda = 514.5$ nm. The morphology of the product was characterized by a JSM-6335F scanning electron microscope (SEM, JEOL Ltd., Japan) and JEM-2010 transmission electron microscope (TEM, JEOL Ltd., Japan). The room temperature UV–vis spectrum was collected on a UV/VIS spectrometer PerkinElmer LAMBDA 40 at wavelength range of 200–1300 nm with the scanning rate of 0.5 nm s^{-1}.

* Corresponding authors. Tel.: +66 53 943344; fax: +66 53 892277.
E-mail addresses: ttpthongtem@yahoo.com (T. Thongtem), phuruangrat@hotmail.com (A. Phuruangrat).

0925-8388/$ – see front matter © 2010 Elsevier B.V. All rights reserved.
doi:10.1016/j.jallcom.2010.03.240

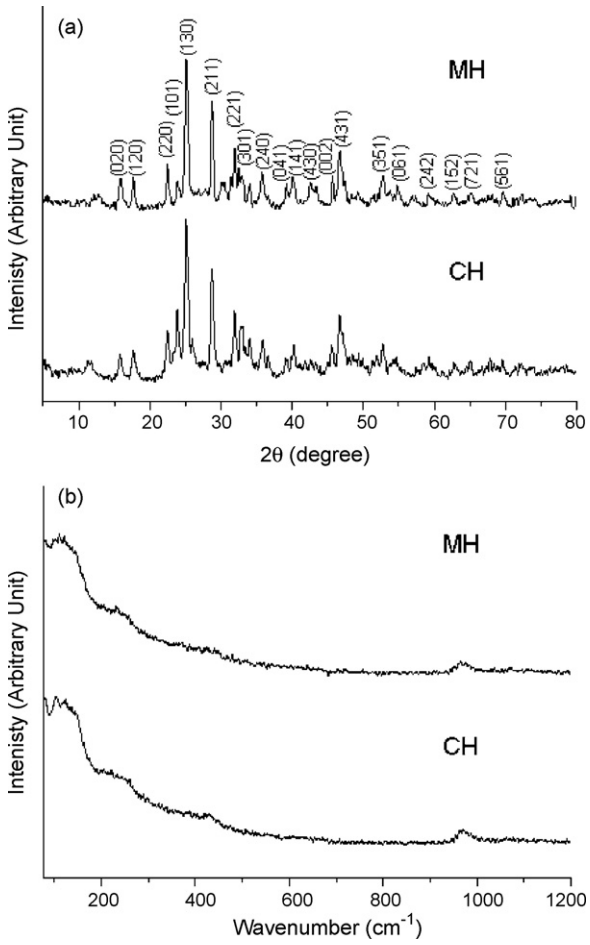


Fig. 1. (a) XRD patterns and (b) Raman spectra of Bi_2S_3 synthesized by the conventional hydrothermal and microwave-assisted hydrothermal methods.

3. Results and discussion

Fig. 1a shows the XRD patterns of the products synthesized by the MH and CH methods. All diffraction peaks match very well with the Bi_2S_3 JCPDS no. 17-0320 [11] with no detection of any impurities. The XRD intensity synthesized by the MH is higher than that synthesized by the CH. It implies that Bi_2S_3 synthesized by the first is better crystalline than Bi_2S_3 synthesized by the second. All the diffraction peaks of the Bi_2S_3 nanorods in flower-shaped bundles were shifted towards the lower angles, as compared to the JCPDS database, caused by an increase in their interplanar spaces. This may be attributed to the existence of the stress in the lattice of Bi_2S_3 nanorods in flower-shaped bundles. EDX spectrum of Bi_2S_3 produced by the MH method (un-shown result) detected only Bi and S peaks, in accordance with its constituents. Quantitative EDX analysis showed that the atomic ratio of Bi:S is 38:62, very close to the composition of Bi_2S_3. A definite existence of Bi_2S_3 was analyzed using a Raman spectrometer as shown in Fig. 1b. The spectra show four vibration modes, at 139.6, 253.7, 310.0 and 968.9 cm^{-1}. The first is in accordance with the 139.4 cm^{-1} mode of Bi_2S_3 nanorods, specified as the surface phonon vibration [12]. The second corresponds with the vibration mode of Bi_2S_3 nanorods at 252.0 and 259 cm^{-1} [12,13] and Bi_2S_3 nanoribbons and hierarchical nanostructures at 250 cm^{-1}, specified as the vibration mode of Bi–S bonds [14,15]. The detections of the third and fourth were in accordance with those of Bi_2S_3 nanorods at 312 and 975 cm^{-1} [13]. In the FTIR spectrum of PVP, it shows the wave numbers at 3450, 2930, 1675, 1420 and 1290 cm^{-1} – assigned to be the OH stretching vibration, CH_2 unsymmetrical stretching vibration, CO stretching vibration, CH_2 bending vibration and CN stretching vibration, respectively [16,17]. There was no detection of these impurity peaks in the FTIR spectrum of Bi_2S_3 (un-shown result), which implied that the product was pure phase.

SEM images of Bi_2S_3, prepared by the MH and CH methods, are given in Fig. 2. Only Bi_2S_3 irregular crystalline (Fig. 2a) with the average size of 1.5 μm was synthesized by the CH process. These nanorods agglomerate together to form clusters, and are not separate as independent nanorod bundles. Comparing to the synthesis of large-scale single-crystalline Bi_2S_3 nanowires by a simple one-step hydrothermal reaction of $Bi(NO_3)_3{\cdot}5H_2O$ and $Na_2S_2O_3$ at 180 °C for 2 days, the product contained a large quantity of nanowires with their lengths of hundreds of nanometers to a few microns range [18]. When microwave radiation was used as the heating source, the clearly independent Bi_2S_3 nanorods in flower-shaped bundles were detected. The use of microwave radiation as heating source shows the formation of uniform and perfect Bi_2S_3 flower-like bundles with the approximate diameter of 3–4 μm including the approximate length of the nanorods of 1–2 μm. The anisotropic growth of the Bi_2S_3 crystallites was further confirmed by the TEM analysis.

Fig. 3 shows TEM images of Bi_2S_3 nanorods in flower-shaped bundles synthesized by the MH method. The Bi_2S_3 flowers of Fig. 3a and b are composed of more than a hundred of individual Bi_2S_3 nanorods grow from the Bi_2S_3 cores. It is obvious that the morphology of Bi_2S_3 nanorods in flower-shaped bundles with 3–5.5 μm in size is in accordance with the SEM image (Fig. 2b) shown above. Fig. 3c shows the broken Bi_2S_3 nanorods form the Bi_2S_3 flower-like cores. The length of the individual nanorod of Bi_2S_3 is approximately 500–1500 nm. The growth direction of Bi_2S_3 nanorods in flower-shaped bundles was studied using high resolution trans-

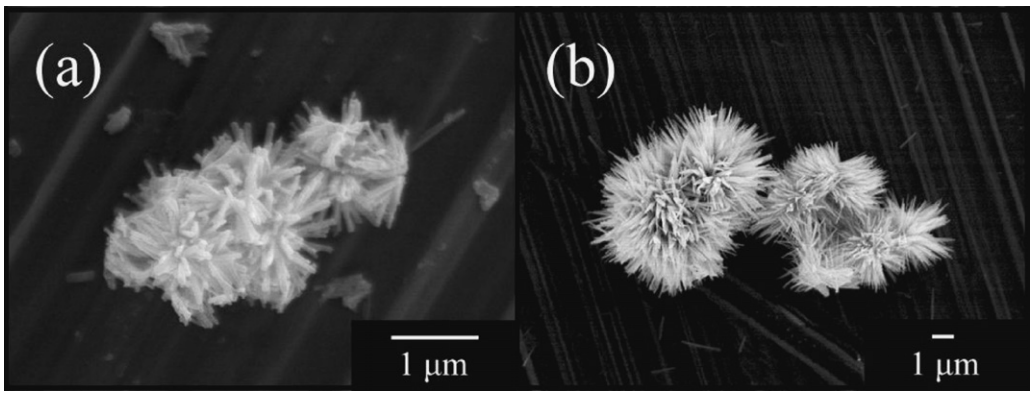


Fig. 2. SEM images of Bi_2S_3 nanorods in bundles synthesized by the (a) conventional hydrothermal and (b) microwave-assisted hydrothermal methods.

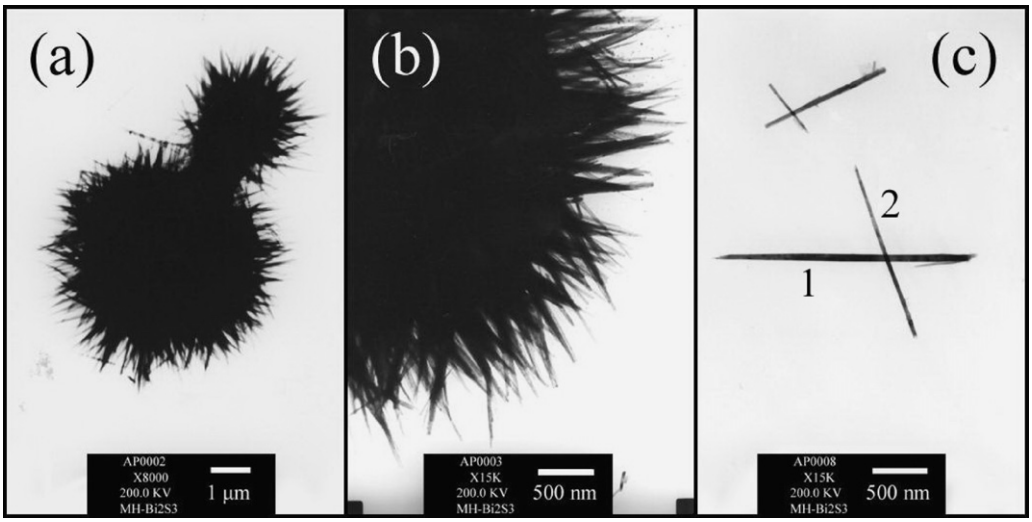


Fig. 3. TEM images of Bi_2S_3 nanorods in flower-shaped bundles synthesized by the MH method at (a) low and (b) high magnifications. (c) The broken nanorods from the flower-like cores.

mission electron microscopy (HRTEM) and selected area electron diffraction (SAED). They were characterized on areas 1 and 2 of TEM image (Fig. 3c). HRTEM images of Fig. 4a and c show lattice fringes of crystallographic planes with 3.96 Å space in parallel with the nanorods, corresponding to the (2 2 0) planes of orthorhombic Bi_2S_3 phase. The HRTEM images demonstrate that the Bi_2S_3 nanorods synthesized by the MH and CH methods grow along the [0 0 1] direction – in accordance with the growth direction of Bi_2S_3 nanorods and nanowires characterized by other researchers [1,3,19]. Both SAED patterns in areas 1 and 2 appear as bright spots composing electron diffraction patterns (Fig. 4b and d), revealing that individual Bi_2S_3 nanorods broken from flower-like cores are single crystal Bi_2S_3 with high degree of crystallinity. The SAED patterns can be indexed as the orthorhombic phase of Bi_2S_3 (JCPDS

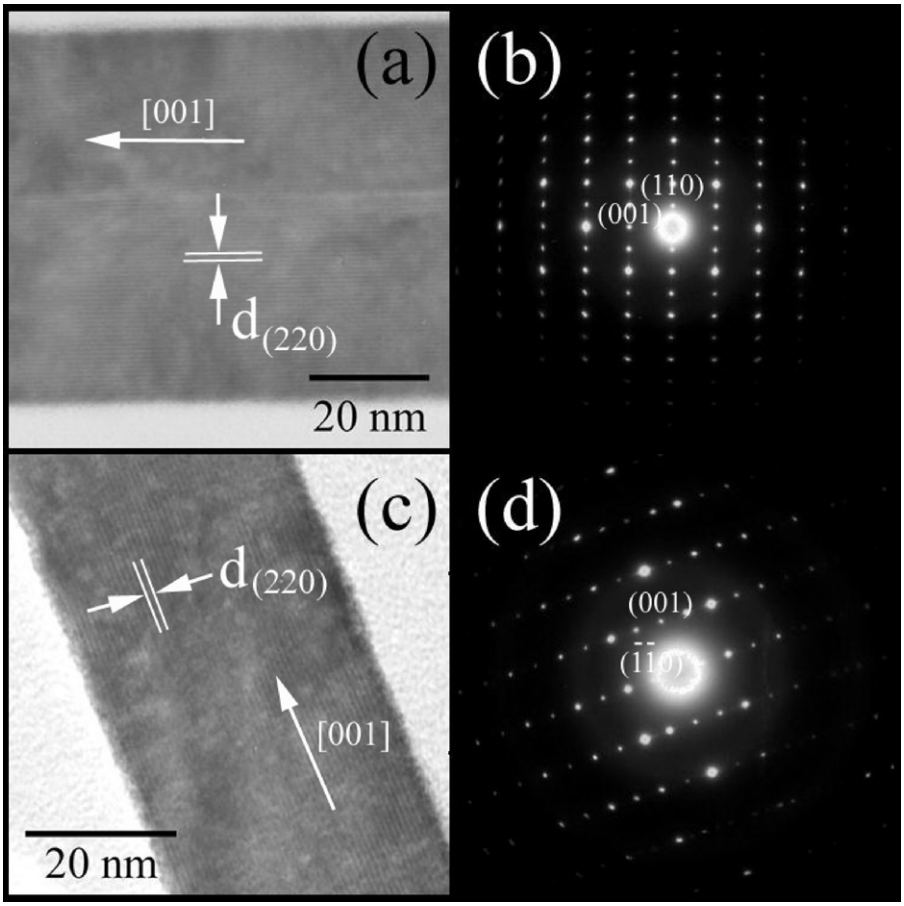


Fig. 4. HRTEM images and SAED patterns of Bi_2S_3 nanorods in bundles synthesized by the (a and b) conventional hydrothermal, and (c and d) microwave-assisted hydrothermal methods.

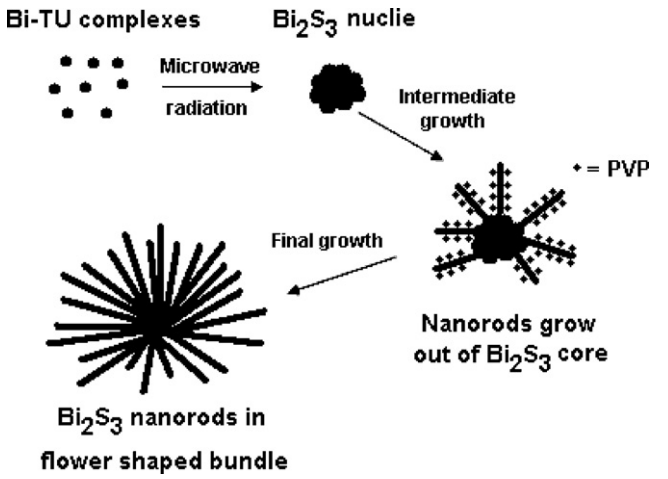


Fig. 5. Schematic illustration for the formation mechanism of Bi_2S_3 nanorods in flower-shaped bundles.

no. 17-0320) with the same [$\bar{1}$ 1 0] zone axes, which further confirm that the structure of the nanorods is orthorhombic phase, in accordance with the XRD analysis.

The formation mechanism of Bi_2S_3 nanorods in flower-shaped bundles is schematically shown in Fig. 5. First, the strong complex action between Bi^{3+} and thiourea (TU) leads to the formation of Bi–TU complexes [9]. For NH_2CSNH_2 compound, it has pair electrons on nitrogen and sulfur atoms, which have the great coordinating ability with inorganic metal cations, such as Cd^{2+}, Cu^{2+} and Pb^{2+} to form the metal–thiourea complexes [20]. Under microwave-assisted hydrothermal process, the Bi–TU complexes decomposed and formed the Bi_2S_3 nuclei. Then the Bi_2S_3 nanorods grew on the surface of Bi_2S_3 nuclei to form Bi_2S_3 nanorods in flower-shaped bundles. The formation reactions may be described as follows.

$$Bi^{3+} + TU \rightarrow \text{Bi–TU complexes} \quad (1)$$

$$\text{Bi–TU complexes} \rightarrow Bi_2S_3 \quad (2)$$

The growth process of Bi_2S_3 nanorods in flower-shaped bundles contains mainly two stages – the nucleation and crystal growth. For the present research, $Bi(NO_3)_3$ reacts with TU to form Bi–TU complexes at the initial stage. At the intermediate stage, the Bi–TU complexes decomposed to produce Bi_2S_3 nuclei by the microwave-assisted hydrothermal process. At this stage, PVP adsorbed on Bi_2S_3 nuclei – leading to the Bi_2S_3 nucleation as seeds which act as initial nuclei for particle growth. When the particles reach the critical dimension, PVP absorbed on the small particles by the side linked Bi_2S_3 units forming infinite chains parallel to the *c*-axis acting as a template for the formation of Bi_2S_3 nanorods in flower-shaped bundles. The final stage is the Bi_2S_3 nanorods in flower-shaped bundles, obtained by a novel microwave hydrothermal method, - homogeneous in size and form much similar to a flower with thorns found in nature [9,10,21]. In general, the growth of 1D Bi_2S_3 nanomaterials is a preferential growth direction along the *c*-axis due to the difference bonding in Bi_2S_3 structure. Bi_2S_3 is a lamellar structure with linked Bi_2S_3 units forming infinite chains parallel to the *c*-axis. The stronger covalent bond between the planes perpendicular to the *c*-axis supports higher growth rate along the *c*-axis. The much weaker van der Waals bonding between the planes perpendicular to the *a*-axis limits the growth of the fibers in the horizontal direction and supports their cleavage to form one-dimensional nanostructure [22].

The optical property of the product was investigated by UV–vis spectroscopy. Fig. 6 presents the UV–vis absorbance spectrum, and $(\alpha h\nu)^2$ vs. $h\nu$ curve of Bi_2S_3 nanorods in flower-shaped bundles synthesized by the MH method. The UV–vis spectrum showed the blue shifted absorption at 596 nm as compared to the 953 nm absorption for bulk Bi_2S_3 [23]. It can be attributed to the excitonic absorbance due to the quantum confinement at low dimension compared to its bulk counterparts [23]. The direct band gap of the product was calculated from its optical absorption spectrum by plotting $(\alpha h\nu)^2$ vs. $h\nu$ curve where α is the absorbance, h the Planck constant and ν the frequency [24] is shown in Fig. 6b. The direct band gap (E_g) of the Bi_2S_3 semiconducting nanorods in flower-shaped bundles was determined to be at 1.82 eV. This value is in good agreement with the 1.85 eV band gap of Bi_2S_3 nanowires [22], and 1.8 eV band gap of Bi_2S_3 thin films [24].

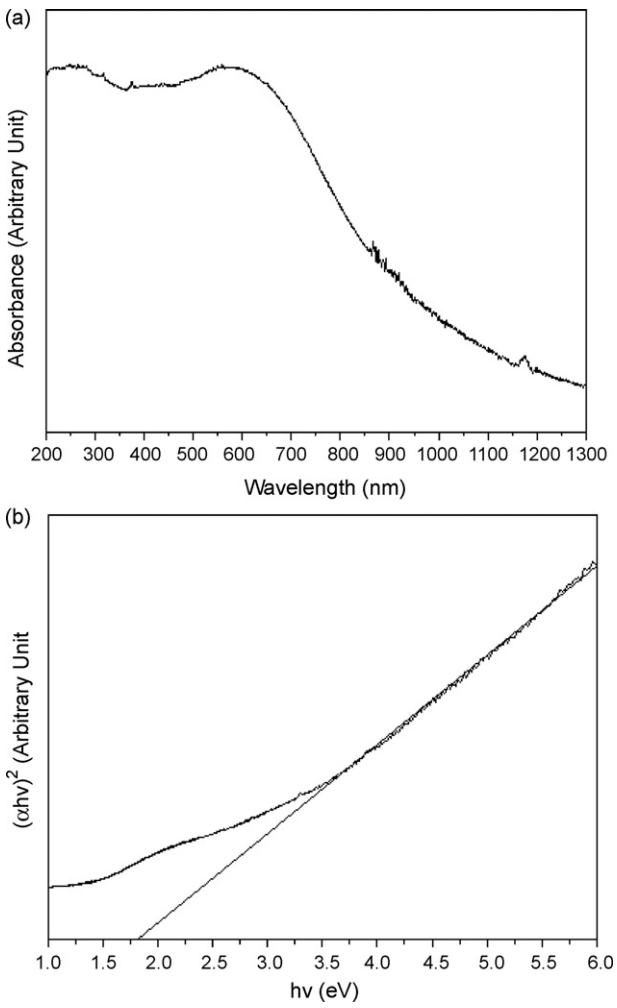


Fig. 6. (a) UV–vis absorbance, and (b) $(\alpha h\nu)^2$ vs. $h\nu$ curve of Bi_2S_3 nanorods in flower-shaped bundles synthesized by the microwave-assisted hydrothermal method.

4. Conclusions

Microwave-assisted hydrothermal reaction has emerged as an alternative route of fine powder synthesis. It was demonstrated that this simple method can be used to synthesize Bi_2S_3 nanostructure. XRD, SEM and TEM analyses proved that the product is orthorhombic Bi_2S_3 nanorods in flower-shaped bundles with the size of 3–5.5 μm. The microwave-assisted hydrothermal process for the synthesis of nanomaterials is shown to be very effective, inexpensive, short reaction time and environmentally benign. The direct energy band gap of the product was determined to be 1.82 eV – in agreement with those of other researchers.

Acknowledgements

This research was supported by the National Nanotechnology Center (NANOTEC), a member of National Science and Technology Development Agency (NSTDA), Ministry of Science and Technology, and the Thailand Research Fund, Bangkok, Thailand.

References

[1] Z.J. Zhang, X.Y. Chen, J. Phys. Chem. Solids 70 (2009) 1121–1131.
[2] L. Tian, H.Y. Tan, J.J. Vittal, Cryst. Growth Des. 8 (2008) 734–738.
[3] C.J. Tang, G.Z. Wang, H.Q. Wang, Y.X. Zhang, G.H. Li, Mater. Lett. 62 (2008) 3663–3665.
[4] Q. Han, J. Chen, X. Yang, L. Lu, X. Wang, J. Phys. Chem. C 111 (2007) 14072–14077.
[5] J. Lu, Q. Han, X. Yang, L. Lu, X. Wang, Mater. Lett. 61 (2007) 3425–3428.
[6] G. Xie, Z.P. Qiao, M.H. Zeng, X.M. Chen, S.L. Gao, Cryst. Growth Des. 4 (2004) 513–516.
[7] X. Zhu, J. Ma, Y. Wang, J. Tao, B. Lin, Y. Ren, X. Jiang, J. Liu, Ceram. Int. 34 (2008) 249–251.
[8] Y. Jiang, Y.J. Zhu, Z.L. Xu, Mater. Lett. 60 (2006) 2294–2298.
[9] A. Phuruangrat, T. Thongtem, S. Thongtem, Mater. Lett. 63 (2009) 1496–1498.
[10] T. Thongtem, A. Phuruangrat, S. Wannapop, S. Thongtem, Mater. Lett. 64 (2010) 122–124.
[11] Powder Diffract. File, JCPDS-ICDD, Newtown Square, PA, USA, 2001.
[12] X. Yang, X. Wang, Z. Zhang, Mater. Chem. Phys. 95 (2006) 154–157.
[13] J. Ota, S.K. Srivastava, J. Phys. Chem. C 111 (2007) 12260–12264.
[14] Y. Sun, Q. Han, J. Lu, X. Yang, L. Lu, X. Wang, Mater. Lett. 62 (2008) 3730–3732.
[15] Q. Han, Y. Sun, X. Wang, L. Chen, X. Yang, L. Lu, J. Alloys Compd. 481 (2009) 520–525.
[16] X. Sui, Y. Liu, C. Shao, Y. Liu, C. Xu, Chem. Phys. Lett. 424 (2006) 340–344.
[17] T.T. Tseng, W.J. Tseng, Ceram. Int. 35 (2009) 2837–2844.
[18] Y. Yu, W.T. Sun, Mater. Lett. 63 (2009) 1917–1920.
[19] Y. Yu, C.H. Jin, R.H. Wang, Q. Chen, L.M. Peng, J. Phys. Chem. B 109 (2005) 18772–18776.
[20] S.H. Yu, J. Yang, Z.H. Han, Y. Zhou, R.Y. Yang, Y.T. Qian, Y.H. Zhang, J. Mater. Chem. 9 (1999) 1283–1287.
[21] D.P. Volanti, D. Keyson, L.S. Cavalcante, A.Z. Simões, M.R. Joya, E. Longo, J.A. Varela, P.S. Pizani, A.G. Souza, J. Alloys Compd. 459 (2008) 537–542.
[22] W. Li, Mater. Lett. 62 (2008) 243–245.
[23] M. Salavati-Niasari, D. Ghanbari, F. Davar, J. Alloys Compd. 488 (2009) 442–447.
[24] V.V. Killedar, S.N. Katore, C.H. Bhosale, Mater. Chem. Phys. 64 (2000) 166–169.

Current Applied Physics 10 (2010) 342–345

Contents lists available at ScienceDirect

Current Applied Physics

journal homepage: www.elsevier.com/locate/cap

Analysis of lead molybdate and lead tungstate synthesized by a sonochemical method

Anukorn Phuruangrat [a,*], Titipun Thongtem [b,*], Somchai Thongtem [a]

[a] Department of Physics and Materials Science, Faculty of Science, Chiang Mai University, Chiang Mai 50200, Thailand
[b] Department of Chemistry and Center for Innovation in Chemistry, Faculty of Science, Chiang Mai University, Chiang Mai 50200, Thailand

ARTICLE INFO

Article history:
Received 19 February 2009
Received in revised form 29 May 2009
Accepted 18 June 2009
Available online 23 June 2009

PACS:
81.07.Bc
81.16.Be

Keywords:
Nanostructures
Chemical synthesis
X-ray diffraction
Raman spectroscopy
Electron microscopy

ABSTRACT

Lead molybdate and lead tungstate nanoparticles were successfully synthesized by a sonochemical method for 1 h. XRD patterns showed the body-centered tetragonal structures of $PbMoO_4$ and $PbWO_4$, and were in accordance with those of the simulation and JCPDS software. Calculated lattice parameters are $a = b = 5.4233$ Å and $c = 12.1253$ Å for $PbMoO_4$, and 5.4570 Å and 12.0995 Å for $PbWO_4$. They are in accordance with those of the corresponding JCPDS software. TEM images show that the particles were 29.09 ± 5.22 nm and 21.05 ± 2.68 nm for $PbMoO_4$ and $PbWO_4$, respectively. Raman and FTIR vibrations were investigated to identify a definite existence of the structures.

© 2009 Elsevier B.V. All rights reserved.

1. Introduction

Metal molybdates and tungstates are the materials, which have highly potential and widely applications: photoluminescence, solid-state lasers, optical fibers, scintillating materials, humidity sensors, magnetic materials and catalysts [1–3]. Recently, $PbMoO_4$ has gained attractive interest for using as acousto-optic deflectors and modulators due to its high figure of merit, low optical loss in the range 420–3900 nm and good mechanical impedance for acoustic matching, ion conductors and effective low-temperature scintillators of nuclear instruments [4,5]. $PbWO_4$ is a good candidate in radiation detection of high energy physics and nuclear physics due to its high density (8.3 g/cm^3), short radiation length (less than 10 ns for a large part of light output), high irradiation damage resistance (10^7 rad for undoped and 10^8 rad for La-doped $PbWO_4$), small Moliere radius, fast decay time and non-hygroscopic materials, and low production cost [6–8].

There are various methods used to synthesize the molybdates and tungstates, such as wet chemical processes [1–3,8], hydrothermal reactions [7] and microwave radiation [9]. It is very interesting to develop other facile methods for the synthesis of these materials with short reaction time under a mild condition. Sonochemical is very attractive process used for synthesizing these nanosized materials. Ultrasonic radiation (20 kHz–10 MHz) is supplied to molecules, which undergo chemical reaction by the acoustic cavitation–formation (nucleation) of bubbles, growth by the diffusion of solute vapor into the bubbles, and collapse of bubbles (mechanical action) in a liquid solution when their maximum sizes are excessive. During the collapsing process (with less than 1 ns), the temperature and cooling rate are extremely high (5000–25,000 K, exceeding 10^{11} K/s), causing chemical bonds to be broken. For volatile precursors, gas phase reactions are predominant and amorphous nanoparticles are synthesized. For non-volatile precursors and the reactions are in liquid solutions, the products are nano-amorphous particles and nanocrystalline – depending on the temperature surrounding the collapsing bubbles. In general, the products synthesized by this process are nanomaterials (amorphous or crystalline) with different shapes, sizes and structures [10]. When ultrasonic radiation is supplied to chemical solutions, their molecules vibrate – the problems of concentration and temperature gradients were solved. The radiation has the influence on the reaction to proceed with efficiency and very short time. Subsequently, pure products were synthesized [11]. At present, a simple and fast sonochemical assisted process for synthesizing nanocrystallines of $PbMoO_4$ and $PbWO_4$ is reported.

* Corresponding authors. Tel.: +66 53 943344; fax: +66 53 892277.
E-mail addresses: phuruangrat@hotmail.com (A. Phuruangrat), ttpthongtem@yahoo.com (T. Thongtem).

1567-1739/$ - see front matter © 2009 Elsevier B.V. All rights reserved.
doi:10.1016/j.cap.2009.06.024

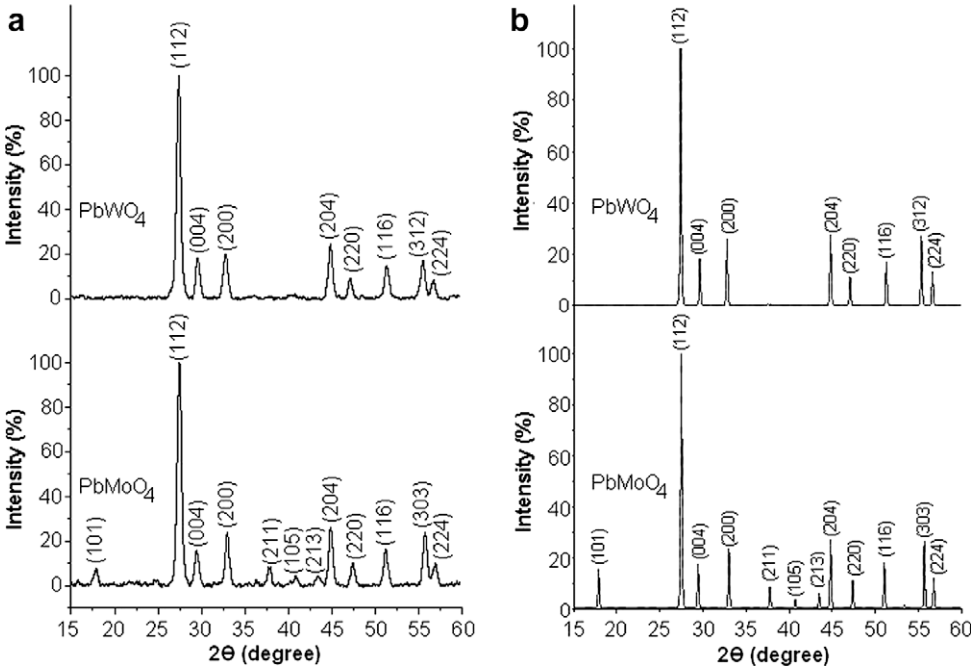


Fig. 1. (a) XRD patterns of $PbMO_4$ and (b) their simulations.

Table 1
The 2θ Bragg's angles (°) and diffraction intensities (%) of $PbMoO_4$ obtained from the experiment, simulation and JCPDS No. 08–0475 [12].

Plane	JCPDS 08–0475		Experiment		Simulation	
	2θ	Intensity	2θ	Intensity	2θ	Intensity
(1 0 1)	17.87	12.00	17.83	7.52	17.90	15.00
(1 1 2)	27.47	100.00	27.44	100.00	27.50	100.00
(0 0 4)	29.48	20.00	29.44	16.03	29.44	17.40
(2 0 0)	32.93	25.00	32.97	32.97	33.01	23.10
(2 1 1)	37.72	8.00	37.74	8.11	37.80	8.50
(1 0 5)	40.76	6.00	40.84	4.41	40.72	3.70
(2 1 3)	43.43	8.00	43.41	4.07	43.48	5.70
(2 0 4)	44.81	30.00	44.87	26.25	44.81	26.60
(2 2 0)	47.31	14.00	47.42	10.06	47.37	10.80
(1 1 6)	51.07	18.00	51.21	16.23	51.04	17.90
(3 0 3)	55.55	25.00	55.74	23.94	55.65	27.60
(2 2 4)	56.71	12.00	56.95	10.23	56.76	11.60

Table 2
The 2θ Bragg's angles (°) and diffraction intensities (%) of $PbWO_4$ obtained from the experiment, simulation and JCPDS No. 08–0476 [12].

Plane	JCPDS 08–0476		Experiment		Simulation	
	2θ	Intensity	2θ	Intensity	2θ	Intensity
(1 1 2)	27.42	100.00	27.40	100.00	27.39	100.00
(0 0 4)	29.66	20.00	29.50	18.17	29.51	18.50
(2 0 0)	32.75	30.00	32.76	20.06	32.80	25.90
(2 1 1)	37.54	2.00	–	–	–	–
(2 0 4)	44.74	35.00	44.84	24.15	44.69	27.70
(2 2 0)	47.02	16.00	47.12	9.44	47.06	11.40
(2 2 2)	49.56	1.00	–	–	–	–
(1 1 6)	51.23	20.00	51.31	14.71	51.06	17.40
(3 1 2)	55.29	35.00	55.50	16.95	55.31	27.00
(2 2 4)	56.57	16.00	56.72	8.16	56.63	12.50

2. Experiment

$PbMO_4$ (M = Mo and W) nanocrystals were synthesized using 0.005 mol each of $Pb(NO_3)_2{\cdot}2H_2O$ and $Na_2MO_4{\cdot}2H_2O$ dissolved in 50 ml ethylene glycol. The solution was transferred in an ultrasonic bath (BANDELIN SONOREX – RK 102 H, 120/480 W, 35 kHz), and sonicated for 1 h. The final products were washed with de-ionized water and absolute ethanol, dried at 70 °C for 12 h, and intensively characterized: XRD (SIEMENS D500) using Cu K_α line (1.5406 Å [3]), Raman spectrometer (HORIBA JOBIN YVON T64000) with 50 mW and 514.5 nm wavelength Ar laser, FTIR (BRUKER TENSOR27) with KBr as a diluting agent and operated in the range 400–4000 cm^{-1}, and TEM (JEOL JEM-2010) operated at 200 kV. Specimen preparation for TEM analysis was to sonicate the products in a beaker containing absolute ethanol for 15 min each, drop the solutions on copper grids, and dry them in ambient atmosphere for 24 h.

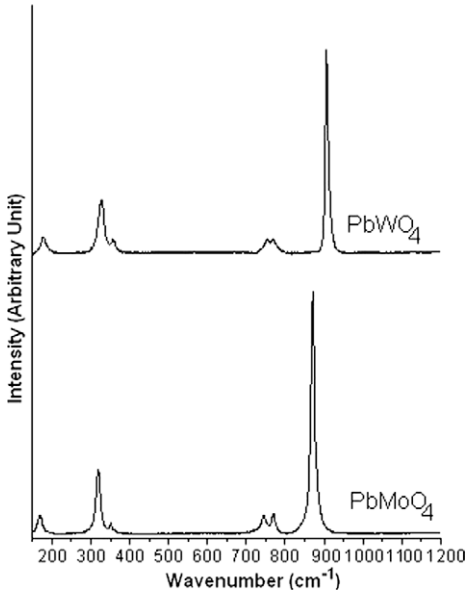


Fig. 2. Raman spectra of $PbMO_4$.

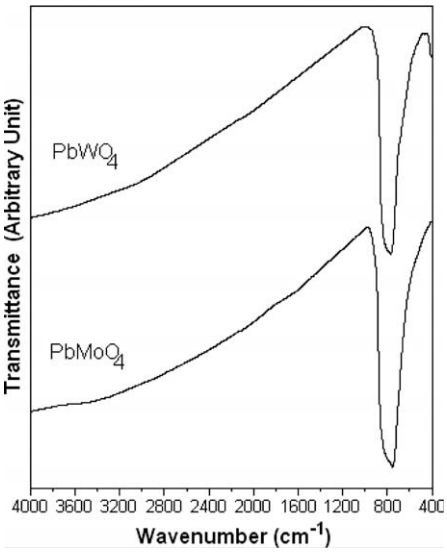


Fig. 3. FTIR spectra of $PbMO_4$.

3. Results and discussion

XRD patterns of $PbMO_4$ synthesized by sonochemical method are shown in Fig. 1a. Their XRD patterns were interpreted to be the tetragonal structures of $PbMoO_4$ and $PbWO_4$ with $I4_1/a$ space group, comparing to the JCPDS Nos. 08-0475 for $PbMoO_4$ and 08-0476 for $PbWO_4$ [12]. Lattice parameters were calculated using an equation of plane spacing for the tetragonal structure and Bragg's law for diffraction [13]: $a = b = 5.4233$ Å and $c = 12.1253$ Å for $PbMoO_4$, and 5.4570 Å and 12.0995 Å for $PbWO_4$, respectively. They are in accordance with the corresponding values of the JCPDS software [12].

To specify that the diffraction patterns of the products could exist in reality, XRD patterns of $PbMO_4$ with $I4_1/a$ space group were simulated using CaRIne Version 3.1 program [14]. The simulated XRD patterns are shown in Fig. 1b. The 2θ Bragg's angles and intensities of different crystallographic planes from the experiment, simulation and JCPDS Nos. 08-0475 and 08-0476 [12] were summarized in Tables 1 and 2. These values for both products are in good accordance. Low intensity peaks of the (2 1 1) and (2 2 2) planes of JCPDS No. 08-0476 [12] were not detected by the experiment and simulation.

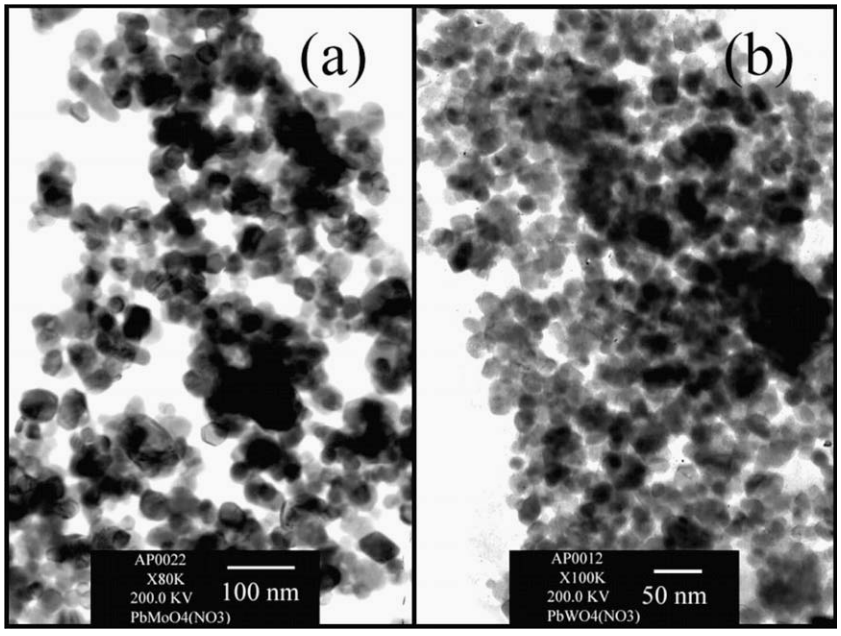


Fig. 4. TEM images of (a) $PbMoO_4$ and (b) $PbWO_4$ nanoparticles.

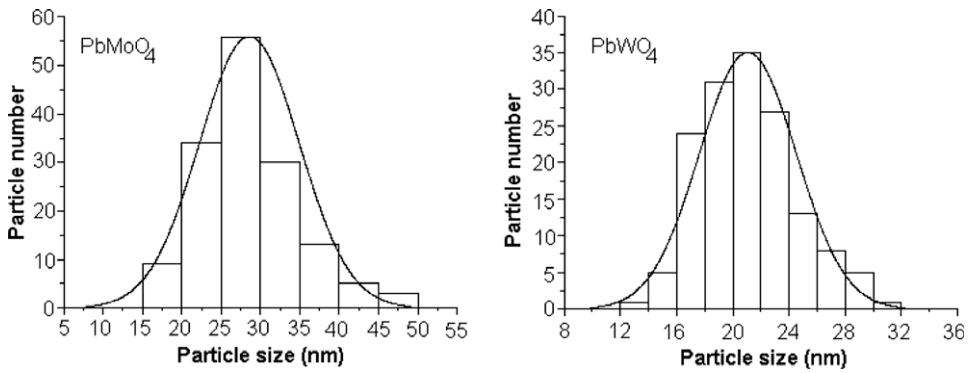


Fig. 5. Particle size distribution curves of $PbMO_4$.

For body-centered tetragonal $PbMO_4$ structure, $(MO_4)^{2-}$ tetrahedrons have S_4 symmetry in crystallographic lattice [15]. Raman spectra of the products (Fig. 2) show wavenumbers at 872.57 cm^{-1} for $PbMoO_4$ and 906.43 cm^{-1} for $PbWO_4$, associated with $\nu_1(A_g)$ vibrations in the tetrahedral $(MO_4)^{2-}$ units. Those at 769.92 and 744.87 cm^{-1} for $PbMoO_4$, and 769.57 and 752.93 cm^{-1} for $PbWO_4$ were split from the ν_3 mode to become $\nu_3(B_g)$ and $\nu_3(E_g)$, respectively. Two modes at 300–400 cm^{-1} were interpreted as the stronger $\nu_2(A_g)$ and weaker $\nu_4(B_g)$ of the regular $(MO_4)^{2-}$ tetrahedrons. Vibration modes at 169.12 cm^{-1} for $(MoO_4)^{2-}$ and 178.35 cm^{-1} for $(WO_4)^{2-}$ rotating about the z axis are much less energies than those of other modes [8,15–17]. Vibrational energies of $(MO_4)^{2-}$ ions were rather small. Thus, bonding of the $(MO_4)^{2-}$ anionic tetrahadrons is quite strong, comparing to the bonding between the anionic and cationic units.

FTIR transmittance modes (Fig. 3) of the products were detected at 730–879 cm^{-1} for $PbMoO_4$, and 738–879 cm^{-1} for $PbWO_4$, specified as the antisymmetric stretching vibrations of $(MO_4)^{2-}$ tetrahedrons [18,19].

TEM analysis shows that each product (Fig. 4) was composed of a number of dispersed nanosized particles with round shape. By respective measuring of 160 and 150 particles for $PbMoO_4$ and $PbWO_4$ on the TEM images, their particle size distribution curves (Fig. 5) are very close to bell shapes with normal distribution. The averages and standard deviations are 29.09 ± 5.22 nm for $PbMoO_4$, and 21.05 ± 2.68 nm for $PbWO_4$. The narrow particle size distributions and homogenous particles favor luminescent properties [11].

4. Conclusions

$PbMoO_4$ and $PbWO_4$ nanoparticles were successfully synthesized from $Pb(NO_3)_2{\cdot}2H_2O$ and $Na_2MO_4{\cdot}2H_2O$ in ethylene glycol by a sonochemical method. XRD patterns obtained by the experiment are in good accordance with those obtained by the simulation and JCPDS software [12]. A definite existence of the tetragonal $PbMO_4$ structures was confirmed by the Raman and FTIR vibrations of these products. TEM images showed that they were composed of dispersed nanoparticles with normal size distributions, having the influence on the photoluminescent properties.

Acknowledgements

We are extremely grateful to the Thailand Research Fund, and Center for Innovation in Chemistry (PERCH-CIC), Commission on Higher Education, Ministry of Education, Thailand, for financial support, and the Graduate School of Chiang Mai University for general funding.

References

[1] F.M. Pontes, M.A.M.A. Maurera, A.G. Souza, E. Longo, E.R. Leite, R. Magnani, M.A.C. Machado, P.S. Pizani, J.A. Varela, J. Eur. Ceram. Soc. 23 (2003) 3001–3007.
[2] J. Liu, J. Ma, B. Lin, Y. Ren, X. Jiang, J. Tao, X. Zhu, Ceram. Int. 34 (2008) 1557–1560.
[3] J.C. Sczancoski, L.S. Cavalcante, M.R. Joya, J.A. Varela, P.S. Pizani, E. Longo, Chem. Eng. J. 140 (2008) 632–637.
[4] N. Senguttuvan, S.M. Babu, R. Dhanasekaran, Mater. Chem. Phys. 49 (1997) 120–123.
[5] D. Piwowarska, S.M. Kaczmarek, M. Berkowski, J. Non-Cryst. Solids 354 (2008) 4437–4442.
[6] G. Wang, C. Hao, Mater. Res. Bull. 44 (2009) 418–421.
[7] W. Zhao, X. Song, G. Chen, G. Tian, S. Sun, Mater. Lett. 63 (2009) 285–288.
[8] L.S. Cavalcante, J.C. Sczancoski, V.C. Albarici, J.M.E. Matos, J.A. Varela, E. Longo, Mater. Sci. Eng. B 150 (2008) 18–25.
[9] T. Thongtem, A. Phuruangrat, S. Thongtem, Curr. Appl. Phys. 8 (2008) 189–197.
[10] A. Gedanken, Ultrason. Sonochem. 11 (2004) 47–55.
[11] T. Thongtem, A. Phuruangrat, S. Thongtem, Appl. Surf. Sci. 254 (2008) 7581–7585.
[12] Powder Diffract File, JCPDS-ICDD, 12 Campus Boulevard, Newtown Square, PA 19073-3273, U.S.A., 2001.
[13] C. Suryanarayana, M.G. Norton, X-ray Diffraction a Practical Approach, Plenum Press, New York, 1998.
[14] C. Boudias, D. Monceau, CaRIne Crystallography 3.1, DIVERGENT S.A., Centre de Transfert, 60200 Compiègne, France, 1989–1998.
[15] A.A. Kaminskii, C.L. McCray, H.R. Lee, S.W. Lee, D.A. Temple, T.H. Chyba, W.D. Marsh, J.C. Barnes, A.N. Annanenkov, V.D. Legun, H.J. Eichler, G.M.A. Gad, K. Ueda, Opt. Commun. 183 (2000) 277–287.
[16] H.S. Lee, S.D. Lee, J.H. Lee, M.S. Jang, Ferroelectrics 107 (1990) 151–154.
[17] J. Xu, S. Wang, M.H. Manghnani, L.C. Ming, J. Bologh, High Pressure Res. 3 (1990) 254–256.
[18] A.P. de Azevedo Marques, D.M.A. de Melo, C.A. Paskocimas, P.S. Pizani, M.R. Joya, E.R. Leite, E. Longo, J. Solid State Chem. 179 (2006) 671–678.
[19] G.M. Clark, W.P. Doyle, Spectrochim. Acta 22 (1966) 1441–1447.